

ACS SYMPOSIUM SERIES

692

Spectroscopic Methods in Bioinorganic Chemistry

Edward I. Solomon, EDITOR
Stanford University

Keith O. Hodgson, EDITOR
Stanford University

Developed from a symposium sponsored by the Division
of Inorganic Chemistry at the 213th National Meeting
of the American Chemical Society,
San Francisco, California,
April 13–17, 1997



American Chemical Society, Washington, DC
**American Chemical Society
Library**
1155 16th St., N.W.
Washington, D.C. 20036

**Spectroscopic methods in
bioinorganic chemistry**



Library of Congress Cataloging-in-Publication Data

Spectroscopic methods in bioinorganic chemistry / Edward I. Solomon, editor,
Keith O. Hodgson, editor.

p. cm.—(ACS symposium series, ISSN 0097-6156; 692)

“Developed from a symposium sponsored by the Division of Inorganic
Chemistry at the 213th National Meeting of the American Chemical Society,
San Francisco, California, April 13-17, 1997.”

Includes bibliographical references and indexes.

ISBN 0-8412-3560-0

1. Spectrum analysis—Congresses. 2. Bioinorganic chemistry—Congresses.

I. Solomon, Edward I. II. Hodgson, K. O. (Keith O.), 1947— . III. American
Chemical Society. Division of Inorganic Chemistry. IV. American Chemical
Society. Meeting (213rd : 1997 : San Francisco, Calif.) V. Series.

QD95.S6345 1998
543'.0858—dc21

98-6347
CIP

Copyright © 1998 American Chemical Society

Distributed by Oxford University Press

All Rights Reserved. Reprographic copying beyond that permitted by Sections 107 or 108 of the U.S. Copyright Act is allowed for internal use only, provided that a per-chapter fee of \$20.00 plus \$0.25 per page is paid to the Copyright Clearance Center, Inc., 222 Rosewood Drive, Danvers, MA 01923, USA. Reproduction or reproduction for sale of pages in this book is permitted only under license from ACS. Direct these and other permissions requests to ACS Copyright Office, Publications Division, 1155 16th Street, N.W., Washington, DC 20036.

The citation of trade names and/or names of manufacturers in this publication is not to be construed as an endorsement or as approval by ACS of the commercial products or services referenced herein; nor should the mere reference herein to any drawing, specification, chemical process, or other data be regarded as a license or as a conveyance of any right or permission to the holder, reader, or any other person or corporation, to manufacture, reproduce, use, or sell any patented invention or copyrighted work that may in any way be related thereto. Registered names, trademarks, etc., used in this publication, even without specific indication thereof, are not to be considered unprotected by law.

PRINTED IN THE UNITED STATES OF AMERICA

**American Chemical Society
Library
1155 16th St., N.W.
Washington, D.C. 20036**

Advisory Board

ACS Symposium Series

Mary E. Castellion
ChemEdit Company

Arthur B. Ellis
University of Wisconsin at Madison

Jeffrey S. Gaffney
Argonne National Laboratory

Gunda I. Georg
University of Kansas

Lawrence P. Klemann
Nabisco Foods Group

Richard N. Loepky
University of Missouri

Cynthia A. Maryanoff
R. W. Johnson Pharmaceutical
Research Institute

Roger A. Minear
University of Illinois
at Urbana-Champaign

Omkaram Nalamasu
AT&T Bell Laboratories

Kinam Park
Purdue University

Katherine R. Porter
Duke University

Douglas A. Smith
The DAS Group, Inc.

Martin R. Tant
Eastman Chemical Co.

Michael D. Taylor
Parke-Davis Pharmaceutical
Research

Leroy B. Townsend
University of Michigan

William C. Walker
DuPont Company

Foreword

THE ACS SYMPOSIUM SERIES was first published in 1974 to provide a mechanism for publishing symposia quickly in book form. The purpose of the series is to publish timely, comprehensive books developed from ACS sponsored symposia based on current scientific research. Occasionally, books are developed from symposia sponsored by other organizations when the topic is of keen interest to the chemistry audience.

Before agreeing to publish a book, the proposed table of contents is reviewed for appropriate and comprehensive coverage and for interest to the audience. Some papers may be excluded in order to better focus the book; others may be added to provide comprehensiveness. When appropriate, overview or introductory chapters are added. Drafts of chapters are peer-reviewed prior to final acceptance or rejection, and manuscripts are prepared in camera-ready format.

As a rule, only original research papers and original review papers are included in the volumes. Verbatim reproductions of previously published papers are not accepted.

ACS BOOKS DEPARTMENT

Preface

This volume is based on a symposium of the same title held at the San Francisco American Chemical Society meeting in April 1997. It brought together many of the major international researchers in the field of spectroscopy in bioinorganic chemistry. It was also designed to have a broad-based appeal to researchers in the fields of bioinorganic, physical-inorganic, inorganic, and biochemistry. This was accomplished through a significant tutorial component emphasizing recent advances in the key spectroscopic and related methods and through a series of sessions focusing on general topics in bioinorganic chemistry where spectroscopy has had a strong impact. The organization of this volume parallels the symposium.

The first part (Recent Advances in Ground-State and in Excited-State Methods) emphasizes important new directions in the different methods of bioinorganic spectroscopy. Included with the ground-state methods is X-ray diffraction. Spectroscopy and protein crystallography strongly complement each other and through their combination one can maximize insight into the geometric and electronic structure of an active site and their contributions to function in biology. Also included with the excited-state spectroscopic methods is a contribution on electronic structure calculations. Spectroscopy probes the electronic structure of an active site and if calculations correlate well with data they can define specific bonding interactions that can activate a metal center for reactivity.

The second part of this volume focuses on four areas of bioinorganic chemistry where spectroscopy has had a huge impact: electron transfer, cluster interactions, active site geometric and electronic structure, and intermediates. This list was limited only by the number of sessions available to the symposium. Contributors to each topic include both researchers who focus on the detailed application of specific spectroscopic methods and those who apply a range of methods to achieve insight into reactivity. Thus for example, in the electron transfer section contributions include both detailed resonance Raman and X-ray absorption spectroscopy of blue copper, iron sulfur, and the Cu_A center in cytochrome *c* oxidase and the use of absorption and resonance Raman spectroscopies to probe electron transfer induced protein folding in heme proteins.

A few of the contributors to the symposium were not able to submit a manuscript within the time constraints for this volume and we suggest the reader go to the following references for the topic they covered in the symposium.

“The Electron Structure of Cu_2 : A Novel Mixed-Valence Dinuclear Copper Electron-Transfer Center”, Farrar, Jacqui A.; Neese, Frank; Lappalainen, P.; Kroneck, Peter M. H.; Sarraste, M.; Zumft, W. G.; **Thomson, Andrew J.** *J. Am. Chem. Soc.* **1996**, *118*, 11501–11514.

Stephens, Philip (Presenter) Two Ph.D. theses: “Azotobacter Vinelandii Ferredoxin I: Spectroscopic and Theoretical Studies,” Jensen, G. M. 1995; “Spectroscopic Studies of Chemically and Mutated Forms of Azotobacter Vinelandii Ferredoxin I”, Reyntjens, B. R. University of Southern California, Los Angeles, CA, 1996.

“Molybdenum-Iron Sulfide-Bridged Double Cubanes”, Huang, Jiesheng; Mukerjee, Subhashish; Segal, Brent M.; Akashi, Haruo; Zhou, Jian; **Holm, R. H.** *J. Am. Chem. Soc.* **1997**, *119*, 8662–8674.

“X-ray Absorption and EPR Studies on the Copper Ions Associated with the Particulate Methane Monooxygenase from *Methylococcus capsulatus* (Bath)”, Nguyen, Hiep-Hoa T.; Nakagawa, Kent H.; Hedman, Britt; Elliot, Sean J.; Lidstrom, Mary E.; Hodgson, Keith O.; and **Chan, Sunney I.** *J. Am. Chem. Soc.* **1996**, *118*, 12766–12776; “Regio- and Stereoselectivity of Particulate Methane Monooxygenase from *Methylococcus capsulatus* (Bath)”, Elliot, Sean J.; Zhu, Mei; Tso, Luke; Nguyen, H.-Hoa T.; Yip, John H.-K.; Chan, Sunney I. *J. Am. Chem. Soc.* **1997**, *119*, 9949–9955.

“EXAFS Studies of FeMo-Cofactor and MoFe Protein: Direct Evidence for the Long Range Mo–Fe–Fe Interaction and Cyanide Binding to the Mo in FeMo-Cofactor,” Liu, H. I.; Filipponi, A.; Gavini, N.; Burgess, B. K.; Hedman, B.; Di Cicco, A.; Natoli, C. R.; **Hodgson, K. O.** *J. Am. Chem. Soc.* **1994**, *116*, 2418–2423.

“Heme/Copper Terminal Oxidases”, Ferguson-Miller, S.; **Babcock, G. T.** *Chem. Rev.* **1996**, *96* 2889–2907; “Low-Powered Picosecond Resonance Raman Evidence for Histidine Ligation to Heme a_3 after Photodissociation of CO from Cytochrome *c* Oxidase”, Schelvis, J. P. M.; Deinum, G.; Varotsis, C. A.; Ferguson-Miller, S.; Babcock, G. T. *J. Am. Chem. Soc.* **1997**, *119*, 8409–8416.

Acknowledgments

We want to thank the participants for their excellent and timely contributions to the field of bioinorganic chemistry. The symposium was made possible through the generous support of the U.S. Department of Energy Biological and Environmental Research Program, which provided general support and student travel

awards. Additional funding was provided by the Inorganic Division of the American Chemical Society and by the Society of Biological Inorganic Chemistry.

EDWARD I. SOLOMON
Department of Chemistry
Stanford University
Stanford, CA 94305

KEITH O. HODGSON
Department of Chemistry
Stanford University
Stanford, CA 94305

Chapter 1

Structure Determination by Combination of CW and Pulsed '2-D' Orientation-Selective ^1H Q-Band Electron-Nuclear Double Resonance

Identification of the Protonated Oxygenic Ligands of Ribonucleotide Reductase Intermediate X

Jean-Paul Willems¹, Hong-In Lee¹, Doug Burdi², Peter E Doan¹,
JoAnne Stubbe^{2,3}, and Brian M. Hoffman^{1,3}

¹Department of Chemistry, Northwestern University, Evanston, IL 60208–3113

²Department of Chemistry, Massachusetts Institute of Technology,
Cambridge, MA 02139–4307

The structure of a paramagnetic center can be determined by analysis of the electron-nuclear hyperfine and nuclear-quadrupole coupling tensors of interacting nuclei. These tensors can be determined for a frozen-solution sample by analyzing the orientation-selective 2-D pattern generated by collecting ENDOR spectra at multiple fields across the entire EPR envelope. This process requires careful comparison of experimental and simulated ENDOR patterns, which requires that the spectra must be collected in such a manner as to give reliable peak intensities and shapes as well as frequencies. This requirement usually cannot be met by either CW or pulsed-ENDOR protocols *alone*, but the goal can be reached by a combination of CW *and* pulsed-ENDOR measurements. This process is illustrated by showing how continuous wave (CW) and pulsed Q-Band ^1H ENDOR measurements have been used to identify the types of protonated oxygen (OH_x) species coordinated to diiron center of Intermediate X formed during oxygen activation by the R2 subunit of *Escherichia coli* Ribonucleotide Reductase (RNR), as well as their disposition relative to the ferric and ferryl iron ions: X contains the $[(\text{H}_x\text{O})\text{Fe}^{\text{III}}\text{OFe}^{\text{IV}}]$ fragment.

Electron-nuclear double resonance (ENDOR)¹ and electron spin-echo envelope modulation (ESEEM)² spectroscopies are advanced magnetic resonance techniques that provide an NMR spectrum of nuclei that interact with the electron spin of a paramagnetic center.³⁻⁷ As discussed in detail,^{4;7;8} the electron-nuclear hyperfine and nuclear-quadrupole coupling tensors of interacting nuclei can be determined by analyzing the orientation-selective '2-D' pattern generated by collecting ENDOR spectra at multiple fields across the entire EPR envelope of a frozen-solution sample. The structure of a paramagnetic center can be determined by analysis of these tensors through a process that involves careful comparison of experimental and simulated

³Corresponding authors.

ENDOR patterns (*eg.*, see the recent reference, # 9). This requires that the spectra must be collected in such a manner as to give reliable peak intensities and shapes as well as frequencies, a requirement that usually cannot be met by either CW or pulsed-ENDOR protocols *alone*. However, the goal can be reached by a combination of CW *and* pulsed-ENDOR measurements. We illustrate this process with a study of oxygen activation in the R2 subunit of *Escherichia coli* Ribonucleotide Reductase (RNR).

Catalytically active RNR contains a nonheme diferric center and a catalytically-essential tyrosyl radical^{10;11} that are formed via a pathway that includes reaction of dioxygen with a diferrous center. A paramagnetic diiron intermediate (X) has been observed that is one-electron oxidized above the diferric resting state and is catalytically competent to oxidize tyrosine to tyrosyl radical.^{12;13} In order to define the composition and structure of X, we have extended the RFQ technique¹² to Q-band ENDOR spectroscopy. An ⁵⁷Fe ENDOR study¹⁴ clarified the electronic properties of the diiron center of X and offered a revised spin-coupling paradigm which describes X as having an $S = \frac{1}{2}$ diiron center with antiferromagnetic coupling between Fe^{III}($S = 5/2$) and Fe^{IV}($S = 2$) ions. The observed antiferromagnetic exchange coupling between iron ions requires the presence of one or more oxy and/or hydroxo bridges. A preliminary Q-Band CW ENDOR study of X by Burdi et al.¹⁵ using ¹⁷O₂ and H₂¹⁷O corroborated the earlier observation of ¹⁷O coupling by X-band EPR¹⁶ and demonstrated the presence of one oxygen ligand derived from solvent and at least one from dioxygen. The same report also presented a limited 2-D set of orientation-selective proton CW Q-Band ¹H ENDOR spectra taken at several fields across the EPR envelope of samples of X prepared in both H₂O and D₂O buffer. The published CW data collected at Q band did not allow a distinction between the two models sketched in **Figure 1**. In one model, which we denote B, all exchangeable proton/deuteron signals with substantial couplings are assigned to an hydroxo bridge; in the other, denoted T, these signals are assigned to the two protons of a water molecule bound to Fe^{III}. The number and nature of OH_x ligand(s) to the diiron center of X thus remained undetermined. Here we show how the combination of CW and pulsed Q-Band ^{1,2}H ENDOR measurements of Intermediate X allows us to identify the types of protonated oxygen (OH_x) species coordinated to the iron ions of X and their disposition relative to the ferric and ferryl iron ions.¹⁷ We note that X gives an essentially isotropic EPR spectrum at X band, and hence no orientation selection, but that the EPR spectra at Q band show that the g tensor is rhombic, with $g = [g_1, g_2, g_3] \approx [2.0081(5), 1.9977(5), 1.9926(5)]$,¹⁵ which is adequate to allow a full analysis of Q band ENDOR data.

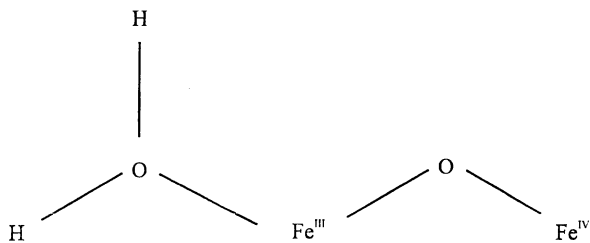
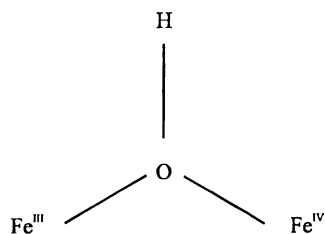
ENDOR Spectroscopy:

The CW ENDOR spectrometer and procedures employed in this study have been briefly described.¹⁹ A description of the 35 GHz pulse ENDOR spectrometer employed in this study has been published recently.²⁰ The proton CW ENDOR spectra reported have been recorded using 'Packet-Shifting' ENDOR.⁴ Although this type of ENDOR has many advantages when studying metalloproteins, including excellent signal/noise ratios, at low sample-temperature where relaxation rates are slow, it also can manifest distortions in peak shapes and intensities. In particular, signals with small hyperfine coupling may not be well resolved, and those with larger couplings that are resolved exhibit line shapes and intensities that depend on the spectrometer settings, such as

e 1:

Model B: Hydroxo bridge

$$A_H \approx [-T, 0, T]$$

**Model T:** Terminal water

$$A_H \approx [-T/2, -T/2, T]$$

Figure 1: Alternate, partial models for exogenous ligands to Intermediate X. Top: hydroxo bridge (B model); Bottom: oxo bridge plus terminal water (T model). Approximate characteristics of the cluster dipolar hyperfine tensors are indicated.

microwave power, field modulation amplitude, RF power, and RF scan rate and direction. The CW ^1H ENDOR spectra presented in this paper have been taken under conditions, given in the appropriate figure legends, where the shapes match those obtained using the Davies pulsed ENDOR protocol,^{21;22} which does give reliable shapes; we note that this was not the case in the original report.¹⁵ The Davies (t_p -T- $t_p/2$ - τ - t_p - τ -echo) ENDOR pulse sequence^{21;22} is hyperfine-selective because the ENDOR response, R , is jointly dependent on the hyperfine coupling, A , and the length of the microwave pulse, t_p , in the preparation phase, through the selectivity factor, $\eta = A \cdot t_p$:

$$R = R_0 \left(\frac{1.4\eta}{0.7^2 + \eta^2} \right)$$

where R_0 is the maximum ENDOR response.²³ The equation shows that an optimal ENDOR response is obtained if $\eta = A \cdot t_p = 0.7$; when $\eta < 0.7$ the response is suppressed. For a given sample, the value of t_p cannot be lengthened beyond some *intrinsic* maximum, t_p^{\max} , because dephasing during the pulse diminishes or abolishes the spin echo observed in the detection phase of the experiment. As a result, the smallest hyperfine coupling, A^{\min} , that can be observed with sufficient signal-to-noise ratios using a Davies ENDOR sequence is roughly, $A^{\min} \approx 1/t_p^{\max}$.

Deuterium ENDOR spectra were collected using the Mims stimulated-echo ENDOR pulse sequence^{22;24} (t_p - τ - t_p -T- t_p - τ -echo). This protocol also is hyperfine selective because its ENDOR response R depends jointly on the nuclear hyperfine coupling A and the interval τ according to:

$$R \propto [1 - \cos(2\pi A\tau)] \quad (1)$$

This equation shows that the ENDOR response will fall to zero for $A\tau = 1, 2, \dots$ and will reach a maximum for $A\tau = 0.5, 1.5, \dots$. Such 'hyperfine selectivity' normally is considered as one of the key benefits of pulsed ENDOR techniques. However, orientation-selective ENDOR analysis of frozen solutions relies on accurate line shapes and intensities. Our experience with Mims ENDOR of powder or frozen-solution samples shows that one obtains ENDOR pattern essentially undistorted by the blind spots only for couplings in the range $A < 1/(2\tau)$.²⁵ Thus, *in practice*, in the study of frozen solutions the maximum hyperfine value, A^{\max} , that should be studied using a Mims ENDOR sequence is restricted by the minimum usable value of τ , denoted as the deadtime, t_d , with the result that $A^{\max} \approx 1/(2t_d)$. The deadtime is defined as the minimum time after the last pulse that the ENDOR effect can be detected against the resonator ringdown, and it depends not only on the spectrometer performance but also on the strength of the ENDOR signal. If the effective spectrometer deadtime is long, thereby reducing A^{\max} in a Mims sequence, or if the sample phase memory is short, thereby increasing A^{\min} in a Davies sequence, it is not possible to obtain undistorted spectra for hyperfine couplings that fall in a 'gap' defined by: $1/(2t_d) < A < 1/t_p^{\max}$.

In the case of Intermediate X, the maximum useful value of t_p typically was of the order of 0.2 μs , which means that an optimized Davies ENDOR response could be achieved for nuclei having hyperfine coupling constants larger than ~ 3.5 MHz (as will be seen below because of other considerations, the minimum ^1H hyperfine coupling that can be well-studied for exchangeable protons is closer to 8 MHz). The effective deadtime of the spectrometer as configured was approximately 0.5 μs for the available samples of Intermediate X. Hence, the maximum hyperfine value accessible using a Mims pulse sequence is roughly 2 MHz. Consequently for this sample there in fact is

a ‘gap’, such that signals with hyperfine couplings $2 \leq A \leq 3.5$ MHz cannot be well-studied by the conventional pulsed-ENDOR protocols and this is crucial for the ^2H ENDOR measurements. To fill this gap we used the recently described ‘Refocused-Mims’ (ReMims) pulse sequence ($t_{p/2}-\tau_1-t_{p/2}-T-t_{p/2}-\tau_2-t_p-(\tau_2\pm\tau_1)$ -echo).²⁶ This is a four-pulse stimulated-echo ENDOR variation of the original Mims ENDOR sequence that eliminates the linkage between hyperfine coupling and spectrometer deadtime by permitting experiments where τ is less than the deadtime of the detection system: the hyperfine selectivity is governed by τ according to eq. 1, but the deadtime must be shorter than $\tau_2\pm\tau_1$, which can be set to an arbitrary value. The ReMims sequence therefore, increases the A^{max} of a Mims ENDOR so as to recover the hyperfine values poorly interrogated by the Davies and Mims ENDOR sequences.

A proton ENDOR signal for a single molecular orientation consists of a doublet centered at the Larmor frequency, ν_{H} , and split by the hyperfine coupling A_{H} ; spectra in this paper are plotted as $\Delta\nu = \nu - \nu_{\text{H}}$. A deuterium signal consists of a doublet centered at ν_{D} and split by A_{D} , with an additional splitting caused by the nuclear quadrupole interaction. The Larmor frequency and hyperfine constants of protons and deuterons are related by the equation: $\nu_{\text{H}}/\nu_{\text{D}} = A_{\text{H}}/A_{\text{D}} = g_{\text{H}}/g_{\text{D}} = 6.5$. The ENDOR simulations were performed on a PC using the program Gensim, a modified version of the simulation program GENDOR,⁵ which speeds calculations when orientation selectivity is poor as in the case of Intermediate X.

Results and Discussion

Alternative Models for the protonated oxygenic species of Intermediate X The preliminary ^1H and ^{17}O ENDOR measurements of Burdi et al.¹⁵ clearly demonstrated the presence of signals from exchangeable proton or protons associated with a hydroxo bridge (Figure 1, top), a terminal water (Figure 1, bottom), or both. This section presents ^1H ENDOR spectra calculated for the two different models using parameters for each that are chosen to optimize the agreement with experiments presented below. The similarities and differences between the two sets of calculations are carefully noted in preparation for comparison with the experiments.

Our prior work^{3;27;28} shows that the protons of a bridge and of a terminal water both exhibit dipolar interactions with an interacting Fe ion. Reference 17 gives equations for the observed cluster dipolar hyperfine tensor of a proton an arbitrary position relative to the two Fe ions of an $S = 1/2$ spin-coupled $[\text{Fe}(S = 5/2)-\text{Fe}(S = 2)]$ diiron center. A limiting form of this treatment, appropriate only for a bridge, was given in a discussion of the ($\text{Fe}^{\text{III}}-\text{Fe}^{\text{II}}$) clusters of ‘mixed-valence’ MMOH.³ For a terminal water (or hydroxide) the dipole interaction with the liganding iron dominates the ^1H hyperfine tensor, which is approximately axial: $\mathbf{A} \sim [-1/2T, -1/2T, T]$. The A_3 axis lies close to the Fe-H vector and $T \sim (7/3)g\beta g_{\text{n}}\beta_{\text{n}}/r_1^3$ when the ligand is bound to the ferric ion, but $T \sim (-4/3)g\beta g_{\text{n}}\beta_{\text{n}}/r_2^3$ when it is bound to the ferryl ion. In contrast, a proton of a bridging hydroxide interacts strongly with both Fe ions and it is characterized by a nearly rhombic hyperfine tensor, $\mathbf{A} \sim [-T, 0, T]$, where A_2 lies normal to the Fe(H)Fe plane and \mathbf{A} is rotated about the A_2 direction.

Figure 2 presents an optimized 2-D set of ^1H ENDOR spectra calculated by assuming the presence of a bridging hydroxyl (B model) with a dipolar hyperfine interaction to the two iron ions. In these calculations an idealized geometry is assumed

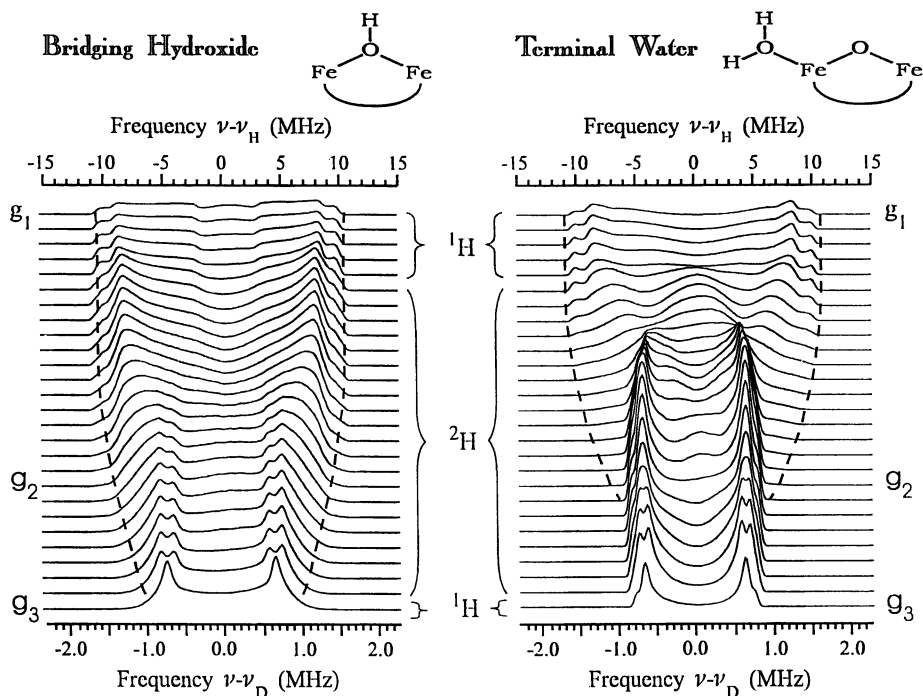


Figure 2: Optimized simulations of the field dependence of ^1H (as indicated) ENDOR responses for Intermediate X within the B model (bridging hydroxide, left), and T model (terminal water plus oxo bridge, right). The ^1H and ^2H signals are displayed in a common axis as ENDOR shifts from the Larmor frequency ($\Delta\nu$) through a scaling of the proton ENDOR shifts by the ratio (g_b/g_H); all spectra have been centered around the nuclear Larmor frequency. The maximum breadth of the ENDOR pattern has been indicated by the dashed lines.

in which the O atom is the apex of an isosceles triangle with the two Fe ions and with H in the plane of the other atoms and forming an Fe-H-Fe isosceles triangle. The Fe-Fe separation was chosen to be 2.5 Å. One obtains a hyperfine tensor whose maximum principal component matches the maximum coupling observed experimentally (see below) by selecting an Fe-H distance of ~ 2.57 Å. The precise metrical parameters and the hyperfine tensor components are listed in **Table I**. As noted in **Table I**, the optimized tensor for the B model includes a small isotropic component, $A_{\text{iso}}(^1\text{H}) = 2$ MHz while those for the T model are purely dipolar, $A_{\text{iso}} = 0$.

For comparison with the experiments, the spectra for g values near g_1 were calculated for a proton while those to lower g values were calculated for a deuteron, with the ^1H and ^2H signals being displayed on a common axis through a scaling of the proton ENDOR shifts by the ratio ($g_{\text{D}}/g_{\text{H}}$). The ^2H quadrupole interaction was idealized as being axial, with the unique axis along the H-O bond (**Table I**).

Figure 2 (right) presents an optimized set of ^1H ENDOR spectra calculated under the alternate assumption that two inequivalent protons of a water are terminally bound to Fe^{III} (T model). As noted above, the hyperfine tensor for a terminal proton is predicted to be approximately axial. We have simplified the problem by working in this limit, as the mildly anisotropic g tensor of X (*vide supra*) gives relatively poor orientation selection even at Q Band, which would not permit an accurate determination of small deviations from axiality. In this case, the hyperfine tensor components for a proton depend almost exclusively on the Fe^{III} -H distance. The distances of the two protons to Fe^{III} were chosen by assuming that the maximum calculated dipolar interactions for each one gives rise to one of the two largest doublet splittings in the experiments (see below). The ranges of acceptable values for the locations of these protons are quite reasonable for a bound water with Fe-O and O-H distances used in the bridging model. The two Fe-H distances chosen to best match the experimental splittings differ by only ~ 4% (**Table I**), corresponding to a minimally distorted water coordination. It is *not* possible to reproduce the breadth of the spectrum by assuming a terminal water bound to Fe^{IV} . The precise distances chosen, the resulting hyperfine tensor components, and the orientational parameters are listed in **Table I**. The calculated 2-D pattern provided by the spectra calculated at fields across the EPR envelope of X **Figure 2 right**, again is a composite of ^1H and ^2H simulations, with ^2H quadrupole parameters chosen as in the B model.²⁹

The parameters defining the B and T model calculations were chosen to generate sets of 2-D spectra that optimize the agreement with experiments presented below, and as a result the two sets are *constrained* to have important similarities. At g_1 , each simulation shows a pair of proton doublets, with splittings of 16.8 and 19.6 MHz. In the B model, **Figure 2 (left)**, these both arise from the single bridge proton, while in the T model, **Figure 2 (right)**, each doublet is from a distinct proton terminal to Fe^{III} , with the two protons having slightly different Fe^{III} -H distances, as noted. The deuterium spectra also agree near g_3 , in revealing a pair of sharp features, a doublet of doublets whose main splitting is approximately 1.38 MHz, with a minor splitting of about 0.12 MHz. However, there are a number of key differences between the models, as well. In the B model the strongly-coupled signals near g_1 exhibit smooth ‘shoulders’, whereas the T model has ‘peak-like’ features. Perhaps the most transparent difference between the two models is in the field dependence of the overall breadth of the ENDOR pattern at intermediate values of g. As indicated by the dashed lines in **Figure**

Table I:

Metrical and ^1H spin-Hamiltonian parameters used to calculate the 2-D ENDOR patterns displayed in Figure 2^a.

	B model ^b		T model ^c			
			Proton 1		Proton 2	
$r_{\text{Fe-H}}$ (Å)	2.56 ± 0.05		2.55 ± 0.03		2.67 ± 0.03	
β_1 (°) ^d	72.3 ± 0.3		140 - 220		135 - 225	
	¹ H	² H	¹ H	² H	¹ H	² H
A_1 (MHz) ^{e,f}	-17.5	-2.686	-10.25	-1.5745	-8.8	-1.3518
A_2 (MHz)	-9	-1.382	-10.25	-1.5745	-8.8	-1.3518
A_3 (MHz)	20.5	3.147	20.5	3.149	17.6	2.7035
ENDOR linewidth (MHz) ^g	0.5	0.07	0.5	0.07	0.5	0.07
EPR Linewidth (MHz) ^g	90		35		35	

^a Components of the ^2H quadrupole tensor, **P**, are idealized from those given for water in Ref. ³⁰: [P_1, P_2, P_3] = [-0.045, -0.045, 0.09]MHz. In other terminology, $e^2qQ = 2P_3 = 4\text{K}$ and $\eta = 0$. Simulations employed $g = [g_1, g_2, g_3] = [2.0081, 1.9977, 1.9926]$.

^b For model B, a small isotropic hyperfine component of $A_{\text{iso}}(^1\text{H}) = 2\text{MHz}$ improved the agreement with the experimental data and is included.

^c This model as implemented is insensitive to Fe-Fe distances. As stated before, a value of 2.5 Å was used, which is in accordance to the EXAFS data.

^d β_1 is defined as the angle between the $\text{Fe}^{\text{III}}\text{-H}$ bond and the $\text{Fe}^{\text{III}}\text{-Fe}^{\text{IV}}$ vector.

^e The Euler angles for **A** in the B model are $\alpha=50^\circ$ and $\beta=90^\circ$. The Euler angles for **A** in the T model are: proton 1, $\alpha=10.3^\circ$ and $\beta=72.8^\circ$; proton 2, $\alpha=20^\circ$ and $\beta=90^\circ$. For definition of angles, see ⁴⁴.

^f The Euler angles for **P** of deuterons in the B model are $\alpha=20^\circ$ and $\beta=90^\circ$. The Euler angles for **P** of deuterons in the T model are: proton 1, $\alpha=45^\circ$, $\beta=61.1^\circ$; proton 2, $\alpha=70^\circ$, $\beta=90^\circ$.

^g FWHM Gaussian.

2, within the T model, the overall breadth decreases rapidly from its maximum value of ~ 20 MHz for ^1H (3 MHz for ^2H) to approximately 9 MHz (1.38 MHz for ^2H) as the magnetic field is increased from g_1 to g_2 . The pattern breadth then remains unchanged between g_2 and g_3 . In contrast, model B predicts that the breadth of the pattern changes little between g_1 and g_2 ; then, as the magnetic field increases further, the width of the ENDOR pattern decreases slowly until at the g_3 edge of the spectrum it becomes ~ 9 MHz. Although both models predict a sharp ~ 9 MHz doublet of doublets near g_3 , in the T model the secondary splitting reflects the fact that the two inequivalent protons have different hyperfine couplings for the g_3 orientation, and it occurs in both ^1H and ^2H calculations. In contrast, in the B model the ^1H spectrum arises from a single hyperfine coupling to the unique bridge proton; the secondary splitting in the ^2H spectrum arises solely from the quadrupole interaction. Finally, in the B model this 9 MHz doublet appears as a sharp feature only for fields between g_3 to g_2 ; the peaks broaden quickly as g increases towards g_1 . In contrast, in the T model the sharp pair of doublets persists from g_3 to g -values well above g_2 .

Proton/Deuteron ENDOR of Intermediate X An extensive 2D set of experimental $^1,^2\text{H}$ ENDOR spectra was taken across the EPR envelope of Intermediate X. The spectrum at each field was taken by the appropriate technique, CW, Davies-pulsed, or ReMims-pulsed ENDOR, chosen so as to ensure that the intensities and shapes of the peaks associated with the strongly-coupled exchangeable protons/deuterons are reliable: a portion of this dataset is displayed in **Figure 4**. The input parameters (**Table I**) for the model calculations presented in **Figure 2**, namely the metrical parameters of the protonated oxygenic species bound to the diiron center and the orientation of the g tensor relative to the center, were optimized so as to make each model fit the experimental data as closely as possible, with particular focus on achieving the best possible match to spectra at the g_1 and g_3 edges of the EPR envelope. Comparison of the experimental results and the calculations permits a definitive conclusion that Intermediate X contains a terminal water molecule (or 2-fold disordered hydroxyl; see above) bound to Fe^{III} and does not contain an hydroxyl bridge.

This conclusion were reached by comparison of the two sets of calculations with the experiment, and is based on the following observations. (i) Spectra taken near g_1 show a pair of strongly-coupled doublets ($A_{\text{H}} \sim 19\text{--}20$ MHz) with 'peak-like' features, not shoulders, in agreement with the T model and in opposition to the B. (ii) As already stated, perhaps the most transparent difference between models seen in **Figure 2** regards the field dependence of the maximum breadth of the ENDOR pattern. The breadth of the experimental pattern does not remain roughly constant at $A_{\text{H}} \sim 20$ MHz from g_1 to g_2 as in the B model, but as indicated, decreases from g_1 to g_2 and then remains constant at $A_{\text{H}} \approx 9$ MHz, as in T; *for fields between g_2 and g_3 there is no intensity from protons with $A_{\text{H}} \geq 9$ MHz, in agreement with the T model and in opposition to the B model*. To be able to make this statement definitively required particular care. As shown by **Figure 2**, in the B model the signals with larger splittings in this field range have low intensity. However, the ReMims protocol permitted us to select a value of τ that optimizes the response to such signals; the baseline in this experiment is flawless, and extensive signal averaging produced spectra with good signal/noise. Thus, even the low-intensity 'wing' signals predicted by the B model would have been cleanly detected if they had been present. We conclude that they are

not. (iii) The ^2H ReMims experiment with $\tau = 204$ ns reveals a sharp doublet of doublets with major splitting of $A_D \approx 1.38$ MHz near g_3 , but the hyperfine selectivity shown by comparison to the spectrum with a larger value of $\tau = 500$ ns (**Figure 3c**) shows that this doublet is not simply a quadrupole splitting as it would be in the B model, but reflects the unequal hyperfine couplings of the two inequivalent protons in the T model (see the discussion above). (iv) The doublet of doublets seen at g_3 persists from g_3 to g values substantially greater than g_2 , rather than abruptly broadening and disappearing at fields near g_2 ; this again is in accord with the T but not the B model. (v) For clarity we emphasize that the absence in the experimental ^1H spectra of *any* unexplained features with the large hyperfine couplings *required* for the proton of a bridging hydroxyl precludes there being both a bridging hydroxyl and a water molecule. (vi) Finally, the current data give no evidence for an additional H_2O terminally bound to the Fe^{IV} , which would have small ^1H couplings, but does not rule out the presence of one.

Conclusions

The striking agreement between the 2D set of experimentally optimized Q-band ^1H ENDOR spectra in **Figure 4** and the simulations based on the T model displayed in the right diagram in **Figure 2** show that the exchangeable proton signals displayed by Intermediate X, belong to two protons associated with a terminal water bound to Fe^{III} . Within the precision of the modeling this picture is indistinguishable from that of a 2-fold disordered terminal hydroxyl. The strong spin coupling between the iron ions and the short Fe-Fe separation observed by EXAFS spectroscopy, requires that Intermediate X contain one or more oxo/hydroxo bridges. The determination that X does not have an hydroxyl bridge, in conjunction with the finding of a terminal water, then establishes that Intermediate X contains the $[(\text{H}_2\text{O})\text{Fe}^{\text{III}}\text{OFe}^{\text{IV}}]$ fragment that defines the T model (**Figure 1**). As stated in the introduction and demonstrated above, these results could not have been achieved with any individual technique. The presence or absence of the second oxo bridge of a diamond core, a determination of the fate of the two atoms of dioxygen, and a confirmation that there is not a second H_2O bound to Fe^{IV} is the subject of ^{17}O ENDOR measurements using enriched solvent and gas.

Acknowledgments

The authors would like to express their gratitude towards C. E. Davoust for his extensive technical support and to the NIH (Grants HL 13531 (B. M. H); GM 29595 (J. S.)).

Literature Cited

1. Abragam, A.; Bleaney, B. *Electron Paramagnetic Resonance of Transition Ions*; 2nd ed.; Clarendon Press: Oxford, 1970, xiv, 911.
2. Mims, W. B. *Electron Spin Echoes*; Mims, W. B., Ed.; Plenum Press: New York, 1972.
3. DeRose, V. J.; Liu, K. E.; Lippard, S. J.; Hoffman, B. M., *J. Am. Chem. Soc.* **1996**, *118*, 121-134.

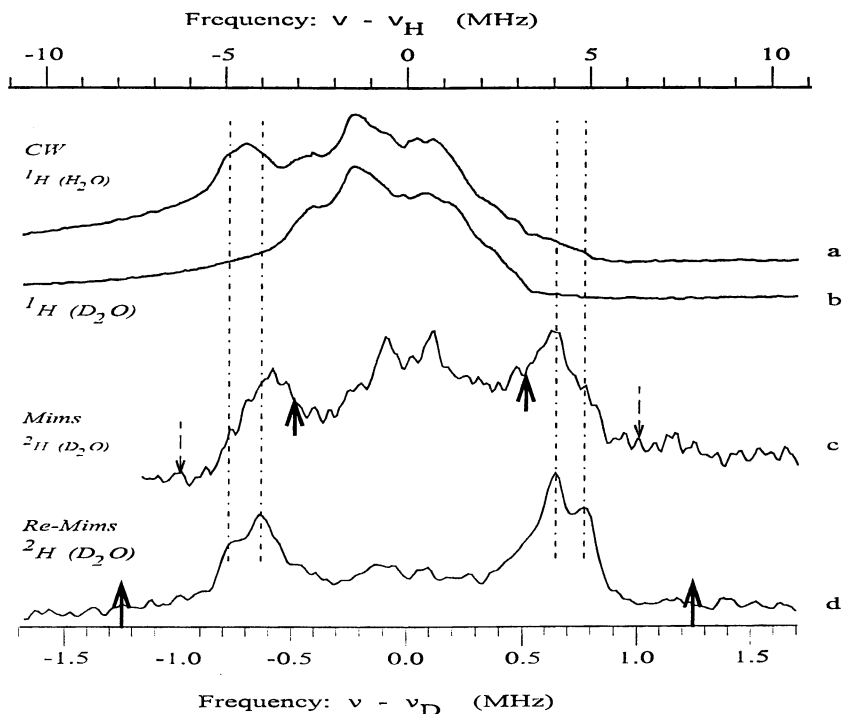


Figure 3: ^{12}H Q-Band ENDOR spectra taken at $\approx g_3$ of **X** using each of the techniques employed in this study. The ^1H and ^2H signals are displayed in a common axis through a scaling of the proton ENDOR shifts by the ratio (g_D/g_H) ; all spectra have been centered around the nuclear Larmor frequency. (Temperature: 2K)

- (a) CW ^1H spectrum of Intermediate **X** in H_2O buffer. *Conditions*: microwave frequency: 35.3 GHz; modulation amplitude: 8 G; modulation frequency: 100 kHz; RF scan speed: 1 MHz/s. RF frequency sweep: from high frequency to low.
- (b) CW proton spectrum of Intermediate **X** in D_2O buffer. Experimental conditions, as (a).
- (c) Mims ^2H pulsed ENDOR spectrum of Intermediate **X** in D_2O buffer. *Conditions*: microwave frequency: 34.975 GHz; $\tau = 500$ ns; microwave pulse width, 28 ns; RF pulse width, 60 μs . The $\eta = 1$ Mims 'hole' (eq. 1) has been indicated by the dashed arrows; the points of maximum sensitivity have been indicated by the solid arrows.
- (d) ReMims ^2H pulsed ENDOR spectrum of Intermediate **X** in D_2O buffer. *Conditions*: microwave frequency: 34.978 GHz; $\tau = 204$ ns; microwave pulse width: 28 ns; RF pulse width: 60 μs ; $\tau_2 = 216$ ns. The RF frequency window has been indicated by the solid arrows. The $\eta = 1$ Mims 'hole' (eq. 1) is out of the frame; the points of maximum sensitivity have been indicated by the solid arrows.

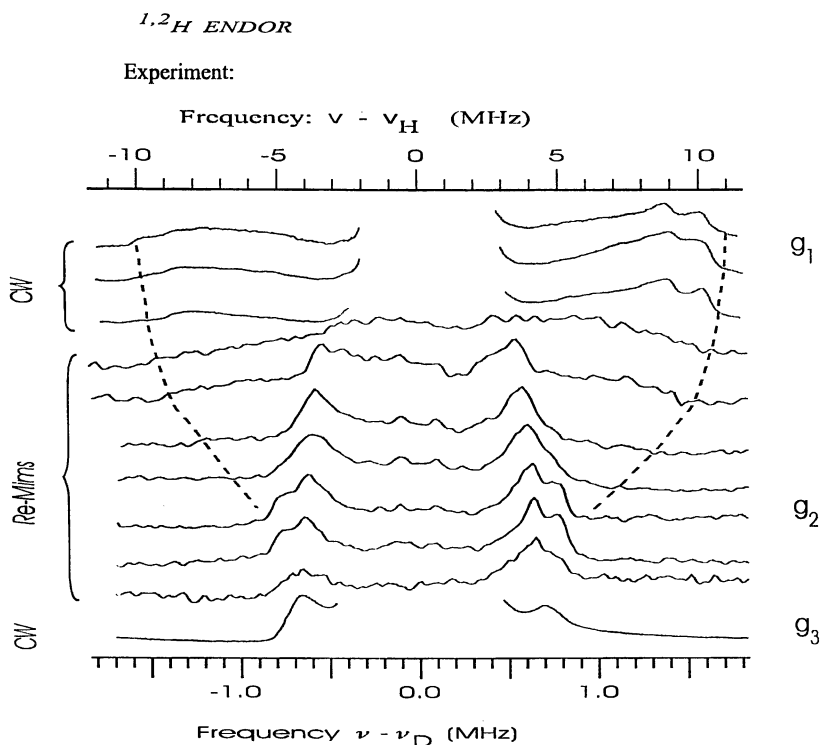


Figure 4: Experimental $^{1,2}\text{H}$ ENDOR spectra taken across the EPR envelope of X. The ^1H and ^2H signals are displayed in a common axis through a scaling of the proton ENDOR shifts by the ratio (g_D/g_H); all spectra have been centered around the nuclear Larmor frequency. (Temperature, 2K). The CW ^1H spectra come from a sample in H_2O buffer, the pulse ^2H spectra come from a sample in D_2O buffer. The maximum breadth of the ENDOR pattern has been indicated by the dashed lines, as in **Figure 2**. Conditions: CW, as in **Figure 3a**; ReMims pulse, as in **Figure 3d**.

4. DeRose, V. J.; Hoffman, B. M., *Methods Enzymol.* **1995**, *246*, 554-589.
5. Hoffman, B. M.; DeRose, V. J.; Doan, P. E.; Gurbiel, R. J.; Houseman, A. L. P.; Telser, J. *Metalloenzyme Active-Site Structure and Function through Multifrequency CW and Pulsed ENDOR*; Hoffman, B. M.; DeRose, V. J.; Doan, P. E.; Gurbiel, R. J.; Houseman, A. L. P.; Telser, J., Ed.; Plenum Press: New York and London, 1993, pp 151-218.
6. Lowe, D. J. *ENDOR and EPR of Metalloproteins*; R. G. Landes Co.: Austin, TX, 1995.
7. DeRose, V. J.; Hoffman, B. M. *Protein Structure and Mechanism Studied by Electron Nuclear Double Resonance Spectroscopy*; DeRose, V. J.; Hoffman, B. M., Ed.; Academic Press: New York, 1995; Vol. 23, pp 555-589.
8. Hoffman, B. M., *Acc. Chem. Res.* **1991**, *24*, 164-170.
9. Randall, D. W.; Gelasco, A.; Caudle, M. T.; Pecoraro, V. L.; Britt, R. D., *J. Am. Chem. Soc.* **1997**, *119*, 4481-4491.
10. Atkin, C. L.; Thelander, L.; Reichard, P.; Lang, G., *J. Biol. Chem.* **1973**, *248*, 7464-7472.
11. Larrson; Sjöberg, B. M., *EMBO J.* **1986**, *5*, 2037-2040.
12. Bollinger, J. M., Jr.; Edmondson, D. E.; Huynh, B. H.; Filley, J.; Norton, J. R.; Stubbe, J., *Science* **1991**, *253*, 292-298.
13. Bollinger, J. M., Jr.; Tong, W. H.; Ravi, N.; Huynh, B. H.; Edmondson, D. E.; Stubbe, J., *J. Am. Chem. Soc.* **1994**, *116*, 8015-8023.
14. Sturgeon, B. E.; Burdi, D.; Chen, S.; Huynh, B.-H.; Edmondson, D. E.; Stubbe, J.; Hoffman, B. M., *J. Am. Chem. Soc.* **1996**, *118*, 1551-7557.
15. Burdi, D.; Sturgeon, B. E.; Tong, W. H.; Stubbe, J.; Hoffman, B. M., *J. Am. Chem. Soc.* **1996**, *118*, 281-282.
16. Ravi, N.; Bollinger, J. M., Jr.; Huynh, B. H.; Edmondson, D. E.; Stubbe, J., *J. Am. Chem. Soc.* **1994**, *116*, 8007-8014.
17. Willems, J.-P.; Burdi, D.; Lee, H.-I.; Doan, P. E.; Stubbe, J.; Hoffman, B. M., *J. Am. Chem. Soc.* **1997**, *in press*.
18. For sample preparation, see Ref. 17.
19. Werst, M. M.; Davoust, C. E.; Hoffman, B. M., *J. Am. Chem. Soc.* **1991**, *113*, 1533-1538.
20. Davoust, C. E.; Doan, P. E.; Hoffman, B. M., *J. Mag. Res., A* **1996**, *119*, 38-44.
21. Davies, E. R., *Phys. Lett.* **1974**, *47A*, 1-2.
22. Gemperle, C.; Schweiger, A., *Chem. Rev.* **1991**, *91*, 1481-1505.
23. Fan, C.; Doan, P. E.; Davoust, C. E.; Hoffman, B. M., *J. Magn. Reson.* **1992**, *98*, 62-72.
24. Mims, W. B., *Proc. Roy. Soc. Lond.* **1965**, *283*, 452-457.
25. Doan, P. E.; Fan, C.; Hoffman, B. M., *J. Am. Chem. Soc.* **1994**, *116*, 1033-1041.
26. Doan, P. E.; Hoffman, B. M., *Chem. Phys. Let.* **1997**, *269*, 208-214.
27. Fann, Y.-C.; Ong, J.-I.; Nocek, J. M.; Hoffman, B. M., *J. Am. Chem. Soc.* **1995**, *117*, 6109-6116.
28. Fann, Y.-C.; Gerber, N. C.; Osmulski, P. A.; Hager, L. P.; Sligar, S. G.; Hoffman, B. M., *J. Am. Chem. Soc.* **1994**, *116*, 5989-5990.

29. The relative orientations of the hyperfine and quadrupole tensors for each protonic species depends on the exact orientation of the water, with indistinguishable results for an appreciable range of choices; such details are irrelevant to this report.
30. Edmonds, D. T., *Phys. Lett.* **1977**, *C 29*, 233-290.

Chapter 2

Combining Mössbauer Spectroscopy and Magnetometry

K. E. Kauffmann and E. Münck

Department of Chemistry, Carnegie Mellon University, Pittsburgh, PA 15213

Combining ^{57}Fe Mössbauer spectroscopy with magnetometry can provide significant insight into the physical and electronic structure of iron-containing compounds. Such multi-instrumental studies are particularly useful for analyzing the magnetic behavior of synthetic complexes, available as polycrystalline powders. In addition to difficulties due to frequently present metal contaminants, the study of powder samples poses problems associated with alignment of individual crystallites by an applied magnetic field and/or texture resulting from packing. Moreover, interactions between neighboring molecules in solid samples complicate the analysis of the magnetic behavior for individual sites. By combining ^{57}Fe Mössbauer spectroscopy with magnetic susceptibility measurements, such problems can be observed and overcome. We address these issues by discussing a simple $S = 5/2$ system and an exchange-coupled diferric complex.

Previous published articles have explored and reviewed the correlations between Mössbauer spectroscopy and Electron Paramagnetic Resonance (EPR) for iron-containing systems with half-integral ($I=3$) and integral electronic spin ($I=4$). These relations provide researchers with strong arguments for establishing the presence of novel structures, or they allow one to correlate EPR signals with specific iron environments in multi-metal systems such as the nitrogenases, hydrogenases and carbon monoxide dehydrogenases, to mention examples from biologically oriented research. Similarly, when ^{57}Fe Mössbauer spectroscopy is used in conjunction with magnetic susceptibility measurements, Mössbauer spectroscopy becomes an extremely powerful technique in characterizing the magnetic behavior of iron

complexes. Recently in our laboratory, we have studied model compounds using both Mössbauer spectroscopy and SQUID magnetometry (5). These studies show that by using magnetic susceptibility to limit the range of values in the electronic parameters of a given spin system it is possible to obtain consistent fits to both Mössbauer and susceptibility data. In the following, we describe some aspects of the methodology of our combined studies. We will assume that the reader is familiar with the relevant aspects of Mössbauer spectroscopy and magnetometry, in particular with the spin Hamiltonian formalism. Suitable introductions into the Mössbauer technique, for instance, are given in (1-3); magnetometry studies have been described by Day (6), Butzlaff et al. (7), and Trautwein et al. (8).

Theoretical Considerations

This section briefly reviews the theoretical basis of the connections between magnetization studies and certain aspects of Mössbauer spectroscopy. Let us consider a mononuclear iron compound with spin S , and assume that the energy levels of interest are well described in the spin Hamiltonian approximation. In the presence of an applied magnetic field, the electronic part of the spin Hamiltonian can be written as

$$H_e = D \left\{ S_z^2 - \frac{S(S+1)}{3} + \frac{E}{D} (S_x^2 - S_y^2) \right\} + \beta \mathbf{S} \cdot \mathbf{g} \cdot \mathbf{B}. \quad (1)$$

where D and E are the axial and rhombic zero-field splitting parameters, respectively, and \mathbf{g} is the g -tensor. For simplicity we assume that the g -tensor is collinear with the zero-field splitting tensor. This assumption frequently does not hold for exchange-coupled clusters; however, because the g -values are generally close to $g = 2$, violation of this assumption does not seriously affect the data analysis. For a given orientation of the applied field, the magnetic moment, $\langle \mu^n \rangle$, of the n^{th} eigenstate due to H_e can be written as

$$\langle \mu^n \rangle = - \frac{\partial E^n}{\partial B} \hat{\mathbf{e}} \quad (2)$$

where $\hat{\mathbf{e}}$ is the unit vector along \mathbf{B} and B is the magnitude of \mathbf{B} . The net magnetic moment, \mathbf{M} , observed for N paramagnetic sites at temperature T is the thermal average of $\langle \mu^n \rangle$,

$$\mathbf{M} = -N \frac{\sum_{\text{all } n} \langle \mu^n \rangle e^{-E^n/kT}}{\sum_{\text{all } n} e^{-E^n/kT}} \quad (3)$$

This expression is fundamental to the study of molecular magnetism (9). From eqs. 1 and 2, it follows that

$$\langle \mu^n \rangle = -\beta \langle S^n \rangle \bullet \mathbf{g} \quad (4)$$

where $\langle S^n \rangle$ is the expectation value of the electronic spin taken for level n . Using eq. 4 we can write eq. 3 as

$$\begin{aligned} \mathbf{M} &= -N\beta \frac{\sum_{\text{all } n} \langle S^n \rangle e^{-E^n/kT}}{\sum_{\text{all } n} e^{-E^n/kT}} \bullet \mathbf{g} \\ &= -N\beta \langle S \rangle_{\text{th}} \bullet \mathbf{g} \end{aligned} \quad (5)$$

where $\langle S \rangle_{\text{th}}$ is the thermally averaged electronic spin. In magnetization studies of samples containing randomly oriented molecules (a powder sample), \mathbf{M} is averaged over all orientations to yield

$$M_{\text{powder}} = \chi B = -N\beta \int_{\text{all space}} (\langle S \rangle_{\text{th}} \bullet \mathbf{g} \bullet \hat{\mathbf{e}}) d\tau \quad (6)$$

In eq. 6, χ is the powder-averaged magnetic susceptibility. By computing χ as a function of temperature and applied field, we can determine D , E , and \mathbf{g} of eq. 1 by comparison with experimental data.

For analyzing Mössbauer spectra, eq. 1 has to be augmented by terms describing the magnetic hyperfine interactions, $H_{\text{hyp}} = \mathbf{S} \bullet \mathbf{A} \bullet \mathbf{I}$, the nuclear Zeeman term, $H_z = -g_n \beta_n \mathbf{I} \bullet \mathbf{B}$, and the electric quadrupole interactions, H_Q . Since H_Q does not depend on \mathbf{S} , it is not important for the arguments presented here. The total Hamiltonian then becomes:

$$H = H_e + H_Q + H_{\text{hyp}} + H_z \quad (7)$$

Since the nuclear terms are extremely small compared H_e , the expectation value of the electronic spin, $\langle S \rangle$, is solely determined by eq. 1. This allows us to replace the operator \mathbf{S} in H_{hyp} by its expectation value, i.e. $H_{\text{hyp}} = \langle S \rangle \bullet \mathbf{A} \bullet \mathbf{I}$. The term $\langle S \rangle \bullet \mathbf{A}$ has the dimensions of a vector. As a result, we can combine the hyperfine term with the nuclear Zeeman term in the following manner:

$$\begin{aligned} H_z &= -g_n \beta_n \left(\mathbf{B} - \langle S \rangle \bullet \frac{\mathbf{A}}{g_n \beta_n} \right) \bullet \mathbf{I} \\ &= -g_n \beta_n (\mathbf{B} + \mathbf{B}_{\text{int}}) \bullet \mathbf{I} \end{aligned} \quad (8)$$

The quantity

$$\mathbf{B}_{\text{int}} = - \langle \mathbf{S} \rangle \bullet \frac{\mathbf{A}}{g_n \beta_n} \quad (9)$$

is known as the internal magnetic field. \mathbf{B}_{int} acts on the nuclear magnetic moment producing the magnetic splittings observed in the Mössbauer spectrum (1-3). Since \mathbf{B}_{int} depends on $\langle \mathbf{S} \rangle$ and therefore on the spin Hamiltonian parameters D , E , and \mathbf{g} , Mössbauer spectroscopy can be used to determine these pure electronic quantities.

If the electronic spin S fluctuates slowly compared to the nuclear precession frequencies (the latter are typically ≈ 10 MHz), each thermally populated electronic level n has an associated Mössbauer spectrum for which the internal field is computed by using in eq. (9) for $\langle \mathbf{S} \rangle$ the spin expectation value $\langle \mathbf{S}^n \rangle$. The resulting Mössbauer spectrum is then a sum of the spectra of the individual electronic levels, weighted by the appropriate Boltzmann factor. In the fast fluctuation limit, on the other hand, only one spectrum is observed for which \mathbf{B}_{int} is computed by using in eq. 9 the thermal expectation value $\langle \mathbf{S} \rangle_{\text{th}}$. For this case, the connection between magnetization data and Mössbauer spectra is particularly apparent since $\langle \mathbf{S} \rangle_{\text{th}}$ is related to the thermal averaged magnetic moment, M , through eq. 5.

A Simple Example

In the following, we discuss for a high-spin ($S = 5/2$) ferric system how a combined magnetization and Mössbauer study can lead to a reliable determination of the zero-field splitting parameter D . While the example is fairly simple, it will allow us to focus on the essential points without getting lost in the details of more complex systems such as exchange-coupled clusters containing inequivalent iron sites with anisotropic magnetic hyperfine interactions. Rather than illustrating the various points with examples from the literature, we will present theoretical Mössbauer spectra and magnetization curves.

Consider an $S = 5/2$ system described by the Hamiltonian of eq. 1 for the axial case $D = +5 \text{ cm}^{-1}$, $E = 0$, and $\mathbf{g} = \mathbf{g}_0 = 2.00$. These parameters are typical of ferric porphyrins. Figure 1 shows the energy levels resulting from eq. 1 for the case where the magnetic field is applied either along the z -axis or in the xy plane. EPR spectroscopists like to treat each of the three Kramers doublets as a system with effective spin $S' = 1/2$ (2). In our example, only the $M_S = \pm 1/2$ ground doublet is EPR-active; if described by a Hamiltonian with an effective spin $S' = 1/2$, its effective g -tensor has $g_x = g_y = 3g_0 = 6.0$ and $g_z = g_0 = 2.0$. By observing these g -values in an EPR experiment, $E = 0$ is readily established. For polycrystalline samples intermolecular spin-spin interactions may prevent observation of EPR; in this case, the parameter E can be determined with high precision from Mössbauer spectroscopy (10). More generally, we can use EPR in conjunction with so-called rhombograms (11) (plots of effective g -values as a function of E/D) or Mössbauer spectroscopy to determine the ratio E/D . Saturation magnetization can also be used

to determine the value of E ; however, its sensitivity to small variances in E is not as high as that inherent to Mössbauer and/or EPR spectroscopy.

Suppose that the Mössbauer spectrum of Figure 2A is observed for our $S = 5/2$ complex at 4.2 K and for an applied magnetic field of 0.05 T. The observation of magnetic splittings in the presence of such a weak applied field implies that the electronic spin fluctuates slowly compared to the nuclear precession frequencies. Suppose also that we observe the spectrum of Figure 2B at $T = 20$ K. Note that new absorption lines have appeared. The lines marked by the triangles are the outermost features of the 6-line spectrum associated with the $M_S = \pm 5/2$ doublet, while those marked by the arrows belong to the $M_S = \pm 3/2$ doublet. By determining the absorption of these components relative to the total absorption, the population of the $M_S = \pm 5/2$ and $M_S = \pm 3/2$ doublets at 20 K and, therefore, the parameter D is readily determined. The accuracy for the determination of D is typically $\pm 10\%$.

Suppose, on the other hand, that under the experimental conditions of Figure 2A we observe the spectrum of Figure 3A. The observation of a quadrupole doublet shows that the electronic spin relaxes rapidly among the thermally accessible energy levels, namely the two sublevels of the $M_S = \pm 1/2$ doublet. Because $\beta B/kT \ll 1$ under the stated experimental conditions and because only the $M_S = \pm 1/2$ doublet is populated at 4.2 K, $\langle S \rangle_{th} \approx 0$ and therefore $B_{int} = 0$. Figures 3B-E show a series of 4.2 K Mössbauer spectra computed for applied magnetic fields of 1.0, 2.0, 4.0 and 8.0 T; examples of experimental spectra can be found in (10). Spectra such as those shown in Figure 3 can be readily analyzed to determine B_{int} and plotted as a function of applied magnetic field (Figure 4, left ordinate scale). Plotted also in Figure 4 is the powder-averaged magnetization (dashed line) of the sample, assuming that the molecules in the sample are randomly oriented. Note that the shapes of the two curves are quite similar, as expected on the basis of eqs. 6 and 9. In the present example, the low temperature Mössbauer spectra primarily measure the thermal expectation value of the electronic spin in the xy plane (2, 10). By comparison, M_{powder} is a powder-averaged quantity over all space (This explains small discrepancies in the lineshapes of both curves).

Experimental Considerations

The presence of paramagnetic or magnetically ordered impurities are a substantial impediment for magnetization studies. For the study of synthetic iron complexes, the most likely impurities are iron-containing contaminants. The presence of such impurities does not seriously impede determination of the desired parameters with Mössbauer spectroscopy because this technique resolves, in most cases, the contributions from different Fe sites. Under some conditions, however, it is very difficult to extract much information from the Mössbauer spectra alone. For example, when the relaxation rates of the electronic spin are neither fast nor slow on the Mössbauer time scale, the spectra are poorly resolved and exceedingly difficult to analyze. Since susceptibility measurements always measure a thermally averaged property of a sample, the data are not affected by electronic relaxation rates. By

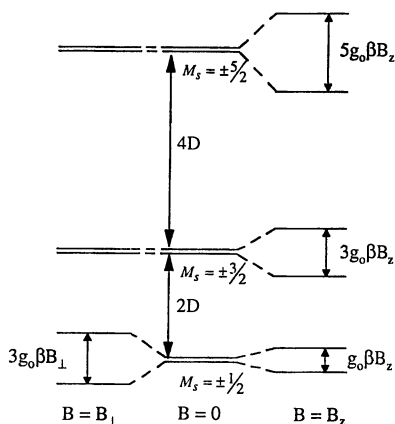


Figure 1. Energy levels of an $S = 5/2$ system with $D > 0$ and $E = 0$. The magnetic splittings of the three Kramers doublets are indicated for magnetic fields applied either along the spin Hamiltonian z -axis or perpendicular to z .

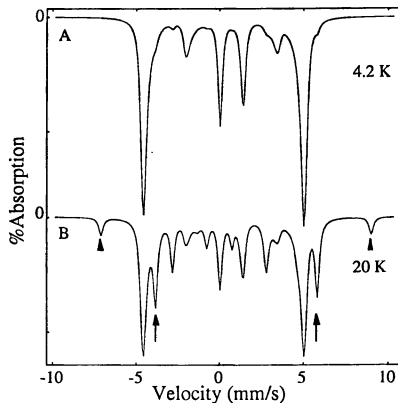


Figure 2. Calculated Mössbauer spectra of a high-spin ferric system with $D = +5 \text{ cm}^{-1}$, $E = 0$, $a_{\text{iso}} = -27.4 \text{ MHz}$, $\Delta E_Q = 1.0 \text{ mm/s}$, and $\eta = 0$. The spectra were calculated for slow relaxation of the electron spin for a magnetic field $B = 0.05 \text{ T}$ applied parallel to the incident γ -radiation. (A) $T = 4.2 \text{ K}$ and (B) $T = 20 \text{ K}$. At $T = 20 \text{ K}$, all three Kramers doublets of the $S = 5/2$ system are populated. The absorption bands marked by the triangles and arrows are the outermost lines of the Mössbauer spectra associated with the $M_S = \pm 5/2$ and $M_S = \pm 3/2$ doublets, respectively.

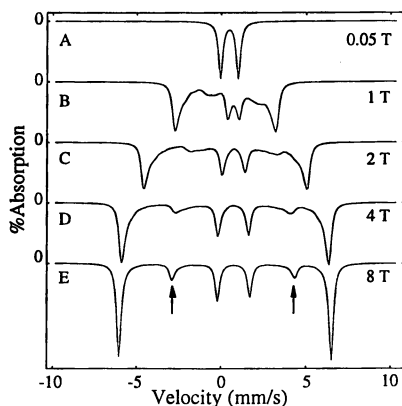


Figure 3: 4.2 K Mössbauer spectra of the $S = 5/2$ system of Figure 2 calculated in the fast relaxation limit for the applied fields indicated. The internal magnetic fields B_{int} extracted from analysis of the magnetic splittings are plotted in Figure 4. The arrows in (E) mark the two nuclear $\Delta m = 0$ transitions. Similarly, one can obtain B_{int} at constant field and variable temperature; for examples see (10).

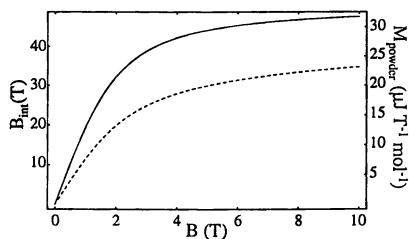


Figure 4: Plots of the powder-averaged magnetization M_{powder} and the internal magnetic field B_{int} versus applied field B . Assumed temperature is 4.2 K.

combining a magnetization study with Mössbauer data, we are able to overcome the problems inherent to any one of the techniques alone. Using Mössbauer spectroscopy we can establish the nature of impurities (spin and oxidation state) and determine the concentration of the contaminant relative to the species of interest. Using this information the analysis of the magnetization data for determination of electronic parameters can then proceed in a straightforward manner. Such a procedure was used by our lab in deriving the electronic parameters for a set of iron porphyrin model complexes (5, 10).

Besides impurities and relaxation problems, sample texture can significantly complicate analysis of Mössbauer data. Most paramagnetic compounds with $S > 1/2$ exhibit at low temperatures ($kT < D$) substantial magnetic anisotropies. For instance, the magnetic moment of the fictitious heme complex discussed above is at 4.2 K much larger when the field is applied in the xy plane than when it acts along z . As a result of this large magnetic moment in the plane, the molecules of the sample will experience a torque due to the applied field. If the sum of the magnetic moments over all molecules in a single crystallite is sufficiently large to overcome packing forces, the crystallite can rotate to align its net magnetic moment with the applied magnetic field (5). Such magnetically induced texture effects have been observed many times for applied fields as low as 1 T. If these effects are not recognized, the data analysis is in peril. Although alignment by the applied magnetic field is readily recognized once a researcher is alerted to the problem, the newcomers in the field may fall into the trap of recording one or two magnetization curves, remove the sample from the magnetometer and analyze the magnetization curve at some later date. Rather, any magnetization study of a complex with a suspected anisotropic moment, in general a compound with $S > 1/2$, should start at low field and at high temperature. At high temperature most paramagnetic systems are quite isotropic. By recording data for decreasing temperature and then retracing the data for increasing temperature, alignment of the sample by the field can be recognized. In our laboratory, we disperse polycrystalline materials, whenever feasible, in a mineral oil such as Nujol; under these conditions we have not observed any alignment in fields up to 8 T. Alignment may also be caused by the physical shape of the microcrystallites. Many complexes form needle-like crystals which tend to pack such that their long axis is parallel to the bottom of the sample cuvette. Grinding the compound in a mortar often increases the texture. Here, again, suspension of the material in Nujol should solve the problem.

Alignment of a sample by a magnetic field or texture induced by packing can be recognized with Mössbauer spectroscopy because the intensities of the absorption lines depend on the direction of the observed γ -radiation relative to the nuclear quantization axis (for compounds with small quadrupole splittings this is the direction of B_{int}) (3). Figure 5A shows a 4.2 K Mössbauer spectrum of our fictitious heme complex recorded in the absence of an applied field. For a sample containing randomly oriented molecules, the area under both absorption lines are equal. For the 8.0 T spectrum of Figure 5B, we have assumed that the magnetic field has affected the sample such that all hemes are aligned and the applied field is in the xy plane

(because our system is axial around z , the distribution of the field in the xy plane is random). Note that the nuclear $\Delta m = 0$ lines (arrows in Figure 3E) have disappeared in the spectrum of Figure 5B. Recording a Mössbauer spectrum after switching off the magnetic field (Figure 5C) reveals alignment by the observation of an asymmetric quadrupole doublet. Sample texture can also be observed using susceptibility measurements. Figure 6 shows plots of χ for a sample containing randomly oriented molecules (solid line) and for a sample aligned (dashed line) like the Mössbauer sample of Figure 5. The insert shows for the same samples a plot of χT versus T . Of course, full alignment is rarely achieved and the actual effects are much less pronounced. In general, a consideration of a full magnetization data set (multiple applied magnetic fields over a wide range of temperatures) collected for a particular sample can identify such problems. However, such alignment effects can be quite subtle, and therefore difficult to diagnose.

An Exchange Coupled Diiron(III) Dimer

We wish to discuss briefly a Mössbauer study of a diiron(III) dimer that shows how one can determine an exchange coupling constant by Mössbauer spectroscopy. The study (12), performed in collaboration with L. Que's group at the University of Minnesota, involved the diferric bis(μ -oxo)bridged complex of Figure 7, **1**. Complex **1** contains two equivalent high-spin ferric sites, as judged from the X-ray structure and the observation of *one* doublet with quadrupole splitting $\Delta E_Q = 1.93$ mm/s and isomer shift $\delta = 0.51$ mm/s (Figure 8A). In an applied magnetic field of 8.0 T, the 4.2 K Mössbauer spectrum (Figure 8B) exhibits magnetic splittings that can be attributed entirely to the nuclear Zeeman term, i.e. the complex is diamagnetic at 4.2 K. However, 8.0 T Mössbauer spectra recorded at temperatures above 20 K exhibit magnetic splittings slightly smaller than those observed at 4.2 K, indicating population of low-lying paramagnetic states. Because only one Mössbauer spectrum is observed at each temperature, the electronic system is in the fast relaxation regime.

The magnetic properties of the diiron(III) complex can be described by the Hamiltonian

$$H = JS_1 \cdot S_2 + 2\beta \sum_{i=1}^2 S_i \cdot B + a_{iso} S_i \cdot I_i - g_n \beta_n I_i \cdot B \quad (10)$$

where J is the exchange coupling constant and a_{iso} the isotropic magnetic hyperfine coupling constant of each high-spin ferric site ($S_1 = S_2 = 5/2$). (For complex **1** the zero-field splitting parameters D_1 and D_2 are small and can be ignored for the analysis). Because the thermally-averaged electronic spin $\langle S \rangle_{th}$ occurs in the expressions of the powder-averaged magnetic susceptibility χ and the internal magnetic field B_{int} , we can write the magnetic hyperfine term as (5)

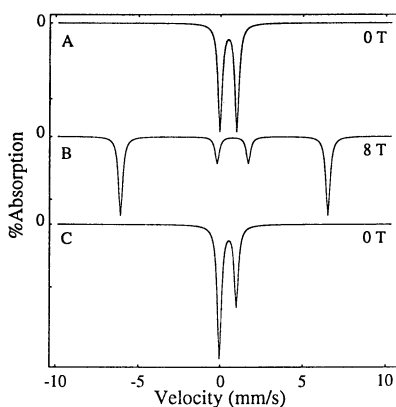


Figure 5: Calculated Mössbauer spectra for an $S = 5/2$ sample with $D = 5 \text{ cm}^{-1}$ and $E = 0$. The sample is aligned such that the applied field is in the xy plane of the molecule. Zero-field spectra of a randomly oriented powder (A), of an aligned sample (C) and 8.0 T spectrum of an aligned sample (B).

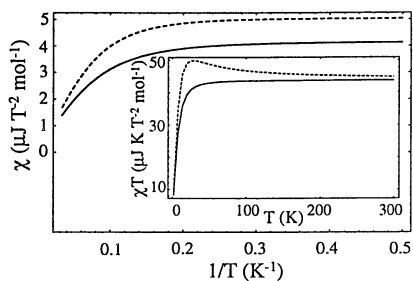


Figure 6: 5.0 T magnetization curves of a sample with randomly oriented molecules (solid line) and oriented sample (dashed) of Figure 5. Insert displays χT vs. T plots for the same samples.

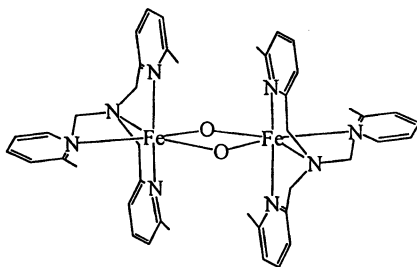


Figure 7: Structure of $[\text{Fe}_2(\text{O})_2(6\text{-TLA})_2]^{2+}$, **1**; 6-TLA = tris(6-methylpyridyl-2-methyl)amine (**12**).

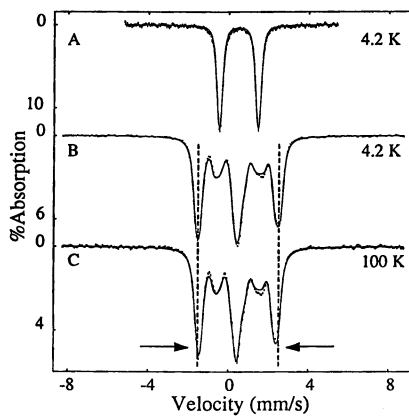


Figure 8: Mössbauer spectra of **1** recorded at 4.2 K in zero field (A), in a parallel field of 8.0 T (B), and at 100 K in a field of 8.0 T (C). Solid lines are theoretical curves. Dashed lines emphasize the difference in the magnetic hyperfine splittings at 4.2 K and 100 K.

$$H_{hyp} = \sum_{i=1}^2 \left(\frac{B}{N_A \beta} \right) \left(\frac{a_{iso} \chi}{2g_0} \right) \hat{e} \cdot \mathbf{I} \quad (11)$$

For a typical high-spin ferric complex with octahedral N/O coordination a_{iso} has, within $\pm 5\%$, the value -29 MHz. Using this value for the two sites of the diferric complex and $g_0 = 2$, we can write the internal field at each iron site as

$$B_{int} = -0.948B\chi \quad (12)$$

where B and B_{int} are in units of T and χ is in units of $\mu\text{J}/(\text{T}^2\text{mol})$. From an analysis of the 8.0 T Mössbauer spectra of complex 1 we obtain B_{int} and χ as a function of temperature. Figure 9 shows the results obtained from analysis of the Mössbauer spectra at seven temperatures, plotted as χT versus T . The solid line is a theoretical curve plotted for $J = 70.5 \text{ cm}^{-1}$, and $g_0 = 2.0$. Figure 10 shows SQUID magnetization data obtained for a sample of the same batch. These data are best fitted with $J = 54 \text{ cm}^{-1}$ (solid line). The estimated errors are about $\pm 10 \text{ cm}^{-1}$ for each technique.

A few comments are in order here. First, the results of both techniques agree within the stated uncertainties, although we would prefer a better agreement. The case just discussed was the first instance where we have tried to measure χ by Mössbauer spectroscopy, and the combined technique was not carried out as well as we would do it in our present studies. In particular, we have recently improved our methods of analysis of magnetization data by analyzing a larger set of applied fields for a given set of temperatures. Moreover, we have written our own programs to analyze magnetization data in both the high temperature and the saturation (low temperature) regions. Second, the Mössbauer data are not treated as indicated in Figure 9. Rather, the spectra are fit to the Hamiltonian of eq. 9 (amended by the quadrupole interaction). Fitting the data yields the quantity of interest, namely J . Using this value of J , we can compute B_{int} and χ .

Summary

We have described here some of the advantages of combining Mössbauer spectroscopy with magnetometry. Although the examples discussed were very simple systems, they served to elaborate on some principal points. We have recently described (5, 10) Mössbauer and magnetization studies of some exchange coupled Cu(II)-Fe(III) heme model complexes for the $a_3\text{-Cu}_B$ site of cytochrome oxidase. This study demonstrates that application of both techniques yields J - and D -values more precise than that which can be obtained from either method alone. We have not addressed here another frequently occurring problem, namely the presence of intermolecular exchange interactions in magnetically concentrated materials. While such interactions pose formidable problems for the data analyses, there is no simple general strategy to solve the problem, although fitting the data with suitable theoretical models can go a long way towards a solution. Paramagnetic dilution by

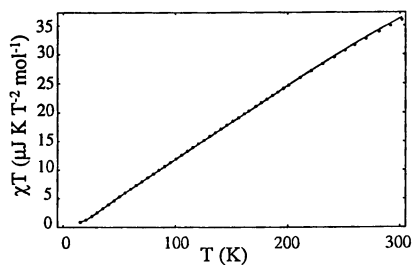


Figure 10: Magnetization data (χT) of **1** and fit to the Hamiltonian $H = J\mathbf{S}_1 \cdot \mathbf{S}_2 + 2\beta \sum_{i=1}^2 \mathbf{S}_i \cdot \mathbf{B}$ for $J = 54 \text{ cm}^{-1}$.

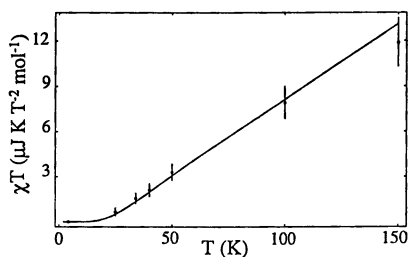


Figure 9: Data points for χT of complex **1** extracted from Mössbauer spectra. Solid line is a theoretical curve for $J = 70.5 \text{ cm}^{-1}$.

dissolving the compound into a solvent that maintains the integrity of the structure or embedding the complex into the matrix of an isomorphous complex have been successful approaches.

Acknowledgment

This work was supported by NIH grant GM 22701.

Literature Cited

1. Münck, E. (1978) in *The Porphyrins*, Vol. IV (D. Dolphin Ed.), Academic Press, pp. 379-423.
2. Münck, E. *Meth. Enz.* **1978**, *54*, 346-379.
3. Münck, E., and Huynh, B.H. (1979) in *ESR and NMR of Paramagnetic Species in Biological and Related Systems*, (eds. I. Bertini and R.S. Drago) pp. 275-288, Reidel Publishing Company, Holland.
4. Münck, E.; Surerus, K.K.; Hendrich, M. *Methods Enzym.* **1993**, *227*, 463-479.
5. Kauffmann, K. Ph.D. Thesis, Carnegie Mellon University, 1996.
6. Day, E.P. *Meth. Enzym.* **1993**, *227*, 437-463.
7. Butzlaff, C.; Trautwein, A.X.; Winkler, H. *Meth. Enzymol.* **1993**, *227*, 412-463.
8. Trautwein, A.X.; Bill, E.; Bominaar, E.L.; Winkler, H. *Structure and Bonding* **1991**, *78*, 1-96.
9. Kahn, O. *Molecular Magnetism*, VCH Publishers, Inc: New York, NY, 1993.
10. Kauffmann, K.E.; Goddard, C.A.; Zang, Y.; Holm, R.H.; Münck, E. *Inorg. Chem.* **1997**, *36*, 985-993.
11. Hagen, W.R. in *Adv. Inorg. Chem.*, Cammack, R.; Sykes, A.G., Ed.; Academic Press, Inc., 1992, Vol. 38. pp 165-216.
12. Zang, Y.; Dong, Y.; Que, L.; Kauffmann, K.; Münck, E. *J. Am. Chem. Soc.* **1995**, *117*, 1169-1170.

Chapter 3

Advances in Single- and Multidimensional NMR Spectroscopy of Paramagnetic Metal Complexes

F. Ann Walker

Department of Chemistry, University of Arizona, Tucson, AZ 85721

Proton (and ^{13}C) NMR signals of paramagnetic metal complexes (and metalloproteins) can often, but not always, be detected by suitable modification of the standard experiments that are a part of the software of any modern NMR spectrometer. These NMR spectra potentially contain important information concerning the electronic and geometrical structure of the complex. Successfully obtaining 1D spectra is usually not difficult, because rapid recycle times can usually be used, and good S/N can usually be obtained in a relatively short time. To successfully obtain 2D spectra of paramagnetic complexes, however, requires careful optimization of the experimental parameters, in line with the relaxation times T_1 and T_2 of the signals of interest. ROESY spectra are in many cases more informative for small to medium-sized inorganic complexes than are NOESY spectra, because ROEs are non-zero for all rotational correlation times. For heteronuclear 2D experiments such as HMQC and HMBC, experiments that include gradient pulses greatly improve S/N and decrease t_1 noise, making it possible to detect weak correlations.

NMR spectroscopic investigations of a wide variety of paramagnetic transition or rare earth metal complexes and metalloproteins have been reported over the years, yet many chemists are still convinced that it is impossible to obtain NMR spectra of paramagnetic compounds. Certainly, there are a number of limitations, which will be discussed below, but there are often simple ways of getting around these limitations, and sometimes they can be used to advantage. Thus, it should never be assumed that just because a complex contains one or more unpaired electrons, it is not worth obtaining an NMR spectrum of it!

Why should one study the NMR spectra of paramagnetic complexes? Because they are usually exquisitely sensitive to molecular structure (metal-nuclear distances) and

to the molecular orbital into which the unpaired electron is delocalized. This not only allows one to confirm that the proper product has been obtained, but also, in many cases, to obtain detailed information about molecular shape and conformation and intimate details about covalency and the nature of the molecular orbital(s) of the ligands that interact with the unpaired electron(s) of the metal. One or more unpaired electrons on a metal center cause the protons (or ^{13}C nuclei) that are close to the metal through bonds and/or through space to be "illuminated." This "illumination" comes in the form of 1) a much wider range of chemical shifts than are typically observed for diamagnetic compounds and 2) linewidths that vary strongly with the distance between the metal and the nucleus of interest. In some of the most extreme cases reviewed herein, ^1H and ^2H chemical shifts of greater than ± 600 ppm and linewidths of greater than 2 kHz have been detected, and these are by no means limits! (1,2) To observe these large chemical shifts and very broad lines, certain modifications of the typical NMR experiments used by organic chemists are often necessary, as we will discuss in detail, but these modifications are not difficult for the experimenter to make. However, to the novice NMR user, who has been taught how to carry out NMR experiments on diamagnetic compounds, it may appear as though 1D and typical 2D experiments such as COSY, NOESY, ROESY, etc. are "abused" by those who study paramagnetic compounds! On the other hand, the more experienced NMR user, who understands the consequences of short nuclear relaxation times and large spectral bandwidths on the acquisition times of free induction decays, both in one and two dimensions, will immediately see that although the resonances of paramagnetic complexes are typically much broader than those of their diamagnetic analogs, the short relaxation times permit much shorter acquisition times and relaxation delays between repetitions of the pulse sequence, and hence allow many more transients to be obtained in a given period of time. It is also worth noting that optimization of the 1- and 2D NMR spectra of quadrupolar nuclei, such as those of ^{51}V complexes (3), rely on exactly the same considerations regarding short acquisition times, etc., as do ^1H spectra of paramagnetic complexes.

The intended audience of this chapter is people who already have some familiarity with NMR spectroscopy and who would like to know how to optimize 1D and 2D NMR experiments for paramagnetic complexes. The major problems, benefits and techniques relating to NMR spectroscopy of paramagnetic metal complexes will be discussed and summarized. Methods for optimizing both 1D and 2D experiments will be summarized. Specifically excluded from detailed discussion are paramagnetic metalloproteins, on which there have been a number of recent reviews. (4-8) In some cases the references given are to recent reviews or books on a topic, rather than to the original publications that described the pulse sequence, for example. In cases where this has occurred the indulgence of the original authors is begged. Each topic covered herein will be illustrated with one or more examples from the recent literature.

Background

Energy Levels and NMR Transitions. For the case of a single nucleus of spin $I = 1/2$ interacting with a single electron, $S = 1/2$, such as the hydrogen atom, H^\bullet , the energy level diagram is that shown in Figure 1. The energies of the four states $|\beta_e\alpha_N\rangle$, $|\beta_e\beta_N\rangle$, $|\alpha_e\beta_N\rangle$ and $|\alpha_e\alpha_N\rangle$ result from the combination of the electronic and nuclear Zeeman terms and

the electron-nuclear hyperfine interaction (9), and as shown in Figure 1, the two allowed NMR transitions, between states 1 and 2 and states 3 and 4, are of different energies. This would suggest that there should be *two* NMR lines, as there typically are two EPR lines, the latter resulting from transitions between states 1 and 4 and states 2 and 3 of Figure 1.

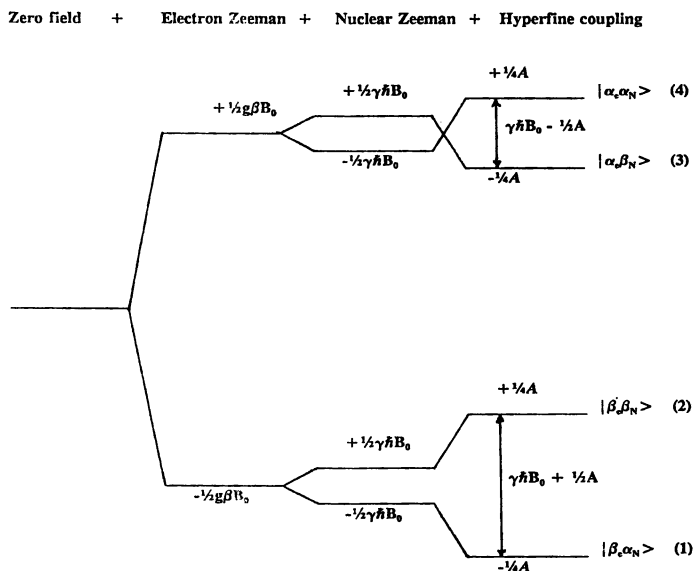


Figure 1. Energy level diagram for the hydrogen atom in the presence of a magnetic field. The NMR transitions (between levels 1 and 2 and between 3 and 4) are marked. The corresponding EPR transitions would be between levels 1 and 4 and also 2 and 3.

The separation of the two lines in each case should be A (10), the electron-nuclear hyperfine coupling constant, as shown in Figure 2. Hyperfine coupling constants are a measure of the unpaired electron density at the nucleus of interest (9), and hence require that there be some s -electron wave function contribution to the orbital of the unpaired electron. For the hydrogen atom, where the single electron is localized in the $1s$ orbital, which has some finite electron density at the (proton) nucleus, A has been measured by EPR techniques and is quite large--- $A/g\beta = 507$ gauss or $A/h = 1420$ MHz! (11) Hence, even if A for a proton of a ligand bound to a paramagnetic metal is only 0.01-0.02% of that for the hydrogen atom (a typical finding), it is still larger than the typical spectral bandwidth achievable on a high-resolution NMR spectrometer!

How, then, can we ever hope to observe the two NMR resonances of Figure 2? The answer lies in a fortunate consequence of short electron spin relaxation times---essentially, a type of chemical exchange phenomenon. We can observe the NMR resonances of the ligands bound to transition metals that have electron spin relaxation times *short enough* to average the positions of the two predicted resonances. (12) That average is the population *weighted* average of the two proton signals because the

populations of the four energy levels of Figure 1 are unequal, as determined by the Boltzmann distribution. Thus, the resulting resonance will not be at the diamagnetic position (the position marked by the dotted line in Figure 2), but rather either to higher or lower frequency (13) of the frequency of the same nucleus in the corresponding diamagnetic complex. The chemical shifts of the nuclei of the paramagnetic complex vary linearly with inverse temperature (usually---see the section on temperature dependence below) as a result of the expansion of the Boltzmann terms.

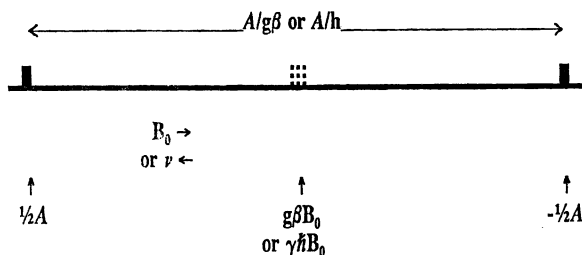


Figure 2. Expected NMR (or EPR) spectrum for the hydrogen atom, H•. The dotted line represents the position of the expected resonance if there were no hyperfine interaction, *i.e.*, the resonance of a diamagnetic analog.

Definition of Shifts. Chemical shifts, δ_{obs} , of paramagnetic complexes are the sum of the diamagnetic and paramagnetic contributions,

$$\delta_{\text{obs}} = \delta_{\text{dia}} + \delta_{\text{para}} \quad (1)$$

where δ_{para} is often also called the isotropic shift, δ_{iso} , or the hyperfine shift, δ_{hf} . The paramagnetic or isotropic or hyperfine shift is in turn composed of two contributions, the contact, δ_{con} , and dipolar, δ_{dip} , terms. (14) The dipolar shift is sometimes (especially in the field of NMR of paramagnetic metalloproteins) called the *pseudocontact shift*. The contact shift arises from electron spin delocalization or polarization *through bonds*, while the dipolar shift arises from spin delocalization *through space*. Let us look at each of these two contributions to the paramagnetic shift.

The contact shift, δ_{con} . The contact contribution to the paramagnetic shift arises from the Fermi contact interaction, which requires through-bond delocalization of the unpaired electron(s) to the nuclei of interest. The contact shift is expressed as (14,15)

$$\delta_{\text{con}} = A(\chi_{xx}/g_{xx} + \chi_{yy}/g_{yy} + \chi_{zz}/g_{zz})/6\gamma_N\hbar kT \quad (2)$$

or, if $\chi_{ii} = g_{ii}^2\beta^2S'(S' + 1)/3kT$ (*i.e.*, if second-order Zeeman contributions are small (24)),

$$\delta_{\text{con}} = A\langle g \rangle \beta S'(S' + 1)/18\gamma_N\hbar kT \quad (3)$$

In these expressions, A is the electron-nuclear hyperfine coupling constant, χ_{ii} = magnetic susceptibilities along each of the three principal axes, g_{ii} = principal g -values of the metal

complex, with g_{zz} often being oriented along or close to the molecular z-axis, $\langle g \rangle =$ average g-value, S' = total spin of the metal and may be slightly larger than S due to orbital contributions, β = Bohr magneton, k = Boltzmann constant, γ_N = magnetogyric ratio of the NMR nucleus. In order to determine the contact contribution to the paramagnetic shift, we must be able to separate off the dipolar or pseudocontact contribution, which may or may not be sizeable. This is often relatively easy to do, if we have assigned the spectrum, have measured the g-values by EPR spectroscopy, know the molecular structure, and can thus calculate the dipolar contribution, as discussed below.

For the complexes of interest, we often wish to determine the mechanism of electron spin delocalization and hence identify the orbital(s) that are involved in the bonding interactions that allow this delocalization. Either σ - or π -delocalization (or both) may occur for a given complex, and it is thus useful to know that the sign of A gives us immediate information as to the nature of the predominant means of spin delocalization: If A is negative, then according to equation 2 or 3 we will have a negative contact shift, or the resonance will appear at lower frequency ("upfield") than it would for the corresponding diamagnetic complex. It has been shown that if A_H is negative for a proton directly bound to a π system, then π delocalization predominates. (16,17) The McConnell equation (18),

$$A = Q\rho_C/2S \quad (4)$$

(where $Q \sim -63$ MHz for protons bound to a carbon that is a member of a π system (17), $Q \sim -39(\gamma_H/\gamma_C) = -155$ MHz for the same carbon in a π system (19,20), ρ_C is the unpaired electron density on the carbon of interest, and S is the total electron spin) is typically used to determine the amount of unpaired spin at particular carbons (ρ_C) having attached protons. If another complex can be made with methyl groups attached at the same carbon positions where the protons were attached in the original complex, then A_H for the methyl protons is positive, and the resonance will appear at higher frequency ("downfield") than that of the related diamagnetic complex. (16,17) For methyl protons, $Q \sim +70-75$ MHz (21), but for larger alkyl groups where restricted rotation may occur Q for the α -CH₂ protons is difficult to predict and may vary all the way from about 14 to 100 MHz according to a Karplus-like angular function (21), and will, for a given proton, undoubtedly vary with temperature.

If σ delocalization predominates, A_H is expected to be positive and the resonance will again appear at higher frequency ("downfield"). (16,17) Substitution of a methyl group for a proton in this case simply diminishes the magnitude of A_H , but still leaves it positive. (16,17) It should be noted that π delocalization may predominate at one position while σ delocalization predominates in another position of a macrocycle, as in the case of 5-coordinate high-spin Fe(III) porphyrins and chlorins, where *meso*-H shifts are negative and very large (π - delocalization) while pyrrole-H shifts are positive and again very large (σ -delocalization). (22,23)

The dipolar or pseudocontact shift, δ_{dip} . The dipolar contribution to the paramagnetic shift arises from the magnetic dipole interaction between the unpaired electron(s) and the nuclei of interest. The dipolar shift is expressed as (14,15)

$$\delta_{\text{dip}} = \{[\chi_{zz} - 1/2(\chi_{xx} + \chi_{yy})](3\cos^2\Theta - 1)/r^3 + (3/2)[\chi_{xx} - \chi_{yy}]\sin^2\Theta\cos 2\Omega/r^3\} \quad (5)$$

Again, if $\chi_{ii} = g_{ii}^2\beta^2S'(S' + 1)/3kT$,

$$\delta_{\text{dip}} \approx [\beta^2S'(S' + 1)/18kT]\{[2g_{zz}^2 - (g_{xx}^2 + g_{yy}^2)](3\cos^2\Theta - 1)/r^3 + 3[g_{xx}^2 - g_{yy}^2]\sin^2\Theta\cos 2\Omega/r^3\} \quad (6)$$

As for the contact shift, the χ_{ii} are the magnetic susceptibilities along each of the three principal axes, g_{zz} , g_{yy} , g_{xx} are the principal g-values of the metal complex, and in many (but not all) cases g_{zz} is along or close to the highest-symmetry molecular axis. Because the dipolar shift arises from a through-space interaction, the distance and angular relationship of the nuclei relative to the metal center are an important part of the expression, and are given by the polar coordinates r , Θ and Ω . If the structure of the complex is known and the g-values can be measured by EPR spectroscopy, then it is possible to calculate the approximate dipolar contribution to the isotropic shift. However, g-values measured at low temperatures may not be good measures of the magnetic susceptibilities at the temperatures at which NMR spectra are usually recorded because of additional contributions to the magnetic susceptibilities due to the second order Zeeman interaction (24) or to low-lying excited electronic states. This is the reason that χ_{ii} may not be proportional to g_{ii}^2/T , and thus equation 6 may not be directly derived from equation 5. Furthermore, at least in systems such as low-spin Fe(III) porphyrinates, the in-plane g-values g_{xx} and g_{yy} usually (but not always) rotate about the z-axis counter to the direction of rotation of a planar axial ligand away from the N-Fe-N axis (25), and this must be taken into account in systems that have at least one planar axial ligand in a fixed orientation that is not along the porphyrin nitrogens.

Alternatively, if the orbital of the unpaired electron is known well enough to conclude that there will be no contact shift at a given position or positions (most frequently due to there being a node or nodes in a π orbital used for spin delocalization), then it may be assumed that the observed paramagnetic shift at these position(s) is entirely due to the dipolar contribution. (16) If the structure is known, then the axial and rhombic geometric factors, $(3\cos^2\Theta - 1)/r^3$ and $(\sin^2\Theta\cos 2\Omega/r^3)$, respectively, can be readily calculated and used to calculate the dipolar shifts at other positions in the molecule by simple factoring from the known position(s). (26) In other cases, including tetrahedral Ni(II) and high-spin Fe(III), for example, the g-tensor is isotropic and the dipolar shift arising from equations 3 or 4 is zero, although there may be other higher-order terms that arise from zero-field splitting, as in the case of HS Fe(III) porphyrinates. (16)

It was implied above, perhaps unfairly, that our desire is to "get rid" of the dipolar contribution so that we can investigate the contact interaction. However, this is not always our desire; the dipolar shifts can in principle be used as the input data of equation 5 or 6 to *determine* the orientation of the magnetic axes of the molecule, and this is more and more frequently done for paramagnetic proteins. (27,28) Or, they could also be used to determine the structure of a group complexed to the metal, if the orientation of the magnetic axes is known, as has been done for many years by organic chemists who use lanthanide shift reagents to determine the structures of organic molecules containing Lewis base functional groups that can bind to the lanthanide complex. (29,30) However, to use the paramagnetic shifts of small molecules for either of these purposes, one must have certain knowledge that the *contact* contribution is negligible, *or*, if it is not, a certain

means of separating it! This is not a trivial problem, and it has been debated for some time with respect to the use of lanthanide shift reagents for structure determination of organic molecules. (31)

Relaxation Times: T_{1e} , T_{1M} , T_{2M} . All three of these relaxation times have important consequences for whether or not the resonances of interest will be detectable.

Electron spin relaxation time, T_{1e} or τ_s . How short does T_{1e} (τ_s) have to be in order to observe a single NMR resonance resulting from the two energy transitions of the nuclei of our complex, Figure 1? In a word, it must at the least be short compared to the inverse of the electron-nuclear hyperfine coupling constant of the nuclei of our complex, $T_{1e} \ll (A/h)^{-1}$, and there are additional factors that make it typically necessary that it be much shorter than that. (32) Organic free radicals typically have T_{1e} s of 10^{-5} to 10^{-7} s, which is too long to achieve this averaging, while metal complexes may have T_{1e} s ranging anywhere from 10^{-7} to 10^{-13} s. (33) The T_{1e} s and typical calculated ^1H linewidths of some metal ions whose complexes might be studied by NMR spectroscopy are listed in Table I (34); of these, ^1H NMR resonances have been detected for very few (if any) VO^{2+} complexes and one monomeric Cu^{2+} protein complex (35), and none have been reported for Mn^{2+} and Gd^{3+} complexes. On the other hand, both HS (high-spin) and LS (low-spin) Fe(III), Fe(II) and Co(II), HS Ni(II), Cr(II), and a number of Ln(III) complexes (36,37) of many types of ligands have been well studied by NMR spectroscopy. In addition, in certain cases, such as tetrahedral Cu(II) (35,38), or many metals involved in dimeric or multimeric metal clusters, it is possible to push the limits of the generalizations summarized in Table I because there are additional pathways available to shorten electron spin relaxation times (energy level manifolds of antiferromagnetically coupled multi-metal complexes, different symmetries for complexes that create low-lying energy levels, dynamic Jahn-Teller distortions, etc.). In a word, it is often not a good idea to *assume* that it is impossible to detect a resonance, at least for borderline cases such as VO^{2+} , Cu^{2+} , Ti^{3+} and others.

Nuclear spin-lattice relaxation time, T_{1M} . The longitudinal or spin-lattice relaxation time of the nucleus of the paramagnetic complex under investigation is typically abbreviated T_1 ; the general subscript M indicates the T_1 of the nucleus of interest in the presence of a paramagnetic metal. T_1 s are typically measured by the Inversion-Recovery experiment, for which the pulse sequence is π - t_1 - $\pi/2$ -Acq, and the t_1 delay is incremented in a series of separate experiments, the intensity of the resulting peaks is plotted as a function of the t_1 delay, and this plot is used to determine the T_1 of each resonance, as described in a number of textbooks. (39,40) T_1 s should be measured before 2D experiments are attempted, in order to allow the investigator to optimize the experiment, as will be discussed below. Usually, those wishing to obtain NOESY and ROESY spectra of paramagnetic complexes would prefer to have their T_1 s be as long as possible, in order to allow time for NOEs to build up, and to achieve this it is always a good idea to purge the solution sample with argon or nitrogen in order to remove dissolved oxygen, which, because it is paramagnetic, shortens T_1 s and T_2 s by spin exchange.

Table I. Electronic Relaxation Times for Various Metal Ions and Nuclear Line Broadening Due to Dipolar Relaxation.^{a,b}

Metal Ion (Hz)	T_{1e} or τ_s (s)	Nuclear Line Broadening
Ti ³⁺	10^{-9} - 10^{-10}	500-3000
VO ²⁺	10^{-8} - 10^{-9}	3000-20,000
V ³⁺	5×10^{-12}	100
V ²⁺	5×10^{-10}	9000
Cr ³⁺	5×10^{-10}	9000
Cr ²⁺	10^{-11}	300
Mn ³⁺	10^{-10} - 10^{-11}	300-3000
Mn ²⁺	10^{-8} - 10^{-9}	40,000-200,000
Fe ³⁺ (HS)	10^{-10} - 10^{-11}	400-5000
Fe ³⁺ (LS)	10^{-11} - 10^{-12}	10-40
Fe ²⁺ (HS)	10^{-12}	70
Co ²⁺ (HS)	10^{-11} - 10^{-12}	50-200
Co ²⁺ (LS)	10^{-9} - 10^{-10}	500-3000
Ni ²⁺	10^{-10} - 10^{-12}	25-1000
Cu ²⁺	1 - 3×10^{-9}	3000-9000
Ru ³⁺ (LS)	10^{-11} - 10^{-12}	10-40
Re ³⁺	10^{-11}	100
Gd ³⁺	10^{-8} - 10^{-9}	60,000-400,000
Other Ln ³⁺	10^{-12}	30-100

a) Adapted from reference 32. b) For ¹H, $r = 5 \text{ \AA}$, $H_0 = 2.35 \text{ T}$.

Although both contact (through bonds) and dipolar (through space) relaxation effects may be present, the most common situation is that dipolar relaxation dominates, especially for nuclei that are not directly connected to the metal through π bonds. Such dipolar relaxation results from dipolar coupling between the electron spin and the nuclear spin of the nucleus of interest, within a given molecule, which is not averaged to zero by rapid rotation of the molecule. (32) At the risk of vastly over-simplifying the situation, we may say that in many cases the inverse relaxation times, or relaxation rates, $R_{1M} = T_{1M}^{-1}$ are proportional to τ_c/r^6 , where τ_c is the rotational correlation time of the molecule. A very rough rule of thumb is that

$$\tau_c \sim 4\pi\eta a^3/3kT \sim \text{MW in picoseconds.} \quad (7)$$

where η is the viscosity of the solvent, a is the radius of the molecule, and T is the temperature (K). A more detailed look at the dependence of R_1 on molecular correlation time, however, shows that the τ_c dependence is actually $\tau_c/[1 + (\omega_1 - \omega_s)^2\tau_c^2]$ (32), (or approximately $\tau_c/[1 + \omega_1^2\tau_c^2]$ (32)) where ω_1 is the nuclear Larmor frequency and ω_s is the electronic Larmor frequency. Thus, T_1 s may differ if measurements are made on instruments of different field strength. Clearly, the interested reader should consult chapters (32,41) and books (15,42) on the topic for more complete information! The important point regarding the basic τ_c/r^6 dependence of R_1 is that the resonances of

protons closest to the metal center will typically have the shortest T_1 s and thus their connectivities will be hardest to detect in 2D NMR experiments. Also, because R_1 s depend upon the molecular correlation time, which in turn depends upon molecular size, solvent viscosity and temperature (equation 7), changes in any or all of these factors may make significant changes in the T_1 s, and one may wish to vary one or more of these parameters in order to obtain T_1 s of the length necessary to successfully obtain NOESY spectra, for example.

Nuclear spin-spin relaxation time, T_{2M} . The transverse, or spin-spin relaxation time of the nucleus of interest in a paramagnetic metal complex is T_2 , for which the inverse (R_2) is also often proportional to τ_c/r^6 if dipolar relaxation dominates. But the more detailed dependence on correlation time τ_c has a different relationship involving nuclear and electronic Larmor frequencies than for T_1 : ($\tau_c + \tau_c/[1 + (\omega_I - \omega_S)^2\tau_c^2]$). (32) Hence, T_2 s vary differently with magnetic field strength than do T_1 s, and again, the interested reader should consult other sources (15,32,42) for more complete information. T_2 s are typically measured using the CPMG (Carr-Purcell-Meiboom-Gill) spin-echo experiment, a series of $\pi/2$ - t_1 - π -Acq sequences (39,40), but can be roughly estimated from the linewidth, assuming that the lineshape of the resonance is Lorentzian,

$$R_2 = T_2^{-1} \sim \pi(LW) \quad (8)$$

where LW is the linewidth at half-height, in Hz. (43) The contact interaction may also affect R_2 , in which case an additive contribution proportional to $S(S+1)A^2\tau_c$ must be added to the dipolar contribution. (32) For systems having multiple unpaired electrons, Curie relaxation (an additional kind of dipolar relaxation) may also contribute a term proportional to $B_0^2 S^2(S+1)^2\tau_c/T^2r^6$ to the linewidths (32), which *could* cause the resonances of such complexes to be broader at higher magnetic fields. However, for $S = 1/2$ systems, where the small value of S usually means that Curie relaxation is not an important contribution (44), the benefits of higher magnetic field (better S/N) always outweigh any (usually undetectable) contribution from Curie relaxation. Peak overlap is usually not a problem for paramagnetic complexes, so if the S/N is adequate, lower-field (200-300 MHz) spectrometers will provide just as well resolved spectra as will higher-field (500 or 600 MHz) spectrometers. However, the spectroscopic signature of any kinetic process may be strongly affected by the frequency of the NMR spectrometer, because NMR-active chemical exchange processes depend on the *difference in frequency*, $\nu_A - \nu_B$, in Hz, of the two resonances (45); this difference triples on going from 200 to 600 MHz, so a system that is in fast exchange at 200 MHz may be in slow exchange at 600 MHz!

The bottom line of the above discussion of T_2 s is that they are usually shortest for the nuclei closest to the unpaired electron(s) of the metal, as is also true of T_1 s. An example of the effect of distance of the nucleus of interest from the metal center is shown in Figure 3, where a Mo(V) complex is appended to one of the phenyl rings of a low-spin ($S = 1/2$) iron(III) tetraphenylporphyrinate complex. (46) Mo(V), like V(IV), Table I, has very long electron spin relaxation times, T_{1e} , and hence none of the resonances of the hydrotris-(3,5-dimethylpyrazolyl) borate moiety or the catecholate connecting ring are detected. Furthermore, the eight pyrrole-H signals of the TPP ligand are differentially broadened with the Mo(V) complex appended to the 2,3-phenyl positions, depending

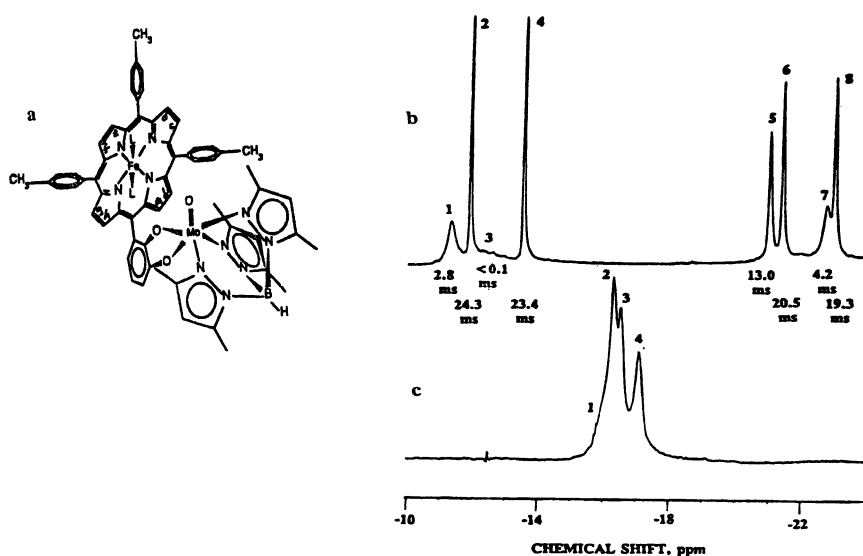


Figure 3. (a) Structure of the Mo(V)-appended iron tetraphenylporphyrinate, where the LMoO moiety may be bound either to the 2,3- or 3,4-positions of the catecholate ring; (b) the pyrrole-H region of the 1D ¹H NMR spectrum of the 2,3-isomer, recorded in CD₂Cl₂ at -296 K, showing the large differences in linewidths of the eight pyrrole protons; (c) the pyrrole-H region of the 1D ¹H NMR spectrum of the 3,4-isomer, showing that resonance 1 is much broader than the other three. Reprinted from reference 46 with permission from the American Chemical Society.

upon their distance from the Mo(V). This effect can be used to help assign the pyrrole resonances: We know, just from a quick inspection of Figure 3, that these distances increase in the order H₃<H₁<H₇<H₅, while the other four protons are at significantly greater distances from the Mo(V) center. T₁s measured by inversion-recovery methods are in line with the impressions gained from the relative linewidths, and can be used to quantitatively estimate the distances of each of the four closest protons to the Mo(V) center, in line with the expected r⁻⁶ dependence of the R₁s. The first four can then confidently be assigned to H_a, H_b, H_c and H_d, respectively. (46) For the molecule in which the Mo(V) center is appended to the 3,4-phenyl positions (Figure 3c), only four resonances are observed, and it is clear that H₁ is the closest to the Mo(V) center. (46,47) Differential linewidths are also quite useful in assigning the NMR spectrum of the dicopper complex (48) shown in Figure 4, and other dicopper complexes studied recently. (49)

An example of the effect of complex correlation time τ_c on T₁⁻¹ and T₂⁻¹ for a water-soluble Fe(III) tetraphenylporphyrinate complex (50) is shown in Figure 5, where the correlation time was varied at a given temperature by nearly a factor of 100 by adding deuterated glycerol to D₂O, up to 80% glycerol. As is clear from Figure 5, T₂ varies much more strongly with τ_c than does T₁. (50)

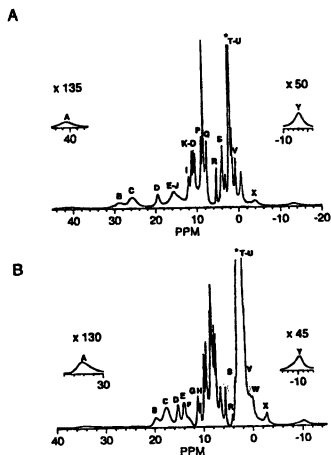
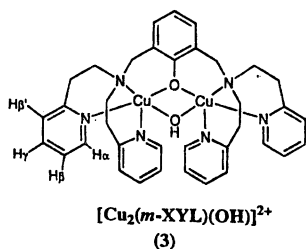
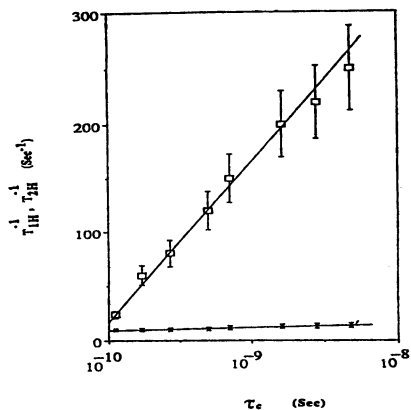


Figure 4. ¹H NMR spectra of the binuclear complex **3** in CD₃CN (A) at 25 °C and (B) at -20 °C. Spectra were referenced to the residual protic solvent signals (*) at 1.92 ppm for acetonitrile. Reprinted from reference 48 with permission of the American Chemical Society.

Figure 5. Plot of the pyrrole ¹H relaxation rates, T_{1H}⁻¹ (closed symbols) and T_{2H}⁻¹ = π(LW) (open squares), of [(TPPS)Fe^{III}(CN)₂] as a function of the molecular correlation time obtained through alteration of solvent viscosity. The data were obtained at 360 MHz at 25 °C from a variety of mixed solvents ranging from neat D₂O (least viscous) to 80% glycerol-d₈ (most viscous). The effective viscosity is converted to τ_c for the complex by equation 4. Reprinted from reference 50 with permission of the American Chemical Society.



Temperature Dependence of Paramagnetic Shifts. It was mentioned in the Introduction that the paramagnetic shifts of the nuclei of interest follow the Curie law, $\delta_{\text{para}} \propto 1/T$. However, there is some looseness with which the $1/T$ dependence of δ_{para} is termed "Curie behavior." Furthermore, the terms "non-Curie" and "anti-Curie" are now in use by various investigators, and the same behavior is not always described by the same name by all investigators. Curie behavior implies that:

$$\delta_{\text{para}} = F/T \quad (9)$$

with the paramagnetic shift extrapolating linearly to zero at infinite temperature ($1/T = 0$). F is the Curie factor, which must be determined in each case, since it will depend on

the mechanism of electron spin delocalization. This assumes, of course, that one *knows* the diamagnetic shifts of the nuclei of interest and has subtracted them from the observed shifts, δ_{obs} . If one has corrected for the diamagnetic shifts and the intercepts are still non-zero at $1/T = 0$, then terms such as "Curie" or "almost Curie" are sometimes used if the intercepts are small, and "anti-Curie" if the intercepts are very large, especially if they are positive for a resonance having negative slope, or vice-versa. Sometimes the temperature dependence is obviously non-linear (a euphemistic term indicating markedly curved), and this type of behavior is often called "non-Curie." No matter what the shape of the plot of δ_{para} vs. $1/T$, such plots are universally called "Curie plots."

Very often the deviations from equation 9 result from low-lying thermally-accessible excited electronic states of the complex. This has long been understood for dimeric or multimeric metal complexes in which the metals are either ferromagnetically or antiferromagnetically coupled, and the Bleany-Bowers expressions have often been used to explain curved or apparent "anti-Curie" temperature dependences for such complexes. (51) More recently, we have noted that even a monomeric metal complex may have a thermally-accessible excited state that can give rise to apparent "non-Curie" or "anti-Curie" temperature dependence. (52) The examples that we have published thus far all involve low-spin Fe(III) porphyrinates which have either a covalently attached axial ligand or one which is crowded into a particular orientation and prevented from rotating freely. (52) Since the spin delocalization of low-spin Fe(III) porphyrinates involves Por-Fe π donation from the filled e-symmetry $3e(\pi)$ orbitals, and since the fixed planar axial ligand plane imposes its nodal plane orientation onto the porphyrin ring, the $3e(\pi)$ orbital preferred for spin delocalization to the half-filled d_{π} orbital is that which has the same orientation of its nodal plane as does the axial ligand. However, excitation of one of the paired electrons from the *other* $3e(\pi)$ orbital, which is oriented at 90° to the one just mentioned, produces an excited state that is likely not much higher in energy---perhaps 200-600 cm^{-1} higher, depending on the crystal field strength of the axial ligands and the exactness to which their orientation is fixed. (52) Because the two $3e(\pi)$ orbitals predict opposite-sized orbital electron density coefficients at a given carbon atom (Figure 6 left), this thermal excitation can lead to curvature in the Curie plot if the NMR spectra are acquired over a wide enough temperature range, or simply to non-zero intercepts of the Curie plots if linear dependence is assumed. The general equation that describes such behavior is simply an expansion of the Curie law to include a Boltzmann population of a thermally-accessible excited state (52):

$$(\delta_{\text{para}})_n = (1/T) \{ [W_1 F_{n,1} + W_2 F_{n,2} e^{-\Delta E/kT}] / [W_1 + W_2 e^{-\Delta E/kT}] \} \quad (10)$$

where W_1 and W_2 are the weighting factors for the ground and excited state ($= 2S+1$), F_n are the Curie factors for each nucleus n in the ground (1) and excited (2) states, and ΔE is the energy difference between the ground and excited states. The Curie factors F_n encompass all of the terms of equations 2 or 3 and 6 *except* the inverse temperature dependence for each proton (or carbon) of interest. Shokhirev has created a computer program (53) that fits the temperature dependence of one or a series of lines, imposing a zero intercept for all, and provides, as output, the energy separation between the ground and excited state and the Curie factors (or electron densities ρ_C) for each resonance in the ground and excited state. (52) For the curved lines of Figure 6 that result from the best

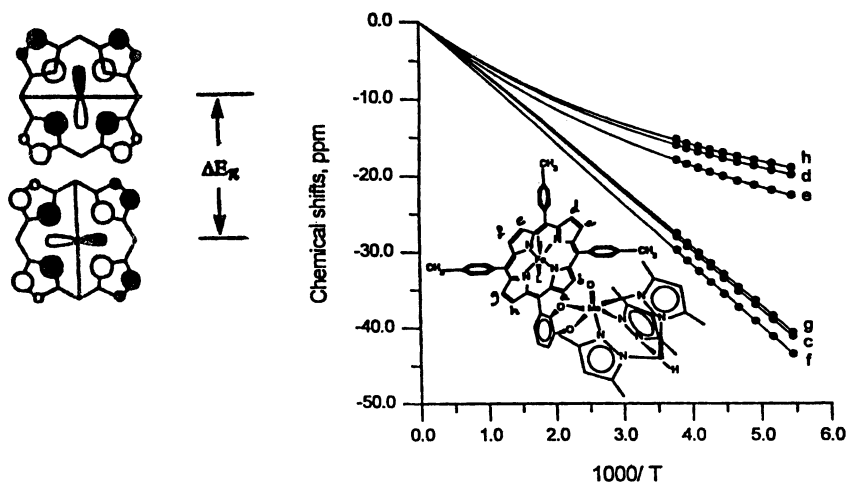


Figure 6. Left: Diagram of the two $3e(\pi)$ orbitals involved in electron donation to the hole in the d_{xz}, d_{yz} orbitals of low-spin d^5 porphyrinates, assuming the axial ligand lies along the horizontal *meso* positions. Right: Temperature dependence of the six sharpest pyrrole-H resonances obtained from fitting of equation 10 to the data. Reprinted from reference 52 with permission of the American Chemical Society.

fit of equation 10, the intercepts of all lines *would* have been non-zero if straight lines through the measured points had been plotted. The energy separation obtained for this system is about 210 cm^{-1} , and the electron densities ρ_C (52) are very similar to those calculated from a simple Hückel program. (54) (As might be expected for such a fitting procedure, excited state coefficients ρ_C are much less accurately determined than ground state coefficients.) Similar analysis of several heme proteins has also provided reasonable energy separations and orbital coefficients. (20,52)

Equation 10 actually predicts the very same temperature dependence as predicted by the Bleany-Bowers expressions for a ground state of one spin multiplicity and an excited state of a different spin multiplicity. (51,52)

Another source of "non-Curie" temperature dependence is the less-than-rapid rotation on the NMR time scale of longer-chain aliphatic groups. Ethyl groups in Fe(III) octaethylporphyrinates (55) are typical examples of this variable rate of rotation, which leads to a variable McConnell Q value as a function of temperature. There is no simple way to treat such systems theoretically, and thus the non-Curie temperature dependence is not very helpful in determining spin densities, etc.

Experimental Methods

Simple 1D NMR Spectroscopy of Paramagnetic Complexes. The typical experience of the novice investigator is that the first attempt at obtaining the NMR spectrum of a paramagnetic complex results in the observation of mainly the resonances of the excess

free ligand and of solvent impurities. Besides removing these from the sample (56), the experimenter must know *how* to obtain a meaningful spectrum. In general this means adjusting the spectral width and/or number of data points in the FID so that the acquisition time is of the order of $2-3T_2$ (57), where T_2 is the transverse relaxation time of the nuclei in question. (Acquiring noise after the FID has dropped to nearly zero simply reduces the S/N of the transformed spectrum.) This, *of necessity*, will mean that the digital resolution will appear to be *terrible*. (A spectral bandwidth of 20 kHz and 1024 data points will produce an acquisition time of 50 ms, but the digital resolution will be 39 Hz/point.) Zero-filling one or several times will improve the digital resolution, and the typical broadness of the lines of paramagnetic complexes does not require high digital resolution.

Since T_1 s are much shorter for paramagnetic complexes than for their diamagnetic analogs, the relaxation delay (58) can be shortened dramatically. The combination of short acquisition times of $2-3T_2$ and short relaxation delays of $\sim 1.3T_1$ typically makes it possible to obtain at least ten times as many transients for a paramagnetic complex in a given period of time as for the diamagnetic analog. Further enhancement of very broad peaks can be achieved by varying the amount of line broadening applied to the window function before Fourier transformation. If a line is 400 Hz wide, a line broadening exponential multiplication factor of 100-200 Hz before Fourier transformation would certainly help to "bring it out of the baseline," without dramatically distorting the lineshape, and even peaks that are 20-50 Hz wide benefit greatly from application of a exponential line broadening factor of about 1/4 their width. A range of different exponential line broadening factors may be necessary to optimize the chances of detection of all signals. Note that the default setting for many "automatic" 1D NMR macros is often $LB = 0.1$ Hz, a value that is guaranteed to produce the spectrum of the diamagnetic impurities!

In cases of the most extremely broadened lines, isotopic substitution (deuterium for protium) produces significantly sharper ^2H lines that are easier to detect than the broader ^1H lines. (2) Although there are only $\gamma_{\text{D}}/\gamma_{\text{H}}$ or 1/6.48 as many Hz/ppm in the ^2H NMR spectrum, the resonances are $(\gamma_{\text{H}}/\gamma_{\text{D}})^2$ or 42 times sharper, which significantly aids in detecting of very broad resonances. The chemical shifts for ^1H and ^2H are essentially identical, aside from an almost undetectably small isotope shift. Having detected the ^2H signal, it is then usually possible to go back to the original complex and optimize the 1D experiment to allow detection of the very broad ^1H signal, if desired.

1D NOE Difference Spectroscopy. The design of the experiment can be summarized as:

Expt. (1):	Irradiate $f_A - \pi/2$ -Acq
Expt. (2):	Irradiate $f_B - \pi/2$ -Acq

where f_A is the frequency of the resonance of interest and f_B is an off-resonance frequency not too far away from f_A . Experiments 1 and 2 are usually acquired in an interleaved manner of 16 or 32 transients each, in order to minimize artifacts due to instrumental noise, etc. The FID (or transformed spectrum) of experiment 2 is then subtracted from that of experiment 1 (or vice-versa). The irradiated resonance will then appear as a large negative (or positive) peak, while resonances to which the resonance at f_A is connected

by the nuclear Overhauser effect will appear as smaller, either positive or negative peaks, depending on the rotational correlation time of the molecule. (59) Exactly this procedure is also used for the Saturation Transfer experiment (60), which differs only in name and in the source (chemical exchange) of the small peaks. (The small peaks have the same phase as the irradiated peak in this case.) The first report of a saturation transfer experiment on a paramagnetic complex (cytochrome *c*) was by Redfield and Gupta. (61)

While several other variations on the 1D NOE difference experiment can be performed (truncated driven NOE (TOE), transient NOE), the most common experiment used for paramagnetic complexes is the steady-state NOE experiment, where, as in the Saturation Transfer experiment, the resonance of interest is irradiated for at least $10T_1$ to allow buildup of the steady-state NOE signals. Because the sign of the NOE changes as the rotational correlation time τ_c increases (62), one could *definitely* be so unlucky as to have NOE = 0, if $\omega\tau_c = 1.12$, where ω is the spectrometer frequency in angular units ($2\pi\nu$), (Figure 7) for relatively small inorganic complexes.

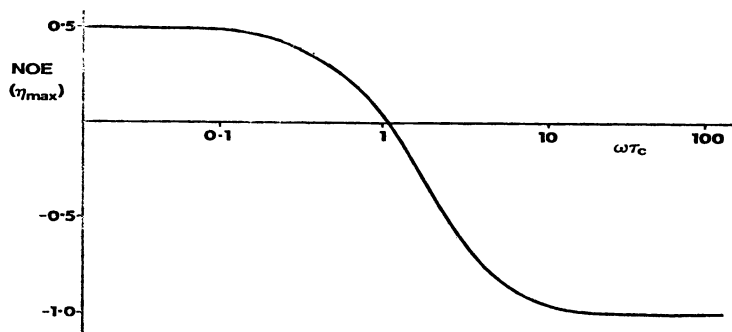


Figure 7. Dependence of maximum homonuclear NOE enhancement on $\omega\tau_c$. Note the logarithmic scale of $\omega\tau_c$; NOE = 0 when $\omega\tau_c = 1.12$. Reprinted from reference 59 with permission of John Wiley and Sons.

Because of the approximate relationship between molecular weight and τ_c (equation 7), we can predict that at 300 MHz in typical solvents at room temperature, the zero-crossing point could be at about a molecular weight of about 590, while at 500 MHz it *could* be at about 350 g/mol. While these particular values will vary with the degree of tight solvation of the complex, solvent viscosity and temperature, and may also be inaccurate in number due to the approximate nature of equation 7 or to the particular shape of the molecule, the point is that the inorganic chemist should use the following strategies to insure that he/she is not at the NOE = 0 point: 1) work with *really* small molecules at high temperatures and low magnetic fields (+NOEs), or 2) work in viscous solvents at low temperatures (-NOEs). The latter is obviously much easier to achieve, for many metal complexes are not stable at high temperatures due to ligand dissociation. Mixed solvents such as D_2O /glycerol- d_8 , or DMSO- d_6 or toluene- d_8 at low temperatures are three possibilities for achieving this. High magnetic field (a 500 or 600 MHz spectrometer) will further help to insure that NOEs are negative.

The first example of an NOE difference spectrum of a low-spin Fe(III) porphyrin were reported by Dixon and coworkers in 1985 (63), Figure 8. Later studies extended this work and were able to show not only the connectivities of the protoporphyrin ring, but also the conformation of the vinyl groups (64,65); in Figure 9, left side, trace d, are shown the NOEs between the 3-methyl and the α -meso and 4- β -vinyl protons, indicating that the 4-vinyl group is actually, on the average, flipped by 180° about the pyrrole-C $_{\alpha}$ bond from the conformation shown. NOESY spectra confirm this structure (Figure 9, right). Figure 9, left side, trace b, illustrates the fact that low solvent viscosity precludes the observation of NOEs at the field strength (360 MHz) and temperature (30 °C) used. NOE difference spectra were also used to assign part of the resonances of the Mo(V)-appended low-spin iron(III) porphyrinate, whereas 2D NOESY spectra showed no cross peaks. (46) Steady-state NOE difference spectroscopy is often more sensitive than NOESY because the latter rely upon transient NOEs, which will of necessity be weaker for complexes with very short T $_{1}$ relaxation times. (59) However, it suffers from irradiation spillover if there is significant spectral crowding. Note that irradiation times ($\sim 10T_{1}$) will be much shorter for paramagnetic complexes than for their diamagnetic analogs.

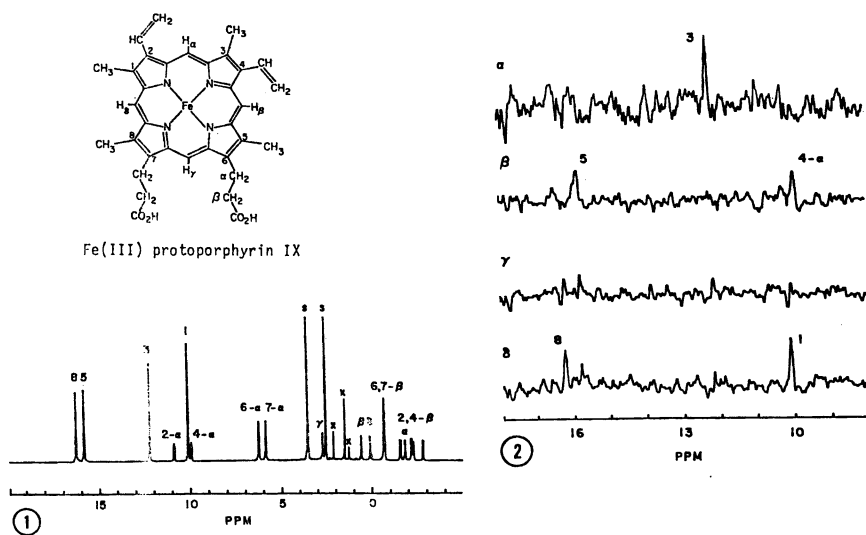


Figure 8. 1) 1D ^1H NMR spectrum of bis-(cyano)Fe(III) protoporphyrin IX in DMSO- d_6 with traces of H_2O at 30 °C, recorded at 200 MHz. Peak assignments indicated on the spectrum refer to the structure inset above. The symbol *s* indicates solvent resonances, *x* indicates impurities. 2) NOEs resulting from irradiating in turn each of the four *meso*-H resonances (-2 to +3 ppm), showing NOEs from each *meso*-H to the neighbor heme methyl(s) and α -vinyl-H. Note that only the δ -*meso*-H can have NOEs to two methyls, and that only the γ -*meso*-H can have NOEs to none of the four methyls. Reprinted from reference 63 with permission of Academic Press.

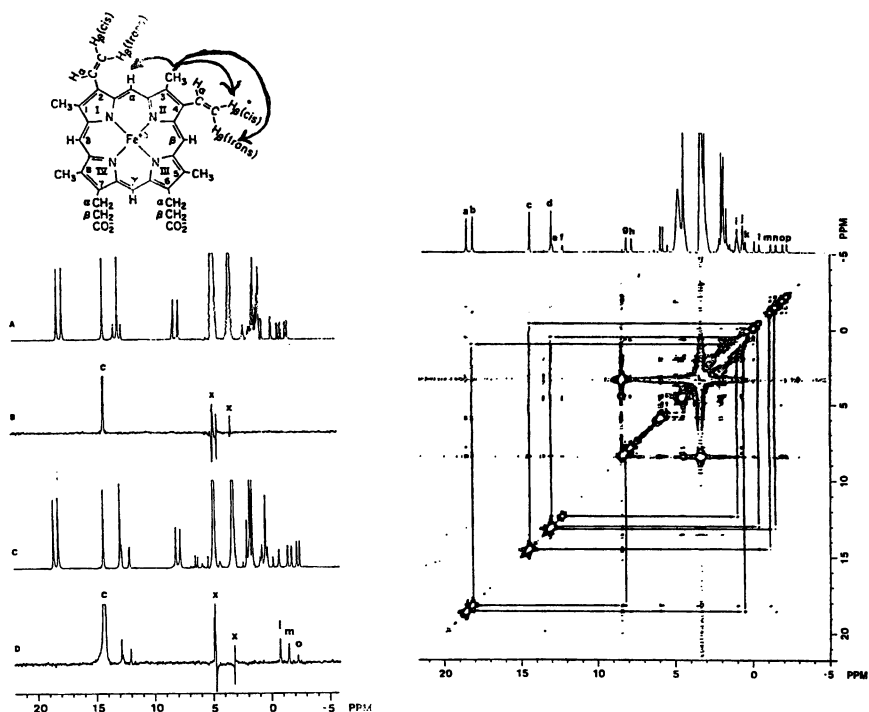


Figure 9. Left: (A) Control ^1H NMR spectrum of 2 mM protohemin-bis-cyanide in methanol- d_4 at 30 $^\circ\text{C}$, recorded at 360 MHz. (B) NOE difference spectrum which results from saturation of the 3- CH_3 (peak c) in methanol- d_4 ; only artifacts are observed. (C) Control ^1H NMR spectrum of 2 mM protohemin-bis-cyanide in ethylene glycol- d_6 . (D) NOE difference spectrum resulting from saturation of the 3- CH_3 (peak c) in ethylene glycol- d_6 yielding NOEs to the α -*meso*-H (peak l), 4-vinyl- H_β (*trans*) (peak m), and 4-vinyl- H_β (*cis*) (peak o). Right: 2D NOESY spectrum of 2 mM hemin-bis-cyanide in ethylene glycol- d_6 at 30 $^\circ\text{C}$. The 1D spectrum is given above the contour plot. The arrows illustrate the detected connectivities: 8- CH_3 - δ -*meso*-H-1- CH_3 -2-vinyl- H_β (*trans*)-2-vinyl- H_α - α -*meso*-H-3- CH_3 -4-vinyl- H_β (*trans*)-4-vinyl- H_α - β -*meso*-H-5- CH_3 -6- α - CH_2 . While the 6- α - CH_2 to 7- α - CH_2 connectivity is not observable because of the intense diagonal peak, the 7- α - CH_2 is assignable based on its connectivity to the 8- CH_3 . Numerous artifacts arising from the intense solvent resonances are observed. Carrier noise is apparent at 8.3 ppm. Peak assignments: (a) 8- CH_3 , (b) 5- CH_3 , (c) 3- CH_3 , (d) 1- CH_3 , (e) 2-vinyl- H_α , (f) 4-vinyl- H_α , (g) 6- α - CH_2 , (h) 7- α - CH_2 , (i) β -*meso*-H, (j) 6,7- β - CH_2 , (k) δ -*meso*-H, (l) α -*meso*-H, (m) 4-vinyl- H_β (*trans*), (n) 2-vinyl- H_β (*trans*), (o) 4-vinyl- H_β (*cis*), (p) 2-vinyl- H_β (*cis*). The γ -*meso*-H, which is buried under the strong solvent resonance at about 3 ppm, is not observed. Reprinted from reference 65 with permission of Academic Press.

NOESY and ROESY Experiments. Both the laboratory frame and rotating frame Overhauser experiments are extremely valuable in obtaining information about close through-space distances between nuclei in paramagnetic complexes, as well as chemical exchange information. (59,66,67) The drawback of the NOESY experiment is that the NOEs will be zero at some temperature/solvent viscosity, as indicated by Figure 7. The same drawback does *not* hold for the ROESY experiment, which is *extremely* valuable for investigating molecules of small or intermediate size! For large molecules, such as proteins, the ROESY experiment has been said to be less useful than the NOESY experiment (6), but the opposite is true for smaller molecules such as many inorganic complexes. (68)

The pulse sequences for the two experiments are similar (59):

$$\text{NOESY:} \quad \text{RD} - \pi/2 - t_1 - \pi/2 - \tau_m - \pi/2 - t_2 \quad (11)$$

$$\text{ROESY:} \quad \text{RD} - \pi/2 - t_1 - \pi/2 - \text{SL}(\tau_m) - \pi/2 - t_2 \quad (12)$$

where RD = relaxation delay $\sim 4-5T_1$, $\tau_m \sim T_1$ for the NOESY experiment or somewhat shorter (about $1/2T_1$ (59)) for the ROESY experiment, and the acquisition time $t_2 \sim 2-3T_2$. (Equation 12 is not the simplest ROESY sequence, but is rather the one recommended by Griesinger and Ernst (69), which uses a pulsed spin-lock field that quells the transfer of spin through most J coupled protons and hence suppresses most TOCSY effects.) The number of t_1 increments used is sometimes no more than 256, or even half or a quarter of that number, but this number can be adjusted: The reason for using a relatively small number of t_1 increments is that for the later experiment blocks, in which the t_1 delay is longer, less and less signal will exist at the time of detection (during t_2), and hence mainly noise will be acquired in these blocks. The data sets can always be zero-filled once or several times before Fourier transformation in the t_1 domain, in order to improve digital resolution. Another alternative is to use a larger number of t_1 increments (512, 1028 or even more) and then terminate the experiment either when the FID in the t_1 dimension has decayed to zero, and then zero-fill, or *before* the FID in the t_1 dimension has decayed to zero, and then use the linear prediction software available on newer spectrometers and FELIX to fill in the remaining data blocks.

All of the above considerations make for a very rapid 2D NOESY or ROESY experiment for a paramagnetic complex, compared to one carried out on a diamagnetic compound. The simpler, original sequence for the ROESY experiment introduced by Bothner-By and coworkers was originally called the CAMELSPIN experiment. (70) Buildup of TOCSY coherences (originally called HOHAHA, Homonuclear Hartmann-Hahn (71)) can be suppressed by transmitter offset. (71,72) All of the same considerations as discussed above for the NOESY experiment apply to the ROESY experiment. In addition, the rule of thumb is that the strength of the B_1 field for the spin lock (SL) should be about equal to the spectral bandwidth, but for paramagnetic complexes this usually makes the B_1 field quite large (≥ 12 kHz) (68), which is in the range used for TOCSY experiments on diamagnetic complexes. (66,67) However, we have found that TOCSY effects are weak for paramagnetic complexes at B_1 fields of about 10 kHz, especially if the transmitter is offset from the center of the spectrum (by increasing the spectral width), and more than twice as large values of the B_1 field (25

kHz) are required to observe mainly TOCSY cross peaks, and even at those large spin-lock fields there may still be some ROESY effects present. (73) ROESY spectra usually suffer from less two-or-more-step NOEs than do NOESY spectra, although we have observed several 2-step NOEs in a recent study of a paramagnetic complex. (68) The only disadvantage of the ROESY experiment for small to intermediate-sized molecules is the difficulty in phasing the 2D spectra. (74) This difficulty can be minimized with practice, especially if FELIX software is used. Baseline roll can be minimized by adjusting the delay between the last pulse and the first digitized data point.

Initially, most investigators tend to try the magnitude NOESY experiment, which is very forgiving in terms of experiment setup. However, the phase cycling used for a magnitude experiment (4-step) produces twist-phase peaks in the 2D spectrum (39), and the twist-phase problem is then solved by using a fairly large line-broadening function, and then carrying out a magnitude calculation. (39) Such spectra typically give "intense"-looking, broad cross peaks (54,75), which, however, may derive quite a bit or all of their intensity from overlap of the wings of the (broad) diagonal peaks. Hence, *false* cross peaks arising from overlap of the wings may be detected and believed to be real. This has happened in our own research program, where apparent NOE cross peaks, between the very resonances that we expected *should* give NOE cross peaks, were reported as real. (54) We have not been able to detect these cross peaks in phase-sensitive NOESY spectra (44), where full (usually 16-step) phase cycling is used, and we have shown by measurements of the NOE buildup curve for a related complex and by calculations (44) that the protons which gave the apparent NOE cross peaks in the earlier study are too far apart ($>5\text{\AA}$) to give a measureable NOE cross peak with the solvent viscosity used in that study (CD_2Cl_2 at -40 to -50 °C). (54) In general, if the T_1 s are less than 10 ms, the likelihood of observing an NOE for protons that are 2.5\AA or more apart for a compound in a non-viscous solvent is very small to negligible. (44) Hence, although we are still convinced that the peak assignments reported earlier are correct, based upon the molecular orbital pictures that had been derived for each of the complexes (54), we cannot *prove* the assignments by NOESY (or ROESY or 1D NOE difference spectroscopy) experiments, because the T_1 s of the protons involved are just too short to allow buildup of NOEs. Thus, *magnitude*-NOESY cross peaks can be *extremely* misleading, and we recommend that magnitude experiments in general, whether NOESY or COSY, not be used, and that spectra *never* be symmetrized!

If the T_1 s of the two protons between which an NOE is expected are very different, then the cross peaks may be extremely weak or undetectable. Reference 6 provides a useful table of calculated cross peak intensities for two protons at a fixed distance where the T_1 s differ by varying amounts.

WEFT-NOESY, WEFT-1D and super-WEFT (WEFT = water-suppressed equilibrium Fourier transform) sequences can be used to suppress intense resonances from diamagnetic protons of the solvent, large ligand or protein. (35) Such intense resonances tend to fill up the ADC (analog-to-digital converter), leaving little chance to properly digitize the frequencies of broad, low-intensity resonances from protons that are close to the paramagnetic center. By nulling the signals of the diamagnetic resonances, the paramagnetically relaxed protons become much more clearly observed, as was earlier demonstrated for a heme protein (76), and more recently for the Cu(II) protein amicyanin. (35) The procedure is to give a 180° pulse to the protons and then wait for the time

necessary for the magnetization of the slow-relaxing diamagnetic protons to reach its null point, while the fast-relaxing protons will have rapidly returned to equilibrium. Then the desired pulse sequence, optimized for the expected T_1 s of the protons of interest, is applied. The delay between the 180° pulse and the 90° pulse at the start of the desired pulse sequence that produces the smallest signals from the diamagnetic protons is usually best found by trial and error. For the amicyanin case, this optimum delay was found to be 40 ms, and the acquisition time used was 50 ms, giving a repetition rate of 10 s^{-1} for the 1D spectrum; for the NOESY spectrum the optimum delay was found to be 24 ms, the acquisition time used was 25 ms, giving a repetition rate of 17 s^{-1} . For 4096 transients for each of the 256 t_1 increments, the NOESY/EXSY spectrum was acquired in 17 h. (35)

In addition to through-space NOEs, the NOESY and ROESY experiments are also sensitive to chemical exchange. For molecules on the left side of the zero-crossing point of Figure 7 ("small" molecules), NOEs are positive and NOE cross peaks are of opposite sign to the diagonal peaks, while chemical exchange cross peaks are the same sign as the diagonal peaks. In comparison, for molecules on the right side of the zero-crossing point of Figure 7 ("large" molecules), NOE cross peaks are of the same sign as the diagonal peaks, and hence cannot be distinguished from chemical exchange cross peaks. However, for molecules of *all* sizes, ROE cross peaks are of opposite sign to the diagonal while chemical exchange cross peaks are the same sign as the diagonal peaks. Thus, ROESY spectra can be extremely helpful in identifying the source of 2D cross peaks. (68)

An example of this comparison is shown in Figure 10, where NOESY and ROESY spectra of an iron(III) porphyrinate, $[\text{TMPFe}(2\text{-MeImH})_2]\text{ClO}_4$ in CD_2Cl_2 at similar low temperatures are shown. The chemical exchange cross peaks arise from rotation of the perpendicularly-oriented unsymmetrical 2-methylimidazole ligands, which create four pyrrole-H, four *o*- CH_3 , four *m*-H, and two *p*- CH_3 environments. (68,74) NOE cross peaks arise from pairs of protons that are spatially close, and include the pyrrole-H protons in a given pyrrole ring: pyrrole-H resonances (2) and (4). This set of cross peaks is not observed in the ROESY spectrum at -65°C (right side of Figure 10) due to interference from the opposite-phase chemical exchange and TOCSY cross peaks that arise from use of a spin-lock B_1 field of 10.3 kHz (68), and they are obscured by chemical exchange in the NOESY spectrum (left side of Figure 10). At lower temperatures (-75°C), however, the NOEs between pyrrole-H (2) and (4) are clearly observed in both NOESY (75) and ROESY (68) spectra. (See also below, Figure 13, where the J-coupling of pyrrole-H resonances (2) and (4) is revealed in the DQF-COSY spectrum.)

Derivation of the equations for a 4-site chemical exchange process with one common rate constant has allowed the use of phase-sensitive NOESY cross peak intensities to measure the rate constant as a function of temperature. (74) Saturation transfer techniques have also been used to measure the same rate constant as a function of temperature. (60) That these complexes, MW $\sim 1100\text{ g/mol}$, have negative phase NOESY cross peaks (*i.e.*, positive NOEs) at room temperature but positive phase cross peaks (negative NOEs) at low temperatures, is an indication that they fall very close to the zero-crossing point of Figure 7 at 300 MHz. These molecular weights are considerably higher than those predicted by equation 7.

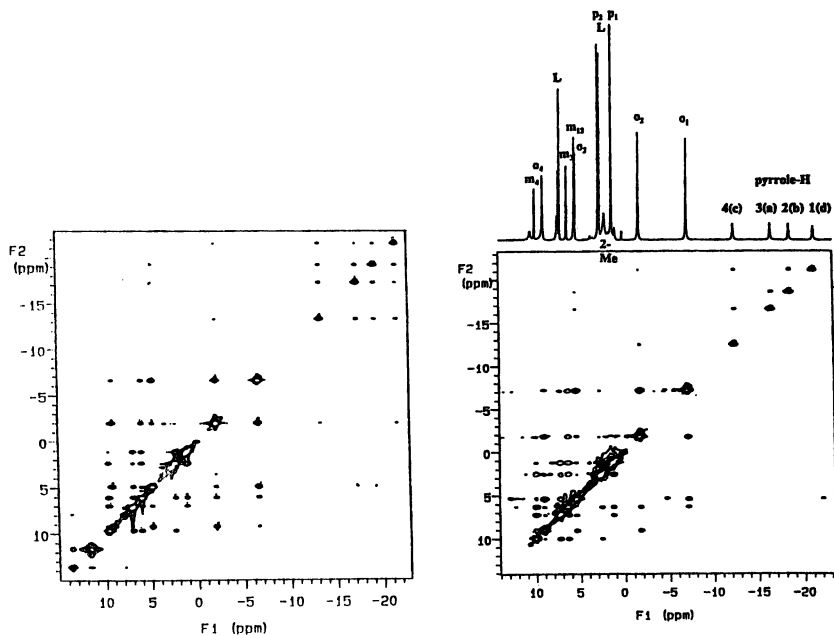


Figure 10. Left: 300 MHz ^1H - ^1H Phase-sensitive NOESY spectrum of $[\text{TMPFe}(2\text{-Me-ImH})_2]\text{ClO}_4$ recorded at -61°C in CD_2Cl_2 . Conditions: Spectral bandwidth 11.35 kHz, 512 t_2 data points, 23 ms t_2 acquisition time, relaxation delay 600 ms, $\tau_m = 70$ ms, 128 t_1 blocks, 32 transients per t_1 block, Gaussian window multiplication function 0.011, final data size 1024x1024. (T. Kh. Shokhireva, unpublished data.) Right: 300 MHz ^1H - ^1H Phase-sensitive ROESY spectrum of $[\text{TMPFe}(2\text{-MeImH})_2]\text{ClO}_4$ recorded at -65°C in CD_2Cl_2 . Note in particular the chemical exchange cross peaks among pyrrole-H in the NOESY spectrum that prevent observing the NOE between pyrrole-H (2) and (4); this is not observed as either positive phase chemical exchange or negative phase ROE cross peaks in the ROESY spectrum, where the temperature is 4° lower and the two contributions (plus TOCSY effects) apparently cancel. Weak NOEs/ROEs are observed in both spectra between *o*-CH₃(2) and pyrrole-H(1) and (4), between *o*-CH₃(3) and pyrrole-H(2) and (3), and among the *o*-CH₃ and *p*-CH₃ with their neighbor *m*-H resonances. Chemical exchange cross peaks among the *o*-CH₃ resonances are also observed in the NOESY spectrum at -61° , and more weakly in the deep contour streaks above the diagonal of the ROESY spectrum at the slightly lower temperature of -65° . Cross peaks resulting from a combination of a NOE between an *o*-CH₃ and its neighbor *m*-H or between a *m*-H and its neighbor *p*-CH₃, and chemical exchange between *m*-H are also observed in the NOESY spectrum on the left, and more weakly on the ROESY spectrum on the right. ROESY spectrum reprinted from reference 74 with permission of Elsevier Science S. A.

The dynamic behavior of the paramagnetic Yb(III) macrocyclic chelate complex of DOTA (1,4,7,10-tetraazacyclododecane-N,N',N'',N'''-tetraacetate) has been studied quantitatively by EXSY spectroscopy. (37) Pure absorption mode EXSY spectra were used for this study, in which there are two diastereomeric major (M_1 and M_2) and minor (m_1 and m_2) conformers undergoing exchange. The intensities of the cross peaks were expressed in terms of the exponential decay of the dynamic matrix L , and the experimental intensities were used to solve L as a function of mixing time τ_m at a series of temperatures. Activation parameters for the reactions $M_1 \rightarrow m_1$, $m_1 \rightarrow M_1$, $M_1 \rightarrow m_2$, $m_1 \rightarrow M_2$ and $M_1 \rightarrow M_2$ were determined. (37)

COSY and TOCSY Experiments. As for the NOESY and ROESY experiments, the laboratory and rotating frame correlation spectroscopy experiments are extremely valuable, in these cases in providing J-coupling information about the nuclei in the paramagnetic complex. The two experiments provide the same information, but because of the large B_1 fields required for the TOCSY experiment (called by Bax the HOHAHA, or Homonuclear Hartmann-Hahn experiment (71)), the COSY experiment is probably preferable for paramagnetic complexes in almost all cases (but see reference 1 for an opposing view and experimental evidence to the contrary).

The pulse sequences for the two experiments are:

$$\text{COSY:} \quad \text{RD} - \pi/2 - t_1 - \pi/2 - t_2 \quad (13)$$

$$\text{TOCSY:} \quad \text{RD} - \pi/2 - t_1 - \pi/2 - \text{SL}(\tau_m) - \pi/2 - t_2 \quad (14)$$

As can be seen, the TOCSY pulse sequence given (equation 14) is identical to the ROESY pulse sequence (equation 12), with the only difference being that the spin-lock field used for TOCSY experiments should be about double to triple that used for ROESY experiments, and the transmitter should be placed in the center of the spectrum. The spin-lock mixing time should be varied to find the optimum value. The upper limit on the strength of the spin-lock field B_1 is probably 25 kHz, or perhaps smaller for some instruments, in order to avoid frying the probe and the sample! CLEAN-TOCSY spin locks (77) can also be used to virtually eliminate ROE peaks.

The first application of COSY (and NOESY) spectra to paramagnetic complexes was the study of Jenkins and Lauffer of the lanthanide complexes of DTPA. (78) Using the COSY experiment, assignments of diastereotopic protons in methylene groups could be made, while the NOESY experiment provided chemical exchange information. Since then, the magnitude experiment, MCOSY, has been applied to low-spin iron chlorins (79), Figure 11, to octahedral Ni(II) dimeric complexes (80), and to dimeric Cu(II) complexes (48,81), Figure 12, among many other systems. An example of the effect of either poor shimming or temperature fluctuation on the shapes of diagonal and cross peaks (48) is also illustrated in Figure 12; because the chemical shifts of paramagnetic complexes are so sensitive to temperature, careful temperature control is a must in 2D experiments on such complexes!

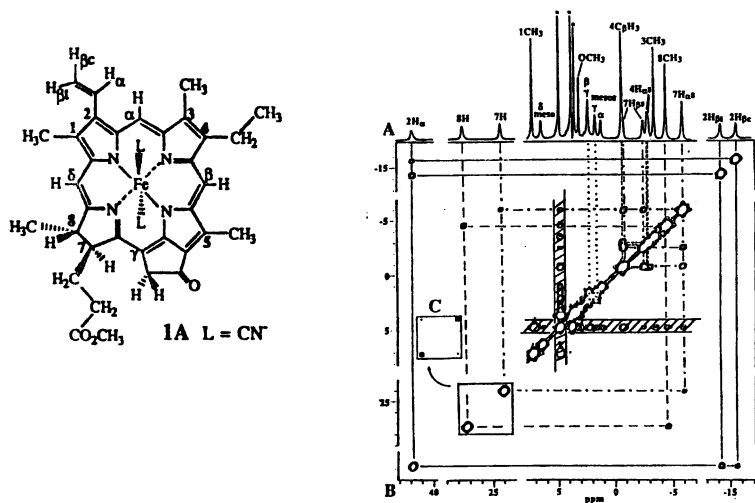


Figure 11. 300 MHz symmetrized MCOSEY map of the bis-cyano complex of Fe(III) pyropheophorbide *a* illustrating cross peaks between spin-coupled resonances. Reprinted from reference 79 with permission of the American Chemical Society.

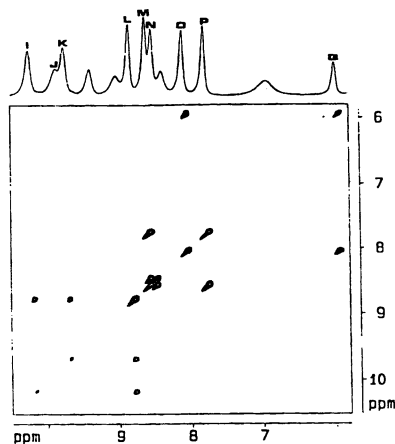


Figure 12. Magnitude ^1H COSY spectrum of the Cu(II) dimer complex of Figure 4 obtained at 400.13 MHz at -20°C in CD_3CN . J-coupling connectivities are observed. In addition, the shape of the diagonal and cross peaks suggests some drift in temperature during the experiment. Reprinted from reference 48 with permission from the American Chemical Society.

Not only simple MCOSEY spectra, but also phase-sensitive COSY spectra can be obtained on paramagnetic complexes, and again, the phase-sensitive experiments (with full 16-step phase cycling) are more likely to give reliable cross peaks where questions of possible overlap of broad diagonal peaks arise. Caution should also be exercised in

symmetrizing *any* 2D spectra, since this can create false cross-peaks! There has been considerable discussion of the possibility of cancellation of the antiphase components of COSY cross peaks due to the larger linewidths of such peaks for paramagnetic complexes. (82) In addition, Curie relaxation can produce cross peaks that can be mistaken for J-coupling cross peaks in either COSY or TOCSY spectra. (83,84) We have found recently that antiphase components are clearly displayed in the double quantum filtered (DQF) COSY spectrum of [TMPFe(2-MeImH)₂]ClO₄ (85), as demonstrated in Figure 13 for both pyrrole-H at -11.7 and -17.4 ppm and *m*-H resonances at 6.4 and 7.1 and 6.4 and 9.8 ppm. The antiphase components are *not* separated by distances indicative of the J coupling constants of the protons involved, which may suggest that the

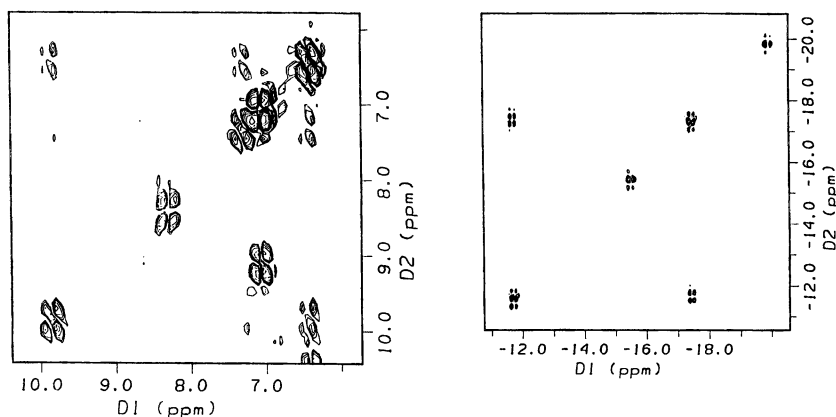


Figure 13. Phase-sensitive 300 MHz DQF-COSY spectra of [TMPFe(2-MeImH)₂]ClO₄ recorded at -55 °C in CD₂Cl₂. Left: *meta*-H region, right: pyrrole-H region. Conditions: Spectral bandwidth 11.19 kHz, 512 *t*₂ data points, 25 ms *t*₂ acquisition time, relaxation delay 150 ms, 128 *t*₁ blocks, 512 transients per *t*₁ block, processed with an unshifted sine bell window function, final data size 1024x1024. Note artifact at 7.1,9.2 ppm, discussed in the text. (Shokhireva, unpublished data.)

cross peaks are actually a result of cross-relaxation between spatially proximal protons. (84) (This does not invalidate their use in assigning the spectra.) The off-diagonal peak at 7.1,9.2 ppm that has no off-diagonal partner or diagonal peak at 9.2 ppm is an anti-diagonal artifact peak; such artifacts are often seen in phase-sensitive COSY spectra, especially DQF-COSY. (86)

¹³C-¹H Correlation Spectra. Both HETCOR (¹³C-detected) and HMQC (¹H-detected) spectra have been obtained in our laboratory and that of Simonis on low-spin Fe(III) porphyrinate complexes. Other groups have previously used these heteronuclear experiments to assign the spectra of diamagnetic (71) and paramagnetic (87) transition metal complexes, and several recent multi-experiment approaches discussed below have also reported HMQC spectra. Inverse spectra (HMQC) are generally of superior quality

because of the greater sensitivity of ^1H as compared to ^{13}C , as well as the shorter relaxation times of ^1H compared to ^{13}C resonances. The basic HETCOR and HMQC pulse sequences are:

$$\begin{array}{ll} \text{HETCOR:} & \begin{array}{l} ^1\text{H:} \quad (\pi/2) - t_1 - (\pi/2) - \text{Dec} \\ ^{13}\text{C:} \quad (\pi/2) - \text{Acq}(t_2) \end{array} \end{array} \quad (15)$$

$$\begin{array}{ll} \text{HMQC (HMBC):} & \begin{array}{l} ^1\text{H:} \quad (\pi/2) - \Delta - t_1/2 - \pi - t_1/2 - \Delta - \text{Acq}(t_2) \\ ^{13}\text{C:} \quad \Delta - (\pi/2) - t_1 - (\pi/2) - \Delta \end{array} \end{array} \quad (16)$$

In equations 15 and 16 the phase relationships of the pulses have not been given, but are very important. (39,40,66,67) The delay Δ in the HMQC (and HMBC) experiments is usually set for up to ~20% less than the expected $1/2J_{\text{CH}}$. (67)

HMQC spectra suffer from streaks arising from poor ^{12}C -H suppression, and thus can appear to be more noisy than HETCOR spectra. However, HETCOR spectra require longer experiment times, both because of the lower sensitivity of ^{13}C and because of the longer T_1 and T_2 relaxation times of this nucleus than of ^1H . Single-bond H-C correlations are readily obtained from either experiment, and have been reported for a number of systems. (87-90) However, multiple-bond H-C correlations have only been reported for one paramagnetic complex, a low-spin Fe(III) unsymmetrically-phenyl-substituted tetraphenyl-porphyrinate. (90) Since all H-C correlation experiments require an evolution time of $1/2J_{\text{CH}}$, it is necessary to have some idea as to what the long-range coupling constant J_{CH} is for the HMBC experiment. Thus far, it has been possible to detect 2- and 3-bond couplings from the pyrrole-H to the α -C of the unsymmetrically-substituted porphyrin ligand, where $1/2J_{\text{CH}} = 25$ ms (indicating $^3J \sim 15\text{-}20$ Hz) (90), Figure 14, but no 3-bond couplings from the pyrrole-H to the *meso*-C have yet been detected, despite wide variations of the $1/2J_{\text{CH}}$ evolution time. (91) This suggests that $^3J_{\text{CH}}$ for coupling of the *meso*-carbon and β -H is very small, perhaps too small to be compatible with the T_1 of the β -H, such that no magnetization remains after the $1/2J_{\text{CH}}$ evolution time. The gradient version of the HMBC experiment (92) provides spectra with considerably better ^{12}C -H suppression and significantly reduced t_1 noise (because only the magnetization pathways of interest are selected), making it possible to detect the 3-bond couplings between β -H and α -C. (90) In addition, since the optimal value of $1/2J_{\text{CH}}$ may not be known, the use of gradients is particularly valuable for paramagnetic systems, in order to suppress undesirable coherences. It can be expected that gradient experiments will significantly improve the quality of all 2D NMR experiments, especially on paramagnetic complexes having short T_1 and T_2 relaxation times.

Multi-Experiment Approaches to Structure Determination and Complex Dynamics.

A number of recent examples of such studies have been reported. Due to page limitations, spectra are not included herein, but the reader is referred to the following:

LnH(OEP)(TPP). COSY, NOESY, TOCSY, ROESY and HMQC spectra have been obtained for several lanthanide ions bound in sandwich form to two different porphyrins (88). Complete assignment of the spectra was achieved.

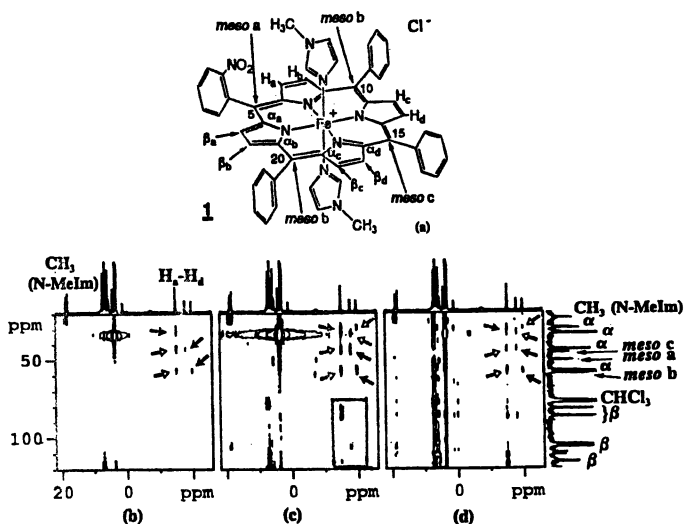


Figure 14. HMBC spectra of the unsymmetrical $[\text{TPPFe}(\text{N-MeIm})_2]^+$ complex **1** recorded at 300 MHz at 302 K in CD_2Cl_2 . (a) Structure of **1**; (b) HMBC spectrum recorded with pulse field gradients and 1024 transients per FID; (c) pulsed-field gradients and 8192 transients per FID; (d) phase-cycling and 8192 transients per t_1 increment. The 2D data for all maps were recorded in the proton dimension with a spectral width of 15,625 Hz, 2048 t_1 increments, and a 11.3 μs 90° pulse width. In the carbon dimension, a spectral width of 13,576 Hz, a 14.6 μs 90° pulse, and 64 FIDs were used to give total acquisition times of 3.5 h for (b), 29.5 h for (c) and 28.9 h for (d). For (b) and (c) sine-shaped pulsed-field gradient pulses of 1 ms duration, a pulse ratio of 50:30:40, and strengths of 15, 9, and 12 G/cm were used, with the pulse sequence given in reference 92. The data were multiplied with a phase-shifted sine-squared window function in f_2 and a sine function in f_1 prior to Fourier transformation. The cross peaks marked with solid arrows are due to two-bond pyrrole β -H-pyrrole- α -C correlations, and those marked with open arrows are due to $^3J^{1\text{H}}_{\beta}-^{13\text{C}}_{\alpha}$ couplings. The cross peaks in the boxed area of Figure 1c are due to nonsuppressed one-bond scalar correlations linking the pyrrole β -H to the pyrrole β -C signals. Reprinted from reference 90 with permission of the American Chemical Society.

Fe(II) Bleomycin. This large antibiotic molecule, Figure 15, which has numerous sites at which it can bind to a metal, has been studied as the Fe(II) complex by a battery of 2D NMR experiments, including MCOSY, NOESY, and HMQC. (89) In each case, the experimental conditions were adjusted (mixing time, acquisition time, recycle delay) in order to emphasize the resonances of nuclei close to the paramagnetic center, and in separate experiments, to emphasize the resonances of nuclei far from the paramagnetic center. (89) The paper is a nice example of how 2D NMR experiments can be optimized to obtain the maximum amount of information about a relatively complicated system of interest.

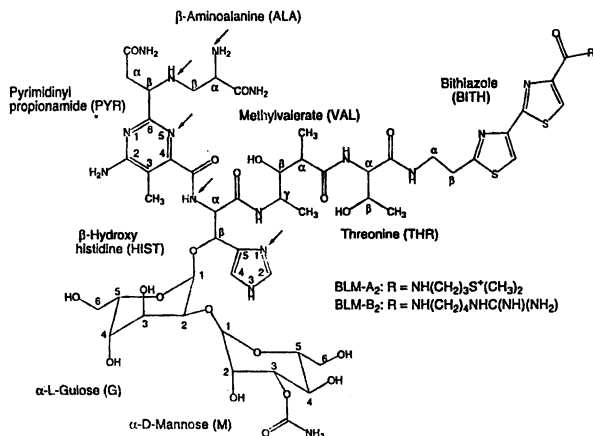


Figure 15. Structure of the bleomycin ligands BLM-A₂ and BLM-B₂, the most abundant components of the clinically employed mixture of bleomycins. The arrows indicate the ligating atoms to the Fe(II) center, proposed on the basis of the results of the study presented in reference 89. Reprinted with permission of the American Chemical Society.

Miscellaneous Techniques: CIDNP. Chemically-induced dynamic nuclear polarization (CIDNP), a phenomenon that was studied in some detail in the early 1970s (93-95), has recently been utilized to develop a mechanistic scheme for the collapse of the photo-excited vitamin B₁₂ model complex, (CH₃CH₂)Co^{III}(SALEN) (90), to show that the preferred pathway involves collapse of the singlet radical pair, (CH₃CH₂•)(Co^{II}(SALEN)) to the starting material, rather than a pathway involving singlet-triplet conversion and then re-conversion to the singlet state. The strong enhancement of the methyl resonance, and the weak emission of the methylene resonance, Figure 16, are consistent with the singlet-collapse mechanism. (96)

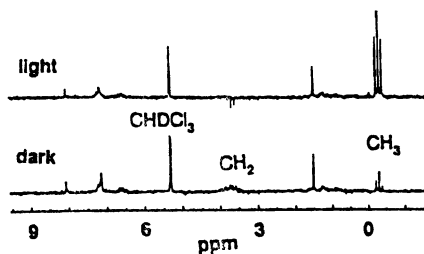


Figure 16. ¹H NMR spectra for 1 mM CH₃CH₂Co^{III}(SALEN) in aerated CD₂Cl₂ acquired without irradiation, as well as after 10 s irradiation with 300-400 nm light. Note the strong positive enhancement of the CH₃ resonance and the weak negative enhancement of the CH₂ resonance of the ethyl group that arise from chemically-enhanced dynamic nuclear polarization (CIDNP) arising from the electron spin polarization of the nuclear states of the ethyl radical intermediate in the photolysis of the Co-C bond. Reprinted from reference 96 with permission of the American Chemical Society.

Summary

In this report we have shown that most simple 1D and 2D NMR experiments used for studying diamagnetic organic compounds can be successfully carried out on paramagnetic complexes with proper optimization of experimental conditions and processing parameters. Exceptions to this are experiments with built-in delays that are long compared to the T_1 relaxation times of the nuclei of interest, and this can be a limitation of the HMBC experiment, for example, when $^3J_{\text{CH}}$ values are small. (In general, simpler versions of 2D experiments, which require the minimum necessary time delays, are always preferable to "fancier" versions that may contain extra spin-echo sequences, etc.) We have also shown that the temperature dependence of both chemical shifts and linewidths can be used to determine detailed information about the energy level structure of a paramagnetic complex. But we have also pointed out that it is extremely important that the temperature remain constant during an experiment! We have stressed the point that magnitude mode 2D spectra should not be collected, and that spectra should *never* be symmetrized. We have further shown that the ROESY experiment is very valuable for molecules of intermediate size, whose value of $\omega\tau_c$ could place them near the point where $\text{NOE} = 0$ for the NOESY experiment. However, because the ROESY experiment requires higher B_1 fields for the larger spectral bandwidths of paramagnetic complexes, the spectra *may* be complicated by TOCSY effects; these can be detected and minimized by placing the transmitter on one end or the other of the spectrum (by changing the spectral width). Pulsed field gradient versions of 2D NMR experiments, available on modern NMR spectrometers, will probably not save much in total experiment time, but can eliminate artifacts arising, for example, from incomplete ^{12}C -H suppression, that will significantly aid the chemist working with paramagnetic complexes in detecting weak cross peaks.

Acknowledgements

The author wishes to thank her very able coworkers, in particular Dr. Nikolai V. Shokhirev, Dr. Tatjana Kh. Shokhireva, Mr. Konstantin I. Momot, Mr. Hiroshi Ogura, and her former coworker, Prof. Ursula Simonis of San Francisco State University, for carrying out the experimental and theoretical work reported from this laboratory that is described herein. The support of the National Institutes of Health, grant DK 31038, and the University of Arizona Materials Characterization Program is also gratefully acknowledged.

Literature Cited

1. Luchinat, C.; Steuernagel, S.; Turano, P. *Inorg. Chem.* **1990**, *29*, 4351.
2. Chmielewski, P. J. Latos-Grazynski, L. *Inorg. Chem.* **1992**, *31*, 5231.
3. Crans, D. C.; Rithner, C. D.; Thiesen, L. A. *J. Am. Chem. Soc.* **1990**, *112*, 2901.
4. Berliner, L. J.; Reuben, J., Eds. *Biological Magnetic Resonance: NMR of Paramagnetic Molecules*; Plenum: New York, 1993; Vol. 12.
5. La Mar, G. N., Ed. *NMR of Paramagnetic Macromolecules*; Kluwer-Academic: Dordrecht, 1994.
6. Banci, L.; Bertini, I.; Luchinat, C. In *Methods in Enzymology*; James, T. L., Oppenheimer, N. J., Eds.; Academic Press: New York, 1994; vol 239, pp. 485-514.

7. Bertini, I.; Luchinat, C. *NMR of Paramagnetic Molecules in Biological Systems*; Benjamin/Cummings: Menlo Park, CA, 1986.
8. Bertini, I.; Turano, P.; Vila, A. *Chem. Revs.* **1993**, *93*, 2833.
9. Carrington, A.; McLachlan, A. D. *Introduction to Magnetic Resonance with Application to Chemistry and Chemical Physics*; Harper and Row: New York, 1967; Chapter 1.
10. Actually, $A/g\beta$ (in gauss or mT) for EPR and A/h (in MHz) for NMR spectra.
11. Beringer, R.; Heald, M. A. *Phys. Rev.* **1954**, *95*, 1474. Kusch, P. *Phys. Rev.* **1955**, *100*, 1188.
12. Note that this “fast chemical exchange” of the electron spin on the NMR time scale is the opposite of the “slow chemical exchange” of the electron spin on the EPR time scale that gives rise to the two hyperfine lines discussed in the preceding paragraph and shown in Figure 2. In spite of the difference in time scales between EPR and NMR spectroscopy, this “fast” vs. “slow” electron spin relaxation rate is responsible for the rule of thumb that if you see the EPR spectrum of the complex at room temperature, you will not see the NMR spectrum of the same complex at room temperature. However, rules of thumb are meant to be broken, or at least bent, as is the case with certain monomeric, tetrahedral Cu(II) complexes.
13. Downfield or upfield in the jargon that has developed over the years.
14. Jesson, J. P. In *NMR of Paramagnetic Molecules*; La Mar, G. N.; Horrocks, W. D.; Holm, R. H., Eds.; Academic Press: New York, 1973; pp. 1-53.
15. Bertini, I.; Luchinat, C. *NMR of Paramagnetic Substances*; Elsevier: Amsterdam, 1996.
16. La Mar, G. N.; Walker, F. A. In *The Porphyrins*; Dolphin, D., Ed.; Academic Press: New York, 1979; Vol. IV; pp. 57-61.
17. Walker, F. A.; Simonis, U. In reference 4, pp. 133-274.
18. McConnell, H. M. *J. Chem. Phys.* **1956**, *24*, 764.
19. Karplus, M.; Fraenkel, G. K. *J. Chem. Phys.* **1961**, *35*, 1312.
20. Banci, L.; Bertini, I.; Luchinat, C.; Pierattelli, R.; Walker, F. A. Manuscript in preparation.
21. Derbyshire, W. *Mol. Phys.* **1962**, *5*, 225.
22. La Mar, G. N.; Eaton, G. R.; Holm, R. H.; Walker, F. A. *J. Am. Chem. Soc.* **1973**, *95*, 63.
23. Pawlik, M. J.; Miller, P. K.; Sullivan, E. P.; Levstik, M. A.; Almond, D. A.; Strauss, S. H. *J. Am. Chem. Soc.* **1988**, *110*, 3007.
24. (a) Horrocks, W. D.; Greenberg, E. S. *Biochim. Biophys. Acta* **1973**, *322*, 38. (b) Horrocks, W. D.; Greenberg, E. S. *Mol. Phys.* **1974**, *27*, 993.
25. Shokhirev, N. V.; Walker, F. A. Submitted to *J. Am. Chem. Soc.* **1997**.
26. Taking into account the counter-rotation of g_{xx} and g_{yy} (25), if necessary.
27. Emerson, S. D.; La Mar, G. N. *Biochemistry* **1990**, *29*, 1556.
28. Reference 20 and references therein.
29. Sievers, R. E., Ed. *Nuclear Magnetic Shift Reagents*; Academic Press: New York, 1973.
30. Reference 32, pp. 549-552.

31. Abraham, R. J.; Fisher, J.; Loftus, P. *Introduction to NMR Spectroscopy*; John Wiley & Sons: New York, 1988; pp. 211-217.
32. Bertini, I.; Luchinat, C. In *Physical Methods for Chemists*, Ed. 2; Drago, R. S., Ed.; Saunders: Mexico, 1992; Chapter 12.
33. Reference 32, p. 519.
34. Reference 32, p. 527.
35. Kalverda, A.; Salgado, J.; Dennison, C.; Canters, G. W. *Biochemistry* **1996**, *35*, 3085.
36. Peters, J. A.; Huskens, J.; Raber, D. J. *Progr. NMR Spectrosc.* **1996**, *28*, 283-350.
37. Jacques, V.; Desreux, J. F. *Inorg. Chem.* **1994**, *33*, 4048.
38. The protons that have been detected near the Cu(II) center of amicyanin are those that have a hyperfine coupling constant less than 4.2 MHz and are at a distance of $>4 \text{ \AA}$ from the copper. (35)
39. Derome, A. E. *Modern NMR Techniques for Chemistry Research*; Pergamon: New York, 1987.
40. Sanders, J. K. M.; Hunter, B. K. *Modern NMR Spectroscopy, A Guide for Chemists*, Ed. 2; Oxford University Press: Oxford, 1993.
41. Sigel, H.; Sigel, A., Eds. *Metal Ions in Biological Systems*; Dekker: New York, 1989; Vol. 21, "Applications of Nuclear Magnetic Resonance to Paramagnetic Species."
42. Banci, L.; Bertini, I.; Luchinat, C. *Electron and Nuclear Relaxation*; VCH: Heidelberg, 1991.
43. Reference 40, p. 22.
44. Momot, K. I.; Walker, F. A. *J. Phys. Chem. A* **1997**, in press.
45. a) Pople, J. A.; Schneider, W. G.; Bernstein, H. J. *High Resolution Nuclear Magnetic Resonance*; McGraw-Hill: New York, 1959; chapter 10. b) Sandstrom, J. *Dynamic NMR Spectroscopy*; Academic Press: New York, 1982; chapter 9.
46. Basu, P.; Shokhirev, N. V.; Enemark, J. H.; Walker, F. A. *J. Am. Chem. Soc.* **1995**, *117*, 9042.
47. The reason for eight resonances for the 2,3-isomer but only four for the 3,4-isomer is that the bulky Mo(V) complex hinders the rotation of one axial ligand in the former complex in such a way as to make H_a different from H_b , H_b different from H_c , etc., but in the latter complex both axial ligands rotate freely and thus average H_a and H_b , H_b and H_c , etc. (42)
48. Brink, J. M.; Rose, R. A.; Holz, R. C. *Inorg. Chem.* **1996**, *35*, 2878.
49. Murthy, N. N.; Karlin, K. D.; Bertini, I.; Luchinat, C. *J. Am. Chem. Soc.* **1997**, *119*, 2156.
50. Dugad, L. B.; La Mar, G. N.; Unger, S. W. *J. Am. Chem. Soc.* **1990**, *112*, 1386.
51. O'Connor, C. J. "Magnetochemistry---Advances in Theory and Experimentation;" In *Progress in Inorganic Chemistry*; Lippard, S. J., Ed.; Wiley-Interscience: New York, 1982; Vol. 29, pp. 203-283.
52. Shokhirev, N. V.; Walker, F. A. *J. Phys. Chem.* **1995**, *99*, 17795.
53. Available upon E-mail request to nikolai@u.arizona.edu.
54. Tan, H.; Simonis, U.; Shokhirev, N. V.; Walker, F. A. *J. Am. Chem. Soc.* **1994**, *116*, 5784.

55. Isaac, M. F.; Lin, Q.; Simonis, U.; Suffian, D. J.; Wilson, D. L.; Walker, F. A. *Inorg. Chem.* **1993**, *32*, 4030.
56. In the case of solvent molecules that remain in the crystals, it is often necessary to pump on the sample extensively on a high vacuum line, and also to evaporate the sample from the deuterated solvent to be used, or preferably both.
57. Reference 4, p. 38.
58. The relaxation delay is sometimes set for as long as 1-2 s for a diamagnetic compound, but in fact the rule of thumb is that the repetition rate should be $1.27T_1$. (59)
59. Neuhaus, D.; Williamson, M. P. *The Nuclear Overhauser Effect in Structural and Conformational Analysis*; VCH: New York, 1989; Chapter 7.
60. Momot, K. I.; Walker, F. A. *J. Phys. Chem. A* **1997**, *101*, 2787.
61. Redfield, A. G.; Gupta, R. K. *Cold Spring Harbor Symp. Quant. Biol.* **1971**, *36*, 405.
62. Reference 59, p. 37.
63. Barbush, M.; Dixon, D. W. *Biochem. Biophys. Res. Commun.* **1985**, *129*, 70.
64. Unger, S. W.; LeComte, J. T. J.; La Mar, G. N. *J. Magn. Reson* **1985**, *64*, 521.
65. Yu, C.; Unger, S. W.; La Mar, G. N. *J. Magn. Reson.* **1986**, *67*, 346.
66. Cavanagh, J.; Fairbrother, W. J.; Palmer, A. G.; Skelton, N. J. *Protein NMR Spectroscopy. Principles and Practice*; Academic Press: New York, 1996.
67. Evans, J. N. S. *Biomolecular NMR Spectroscopy*; Oxford University Press: New York, 1995.
68. Shokhireva, T. Kh.; Nasset, M. J. M.; Walker, F. A. *Inorg. Chim. Acta* **1997**, in press.
69. Griesinger, C.; Ernst, R. R. *J. Magn. Reson.* **1987**, *75*, 261.
70. Bothner-By, A. A.; Stephens, R. L.; Lee, J.; Warren, C. D.; Jeanloz, R. W. *J. Am. Chem. Soc.* **1984**, *106*, 811.
71. Summers, M. P.; Marzilli, L. G.; Bax, A. *J. Am. Chem. Soc.* **1986**, *108*, 4285.
72. Cavanagh, J.; Keeler, J. *J. Magn. Reson.* **1988**, *80*, 186.
73. Ogura, H. Unpublished data.
74. Shokhiev, N. V.; Shokhireva, T. Kh.; Polam, J. R.; Watson, C. T.; Raffii, K.; Simonis, U.; Walker, F. A. *J. Phys. Chem. A* **1997**, *101*, 2778.
75. Walker, F. A.; Simonis, U. *J. Am. Chem. Soc.* **1991**, *113*, 8652; **1992**, *114*, 1929.
76. Chen, Z.; de Ropp, J. S.; Hernandez, G.; La Mar, G. N. *J. Am. Chem. Soc.* **1994**, *116*, 8772.
77. a) Briand, J.; Ernst, R. R. *Chem. Phys. Lett.* **1991**, *185*, 276. b) Cavanagh, J.; Rance, M. *J. Magn. Reson.* **1992**, *96*, 670.
78. Jenkins, B. G.; Lauffer, R. B. *Inorg. Chem.* **1988**, *27*, 4730.
79. Keating, K. A.; de Ropp, J. S.; La Mar, G. N.; Balch, A. L.; Shiau, F.-Y.; Smith, K. M. *Inorg. Chem.* **1991**, *30*, 3258.
80. Holz, R. C.; Evdokimov, E. A.; Gobena, F. T. *Inorg. Chem.* **1996**, *35*, 3808.
81. Murthy, N. N.; Karlin, K. D.; Bertini, I.; Luchinat, C. *J. Am. Chem. Soc.* **1997**, *119*, 2156.
82. La Mar, G. N.; Chien, Z.; de Ropp, J. S., Reference 5, pp. 55-74.
83. Bertini, I.; Luchinat, C.; Tarchi, D. *Chem. Phys. Lett.* **1993**, *203*, 445.

84. Qin, J.; Delaglio, F.; La Mar, G. N.; Bax, A. *J. Magn. Reson., Series B* **1993**, *102*, 332.
85. Shokhireva, T. Kh. Unpublished data.
86. Reference 66, Figure 6.21, p. 335.
87. Timkovich, R. *Inorg. Chem.* **1991**, *30*, 37.
88. Bertini, I.; Coutsolelos, A.; Dikiy, A.; Luchinat, C.; Spyroulias, G. A.; Troganis, A. *Inorg. Chem.* **1996**, *35*, 6308.
89. Lehmann, T. E.; Ming, L.-J.; Rosen, M. E.; Que, L., Jr. *Biochemistry* **1997**, *36*, 2807.
90. Skidmore, K.; Simonis, U. *Inorg. Chem.* **1996**, *35*, 7470.
91. Simonis, U. Personal communication.
92. Hurd, R. E.; John, B. K. *J. Magn. Reson.* **1991**, *91*, 648.
93. Lepley, A. R.; Closs, G. L. *Chemically Induced Magnetic Polarization*; Wiley-Interscience: New York, 1973.
94. Ward, H. R. *Accounts Chem. Res.* **1972**, *5*, 18.
95. Lawler, R. G. *Ibid.* **1972**, *5*, 23.
96. Kruppa, A. I.; Taraban, M. B.; Leshina, T. V.; Natarajan, E.; Grissom, C. B. *Inorg. Chem.* **1997**, *36*, 758.

Chapter 4

Metalloprotein Crystallography

H. C. Freeman

School of Chemistry, University of Sydney, Sydney, New South Wales 2006,
Australia

The steps in the crystal structure analysis of a biological macromolecule are described, with emphasis on some of the spectacular advances that have occurred in recent years. The description of crystallographic concepts and procedures is largely qualitative. References to more detailed and rigorous treatments are provided. The need for a critical assessment of the accuracy and precision of each macromolecular structure is stressed.

This 'tutorial' is addressed to bioinorganic chemists who are not already familiar with macromolecular crystallography. The aim is to describe what a contemporary protein crystallographer can do if she/he is entrusted with a few milligrams of a new metalloprotein. The treatment of crystallographic concepts and procedures is necessarily impressionistic rather than mathematically rigorous.

For those who wish to read more, an excellent and largely pictorial introduction to macromolecular crystal structure analysis is given in a monograph by Perutz (1). A more detailed treatment of many fundamental aspects is available in the classic text by Blundell and Johnson (2). The recent book by Drenth is recommended as a state-of-the-art 'how-to-do-it' guide (3). A condensed overview, which conveys much of the excitement of current developments, can be found in a review by Hendrickson (4). Short reviews and discussion papers on specialized topics, mainly from the journals *Structure* and *Synchrotron Radiation News*, are cited in the relevant sections of this tutorial.

Outline

Most of the examples in this tutorial are taken from the structure analyses of several small (~10 kDa) 'blue' copper proteins and two much larger (~140 kDa) copper enzymes. The first objective in the crystal structure analysis of such metalloproteins is to discover how the polypeptide chain is folded and where the metal site is located.

Various types of computer-graphics idealization are used to make the information digestible, the most common being ribbon diagrams (Figure 1). The structure analysis then generally proceeds to the detailed study of specific structural features such as the dimensions of the metal site, the location and conformation of particular amino acid side chains, the location and characteristics of a substrate binding site, and so on. The relevant parts of the structure have to be represented in atomic detail. Examples that we shall need later in the tutorial are shown in Figure 2. Bio-inorganic chemists who cannot achieve stereoscopy have only half the fun (Figure 2b).

The steps that lead to such an intimate knowledge of a metalloprotein are shown in Figure 3. They are (i) the purification of the protein, and the discovery of conditions that lead to the formation of suitable crystals, (ii) measurements of the intensities of the X-ray beams reflected ('diffracted') by the crystals, (iii) the determination of the phases of the X-ray reflections, leading directly to the calculation of an electron-density map, (iv) the interpretation of the electron-density map, resulting in a molecular model, and (v) the refinement of the molecular model to make it as accurate and precise as the available data allow. A final step, which has only recently received the attention that it deserves, is (vi) the assessment of the accuracy and precision of the results.

Crystallization

The discovery of conditions that lead to the formation of suitable crystals (where the meaning of *suitable* will shortly become clear) used to be entirely a matter of trial-and-error. Crystallization is still largely a matter of trial-and-error, but the trials are becoming more systematic and some general principles are emerging (5).

Purity. It is now generally agreed that purity is a pre-condition for the production of crystals with good diffraction properties. The size and flexibility of a protein make one wonder how the molecules ever arrange themselves in a regular lattice. It is not surprising that impurities - especially traces of other proteins - interfere with this process, and either inhibit crystallization altogether or cause the crystals to be disordered. In the case of metalloproteins, even small amounts of the apo-protein are thought to hinder crystallisation, unless the pure apo-protein is the object of the exercise. A recombinant protein is frequently a better target for crystallization than the same protein from a natural source, since it is more likely to be homogenous and less likely to be glycosylated.

Crystallization Experiments. In a crystallization experiment, the solubility of a protein is depressed very slowly by adding a 'precipitant' until the protein drops out of the solution. The aim is to create conditions for the formation of nuclei around which crystals will grow. Initially the concentration of the precipitant is insufficient to cause precipitation of the protein. The protein solution is allowed to equilibrate by vapor diffusion against a solution containing a higher concentration of the precipitant, causing the concentration of precipitant in the protein solution to increase at a slow and controllable rate.

A typical experiment involves only a small quantity of protein (say, 0.05-0.2 mg in a 5-20 μ L droplet of solution). In the 'hanging-drop' method, a droplet of the protein

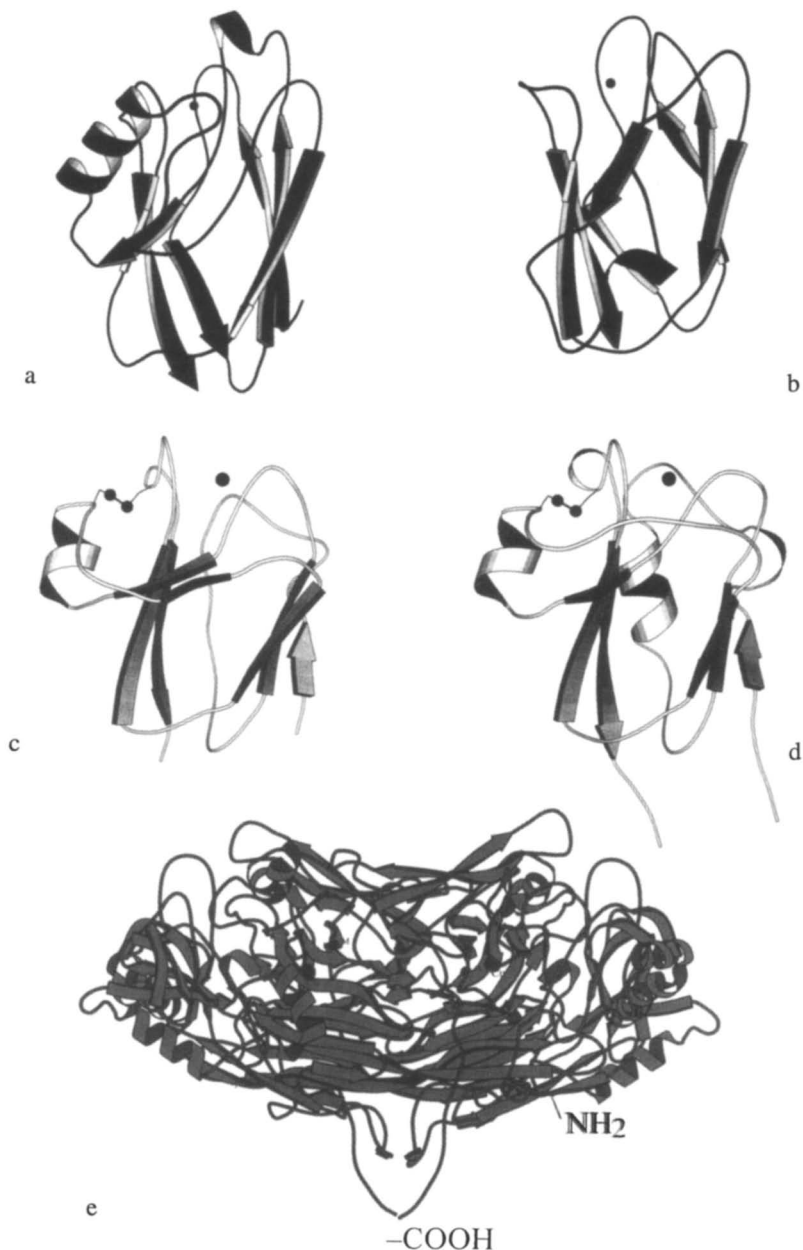


Figure 1: Polypeptide Folds Represented as Ribbon Diagrams

Molecular structures of four 'blue' (type-1) Cu proteins and two Cu enzymes mentioned in the text: (a) plastocyanin, (b) azurin, (c) cucumber basic protein (CBP), (d) cucumber stellacyanin (CuSc), and (e) pea seedling amine oxidase (PSAO). [Figure 1(c) is reproduced with permission from ref. 21. Copyright 1996 Academic Press Limited.]

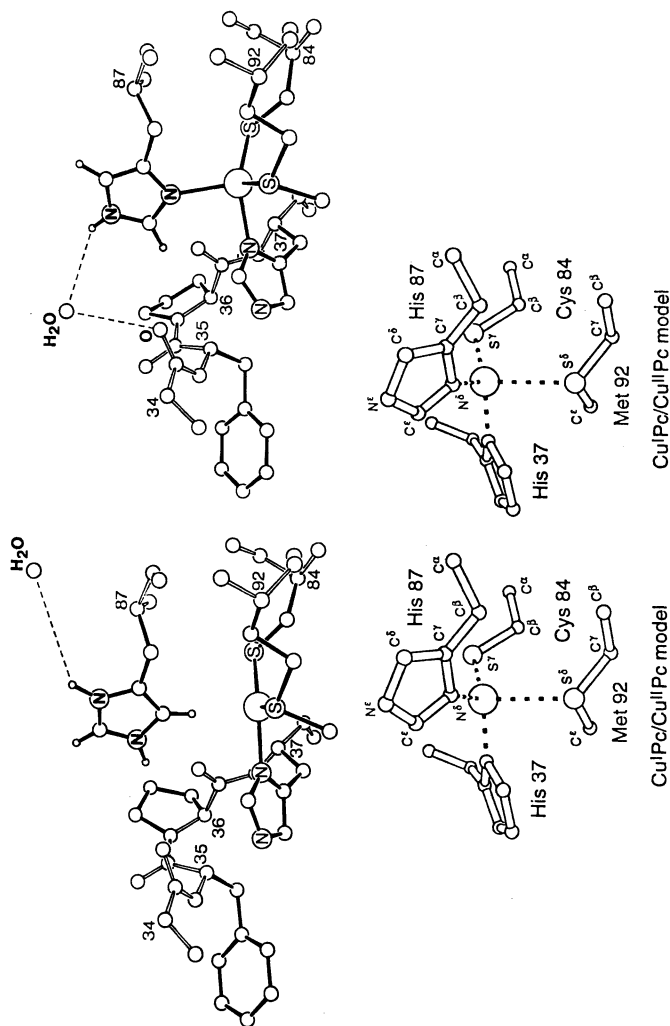


Figure 2: Structural Details of the Metal Site in a Metalloprotein

Top: The Cu site and its surroundings in reduced (Cu^I) poplar plastocyanin (*left*) at low pH and (*right*) at high pH. *Bottom:* Stereoscopic view of the Cu atom and its ligands. The high-pH form of the reduced (Cu^I) protein has the same coordination geometry as the oxidized (Cu^{II}) protein, except that corresponding Cu-ligand bonds are 0.1–0.2 Å longer. [The top figure is reproduced with permission from ref. 7. Copyright 1986 Academic Press Limited.]

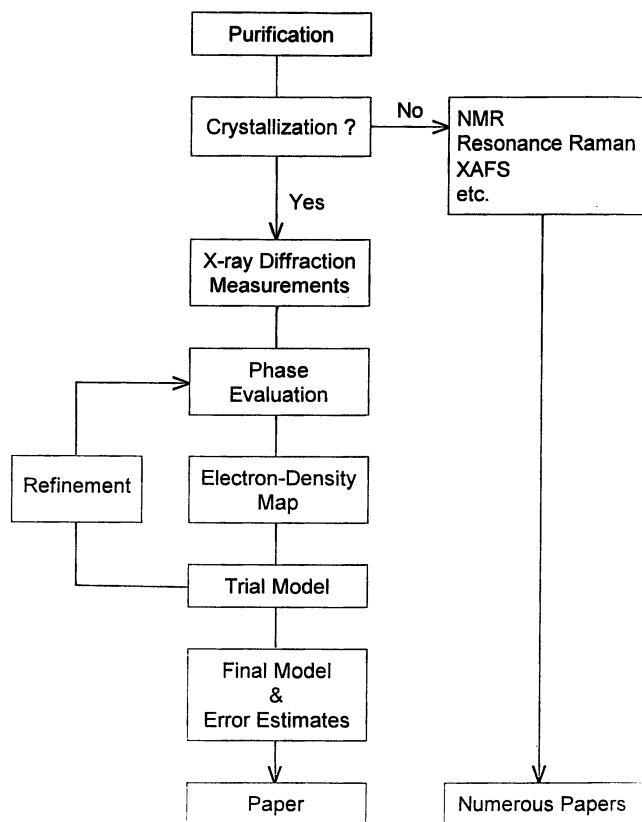


Figure 3: The Crystal Structure Analysis of a Metalloprotein

solution is placed on a siliconized microscope cover slip. This is inverted, and is used to seal a reservoir containing 0.5-1 mL of the precipitant solution. In the 'sitting-drop' method, droplets of the protein solution are placed on multi-depression glass plates in a sealed container containing a larger volume of the precipitant solution. For a long time, 'sitting-drop' experiments were carried out in cheap plastic sandwich boxes, but more professional equipment is now available.

Screening Procedures. The variables that may affect the crystallization behavior of a protein include the concentration of the protein, the nature of the precipitant, the pH, the nature and concentration of the buffer, the nature and concentration of other additives (metal ions, small organics), the ionic strength, and the temperature. The search for the ideal combination of these variables for a particular protein is still "an empirical process that relies on our knowledge of what has worked in the past for other biological macromolecules" (5). Attempts to use that knowledge in a systematic and focussed way have led to the development of screening procedures in which the initial crystallization experiments use a random sampling of precipitants, buffers, metal ions and other additives that have "worked in the past". The most promising combinations identified in the initial screening are then explored in greater detail. Kits of solutions for these procedures are commercially available.

Suitability of Crystals for X-ray Measurements. Ideal protein crystals have dimensions of the order of ≥ 0.1 mm, are single crystals, have well developed faces, are sufficiently robust to be manipulated, are stable in the X-ray beam, and yield a diffraction pattern to adequate resolution (to be defined below). Figure 4 shows the crystals that were used to solve the structures of two of the proteins in Figure 1.

Dependence of Metalloprotein Structures on Crystallization Conditions. When crystals suitable for diffraction measurements have finally been produced - sometimes after the investment of much time and effort - it is tempting to talk about "the crystals" and (later) about "the protein structure". This involves the assumptions (i) that the crystals grown under a particular set of crystallization conditions are unique, and (ii) that the structure of the protein has not been affected by the crystallization conditions.

The first of these assumptions is simply not valid. If a protein crystallizes at all, then it is quite common to find that even a small change in the crystallization conditions can lead to the formation of crystals with a different unit cell ('polymorphism'). An example is shown in Table I. Polymorphism implies that the arrangement of the molecules in the crystals has changed in response to the crystallization conditions.

A similar word of caution applies to the assumption that a crystal structure analysis results in "the" structure of a protein molecule. While changes in the crystallization conditions are unlikely to cause gross changes in the polypeptide fold, it is easy to understand why particular regions in the interior as well as on the surface of a protein molecule may be affected. The network of hydrogen bonds, electrostatic interactions and Van der Waals contacts that hold the polypeptide together provides many pathways by which effects due to the ionic strength, pH and chemical composition of the mother liquor can be transmitted.

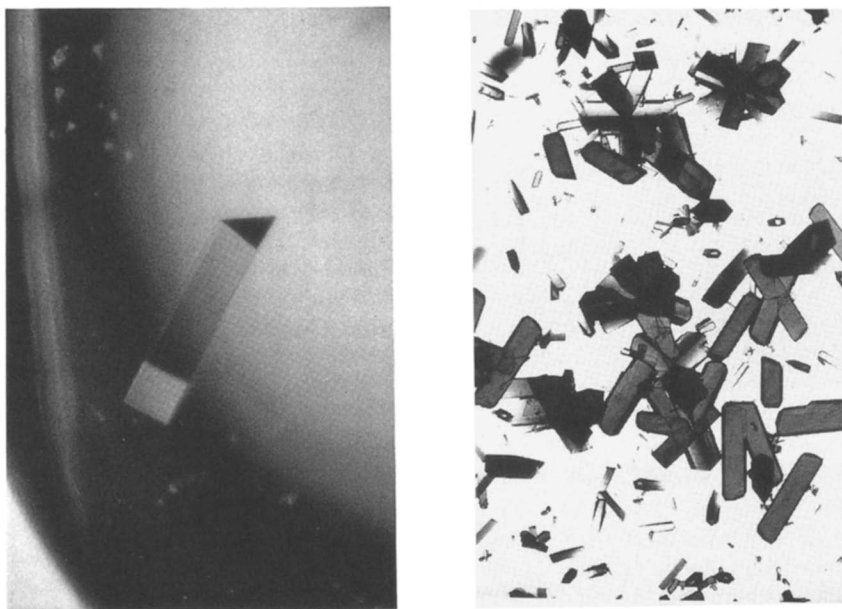


Figure 4: Crystals

Left: A 0.4-mm crystal of pea seedling amine oxidase. *Right:* Crystals of poplar plastocyanin. The large crystals are ~1 mm long.

Table I. An Example of Polymorphism

Crystals of *Arthrobacter globiformis* amine oxidase have different unit cells under different crystallization conditions. (Adapted from ref. 6).

Crystallization conditions ^a	10% w/v PEG8000 0.2M Ca(Ac) ₂ pH 6.5	25% Saturated (NH ₄) ₂ SO ₄ pH 8.7	30% w/v PEG4000 0.1M Tris pH 8.5
Crystal size (μm)	400 × 250 × 50	300 × 150 × 50	1100 × 400 × 60
Symmetry	Monoclinic	Monoclinic	Orthorhombic
Space group	<i>C</i> 2	<i>C</i> 2	<i>P</i> 2 ₁ 2 ₁ 2 ₁
Cell parameters			
<i>a</i> (Å)	159.0	157.6	112.2
<i>b</i> (Å)	65.1	64.3	162.6
<i>c</i> (Å)	71.2	92.6	69.4
<i>β</i> (deg.)	112.5	112.6	90.0
No. of subunits in asymmetric unit	1	1	2
Resolution ^b (Å)	3.0	2.8	3.0

^a PEG = polyethyleneglycol. ^b Resolution is defined as the limit beyond which fewer than 50% of reflections have intensity $I \geq 3\sigma(I)$. See equation 1.

In the following two examples, the metal site in a metalloprotein was found to be highly susceptible to changes in the crystallization medium. The take-home lesson is that, whenever a protein can be crystallized under more than one set of conditions, it is a worthwhile precaution to carry out more than one structure analysis. (This can be done without solving the structure all over again.) If only one structure analysis can be carried out, then the invariance of the protein has to be tested in some other way, for example by observing appropriate spectroscopic properties under a variety of conditions.

Example 1: The Cu^I Site in Reduced Plastocyanin. During the structure analysis of plastocyanin in the reduced (Cu^I) state, complete sets of diffraction data were recorded after adjusting the pH of the crystallization medium to six values between pH 3.8 and pH 7.8 (7). The six structures were refined independently, yielding six sets of Cu^I-site dimensions. These dimensions were strongly dependent on the pH of the crystallization medium (Figure 5), consistent with non-crystallographic evidence for a low-pH form and a high-pH form of the Cu^I site.

It is important to note that there are *no* Cu^I-plastocyanin molecules with the Cu^I-site dimensions found, for example, at pH 5.9: what we see at pH 5.9 is a weighted mean of the two extreme forms whose Cu^I sites are shown in Figure 2a (7). If the

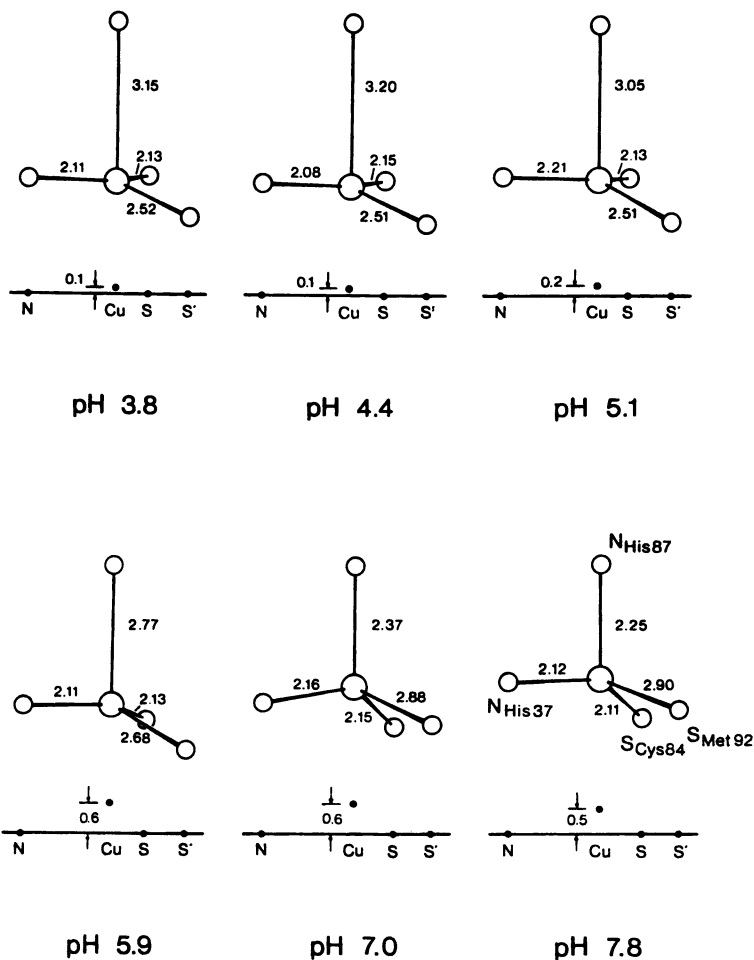


Figure 5: Dimensions of the Cu Site in Reduced (Cu^I) Poplar Plastocyanin as a Function of pH

Only a low-pH and a high-pH form of the Cu^I site actually exist. At intermediate pHs, the crystals contain mixtures of the two types of molecule, and the dimensions of the Cu^I site are weighted means of the two extreme forms. Adapted with permission from ref. 7. Copyright 1986 Academic Press Limited.

structure had been studied only at pH 5.9, the geometry of the Cu^I site would have been described incorrectly.

Example 2: The Active Site in Amine Oxidases. A more dramatic example is provided by the structure analyses of two copper-containing amine oxidases. The catalytic site of these enzymes includes a Cu atom and a topa quinone (TPQ) cofactor. Under some crystallization conditions, the Cu atom is 5-coordinate, and there is no bond between it and the TPQ cofactor (Figure 6a). Under slightly different crystallization conditions, the Cu atom becomes 4-coordinate, and has the TPQ cofactor as one its ligands (Figure 6b). Only the first of these forms of the Cu site is thought to be catalytically competent.

The existence of two forms of the amine oxidase catalytic site was originally reported for the enzyme from *Enterobacter coli*, where the difference was ascribed to the absence or presence of (NH₄)₂SO₄ in the crystallization medium (8). The structure analysis of the amine oxidase from *Arthrobacter globiformis* later revealed the same two forms of the catalytic site, but in this case the crystals of both forms of the enzyme were grown using (NH₄)₂SO₄ as the precipitant (9). The solution from which the 'TPQ-off' form crystallized had a slightly lower pH and a slightly higher ionic strength than the solution which yielded the 'TPQ-on' form, but the trigger responsible for switching the crystals of the enzyme from one form to the other is not yet clear.

X-ray Diffraction Measurements

When a crystal is exposed to a fine parallel beam of X-rays, the X-rays are reflected only in specific directions. The directions depend on the orientation of the crystal and on the dimensions of its unit cell. The diffraction pattern is a record of the directions and intensities of all the reflected X-ray beams. In order to record a diffraction pattern, we need an X-ray source and an X-ray detector.

A single set diffraction data for a protein commonly comprises tens to hundreds of thousands of reflections, and - as will be seen shortly - a single structure analysis may require several sets of data. The ability to measure diffraction data on a semi-industrial scale depends on the availability of intense X-ray sources and fast X-ray detectors. The development of such devices has played a crucial role in making protein crystallography widely available as a research tool.

X-ray Detectors: Films. In the early days of protein structure analysis, diffraction data were recorded as patterns of spots on photographic films. Two properties of each spot had to be recorded: its blackness, which was proportional to the intensity *I* of the reflected beam, and its position on the film, which was obviously related to the direction in which the X-ray beam had been reflected. Each spot and the reflection that had generated it were identified by means of three integers known as the Miller indices *h*, *k* and *l*. The intensity measurements were made by visually comparing each spot with a pre-recorded series of standard spots. The values of *h*, *k* and *l* could be read from a template, though most operators with a bit of experience could dispense with this aid. Meticulous concentration was required. Being recruited to "read spots" was a

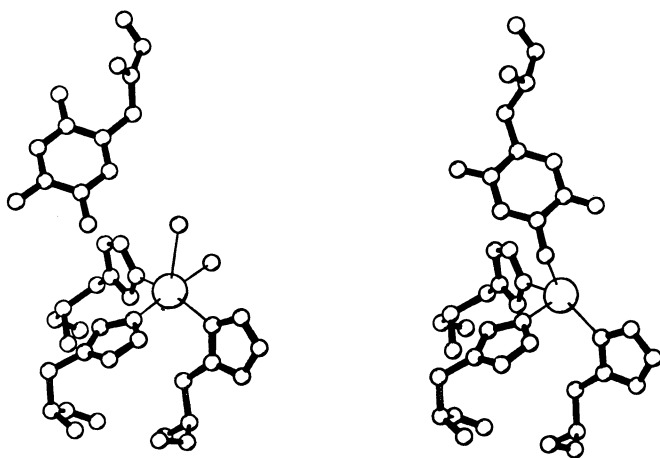


Figure 6: Dependence of the Active Site in *Arthrobacter globiformis* amine oxidase on the Crystallization Conditions

Left: In the catalytically active form of the enzyme, the Cu atom at the catalytic site is 5-coordinate. The TPQ (topa quinone) cofactor is close to the Cu atom but is not bonded to it. *Right:* Under slightly different crystallization conditions, the Cu atom is 4-coordinate, and has the TPQ cofactor as one of the ligands.

considerable hazard for anybody who happened to be the student, spouse or friend of a protein crystallographer.

X-ray Detectors: Counters. Photographic films were in due course replaced by a counter which recorded a single reflection at a time. In a single-counter diffractometer, the crystal and counter were moved under computer control into the orientation appropriate for the measurement of each reflection. At a rate of, say, one reflection per 2 min, a medium-resolution data set of 6,000 reflections for a small protein could be recorded in about a week.

Apart from the obvious advantages of automation, counter instruments offered another benefit: the random (counting) errors in the intensities of the reflections could be deduced directly from the measurements, and the correction of some types of systematic error was relatively simple. In particular, corrections for the absorption of X-rays by the crystal, and for the deterioration of the crystal specimen in the X-ray beam, could be made empirically after some additional measurements on a small sample of reflections. We shall return later to the theme of accuracy and precision.

X-ray Detectors: Two-Dimensional Detectors. More recent developments in detector technology are represented by multi-wire proportional counters ('area detectors', effectively 2-dimensional counters), phosphor image plates, and charge-coupled devices (10). All three types of detector have been incorporated in commercially available instrumentation for 'in-house' use, as well as in multi-user facilities at synchrotron radiation sources. The rates of data acquisition increase in the order: multi-wire detector < image plate < charge-coupled device.

Image Plates. Image plates offer the advantages of a large dynamic range (ratio of the strongest to the weakest measurable intensities), low background noise, and the ability to record data over a large area, i.e., over a large range of diffraction angles. These advantages come at a price in terms of experimental efficiency, since the diffraction patterns recorded on image plates have to be scanned by a laser reader. This can be done off-line or on-line. If scanning is done off-line, the camera cassette has to be re-loaded after each exposure. If scanning is done on-line, data-recording is interrupted while data-readout takes place. Either way, the readout times tend to be longer than the X-ray exposures. In one commercially available instrument, the interruption to data collection is minimized by scanning one plate while another is being recorded. However, few crystallographers lose sleep over the sub-optimal use of their instrumentation. In the euphoria following the crystallization of a protein and the recording of a data set, slight inefficiencies are easily forgiven.

Charge-Coupled Devices. Charge-coupled device detectors (CCDs), the most recent arrivals on the detector scene, offer the ability to record diffraction data at an unprecedented rate. When area detectors and image-plate devices came on the market, they increased the rate of data collection by two orders of magnitude. The readout from CCDs is faster by two more orders of magnitude. At the present time, the high cost of CCDs limits their size (and hence the area over which data can be recorded), but the cost will no doubt decrease when production is scaled up to meet demand.

X-ray Sources: In-house X-ray Generators. Conventional X-ray generators using a sealed X-ray tube are still a tool-of-trade for small-molecule crystallographers, but are now seldom used in macromolecular crystallography. More intense X-ray beams are available from rotating-anode generators. A typical in-house data collection facility comprises a rotating-anode generator and a multi-wire, image-plate or CCD detector. The X-rays emitted by the rotating anode pass through an elaborate arrangement of shutters, slits and mirrors to ensure that the crystal is exposed to a fine, parallel beam of radiation at a single wave length. The whole lot can be purchased for \$0.5-1.0M, depending on one's bargaining ability and choice of detector. Such in-house instrumentation yields perfectly adequate diffraction data for many protein crystal structure analyses.

X-ray Sources: Synchrotron Radiation Sources. Entirely new types of diffraction measurement have been made possible by the high intensity, low divergence and large energy range of the X-ray beams available at synchrotron radiation sources. The high intensity of a synchrotron X-ray beam not only increases the speed of data acquisition, but also enables data to be recorded from smaller crystal specimens (a great advantage in cases where only small crystal specimens can be grown). Time-dependent protein crystallography becomes feasible (11). The low divergence of the X-ray beam reduces the overlap between adjacent reflections, so that resolved diffraction patterns can be recorded from larger unit cells. Finally, the large wave-length range of a synchrotron X-ray beam gives the crystallographer unprecedented flexibility and unprecedented advantages in designing diffraction experiments: (i) Data can be recorded at a single wave length, selected to enhance a particular feature of the experiment (for example, anomalous scattering effects). (ii) Data can be recorded at several selected wave lengths, as required for multiple-wavelength anomalous dispersion analyses ('MAD', see below). (iii) The use of white X-radiation can yield a complete 'Laue' diffraction pattern for a protein on a millisecond time scale.

The availability of synchrotron X-ray sources for protein crystallography depends on the willingness of national or international agencies to foot the bill, which is substantial. The capital cost of a typical multiple-beamline facility is several \$100Ms, and the annual running costs are several \$10Ms. Incidentally, this is one more reason why the CCD detectors mentioned above are potentially very important for macromolecular crystallography at synchrotron X-ray sources: the more expensive the X-ray source, the greater is the saving made by fast data acquisition.

X-ray Measurements at Low Temperature: Cryocrystallography. An important and relatively recent advance in protein crystallography has been the development of methods whereby protein diffraction data can be recorded routinely at liquid-N₂ temperature (~110K) (12). In a cryocrystallographic experiment, a crystal surrounded by a drop of a 'cryoprotectant' is picked up in a tiny loop made from a fine fiber of nylon or glass wool, is snap-frozen, and is mounted in the same loop on a diffractometer (Figure 7). The purpose of the cryoprotectant (glycerol and ethylene glycol are typical (12)) is to prevent the nucleation of ice in the protein crystal. The snap-freezing is achieved by exposing the crystal to a stream of cold nitrogen gas from

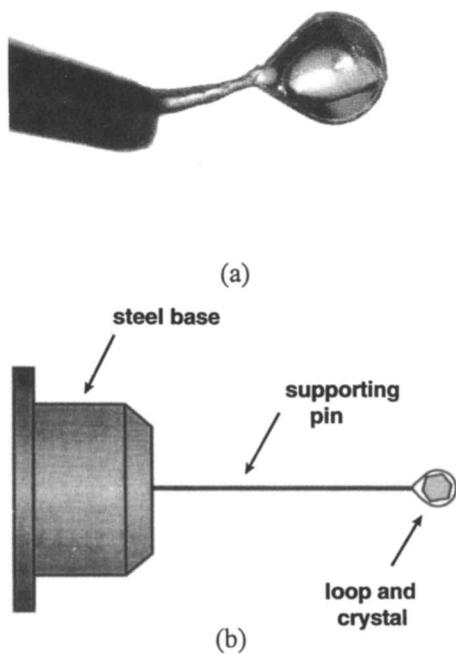


Figure 7: Protein Crystallography at Low Temperatures

(a) A protein crystal held in a nylon loop by means of a drop of cryo-protectant liquid. (b) Diagram of a loop assembly. Reprinted from ref. 12 with permission of Gordon and Breach Publishers. Copyright 1996 Overseas Publishers Association Amsterdam B.V.

a cryostat, or by dipping the crystal into liquid N₂ or a cryogen such as liquid propane. The crystal can be maintained at a low temperature during the entire period of data acquisition.

The most significant benefit of low-temperature diffraction measurements is that X-radiation damage to the crystal is reduced. In many cases, a complete data set can be recorded from a single crystal specimen. This helps to improve the quality of the diffraction data, since it eliminates the need to place several partial data sets recorded from different crystal specimens on a single scale. At low temperature there is usually also a reduction of the dynamic disorder ('temperature factors') in the crystals, so that the resolution of the data and the quality of the final structure are improved.

Once the manipulations required for cryocrystallography have been mastered and the conditions for freezing a particular type of specimen have been optimized, the loop and crystal can be inserted into a plastic phial and stored at liquid-N₂ temperature until required for X-ray data acquisition. Among other practical advantages, this facilitates the transport of diffraction-ready crystals to a synchrotron X-ray source.

The Quality of a Diffraction Pattern: Resolution. Despite the power of contemporary computing methods and the appeal of stereoscopic color graphics, a protein structure is only as good as the diffraction data from which it is derived. A diffraction pattern of high quality has the following characteristics: the background noise is low, the data extend to high values of the reflection angle θ , the reflections at high angles do not overlap, there is a wide range of intensities between the weakest and the strongest reflections, the strongest reflections lie in the linear-response range of the detector, and there is good agreement between the intensities of reflections which should be identical because they are crystallographically equivalent. The 'resolution' d_{\min} depends on the angular range of the X-ray reflections, and on the wave length λ of the X-rays used to record the data:

$$d_{\min} = \lambda/2\sin\theta_{\max} \quad (1)$$

An operational definition of resolution is that d_{\min} is the limit beyond which more than half of the reflections in a narrow range of θ values are too weak to be detected.

Protein Structures at Atomic Resolution. Many perfectly acceptable protein structures have been determined at resolutions in the range 1.5–3 Å. Until recently, structures at higher resolutions (i.e., <1.5 Å) were comparatively rare. An important trend is that increasing numbers of diffraction patterns are now being recorded at resolutions around 1 Å. Not only do the electron-density maps calculated with such high-resolution data lead to more accurate and precise structures, but *ab initio* methods of structure analysis akin to those used for small-molecule structures become accessible. [For purposes of comparison, the resolution of a small-molecule data set recorded with Cu K α radiation ($\lambda = 1.542$ Å) to $\theta_{\max} \approx 75^\circ$ is 0.8 Å.]

The ability to record diffraction data to high resolution has been made possible largely by improvements in crystallization techniques, the development of cryocrystallography, and the availability of synchrotron X-ray sources. In a short 1997 review, Dauter has listed 4 protein structures which have been refined at ≤ 1.2 Å

resolution, and 11 more for which high-resolution data are known to have been recorded (13). The list starts with the classical 1979 (!) refinement of rubredoxin, and includes the 1996 analysis and refinement of cytochrome c_6 by quasi small-molecule methods (14). Two more metalloproteins, concanavalin and liver alcohol dehydrogenase, are among the 11 proteins for which atomic-resolution structures are presumably on the way.

Phase Evaluation

At this stage of the tutorial we need to introduce just a few crystallographic terms which will be helpful in the rest of the discussion.

Intensity and Phase of an X-ray Reflection. Every X-ray beam reflected ('diffracted') by a crystal has a *direction* and an *intensity*. The direction determines the position of the reflection in the diffraction pattern. It is described by three integers, the Miller indices h, k, l , which are uniquely defined by the geometry of the experiment.

The intensity of the reflection, I_{hkl} , is proportional to the square of the *structure factor amplitude* of the diffracted waves, F_{hkl} . Thus

$$|F_{hkl}| = (I_{hkl})^{1/2} \quad (2)$$

However, the structure factor is a vector. For a complete description of it we need to not only its magnitude $|F_{hkl}|$, but also its 'phase'. The phase is represented by the symbol α_{hkl} :

$$\begin{aligned} F_{hkl} &= |F_{hkl}| \exp(i\alpha_{hkl}) \\ &= |F_{hkl}| [\cos\alpha_{hkl} + i\sin\alpha_{hkl}] \end{aligned} \quad (3)$$

When we measure I_{hkl} and take its square root, we obtain only the modulus of the structure factor amplitude $|F_{hkl}|$. The phase α_{hkl} is destroyed by the act of measuring I_{hkl} .

Why Phases are Important: Electron Density. The reason why the loss of the phase information is a pity is that we need to know the phase α_{hkl} of every reflection before we can calculate an electron-density map. This can be seen from the equation for the electron density $\rho(xyz)$ at a point x, y, z in a unit cell:

$$\rho(xyz) = \frac{1}{V} \sum_{hkl} |F_{hkl}| \cos[2\pi(hx + ky + lz) - \alpha_{hkl}] \quad (4)$$

In equation 4 and elsewhere, V is the volume of the unit cell.

The electron density has to be calculated at a large number of points x, y, z . It can be represented graphically in various ways. In the days before computer graphics, electron-density contours were plotted on plastic sheets representing slices through the unit cell. Most current computer graphics programs draw 'chicken-wire' contours that

enclose a volume where the electron density is above a selected threshold. By raising the threshold, the map can be re-drawn to emphasize regions of higher electron density; by lowering the threshold, the electron density can be re-drawn to include regions of lower electron density.

It is important to calculate the electron density as accurately as possible, because the next step in the structure analysis uses the electron density to guide the building of a molecular model. The electron-density map can be only as good as the structure factor amplitudes and phases. We have already seen that the quality of the structure factor amplitudes depend on the quality of the crystals and on the way in which the intensities of the X-ray reflections were measured. The phases, having been destroyed by the act of measuring the intensities, have to be rediscovered.

Calculated Structure Factors for a Molecular Model. The magnitudes and phases of the structure factors for any model consisting of atoms j at positions x_j, y_j, z_j in the unit cell can be calculated:

$$F_{hkl} = V \sum_j \left[f_j \exp(-B_j \sin^2 \theta / \lambda^2) \right] \exp \left[2\pi i (hx_j + ky_j + lz_j) \right] \quad (5)$$

$$= V \sum_j \left[f_j \exp(-B_j \sin^2 \theta / \lambda^2) \right] \left[\cos \left[2\pi (hx_j + ky_j + lz_j) \right] + i \sin \left[2\pi (hx_j + ky_j + lz_j) \right] \right]$$

In equation 5, the contribution of the j th atom depends on the X-ray scattering factor f_j , which is a function of the number of electrons Z_j . The term $\exp(-B_j \sin^2 \theta / \lambda^2)$ is a so-called temperature factor, in which the displacement parameter B_j represents the combined effects of static and dynamic disorder, the angle θ is related to the direction in which the hkl reflection was observed, and λ is the wave length of the X-rays.

Equation 5 tells us that every atom in the structure contributes to every F_{hkl} , but that atoms with a small Z_j and/or a large B_j contribute less than atoms with a large Z_j and/or a small B_j .

Further, equation 5 gives both the real and imaginary components of F_{hkl} , so that the phase α_{hkl} is determined.

While it is nice to know that we can calculate the structure factor amplitudes and phases when we know where the atoms are, this is not what crystallographers are paid to do. Their job is to use the observed structure factor amplitudes $|F_{hkl}|$ to find the positions x_j, y_j, z_j and the displacement parameters B_j . At the end of the process, when correct values of the atomic parameters have been found, the calculated values of $|F_{hkl}|$ should agree with the observed values within the limits of precision of the experiment.

Methods for Evaluating the Phases. The main methods for evaluating the phases for protein structures are summarised in Table II. Each method has its own technical requirements. Multiple isomorphous replacement (MIR) depends on complete data sets recorded from the native protein and at least two isomorphous heavy-atom derivatives. In single isomorphous replacement with anomalous scattering (SIRAS),

Table II. Methods for Evaluating Phases

<i>Abbreviation</i>	<i>Method</i>	<i>Requirements</i>
MIR	Multiple Isomorphous Replacement	Requires several heavy-atom derivatives which are <i>isomorphous</i> with the native protein. The heavy atoms must perturb neither the molecular structure of the protein nor the dimensions of the unit cell of the crystals.
SIRAS	Single Isomorphous Replacement with Anomalous Scattering	Requires a single isomorphous heavy-atom derivative, the data being recorded at an X-ray wavelength where the heavy atoms behave 'anomalously'. Certain pairs of reflections which are normally equivalent become non-equivalent.
MAD	Multiple Wavelength Anomalous Dispersion	Requires complete sets of X-ray diffraction data at several (general 3 or 4) X-ray wavelengths. The wavelengths are selected to lie below, close to, and above the X-ray absorption edge of an atom type in the crystals, so as to exploit energy-dependent differences in the anomalous scattering characteristics of that atom type. The anomalous scatterer may be the endogenous metal of a metalloprotein, or an exogenous heavy-atom type added <i>via</i> the crystallization medium, or an atom type such as Se introduced by protein engineering or biosynthetic labelling of the protein molecules.
MR	Molecular Replacement	Requires a known and closely related protein structure as a 'search model'.
AI	<i>Ab Initio</i>	Requires X-ray diffraction data to very high resolution (at least 1.2Å).

data are required for the native protein and only one isomorphous heavy-atom derivative, but the data for the derivative have to be recorded under special conditions. Multiple wavelength anomalous dispersion (MAD) uses complete data sets recorded at three or four wavelengths, requiring only a single crystal in favorable cases (15,16). There are several ways to incorporate anomalous scatters into a protein that does not have a natural one (17). When a known and closely related protein structure is available, phase evaluation by molecular replacement (MR) is frequently the method of choice (18). Finally, although *ab initio* (AI) methods are still in their infancy, it is already clear that they represent an exciting challenge when atomic-resolution data are accessible.

Phase Evaluation = Solving the Structure. The phases evaluated by one or more of these methods are only approximate. In favorable cases, they lead to the calculation of an interpretable electron-density map, i.e., a map to which a reasonable model can be fitted. The phases can be improved ('refined') in various ways that will be discussed under the headings **Model Building** and **Model Refinement**. As already stated, the structure can be described as solved when the values of $|F_{hkl}|$ calculated *via* equation 5 agree with the observed values within the limits of precision of the experiment.

Recent Progress in *Ab Initio* Phase Evaluation. The statistical ('direct') methods which are now used routinely to find the phases for - and thus solve - a large proportion of 10-to-200-atom structures are not generally applicable to macromolecular structures. However, there has recently been progress in two methods for solving protein structures *ab initio*, using no information other than a single set of diffraction data. Both methods require diffraction data to atomic resolution.

In the 'shake-and-bake' method (19), a trial structure is generated by placing an appropriate number of atoms at random positions in the unit cell. Structure factors are calculated, their phases are refined by optimizing a 'minimal function', and the highest peaks in an electron-density map based on the refined phases are used as a trial structure for the next cycle. In addition to high-resolution (~1 Å) data, the calculations require a lot of computer time.

The second new *ab initio* method is of particular interest for bio-inorganic chemists, since it is applicable to proteins that contain a small number of heavier atoms such as Fe and S (14). Provided that the X-ray data extend to atomic resolution, the positions of the heavier atoms can be found by a well-established variant of a well-established small-molecule procedure (the superposition of super-sharpened Patterson functions). Once the heavier atoms have been located, phases calculated from the heavier-atom contributions using are combined with the observed structure factor amplitudes to produce an electron-density map. The peaks in this map are listed in order of height. Starting with the weakest peak, the effect of deleting each peak in turn is tested. If deleting an atom improves the agreement between the calculated and observed structure factors, the peak remains deleted; if the agreement gets worse, the deleted peak is restored, and is assigned as an atom. When all the peaks have been tested, new phases are calculated and the procedure is repeated.

The first unknown protein structure to be solved by this method was that of *Monoraphidium braunii* cytochrome c_6 , an 89-residue protein with a heme-Fe and

three S atoms (14). The analysis used data to 1.2 Å resolution, 85% of the atoms being generated automatically. The remaining gaps in the model were filled by inspecting electron-density maps.

Molecular Replacement *versus* Other Methods of Phase Evaluation. Among the methods listed in Table II, MR has the distinct advantage that it requires only one set of diffraction data for the unknown protein. This advantage has to be balanced against the possibility that phases evaluated by MR may be biased towards the search model. Phases evaluated by MIR, SIRAS, MAD and *ab initio* methods are free from this type of bias, since all the information used in the calculations is derived from the protein that is being studied. Experimental phases are more likely to be distributed randomly around the 'correct' values, and their refinement to the 'correct' values is, in principle, easier.

Some applications of MR and other methods of phase determination are illustrated by the following examples, which are taken from the structure analyses of three of the proteins in Figure 1.

Example 3: Cucumber Basic Protein (CBP). CBP was one of the first 'blue' copper proteins to be crystallized, but the structure analysis took a long time. Attempts to prepare heavy-atom derivatives for MIR were frustrated by the fact that the crystals were extremely fragile and fell apart during most experiments. MR calculations were unsuccessful, even though two other 'blue' copper proteins, azurin and plastocyanin, were available as search models. The phases were finally found by the MAD method, using synchrotron X-ray data recorded at 4 wavelengths near the Cu absorption edge (20). The reason for the failure of MR then became apparent: contrary to expectation, the polypeptide folds of azurin (Figure 1a) and plastocyanin (Figure 1b) are sufficiently different from that of CBP (Figure 1c) to render them ineffective as search models.

Example 4: Cucumber Stellacyanin (CuSc). In contrast to the previous example, MR enabled the phases for yet another 'blue' copper protein, CuSc, to be found in a single step. When CuSc was crystallized in 1995, a high level of sequence identity and spectroscopic similarities with CBP suggested that the polypeptide folds of the two proteins are closely similar. Phases evaluated by MR using the refined CBP coordinates (21) as a search model indeed yielded an electron-density map from which the structure of CuSc could be deduced directly (22). As expected, the polypeptide fold of CuSc (Figure 1d) has key features in common with that of CBP (Figure 1c). This example illustrates the effectiveness of MR when the search model is sufficiently similar to the target protein.

Example 5: Pea Seedling Amine Oxidase (PSAO). In the structure analysis of PSAO, a combination of SIRAS and MR was used in an innovative way which avoided biasing the final phases towards the MR search model (23).

Extensive attempts to find isomorphous heavy-atom derivatives for phase evaluation by MIR were unsuccessful. Only one isomorphous heavy-atom derivative was ever characterized. The "heavy atom" was a phosphotungstate ion, $\text{PW}_{12}\text{O}_{40}^{5-}$.

Complete sets of X-ray diffraction data were recorded for the native protein and for the $\text{PW}_{12}\text{O}_{40}^{5-}$ derivative. The data for the $\text{PW}_{12}\text{O}_{40}^{5-}$ derivative were recorded near the tungsten X-ray absorption edge, where W atoms exhibit strong anomalous scattering effects. For the purpose of interpreting the data it was assumed that a $\text{PW}_{12}\text{O}_{40}^{5-}$ ion could be treated as a single composite atom, i.e., a ball of electron density equivalent to all the electrons in a W_{12} cluster. The positions of the W_{12} composite atoms in the unit cell were found by a standard computational procedure ('difference Patterson' maps). Phases could then be evaluated by the SIRAS method. The measured anomalous scattering effects were included in the SIRAS calculations as though they originated from W_{12} composite atoms. However, the electron-density maps calculated with these SIRAS phases were uninterpretable.

While this work was in progress, the structure of the amine oxidase from *E. coli* (ECAO) was reported by another laboratory (8). When the atomic coordinates for ECAO became available, the obvious next step was to use ECAO as a search model in a MR calculation. This was done. However, instead of using the MR calculation to evaluate phases for PSAO itself, phases were derived for the $\text{PSAO-PW}_{12}\text{O}_{40}^{3-}$ derivative. An electron-density map calculated with these phases had features that clearly corresponded to the W_{12} clusters. Since the shape and dimensions of a $\text{PW}_{12}\text{O}_{40}^{3-}$ anion are well known from several inorganic crystal structures, it was possible to find the positions of all 12 W atoms in the W_{12} clusters by fitting a model of $\text{PW}_{12}\text{O}_{40}^{3-}$ to the electron density. In this way the positions of all 12 W atoms in the W_{12} clusters could be located (Figure 8a).

New phases for the structure factors of the native protein crystals were then evaluated by means of a SIRAS calculation based on the scattering contributions of the 12 individual W atoms in the W_{12} clusters. Electron-density maps calculated with these new phases were interpretable, and led to the solution of the structure (Figures 1e and 8b) (23).

In this strategy MR was used only to discover the W atom positions in the heavy-atom derivative. Thus the risk of biasing the PSAO structure towards the ECAO search model was avoided.

Model Building and the Interpretation of Electron-Density Maps

Model Building. The model of a protein is built by using computer graphics to move atoms or groups of atoms into the electron-density contours. The challenge of doing this for a new protein is considerable. It is a part of the structure analysis which many crystallographers find most exciting, and where subjective judgments based on experience and intuition can still play an important role.

Many structures are solved at a resolution of 2–3 Å, but even 3.5-Å maps can be interpretable. At such resolutions, the electron density lacks features that correspond to individual atoms. Further, the initial phases and the electron-density map calculated from them are - at best - only approximately correct. Even when high-resolution data are available, the investigator may decide not to include them since the accuracy of the calculated phases tends to decrease at high resolution.

In favorable cases, the boundary between the protein and solvent can be distinguished, and the electron density in the protein region includes continuous

segments that look like parts of a polypeptide chain. The investigator inspects computer graphics images of the electron-density contours, hoping to recognize segments that are continuous and have a shape consistent with the geometry of an α -helix, a β -strand or a plausible loop. With a bit of luck, these potential elements of secondary structure can be joined in a rational way to yield a model of the polypeptide backbone. Discontinuities and noise in the electron density may create problems in deciding the order in which the bits of polypeptide are to be connected.

As the model of the polypeptide backbone is developed, atomic positions derived from it are used to improve the phases. Better phases result in a better electron-density map, which is used to improve the model, which in turns results in better phases. The process is iterative. If all goes well, the electron density progressively becomes clearer and cleaner, permitting side chains and solvent molecules to be identified and added to the model.

Objective (Computer) Methods to Assist Model Building. The problem of identifying a polypeptide in an electron-density map has been likened (I have forgotten by whom) to finding a long noodle in a bowl of thick soup. Software developments are helping to make the process more objective and more automatic. In the early stages of an analysis, automatic procedures for solvent flattening can facilitate the recognition of the molecular boundary, and thus improve the phases. Software for tracing the highest ridge through the 3-dimensional electron density automatically is available, and frequently enables segments of secondary structure to be recognized. Pattern recognition may be aided by the use of data bases of known structures.

Avoidance of errors in connectivity. At first sight, protein structures are sufficiently complicated to make it unlikely that more than one model (i.e., more than one set of atomic coordinates) can adequately account for the observed diffraction pattern. Unfortunately this assumption has turned out to be incorrect. Even experienced investigators can make mistakes in assigning the connectivity of a polypeptide chain. In other words, it is possible to identify the helices, β -strands and loops in a protein structure correctly, and then to join them up in an incorrect order. This is not the place to discuss specific examples. Most protein crystallographers are now well aware of the need to apply objective tests designed to reduce the risk of errors in the connectivity and conformation of the polypeptide backbone (24).

Model Refinement

The aim of 'refinement' is to make a molecular model as accurate and precise as the available data allow. Although effective refinement methodologies have been in place for quite a long time, research on better refinement strategies is still an active field.

In a refinement calculation, the model is adjusted until the structure factor amplitudes calculated from the model agree as well as possible with the observed structure factor amplitudes. The parameters that are varied are the atomic positions x_j, y_j, z_j , the displacement parameters ['temperature factors'] B_j , and possibly some fractional site occupancies q_j .

The model may be adjusted (i) in 'real' space, by moving, adding or subtracting atoms or groups of atoms so as to optimize agreement with the current computer-graphics images of the electron density, or (ii) in 'reciprocal space' (a concept used to discourage interference from non-crystallographers), by least-squares adjustment of the atomic parameters so as to optimize the agreement between the observed and calculated values of the structure factor amplitudes. In most refinements, cycles of automatic reciprocal-space adjustment alternate with 'hands-on' real-space adjustment of the model by the investigator. As the model gets better, so do the phases calculated from it, and so also do the electron-density maps calculated from the phases.

Least-Squares Refinement. In least-squares refinement, the atomic parameters are systematically adjusted so as to minimize the sum of the squares of the discrepancies between the observed and calculated structure factor amplitudes (equation 7).

Quantity Minimized in Least-squares Refinement

$$= Q = \sum_{hkl} w_{hkl} \left(|F_{hkl}(\text{obs})| - k |F_{hkl}(\text{calc})| \right)^2 \quad (7)$$

[where $w_{hkl} = 1/\sigma^2(F_{hkl})$, $\sigma^2(F_{hkl}) = \text{variance of } F_{hkl}$, and k is a scale factor]

Since the relationship between the variables x_j , y_j , z_j , B_j and the discrepancies ($|F_{hkl}(\text{obs})| - |F_{hkl}(\text{calc})|$) is non-linear, the refinement is an iterative process.

Restrained Least-squares Refinement. The effectiveness of least-squares fitting depends partly on the extent to which a problem is over-determined, i.e., the ratio of observations to variables. In the refinement of small-molecule structures the ratio of observations to variables is frequently ≥ 5 , even when each atom is represented by 9

Table III. Comparisons between the Structure Analyses of Small Molecules and Macromolecules^a

<i>Small Molecules</i>		<i>Macromolecules</i>		
4%	Typical Final Residual R	15-20%		
9	Parameters per Atom ^b	4		
0.85 Å	Typical Resolution of Data	1 Å	2 Å	3 Å
≥ 5	Observations per Variable	14	2	<1

^a Adapted from ref. 4. ^b Small molecules: 3 positional and 6 anisotropic displacement parameters per atom. Macromolecules: 3 positional and 1 isotropic displacement parameters per atom.

variables (3 positional and 6 anisotropic displacement parameters). In the refinement of many protein structures, the degree of over-determination is much smaller (Table III).

The remedy is to introduce additional 'observations' in the form of geometrical data taken from well-authenticated small-molecule structures. After all, there is no need to use a protein structure analysis to find the lengths of C–C bonds or the bond angles in amide groups: the values of such parameters are assumed to be known accurately and are used as data. The sum of the squares of the discrepancies from each of the standard values is minimized, along with the sum of the squares of the discrepancies between the observed and calculated structure factor amplitudes (equation 8).

Quantity Minimized in Geometrically Restrained Least-Squares Refinement

$$\begin{aligned}
 = Q = & \sum_{hkl} w_{hkl} \left(|F_{hkl}(\text{obs})| - k |F_{hkl}(\text{calc})| \right)^2 \\
 & + \sum_{\text{distances}} w_{\text{dist } j} \left(d_j^{\text{ideal}} - d_j^{\text{model}} \right)^2 + \sum_{\text{angles}} w_{\text{ang } j} \left(\theta_j^{\text{ideal}} - \theta_j^{\text{model}} \right)^2 \\
 & + \sum_{\text{coplanar atoms}} \dots + \sum_{\text{chiral centres}} \dots + \sum_{\text{non-bonded contacts}} \dots \quad (8)
 \end{aligned}$$

The currently accepted dictionary of standard geometrical criteria was compiled by Engh and Huber (25). The weights $w_{\text{dist } j}$, $w_{\text{ang } j}$, etc., of the restraints in relation to the crystallographic data are arbitrary, and are usually allocated in accordance with past experience combined with trial-and-error.

Simulated Annealing. There remains a danger that a least-squares refinement calculation will converge to a false minimum, i.e., a local minimum in the sum of the squares of the discrepancies, but not the global minimum corresponding to the 'best' structure. A false least-squares minimum with respect to the diffraction data will also be a false minimum with respect to the energy of the molecule (Figure 9). In 'simulated annealing' calculations, the structure is perturbed sufficiently to escape from a false energy minimum if necessary, is permitted to undergo internal motions corresponding to those that would be expected if the molecule were heated to a high temperature, and is then allowed to 'cool' under the influence of the crystallographic data and the geometrical restraints mentioned above (26).

Maximum Likelihood Method. While least-squares methods have served protein crystallography well for about 20 years, it has become apparent that the minimization of Q in equations 7 and 8 may be achieved not only by improvements in the model, but also by an accumulation of systematic errors or by fitting the model to noise in the data. A better target function for the refinement is obtained by incorporating the concept of 'maximum likelihood', which takes into account estimates of the model

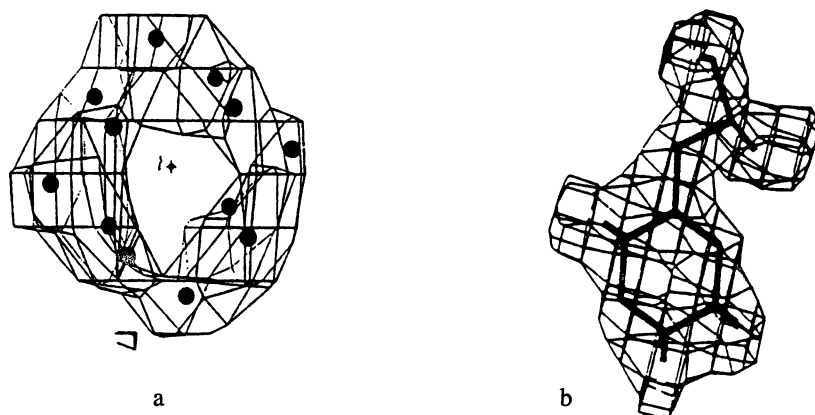


Figure 8: Electron-density Maps and Models at Two Stages of a Structure Analysis.

(a) During the structure analysis of pea seedling amine oxidase (PSAO), a cluster of 12 W atoms was fitted to the electron-density map for a PSAO-phospho-tungstate derivative by using the known structure and dimensions of the phospho-tungstate ($\text{PW}_{12}\text{O}_{40}^{3-}$) anion. The phases for the electron density of the $\text{PW}_{12}\text{O}_{40}^{3-}$ derivative had been evaluated by MR. The positions of the 12 W atoms were then used to evaluate phases for PSAO itself by SIRAS.

(b) At the end of the refinement of the PSAO structure, features such as the TPQ (topa quinone) cofactor could be modelled unequivocally.

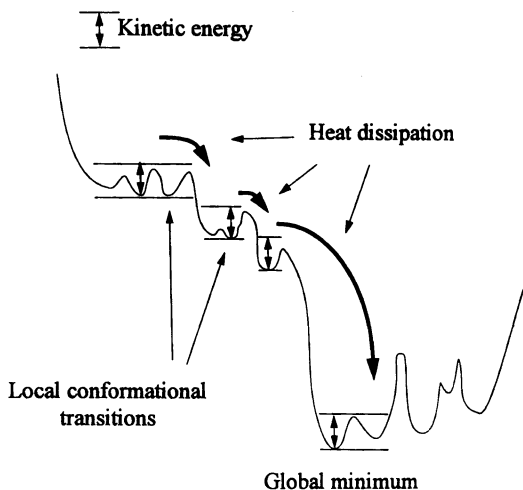


Figure 9: Simulated Annealing

The kinetic energy of the system permits local conformational transitions provided that the barriers are smaller than the kinetic energy. Refinement without simulated annealing may leave the structure in one of the false minima. (Reprinted with permission from ref. 26. Copyright 1997 Current Biology Ltd.

error, the incompleteness of the model, and estimates of the errors in the experimental data. New algorithms using maximum-likelihood refinement are being implemented and tested (27,28). The improvement of phases is reported to be greater, electron-density maps resulting from the refinement are cleaner, and model bias in electron-density maps is reduced. A particular benefit in the refinement of metalloprotein structures is that variations in the quality of diffraction from different parts of a molecule (for example, at a metal site) can be taken into account.

Assessment of the Accuracy and Precision of a Metalloprotein Structure

The Residual R as an Indicator of Accuracy. The most common of the criteria that are used to follow the progress of a refinement is the crystallographic residual R , which expresses the agreement between the calculated and observed structure factor amplitudes (equation 9):

$$R = \frac{\sum_{hkl} \left| |F_{hkl}(\text{obs})| - |F_{hkl}(\text{calc})| \right|}{\sum_{hkl} |F_{hkl}(\text{obs})|} \quad (9)$$

When a structure has been solved, i.e., when all the atomic parameters are thought to be known, the calculated values of the structure factor amplitudes should agree with the observed values within the limits of precision. In small-molecule crystallography, final R values of 0.02-0.03 are not uncommon. Protein crystallographers cheerfully accept final R values of 0.15-0.2. The higher R values for macromolecular structures reflect the greater uncertainties in both F_{obs} and F_{calc} . We have to remember that protein diffraction data are recorded from crystal specimens of less-than-perfect regularity, and that very few protein structures have so far been refined with atomic-resolution data.

The 'Free' Residual. At first sight, the use of the residual R as an indicator of the progress of a refinement is perfectly reasonable. If a model is getting 'better' (i.e., if it is approaching the true structure), R should be getting smaller.

There is a flaw in this reasoning. A decrease in R can nearly always be achieved by simply introducing additional variables (for example, by adding solvent atoms, or by converting isotropic to anisotropic displacement parameters). The additional flexibility introduced by the additional variables leads to better agreement with the data, even if the structural model that is being refined is incorrect. A new criterion, the 'free' residual R_{free} , has therefore been introduced (29).

In order to calculate R_{free} , a small proportion of reflections - say, 5% - are chosen at random and are excluded from the refinement calculations. If the model is truly getting 'better', the residual for the excluded reflections R_{free} should decrease just as rapidly as the residual R for the reflections used in the refinement. A decrease in R without a similar decrease in R_{free} is an indicator that the apparent improvement in the model may be artefactual.

Error Alerts. The explosion in the number of protein crystal structures that are solved each year has created a demand for additional objective (and, if possible, automatic) methods for assessing accuracy and precision. A number of programs have been developed with the specific aim of detecting significant errors before they become part of the literature. A program in frequent use at the present time is *PROCHECK*, which compares selected geometrical parameters of a structure with averaged values taken from a data base of reliable structures at the same resolution (30). The program alerts authors (and referees) to any exceptional features.

One of the outputs from *PROCHECK* is a Ramachandran diagram - a type of diagnostic which has been in use for 30 years (Figure 10). The Ramachandran diagram is a plot of ψ versus ϕ (the dihedral angles) for all main-chain amide groups. Many



combinations of ψ and ϕ are improbable or forbidden, since they represent conformations which would lead to steric hindrance. The parts of a Ramachandran diagram that represent allowed combinations of ψ and ϕ occupy a relatively small proportion of the total area. The usefulness of the amide-group dihedral angles ψ and ϕ as diagnostics at the end of a restrained least-squares refinement is due partly to the fact that ψ and ϕ are seldom included among the restraints. Any combination which falls into an improbable or forbidden part of the Ramachandran plot is therefore a powerful indicator of a potential error.

Deviations from Ideal Dimensions. The results listed in protein crystallographic papers often include the r.m.s. deviations of structural parameters from their ideal values. The reason for presenting this information is that a well refined structure should not only have a low residual and a low free residual, but should also have low r.m.s. deviations from ideal geometry. In the absence of close agreement with the diffraction data, compliance with ideal geometry says little about the accuracy of a structure. It shows only that the dimensions have been restrained effectively by means of the weights in equation 8.

Precision of Metal-Site Geometries. In the case of metalloproteins, the dimensions of the metal site are usually among the quantities that bio-inorganic chemists want to know. The fact that these dimensions have standard deviations has perhaps not been stated sufficiently clearly. When non-crystallographers use crystallographically determined atomic positions to interpret metal-site spectra or to calculate energy levels, the uncertainties in the atomic positions are not always apparent in the quantities derived from them.

The following example is based on data for plastocyanin, where we have quite a lot of empirical evidence about the precision of the metal-site dimensions.

Example 6: The Cu-Ligand Bond Lengths in Plastocyanin. Five refinements of the structure of poplar Cu^{II} -plastocyanin have been published (31-33). They are based on data recorded at ambient and low temperatures, at 1.3 Å and 1.6 Å

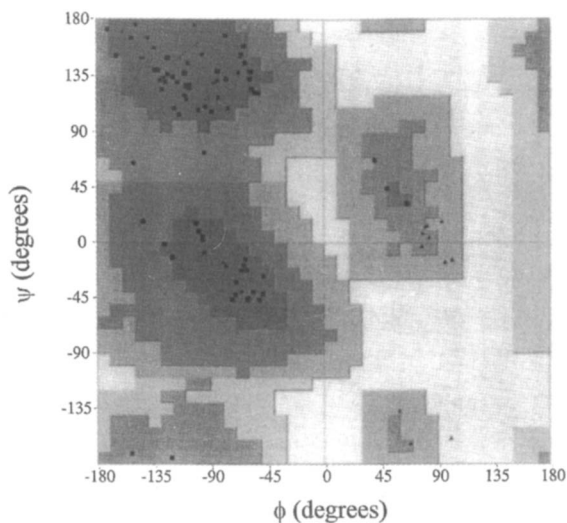


Figure 10. A Classical Error Diagnostic: the Ramachandran Plot

The darker the shading, the more favored are the combinations of the peptide-group dihedral angles ϕ and ψ falling within a region of the diagram. Individual data points are indicated by the symbols ■ and ▲. Diagram from the refinement of cucumber basic protein (21), reproduced with permission. Copyright 1996 Academic Press Limited.

resolution, with a sealed tube and a synchrotron radiation source as X-ray sources, and using single-counter and photographic intensity measurements. Two of the refinements are based the same data set, and were conducted independently by investigators who used different software packages and did not communicate with each other until the calculations were complete. There are remarkable differences among the five sets of Cu-ligand bond lengths (Table IV).

The results for poplar plastocyanin in Table IV, and similar results for the plastocyanins of some other species, suggest values for the precision of the Cu-ligand bond lengths as a function of the resolution of the diffraction data (Table V). The estimate in Table V for 1.6 Å resolution was derived from two independent refinements using independently recorded data sets (31). The other estimates are unpublished 'guesstimates' based on empirical correlations and qualitative arguments. The estimated standard deviations in Table V are such that the bond-length differences in Table IV are within the limits of precision.

Factors Affecting Metal-Site Geometry. The differences among the Cu-ligand bond lengths in plastocyanin (Table IV) can be traced to both technical and personal factors (32,33). The *technical factors* include the 'dictionary' of standard dimensions used in the restraints on molecular geometry, the inclusion/exclusion of hydrogen atoms, the resolution and quality of the diffraction data, the treatment of anomalous scattering by the Cu and S atoms, and the treatment of partially occupied solvent sites. The *personal factors* comprise the decisions that investigators make when they use computer graphics to adjust a model. The adjustments generally involve subjective judgments on the significance of features in various types of electron-density map: For example, should a particular electron-density feature be modelled as a disordered side chain or as a solvent molecule?

One of the conclusions that was drawn from a comparison between the refinements of Cu^{II}-plastocyanin at 1.6 Å and 1.3 Å resolution is that operator intervention in other parts of a structure had contributed to significantly to the differences between corresponding Cu-ligand bond lengths (32). This was predictable: since the structure factors are functions of all the atoms (equation 5), even changes in a distant part of a metalloprotein molecule may have a finite effect on the dimensions of the metal site. What was surprising was the size of the effect. It follows that the estimated precision of the metal-site dimensions should be linked not only to the resolution as in Table V, but also to our confidence in the rest of the structure.

Luzzati Plots. For about 45 years, a statistic proposed by Luzzati (34) has been used as a global estimate of the maximum average error in atomic positions. The Luzzati Plot for a crystal structure is a graph of the residual R , calculated for reflections in ranges of $\sin\theta/\lambda$, as a function of $\sin\theta/\lambda$. The graph is compared with theoretical curves for various values of the maximum average error in position. The Luzzati statistic was proposed long before protein crystal structures were amenable to study. Its subsequent adoption by protein crystallographers led to plausible error estimates, but has recently been criticized as being formally incorrect and invalid

Table IV. Dimensions of the Cu Site in Poplar Plastocyanin

<i>Temperature</i>	295 K			173 K	
<i>Resolution</i>	1.6 Å		1.3 Å	1.6 Å	
<i>pH of Crystals</i>	pH 4.2 ^a	pH 6.0 ^a	pH 6.0 ^b	6.0 ^c	6.0 ^d
<i>Software</i>	PROLSQ	PROLSQ	PROLSQ	PROLSQ	EREF
<i>Bond</i>					
Cu–N(His 37)	2.07	2.04	1.91	1.98	2.05
Cu–N(His 87)	2.17	2.10	2.06	1.95	1.96
Cu–S(Cys 84)	2.11	2.13	2.07	2.14	2.21
Cu–S(Met 92)	2.87	2.90	2.82	2.78	2.78

^a Single-counter data (31). ^b Synchrotron film data (32). ^c Synchrotron film data. Refined in Sydney (33). ^d Same data set as in previous column. Refined independently in Hamburg using a different protocol (33).

Table V. Precision of Metal-Ligand Bond Lengths in a Small Metalloprotein

Example: Poplar plastocyanin (~10,000 Da, 99 aminoacids, 1 Cu).

<i>Resolution (Å)</i>	$\sigma_{\text{Cu-L}}$ (Å)
1.3	0.04
1.6	0.05
1.8	0.06
1.9	0.07

The estimated standard deviation $\sigma_{\text{Cu-L}}$ at 1.6 Å resolution is derived from two independent refinements of the structure (31). The other values of $\sigma_{\text{Cu-L}}$ are based on empirical arguments.

(35,36). It is mentioned here because there are frequent references to it in the literature.

Cruickshank's 'Diffraction Precision Indicator'. A new indicator for the overall precision of a protein structure has recently been proposed by Cruickshank (35). The Diffraction Precision Indicator (DPI) takes the form:

$$\sigma_w(x) = k(N/P)^{1/2}C^{-1/3}d_{\min}R \quad (9)$$

where $\sigma_w(x)$ is the average uncertainty in the position of an atom, k is a constant, N is the number of atoms, P is the number of degrees of freedom [= no. of observations - (no. of atoms x no. of variables/atom)], C is the completeness of the data [(no. of observations) ÷ (no. of reflections theoretically observable in the same resolution range)], d_{\min} is the resolution, and R is the crystallographic residual. The actual value of the constant k is ~ 0.7 , but Cruickshank recommends the use of $k = 1.0$ "as a matter of caution" (35). (The lower value is cited in ref. 36.)

It is noteworthy that the DPI depends linearly on the resolution d_{\min} and the residual R .

As defined in equation 9, the DPI applies to an atom with an average atomic number Z and an average displacement parameter B . A more sophisticated form of equation 9 accommodates the fact that atoms with a higher Z and/or lower B are expected to be located with greater precision than atoms with a lower Z and/or higher B (23).

Values of $\sigma_w(x)$ for some of the structures that have been discussed in this tutorial are shown in Table VI. The values have been calculated using equation 9 with $k = 1.0$.

Table VI. Examples of Diffraction Precision Indicators

	Cyt c_6 ^a	PoPc ^b	PoPc ^c	PSAO ^d	AGAO ^e
Resolution of Data (Å)	1.2	1.3	1.6	2.2	2.3
Completeness of Data	0.985	0.760	0.740	0.865	0.901
No. of Observations	32,653	14,303	7,393	86,780	33,778
No. of Atoms ^f	913	895	936	~10,400	5,353
No. of Variables ^g	8,217	3,580	3,744	~41,600	21,412
Degrees of Freedom ^h	24,426	10,723	3,649	~45,000	12,366
Residual	0.14	0.15	0.15	0.18	0.20
DPI (Å)	0.03	0.06	0.13	0.20	0.31

^a Cytochrome c_6 (14). ^b Poplar plastocyanin (32). ^c Poplar plastocyanin (31).

^d Pea seedling amine oxidase (23). ^e *Arthrobacter globiformis* amine oxidase (9).

^f No. of atoms in asymmetric unit.

^g Cyt c_6 : 9 parameters per atom (x_j, y_j, z_j , plus 6 anisotropic displacement parameters).

Other proteins: 4 parameters per atom (x_j, y_j, z_j, B_j).

^h Degrees of freedom = no. of observations - no. of variables.

At first sight, the values of $\sigma_w(x)$ for plastocyanin in Table VI are surprisingly large in comparison with the estimated uncertainties of the Cu–ligand bond-lengths in Table V. There are reasonable explanations for the difference. Firstly, the DPI includes formal criteria for the quality of a refinement, whereas the estimates in

Table V were derived empirically by comparing corresponding structural parameters in a group of closely related structures. The estimates in Table V were intended to be conservative, but they may not have been conservative enough. Secondly, equation 9 applies to atoms with an average value of the displacement parameter B , so that it over-estimates the $\sigma_w(x)$'s of atoms that have a lower B_j . The donor atoms at the Cu site in plastocyanin have B_j s that are significantly lower than the average value of B for the whole molecule, so that the expanded form of equation 9 should lead to lower estimates of the positional uncertainty. This argument should apply generally to the metal sites of metalloproteins.

Conclusions

This tutorial has aimed to give an impression of the steps involved in using X-ray crystal structure analysis to discover the molecular structure of a metalloprotein. Exciting contemporary advances in instrumentation and methodology are likely to increase the power of macromolecular crystallography yet further: within the foreseeable future, metalloprotein structures will be determined faster, many of them will be determined at atomic or near-atomic resolution, and time-dependent structure analyses are likely to contribute new insights to the understanding of metalloprotein chemistry.

On the other hand, it is appropriate to include a note of caution. The results of a protein structure analysis should be read not only with enthusiasm but also with care. The structural model resulting from an analysis may not be unique; the hypothesis that a particular molecular structure is independent of the crystallization conditions cannot be taken for granted until it has been tested by crystallographic or other experiments; and there are limits to the accuracy and precision of even the most successful and careful crystal structure analysis. While the crystal structure analysis of a metalloprotein is uniquely capable of identifying the metal-binding groups, the precision of the metal-site dimensions may well be improved by XAFS or vibrational spectroscopy. The invaluable contributions that spectroscopic methods can make to our knowledge of metal-ligand bond lengths, molecular structure and dynamics are illustrated in other contributions to this Symposium.

Acknowledgments

Figures 1a–1d and 6 were kindly supplied by Dr. Mitchell Guss, Figure 2 by Dr. Paul Ellis, and Figures 1e and 8b by Dr. Vinay Kumar. Helpful discussions with Dr. Mitchell Guss and Dr. Matthew Wilce are gratefully acknowledged. Research on metalloprotein structures at the University of Sydney is supported by the Australian Research Council (Grant A29601726 to J. M. Guss and H. C. Freeman).

Literature Cited

1. Perutz, M. *Protein Structure. New Approaches to Disease and Therapy*; W. H. Freeman: New York, 1992; Chapter 1, pp 1-40.
2. Blundell, T. L.; Johnson, L. N. *Protein Crystallography*; Academic Press: London, 1976.
3. Drenth, J. *Principles of Protein X-ray Crystallography*; Springer-Verlag: New York, 1994.
4. Hendrickson, W. A. *Physics Today* **1995**, 42-48.
5. Gilliland, G. L.; Ladner, J. E. *Curr. Opinion Struct. Biol.* **1996**, *6*, 595-603.
6. Freeman, H. C.; Guss, J. M.; Kumar, V.; McIntire, W. S.; Zubak, V. M. *Acta Crystallogr.* **1996**, *D52*, 197-198.
7. Guss, J. M.; Harrowell, P. M.; Murata, M.; Norris, V. A.; Freeman, H. C. *J. Mol. Biol.* **1986**, *192*, 361-387.
8. Parsons, M. R.; Convery, M. A.; Wilmot, C. M.; Yadav, K. D. S.; Blakeley, V.; Corner, A. S.; Phillips, S. E. V.; Knowles, P. F. *Structure*, **1995**, 1171-1184.
9. Wilce, C. J. M.; Dooley, D. M.; Freeman, H. C.; Guss, J. M.; Matsunami, H.; McIntire, W. S.; Ruggiero, C. E.; Tanizawa, K.; Yamaguchi, H. Submitted for publication.
10. Tate, M. W.; Eikenberry, E. F.; Gruner, S. M. *Synchr. Rad. News* **1996**, *9*, 19-23.
11. Moffat, K. *Synchr. Rad. News* **1996**, *9*, 15-18.
12. Rodgers, D. W. *Synchr. Rad. News* **1996**, *9*, 4-11.
13. Dauter, Z. *Synchr. Rad. News* **1997**, *10*, 22-25.
14. Frazão, C.; Soares, C. M.; Carrondo, M. A.; Pohl, E.; Dauter, Z.; Wilson, K. S.; Hervás, M.; Navarro, J. A.; De la Rosa, M. A.; Sheldrick, G. M. *Structure* **1995**, *3*, 1159-1169.
15. Ogata, C. M.; Hendrickson, W. A. *Synchr. Rad. News* **1995**, *8*, 13-18.
16. Smith, J. L.; Thompson, A.; Ogata, C. M. *Synchr. Rad. News* **1996**, *9*, 12-14.
17. Pappa, H. S.; Stewart, A. E.; McDonald, N. Q. *Curr. Opinion Struct. Biol.* **1996**, *6*, 611-616.
18. Turkenburg, J. P.; Dodson, E. J. *Curr. Opinion Struct. Biol.* **1996**, *6*, 604-610.
19. Ealick, S. E. *Structure* **1997**, *5*, 469-472.
20. Guss, J. M.; Merritt, E. A.; Phizackerley, R. P.; Hedman, B.; Murata, M.; Hodgson, K. O.; Freeman, H. C. *Science*, **1988**, *241*, 806-811.
21. Guss, J. M.; Merritt, E. A.; Phizackerley, R. P.; Freeman, H. C. *J. Mol. Biol.* **1996**, *262*, 686-705.
22. Hart, P. J.; Nersissian, A. M.; Herrmann, R. G.; Nalbandyan, R. M.; Valentine, J. S.; Eisenberg, D. *Protein Sci.* **1996**, *5*, 2175-2183.
23. Kumar, V.; Dooley, D. M.; Freeman, H. C.; Guss, J. M.; Harvey, I.; McGuirl, M. A.; Wilce, M. C. J.; Zubak, V. M. *Structure*, **1996**, *4*, 943-955.
24. Brändén, C. I.; Jones, T. A. *Nature* **1990**, *334*, 687-689.
25. Engh, R. A.; Huber, R. *Acta Crystallogr.* **1991**, *A47*, 392-400.
26. Brünger, A. T.; Adams, P. D.; Rice, L. M. *Structure* **1997**, *5*, 325-336.
27. Pannu, N. S.; Read, R. J. *Acta Crystallogr.* **1996**, *A52*, 659-668.
28. Murshudov, G. N.; Vagin, A. A.; Dodson, E. J. *Acta Crystallogr.* **1997**, *D53*, 240-255

29. Kleywegt, G. J.; Brünger, A. T. *Structure* **1996**, *4*, 897-904.
30. Laskowski, R. A.; MacArthur, M. W.; Moss, D. S.; Thornton, J. M. *J. Appl. Cryst.* **1993**, *26*, 283-291.
31. Guss, J. M.; Freeman, H. C. *J. Mol. Biol.* **1983**, *169*, 521-563.
32. Guss, J. M.; Bartunik, H. D.; Freeman, H. C. *Acta Crystallogr.* **1992**, *B48*, 790-811.
33. Fields, B. A.; Bartsch, H. H.; Bartunik, H. D.; Cordes, F.; Guss, J. M.; Freeman, H. C. *Acta Crystallogr.* **1994**, *D50*, 709-730.
34. Luzzati, V. *Acta Crystallogr.* **1952**, *5*, 802-810.
35. Cruickshank, D. W. J. In *Proceedings of the CCP4 Study Weekend, January 1996*; Dodson, E.; Moore, M.; Ralph, A.; Bailey, S., Eds.; CLRC Conference Proceedings DL-Conf-96-001; Council for Central Laboratory of the Research Councils, Daresbury, Cheshire, U.K. 1996; pp 11-22.
36. Dodson, E.; Kleywegt, G. J.; Wilson, K. *Acta Crystallogr.* **1996**, *D52*, 228-234.

Chapter 5

Recent Advances in Electronic Absorption Spectroscopy

Felix Tuzek

Institut für Anorganische Chemie und Analytische Chemie, Johannes Gutenberg
Universität Mainz, Staudingerweg 9, D-55099 Mainz, Germany

Many proteins in general and metalloproteins in particular exhibit characteristic optical absorptions which can be used in the investigation of these systems in various ways. Possible applications are the spectrometric quantitation of a protein solution, the spectroscopic monitoring of an enzymatic reaction or the interpretation of the absorption spectrum itself. It is the last aspect this article is dealing with.

The aim of a spectral interpretation in bioinorganic chemistry is to obtain structural information of a metal-containing active site (1). In particular *ligand-field transitions* provide a sensitive probe of the local geometry around the transition-metal center. In this respect, electronic absorption spectroscopy is - like other spectroscopic techniques - complementary to X-ray structure determination. In addition, however, spectroscopy provides electronic-structural information which can be used to define the reactivity of an active site and thus understand its function. This aspect is complementary to electronic-structure calculations. Of central interest is the determination of *covalency* which describes the interaction of the ligands with the metal site beyond electrostatic effects and, in particular, provides a measure of how much *charge* has been transferred from the ligands to the metal (or *vice versa*). Here, "ligands" either denote the amino-acid residues surrounding the metal center or a substrate that is bound to the active site. The total charge or partial charges on a substrate are in many cases critically important for enzymatic reactions. Information regarding covalency is contained in the *charge-transfer spectrum* of the metal-substrate complex. Comparison of this spectrum with that of simple model complexes exhibiting various coordination geometries further allows a systematic study of the metal-substrate bond. In the present article this is exemplified on Cu(II) azide systems with relevance to hemocyanin and tyrosinase. Azide serves as an electronic-structural analogue for peroxide and is also bound by these metalloproteins.

An important feature of the binuclear Cu unit involved in O₂ binding and activation is the *bridging coordination* of O₂ or azide (2). In the electronic ground state, this gives rise to magnetic exchange interactions of the unpaired metal electrons leading in general to strong antiferromagnetic coupling. However, the bridging coordination also has profound effects on the CT excited states of the dimer systems and thus greatly influences

their CT spectra (3). This can be used to *obtain geometric as well as electronic-structural information from CT spectra*. A model is presented which analyzes the CT spectral features of monomers and analogous bridged dimers in terms of a valence-bond configuration interaction (VBCI) formalism. As an introduction to this description and the corresponding nomenclature, the CT spectrum of a mononuclear copper azide system and its information content are described first. Then, the complications arising for a parallel treatment of binuclear systems are demonstrated. It is shown that if the additional features are analyzed the dimer CT spectrum contains more detailed information than the monomer CT spectrum. In particular, it provides insight into the superexchange pathways leading to the observed ground-state magnetic behavior. Finally, a summary and generalization of these results are presented.

Charge transfer transitions in mononuclear Cu(II) complexes

The optical absorption spectrum of a monomeric Cu(II) azide complex displayed in Figure 1a (4) contains one absorption band at 25000 cm⁻¹ which can be assigned to a one-electron transition from the mainly azide-type orbital

$$(\pi^{nb})' = \frac{1}{\sqrt{1+2\gamma S+\gamma^2}} (\pi^{nb} + \gamma d) \quad (1a)$$

to the mainly copper-type orbital

$$d' = \frac{1}{\sqrt{1-2\lambda S+\lambda^2}} (d - \lambda \pi^{nb}) \quad (1b).$$

d is the highest, singly occupied metal orbital which is of $d_{x^2-y^2}$ type, and π^{nb} is the doubly occupied HOMO of azide. S , the overlap integral, is defined by

$$S = \langle d | \pi^{nb} \rangle \quad (2),$$

and the mixing coefficients γ and λ are related by (5)

$$\lambda = \frac{\gamma + S}{1 + \gamma S} \quad (3).$$

Insertion of (1a) and (1b) in the molecular orbital (MO) ground state Slater determinant

$$(\Psi^{GS})' = \left| d'^+ (\pi^{nb})' (\pi^{nb})' \right| \quad (4)$$

gives

$$\begin{aligned}
 (\Psi^{GS})' &= \frac{1}{\sqrt{1+2\gamma S+\gamma^2}} \frac{1}{\sqrt{1-S^2}} \left[\left| d^+ \pi^{nb+} \pi^{nb-} \right| + \gamma \left| d^+ \pi^{nb+} \bar{d} \right| \right] \\
 &= \frac{1}{\sqrt{1+2\gamma S+\gamma^2}} \frac{1}{\sqrt{1-S^2}} \left[\Psi^{GS} + \gamma \Psi^{CT} \right]
 \end{aligned} \tag{5}$$

where the first term corresponds to the *ionic* configuration with two electrons being in the ligand orbital, and the second contribution corresponds to the *charge-transfer* configuration with two electrons at the metal and an unpaired electron on the ligand. The admixture of the CT configuration introduces *covalency* into the system, and hence γ is referred to as *covalency parameter* (5). The wavefunction (5) corresponds to the *Heitler-London* (HL) or *valence-bond* (VB) description of the ground state. Likewise, the CT state of the system is represented by

$$\begin{aligned}
 (\Psi^{CT})' &= \left| d^+ (\pi^{nb})' \bar{d}' \right| \\
 &= \frac{1}{\sqrt{1-2\lambda S+\lambda^2}} \frac{1}{\sqrt{1-S^2}} \left[\left| d^+ \pi^{nb+} \bar{d} \right| - \lambda \left| d^+ \pi^{nb+} \pi^{nb-} \right| \right] \\
 &= \frac{1}{\sqrt{1-2\lambda S+\lambda^2}} \frac{1}{\sqrt{1-S^2}} \left[\Psi^{CT} - \lambda \Psi^{GS} \right]
 \end{aligned} \tag{6}$$

and thus contains some admixture λ of the ionic ground state. In a perturbation limit, γ and λ are given by

$$\gamma = -\frac{\beta_0}{\Delta} \qquad \lambda = -\frac{\beta_1}{\Delta} \tag{7}$$

where

$$\beta_1 = \langle d | \hat{H} | \pi^{nb} \rangle - S \langle d | \hat{H} | d \rangle \tag{8a}$$

$$\beta_0 = \langle d | \hat{H} | \pi^{nb} \rangle - S \langle \pi^{nb} | \hat{H} | \pi^{nb} \rangle \tag{8b}$$

and Δ is the zeroth-order energy difference between Ψ^{GS} and Ψ^{CT} (5). In this limit ($\beta_0, \beta_1 \ll \Delta$),

$$\lambda \cong \gamma + S \tag{9}$$

(cf eqn (3)), and the magnitudes of the ground and CT state shifts, δ_0 and δ_1 , are given by

$$\delta_0 = \beta_0^2 / \Delta \tag{10a}$$

$$\delta_1 = \beta_1^2 / \Delta \tag{10b}$$

Note that the ground-state stabilization energy $-\delta_0$ essentially determines the heat of formation of the metal-ligand complex. In the present context, we are interested in the energy of the optical CT transition which is given by

$$\tilde{\nu}_{CT} = \Delta + \delta_0 + \delta_1 = \Delta + \frac{\beta_0^2}{\Delta} + \frac{\beta_1^2}{\Delta} \quad (11).$$

In general, it is more practical to use orthogonal wavefunctions. To this end, the ligand wavefunctions are orthogonalized to the metal d-orbitals, i.e.

$$\pi_o^{nb} = \frac{1}{\sqrt{1-S^2}} (\pi^{nb} - S d) \quad (12).$$

With (12) the zeroth-order ground and excited state wavefunctions are given by

$$\Psi_o^{GS} \equiv \left| \begin{matrix} + & + & - \\ d & \pi_o^{nb} & \pi_o^{nb} \end{matrix} \right| \quad \Psi_o^{CT} \equiv \left| \begin{matrix} + & + & - \\ d & \pi_o^{nb} & d \end{matrix} \right| \quad (13)$$

and the admixed GS and CT states can be written as

$$(\Psi_o^{GS})' = \frac{1}{\sqrt{1+\lambda_0^2}} (\Psi_o^{GS} + \lambda_0 \Psi_o^{CT}) \quad (14a)$$

$$(\Psi_o^{CT})' = \frac{1}{\sqrt{1+\lambda_0^2}} (\Psi_o^{CT} - \lambda_0 \Psi_o^{GS}) \quad (14b)$$

In this basis, the covalency parameter is

$$\lambda_0 = -(\beta_1)_0 / \Delta_0 \quad (15)$$

(cf (7)) with Δ_0 being the energy difference between the zeroth-order states (13), and

$$(\beta_1)_0 = \langle d | \hat{H} | \pi_o^{nb} \rangle = \frac{1}{\sqrt{1-S^2}} \left[\langle d | \hat{H} | \pi^{nb} \rangle - S \langle d | \hat{H} | d \rangle \right] \quad (16).$$

From (16), $(\beta_1)_0$ has the simple meaning of a *transfer matrix element* between a metal and a ligand orbital that is orthogonal to the metal orbital. The corresponding splitting scheme is symmetric, i.e. both the ground-state stabilization and the CT excited state shift are given by

$$(\delta_1)_0 = (\beta_1)_0^2 / \Delta_0 \quad (17).$$

(cf Fig. 1b). Throughout the remainder of this paper, orthogonal wavefunctions will be used and the suffixes "0" are omitted.

In the case of a monomer, the ground and CT excited state shifts δ_1 cannot be measured spectroscopically. This is different in a dimer, as will be shown below. However, λ can always be determined from the *intensity of a CT transition* and thus an estimate of these shifts also becomes possible for a monomer. A measure for the intensity of a transition is the oscillator strength (f) which is proportional to the area of an absorption band

$$f_{\text{exp}} = 4.32 \cdot 10^{-9} \int \epsilon(\tilde{\nu}) d\tilde{\nu} \quad (18)$$

with ϵ , the molar decadic absorption coefficient, in $\text{M}^{-1}\text{cm}^{-1}$, and $\tilde{\nu}$ in cm^{-1} . On the other hand, f is related to the square of the transition dipole moment by

$$f_{\text{theo}} = 1.085 \cdot 10^{-5} \bar{\tilde{\nu}} \left| \langle \psi^g | \underline{\mu} | \psi^e \rangle \right|^2 \quad (19)$$

where $\bar{\tilde{\nu}}$ is a suitably averaged transition energy (in cm^{-1}) and the transition dipole moment is given in $\text{e}\text{\AA}$. If ψ^g is identified with the ground state function (14a) and ψ^e with the CT state function (14b) and the CT transition is associated with the transfer of one electron over the distance \underline{R} (in \AA) from the ligand to the metal, the transition dipole moment results as

$$\langle \psi^g | \underline{\mu} | \psi^e \rangle = \frac{1}{1 + \lambda^2} \lambda \text{ e } \underline{R} \equiv \underline{M} \quad (20)$$

Hence

$$\frac{f_{\text{exp}}}{\bar{\tilde{\nu}}} \frac{1}{1.085 \cdot 10^{-5}} \frac{1}{(eR)^2} = \frac{1}{(1 + \lambda^2)^2} \lambda^2 \quad (21)$$

and if the quantities f , $\bar{\tilde{\nu}}$ and R are known, λ is determined. For the structurally characterized Cu(II) azide monomer $[\text{py}_2\text{Cu}(\text{NO}_3)(\text{N}_3)]$ (7), $f = 0.05$, $\bar{\tilde{\nu}} = 25000 \text{ cm}^{-1}$ (4) and $R \approx 2 \text{ \AA}$ and thus $\lambda = 0.23$. With (15) and (17),

$$\tilde{\nu}_{\text{CT}} = \bar{\tilde{\nu}} = \Delta (1 + 2\lambda^2) \quad (22)$$

and thus $\Delta = 22600$, $\beta_1 = -5200$ and $\delta_1 = 1200$ (all in cm^{-1} , cf Table I).

Charge transfer transitions in binuclear bridged Cu(II) complexes

General considerations. First, a binuclear complex bridged by one ligand L with one „active“ bridging orbital is considered (8); specific examples will be given below. Let the symmetry of the dimer be C_{2v} . In the ground state (GS) of the dimer, the two electrons in the Cu orbitals couple to form a 1A_1 and a 3B_1 state. LMCT transitions can take place to the left Cu (Cu_A) or the right Cu (Cu_B). Linear combinations of these two degenerate, locally excited CT configurations generate two symmetry-adapted CT states, A_1^{CT} and B_1^{CT} . In addition, each CT configuration leaves one unpaired electron in the bridging

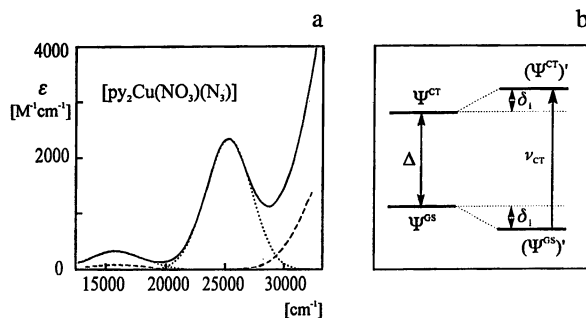


Figure. 1a (left): Optical absorption spectrum of a mononuclear azido complex with azide \rightarrow Cu CT band (dotted); dashed: spectrum of a non-azide containing analogue (adapted from ref. 4). Figure 1b (right): Energy-level scheme of a mononuclear complex indicating the zeroth-order CT energy Δ , the interaction energy δ_1 and the optical CT transition.

Table I. VBCI parameters of mono- and binuclear Cu(II) azide complexes (in cm^{-1})

	end-on terminal ^a	cis μ -1,3 ^b	mono μ -1,1 ^c	bis μ -1,1 ^c
Δ	22600	23900	22900	24800
U		52400	52400	52400
Π		43500	43500	43500
β_1	-5200	-8350	-7070	-7020
β_2		-4350	-6580	-5700
λ	0.23	0.49	0.44	0.57

^a From intensity of CT band (see text)

^b Differs from parametrization of ref. 8 by taking into account π^* orbital

^c From ref. 17

ligand orbital that couples with the other unpaired electron on a Cu center to a singlet and a triplet state. Hence, *there exist in total four CT excited states for each CT state in the monomer*. In analogy to the monomer (eqn (14)), the GS and CT wavefunctions are to a first approximation given by

$$({}^1A_1^{GS})' = \frac{1}{\sqrt{1+\lambda^2}} ({}^1A_1^{GS} + \lambda {}^1A_1^{CT}) \quad (23a)$$

$$({}^1A_1^{CT})' = \frac{1}{\sqrt{1+\lambda^2}} ({}^1A_1^{CT} - \lambda {}^1A_1^{GS}) \quad (23b)$$

$$({}^3B_1^{GS})' = \frac{1}{\sqrt{1+\lambda^2}} ({}^3B_1^{GS} + \lambda {}^3B_1^{CT}) \quad (23c)$$

$$({}^3B_1^{CT})' = \frac{1}{\sqrt{1+\lambda^2}} ({}^3B_1^{CT} - \lambda {}^3B_1^{GS}) \quad (23d)$$

with

$$\lambda = -\sqrt{2} \frac{\beta_1}{\Delta} \quad (24),$$

whereas ${}^3A_1^{CT}$ and ${}^1B_1^{CT}$ do not interact. Correspondingly the energy level scheme of Figure 2 is obtained which is an immediate generalization of the monomer level scheme (Fig. 1b). Both singlet and triplet CT states split by an amount

$$\delta_1 = \frac{2\beta_1^2}{\Delta} \quad (25)$$

providing an experimental information about the transfer matrix element β_1 and thus the covalency parameter λ . Note that δ_1 which also corresponds to the ground-state stabilization is twice as large as for the monomer (eqn (17)). At the present level of approximation, both singlet and triplet GS components are lowered in energy by δ_1 and are therefore degenerate. Hence, four symmetry-allowed CT transitions are predicted as indicated in the figure, two singlet \rightarrow singlet and two triplet \rightarrow triplet transitions.

An alternative measure of covalency is provided by the *intensity* of the CT transition. If the metal-ligand distance does not change, the transition dipole moments of the, e.g. ${}^1A_1 \rightarrow {}^1A_1$ and ${}^1A_1 \rightarrow {}^1B_1$ transitions are given by the vector sum and difference, resp., of the transition moments from the ligand to the individual Cu sites \underline{M}_A and \underline{M}_B which each correspond to the transition moment \underline{M} of the monomer (20) („transition dipole vector coupling“ (4)):

$$\langle ({}^1A_1^{GS})' | \underline{\mu} | ({}^1A_1^{CT})' \rangle = \frac{1}{\sqrt{2}} (\underline{M}_A + \underline{M}_B) \quad (26a)$$

$$\langle ({}^1A_1^{GS})' | \underline{\mu} | ({}^1B_1^{CT})' \rangle = \frac{1}{\sqrt{2}} (\underline{M}_A - \underline{M}_B) \quad (26b)$$

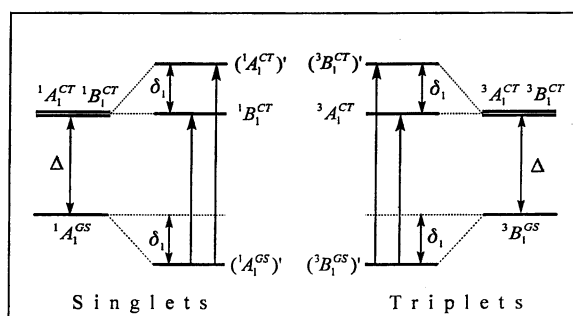


Figure 2. Energy-level scheme of a binuclear complex (symmetry C_{2v}) along with interaction parameters and optical CT transitions.

Hence, the total intensity of the singlet \rightarrow singlet CT transitions in the dimer unit should be about twice as large as the intensity of the monomer CT transition:

$$\left(\frac{f({}^1A_1^{GS} \rightarrow {}^1A_1^{CT})}{\tilde{\nu}({}^1A_1^{GS} \rightarrow {}^1A_1^{CT})} + \frac{f({}^1A_1^{GS} \rightarrow {}^1B_1^{CT})}{\tilde{\nu}({}^1A_1^{GS} \rightarrow {}^1B_1^{CT})} \right) / \frac{f(\text{mono})}{\tilde{\nu}(\text{mono})} = \frac{|M_A + M_B|^2 + |M_A - M_B|^2}{2|M|^2} = 2 \quad (27),$$

and the intensity ratio of the two CT transitions should be given by

$$\frac{f({}^1A_1^{GS} \rightarrow {}^1A_1^{CT})}{f({}^1A_1^{GS} \rightarrow {}^1B_1^{CT})} \frac{\tilde{\nu}({}^1A_1^{GS} \rightarrow {}^1B_1^{CT})}{\tilde{\nu}({}^1A_1^{GS} \rightarrow {}^1A_1^{CT})} = \frac{|M_A + M_B|^2}{|M_A - M_B|^2} = \frac{\cos^2(\alpha/2)}{\sin^2(\alpha/2)} \quad (28)$$

where α is the angle between the two Cu-L bonds. The same relations apply to the total intensity and the intensity ratio, resp., of the triplet \rightarrow triplet CT transitions. Note that (27) equally follows from the evaluation of the transition dipole matrix element using the dimer wavefunctions (23) with (24) and (21): the CT intensity is proportional to λ^2 , and the covalency parameter of the dimer is $\sqrt{2} \cdot \lambda(\text{mono})$.

In the examples which now follow, this simple, prototype picture of CT energies and intensities is modified by several factors:

- the presence of additional interactions influencing the CT state energies,
- the presence of more than one important bridging orbital,
- the presence of more than one bridging ligand.

Cis μ -1,3 bridging azide. The first binuclear system being considered, $[\text{Cu}_2(\text{L-Et})(\text{N}_3)][\text{BF}_4]_2$ contains a cis μ -1,3 bridging azide ligand between two Cu(II) centers, in addition to a bridging alkoxide group deriving from the binucleating ligand L-Et (= N,N,N',N' tetrakis[2-(1-ethylbenzimidazolyl)]2-hydroxy-1,3-diaminopropane). This system has been synthesized as a model for met-N₃ Hemocyanin by McKee et al. (9). The coordination of each Cu is completed by three benzimidazolyl groups simulating the three histidine ligands of hemocyanin. The two copper centers are strongly antiferromagnetically coupled ($-2J \geq 1200 \text{ cm}^{-1}$). In contrast to the earlier structure determination, we found that the Cu coordination is closer to trigonal-bipyramidal than quadratic-planar (10). Hence, the two unpaired electrons are primarily in d_{z^2} -type orbitals and the major part of the strong antiferromagnetic coupling is due to the bridging azide group.

The optical spectrum of this compound shows two bands at 23800 and 27400 cm^{-1} (Figure 3, top) which by comparison with the non-azide containing analogue are associated with the bound azide. From a comparison of this spectrum with that of met-azide hemocyanin, Solomon and coworkers inferred a cis μ -1,3 coordination of azide in this Hc derivative (4). As the triplet ground state is not populated, both transitions correspond to singlet \rightarrow singlet CT transitions. In accordance with the prototype energy

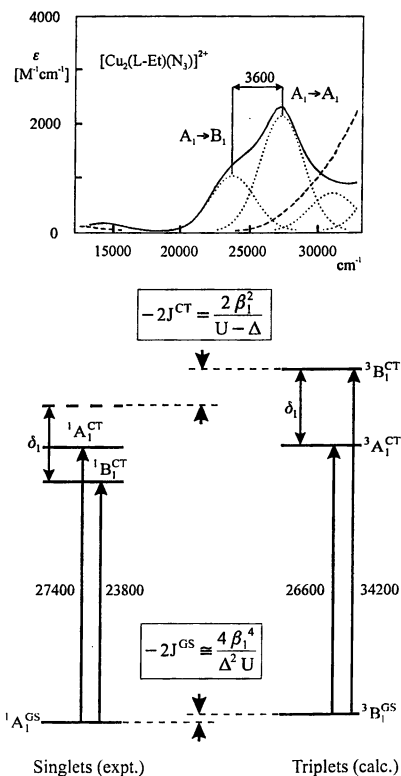


Figure 3. Top: Optical absorption spectrum of the binuclear cis μ -1,3 azido Cu(II) complex $[\text{Cu}_2(\text{L-Et})(\text{N}_3)]^{2+}$ with Gaussian resolution (dotted), spectrum of a non-azide containing analogue (dashed) and assignments of the azide \rightarrow Cu CT bands (adapted from ref. 4). Bottom: Corresponding energy level scheme with observed and calculated transitions, interaction energies and ground-state/excited-state coupling constants.

level scheme (Fig.2), these transitions appear split, and the splitting δ_1 is about twice as large as the monomer- δ_1 (see above). The assignment of the higher-energy transition to ${}^1A_1^{GS} \rightarrow {}^1A_1^{CT}$ is qualitatively in line with the intensity ratio from eqn (28) which, based on the angle α between the two Cu-azido bonds, gives a value of 8.6. The deviation from the experimentally determined ratio of 2.1 has been explained by vibronic mixing between the ${}^1A_1^{CT}$ and ${}^1B_1^{CT}$ states (4). The total intensity of the singlet CT bands in the dimer, however, does not double with respect to the monomer as predicted by the vector coupling model (cf eqn (24)), but is only 30% larger than in the monomer.

In view of the fact that the triplet CT transitions cannot be observed in this system an estimate of their energies has been obtained by SCF-X α transition-state calculations (8). These are indicated on the right half of the energy level scheme in Figure 3, bottom. Obviously, the predicted triplet energies are by several thousand cm^{-1} higher than the observed singlet energies (left half of Fig.3, bottom), and the calculated triplet CT state splitting is about twice as large as the observed singlet CT state splitting. The first result is consistently found in this type of calculation for bridged dimers and is explained by a *large antiferromagnetic interaction in the CT excited state (ESAF) (11)* which lowers the singlet with respect to the triplet CT states by several 1000 cm^{-1} in energy. This effect cannot be described by MO theory at the Hartree-Fock level and is due to direct overlap between the unpaired electron in a ligand orbital with an unpaired electron in a Cu orbital in the CT excited state. In terms of the HL or VB description, this interaction is accounted for by CI with a metal \rightarrow metal CT (MMCT) state, i.e. a state where one electron has been transferred from one Cu to the other (8). The energy of this state is the so-called Mott-Hubbard U which for Cu(II) compounds has been determined to 6.5 eV (12). The second effect, i.e. the decrease of the singlet with respect to the triplet CT state splitting, is due to another excited-state interaction which is described below. Without taking this contribution into account, the ${}^1A_1^{CT}$ state is lowered with respect to the ${}^3B_1^{CT}$ state by

$$-2 J^{CT} \equiv E [({}^3B_1^{CT})'] - E [({}^1A_1^{CT})'] = 2 \frac{\beta_1^2}{U - \Delta} \quad (29)$$

As a consequence, the 1A_1 ground state component is lowered with respect to the 3B_1 component by (8,13)

$$-2 J^{GS} \equiv E [({}^3B_1^{GS})'] - E [({}^1A_1^{GS})'] = 4 \frac{\beta_1^4}{\Delta^2 U} \equiv \lambda^2 (-2 J^{CT}) \quad (30);$$

the last equality follows with (24) and $(U-\Delta) \cong U$. Hence, the origin of the antiferromagnetic coupling in the ground state is the depression of the ${}^1A_1^{CT}$ with respect to the ${}^3B_1^{CT}$ state, and the corresponding GS coupling constant is given by the excited-state $-2J$ scaled down by λ^2 . This mechanism of antiferromagnetic coupling is referred to *super-exchange (14)*. The parameters resulting from the VBCI analysis are given in Table I.

Ferromagnetically coupled Cu(II) azido dimers. The following CT spectra derive from μ -1,1 azido bridged Cu(II) dimers. The first system, $[\text{Cu}_2(\text{tmen})(\text{N}_3)(\text{OH})](\text{ClO}_4)_2$ (tmen = N,N,N',N'-tetramethylethylenediamine), has one μ -1,1 azido and one bridging

OH group (15) and the second one, $[\text{Cu}_2(\text{tbupy})_4(\text{N}_3)_2](\text{ClO}_4)_2$ (tbupy = tert-butylpyridine), two μ -1,1 bridging azido groups (16). In contrast to the cis μ -1,3 azido Cu(II) complex described above, both molecules exhibit strong ferromagnetic coupling with $2J$ being $> 200 \text{ cm}^{-1}$ for the mono- (15) and 120 cm^{-1} for the bis μ -1,1 dimer (16).

$[\text{Cu}_2(\text{tmen})(\text{N}_3)(\text{OH})](\text{ClO}_4)_2$. Figure 4, top displays the optical spectrum of this compound in CHCl_3 at room temperature (17). Five bands can be distinguished: the band at 17000 cm^{-1} (band I) is a ligand-field transition, bands II, IIIb and IIIc are azide \rightarrow Cu CT transitions and band IV at 37000 cm^{-1} is a CT transition which is not related to azide. These assignments have been made with the help of variable-temperature single-crystal polarized absorption spectra which are displayed in Figure 5. As the crystal symmetry is tetragonal, α , σ and π spectra can be recorded. The π -spectrum probes transitions that are polarized along the azide axis (A_1 symmetry), and the σ -spectrum probes transitions that are polarized along the Cu-Cu vector (B_1 symmetry). In terms of electric-dipole selection rules, the α -is equivalent of the σ -spectrum. Fig. 5 shows that the LF transition splits and displays little T-dependence. However, band II is strongly temperature dependent and vanishes at low temperature (32K). Since band II is present in the α and σ spectrum but is absent in the π -spectrum, it must be a singlet \rightarrow singlet transition of symmetry B_1 , i.e. $^1A_1 \rightarrow ^1B_1$. In contrast, bands III do not vanish at low temperature and therefore must correspond to triplet \rightarrow triplet CT transitions. In addition to the relatively intense bands II and IIIb, there are additional small intensity bands IIa and IIIa at lower energy that are members of a progression in the antisymmetric azide stretching mode (2500 cm^{-1}) transforming totally symmetric in the dimer point group. Band IIIa observed at 25200 cm^{-1} in the σ -spectrum is assigned to the electronic origin of the $^3B_1 \rightarrow ^3A_1$ CT transition and band IIIa observed at 24800 cm^{-1} in the π -spectrum is assigned to the electronic origin of the $^3B_1 \rightarrow ^3B_1$ CT transition. Therefore the $^3B_1 \rightarrow ^3B_1$ CT transition is shifted by 400 cm^{-1} to lower energy with respect to the $^3B_1 \rightarrow ^3A_1$ CT transition.

Figure 4, bottom displays the energy levels along with the measured CT transition energies. Importantly, the triplet CT state splitting is now extremely small (400 cm^{-1}), and the 1B_1 CT state is lowered by 7000 cm^{-1} with respect to the triplet CT states. In order to understand these deviations from the prototype splitting scheme (Fig.3), second excitations have to be considered which are different from the MMCT excitation (see above). An important excitation of this kind is the transfer of an electron to the azide π^* orbital leading to the "ligand excited" (LE) configurations which have B_1 symmetry. CI selectively lowers CT states of B_1 symmetry thus leading to the observed energetic lowering of the $^3B_1^{\text{CT}}$ and (in part) of the $^1B_1^{\text{CT}}$ state. The stabilization of the $^3B_1^{\text{CT}}$ state is a ferromagnetic contribution with an interaction energy of

$$2 \frac{\langle d | \hat{H} | \pi^* \rangle^2}{\Pi - \Delta} \equiv 2 \frac{\beta_2^2}{\Pi - \Delta} \quad (31)$$

where Π denotes the energy of the azide π^* orbital and β_2 the transfer matrix element between the d and π^* orbital. For the singlets, the effect of the MMCT states has to be added resulting in an excited-state coupling constant given by

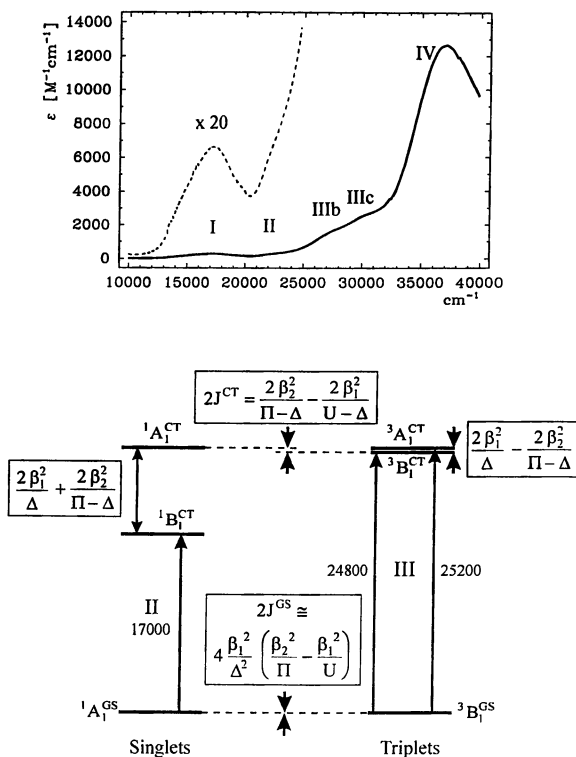


Figure 4. Top: Optical absorption spectrum of the complex $[\text{Cu}_2(\text{tmen})_2(\text{N}_3)(\text{OH})]^{2+}$ with band designations (adapted from ref. 17). Bottom: Corresponding energy-level scheme along with transition energies, splitting energies and excited-state/ground-state $2J$'s

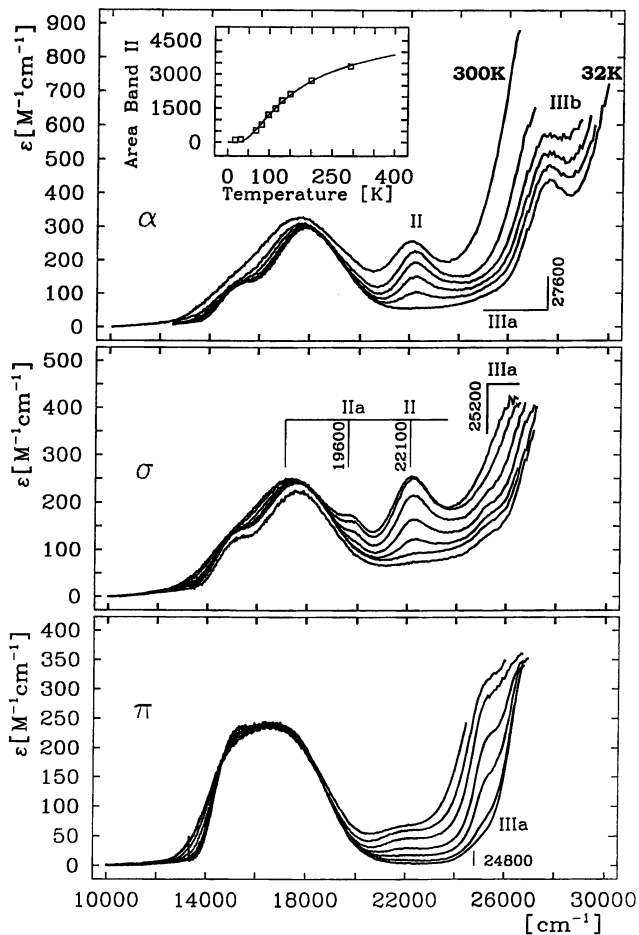


Figure 5. Variable temperature single crystal spectra of $[\text{Cu}_2(\text{tmen})_2(\text{N}_3)(\text{OH})](\text{ClO}_4)_2$. Top: α spectrum from $T = 293$ to 32 K (top to bottom); inset: area of band II vs temperature. Center: σ spectrum from $T = 240$ to 32 K (top to bottom). Bottom: π spectrum from $T = 250$ to 32 K (top to bottom). Stick spectra are included to indicate progressions in $\nu_{\text{as}}(\text{N}_3)$. (Reproduced with permission from ref. 17. Copyright 1995 American Chemical Society).

$$2J^{CT} = E(^1A_1^{CT}) - E(^3B_1^{CT}) = 2 \frac{\beta_2^2}{\Pi - \Delta} - 2 \frac{\beta_1^2}{U - \Delta} \quad (32)$$

Since the first term is larger than the second one, $2J^{CT}$ is positive corresponding to an excited-state ferromagnetic interaction (ESF). The ground state coupling constant is given by

$$2J^{GS} = E(^1A_1^{GS}) - E(^3B_1^{GS}) = 4 \frac{\beta_1^2}{\Delta^2} \left(\frac{\beta_2^2}{\Pi} - \frac{\beta_1^2}{U} \right) \cong \lambda^2 (2J^{CT}) \quad (33)$$

with λ being determined by (24). $2J^{GS}$ is also positive corresponding to the observed ferromagnetic interaction in the ground state. Thus the CT spectrum shows in fact that there is an interaction that is able to compete with the antiferromagnetic contribution of the MMCT state. The VBCI parameters are collected in Table I. Note that the interaction with the LE states leading to a ferromagnetic contribution in the μ -1,1 azide compound corresponds to an antiferromagnetic contribution in the case of *cis* μ -1,3 bridging as it lowers the energy of the A_1 states (17). This explains the reduction of the calculated triplet CT state splitting leading to the observed singlet CT state splitting (cf Fig.3).

[Cu₂(tbupy)₄(N₃)₂](ClO₄)₂. In Figure 6, top, the chloroform solution spectrum of this compound is displayed (17). The LF transition A is observed at 16500 cm⁻¹. In the CT region, four bands are observed, bands B, C, D1 and D2, and, at 39500 cm⁻¹, a high-intensity band E is found. Comparison with the spectrum of the azide-free compound [Cu(tbupy)₄](ClO₄)₂ shows that bands B, C, D1 and D2 are azide → Cu CT bands whereas band E is associated with the tbupy ligand. In order to obtain further information about the azide CT spectrum, T-dependent single-crystal polarized absorption spectra have been collected of this system as well which are displayed in Figure 7. The compound is monoclinic with the (100) face prominent. Polarized absorption data have been obtained with **k** perpendicular to this plane and **E** along the *b* and *c* axis, resp., but in both cases now contain mixed molecular polarisations. Obviously, bands B and C are much more intense for **E** || *b* than for **E** || *c*, and band B gradually disappears upon cooling the sample. This parallels the behavior of band II in the *tmen* system and shows that this band corresponds to a singlet → singlet CT transition. In contrast, band C has a nonvanishing intensity at low temperature and hence corresponds to a triplet → triplet CT transition. It can be decomposed into a number of progressions in the antisymmetric azide stretching mode the lowest-energy member of which is located at 22500 cm⁻¹ (band C1). Figure 7, bottom shows a deconvolution of this band into 5 vibronic transitions (C1 to C5). In order to determine the molecular polarisations of bands B and C, a further data set is needed which we could not obtain from the single crystals. Taking instead the solution spectrum as third independent piece of information, band B was determined to be polarised along Cu-Cu (symmetry B_{3u}) and band C to be polarised along the azide vector (symmetry B_{2u}). Hence, B corresponds to the ¹A_g → ¹B_{3u} transition and C corresponds to the ³B_{3u} → ³B_{1g} transition (Figure 6, bottom). Finally, band D is assigned to the other electric-dipole allowed triplet → triplet CT transition, ³B_{3u} → ³A_g with the splitting into D1 and D2 again corresponding to a

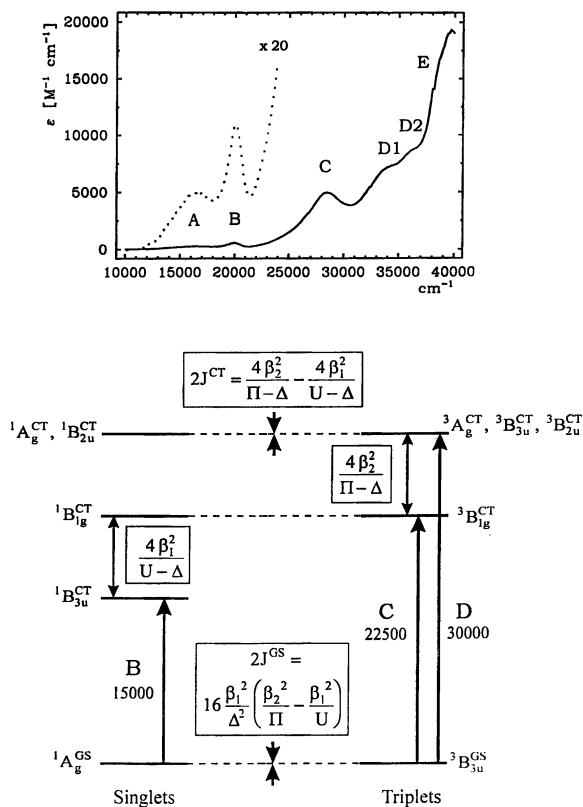


Figure 6. Top: Optical absorption spectrum of $[\text{Cu}_2(\text{tbupy})_2(\text{N}_3)_2]^{2+}$ (adapted from ref. 17). Bottom: Corresponding energy-level scheme along with transition energies, splitting energies and excited-state/ground-state $2J$'s.

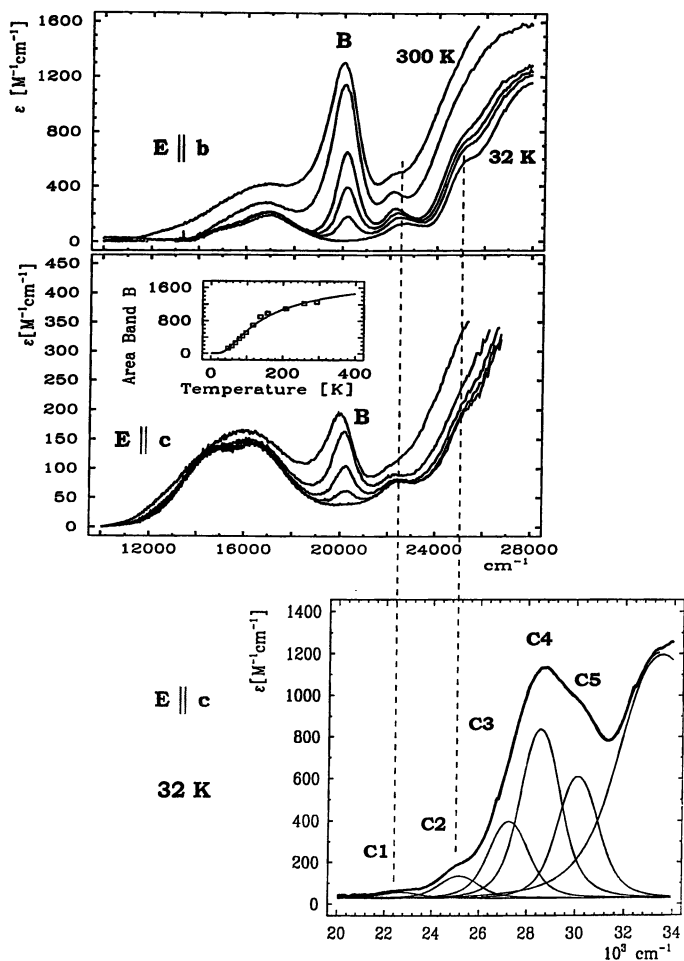


Figure 7. Variable-temperature single-crystal spectra of $[\text{Cu}_2(\text{tbupy})_4(\text{N}_3)_2](\text{ClO}_4)_2$. Top: $E \parallel b$ from 300 to 30 K (top to bottom). Center: $E \parallel c$ from 293 to 38 K (top to bottom); inset: area of band B vs temperature. Bottom: Band C in $E \parallel c$ spectrum at $T = 32$ K with Gaussian resolution indicating the progression in $\nu_{\text{as}}(\text{N}_3)$. (Adapted from ref.17).

progression in the antisymmetric azide stretching mode. Importantly, the energy difference between the ${}^3A_g^{CT}$ and ${}^3B_{1g}^{CT}$ state now provides a direct measure of the excited-state ferromagnetic contribution, and the energy difference between the ${}^1B_{1g}^{CT}$ and ${}^1B_{3u}^{CT}$ state provides a direct measure of the excited-state antiferromagnetic interaction. The VBCI treatment predicts an excited-state $2J$ value corresponding to the difference between these two terms

$$2J^{CT} = E({}^1A_g^{CT}) - E({}^3B_{3u}^{CT}) = 4 \frac{\beta_2^2}{\Pi - \Delta} - 4 \frac{\beta_1^2}{U - \Delta} \quad (34).$$

Since both contributions are of equal magnitude, $2J^{CT} \approx 0$ and ${}^1A_g^{CT}$ and ${}^1B_{3u}^{CT}$ are at the same energy. As a consequence,

$$2J^{GS} = E({}^1A_g^{GS}) - E({}^3B_{3u}^{GS}) = 16 \frac{\beta_1^2}{\Delta^2} \left(\frac{\beta_2^2}{\Pi} - \frac{\beta_1^2}{U} \right) \cong \lambda^2 (2J^{CT}) \cong 0 \quad (35)$$

with $\lambda = -2 \beta_1/\Delta$, and the 1A_g and ${}^3B_{3u}$ ground state components are predicted to be at the same energy leading to net ferromagnetic coupling due to the two-electron exchange integral. The VBCI parameters corresponding to this analysis are given in Table I.

Summary, generalization and conclusion

One and the same azide \rightarrow Cu CT transition has been observed in a Cu(II) azide monomer, in an antiferromagnetically coupled Cu(II) cis μ -1,3 azido dimer and in two ferromagnetically coupled Cu(II) mono- and bis μ -1,1, resp., azide bridged dimers. In the monomer, the intensity of the unsplit ligand \rightarrow metal CT transition allows an estimate of the corresponding transfer matrix element β_1 and the covalency parameter λ . Upon going from the monomer to the dimer, the CT transition splits into several components covering a spectral range of up to 15000 cm^{-1} , and the splitting pattern characteristically depends upon the geometry of ligand binding and the number of the bridging ligands. The VBCI model allows to analyze the CT spectra of monomers and dimers. The splitting of a monomer CT transition in the dimer also contains covalency information, but is influenced by further interactions which can be considered as antiferro- or ferromagnetic contributions to an excited-state magnetic coupling constant $2J^{CT}$. Whereas the antiferromagnetic contribution due to the MMCT configuration also depends on β_1 , the ferromagnetic contribution due to the LE states depends on β_2 , a transfer matrix element between the d-orbitals of the metal and the ligand π^* orbital. The difference between ferro- and antiferromagnetic terms gives the excited-state $2J^{CT}$ which in turn determines the ground-state $2J^{GS}$ value. In the cis μ -1,3 azide bridged Cu(II) dimer, $2J^{CT}$ is negative and the ground-state coupling antiferromagnetic, in the μ -1,1 azide bridged systems, $2J^{CT}$ is positive (or 0) and the ground-state coupling ferromagnetic.

These results can be generalized by including all orbitals i of a bridging ligand. If the metal and ligand orbitals are chosen as zeroth-order wavefunctions and the metal-ligand

interaction is treated as a perturbation, the admixed ground state singlet and triplet ($S=0,1$) wavefunctions are given in second order by

$$\left({}^{2S+1}\Psi^{GS} \right)' = \left(1 - \frac{1}{2} \sum_i \lambda_i^2 \right) {}^{2S+1}\Psi^{GS} + \sum_i \lambda_i \left[{}^{2S+1}\Psi_i^{CT} + \sum_k v_{ik} {}^{2S+1}\Psi_k^{DE} \right] \quad (36)$$

where all Ψ 's on the right side transform as the respective ground state ${}^{2S+1}\Psi^{GS}$. Specifically, Ψ_i^{CT} denotes a CT state corresponding to a transfer of an electron from orbital i to the half-occupied Cu d orbital and Ψ_k^{DE} denotes a doubly excited state, i.e. a state which differs from a CT state by a second ligand \rightarrow metal or metal \rightarrow ligand excitation and from the ground state by two of such excitations. The MMCT ($S=0$) or LE states ($S=0,1$) are examples for DE states, as are the DCT (double CT) states (8) which have not been considered here. In case there exist more than one singly occupied or empty d -orbital, an additional summation over all accepting orbitals j has to be included in (36). The first-order mixing coefficients are given by

$$\lambda_i = \frac{\langle {}^{2S+1}\Psi^{GS} | \hat{H}' | {}^{2S+1}\Psi_i^{CT} \rangle}{E(GS) - E(CT_i)} \quad (37)$$

and the second-order coefficients by $\lambda_i v_{ik}$ with v_{ik} being defined by

$$v_{ik} = \frac{\langle {}^{2S+1}\Psi_i^{CT} | \hat{H}' | {}^{2S+1}\Psi_k^{DE} \rangle}{E(GS) - E(DE_k)} \quad (38)$$

The total covalency (= amount of charge transferred from the ligand to the metal) corresponds to $\sum_i \lambda_i^2$. Evaluation of the expectation values of $H' = H - \epsilon_0$ (with ϵ_0 being the zeroth-order energy) with the singlet and triplet wavefunctions (36) gives the ground-state $-2J$ value as fourth-order energy difference (this expression is actually accurate to 5th order (18))

$$E[({}^3\Phi^{GS})'] - E[({}^1\Theta^{GS})'] = -2J^{GS} = \sum_i \lambda_i^2 \left[\sum_i \frac{|\langle {}^3\Phi_i^{CT} | \hat{H}' | {}^3\Phi_i^{DE} \rangle|^2}{E(GS) - E({}^3DE_i)} - \sum_k \frac{|\langle {}^1\Theta_i^{CT} | \hat{H}' | {}^1\Theta_k^{DE} \rangle|^2}{E(GS) - E({}^1DE_k)} \right] \quad (39)$$

where all Θ 's on the right side transform as ${}^1\Theta^{GS}$ and all Φ 's on the right side as ${}^3\Phi^{GS}$. Note that eqns (33) and (35) are special cases of (39). The interpretation of (39) is obvious: each bridging orbital i opens a superexchange pathway, and the nature of the double excitations determines whether this pathway gives a net antiferromagnetic (square bracket in (39) > 0) or ferromagnetic (< 0) contribution to the ground-state $-2J$ value. Optical absorption spectroscopy, on the other hand, allows the CT excited-state magnetic interaction $-2J_i^{CT}$ to be determined which is defined by the second-order energy difference

$$E[(^3\Phi_i^{CT})'] - E[(^1\Theta_i^{CT})'] = -2J_i^{CT} = \sum_i \frac{|\langle ^3\Phi_i^{CT} | \hat{H}' | ^3\Phi_i^{DE} \rangle|^2}{E(CT_i) - E(^3DE_i)} - \sum_k \frac{|\langle ^1\Theta_i^{CT} | \hat{H}' | ^1\Theta_k^{DE} \rangle|^2}{E(CT_i) - E(^1DE_k)} \quad (40)$$

and thus is related to the square bracket in (39). As the energy denominators in (39) and (40) are of the same order of magnitude, the ground-state $-2J$ value is approximately given by

$$-2J^{GS} \cong \sum_i \lambda_i^2 (-2J_i^{CT}) \quad (41).$$

Beyond the determination of covalency, optical spectroscopy of CT bands is therefore able to monitor specific superexchange pathways contributing to the ground-state $-2J$ value in bridged dimers. The limitation to the UV/Vis/NIR spectral region is not a serious one as in general CT transitions from bridging orbitals contributing strongly to covalency (i.e. with large λ values) fall into this range. In the present article, this methodology has been exemplified on the $\pi^{nb} \rightarrow \text{Cu}$ CT transition of Cu azide systems where the dominant metal-ligand interaction derives from the azide HOMO of π^{nb} type. Further applications include the peroxide $\pi^* \rightarrow \text{Cu(II)}$ CT spectrum of oxy-Hemocyanin (19) and the $\text{O}^{2-} \rightarrow \text{Fe(III)}$ CT spectra of μ -oxo iron(III) dimers (20).

Literature Cited:

- (1) Solomon, E.I.; Kirk, M.L.; Gamelin, D.R.; Pulver, S. In *Biochemical Spectroscopy*; K.Sauer, Ed.; Methods in Enzymology; Academic Press 1995, Vol. 246, pp 71-110.
- (2) Solomon, E.I.; Lowery, D.L.; Root, D.E.; Hemming, B.L. In *Mechanistic Bioinorganic Chemistry*; Thorp, H.H. and Pecoraro, V.L., Eds.; Adv. in Chemistry Series, American Chemical Society, Washington DC 1995, Vol. 246, pp 121-164.
- (3) Solomon, E.I.; Tuzcek, F.; Root, D.E.; Brown, C.A. *Chem. Rev.* **1994**, *94*, 827-856
- (4) Pate, J.E.; Ross, P.K.; Thamann, T.J.; Reed, C.A.; Karlin, K.D.; Sorrell, T.N.; Solomon, E.I. *J. Am. Chem. Soc.* **1989**, *111*, 5198-5208
- (5) Sugano, S.; Tanabe, Y.; Kamimura, H. *Multiplets of Transition-Metal Ions in Crystals*; Academic Press, 1970
- (6) Haken, H.; Wolf, B. *Molekülphysik und Quantenchemie*; Springer-Verlag, 1991
- (7) Karlin, K.D.; Cohen, B.I.; Hayes, J.C.; Farooq, A.; Zubieta, J. *Inorg. Chem.* **1987**, *26*, 147-153
- (8) Tuzcek, F.; Solomon, E.I. *Inorg. Chem.* **1993**, *32*, 2850-2862
- (9) McKee, V.; Zvagulis, M.; Dagdigian, J.V.; Patch, M.G.; Reed, C.A. *J. Am. Chem. Soc.* **1984**, *106*, 4765-4772
- (10) Tuzcek, F.; Bensch, W. *Inorg. Chem.* **1995**, *34*, 1482-1486
- (11) Desjardins, S.R.; Wilcox, D.E.; Musselman, R.L.; Solomon, E.I. *Inorg. Chem.* **1987**, *26*, 288
- (12) Didziulis, S.V.; Cohen, S.L.; Gewirth, A.A.; Solomon, E.I. *J. Am. Chem. Soc.* **1988**, *110*, 250-268
- (13) Shen, Z.-X.; Allen, J.W.; Yeh, J.J.; Kang, J.-S.; Ellis, W.; Spicer, W.J.Z.; Geballe, T.H. *Phys. Rev. B* **1987**, *36*, 8414-8428

- (14) Anderson, P.W. *Solid State Physics* **1963**, *14*, 99-214
- (15) Kahn, O.; Sikorav, S.; Gouteron, J.; Jeannin, S.; Jeannin, Y. *Inorg. Chem.* **1983**, *22*, 2877
- (16) Sikorav, S.; Bkouche-Waksman, I.; Kahn, O. *Inorg. Chem.* **1984**, *23*, 490
- (17) von Seggern, I.; Tuzcek, F.; Bensch, W. *Inorg. Chem.* **1995**, *34*, 5530-5547
- (18) A wave function accurate through the n-th order permits the energy to be calculated to (2n+1)-st order: cf Hirschfelder, J.O. In *Perturbation Theory and Its Applications in Quantum Mechanics*; C.H. Wilcox, Ed.; J. Wiley, 1966, pp 3-34.
- (19) Tuzcek, F.; Solomon, E.I. *J. Am. Chem. Soc.* **1994**, *116*, 6916
- (20) Brown, C.A.; Remar, G.J.; Musselman, R.L. Solomon, E.I. *Inorg. Chem.* **1995**, *34*, 688

Chapter 6

Recent Advances in Magnetic Circular Dichroism Spectroscopy

Elizabeth G. Pavel and Edward I. Solomon¹

Department of Chemistry, Stanford University, Stanford, CA 94305-5080

Magnetic circular dichroism (MCD) spectroscopy has proven to be a useful tool for investigating the electronic and magnetic properties of metal centers in bioinorganic systems. A brief background of this important technique is presented, followed by a discussion of the information available from observed excited-state transitions. Ground-state electronic structure information is obtained through variable-temperature, variable-field (VTVH) MCD data, which can be analyzed to extract ground-state sublevel splittings and g values. More recently, the methodology to analyze VTVH MCD data of non-Kramers $S = 2$ systems has been developed for both negative and positive zero-field splitting. MCD and VTVH MCD have proven particularly valuable for investigating high-spin ($S = 2$) non-heme Fe^{2+} sites, which are EPR-silent and have very weak absorption bands. Application of this methodology to non-heme enzymes is presented to demonstrate how this technique provides active site geometric and electronic structure information which can be used to probe oxygen and substrate reactivity and lend insight into catalytic mechanism.

MCD Theory.

Like circular dichroism (CD) spectroscopy, magnetic circular dichroism (MCD) spectroscopy measures the difference between left and right circularly polarized (LCP and RCP) extinction coefficients: $\Delta\varepsilon = \varepsilon_{\text{LCP}} - \varepsilon_{\text{RCP}} = \Delta A/cl$, where ΔA is the differential absorption, c is the concentration, and l is the path length. Experimentally, MCD differs from CD by adding a longitudinal magnetic field. While CD activity is restricted to chiral centers, the origin of MCD activity lies in the universal phenomenon known as the Faraday effect, whereby optical activity is induced in all matter when a magnetic field is applied parallel to the direction of the light propagation, and all substances exhibit some form of MCD activity (I). Under the applied magnetic field, electronic levels split so that MCD probes the Zeeman splittings of both the ground and excited states and the selection rules for transitions between these states. Therefore, while CD spectroscopy probes spatial arrangements, MCD spectroscopy applied to bioinorganic systems provides both geometric and electronic structure information for a metal site.

¹Corresponding author.

The standard selection rules for MCD transitions are $\Delta M_L = +1$ for LCP and $\Delta M_L = -1$ for RCP, where L is the orbital angular momentum. The formalism for MCD intensity using the Rigid Shift model (assuming that the band shape does not change with magnetic field) is given in equation 1 (2-4),

$$\frac{\Delta A}{E} = \gamma \beta H \left[\mathcal{A}_1 \left(-\frac{\partial f(E)}{\partial E} \right) + \left(\mathcal{B}_0 + \frac{C_0}{kT} \right) f(E) \right] \quad (1)$$

where γ is a collection of spectroscopic constants, β is the Bohr magneton, k is Boltzmann's constant, H is the applied magnetic field, T is the temperature, $f(E)$ is a bandshape function (often approximated as a Gaussian), and $\partial f(E)/\partial E$ its first derivative. Within this formalism, the MCD intensity has three components, \mathcal{A}_1 , \mathcal{B}_0 , and C_0 , which give rise to \mathcal{A} -, \mathcal{B} -, and C -terms (4).

MCD \mathcal{A} -terms require orbital degeneracy in either the ground (A) or excited (J) state or in both. The quantum mechanical formalism (4) for an \mathcal{A} -term is presented in equation 2, where d_A is the degeneracy of the ground state, $\mu_z = L_z + 2S_z$ is the Zeeman operator for the magnetic field along the z -axis, and $m_{\pm} = (m_x \pm i m_y)/\sqrt{2}$ is the electric dipole transition moment operator.

$$\mathcal{A}_1 = \frac{1}{d_A} \sum \left(\langle J | \mu_z | J \rangle - \langle A | \mu_z | A \rangle \right) \left(\left| \langle A | m_- | J \rangle \right|^2 - \left| \langle A | m_+ | J \rangle \right|^2 \right) \quad (2)$$

\mathcal{A} -terms are distinguished by their derivative bandshape and the fact that their intensity is independent of temperature.

C -terms also require orbital degeneracy, but only in the ground state. The formalism for a C -term, shown in equation 3, is similar to that for an \mathcal{A} -term, except that the Zeeman coupling term for the excited state is now absent.

$$C_0 = -\frac{1}{d_A} \sum \langle A | \mu_z | A \rangle \left(\left| \langle A | m_- | J \rangle \right|^2 - \left| \langle A | m_+ | J \rangle \right|^2 \right) \quad (3)$$

Note that because equations 2 and 3 contain squares of transition dipole moments, \mathcal{A} - and C -terms both require two non-zero perpendicular transition moments. C -terms have absorption bandshapes and intensity which is inversely proportional to the temperature. This temperature dependence arises from differential population of the components of the Zeeman-split ground state: as the population of the lowest-energy component increases with decreasing temperature, the C -term intensity increases.

Unlike \mathcal{A} - and C -terms, MCD \mathcal{B} -terms have no degeneracy requirements and instead arise from field-induced mixing between states. The formalism for a \mathcal{B} -term is given in equation 4, where K is some state which mixes with the ground or excited state(s) in a magnetic field.

$$\mathcal{B}_0 = -\frac{2}{d_A} \text{Re} \sum \left\{ \sum_{K \neq J} \frac{\langle J | \mu_z | K \rangle}{\Delta E_{KJ}} \left(\langle A | m_- | J \rangle \langle K | m_+ | A \rangle - \langle A | m_+ | J \rangle \langle K | m_- | A \rangle \right) + \sum_{K \neq A} \frac{\langle K | \mu_z | A \rangle}{\Delta E_{KA}} \left(\langle A | m_- | J \rangle \langle J | m_+ | K \rangle - \langle A | m_+ | J \rangle \langle J | m_- | K \rangle \right) \right\} \quad (4)$$

\mathcal{B} -terms require that $A \rightarrow J$ and $A \rightarrow K$ (or $J \rightarrow K$) be perpendicularly polarized and that K and A (or K and J) mix with the Zeeman effect; therefore, \mathcal{B} -terms can occur for an $A \rightarrow J$ transition which is polarized along a single direction. Because \mathcal{B} -term intensity

is inversely proportional to the energy separation between the mixing states (ΔE_K or ΔE_{K_A}) and most mixing states are at much higher energy, \mathcal{B} -terms have an absorption bandshape and their intensity is generally weak, temperature-independent, and linear with field. However, if ΔE_{K_A} is small and on the order of kT , there can be differential population between A and K which gives rise to a temperature-dependent \mathcal{B} -term.

Since the observed MCD spectrum can be a combination of \mathcal{A} -, \mathcal{B} -, and \mathcal{C} -terms, it is worth considering their relative intensities. The $\mathcal{A} : \mathcal{B} : \mathcal{C}$ intensity ratio is $(1/\Gamma) : (1/\Delta E) : (1/kT)$, where Γ is the transition full-width-at-half-height, ΔE is the energy separation between mixing states, and kT is Boltzmann's constant times the experimental temperature. For transition metal complexes, a typical bandwidth is $\Gamma \approx 1000 \text{ cm}^{-1}$ and a typical energy separation is $\Delta E \approx 10,000 \text{ cm}^{-1}$ for a temperature-independent \mathcal{B} -term. At room temperature, $kT \approx 200 \text{ cm}^{-1}$ so that $\mathcal{A} : \mathcal{B} : \mathcal{C} \approx 10 : 1 : 50$ and \mathcal{C} -terms contribute most to the MCD intensity. At liquid helium temperatures, $kT \approx 3 \text{ cm}^{-1}$ and $\mathcal{A} : \mathcal{B} : \mathcal{C} \approx 10 : 1 : 3300$. Thus at the low temperatures where much bioinorganic spectroscopy is performed, \mathcal{C} -terms fully dominate the MCD spectrum.

Excited State Information.

\mathcal{C} -terms require ground-state orbital degeneracy, yet metal sites in biology often have not orbital, but rather spin degeneracy. The selection rules for MCD require that $\Delta M_L = \pm 1$ and also that $\Delta M_S = 0$. Therefore, with only spin degeneracy in the ground state, non-zero \mathcal{C} -term intensity can only occur via spin-orbit coupling. (MCD selection rules are often given as $\Delta M_J = \pm 1$, taking into account this spin-orbit coupling mechanism.) When considering the excited state information content, it is convenient to divide metalloprotein sites into two categories: those with high symmetry, and thus possible excited-state orbital degeneracy, and those with low symmetry.

High-symmetry metalloenzyme systems are those with approximate C_3 , C_4 , or S_4 axes, such as heme and iron-sulfur centers. In these cases, it is possible to have orbitally degenerate excited states which are xy -polarized and thus satisfy the \mathcal{C} -term condition of two non-zero perpendicular transition dipole moments. The orbital angular momentum of the excited state will spin-orbit couple with the spin degeneracy to split the excited state, as demonstrated in Figure 1 for the case of an $S = 1/2$ system with an $M_L = 0$ ground state and an $M_L = \pm 1$ excited state. As shown in Figure 1, there will be one \mathcal{C} -term to the lower-energy component of the spin-orbit-split excited state and a second \mathcal{C} -term to the higher-energy component which is oppositely signed. The resulting MCD signal is a pseudo- \mathcal{A} -term, composed of equal and opposite \mathcal{C} -terms (4). The energy splitting between the two \mathcal{C} -terms gives the in-state spin-orbit coupling (λ), and the sign of the pseudo- \mathcal{A} -term, defined to be that of the higher-energy component, gives insight into the one-electron orbitals involved in the transition (5).

Many metal sites in proteins are highly distorted and have low symmetry so that there is no orbital degeneracy in the excited states. In these cases, the MCD transitions are electric dipole allowed, but with the transition moment polarized in only one direction. The \mathcal{C} -term intensity formalism can be rewritten in terms of the electric dipole transition moments, M_i ($i = x, y, z$), and the components of the g tensor, g_i , as given in equation 5 (6).

$$C_0 \propto g_z(M_x M_y) + g_y(M_x M_z) + g_x(M_y M_z) \quad (5)$$

From equation 5, it is clear that two perpendicular transition moments are required for \mathcal{C} -term intensity. With all transitions polarized in only one direction, the only way to obtain a second perpendicular polarization component is through spin-orbit coupling (7). Spin-orbit coupling between two excited states which are close in energy

produces a pseudo- \mathcal{A} -term, as described above. Spin-orbit coupling over all excited states will produce equal and opposite C -terms which sum to zero intensity. Non-zero C -term intensity summed over excited states for low symmetry sites must therefore arise from spin-orbit mixing into the ground state (8).

Because spin-orbit coupling governs the C -term intensity, the magnitude of the spin-orbit coupling parameter (ζ) can provide insight into relative intensities. Spin-orbit coupling is much stronger for metals (for example, $\zeta(\text{Cu}^{2+}) \approx 830 \text{ cm}^{-1}$, $\zeta(\text{Fe}^{2+}) \approx 400 \text{ cm}^{-1}$, $\zeta(\text{Fe}^{3+}) \approx 460 \text{ cm}^{-1}$) than for biologically relevant ligands ($\zeta(\text{O,N}) \approx 60\text{--}70 \text{ cm}^{-1}$, $\zeta(\text{S}) \approx 325 \text{ cm}^{-1}$). From these values, one expects that metal-based excited states will be more spin-orbit-mixed than ligand-based states; therefore $d \rightarrow d$ transitions will exhibit a larger MCD intensity relative to the absorption intensity than will charge transfer transitions. The ratio of MCD to absorption intensities is often expressed as C_0/\mathcal{D}_0 (equation 6), where \mathcal{D}_0 is the dipole strength as defined in equation 7 and can be obtained from the experimental low-temperature absorption spectrum.

$$\frac{C_0}{\mathcal{D}_0} = \frac{kT}{\beta H} \left(\frac{\Delta\mathcal{E}(\text{MCD})}{\mathcal{E}(\text{Abs})} \right) \quad (6)$$

$$\mathcal{D}_0 = \frac{1}{2d_A} \sum \left(\left| \langle A | m_- | J \rangle \right|^2 + \left| \langle A | m_+ | J \rangle \right|^2 \right) \quad (7)$$

It has been found for blue copper systems (7) that C_0/\mathcal{D}_0 is ~ 0.01 for charge transfer transitions, but is an order of magnitude larger, $C_0/\mathcal{D}_0 \approx 0.1$, for $d \rightarrow d$ transitions. Thus assignment of bands can be aided by the relative C_0/\mathcal{D}_0 ratios for a given system.

The energies and splitting of $d \rightarrow d$ bands obtained from low-temperature MCD spectroscopy can be used to probe metal site geometry. In the case of octahedral high-spin Fe(II), the ${}^5T_{2g}$ ground state corresponds to a $(t_{2g})^4(e_g)^2$ configuration, so the ${}^5T_{2g} \rightarrow {}^5E_g$ transition corresponds to a promotion of one electron from the t_{2g} set to the e_g set. Thus the observed ligand field transitions correlate directly to the e_g d-orbital energies. Additionally, the splitting of the 3E_g excited state is sensitive to the surrounding ligands and distortions, and the splittings of the observed bands indicates geometry. Ligand field calculations and spectroscopic studies on high-spin ferrous model complexes with biologically relevant ligands show that 6-coordinate (6C) distorted octahedral sites typically show two transitions centered at $\sim 10,000 \text{ cm}^{-1}$ and split by 2000 cm^{-1} , 5-coordinate (5C) sites have two transitions at $\sim 10,000$ and $\sim 5000 \text{ cm}^{-1}$ with these transitions shifted to higher energy for square pyramidal sites and to lower energy for trigonal bipyramidal sites, and distorted 4-coordinate (4C) sites have two transitions in the $4000\text{--}7000 \text{ cm}^{-1}$ region, depending on the distortion (9).

The excited-state spectral data for the blue copper protein plastocyanin serve as a nice illustration of some of the above methodology. The low-temperature absorption and MCD spectra for plastocyanin (7) are shown in Figures 2a and 2b, respectively, and eight Gaussian bands are required to simultaneously fit both spectra. Bands 1–4 in the high-energy region show a much smaller MCD intensity relative to the absorption intensity, and their C_0/\mathcal{D}_0 ratios are found to be ~ 0.01 . Note that band 4 has an unusually large absorption intensity, signifying significant metal–ligand overlap; this has been found to be due to a large amount of S covalency in the Cu HOMO (10,11). In contrast to bands 1–4, bands 5–8 in the low-energy region have much stronger MCD signals and a C_0/\mathcal{D}_0 ratio of ~ 0.1 , an order of magnitude larger than for the high-energy bands. Thus bands 1–4 are assigned as charge transfer transitions and bands 5–8 as ligand field transitions.

Specific assignments of the $d \rightarrow d$ bands can be made based on calculating the sign of the C -term using group theory and the spin-orbit-corrected many-electron

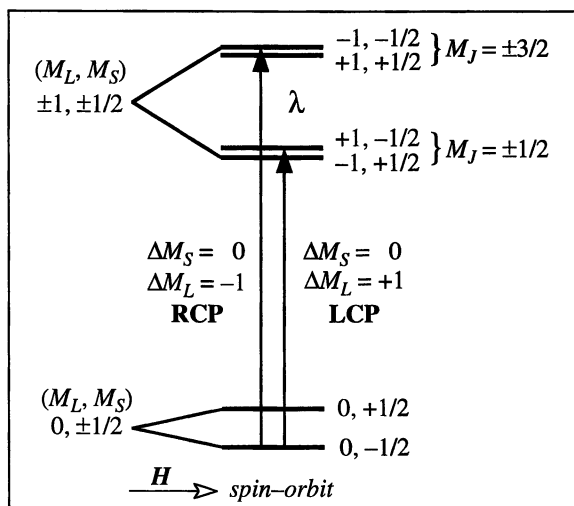


Figure 1. Example of an MCD pseudo- \mathcal{A} -term due to spin-orbit coupling within the orbitally degenerate excited state.

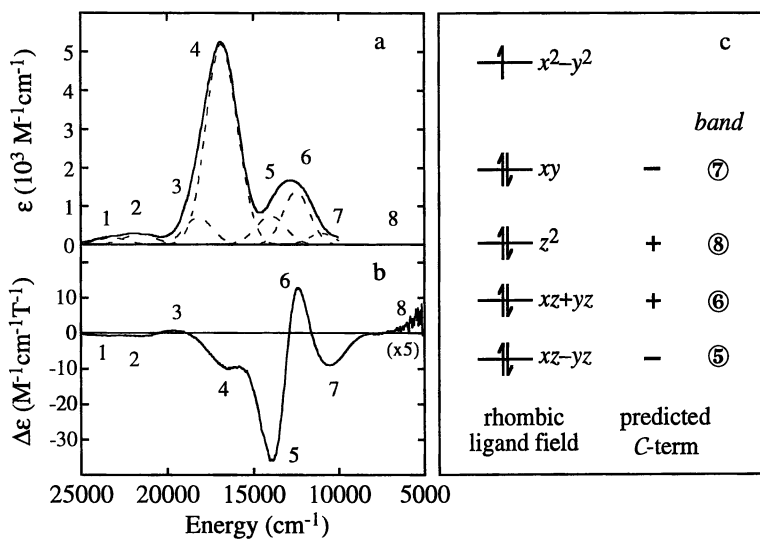


Figure 2. Low-temperature absorption (a) and MCD (b) spectra of plastocyanin and simultaneous Gaussian fit. (c) d-orbital energy level diagram, predicted C-term signs, and assignment of the d→d bands.

wave functions (7,8). The copper center in plastocyanin is a C_{3v} -distorted tetrahedral site with an additional rhombic distortion (12). Figure 2c shows the approximate energy level diagram for the d-orbitals and the predicted C -term signs for the transitions to the singly-occupied $d_{x^2-y^2}$ HOMO. Based on these calculations, bands 5 and 6 are found to be components of a pseudo- A -term from the rhombically-mixed d_{xz} and d_{yz} orbitals; band 7, which has negative intensity, is assigned as the $d_{xy} \rightarrow d_{x^2-y^2}$ transition; and band 8, which is positive, is the $d_{z^2} \rightarrow d_{x^2-y^2}$ transition. The very low energy of band 8 indicates a significant interaction between the Cu d_{z^2} and the axial S(Met) ligand, despite the long Cu-S(Met) bond at 2.9 Å (12). The large rhombic splitting of the $d_{x^2-y^2}$ and d_{xy} orbitals ($\sim 10,000 \text{ cm}^{-1}$ for band 7) is associated with a π^* interaction due to the short Cu-S(Cys) bond at 2.1 Å which quenches the normally large Jahn-Teller effect expected for T_d Cu(II) sites; this leads to a low Franck-Condon barrier to electron transfer in the blue copper proteins (13,14). Thus transitions can be assigned based on C_0/D_0 signs and magnitudes, and specific metal-ligand bonding interactions can be probed which provide insight into electronic structure contributions to reactivity.

Ground State Information.

Although MCD spectroscopy is most often used as an excited-state method, many of the recent advances in this technique have been in obtaining ground-state information from MCD data. Because C -term intensity depends on the differential population between ground-state sublevels, the intensity will increase with increasing magnetic field (larger Zeeman splitting) and with decreasing temperature (lower thermal energy). As H/T increases, the population of the lowest sublevel grows and the MCD intensity increases linearly. At some value of H/T , however, the population of the lowest sublevel starts to maximize, and the MCD intensity will no longer increase in a linear fashion. At this point, the intensity begins to saturate and experimentally becomes independent of temperature and field when only the lowest sublevel is populated (3,6,15). Variable-temperature, variable-field (VTVH) MCD data can be used to probe this saturation magnetization behavior and provide ground-state electronic structure information. Specifically, analysis of VTVH MCD data yields g values and zero-field splittings, as well as spin-state and magnetic coupling information for dimeric sites.

Kramers Systems. We first consider the case of an isolated Kramers (*i.e.*, half-integer spin) doublet ground state. For an isotropic $S = 1/2$ system, the C -term intensity for the $M_S = \pm 1/2$ ground state can be expressed in terms of H/T by equation 8 (16), where A_{satlim} is a C -term intensity scaling factor.

$$\Delta\epsilon = A_{\text{satlim}} \tanh\left(\frac{g\beta H}{2kT}\right) \quad (8)$$

VTVH MCD data can be fit to this expression to extract the g value of the ground state. Alternatively, g can be obtained from the high-temperature data by plotting the MCD intensity *vs.* $\beta H/2kT$ (Figure 3): the intercept (I) of the Curie-Law slope is directly related to the g value by $I = 1/g$ (17). It is also important to notice that for Kramers systems, the MCD isotherms (VTVH MCD data for a single temperature such as shown in Figure 3) superimpose for all temperatures.

If a Kramers doublet has anisotropic g values, then equation 8 must be expanded to include orientation averaging, *i.e.*, the molecular orientation relative to the external magnetic field (θ), as well as the polarization of the MCD transition (M_z/M_{xy}). These additional factors are included in the MCD intensity expression in equation 9 (18),

where the first part describes the C -term intensity for an xy -polarized transition and the second term allows for z -polarization.

$$\Delta\varepsilon = A_{\text{satlim}} \left\{ \int_0^{\pi/2} \frac{\cos^2 \theta \sin \theta}{\Gamma} g_{\parallel} \tanh\left(\frac{\Gamma\beta H}{2kT}\right) d\theta - \sqrt{2} \left(\frac{M_z}{M_{xy}}\right) \int_0^{\pi/2} \frac{\sin^3 \theta}{\Gamma} g_{\perp} \tanh\left(\frac{\Gamma\beta H}{2kT}\right) d\theta \right\} \quad (9)$$

where $\Gamma = \sqrt{(g_{\parallel} \cos \theta)^2 + (g_{\perp} \sin \theta)^2}$

This form for the C -term intensity assumes axial symmetry ($g_x = g_y = g_{\perp}$); however, in the case that $g_x \neq g_y$, one must now orientation average over both Euler angles θ and ϕ (17). As with the isotropic Kramers doublet, the Curie-Law slope can also be used to extract ground-state g values and polarizations for an anisotropic Kramers doublet (see ref. 6).

For Kramers systems with $S > 1/2$, there are $(2S+1) M_s$ sublevels which will split under the applied magnetic field. If these sublevels become thermally accessible, they can partially deplete the population of the ground state. In such a situation, the MCD intensity will change at higher temperatures and the isotherms are no longer superimposing, but instead exhibit nesting behavior (17). The energy of higher-energy doublets can be determined by fitting the VTVH MCD data to an expanded version of equation 9 which includes population of excited states. Another method to extract the energy of higher doublets is by using the Curie-Law region data: variable-temperature MCD data at a fixed low field can be fit to equation 10 (19),

$$\Delta\varepsilon = \sum_i \left(\frac{C_i}{kT} + B_i \right) \alpha_i H \quad \text{where } \alpha_i = \frac{e^{-E_i/kT}}{\sum_j e^{-E_j/kT}} \quad (10)$$

where C_i and B_i are the C -term and B -term intensities, respectively, and α_i accounts for the Boltzmann population of each doublet (i) at an energy E_i .

Non-Kramers Systems. Non-Kramers (*i.e.*, integer spin) systems may have $(2S+1) M_s$ sublevels which are split even in the absence of a magnetic field. Representative VTVH MCD data for an $S = 2$ non-Kramers system with an isolated $M_s = \pm 2$ doublet ground state are shown in Figure 4. The saturation magnetization behavior for this non-Kramers doublet is qualitatively quite different from that of the isolated Kramers doublet (Figure 3) in that the isotherms are nested, even at low temperature, as seen in Figure 4b (20). Furthermore, if these data are plotted *vs.* $1/kT$ (Figure 4c), one finds a non-linear decrease in the intensity at saturating limits (low temperature, high field), which indicates an unusual non-linear magnetic field dependence of the MCD intensity (9,20) that must be explained. In the case of $S = 2$, such as for high-spin d^6 Fe(II) sites, the five M_s sublevels zero-field split into $M_s = 0, \pm 1$, and ± 2 , separated by D and $3D$ respectively, where D is the axial zero-field splitting parameter. The sign of the zero-field splitting (ZFS) is related to the geometry of the site: $-ZFS$ corresponds to a weak tetragonal distortion (d_{yz}, d_{xz} lowest) and $+ZFS$ corresponds to a strong tetragonal distortion (d_{xy} lowest).

$S = 2$ with $-ZFS$. When the ZFS is negative, the $M_s = \pm 2$ doublet is lowest in energy. In the absence of a magnetic field, a rhombic distortion causes this doublet to split by an amount δ and mixes the wave functions to produce $|X\rangle = (|+2\rangle + |-2\rangle) / \sqrt{2}$

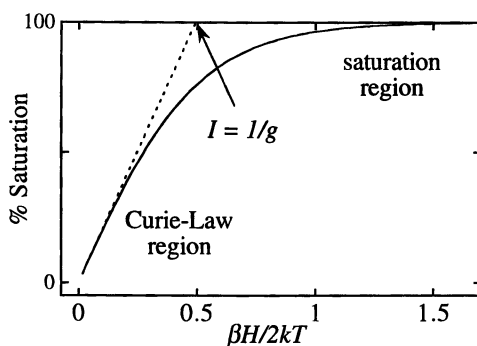


Figure 3. VTVH MCD data for an $S = 1/2$ Kramers doublet with $g = 2$.

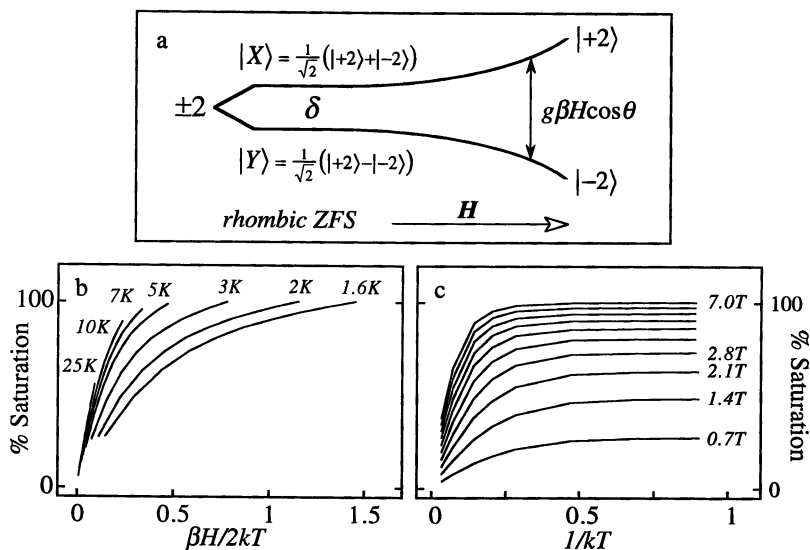


Figure 4. (a) Rhombic zero-field splitting and field-dependence of an $S = 2$ non-Kramers doublet with an $M_s = \pm 2$ ground state. Experimental VTVH MCD data for a non-Kramers doublet with $\delta \approx 6 \text{ cm}^{-1}$ and $g \approx 8.6$ plotted vs. $\beta H / 2kT$ (b) and $1/kT$ (c).

and $|Y\rangle = (|+2\rangle - |-2\rangle)/\sqrt{2}$ (Figure 4a). With equal amounts of $|+2\rangle$ and $|-2\rangle$, there is no net MCD intensity. When a magnetic field is applied, the components of the $M_s = \pm 2$ doublet are further split by an amount $g\beta H \cos\theta$, and the wave functions change so that there are no longer equal amounts of $|+2\rangle$ and $|-2\rangle$ (see Figure 4a) and MCD activity is restored. As the field increases, the wave functions change in a non-linear fashion and approach pure $|+2\rangle$ and $|-2\rangle$. It is this non-linear field-dependence of the wave functions which accounts for the observed saturation magnetization behavior as shown in Figure 4b,c (9,20).

The orientation averaged MCD intensity expression for an isolated non-Kramers doublet is given in equation 11 (9,21), where δ is the zero-field splitting of the doublet.

$$\Delta\varepsilon = A_{\text{satlim}} \left\{ \int_0^{\pi/2} \frac{\cos^2\theta \sin\theta}{\Gamma} g_{\parallel} \beta H \tanh\left(\frac{\Gamma}{2kT}\right) d\theta - \sqrt{2} \left(\frac{M_z}{M_{xy}}\right) \int_0^{\pi/2} \frac{\sin^3\theta}{\Gamma} g_{\perp} \beta H \tanh\left(\frac{\Gamma}{2kT}\right) d\theta \right\} + B_0 H$$

$$\text{where } \Gamma = \sqrt{\delta^2 + (g_{\parallel} \beta H \cos\theta)^2 + (g_{\perp} \beta H \sin\theta)^2}$$
(11)

This equation is very similar to that of the anisotropic isolated Kramers doublet (equation 9), but now the zero-field splitting of the non-Kramers doublet has been included. Also included here is $B_0 H$ which allows for linear, temperature-independent \mathcal{B} -term contributions. VTVH MCD data can be computationally fit to equation 11 to extract the zero-field splitting (δ), the ground-state g values (g_{\parallel} and g_{\perp}), as well as the polarization of the transition (M_z/M_{xy}). Fits of experimental VTVH MCD data and simulations show that the degree of nesting is directly proportional to the magnitude of δ : the larger the value of δ , the more spread out the isotherms appear (9).

$S = 2$ with +ZFS. Recently, the methodology to analyze MCD saturation magnetization behavior for +ZFS systems has been developed (9,22). In order to probe such systems, an $S = 2$ complex with known +ZFS was investigated (22), namely ferrous fluorosilicate, $[\text{Fe}(\text{H}_2\text{O})_6](\text{SiF}_6)$, which has $D = +10 \text{ cm}^{-1}$ and is nearly axial with $E/D \approx 0.07$ (23,24). The experimental VTVH MCD data for ferrous fluorosilicate is found to be qualitatively very similar to that for a -ZFS complex with a large value of δ .

For +ZFS, the non-degenerate $M_s = 0$ sublevel is lowest in energy with the $M_s = \pm 1$ doublet at $D \text{ cm}^{-1}$ above. When a magnetic field is applied parallel to the molecular z -axis ($H \parallel Z$), the $M_s = 0$ level is invariant to field, while the $M_s = \pm 1$ doublet splits with a $g \approx 4$ (Figure 5a). Thus one expects no MCD intensity at low temperatures when only the C -term-inactive $M_s = 0$ is populated and non-zero C -term intensity at higher temperatures when the $M_s = \pm 1$ doublet becomes thermally populated. The expected saturation magnetization behavior for this scenario is shown in Figure 5b and is quite different than that observed for ferrous fluorosilicate.

With the field applied perpendicular to Z , the $M_s = 0$ and $M_s = \pm 1$ sublevels interact through an off-axis Zeeman effect, as shown in Figure 5c for the case of $H \parallel X$. The $M_s = 0$ and one partner of the $M_s = \pm 1$ act as a pseudodoublet ground state with a $g \approx 8$. The other partner of $M_s = \pm 1$ is nearly invariant with field and can be approximated as a C -term-inactive singlet excited state. The predicted VTVH MCD behavior for this "three-level model" is shown in Figure 5d and is similar to that of -ZFS with very large δ . In fact, the pseudodoublet wave functions are composed of

$|+2\rangle^x$ and $|-2\rangle^x$ (where x refers to the $H \parallel X$ quantized labels) which vary with field in a non-linear fashion analogous to that of the $-ZFS$ $M_s = \pm 2$ ground state. While attempts to fit the ferrous fluorosilicate VTVH MCD data with the $-ZFS$ non-Kramers doublet model are unsuccessful, the $+ZFS$ three-level model describes the experimental data quite well (22). Thus for $+ZFS$ systems, the saturation magnetization intensity derives from a temperature-dependent \mathcal{B} -term due to off-axis Zeeman interactions within the ground-state spin manifold (22,25).

Distinguishing the Sign of the ZFS. Although the saturation magnetization behavior of $+ZFS$ and $-ZFS$ systems can look qualitatively similar, it is possible to distinguish the sign of the ZFS through a quantitative analysis of the data. Experimental VTVH MCD data are fit to the MCD intensity expression shown in equation 12 (21), which includes xy - and z -polarized C -term intensity, temperature-independent \mathcal{B} -term intensity, and both doublet and singlet excited states.

$$\Delta\varepsilon = \sum_{i,\text{doublets}} \left\{ A_{\text{satlim}i} \int_0^{\pi/2} \left(g_{\parallel i} \cos^2 \theta - \sqrt{2} \left(\frac{M_z}{M_{xy}} \right)_i g_{\perp i} \sin^2 \theta \right) \frac{\beta H}{\Gamma_i} \alpha_i \sin \theta d\theta \right\} \quad (12)$$

$$+ \sum_{i,\text{doublets}} B_i H \gamma_i + \sum_{m,\text{singlets}} B_m H \eta_m$$

$$\text{where } \Gamma_i = \sqrt{\delta_i^2 + (g_{\parallel i} \beta H \cos \theta)^2 + (g_{\perp i} \beta H \sin \theta)^2}$$

$$\alpha_i = \frac{(e^{-(E_i - \Gamma_i/2)/kT} - e^{-(E_i + \Gamma_i/2)/kT})}{\sum_{j,\text{doublets}} (e^{-(E_j - \Gamma_j/2)/kT} + e^{-(E_j + \Gamma_j/2)/kT}) + \sum_{n,\text{singlets}} (e^{-E_n/kT})}$$

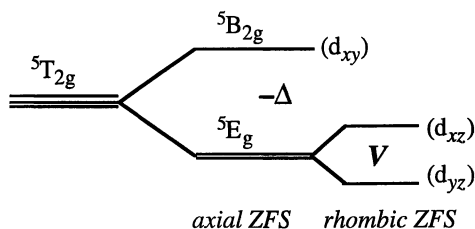
$$\gamma_i = \frac{1}{\tau} (e^{-(E_i - \delta_i/2)/kT} + e^{-(E_i + \delta_i/2)/kT}); \quad \eta_m = \frac{1}{\tau} (e^{-E_m/kT})$$

$$\tau = \sum_{j,\text{doublets}} (e^{-(E_j - \delta_j/2)/kT} + e^{-(E_j + \delta_j/2)/kT}) + \sum_{n,\text{singlets}} (e^{-E_n/kT})$$

(Note that the \mathcal{B} -term Boltzmann factors differ from that for the C -term because field-induced mixing is much greater for perpendicular fields; therefore the Zeeman splitting will be governed by g_{\perp} , which is very small for $S = 2$ systems (9).) When equation 12 is used to fit $+ZFS$ data, " δ " is the zero-field splitting of the pseudodoublet ($\approx D \pm 3E$) (22). $+ZFS$ systems can be distinguished from $-ZFS$ by large values of δ (see ref. 9) and especially by the presence of an additional low-lying singlet excited state. Thus the VTVH MCD data for an unknown ferrous complex can be analyzed to extract not only zero-field splittings, g values, and polarizations, but also the sign of the ZFS.

Relation of Ground State Parameters to Ligand Field Parameters. The ground-state parameters obtained from the fit of VTVH MCD data can be directly related to the ligand field parameters Δ and V which describe the splitting of the ${}^5T_{2g}$ ground state, where Δ is the axial and V is the rhombic zero-field splitting of the t_{2g} orbitals as shown in Scheme 1. When Δ is negative, 5E_g is lowest in energy, corresponding to a weak tetragonal distortion, and the sign of the ZFS is negative ($M_s = \pm 2$ lowest). Because the 5E_g state retains the in-state orbital angular momentum from the ${}^5T_{2g}$ parent state, a spin Hamiltonian is an insufficient description. Instead, a full ${}^5T_{2g}$

Hamiltonian which includes spin-orbit coupling ($\lambda L \cdot S$) and ligand field distortions must be used. Solution of this ${}^5T_{2g}$ Hamiltonian (9), as shown Figure 6, gives the energies of the 15 sublevels (5-fold spin degeneracy \times 3-fold orbital degeneracy), and δ can be directly calculated as the difference between the two lowest sublevels. Applying a Zeeman perturbation allows the calculation of g values for given values of $-\Delta$ and V .



Scheme 1

When Δ is positive, the ${}^5B_{2g}$ state is lowest, corresponding to a strong tetragonal distortion, and the sign of the ZFS is positive ($M_S = 0$ lowest). In this case, the three-level model is used to fit the VTVH MCD data and the spin Hamiltonian parameters D and E must be extracted: " $\delta \approx D \pm 3E$ (+ for $H \parallel X$; - for $H \parallel Y$) and the C -term-inactive singlet excited state lies at $\sim D \mp 3E$ (22). The ${}^5T_{2g}$ Hamiltonian can then be used to relate D to $+\Delta$ and E to V to obtain the axial and rhombic t_{2g} splittings. (This correlation of ground-state parameters with ligand field splittings is described in more detail in ref. 9.)

Therefore, ground-state parameters from VTVH MCD analysis for either $-ZFS$ or $+ZFS$ systems can be related to ${}^5T_{2g}$ ground-state splittings due to the ligand field. This provides a description of the t_{2g} d-orbital energies and, since these orbitals are sensitive to π -bonding, a probe of specific metal-ligand π -interactions. Furthermore, the combination of these t_{2g} d-orbital splittings plus the observed e_g splittings gives a description of all five d-orbitals for a given metal site. Application of this methodology to the iron active sites of non-heme enzymes is now presented to demonstrate how MCD spectroscopy provides geometric and electronic structure information which leads to mechanistic insight and structure/function correlations.

Application to Non-Heme Enzymes: Lipoxygenases.

Lipoxygenases (LOs) are non-heme iron enzymes which catalyze the hydroperoxidation of *cis,cis*-1,4-pentadiene-containing fatty acids. Soybean lipoxygenase-1 (SLO-1) stereoselectively converts linoleic acid to the hydroperoxide product 13(*S*)-hydroperoxy-9,11(*E,Z*)-octadecadienoic acid (13-HPOD), which may be linked to plant growth and development (26). Mammalian LOs convert arachidonic acid to the direct precursors of leukotrienes (5-LOs) and lipoxins (15-LOs) (27), which mediate inflammation, hypersensitivity, and cellular immunity. Thus, there has been pharmacological interest in developing LO inhibitors as anti-inflammatory agents. Sequence analyses on both plant and mammalian LOs show significant homology, particularly in the metal-binding domain (28).

Soybean Lipoxygenase-1 (SLO-1). Because of its ease of isolation and availability, SLO-1 is the most studied of the lipoxygenase enzymes. Native SLO-1 is isolated in the inactive ferrous state and is stable in air. There have been two conflicting crystal structures of the resting ferrous active site (29,30), both of which assign His₄₉₉Ne, His₅₀₄Ne, His₆₀₀Ne, and the C-terminal carboxylate Ile₈₃₉OT2 as iron ligands. One of the crystal structures (29) assigns no further ligands so that the iron site is 4C and

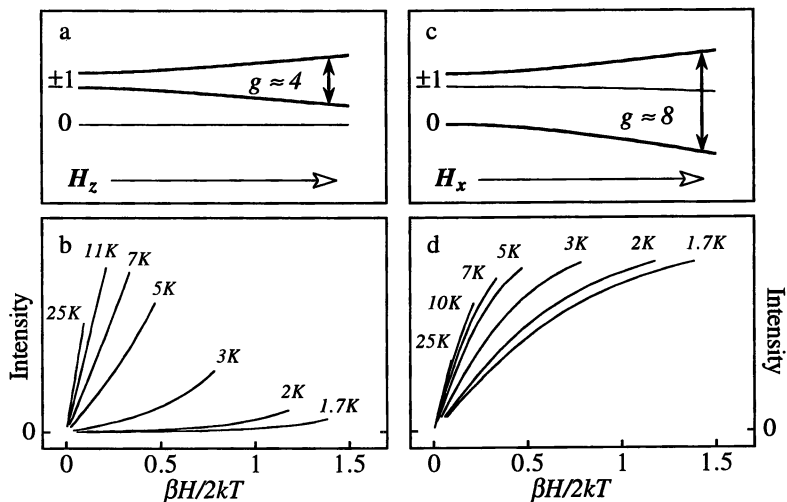


Figure 5. For a +ZFS $S=2$ system, the field-dependence of the $M_S = 0, \pm 1$ levels with (a) $H \parallel Z$ and (c) $H \parallel X$ and the associated predicted VTVH MCD behavior (b,d).

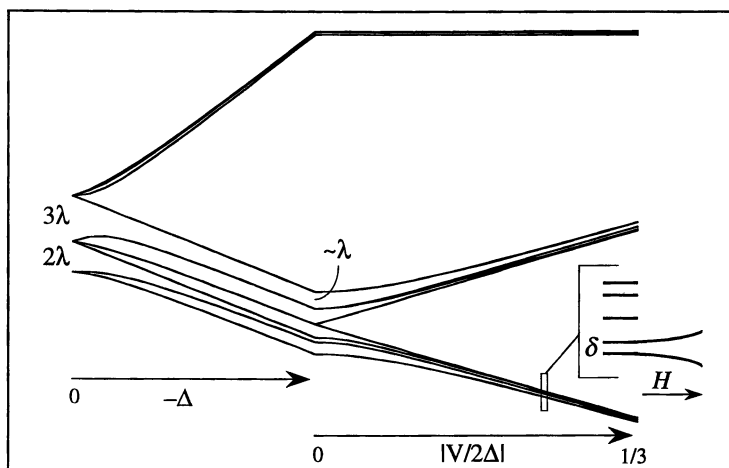


Figure 6. Solution of the $^5T_{2g}$ Hamiltonian for varying values of $-\Delta$ and $V/2\Delta$, where Δ is the axial and V is the rhombic ZFS of the t_{2g} orbitals. The inset shows the Zeeman splitting of the lowest sublevels.

described as distorted octahedral with two unoccupied *cis* positions. The other structure (30) includes a water molecule and Asn₆₉₄Oδ1 as ligands, completing the octahedral coordination sphere for a 6C iron. While the Fe–O(Asn₆₉₄) bond in the 6C structure is significantly longer than the other Fe–L bonds, the 4C structure shows Asn₆₉₄ at a distance too far away from the iron to be considered a ligand. Of the metal-binding residues, His₄₉₉, His₅₀₄, and His₆₉₀ are conserved in all known sequenced LOs, and the C-terminal Ile₈₃₉ is conserved in all but rat leukocyte 5-LO, where there is instead a terminal Val (31). Asn₆₉₄ is found to be conserved in all but rabbit reticulocyte and recombinant human 15-LOs, for which this Asn is replaced by His in the sequence alignment (28).

CD studies on native ferrous SLO-1 show that the addition of glycerol (a common glassing agent) perturbs the active site, while the addition of sucrose as an alternate glassing agent causes no changes in the spectrum (32,33). The low-temperature MCD spectrum of ferrous SLO-1 in sucrose is given in Figure 7a and shows multiple features in the ligand field region. Based on the above methodology, more than two d→d transitions indicates that there must be more than one paramagnetic species present in native SLO-1. In contrast, the low-temperature MCD spectrum of SLO-1 in glycerol (Figure 7b) shows just two d→d features which are indicative of a single distorted octahedral 6C species. Subtraction of 60% of these 6C spectral features from the spectrum of SLO-1 in sucrose produces a clean two-peak spectrum indicative of a 5-coordinate ferrous site (Figure 7c). Thus the CD and MCD data show that native ferrous SLO-1 is in fact a ~60:40 combination of 6C and 5C species, respectively, and that the addition of glycerol shifts this mixture to a pure 6C species (33). This may shed some light on the conflicting crystal structures as it is clear that the resting form of the enzyme in solution is a mixture of species which can shift under differing conditions.

Addition of substrate and exogenous ligands to ferrous SLO-1 has also been investigated (33) to probe changes at the active site which may provide mechanistic insight. The addition of linoleate substrate causes the same shift from a mixture of 5C+6C species to the pure 6C species observed with the addition of glycerol. When ethanol or ethylene glycol are added to ferrous SLO-1, this same change is observed. The fact that the identical 6C spectrum is produced from the addition of substrate or alcohols indicates that alcohols are interacting with the substrate binding site, not directly with the metal. Addition of azide, a small molecule oxygen analog, causes no change when a 500-fold excess of NaN₃ is added either to resting ferrous SLO-1 or to SLO-1 + linoleate (33). Thus spectroscopic studies demonstrate that the addition of substrate to ferrous SLO-1 causes the mixture of species to shift to a pure 6C species, but does not appear to activate the iron site for small molecule binding.

Mammalian Lipoxygenases and Comparison to SLO-1. The mammalian enzymes rabbit reticulocyte 15-LO (15-RLO) and human recombinant 15-LO (15-HLO) differ from SLO-1 (also a 15-LO) by the substitution of His for Asn₆₉₄ according to the sequence alignment. Since His is a stronger-field ligand than Asn, differences in the spectra between these mammalian LOs and SLO-1 might be expected. CD studies show that the addition of glycerol to either 15-RLO or 15-HLO causes no change to the spectra and so does not perturb the active sites (33). The low-temperature MCD spectra of 15-RLO and 15-HLO are shown in Figures 8a and 8b, respectively, and two Gaussians are required to fit each spectrum. These data indicate that unlike native SLO-1, 15-RLO and 15-HLO exist as clean 6C species. This can be explained by the Asn₆₉₄→His substitution since His is a stronger σ-donor ligand and should form a stronger bond to the Fe(II) active sites in 15-RLO and 15-HLO than the weak Asn ligand does in SLO-1.

Additional electronic structure information can be obtained from the saturation magnetization behavior of these systems (33). The VTVH MCD data for 15-RLO and 15-HLO are shown as insets in Figure 8. The data for both mammalian enzymes

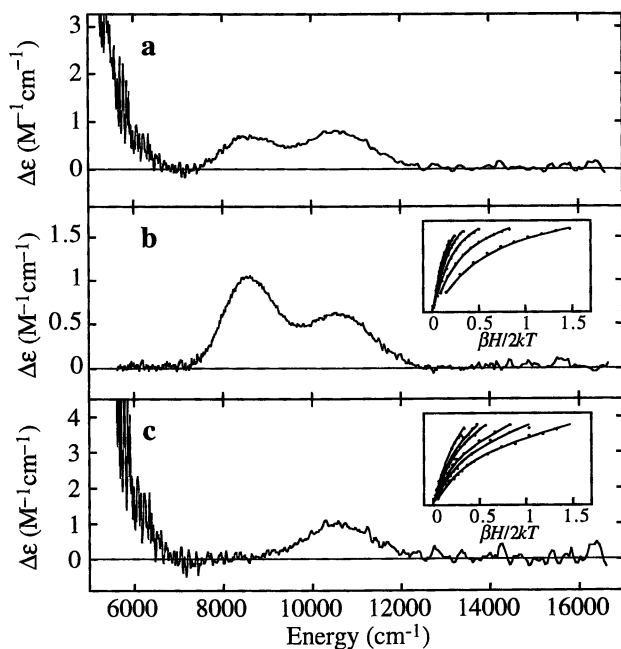


Figure 7. Low-temperature MCD spectra for (a) native SLO-1 in sucrose, (b) SLO-1 in glycerol, and (c) resulting renormalized spectrum when 60% of spectrum b is subtracted from spectrum a. Insets show the VTVH MCD data (points) and fits (lines) for the 6C (b) and 5C (c) species.

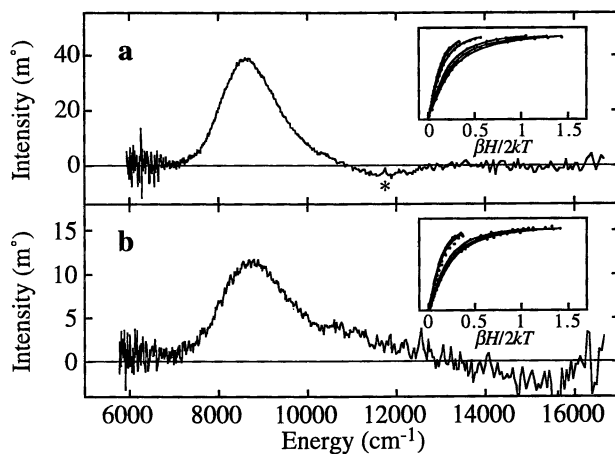
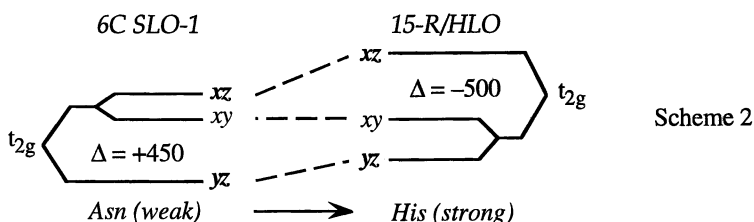


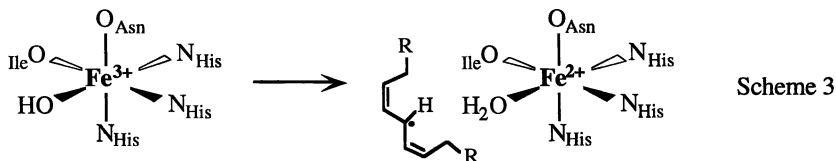
Figure 8. Low-temperature MCD spectra for (a) 15-RLO in glycerol (* <2% heme impurity) and (b) 15-HLO in glycerol. Insets show the respective VTVH MCD data (points) and fits (lines).

are best fit by the $-ZFS$ non-Kramers doublet model with $\delta \approx 4 \text{ cm}^{-1}$ and $g_{\parallel} \approx 9$, values indicative of a 6C site. For comparison, the VTVH MCD data for the 6C and 5C forms of SLO-1 are presented as insets in Figure 7 and are qualitatively different from the mammalian data. (Notice that although native SLO-1 exists as a mixture of species, one can selectively probe each component by collecting VTVH MCD data at specific wavelengths.) Quantitative analysis shows that the SLO-1 data are best fit by the $+ZFS$ three-level model with $D \approx +13$ and $+10 \text{ cm}^{-1}$ for the 6C and 5C species, respectively, and $E/D \approx 0.1$ for both. Application of the above methodology gives $^5T_{2g}$ splittings of $\Delta \approx -500 \text{ cm}^{-1}$ and $|V/2\Delta| \approx 0.27$ for the (6C) mammalian enzymes and $\Delta \approx +450 \text{ cm}^{-1}$ and $|V/2\Delta| \approx 0.16$ for 6C SLO-1. Electronic structure calculations (33) provide more complete orbital descriptions of these levels, as shown below in Scheme 2.



These splitting patterns can be interpreted in terms of replacing a weak Asn ligand with a strong His ligand along z (where z is defined along the unique weak Fe–O(Asn) direction), which causes the d_{yz} and d_{xz} orbitals to shift to higher energy. Therefore, although the excited-state spectra for 6C SLO-1 and 15-RLO/15-HLO are quite similar, the ground-state electronic structures are different, and these differences can be attributed to the substitution of the weak Asn in SLO-1 with a strong His ligand in the mammalian enzymes.

Mechanistic Implications. MCD spectroscopy has indicated electronic structure differences between the soybean and mammalian LOs which may have mechanistic implications. Resting ferrous SLO-1 is activated by the addition of product to give the high-spin ferric enzyme, which is 6C with OH^- in place of H_2O (34). In one proposed mechanism, this ferric center reacts with substrate to abstract a H-atom, generating a ferrous site and a fatty acid radical intermediate (35,36). Because of the strong His electron-donor ligand, 15-RLO and 15-HLO should have more stable ferric sites and lower redox potentials than in SLO-1, making it harder to reduce the mammalian active sites. If reduction of the ferric enzyme is required for catalysis, as proposed in Scheme 3, then one would expect that stabilizing the Fe(III) site in the mammalian enzymes should lower their activity relative to SLO-1.



In fact, 15-RLO and 15-HLO are experimentally found to have comparable K_m values, but lower V_{max} values relative to SLO-1 (37-39), supporting the above proposed mechanism. Thus these results are consistent with the Asn \rightarrow His structural change upon going from the soybean to mammalian LOs (33,40) and show how differences in structure can be related to differences in reactivity.

Summary.

Low-temperature MCD provides a sensitive method for investigating paramagnetic centers in bioinorganic chemistry and is particularly useful in probing low-energy ligand field transitions in the near-infrared region which are often obscured in other techniques. These excited-state ligand field splittings can be directly related to e_g d-orbital energies, as described here for Fe(II), and provide geometric information. VTVH MCD probes ground-state Zeeman effects and allows one to extract zero-field splittings and g values, as well as polarizations for transitions to excited states. This method has recently been extended to encompass non-Kramers ions and both $-ZFS$ and $+ZFS$ systems. Ground-state parameters obtained from the saturation magnetization data can be further correlated with ligand field parameters to give the splitting of the t_{2g} d-orbitals. These, together with the observed e_g splittings, provide a full description of the five d-orbitals for a given ferrous center and provide a direct probe of active site geometric and electronic structure. Additionally, MCD can help assign charge transfer transitions through comparing C_0/D_0 ratios, and the spin-orbit coupling information obtained from the charge transfer bands plus the intensity provide a measure of active site covalency. Thus one can probe specific metal-ligand bonding interactions. This methodology has been illustrated through application to the iron active sites in soybean and mammalian LOs. CD and MCD data have shown that native SLO-1 exists as a mixture of 5C and 6C sites, which may help explain the disparate crystal structures, while 15-RLO and 15-HLO exists as pure 6C species. These results plus the saturation magnetization analysis show that the electronic structure differences between 6C SLO-1 and 15-RLO/15-HLO can be attributed to the substitution of a weak Asn ligand in SLO-1 with a strong His ligand in the mammalian enzymes. Furthermore, these structural differences can be correlated with differences in reactivity and provide mechanistic insight, demonstrating the powerful utility of MCD spectroscopy.

Acknowledgments. This work was supported by the National Institutes of Health (GM 40392).

Literature Cited.

- Schatz, P. N.; McCaffery, A. J. *Quart. Rev.* **1969**, *32*, 552.
- Buckingham, A. D.; Stephens, P. J. *Annu. Rev. Phys. Chem.* **1966**, *17*, 399.
- Stephens, P. J. *Adv. Chem. Phys.* **1976**, *35*, 197.
- Piepho, S. B.; Schatz, P. N. *Group Theory in Spectroscopy: With Applications to Magnetic Circular Dichroism*; John Wiley & Sons: New York, 1983.
- Gebhard, M. S.; Deaton, J. C.; Koch, S. A.; Millar, M.; Solomon, E. I. *J. Am. Chem. Soc.* **1990**, *112*, 2217.
- Thomson, A. J.; Cheesman, M. R.; George, S. J. *Methods Enzymol.* **1993**, *226*, 199.
- Gewirth, A. A.; Solomon, E. I. *J. Am. Chem. Soc.* **1988**, *110*, 3811.
- Gerstman, B. S.; Brill, A. S. *J. Chem. Phys.* **1985**, *82*, 1212.
- Solomon, E. I.; Pavel, E. G.; Loeb, K. E.; Campochiaro, C. *Coord. Chem. Rev.* **1995**, *144*, 369.
- Shadle, S. E.; Penner-Hahn, J. E.; Schugar, H. J.; Hedman, B.; Hodgson, K. O.; Solomon, E. I. *J. Am. Chem. Soc.* **1993**, *115*, 767.
- George, S. J.; Lowery, M. D.; Solomon, E. I.; Cramer, S. P. *J. Am. Chem. Soc.* **1993**, *115*, 2968.
- Guss, J. M.; Bartunik, H. D.; Freeman, H. C. *Acta Crystallogr.* **1992**, *B48*, 790.
- Guckert, J. A.; Lowery, M. D.; Solomon, E. I. *J. Am. Chem. Soc.* **1995**, *117*, 2817.
- Solomon, E. I.; Penfield, K. W.; Gewirth, A. A.; Lowery, M. D.; Shadle, S. E.; Guckert, J. A.; LaCroix, L. B. *Inorg. Chim. Acta* **1996**, *243*, 67.

15. Schatz, P. N.; Mowery, R. L.; Krausz, E. R. *Mol. Phys.* **1978**, *35*, 1537.
16. Stephens, P. J. *Annu. Rev. Phys. Chem.* **1974**, *25*, 201.
17. Thomson, A. J.; Johnson, M. K. *Biochem. J.* **1980**, *191*, 411.
18. Bennett, D. E.; Johnson, M. K. *Biochim. Biophys. Acta* **1987**, *911*, 71.
19. Browett, W. R.; Fucaloro, A. F.; Morgan, T. V.; Stephens, P. J. *J. Am. Chem. Soc.* **1983**, *105*, 1868.
20. Whittaker, J. W.; Solomon, E. I. *J. Am. Chem. Soc.* **1988**, *110*, 5329.
21. Pavel, E. G., Ph.D. Thesis, Stanford University, 1997.
22. Campochiaro, C.; Pavel, E. G.; Solomon, E. I. *Inorg. Chem.* **1995**, *34*, 4669.
23. Champion, P. M.; Sievers, A. J. *J. Chem. Phys.* **1977**, *66*, 1819.
24. Gnezdilov, V. P.; Eremenko, V. V.; Peschanskii, A. V.; Fomin, V. I. *Sov. J. Low Temp. Phys.* **1991**, *17*, 130.
25. Hamilton, C. L.; Scott, R. A.; Johnson, M. K. *J. Biol. Chem.* **1989**, *264*, 11605.
26. Gardner, H. W. *Biochim. Biophys. Acta* **1991**, *1084*, 221.
27. Samuelsson, B.; Dahlén, S.-E.; Lindgren, J. Å.; Rouzer, C. A.; Serhan, C. N. *Science* **1987**, *237*, 1171.
28. Sigal, E. *Am. J. Physiol.* **1991**, *260*, L13.
29. Boyington, J. C.; Gaffney, B. J.; Amzel, L. M. *Science* **1993**, *260*, 1482.
30. Minor, W.; Steczko, J.; Stec, B.; Otwinowski, Z.; Bolin, J. T.; Walter, R.; Axelrod, B. *Biochemistry* **1996**, *35*, 10687.
31. Sigal, E.; Craik, C. S.; Highland, E.; Grunberger, D.; Costello, L. L.; Dixon, R. A. F.; Nadel, J. A. *Biochem. Biophys. Res. Commun.* **1988**, *157*, 457.
32. Pavlosky, M. A.; Solomon, E. I. *J. Am. Chem. Soc.* **1994**, *116*, 11610.
33. Pavlosky, M. A.; Zhang, Y.; Westre, T. E.; Gan, Q.-F.; Pavel, E. G.; Campochiaro, C.; Hedman, B.; Hodgson, K. O.; Solomon, E. I. *J. Am. Chem. Soc.* **1995**, *117*, 4316.
34. Scarrow, R. C.; Trimitsis, M. G.; Buck, C. P.; Grove, G. N.; Cowling, R. A.; Nelson, M. J. *Biochemistry* **1994**, *33*, 15023.
35. Veldink, G. A.; Vliegthart, J. F. G. *Adv. Inorg. Biochem.* **1984**, *6*, 139.
36. Nelson, M. J.; Cowling, R. A.; Seitz, S. P. *Biochemistry* **1994**, *33*, 4966.
37. Schewe, T.; Wiesner, R.; Rapoport, S. M. *Methods Enzymol.* **1981**, *71*, 430.
38. Axelrod, B.; Cheesbrough, T. M.; Laakso, S. *Methods Enzymol.* **1981**, *71*, 441.
39. Sloane, D. L.; Leung, R.; Barnett, J.; Craik, C. S.; Sigal, E. *Protein Eng.* **1995**, *8*, 275.
40. Zhang, Y.; Gan, Q.-F.; Pavel, E. G.; Sigal, E.; Solomon, E. I. *J. Am. Chem. Soc.* **1995**, *117*, 7422.

Chapter 7

Recent Advances in Resonance Raman Spectroscopy

Thomas M. Loehr

Department of Biochemistry and Molecular Biology, Oregon Graduate Institute
of Science and Technology, Portland, OR 97291-1000

Recent advances in Raman spectrometry that have had significant impact on studies of metalloenzymes include the CCD detector, time-resolved spectroscopic methods, and cryogenic techniques for the isolation of short-lived intermediates. The revolutionary charge-coupled device (CCD) photo-detector is robust and offers low noise, high sensitivity, fast response, and a wide spectral window. Time-resolved spectroscopy can be used to follow the kinetics of the appearance and disappearance of chemical species. The study of reaction intermediates may benefit by the adaptation of stopped-flow methodology with freeze trapping in cold liquid isopentane. Examples are given of the application of these methods in the study of metalloenzymes, with particular emphasis on the use of isotopic labeling for the study of oxygenated intermediates.

Raman spectroscopy is the study of the vibrational properties of molecules. The experimental technique requires the input of monochromatic radiation and observing the light scattered by the sample. Spectral frequencies are reported in wavenumber units (cm^{-1}) that are proportional to the vibrational energies, and are given as the difference between the energies of the excitation and scattered rays. Hence, the observed frequencies are also referred to as Raman shifts. The experimental discovery of these satellite frequencies (both Stokes and anti-Stokes shifts) due to molecular light scattering was first reported in 1928 in two landmark papers by C. V. Raman and K. S. Krishnan (1) in Bangalore and by Landsberg and Mandelstam (2) in Moscow. The report by Raman, although much less detailed and insightful, predated the latter by 3½ months and hence carried both the Nobel prize and the eponymous phenomenon. (Facsimiles of these classic papers are given in an excellent book on Raman spectroscopy by Long (3)).

Description of Raman and Resonance Raman Spectroscopy

A depiction of the energetics of some electronic and vibrational processes is given in Figure 1. The transition ν_e represents an electronic absorption from the ground to the first excited state of a molecule; typical energies are in the range of 10,000 to 50,000 cm^{-1} (1000 to 200 nm). For each electronic state, ground and vibrationally excited levels are also indicated. Thus, the transition marked IR is an infrared absorption resulting in a vibrational transition. Typical energies are in the 100 to 3500 cm^{-1} range.

Symmetry restrictions aside, the same vibrational transition may be induced by Raman scattering. Moreover, it should be evident that Raman scattering is independent of the excitation energy (when far from an electronic excited state). The same Raman spectrum would be generated with any input wavelength: it is only the difference between the input and output energies that determine the Raman frequency ($\Delta E_{\text{vib}} = h\nu_0 - h\nu_{\text{scat}}$), and that is dependent on the nature of the scatterer. The most probable scattering contribution, however, is Rayleigh scattering, in which the scattered radiation is of identical energy as the excitation. While this process carries little or no information about the molecule (i.e., frequency = 0 cm^{-1}), it is the dominant effect, and good instrumentation is required to eliminate the Rayleigh contribution from the desired Raman spectrum. Approximately 0.1% (1 in 1000) of the input photons are Rayleigh scattered, and, similarly only 0.1% of the Rayleigh scattered photons are Raman shifted. Thus, only 1 in 10^6 of the incident photons are converted into Raman signal. It is this generally feeble effect that has rendered Raman spectroscopy more of a laboratory curiosity than a standard bench-top technique. Standard Raman measurements require very high concentrations of solutes ($\gg 0.1$ M), neat liquids, or pure solids.

Nonetheless, Raman spectroscopy is a valuable research technique because it does complement IR absorption and has many distinct advantages, especially for the investigation of samples in aqueous media. Whereas water absorbs strongly throughout the infrared, making observation of the IR spectra of samples nearly impossible except in certain window regions, water is a relatively poor Raman scatterer and, thus, a good solvent. Further, Raman scattering depends on a change in the polarizability of the molecule (or chemical bond) whereas IR absorption requires a change in the dipole (3, 4). Thus, totally symmetric vibrations, such as $\nu(\text{O}=\text{O})$ or $\nu_1(\text{SO}_4^{2-})$ are fully allowed in the Raman process but fully disallowed in IR absorption.

Resonance Raman Effect. A process that is unique to Raman scattering is the resonance effect, as indicated by the equation in Figure 1. Because the (square root) Raman scattering intensity is inversely proportional to the difference between the energy of the excited state and the excitation energy, i.e., $(I_R)^{1/2} \propto (\nu_e - \nu_0)^{-1}$, the expression has a resonant denominator. In practice, excitation wavelengths are selected that lie close to or within the electronic absorption band. For efficient resonance Raman scattering, the absorption must involve multiple atoms, such as in a $\pi \rightarrow \pi^*$ or charge-transfer transitions. An electronic transition that is atom localized, as in a $d \rightarrow d$ transition, does not induce resonance. The bonds undergoing the largest change in geometry between the ground and excited states are those that give maximal resonance enhancement. In Hirakawa and Tsuboi's original words: "If a Raman line

becomes stronger when the exciting frequency is brought closer to the frequency of an electronic band, this means that the equilibrium conformation of the molecule is distorted along the normal coordinate for the Raman line in the transition from the ground to the excited electronic state" (5). In more theoretical terms, it is the Franck-Condon factors, that is, the magnitude of the overlap of the vibrational wave functions in the ground and excited states that determine the resonance Raman intensity. A more practical guide to the extent of enhancement is that the resonance effect scales approximately with ϵ^2 , where ϵ is the molar absorptivity of the sample.

Modern Instrumentation

The modern, general-purpose Raman system consists of a single-stage monochromator with a focal length of 0.5 to 1 m utilizing a holographically ruled grating. At least two ports to the spectrograph are required, one serving as an entrance for the scattered light and the second for the detector (Figure 2). The modern charge-coupled device (CCD) detector is a rugged, extremely sensitive array detector. A representative unit may have a physical area of 8×25 mm with some 350×1100 pixels whose quantum efficiency can exceed that of typical photomultiplier tube. In this view, the CCD is a vast collection of PMTs, but one with extremely low dark noise that may be further reduced by thermoelectric or liquid-nitrogen cooling of the detector. Relative to a classical scanning instrument with single-channel PMT detection, the CCD gives the instrument a multiplex advantage in that the entire spectral window, determined by the dispersion of the grating and the focal length of the spectrograph, falls upon the detector. In practice, data accumulation times are reduced from minutes to seconds or hours to minutes. In the author's view, the CCD is the third major technological development in the history of Raman spectroscopy since the transition from photographic plates to photoelectric detectors in the 1940s, and the introduction of lasers as excitation sources in the late 1960s.

The entrance port is fitted with an adjustable slit, a receptacle for a holographic notch filter, and other optics such as a polarization scrambler or f -matching lens. A sample in a glass capillary is illuminated from above (or below) and the scattered light is collected in a 90-degree orientation by an objective lens suitable for the wavelength of the experiment. A variety of gratings (e.g., 600, 1200, 1800, 2400, 3600 grooves mm^{-1}) are available that determine the frequency range on the detector. A denser groove pattern is selected for blue or UV excitation. A 25-mm array illuminated with ~ 500 -nm light in a 0.67-m spectrograph with a 1800-groove grating will give a Raman spectral range of ~ 500 cm^{-1} .

Holographic Notch Filter. This filter is designed to have an optical density of 4 to 6 at the wavelength of the Rayleigh-scattered light. It serves to reduce the undesired Rayleigh component of the scattering to permit access to the low-frequency (≈ 200 - 500 cm^{-1}) Raman region. Thus, it functions like the traditional second and/or third monochromators that reduce stray and Rayleigh scattered light. The single optical element notch filter greatly improves the throughput of the spectrograph when compared to the additional 2 gratings and mirrors of a typical double subtractive filter monochromator. The advantage of the latter, however, is that it can accept any

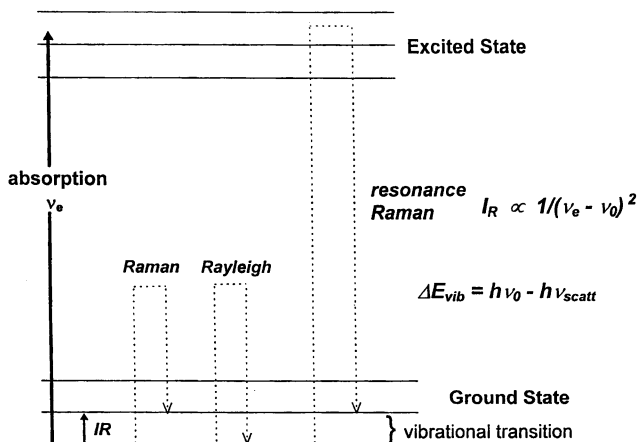


Figure 1. Energy level diagram illustrating optical and infrared absorption (—), and Rayleigh Raman, and resonance Raman scattering (---).

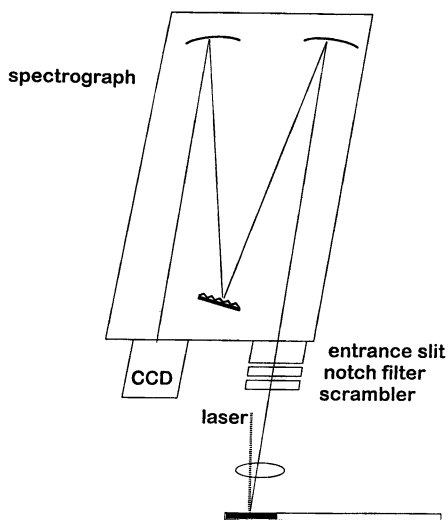


Figure 2. Components of a single-stage grating spectrograph.

excitation wavelength (consider, for example, the use of a tunable dye laser) whereas the notch filter is designed for only a single wavelength.

Calibration of the CCD Detector. The CCD can be used either as an imaging or a spectral detector. The spectrum of CCl_4 is shown in Figure 3 as an image, where it appears as if it had been acquired on a photographic plate (top panel) or as a standard spectrum (lower panel). Prior to calibration, the abscissa of the spectrum is obtained in pixel units. The use of the detector in this image mode serves well to align the detector with respect to the spectrograph. The light from spectral bands falling on the detector should be vertical and evenly distributed across the height of the detector. This image field serves to optimize the choice of the sample image height relative to the slit height and the vertical direction of the array. The CCD controller can be programmed to sum (or bin) the vertical pixels into a 1×1100 array to give the bottom spectrum. The peaks are marked with their pixel number below and with their standardized Raman frequencies above. (Applications of the CCD detector in Raman spectroscopic imaging will not be explored further here; the following references to Morris et al. (6) and Schaeberle et al. (7) illustrate the research capabilities of imaging spectroscopy).

Calibration standards are essential to convert the pixel spectrum to frequency space. An ideal calibrant has 10 or more well-defined, sharp peaks over the full width of the array as shown for the hydrocarbon, indene, an IUPAC frequency standard, in Figure 4. Other useful calibrants include toluene, CCl_4 , powdered aspirin, or neon emission lamps. Once the pixel spectrum of the standard is calibrated against its known frequencies, subsequent spectra are obtained directly in frequency, as shown in the example in the lower trace of Figure 4. However, it is critical that neither the spectrograph nor the sample location be readjusted between the acquisition of the standard and the sample spectra. It is highly advisable to run the standard again after data acquisition to verify that the peak locations have not changed by even as much as one pixel unit. Even a slight repositioning of the sample relative to the entrance optics can "move" the spectrum on the detector plane and, thereby, affect the accuracy of the frequencies.

Sample Integrity. Owing to the very significant decrease in the data acquisition time with a CCD-equipped spectrograph, sample exposure to the laser is also significantly reduced. In cases where sample integrity is of concern due to prolonged exposure, as with most biological specimen, the rapid CCD system offers marked benefits. Sample protection by cryogenic cooling, circulation, use of non-optimal excitation wavelengths, or low power levels was paramount with a scanning system; however, now it is feasible to return to simpler sampling arrangements by taking advantage of the 1000-fold or greater data acquisition factor. With the spectrograph system, we find renewed value in using melting-point capillaries as satisfactory sample cells. They only require a small volume ($\sim 10 \mu\text{L}$), with appropriate collection optics, the image size can be well matched to the detector height, and, importantly, for many chromophoric biological samples, the optical absorption properties can be readily monitored on the same sample in a standard UV/vis spectrophotometer before and after laser exposure. Figure 5 shows the superposition of two absorption spectra (300 -

Carbon tetrachloride - image field on 330 x 1100 pixels

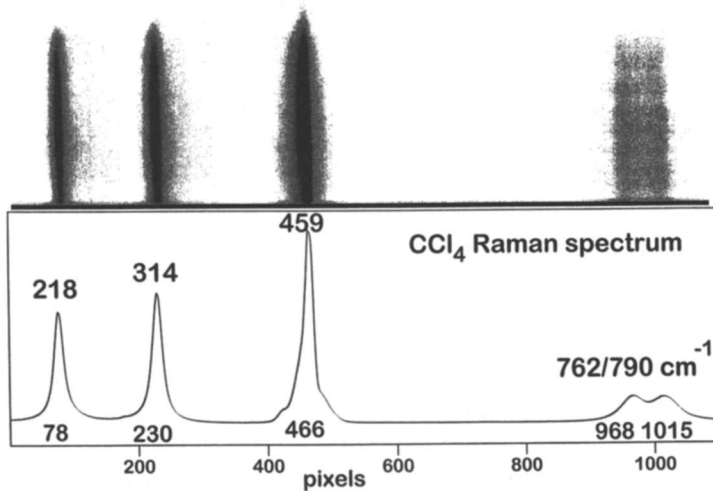


Figure 3. The uncalibrated Raman spectrum of CCl₄ on a CCD detector in image mode (upper panel) and in spectroscopic mode (lower panel).

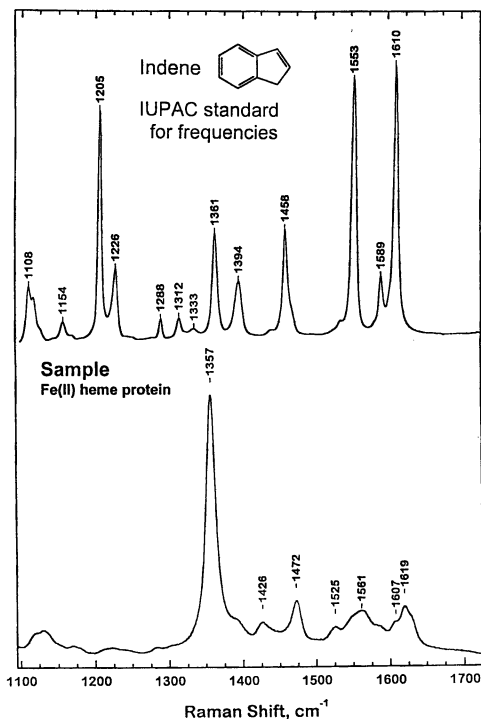


Figure 4. Raman spectrum of indene used as a calibration standard (upper) and a frequency-calibrated spectrum of a heme-protein (lower).

800 nm) of a porphyrin derivative obtained first in the glass capillary used for the Raman experiment, and second, in a narrow path length optical cuvette. Only within the Soret region are data uncertain owing to the very high absorptivity; in the visible region, the data quality for the two cells are identical. As shown in the inset, we use a self-masking black plastic holder sized as a standard cuvette that is bored to fit the capillary and with a ~1-mm wide window for the light path. The spectrophotometer background is initially zeroed with a capillary containing water. Additional experimental details are given elsewhere (8). Raman capillaries may be cooled by insertion into a cold finger that is chilled in ice water or even in liquid nitrogen. A frequent advantage of sampling biological materials near room temperature is the suppression of background fluorescence in liquid as opposed to frozen solution samples. This methodology may be readily adapted to other types of sample cells when sample integrity must be monitored by other means, such as EPR or Mössbauer spectroscopy.

Applications Illustrating Uses of Recent Raman Methodology

Difference Spectroscopy. Interesting applications of Raman difference spectroscopy have been refined by Callender and coworkers. One example is shown in Figure 6 for lactate dehydrogenase (LDH) and its coenzyme, NADH (9). Since this is a non-resonant Raman spectrum, the major peaks observed are due to the protein. High quality data are obtained from two samples in tandem cells mounted on an automated translation stage. Spectrum (a) contains the enzyme plus coenzyme, and (b) contains the enzyme alone. A casual view of these data reveals no significant differences. The quality of repeat data sets is illustrated by difference spectrum (c): enzyme(data set *i*) – enzyme(data set *j*) giving an excellent featureless baseline. The remarkable power of the technique is revealed in difference spectrum (d) = (a) – (b), and this rich spectrum is that of the enzyme-bound cofactor. The large disparity in molecular weights of the enzyme (57,000 Da) and NADH (700 Da) should be noted. Further applications of difference spectra are illustrated below.

Time-Resolved Spectroscopy. One example of a time-resolved experiment is presented here that is based on work carried out in the laboratory of Kitagawa and coworkers on cytochrome *b₀* oxidase (10). This flow-flash experiment was designed to obtain resonance Raman spectroscopic data of oxygenated intermediates of the enzyme. The reaction sequence and the experimental setup are shown in Figure 7. The reduced enzyme is originally reacted with carbon monoxide to form the heme•CO adduct, then exposed to O₂. A laser flash serves both to photodissociate the CO and to probe the time-dependent formation of oxygenated species. The time base is achieved by varying the flow rate of the sample past the laser beam: at faster flow rates, the transit time through the beam is less and earlier species are expected; at slower flow rates, the transit time is longer and species formed by later events are probed. The flow rates were adjusted for the beam dimensions to yield residence times of ≈0 to 20 μs and ≈0 to 40 μs, respectively.

The results of the flow-flash experiments are shown in Figure 8. The raw data, carried out with ¹⁶O₂ and ¹⁸O₂ are shown in traces (A) through (D), and individual

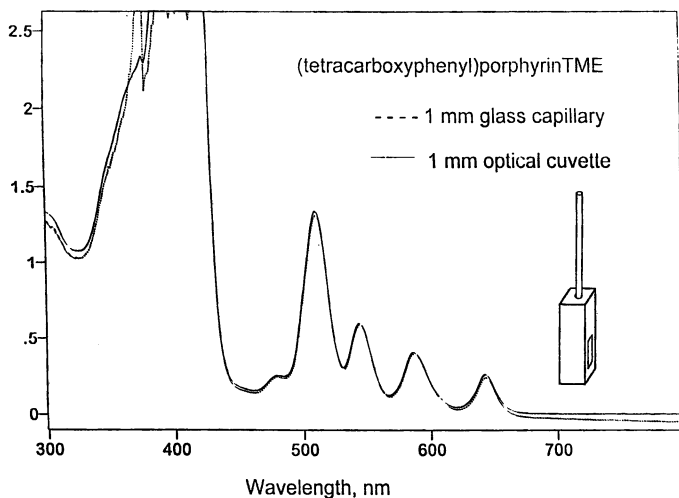


Figure 5. Electronic absorption spectra of a porphyrin specimen obtained in a melting-point capillary vs an optical cuvette.

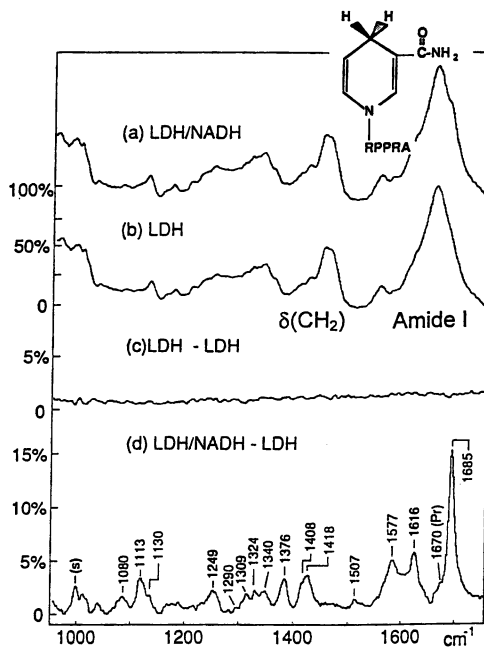


Figure 6. The Raman difference spectrum (d) of the NADH coenzyme bound to lactate dehydrogenase. (Reproduced with permission from ref. 9. Copyright 1994 Annual Reviews, Inc.)

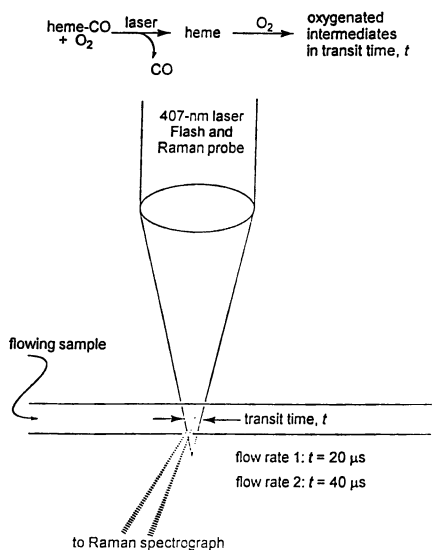


Figure 7. Experimental setup for measuring time-resolved, flow-flash resonance Raman spectra of oxygenated intermediates formed in cytochrome *b₀* oxidase (10).

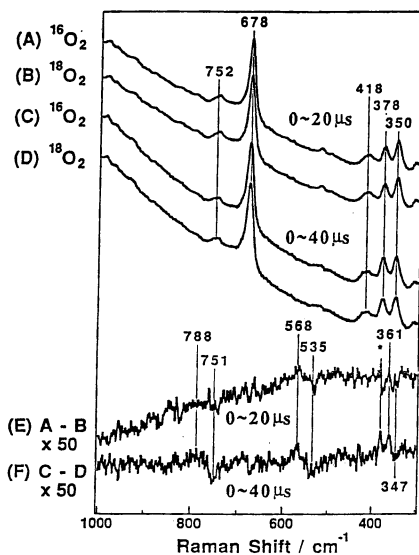
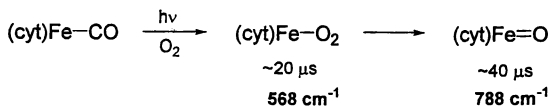


Figure 8. Time-resolved and oxygen-isotope sensitive resonance Raman spectra of the oxygenation of cytochrome *b₀* oxidase. (Reproduced with permission from ref. 10. Copyright 1994, Elsevier Science Co.)

species are identified in the difference spectra, amplified 50× to reveal the small signals. Trace (E), correlating with the earlier (< 20 μs) events, shows a peak at ~568 cm⁻¹ (¹⁶O₂, shifting to ~535 cm⁻¹ in ¹⁸O₂) that is assigned to ν(Fe–O₂). Nearly identical frequencies have been observed in oxy cytochrome *c* oxidase (~570 cm⁻¹, (11-13), oxyhemoglobin and oxymyoglobin (~570 cm⁻¹, (14, 15)), and oxy cytochrome *bd* oxidase (568 cm⁻¹, (16)). At later time (20 - 40 μs), a new signal is observed near 790 cm⁻¹ in trace (F) that is also sensitive to the O₂ isotope. This feature is assigned to the Fe^{IV}=O stretching frequency of ferryl heme. Heme ferryl frequencies are expected and have been observed near 800 cm⁻¹ (11, 12, 17). These results support a reaction sequence in which O₂ initially binds to ferrous heme, and upon subsequent reduction forms the ferryl species after heterolytic O–O bond cleavage. Further details of the chemistry of heme/copper oxidases are given in recent comprehensive reviews by Ferguson-Miller and Babcock (12) and Kitagawa and Ogura (11). Applications of time-resolved resonance Raman spectroscopy on the nanosecond time scale to metalloproteins are given in a review on instrumental methods (18).

Identification of Specific Oxo Intermediates by Resonance Raman Spectroscopy.

O₂ interacts with metal sites during oxygen activation by metalloenzymes and in respiratory proteins, to produce a wide variety of species, coordination geometries, and oxidation states of O and M. A number of these are shown in Figure 9. Many of these, thus far with the exception of methane monooxygenase, can be identified by resonance Raman spectroscopy through judicious study of the isotope, excitation wavelength, and time dependence of oxygen-sensitive vibrational frequencies.

Oxyhemerythrin. A now classic series of experiments on oxyhemerythrin illustrates the appearance of distinct resonance Raman bands under different excitation conditions and how the resulting peaks are identified to specific O₂ or metal-oxo vibrations through isotope exchange (Figure 10; (19, 20)). The electronic absorption spectrum of oxyhemerythrin is shown in the upper left panel, and below it are resonance Raman enhancement profiles that graph the change in intensities of the Raman peaks (shown in the panels to the right) as a function of excitation wavelength. The symmetric μ-oxo-bridge vibration, ν_s(Fe–O–Fe), is at 486 cm⁻¹ and is identified on the basis of its frequency and ¹⁸O-isotope shift. The wavelength dependence of this Raman band shows that it is maximally enhanced with ~370-nm excitation, allowing the assignment of the near-UV absorption band as oxo → Fe(III) charge transfer. In contrast, green to orange colors excite two other bands associated with the O₂ binding site: ν(O–O) at 844 cm⁻¹ and ν(Fe–O₂) at 503 cm⁻¹. The intensities of both of these Raman bands track the optical absorption band that displays a λ_{max} at ~500 nm, and this result serves to identify the absorption as due to O₂ → Fe(III) charge transfer.

All three resonance Raman bands, ν_s(Fe–O–Fe), ν(O–O), and ν(Fe–O₂), also had deuterium isotope effects (data are discussed in Ref. (20)) that led to the proposal that the bound O₂ is in the form of a terminal hydroperoxide that is hydrogen bonded to the μ-oxo bridge oxygen. This proposed structure was entirely consistent with the X-ray structure of oxyhemerythrin (21, 22).

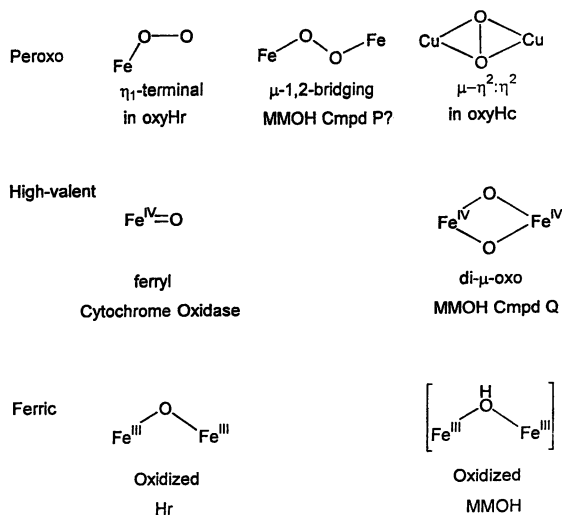


Figure 9. Peroxo adducts that can be identified by resonance Raman spectroscopy and oxidation products.

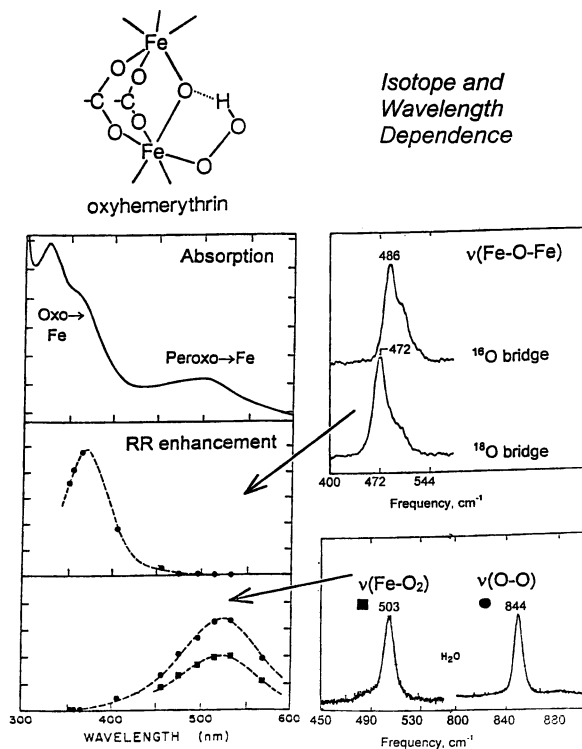


Figure 10. Electronic absorption, resonance Raman spectra, and resonance Raman enhancement profiles for oxyhemerythrin (19, 20).

Binding Mode of Peroxo Adducts. Oxidative addition of O₂ to a binuclear metal site results in reduction of dioxygen to the peroxide level, giving it a vibrational frequency in the 850 - 900 cm⁻¹ range. The peroxo ligand can bind in a number of ways as shown in Figure 9 (see also, (23)). Resonance Raman spectroscopy using mixed-isotope dioxygen provides a powerful and definitive probe of the nature of the binding geometry. The use of ¹⁸O¹⁶O with proteins was first described by Kurtz et al. (24). Examples of spectral interpretations using this technique are given in Figure 11 for oxyhemerythrin (24), oxyhemocyanin (25, 26), and a μ -1,2-bridged iron complex characterized by Kim and Lippard (27). The basis of the spectral differentiation arises from the local symmetry of the peroxo adduct. If the dioxygen species is symmetrically disposed with respect to the metal ions, then a single $\nu(\text{O}-\text{O})$ is expected. That is exactly what has been observed for oxyhemocyanin. Replacing ¹⁶O₂ with the mixed-label ¹⁸O¹⁶O adduct results in the appearance of a single band of the same intensity but downshifted in frequency owing to the increased mass. The extremely low O-O stretching frequency of oxyhemocyanin reflects its novel μ - η^2 : η^2 geometry. However, when the peroxo group is unsymmetrically disposed with respect to the metals, as in oxyhemerythrin, then the shifted frequency is split into two components each of lower intensity owing to the disparate frequencies of the (Fe)¹⁶O-¹⁸O and (Fe)¹⁸O-¹⁶O species. The mixed-isotope effect on the M-O frequency is even more pronounced, with the two bands corresponding to M-¹⁶O and M-¹⁸O being the best diagnostic indicator of asymmetric peroxide binding. An earlier publication from our laboratory reviewed these and similar cases involving ¹⁸O¹⁶O adducts (28).

Freeze-Trapped Intermediates. Isolation of catalytic intermediates in the reactions of O₂ with reduced forms of ribonucleotide reductase and the hydroxylase of methane monooxygenase has been accomplished by rapid-freeze trapping in liquid isopentane at -140 °C. Such resulting "snows" have been investigated by EPR, EXAFS, and Mössbauer spectroscopy to yield valuable structural information on the reductase (29-32) and the monooxygenase (33-35). While, in principle, the study of such isolated intermediates should be possible by resonance Raman spectroscopy, no firm examples can be cited at this time. Complications arise in this method because the cryosolvent itself has a rich Raman spectrum while the effective concentration of the trapped chromophoric intermediate is generally quite low. Approaches to reduce the solvent contribution include pumping the frozen sample to decrease the amount of isopentane or to use subtraction methods. In our laboratory, we have attempted to measure the resonance Raman spectra of intermediate X of protein R2 of ribonucleotide reductase and compound Q of MMO, but to no avail. However, in a feasibility study, we were able to see an excellent signal of $\nu(\text{Fe}-\text{O}-\text{Fe})$ in an isopentane-frozen sample of metmyohemerythrin. Applications of cryogenic methods to absorption and EPR spectroscopy of cytochrome *c* oxidase have also been recently reviewed (11).

High-Valent Metal-Oxo Complexes. Ferryl compounds containing tetra- or pentavalent iron Fe=O moieties have been well studied in porphyrin and heme systems (17, 36). However, the existence of such species in non-heme iron enzymes has been more controversial (34, 37). Of particular research interest in bioinorganic chemistry

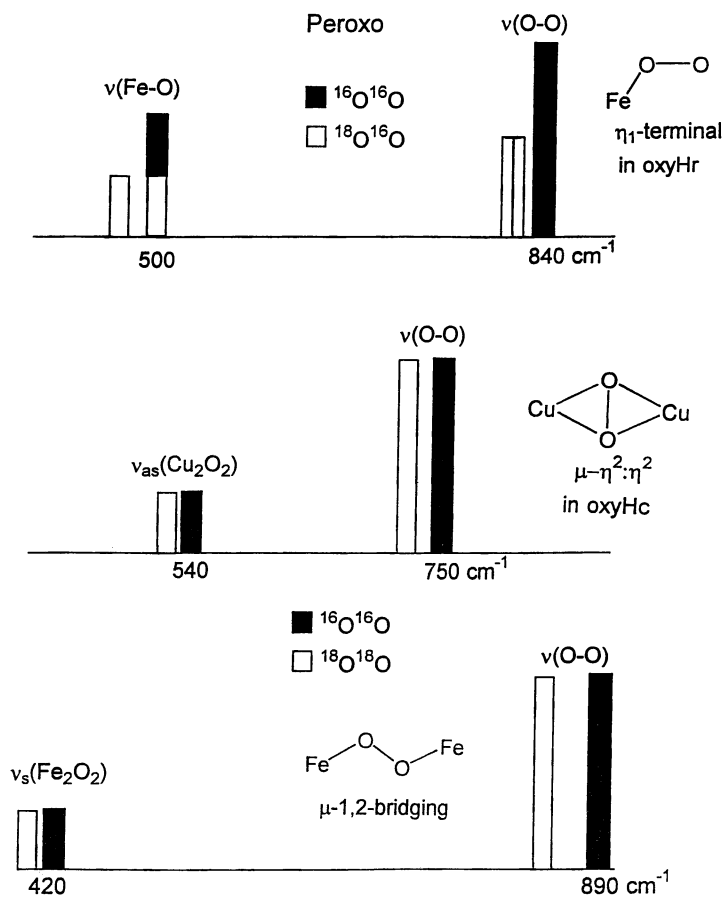


Figure 11. Mixed-isotope O_2 is used to identify the mode of binding of peroxo to metal sites.

is the question whether or not ferryl species appear as catalytic intermediates in enzymes such as ribonucleotide reductase and methane monooxygenase. Resonance Raman spectroscopy could again prove useful in the identification of such species.

Iron-porphyrin ferryl species have been characterized by their Fe=O vibrations in the 790-850 cm^{-1} range (see above under Time-Resolved Spectroscopy), and such a species is illustrated for cytochrome *bd* oxidase in Figure 12. This terminal oxidase has one iron-chlorin and two heme cofactors; hence, the fully reduced enzyme possesses three reducing equivalents and reacts with O_2 to produce an extremely stable ferryl species with a frequency at 815 cm^{-1} (17). Substitution of $^{18}\text{O}_2$ shifts the frequency to 769 cm^{-1} , but reaction with a 50-atom% mixture of mixed label $^{18}\text{O}^{16}\text{O}$ gives equal intensity resonance Raman peaks only at 815 and 769 cm^{-1} (Figure 12). Although these frequencies fall within the range also observed for peroxy species, the identification as a ferryl species is unambiguous. The complete absence of a Raman peak midway between the ^{16}O and ^{18}O features (at 792 cm^{-1}) with an intensity *twice* that of the flanking peaks ascertains that only Fe= ^{16}O and Fe= ^{18}O , and no peroxy species, are present. A further verification that the 815- cm^{-1} mode is from a ferryl is shown by the iron-isotope sensitivity of this Raman band, as shown in Figure 13. No such isotope effect would be expected for a peroxy vibration.

An example of a non-heme ferryl is afforded by an (salen)Fe^{IV}=O complex reported by Proniewicz et al. (38), and its isotope dependence is shown in Figure 14, top panel. As with the cytochrome *bd* oxidase example just mentioned, the salen complex exhibits two well-separated frequencies in the mixed isotope adducts, one due to Fe= ^{16}O and one from Fe= ^{18}O .

Several laboratories have attempted to obtain the resonance Raman spectrum of the freeze-trapped intermediate compound Q of MMO (34), but no successes have yet been described. Mössbauer and EXAFS data on Q of the *M. trichosporium* hydroxylase are consistent with an Fe(IV) formulation in an Fe₂O₂ diamond core (35). An excellent model system for the binuclear sites of MMO and ribonucleotide reductase is a mixed-valence, diamond-core structure characterized by Que and coworkers (39). The oxo bridges of the mixed valence complex undergo exchange with water and can therefore be labeled. The resonance Raman spectrum prepared in H₂¹⁶O and H₂¹⁸O is shown in the middle panel of Figure 14. The diamond-core structure appears to have a characteristically low frequency, relative to terminally bonded oxo groups. However, relative to the spectrum of a representative μ -oxo-bridged Fe^{III}-O-Fe^{III} system as in oxyhemerythrin (Figure 14, lower panel), which has ν_s at ~ 490 cm^{-1} and ν_{as} at ~ 750 cm^{-1} , the high valence of the diamond-core complex is revealed by the high intensity feature at ~ 670 cm^{-1} . These models are of considerable value; from a knowledge of their vibrational properties, the frequencies of the illusive enzyme intermediates can be bracketed and anticipated.

Acknowledgments. This work was supported by grants GM-18862 and GM-34468 of the National Institutes of General Medical Sciences, National Institutes of Health. The CCD-Raman system at OGI was purchased through a grant from the National Science Foundation (BIR-9216592) and matching funds from OGI. The author wishes to acknowledge the research effort of all his coworkers mentioned in the references.

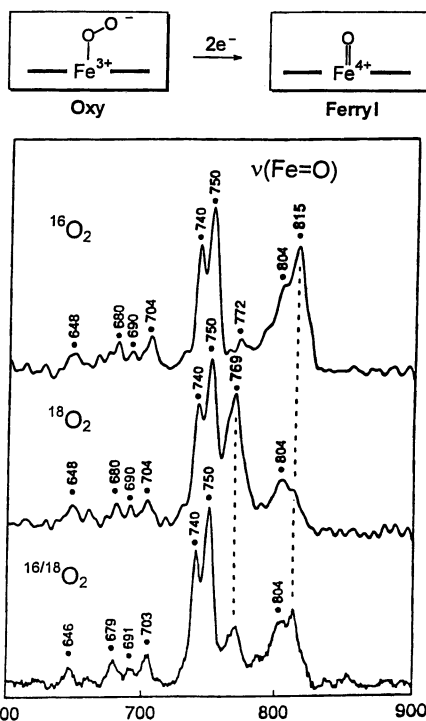


Figure 12. Identification of a ferryl intermediate in cytochrome *bd* oxidase (17).

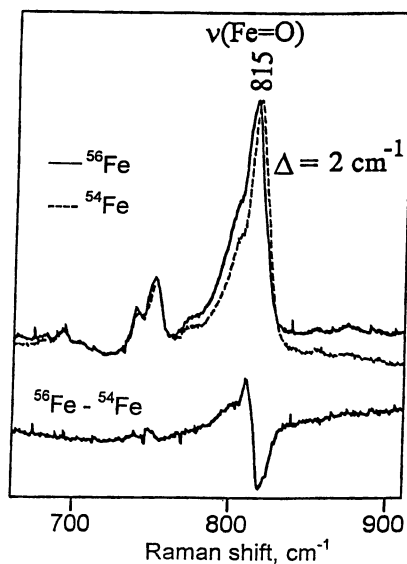


Figure 13. Observation of an iron-isotope shift in the ferryl intermediate of cytochrome *bd* oxidase.

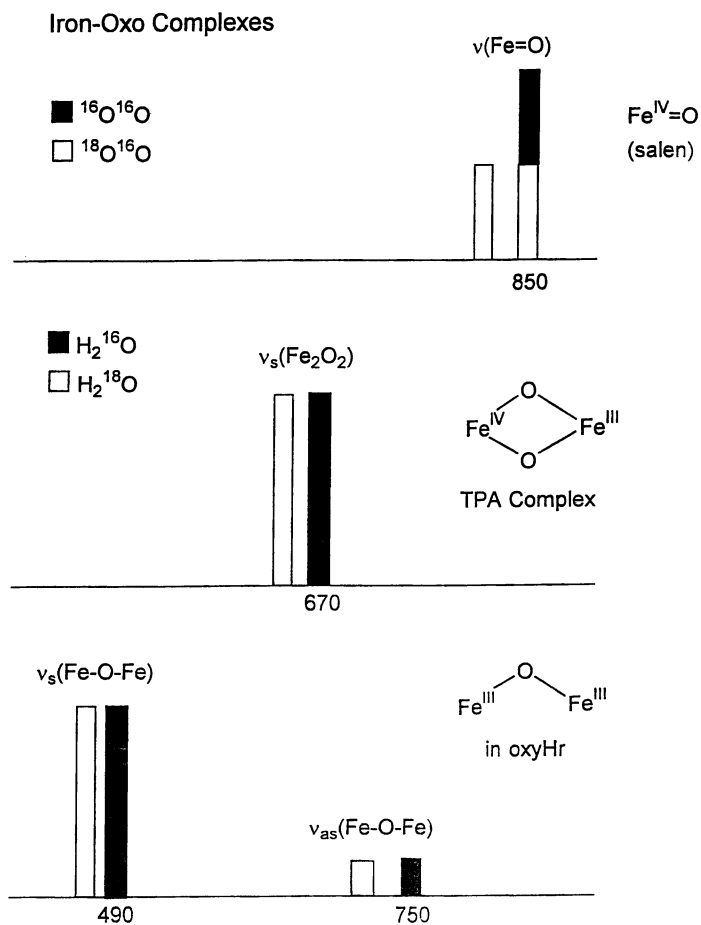


Figure 14. Oxygen-isotope substitutions differentiate between dioxygen adducts and high-valent iron-oxo complexes.

Special thanks go to Dr. Pierre Moënne-Loccoz and Prof. Joann Sanders-Loehr for critical discussions in the preparation of this contribution to the symposium.

Literature Cited

- (1) Raman, C. V.; Krishnan, K. S. *Nature* 1928, 121, 501.
- (2) Landsberg, G.; Mandelstam, L. *Naturwissenschaften* 1928, 16, 557.
- (3) Long, D. A. *Raman Spectroscopy*; McGraw-Hill: London, 1977.
- (4) Diem, M. *Introduction to Modern Vibrational Spectroscopy*; John Wiley & Sons: New York, 1993.
- (5) Hirakawa, A. Y.; Tsuboi, M. *Science* 1975, 188, 359-361.
- (6) Morris, H. R.; Hoyt, C. C.; Miller, P.; Treado, P. J. *Appl. Spectrosc.* 1996, 50, 805-811.
- (7) Schaeberle, M. D.; Kalasinsky, V. F.; Luke, J. L.; Lewis, E. N.; Levin, I. W.; Treado, P. J. *Anal. Chem.* 1996, 68, 1829-1833.
- (8) Loehr, T. M.; Sanders-Loehr, J. *Methods Enzymol.* 1993, 226, 431-470.
- (9) Callender, R.; Deng, H. *Annu. Rev. Biophys. Biomol. Struct.* 1994, 23, 215-245.
- (10) Hirota, S.; Mogi, T.; Ogura, T.; Hirano, T.; Anraku, Y.; Kitagawa, T. *FEBS Lett.* 1994, 352, 67-70.
- (11) Kitagawa, T.; Ogura, T. *Prog. Inorg. Chem.* 1997, 45, 431-479.
- (12) Ferguson-Miller, S.; Babcock, G. T. *Chem. Rev.* 1996, 96, 2889-2907.
- (13) Han, S. W.; Ching, Y. C.; Rousseau, D. L. *Proc. Natl. Acad. Sci. U.S.A.* 1990, 87, 2491-2495.
- (14) Brunner, H. *Naturwissenschaften* 1974, 61, 129.
- (15) Van Wart, H. E.; Zimmer, J. *J. Biol. Chem.* 1985, 260, 8372-8377.
- (16) Kahlow, M. A.; Loehr, T. M.; Zuberi, T. M.; Gennis, R. B. *J. Am. Chem. Soc.* 1993, 115, 5845-5846.
- (17) Kahlow, M. A.; Zuberi, T. M.; Gennis, R. B.; Loehr, T. M. *Biochemistry* 1991, 30, 11485-11489.
- (18) Varotsis, C.; Babcock, G. T. *Methods Enzymol.* 1993, 226, 409-431.
- (19) Shiemke, A. K.; Loehr, T. M.; Sanders-Loehr, J. *J. Am. Chem. Soc.* 1984, 106, 4951-4956.
- (20) Shiemke, A. K.; Loehr, T. M.; Sanders-Loehr, J. *J. Am. Chem. Soc.* 1986, 108, 2437-2443.
- (21) Stenkamp, R. E.; Sieker, L. C.; Jensen, L. H.; McCallum, J. D.; Sanders-Loehr, J. *Proc. Natl. Acad. Sci. U.S.A.* 1985, 82, 713-716.
- (22) Holmes, M. A.; Le Trong, I.; Turley, S.; Sieker, L. C.; Stenkamp, R. E. *J. Mol. Biol.* 1991, 218, 583-593.
- (23) Holm, R. H.; Kennepohl, P.; Solomon, E. I. *Chem. Rev.* 1996, 96, 2239-2314.
- (24) Kurtz, D. M., Jr.; Shriver, D. F.; Klotz, I. M. *J. Am. Chem. Soc.* 1976, 98, 5033-5035.
- (25) Thamann, T. J.; Loehr, J. S.; Loehr, T. M. *J. Am. Chem. Soc.* 1977, 99, 4187-4189.
- (26) Ling, J.; Nestor, L. P.; Czernuszewicz, R. S.; Spiro, T. G.; Fraczkiewicz, R.; Sharma, K. D.; Loehr, T. M.; Sanders-Loehr, J. *J. Am. Chem. Soc.* 1994, 116, 7682-7691.

- (27) Kim, K.; Lippard, S. J. *J. Am. Chem. Soc.* 1996, *118*, 4914-4915.
- (28) Loehr, T. M. *Oxygen binding by the metalloproteins hemerythrin, hemocyanin, and hemoglobin*; Loehr, T. M., Ed.; Plenum: New York, 1988, pp 17-32.
- (29) Ravi, N.; Bollinger, J. M., Jr.; Huynh, B. H.; Edmondson, D. E.; Stubbe, J. J. *Am. Chem. Soc.* 1994, *116*, 8007-8014.
- (30) Bollinger, J. M., Jr.; Tong, W. H.; Ravi, N.; Huynh, B. H.; Edmondson, D. E.; Stubbe, J. J. *Am. Chem. Soc.* 1994, *116*, 8015-8023.
- (31) Sahlin, M.; Lassmann, G.; Pötsch, S.; Sjöberg, B.-M.; Gräslund, A. *J. Biol. Chem.* 1995, *submitted*.
- (32) Sturgeon, B. E.; Burdi, D.; Chen, S.; Huynh, B.-H.; Edmondson, D. E.; Stubbe, J.; Hoffman, B. M. *J. Am. Chem. Soc.* 1996, *118*, 7551-7557.
- (33) Liu, K. E.; Valentine, A. M.; Wang, D.; Huynh, B. H.; Edmondson, D. E.; Salifoglou, A.; Lippard, S. J. *J. Am. Chem. Soc.* 1995, *117*, 10174-10185.
- (34) Wallar, B. J.; Lipscomb, J. D. *Chem. Rev.* 1996, *96*, 2625-2657.
- (35) Shu, L.; Nesheim, J. C.; Kauffmann, K.; Münck, E.; Lipscomb, J. D.; Que, L., Jr. *Science* 1997, *275*, 515-518.
- (36) Oertling, W. A.; Kean, R. T.; Wever, R.; Babcock, G. T. *Inorg. Chem.* 1990, *29*, 2633-2645.
- (37) Feig, A. L.; Lippard, S. J. *Chem. Rev.* 1994, *94*, 759-805.
- (38) Proniewicz, L. M.; Bajdor, K.; Nakamoto, K. *J. Phys. Chem.* 1986, *90*, 1760-1766.
- (39) Que, L., Jr.; Dong, Y. *Acc. Chem. Res.* 1996, *29*, 190-196.

Chapter 8

Soft X-ray Absorption Spectroscopy: Applications to Bioinorganic Chemistry

Stephen P. Cramer¹, Hongxin Wang², Craig Bryant², Mark Legros²,
Craig Horne², Daulat Patel², Corie Ralston², and Xin Wang²

¹Department of Applied Science, University of California, Davis, CA 94306

²Structural Biology Division, Lawrence Berkeley National Laboratory,
Berkeley, CA 94720

The high brightness of modern synchrotron radiation sources enables a number of x-ray spectroscopic experiments on bioinorganic materials. This review emphasizes developments in biological soft x-ray spectroscopy.

For the past two decades, bioinorganic applications of x-ray spectroscopy have primarily involved structure determination by EXAFS and oxidation state characterization using chemical shifts in the XANES region. Although these have been extremely productive techniques, the purpose of this article is to introduce two less familiar probes - soft x-ray absorption and x-ray magnetic circular dichroism. Bioinorganic applications of these and other x-ray techniques such as high resolution x-ray fluorescence are made possible by the increased brightness of modern synchrotron radiation sources.

X-Ray Transitions. X-ray transitions in atoms involve at least one core level electron. A rather archaic terminology evolved when X-rays were discovered serendipitously by Roentgen more than 100 years ago. Promotion of a 1s electron is termed K absorption, while K emission involves filling of a 1s vacancy from higher levels. Similarly, L absorption and emission involve 2s or 2p electrons, and so on. L absorption is subdivided into L₃ and L₂ edges, which come respectively from spin-orbit splitting of the 2p⁵ hole into 2p_{3/2} and 2p_{1/2} final states, and the L₁ edge which results from promotion of the 2s electron. K emission is divided between K α lines for 2p \rightarrow 1s transitions and K β for 3p \rightarrow 1s lines. Finally, K α 1 and K α 2 labels are used to distinguish the spin-orbit splittings of these lines. The many additional intricacies of x-ray nomenclature have been well documented by Agarwal [1].

EXAFS. Extended x-ray absorption fine structure (EXAFS) is a modulation in the absorption cross section past an absorption edge [2]. As illustrated in Figure 1, the final state involves interference between outgoing and backscattered photoelectron waves. Depending on whether this interference is constructive or destructive, there is an enhanced or decreased absorption cross section. As the x-ray energy is changed, the

wavelength of the probe photoelectron changes, and the EXAFS effect periodically alternates in sign. The frequency of this modulation can be used to determine interatomic distances with an accuracy of $\pm 0.02\text{\AA}$, while the amplitude and phase can be used to extract the numbers and elemental types of neighbors. EXAFS has become an almost routine technique for bioinorganic structure determination, and many fine books and reviews are available [2].

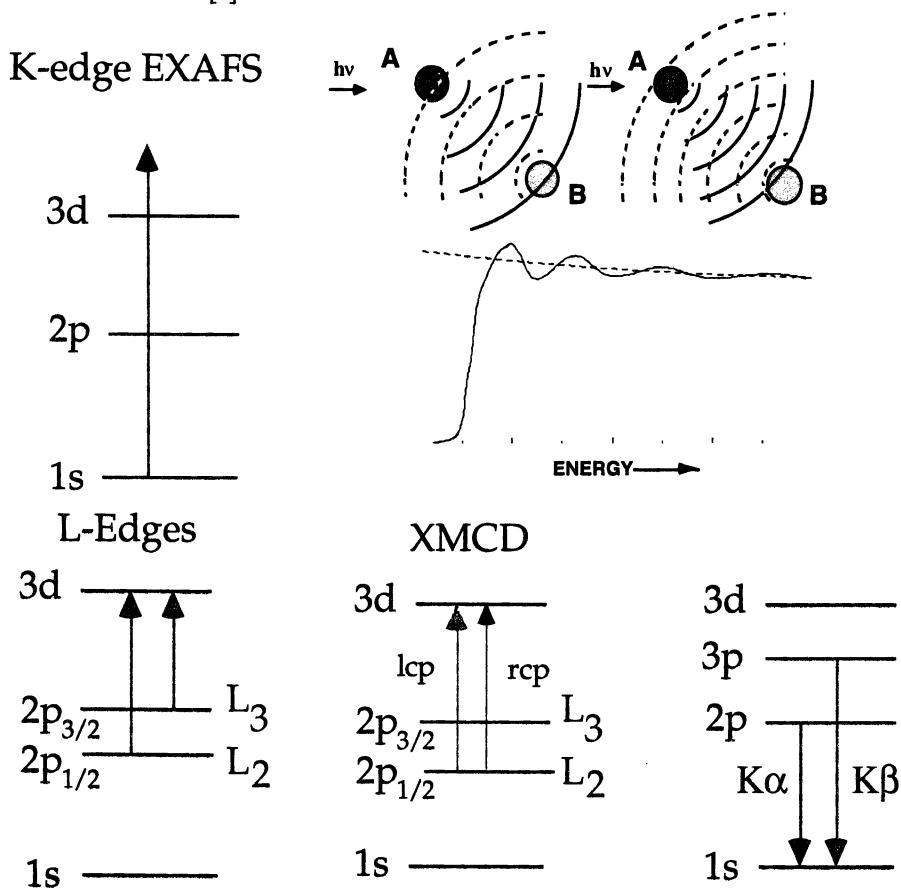


Figure 1. Top panel - (Left) K-edge EXAFS involves a transition from the 1s level to the continuum. (Right) The photoelectron wave from absorber A (—) scatters from neighboring atoms B, and the scattered wave (----) interferes with the original wavefunction to cause the EXAFS effect, as seen in the sample spectrum. Bottom panel - Transitions between discrete levels important for other types of x-ray spectroscopy.

X-Ray Multiplets. When a vacancy is created in a core shell of electrons, the resulting hole can interact with valence electrons to create interesting multiplets. In this way, the core level spectra become sensitive to the valence configuration. Two examples of strong multiplet interactions are first transition metal L-edges, where 2p-3d Coulomb and exchange interactions are important, and K β fluorescence, where the 3p-3d exchange interaction dominates (Figure 1).

Synchrotron Radiation

"For revolutions, however we may be tempted to define them, are not mere changes." H. Arendt [3]

The quantitative change in brightness available from synchrotron radiation sources has been so large that it has qualitatively changed the way x-ray science is done. Synchrotron radiation is emitted when relativistic charged particles are deflected by a magnetic field [4]. Because this radiation is highly collimated, synchrotron sources can produce much brighter x-ray beams than available from conventional bremsstrahlung sources (tubes). The first 'generation' of synchrotron radiation sources involved electron storage rings that were primarily used for high energy physics. For these experiments, the electron beams were kept relatively large around most of the ring, and only focussed to a small diameter in the interaction regions. The second generation consisted of sources designed or modified for synchrotron radiation, using mostly bend magnets and wiggler insertion devices. Over the years, machine physicists have learned how to produce extremely low emittance electron beams. This third generation of low emittance x-ray sources that exploits this progress is now coming on line [5, 6]. These rings use 'undulators' with a large number of magnetic poles, designed for constructive interference at certain wavelengths. The resulting radiation is concentrated in space and in frequency. Third generation soft x-ray rings include the ALS in Berkeley [5], ELETTRA in Trieste [7], and the Pohang Light Source in Korea. Undulator beam lines for hard x-rays are available at the ESRF in Grenoble and the APS near Chicago and will soon be available at SPRING-8 in Japan.

Over the past 2 decades, the x-ray brightness available from synchrotron radiation sources has increased by nearly 8 orders of magnitude. This development is frequently called 'revolutionary', and it compares favorably with two better known advances in technology - microprocessors and lasers. X-ray brightness has increased with a doubling time of approximately 12 months (Figure 2). This is comparable to the rate of change in peak power of tabletop lasers, and it is faster than Moore's law for microprocessors.

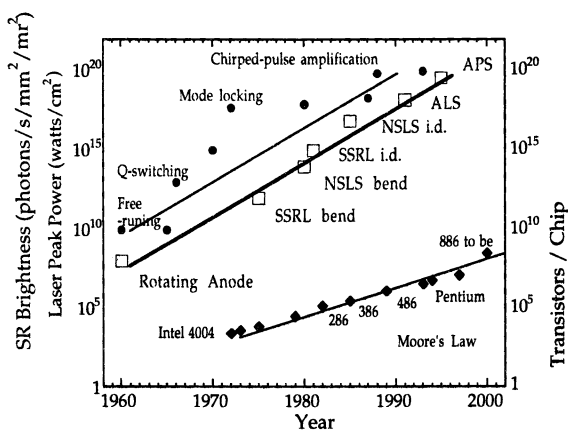


Figure 2. The history of improvement in x-ray brightness from synchrotron sources, compared with other technological revolutions.

Soft X-Ray Absorption

“When I use a word ... it means just what I choose it to mean -- neither more nor less.” -
Humpty Dumpty [8]

The term ‘soft’ for x-rays is used in many ways. For example, in medical technology, 10 keV photons are considered ‘soft’ x-rays, while in the laser literature, the same label is applied to 0.06 keV photons [9]. For the purposes of this article, we will arbitrarily consider the region from ~100-1100 eV, which includes the K-edges of elements from Be to Na and all of the L-edges from P through Zn. In practical terms, this region is often covered by grazing incidence grating monochromator beamlines at synchrotron radiation labs. Lower photon energies are often covered by higher angle grating beamlines, while at higher energies crystal monochromators take over. Efficient high resolution beamlines for this spectral region were only developed in the early 1980’s [10, 11].

Experimental Considerations. Experimental factors make soft x-ray spectroscopy a very different experience from hard x-ray work. Conventional EXAFS measurements can be done in air or helium atmosphere, using moderately thin plastic or Be windows for sample cells, detectors, and cryostats. At many synchrotron radiation labs such as SSRL, NSLS, or the ESRF, a bioinorganic chemist can arrive with a sample and use facility equipment to obtain spectra. In contrast, biological soft x-ray spectroscopy requires a considerable investment in vacuum equipment, primarily because the distance travelled by soft x-rays in aqueous and protein samples is very small.

Absorption Lengths. For example, at the Fe L-edge the 1/e path length for an x-ray in water is only 1.0 micron, and the path length in a helium atmosphere is ~30 cm. This means that any windows used in the apparatus must be extremely thin. One approach is to work in a high vacuum chamber, sometimes in a common vacuum with the beamline and electron storage ring. Setting up the required vacuum conditions often takes days of pumping and ‘baking out’ a chamber. Small leaks that compromise the vacuum can cost extra days to recover, and if the experimenter makes a mistake that compromises the beamline or ring vacuum, he or she will become instantly famous around the facility.

Detection Methods. Direct measurement of an absorption spectrum involves recording the intensity both with (I) and without (I_0) a sample in place, and then deriving the absorbance ($\log I_0/I$) as a function of x-ray energy (E). However, there are many experimental reasons why it is difficult to record soft x-ray spectra in transmission mode. With concentrated samples such as typical inorganic complexes, the proper thickness to achieve 10% transmission (an absorbance of 1) is on the order of 1000 Å. Since this is much smaller than typical particle sizes, it becomes almost impossible to lay down a homogeneous powder sample with the proper thickness and without significant pinholes and other defects. For dilute samples such as metalloproteins, it is difficult to observe the small changes in transmission at the metal edge on top of the large background signal from water and protein absorption. To avoid artifacts and achieve better sensitivity, ‘secondary’ detection methods are used (Figure 3). The derivation of these methods and possible artifacts have been extensively reviewed [12].

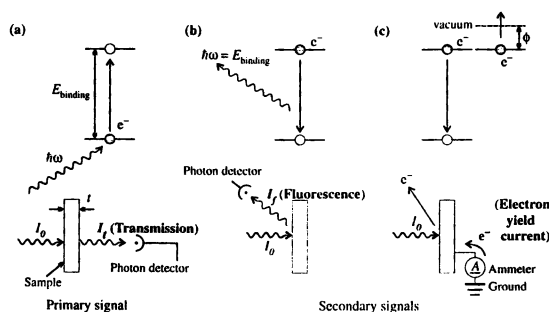


Figure 3. Schematic illustration of different detection modes [49].

In the soft x-ray region, atoms relax after x-ray absorption primarily by emission of an Auger electron. One can measure a signal related to the absorption cross section by recording either the Auger electron yield (I_{Auger}/I_0) or the total yield of electrons (I_{tey}/I_0) which are created in a cascade process as the Auger electron energy is dissipated. Auger yield detection requires an electron energy analyzer, and since only a small fraction of these electrons escape from the sample without energy loss, it is relatively inefficient. The most common detection methods are to either measure secondary electrons emerging from the sample (total electron yield) [13] or to measure the electrons passing through the sample (sample photocurrent) with a charge sensitive amplifier (Figure 3).

Since the electron escape depth is short ($<100 \text{ \AA}$), electron yield techniques are very surface sensitive. Even with excellent glove box or Schlenk techniques, many reactive samples such as Fe-S complexes are coated with a surface oxide that will give unrepresentative and misleading spectra. It is often necessary to sputter or physically scrape samples in vacuum to assure surface integrity. Furthermore, electron yield techniques are not applicable to most metalloproteins. Even if a signal can be observed, it only probes the first protein molecule at the surface of the sample, which may not be representative of the bulk. Furthermore, with total electron yield there is no elemental selectivity and the metal signal will be swamped by the absorption by water and protein background absorption. One is therefore forced to measuring the fluorescence signal (F/I_0) [14], even though L fluorescence yields for transition metals are less than 1%.

Fluorescence detected x-ray absorption is the dominant technique for hard x-ray EXAFS experiments, where its superior sensitivity has long been recognized [15]. The merits and pitfalls of fluorescence detection can be appreciated from the following approximate expression for a 'spectroscopically thick' sample [16]:

$$\frac{F}{I_0} \propto f_s \frac{\mu_s(E)}{\mu_s(E) + \mu_b(E) + \mu_s(E_f) + \mu_b(E_f)} \quad (1)$$

Here f_s represents the fluorescence yield for the sample element of interest, $\mu_s(E)$ and $\mu_s(E_f)$ are the absorption coefficients for this element at the excitation and fluorescence energies respectively, while $\mu_b(E)$ and $\mu_b(E_f)$ are corresponding coefficients for the

background absorption by the matrix. Clearly, if $\mu_s(E)$ is not small compared to $\mu_b(E)$, then the linear relationship between F and $\mu_s(E)$ breaks down. This is properly called fluorescence 'saturation'. The linearity can also break down if the fluorescence and absorption energies of the sample overlap. If E_f changes with excitation energy and $\mu_s(E_f)$ is significant, the amount of escaping fluorescence will vary with E , mimicking a variable fluorescence yield. This is a true 'self-absorption' effect. Both of these problems can be considered 'extrinsic', because they can be solved by making the sample more dilute.

'Intrinsic' artifacts are also possible with fluorescence detection if the fluorescence yield f_s varies significantly across the absorption spectrum or if different fluorescence lines have different angular distributions, as noted by deGroot [17, 18]. Dramatic differences between electron yield and fluorescence spectra have been observed [19] and explained [20] for Tm^{3+} (Figure 4). However, for the later transition metals, the discrepancy between fluorescence yield and true absorption spectra is predicted to be small [21], and this is also what is experimentally observed (Figure 4).

Table 1. Comparison of Different Detection Modes

Technique	Quantity measured	Probe Depth	Typical Detector
Auger yield	Auger electrons	$\sim 20 \text{ \AA}$	CMA
Total electron yield	departing electrons	$\sim 50-75 \text{ \AA}$	channeltron
Sample photocurrent	recharging electrons	$\sim 50-75 \text{ \AA}$	
Fluorescence	fluorescent x-rays	$\sim 50 - 5,000 \text{ \AA}$	Ge or Si detector
Transmission	transmitted x-rays	$\sim 100 - 10,000 \text{ \AA}$	PIN diode

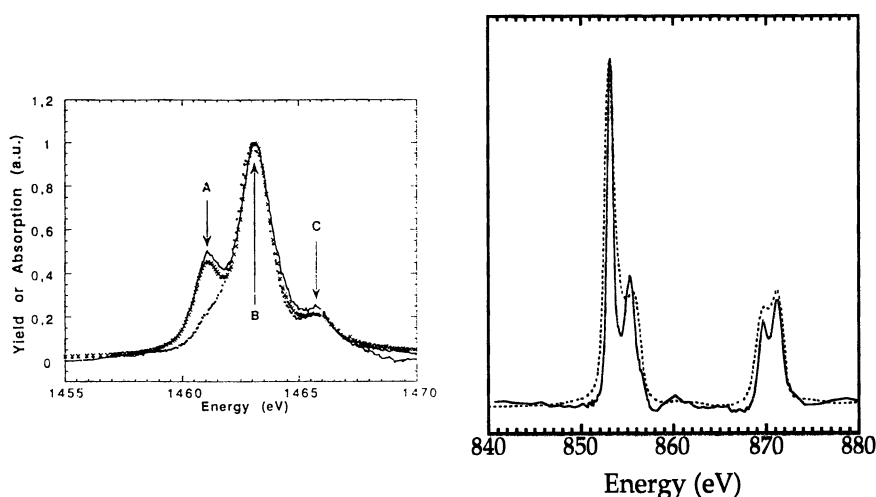


Figure 4. (Left) Transmission (—), electron yield (xxxx) and fluorescence-detected (....) x-ray spectra for Tm_2O_3 [19]. Feature A is almost missing from the fluorescence data (Right) Fluorescence detected absorption for Ni-doped MgO (—) and electron yield for NiF_2 (....). The same features are seen in both spectra.

Radiation Damage. The absorption of x-rays results in ejection of photoelectrons, Auger electrons, and the subsequent production of hydrated electrons and numerous free radicals [22, 23]. Even at low temperatures the electrons can migrate and react with the sample. Because the x-ray path lengths are approximately 3 orders of magnitude shorter than for hard x-rays, while the x-ray energy is only 1 order of magnitude lower, the radiation dose per unit volume is 100 times higher for comparable photon fluxes. Our experience is that proteins with high oxidation potentials are often reduced in the soft x-ray beam (Figure 5). Radiation damage will be an even greater issue in the future when brighter undulator beamlines become available. Crystallographers and microscopists using undulator sources have observed that samples often survive for only a few seconds. However, photoreactivity need not be an insurmountable problem. Because samples only have to be a few microns thick, it should be possible to prepare large sample areas and quickly spin or translate a sample across the photon beam.

What Makes Soft X-Ray Absorption Useful for Bioinorganic Problems? The advantages of the soft x-ray region for inorganic and biological spectroscopy include better energy resolution, favorable selection rules, multiplet splittings and strong magnetic circular dichroism. In the hard x-ray region, transition metal K-edges have linewidths of 1-2 eV, while the intrinsic linewidths of L-levels are much narrower (300-700 meV) [24]. The widths of light element K-edges are even sharper, such that vibrational fine structure can sometimes be seen in gas phase spectra. Better resolution is one factor that makes it easier to distinguish between different oxidation states with L-edges, and it also makes quantitation of mixtures more accurate.

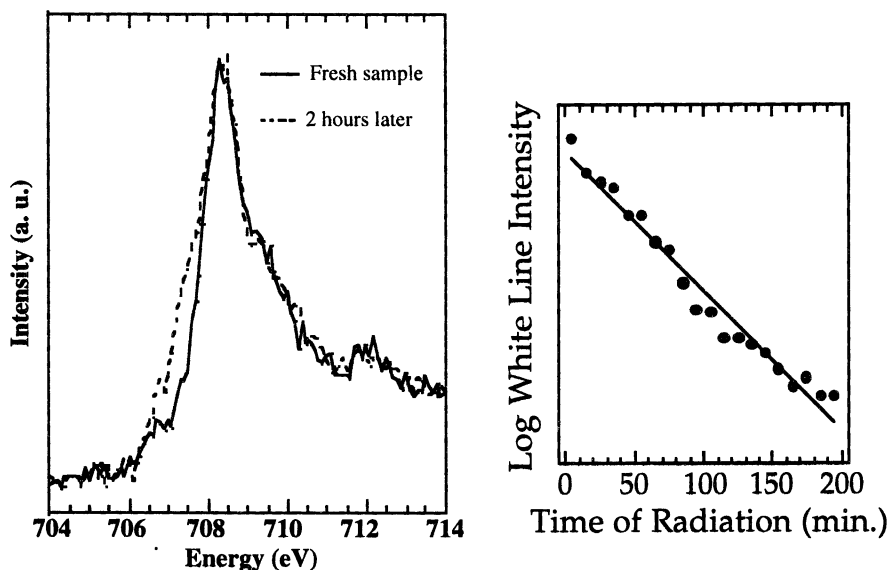


Figure 5. (Left) Mn L-edge spectra of superoxidized *Lactobacillus plantarum* Mn catalase recorded from fresh sample (—) and after 2 hour x-ray exposure (----) [25]. (Right) Time course of the photoreduction of the Cu A site of cytochrome oxidase.

L-edge spectra measure dipole-allowed $2p \rightarrow 3d$ transitions, while at the K-edge the $1s \rightarrow 3d$ transition is a weak quadrupole process (sometimes enhanced by p-d mixing). Since most of the chemistry of the transition metals involves d-orbitals, L-edges are a natural choice for probing the metal electronic structure. L-edges show multiplet structure that is sensitive to the metal oxidation and spin states, and they also have much larger potential XMCD effects. The net result of these factors is illustrated in Figure 6, where the K and L edges of MnCl_2 are compared.

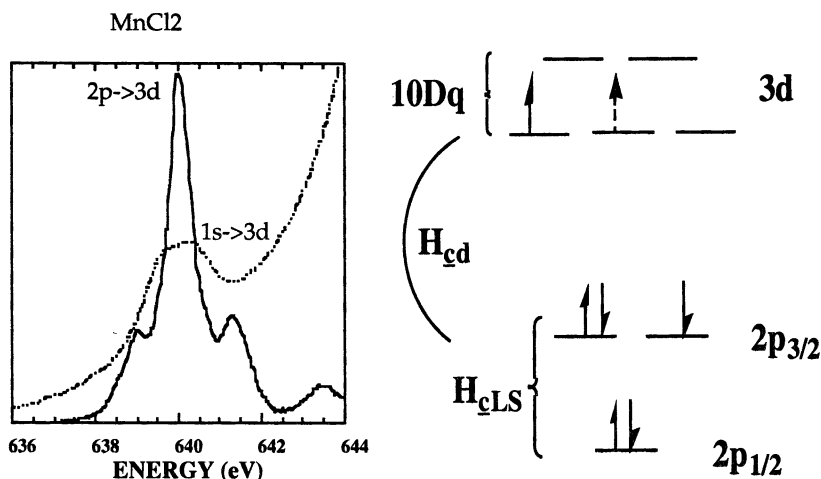


Figure 6. (Left) Comparison of the $1s \rightarrow 3d$ region of the MnCl_2 K-edge with the L_3 edge [26]. (Right) Some of the interactions that give rise to L-edge fine structure.

The Hamiltonian. One way to summarize the factors that affect the position, intensity, and shape of L-edge spectra is to consider the Hamiltonian that describes the initial and final state energies [27]. For inorganic complexes, the most successful procedure for constructing this Hamiltonian is the ligand field multiplet model. Building on ideas developed in the seventies [28, 29], this approach was extensively developed by Thole and coworkers [30], who successfully combined the chain of groups theory of Butler [31] with atomic Hartree-Fock methods from Cowan and coworkers [32]. This method begins by evaluating the atomic multiplets that arise from a given configuration of core hole and valence electrons. Symmetry and ligand field parameters are then used to calculate how these multiplets are split by the ligand environment. In the following examples, we use the notation of deGroot for the relevant Hamiltonians [27].

For example, consider a transition metal ion with N 3d electrons. The L-edge transition can then be described as a $2p^6 3d^N \rightarrow 2p^5 3d^{N+1}$ transition. The Hamiltonian for the ground state atomic multiplets is:

$$\mathcal{H}_{1s} + \mathcal{H}_{\text{mu}} + \mathcal{H}_{3d} \quad (2)$$

where \mathcal{H}_{3d} is the average energy of the 3d states, \mathcal{H}_{mu} includes all 2-electron integrals and \mathcal{H}_{ls} is the 3d spin-orbit coupling. The Hamiltonian for the final state includes extra terms \mathcal{H}_c for the core hole energy, $\mathcal{H}_{c,ls}$ for the core hole spin-orbit splitting, and $\mathcal{H}_{c,3d}$ for the core-valence Coulomb and exchange interactions. We consider the effects of terms in this Hamiltonian in reverse order.

$$\mathcal{H} = \mathcal{H}_{ls} + \mathcal{H}_{mu} + \mathcal{H}_{c,3d} + \mathcal{H}_{3d} + \mathcal{H}_c + \mathcal{H}_{c,ls} \quad (3)$$

Core Hole Spin-Orbit Splitting. L-edges are split into L₃ and L₂ regions by the spin-orbit interaction of the 2p⁵ core hole - $\mathcal{H}_{c,ls}$, which grows stronger with increasing atomic number. Since this splitting is essentially an atomic property, there is probably little chemical information here compared to other features in the spectrum.

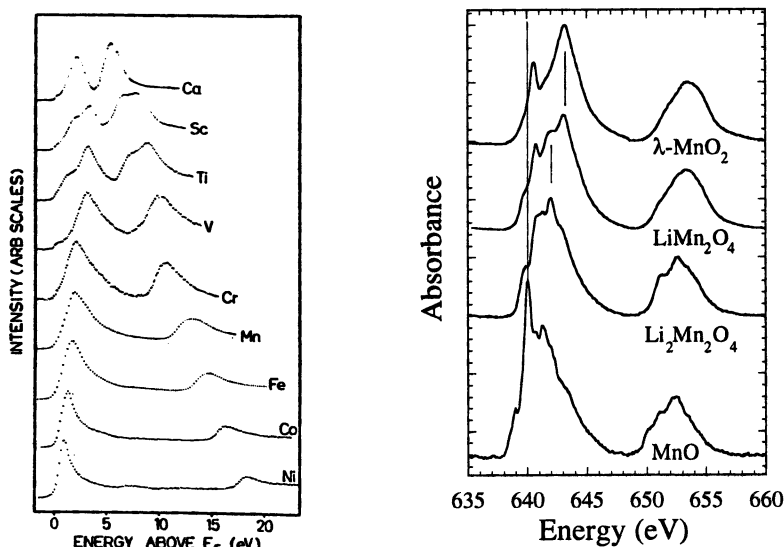


Figure 7. (Left) Changes in spin-orbit splitting in L-edges across the first transition metals. (Right) The shift in L₃ edge position with oxidation state for a series of Mn oxides. LiMn₂O₄ is mixed-valence and shows features both Mn(III) and Mn(IV) features.

Chemical Shifts. The chemical shifts of photoelectron energies to higher energy with increasing oxidation state are often explained as a reduction in the screening of the nucleus by valence electrons - hence an increase in the apparent nuclear charge. However, K-edge shifts are complicated by their dependence on interatomic distance [33], and K-edge shifts are too large to be explained as changes in core-level binding energies. In comparison, L-edge shifts are smaller, and some fraction is certainly due to changes in \mathcal{H}_c . Typical chemical shifts for Mn compounds in different oxidation states are illustrated in Figure 7.

Ligand Field Splittings. The influence of the crystal field \mathcal{H}_{3d} on L-edges is one of the most important reasons why these spectra are chemically useful. When the splitting of 3d orbital energies is large, its effect can be directly observed in L-edge spectra. For example, a ~ 4 eV splitting is seen in the L_3 edge of $K_3[Fe(CN)_6]$ (Figure 8). In many other cases \mathcal{H}_{3d} is of the same order as other terms in the Hamiltonian, such as \mathcal{H}_{mu} and $\mathcal{H}_{c,mu}$, and the complete Hamiltonian has to be considered. It can then be misleading to try to read orbital splittings directly from the spectra (Figure 9).

Another way ligand field splittings can affect the spectra is by changing the initial spin state of the complex. Thole and van der Laan have shown that the ratio of L_3 intensity to total intensity (L_3+L_2), the 'branching ratio', [30] changes with spin state. The so-called 'statistical' branching ratio is 4:(4+2) - the ratio of the number of electrons assigned to $2p_{3/2}$ and $2p_{1/2}$ levels respectively. For high spin complexes, there can be substantial deviations from this ratio of 2/3. For example, a typical branching ratio for high-spin Ni(II) complexes is ~ 0.77 [34], and even higher branching ratios are seen for high spin Fe [35] and Mn complexes [26]. In contrast, branching ratios for low spin Ni(II), Fe(II), and Mn(II) complexes are close to the statistical value.

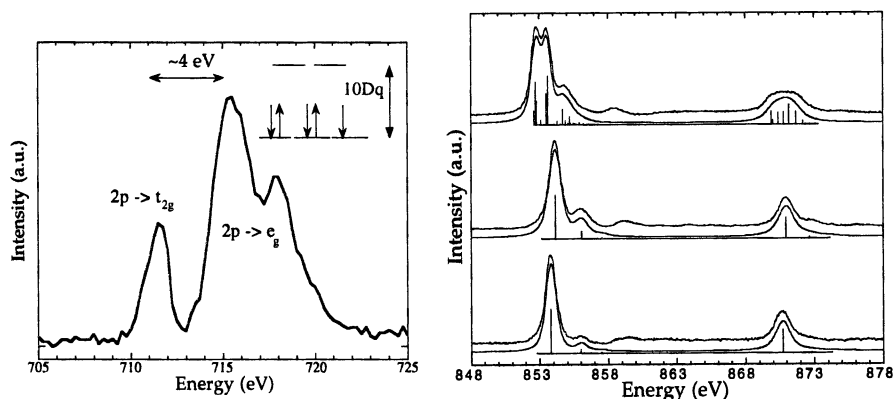


Figure 8. (Left) The L_3 edge for $K_3[Fe(CN)_6]$. (Right) The difference between low-spin and high-spin Ni(II) spectra, illustrated respectively by high spin $[Ni(cyclam)]Cl_2$, low-spin $Ni(salen)$, and low-spin $[Ni(cyclam)](ClO_4)_2$.

Coulomb and Exchange Interactions. For metal complexes with fewer than 9 d electrons, there will be final state vacancies in both the 2p and 3d shells, and the final state will show multiplet structure from 2p-3d interactions - $\mathcal{H}_{c,3d}$. For a $3d^N$ transition metal complex, the final state multiplets derive from $2p^5 3d^{N+1}$ configurations with different couplings between 2p and 3d electrons. The simplest case to consider involves complexes which are originally d^0 , such as K^+ and Ca^{2+} . Theoretical spectra for d^0 complexes have been calculated and explained in great detail by deGroot and coworkers [36]. They show that for isolated ions, the final state symmetry can be obtained as the product of the $2P$ p-hole symmetry and the $2D$ d-valence symmetry:

$$2P \otimes 2D = {}^1P_1 + {}^1D_2 + {}^1P_3 + {}^3P_{0,1,2} + {}^3D_{0,1,2} + {}^3F_{2,3,4} \quad (4)$$

In an octahedral ligand field, the spherical SO_3 atomic symmetries are projected to cubic O_h symmetry. The symmetry of the dipole matrix element:

$$\langle 3d^0 | r | 2p^5 3d^1 \rangle \quad (5)$$

is the product of the symmetries of the initial state (A_1), the dipole operator (T_1) and the final state symmetry, which must also be T_1 for an allowed transition. From the $SO_3 \rightarrow O_h$ branching rules [27, 31], it turns out there are 7 different allowed final states of T_1 symmetry. The relative energies and intensities of the transitions change dramatically with the strength of the crystal field (Figure 9).

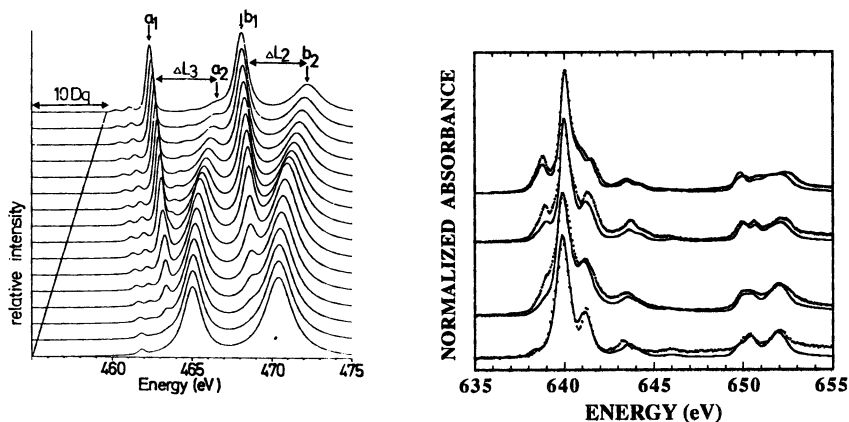


Figure 9. (Left) Calculated L-edges for Ti^{4+} vs. $10Dq$, from 0 (bottom) to 4.5 eV (top) [27, 36]. (Right) Experimental spectra (.....) and theoretical simulations (—) for a series of Mn complexes [26]. $10Dq$ increases from -0.3 eV to +1.05 eV from bottom to top.

Relatively simple spectra are also obtained for low spin Ni(II), where the final state now has a single d hole instead of a single d electron. For other cases, the spectra rapidly become too complex for simple explanation - for a $2p^5d^5$ final state there are 1536 final states! This complexity can nevertheless be handled by the ligand-field multiplet software. Calculations for all of the common transition metals have been published both without [37] and with inclusion of 3d spin-orbit coupling [38].

For completeness, we must mention one last term - \mathcal{H}_{1s} - the 3d spin-orbit coupling. As noted by deGroot [27], this term can be important for the ground state of certain ions with partially filled t_{2g} orbitals, such as $3d^1$, $3d^2$, low-spin $3d^4$, low-spin $3d^5$, high-spin $3d^6$, and high-spin $3d^7$ configurations. Significant changes in the spectrum can occur because of \mathcal{H}_{1s} , as shown in Figure 10.

Covalency Effects. The description of L-edge transitions presented so far works well for ionic complexes such as low oxidation state transition metal oxides, fluorides and chlorides. For more covalent compounds, such as higher formal oxidation states or transition metal sulfides, the single configuration model starts to break down.

Experimentally, the multiplet splittings become less pronounced (and less useful), and one is forced to use integrated quantities such as the centroid position and branching ratio.

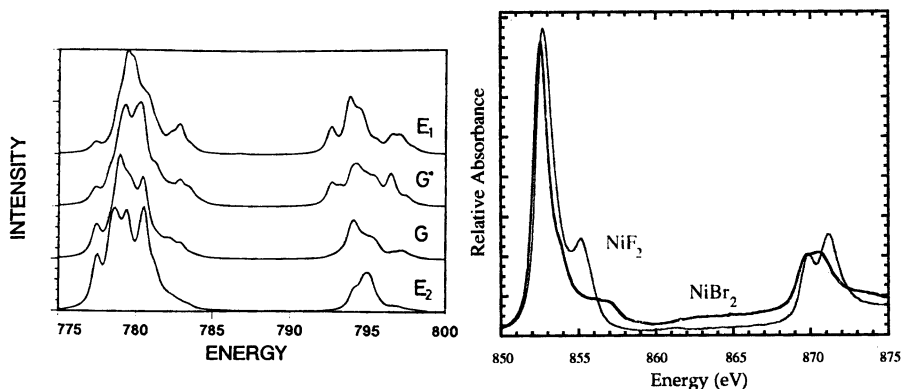


Figure 10. (Left) The effects of 3d spin-orbit coupling on L-edge spectra of cobalt complexes (Right) The loss of multiplet structure in NiBr₂ compared to NiF₂.

Covalency can be accommodated in the ligand field multiplet model empirically by reducing the values of the Slater integrals that produce the multiplet terms. A more rigorous procedure is to include configuration interaction in the initial and final state wave functions. The ground state is written as:

$$\Phi_i = \sin \alpha [3d^N] + \cos \alpha [3d^{N+1} \underline{L}] \quad (6)$$

while the final state is written as:

$$\Phi_f = \sin \beta [2p^5 3d^{N+1}] + \cos \beta [2p^5 3d^{N+2} \underline{L}] \quad (7)$$

If there is a change in the covalency between the initial and final states, then ‘satellite’ transitions can occur. The relative intensity of the main peak is given by $\cos^2(\beta-\alpha)$ and the satellite intensity is $\sin^2(\beta-\alpha)$ [39]. Satellite features can be seen at about 857-8 eV in following Ni enzyme spectra.

Application to Ni Proteins. NiFe hydrogenases catalyze the oxidation and formation of molecular hydrogen and contain a single Ni site as well as several different Fe-S clusters [40]. The NiFe hydrogenase from *D. gigas* is an $\alpha\beta$ heterodimer containing two Fe₄S₄ clusters, an Fe₃S₄ cluster, and a NiFe center. Crystallographic data on the *D. gigas* enzyme reveals a 5-coordinate Ni site, bridged through sulfur ligands to an unusual Fe species [41] now known to have one CO and two CN⁻ ligands. There has been considerable debate about whether the EPR signals from hydrogenase represent Ni(I) or Ni(III) [40], and the redox states of the EPR-silent species are also disputed. L-edge spectroscopy can provide complementary information to magnetic resonance, K-edge, infrared, and crystallographic studies of the enzyme.

We have looked at hydrogenase samples from a number of species, including *Pyrococcus furiosus* [42], *Desulfovibrio baculatus*, and *Desulfovibrio desulfuricans* (Figure 11). Although the multiplet structure is suppressed by the covalency of the Ni site, the features of the as-isolated enzyme spectra are best simulated using high spin Ni(II). Previous magnetic susceptibility data had identified the site as diamagnetic [43], and there is always the possibility that the Ni spin state changes under L-edge experimental conditions. We are currently using FT-IR to investigate the characteristic CO and CN stretching frequencies of the NiFe site in partially dried films. The films yield beautiful IR spectra, and the preliminary results show that redox changes seen in frozen solution spectra also appear in the films.

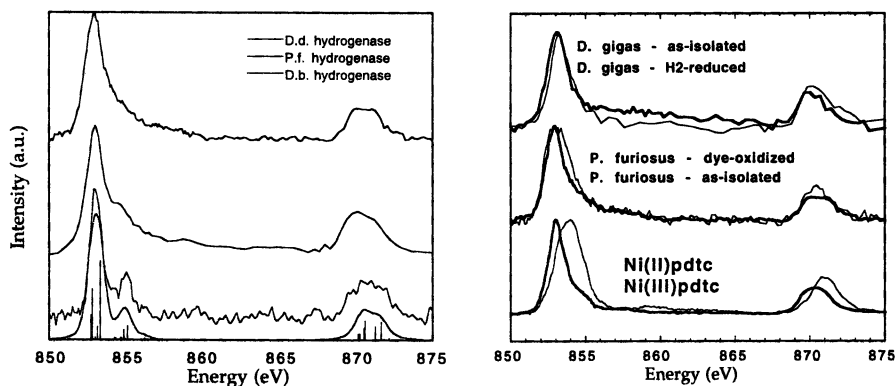


Figure 11. (Left) Ni L-edge spectra for (top to bottom) *P. furiosus* [42], *D. desulfuricans* and *D. baculatus*, as purified, and a high-spin Ni(II) simulation. (Right) Redox shifts in L-edges - (Top to bottom) *D. gigas* as-isolated vs. H₂-reduced, *P. furiosus* oxidized vs. reduced, and [Ni(II)(pdtc)₂]²⁻ vs. [Ni(III)(pdtc)₂]⁻ [42].

L-edge spectroscopy can be used to detect redox activity at the Ni site which is invisible by EPR. For example, the *P. furiosus* enzyme does not show any Ni EPR signals as isolated in the presence of dithionite, nor when oxidized by thionine at 80 C. Nevertheless, the latter sample has a broader L₃ edge and a sharper and more intense L₂ edge. The trend is similar to that seen in the oxidation of the relatively covalent complex [Ni(II)(pyridine-2,6-dithiocarboxylate)₂]²⁻ to the monoanion [42]. In the related system Li_xNi_{1-x}O₂, these kinds of changes have been interpreted as the mixing of low spin character into the d⁸ part of a d⁸L (ligand hole) ground state. Although the terminology is very different, this is similar to proposals that posit significant charge delocalization in the electronic structure of hydrogenase.

Because there is little structure to the hydrogenase Ni L-edges, we have sought other ways to classify the Ni sites. One approach is to look at the correlation between the L₃ centroid energy and the branching ratio (Figure 12). Most Ni model complexes cluster in discrete regions of such a diagram. We found that H₂- or dithionite-reduced hydrogenases resemble high-spin Ni(II), while CO dehydrogenase has more low-spin Ni(II) character [44]. Oxidized samples of both enzymes resemble covalent Ni(III) species. We have also seen evidence for a Ni(I) component under certain conditions.

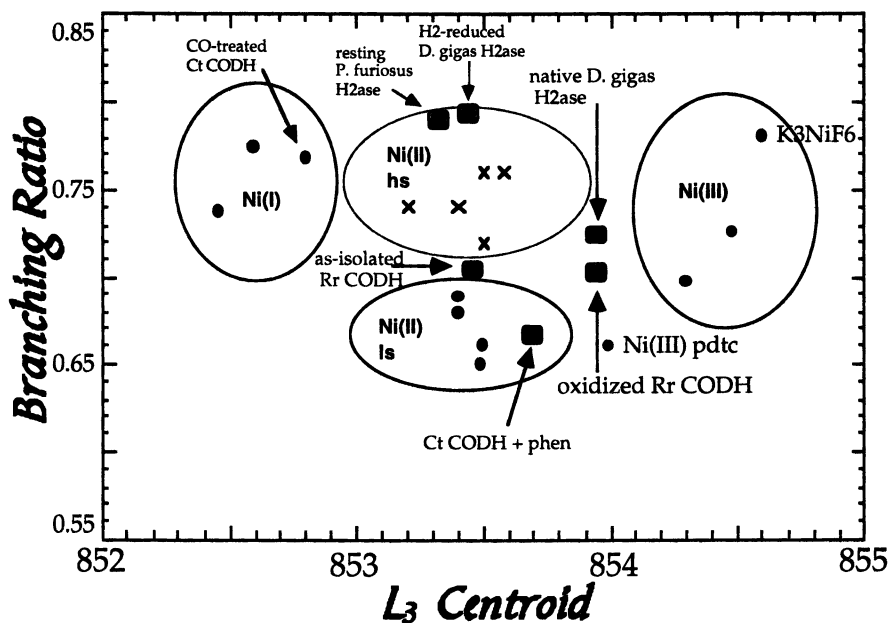


Figure 12. Centroid position and branching ratio for different Ni compounds.

"Is there any point to which you wish to draw my attention?
 'To the curious incident of the dog in the night-time.'
 'The dog did nothing in the night-time.'
 'That was the curious incident.'
 Sherlock Holmes [45]

Integrated Cross Section Sum Rule. Just as the detective inferred a crime from the absence of an event, we can deduce the distribution of electrons in a compound by measuring the presence of 'holes'. The total cross section sum rule for L-edges says that that the intensity integrated over the L_3 and L_2 'white lines' is proportional to the number of empty states. Since the cross sections for $2p \rightarrow 3d$ transitions are 25 times larger than the $2p \rightarrow 4s$ cross section [16], one is primarily sensitive to the 3d character of these states. One can therefore measure the metal 3d vacancies by integrating the L-edges.

In practice, absolute cross sections are difficult to measure. This problem is overcome by normalizing the integrated intensity to a region high above the continuum (Figure 13). With the assumption that the continuum cross section is chemically invariant, the normalized spectra can be calibrated by reference to standard compounds with known electronic structure.

Application to Cu Proteins. Blue copper proteins such as plastocyanin are critical for electron transfer in many living systems, and their electronic structure has been studied for decades [46]. Plastocyanin is thus an ideal system for testing different kinds of sum

rule analysis, because its electronic structure is well understood from a variety of approaches [46, 47]. The integrated L-edge intensity for plastocyanin was compared with values for $[\text{CuCl}_4]^{2-}$ complexes [48], where the electronic structure is well-known. The results are consistent with previous work showing that the half-occupied HOMO is highly covalent with only $\sim 42\%$ Cu $d_{x^2-y^2}$ character (Figure 14).

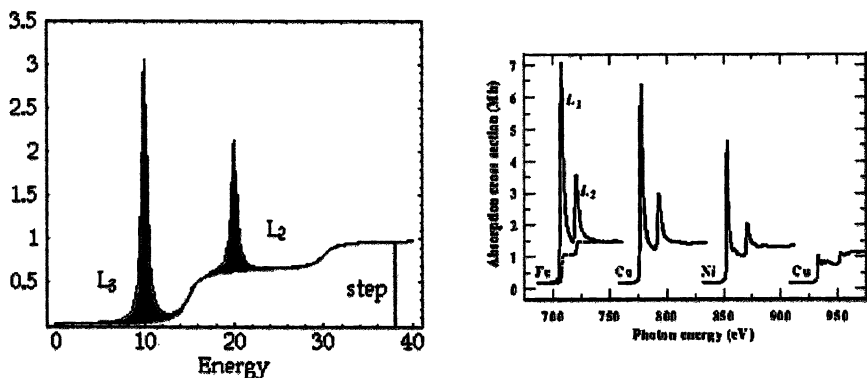


Figure 13. (Left) Schematic illustration of the normalization process. (Right) Normalized L absorption edges for Fe, Co, Ni, and Cu [49].

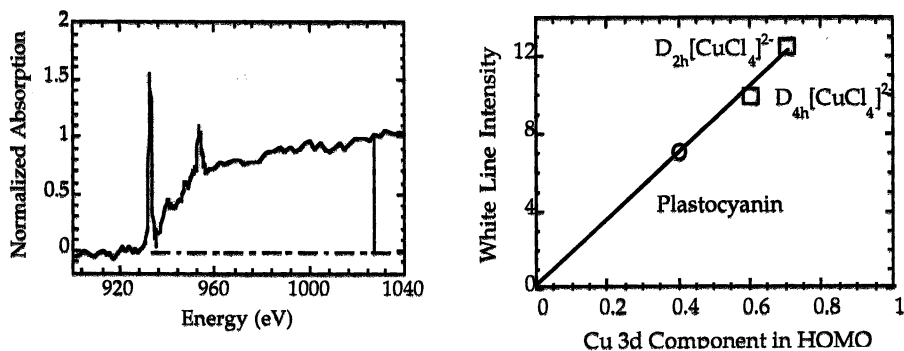


Figure 14. (Left) Representative L-edge spectra for Cu plastocyanin. (Right) Calibration of the Cu white line intensity with respect to $[\text{CuCl}_4]^{2-}$ [48].

X-Ray Magnetic Circular Dichroism

X-ray magnetic circular dichroism (XMCD) measurements involve comparing the absorption of left- and right-circularly polarized light by a magnetized sample [50]. XMCD was first observed with hard x-rays in 1987 [51] and with soft x-rays in 1990 [52]. Since then, XMCD has been used to investigate magnetic thin films [53, 54], magnetic alloys [55], and even to image domains on computer disks [56] (Figure 15). Most studies to date have involved ferro- or ferrimagnets, which are easily magnetized

near room temperature. Experiments on dilute paramagnetic samples require high fields, low temperatures, and fluorescence detection; this was first accomplished for metal centers in proteins using the Fe in rubredoxin [31].

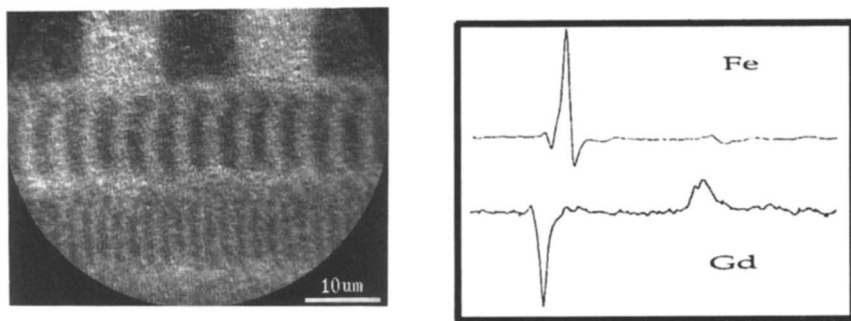


Figure 15. (Left) Photoelectron microscope image of a computer disc test pattern taken by Stöhr and coworkers, with circularly polarized x-rays [56]. The light and dark regions correspond to magnetic domains polarized in different direction. (Right) The Fe L-edge and Gd M-edge XMCD spectra of $\text{Fe}_3\text{Gd}_3\text{O}_{12}$ reported by Chen *et al.* [55]. The opposite signs show that the Gd and Fe sublattices are antiferromagnetically coupled.

The XMCD effect at $3d$ transition metal $L_{2,3}$ edges derives from non-uniform occupation of a Zeeman split initial state, combined with angular momentum rules that determine the intensity of transitions to various final states. Although many transition metal complexes show strong XMCD, the effect is easiest to explain for atomic transitions. For a transition of an atom or ion with angular momentum quantum numbers J and M_J to a new state with quantum numbers J' and $M_{J'}$, one can use the Wigner-Eckart theorem to separate the matrix element into radial and angular parts [32]:

$$\langle \phi(J M_J) | r_q | \phi(J' M_{J'}) \rangle = (-1)^{J-M_J} \begin{pmatrix} J & 1 & J' \\ -M_J & q & M_{J'} \end{pmatrix} \langle \phi(J) | r_q | \phi(J') \rangle \quad (8)$$

The term in large parentheses is the so-called $3j$ symbol. For this term to be nonzero, it is necessary that $q = M_{J'} - M_J$. If we call 'left circularly polarized' x-rays $q=1$, then the ground state can only have transitions to $M_{J'} = M_J + 1$ with left circular polarization or $M_{J'} = M_J - 1$ with right circular polarization. We remind the reader that there is considerable dyslexia in the definition of left and right circular polarization; our convention is that described by Atkins [57], in which the electric field vector moves like a right handed screw.

A more intuitive explanation for the XMCD effect is illustrated in Figure 16. Here it can be seen that the magnetic moment of the sample is oriented by the applied field. This field also dictates the orientation of the Cu^{2+} spin, hence of the spin of the single hole in the d-shell. Since the electron spin does not change during the electric dipole transition, the spin-orientation of the 2p hole is governed by the original 3d hole orientation. The strong spin-orbit coupling in the 2p shell then dictates the required orbital angular momentum for the 2p hole. Only a $q=1$ left circularly polarized photon

can accomplish the required increase in orbital angular momentum. The important point is that the XMCD effect comes out of conservation of angular momentum.

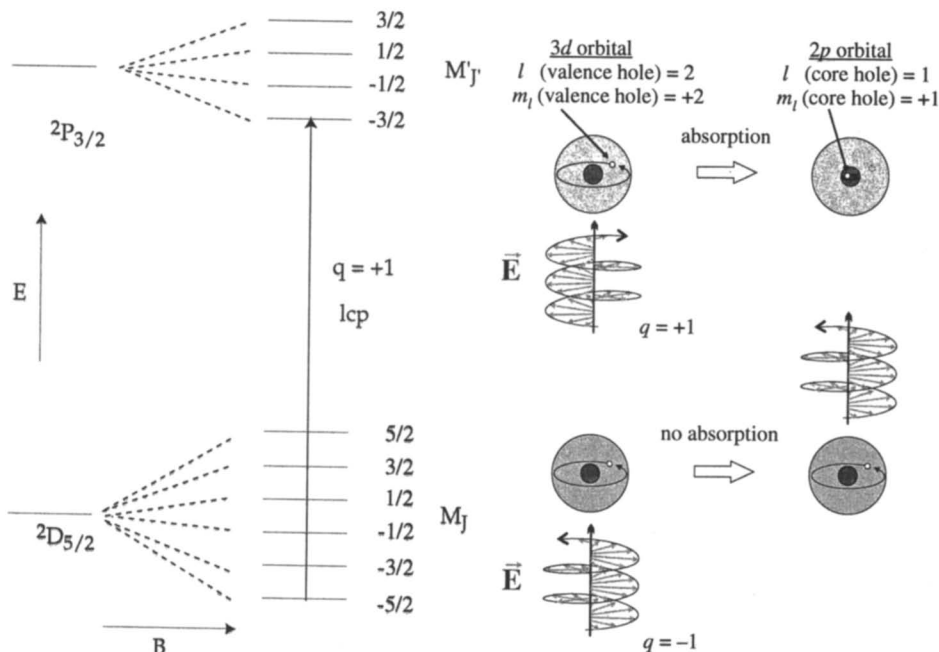


Figure 16. Schematic illustration of the XMCD effect for atomic Cu^{2+} . (Left) The energy levels in a magnetic field, and the allowed transition at 0 K. (Right) An atom interacting with electric field vector of circularly polarized photons [49].

In a ligand field, J is no longer a good quantum number, and the ground state is a mixture of J , M_J wavefunctions. Nevertheless, an XMCD effect is often preserved [58]. The sign of the XMCD effect reveals the local magnetic moment orientation, while the intensities and relative weights can be used to derive spin and orbital moments. Ligand field multiplet programs which calculate L-edges can also simulate metal complex XMCD spectra [59].

Experimental Considerations. The technology for soft x-ray MCD in the transition metal L-edge region differs substantially from UV-visible instrumentation. There are no good quarter wave plate polarizers in this region. Most of the instrument has to be under high vacuum. Transmission experiments are impractical for most metalloproteins. One saving grace is that soft x-ray MCD effects can be quite strong.

Sources of Circular Polarization. One of the simplest ways to obtain circularly polarized synchrotron radiation is to collect the out-of-plane x-rays from bend magnets [60]. As shown in Figure 17, the degree of circular polarization increases rapidly with a small angular excursion from the bending plane, and opposite degrees of

polarization are obtained above and below this plane. However, bend magnet sources are relatively weak, and it is difficult to change from left to right circular polarization without some slight affect on the photon beam energy, spot size or degree of polarization.

A number of insertion device designs provide brighter and more flexible sources of circular polarization, as reviewed by Elleaume [61]. These devices include elliptical wigglers, asymmetric wigglers, crossed undulators, and elliptical undulators. A 75 pole elliptically polarizing undulator is under construction at the Advanced Light Source, and a good fraction of the beamtime will be available for bioinorganic applications.

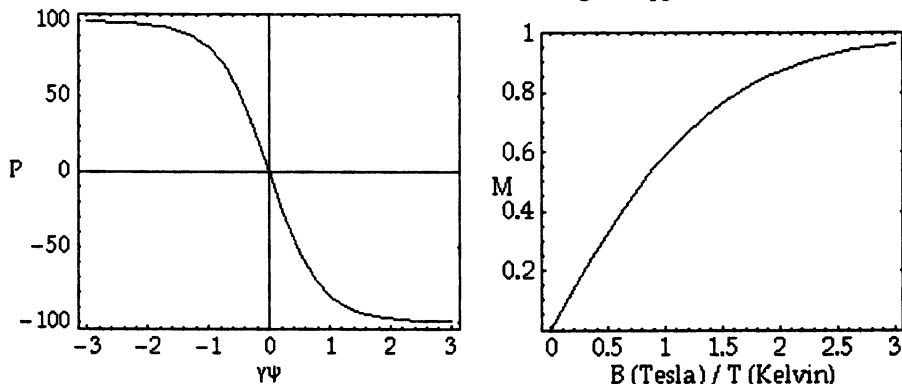


Figure 17. (Left) The degree of circular polarization at 854 eV as a function of off-axis angle ϕ (in radians) from an SSRL bend magnet. γ is the ratio of the electron energy (3 GeV) to its rest mass energy (0.511MeV). At $\phi\psi=1$ the angle is approximately 0.01 degrees. (Right) Magnetization curve for a spin 1/2 system.

Field and Temperature. In conventional MCD terminology, XMCD is primarily a ‘C term’ effect (arising from Zeeman splitting of the ground state) which should have a strong temperature dependence. For a spin 1/2 system, the dependence of the magnetization M on field H and temperature T is given by the Brillouin function [62]:

$$\frac{M}{M_0} = \tanh\left(\frac{g J \mu_B H}{kT}\right) \quad (9)$$

where μ_B is the Bohr magneton and k is Boltzmann’s constant. What this means in practice is that for ~90% magnetization of dilute paramagnetic systems, a $B(\text{Tesla})/T(\text{Kelvin})$ ratio of ~2 is needed (Figure 18). Our approach has been to use a superconducting split-coil magnet system to provide a magnetic field up to 2 Tesla and a dilution refrigerator to keep the sample below 0.5 K (Figure 18).

What Makes X-Ray MCD Useful for Bioinorganic Problems?. X-ray MCD can provide information that is difficult or impossible to obtain by other techniques. The information content and strengths include (1) elemental selectivity - one can examine one particular element at a time, (2) oxidation state selectivity - it is often possible to resolve the XMCD contributions from different chemical species, (3) direct spin orientations - the sign of the XMCD signal can be used to infer the orientation of a particular magnetic

moment, (4) magnetization curves - the B and T dependence of the XMCD can be used to infer spin states, and (5) sum rules - the integrated XMCD signal can be used to deduce the metal-centered orbital and spin moments.

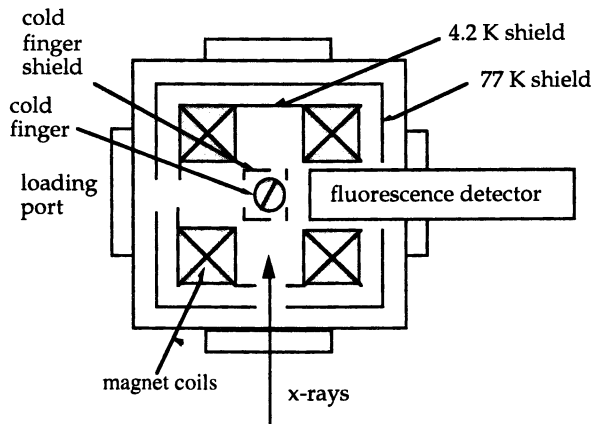


Figure 18. The components of a soft-ray MCD instrument for bioinorganic experiments.

L and S Sum Rules. For 3d transition metal L-edges, the orbital and spin sum rules relate integrated XMCD intensities to element specific projections of the 3d orbital angular momentum $\langle L_z \rangle$, the 3d spin angular momentum $\langle S_z \rangle$ and a magnetic dipole term $\langle T_z \rangle$, as summarized in Equations (10) and (11) respectively. Stöhr and König have shown that the $\langle T_z \rangle$ term averages to zero in 'powder' samples, so this term has been omitted from our equations.

$$\frac{\langle L_z \rangle}{n_h} = \frac{4 \int_{L_2+L_3} [A^+(\omega) - A^-(\omega)] d\omega}{3 \int_{L_2+L_3} [A^+(\omega) + A^-(\omega)] d\omega} = \frac{2(A+B)}{3C} \quad (10)$$

$$\frac{\langle S_z \rangle}{n_h} = \frac{\left(\int_{L_3} [A^+(\omega) - A^-(\omega)] d\omega - 2 \int_{L_2} [A^+(\omega) - A^-(\omega)] d\omega \right)}{\int_{L_2+L_3} [A^+(\omega) + A^-(\omega)] d\omega} = \frac{(A-2B)}{2C} \quad (11)$$

Here n_h represents the number of 3d vacancies in the metal ion and ω is the x-ray frequency. It is common in the XMCD literature to refer to the first integral in the numerator of (10) as 'A', the second integral as 'B', and the average integrated intensity as C. (Figure 19).

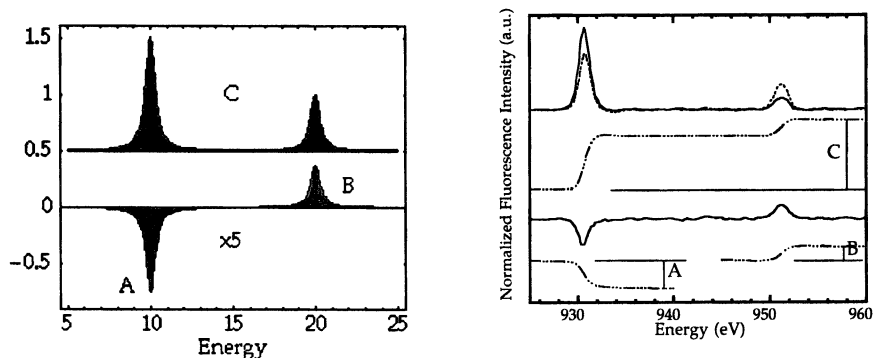


Figure 19. (Left) The integrated quantities important for sum rule analysis. (Right) XMCD spectrum for Cu(II) plastocyanin, along with integrations for sum rule analysis.

Application to Cu Plastocyanin. The XMCD of Cu in oxidized plastocyanin has been used as a test case for sum rule analysis of metalloproteins. After normalizing the overall Cu L-edge jump between 920 and 1050 eV to unity, average numerical values for $A = -3.08 \pm 0.3$, $B = 1.35 \pm 0.2$ and $C = 7.27 \pm 0.3$ were obtained, where the errors refer to the degree of experimental reproducibility. From equation (10), $\langle L_Z \rangle$ is found to be 0.07 ± 0.02 /Cu atom, while from equation (11) we derive 0.18 ± 0.02 /Cu atom for $\langle S_Z \rangle$, all in units of $\hbar/2\pi$. The orbital momentum compares favorably with values using covalent wavefunctions from a converged SCF-X α -SW calculation, which yield a Cu 3d specific, orientation averaged $\langle L_Z \rangle$ value of 0.059 /Cu atom. The SCF-X-SW calculated $\langle S_Z \rangle$ is 0.21 is also not far from the sum rule values of $\langle S_Z \rangle$. XMCD appears to have promise for providing detailed information about electronic structure that is difficult to obtain by other methods.

Prospects for the Future

“... revolution as we know it in the modern age has always been concerned with both liberation and freedom.” Hannah Arendt[3]

The revolution in synchrotron radiation sources has opened the entire realm of x-ray spectroscopy for bioinorganic chemistry. This rapid improvement in technology shows no sign of abating. Plans are already being made for a still brighter fourth generation of synchrotron radiation sources [63], based on ‘free electron lasers’ [64]. Cryogenic detectors with exquisite energy resolution are being developed [65]; these devices will eventually allow much more dilute samples to be examined. New capillary x-ray optics [66], x-ray lenses, and x-ray quarter wave plates [67] will enhance our ability to collect and control high energy photons. With more photons and better detectors, other experiments including x-ray Raman [68] and resonance Raman [69] spectroscopy, x-ray emission dichroism [70, 71], and site-selective EXAFS [72] will become feasible on bioinorganic samples.

Over the past two decades, EXAFS spectroscopy has become a routine tool for structure determination. But although this application is more than 20 years old, in many respects we are just beginning to exploit the potential of x-rays for bioinorganic studies. As more and more molecular structures are conquered by the crystallographers, questions remain that cannot be answered by EXAFS or diffraction. When chemists ask in detail - where are the electrons, where are the spins, and how are they coupled - these are questions that can be addressed by x-ray spectroscopy. The number of photons available is no longer the main issue; we are only limited by our own ingenuity.

Acknowledgements

We thank C. T. Chen, F. Sette, G. Sawatzky, S. George, J. van Elp, and F. deGroot for nurturing the early development of bioinorganic soft x-ray spectroscopy. The staffs of the ALS, NSLS, and SSRL also helped make this work possible. This research was supported by the National Institutes of Health (GM-44380), the National Science Foundation (BIR-9317942 and BIR-9105323), and by the Department of Energy, Office of Biological and Environmental Research. The Stanford Synchrotron Radiation Laboratory is supported by the Department of Energy, Office of Basic Energy Sciences. SPC would also like to acknowledge the memory of Prof. John Fuggle, who helped introduce him to this field.

References Cited

- [1.] Agarwal, B. K. (1991) X-ray Spectroscopy : An Introduction, Springer-Verlag, New York.
- [2.] Koningsberger, D. C., Prins, R. and eds. (1988) X-ray Absorption : Principles, Applications, Techniques of EXAFS, SEXAFS, and XANES, Wiley, New York.
- [3.] Arendt, H. (1963) On Revolution, Viking Press, New York.
- [4.] Margaritondo, G. (1988) Introduction to Synchrotron Radiation, Oxford University Press, New York.
- [5.] Schlacter, A. S. (1994) in New Directions in Research with Third-Generation Soft X-Ray Synchrotron Light Sources (Schlacter, A. S. and Wuilleumier, F. J., eds.), pp. 1-22, Kluwer Academic Publishers, Dordrecht.
- [6.] Hellemans, A. (1997) in Physics Today, vol. 277, pp. 1214-1215.
- [7.] "Ultrabright synchrotron source ELETTRA: First period of operation", Margaritondo, G., Savoia, A., Bernstoff, S., Bertolo, M., Comelli, G., DeBona, F., Jark, W., Kiskinova, M., Paolucci, G., Prince, K., Santaniello, A., Tromba, G., Walker, R. and Rosei, R., *Acta Physica Polonica A*, **91**, 631-640 (1997).
- [8.] Carroll, L. (1872) Through the Looking Glass.
- [9.] "Efficient, high-brightness soft-x-ray laser at 21.2 nm", Rus, B., Carillon, A., Dhez, P., Jaegle, P., Jamelot, G., Klisnick, A., Nantel, M. and Zeitoun, P., *Phys. Rev. A*, **55**, 3858-3873 (1997).
- [10.] "Performance of the Dragon Soft X-Ray Beamline", Chen, C. T. and Sette, F., *Rev. Sci. Inst.*, **60**, 1616-1621 (1989).

- [11.] "A General Purpose Sub-Kev X-Ray Facility at the Stanford-Synchrotron-Radiation-Laboratory", Tirsell, K. G. and Karpenko, V. P., *Nucl. Inst. Meth. A*, **291**, 511-517 (1990).
- [12.] "On Experimental Attenuation Factors of the Amplitude of EXAFS Oscillations in Absorption, Reflectivity, and Luminescence Measurements", Goulon, J., Goulon-Ginet, C., Cortes, R. and Dubois, J. M., *Journal de Physique*, **43**, 539-548 (1982).
- [13.] "Probing Depth of Soft X-Ray Absorption Spectroscopy Measured in Total-Electron-Yield Mode", Abbate, M., Goedkoop, J. B., deGroot, F. M. F., Grioni, M., Fuggle, J. C., Hofmann, S., Petersen, H. and Sacchi, M., *Surface and Interface Analysis*, **18**, 65-69 (1992).
- [14.] "Soft X-Ray Spectroscopy of Metalloproteins Using Fluorescence Detection", Cramer, S. P., Chen, J., George, S. J., van Elp, J., Moore, J., Tench, O., Colaresi, J., Yocum, M., Mullins, O. C. and Chen, C. T., *Nucl. Inst. Meth. A*, **319**, 285-289 (1992).
- [15.] Jaclevic, J., Kirby, J. A., Klein, M. P., Robertson, A. S., Brown, G. S. and Eisenberger, P., *Sol. State Comm.*, **23**, 679 (1977).
- [16.] Stern, E. A. and Heald, S. M. (1983) in Handbook on Synchrotron Radiation, vol. 1B (Koch, E., ed.), pp. 955-1014, North Holland, Amsterdam.
- [17.] "Fluorescence Yield Detection - Why It Does Not Measure the X-Ray Absorption Cross Section", deGroot, F. M. F., Arrio, M.-A., Sainctavit, P., Cartier, C. and Chen, C. T., *Sol. State Comm.*, **92**, 991-995 (1994).
- [18.] "Distortions of X-Ray absorption spectra measured with fluorescence yield", deGroot, F. M. F., Arrio, M.-A., Sainctavit, P., C., C. and Chen, C. T., *Physica B*, **208-209**, 84-86 (1995).
- [19.] "Experimental and Theoretical Comparison Between Absorption, Total Electron Yield, and Fluorescence Spectra of Rare-earth M-5 Edges", Pompa, M., Flank, A. M., Lagarde, P., Rife, J. C., Stekhin, I., Nakazawa, M., Ogasawara, H. and Kotani, A., *Phys. Rev. B*, **56**, 2267-2272 (1997).
- [20.] "Theory of Fluorescence Yield Spectra of Rare Earth Oxides at 3d Threshold Region", Nakazawa, M., Ogasawara, H., Kotani, A. and Lagarde, P., *J. Phys. Soc. Jap.*, in press (1997).
- [21.] "Polarized X-Ray Fluorescence as a Probe of Ground State Properties", van Veenendaal, M., M. Goedkoop, J. B. and Thole, B. T., *Phys. Rev. Lett.*, **77**, 1508-1511 (1996).
- [22.] "On Radiation Damage to Normal Tissues and Its Treatment .1. Growth Factors.", Michalowski, A., *Acta Oncologica*, **29**, 1017-1023 (1990).
- [23.] "DNA Damage and Repair Following Treatment with Ionizing Radiation", Powell, S. and Mcmillan, T. J., *Radiotherapy and Oncology*, **19**, 95-108 (1990).
- [24.] "Natural Widths of Atomic K and L Levels, $K\alpha$ X-Ray Lines and Several KLL Auger Lines", Krause, M. O. and Oliver, J. H., *J. Chem. Phys. Ref. Data*, **8**, 329-337 (1979).
- [25.] "Manganese L-Edge X-Ray Absorption Spectroscopy of *Lactobacillus plantarum* Catalase and Mixed Valence Manganese Complexes", Grush, M. M., Chen, J., Stemmler, T. L., George, S. J., Penner-Hahn, J. E., Christou, G. and Cramer, S. P., *J. Am. Chem. Soc.*, **118**, 65-69 (1996).
- [26.] "Ligand Field Strengths and Oxidation States from Manganese L-Edge Spectroscopy", Cramer, S. P., Degroot, F. M. F., Ma, Y., Chen, C. T., Sette, F., Kipke,

- C. A., Eichhorn, D. M., Chan, M. K., Armstrong, W. H., Libby, E., Christou, G., Brooker, S., Mckee, V., Mullins, O. C. and Fuggle, J. C., *J. Am. Chem. Soc.*, **113**, 7937-7940 (1991).
- [27.] "X-Ray Absorption and Dichroism of Transition Metals and their Compounds", deGroot, F. M. F., *J. Electron Spec. Rel. Phen.*, **67**, 529-622 (1994).
- [28.] "Calculation of Multiplet Structure of Core p-vacancy Levels. II", Gupta, R. P. and Sen, S. K., *Phys. Rev. B*, **12**, 15-19 (1975).
- [29.] Asada, S., Satako, C. and Sugano, S., *J. Phys. Soc. Jap.*, **37**, 855 (1975).
- [30.] Thole, B. T., van der Laan, G. and Butler, P. H., *Chem. Phys. Lett.*, **149**, 295 (1988).
- [31.] Butler, P. H. (1981) Point Group Symmetry Applications, Methods and Tables, Plenum, New York.
- [32.] Cowan, R. D. (1981) The Theory of Atomic Structure and Spectra, University of California Press, Berkeley.
- [33.] "Bond Distance Determination From X-Ray Absorption Near Edge Structure", Mahto, P. and Chetal, A. R., *Physica B*, **158**, 415-416 (1989).
- [34.] "Bioinorganic Applications of X-ray Multiplets - The Impact of Theo Thole's Work", Cramer, S. P., Ralston, C. Y., Wang, H. X. and Bryant, C., *J. Electron Spec. Rel. Phen.*, **86**, 175-183 (1997).
- [35.] "Iron L-edge X-ray absorption Spectroscopy of Myoglobin Complexes and Photolysis Products", Wang, H. X., Peng, G., Miller, L. M., Scheuring, E. M., George, S. J., Chance, M. R. and Cramer, S. P., *J. Am. Chem. Soc.*, **119**, 4921-4928 (1997).
- [36.] " $L_{2,3}$ X-Ray Absorption Edges of d^0 Compounds - K^+ , Ca^{2+} , Sc^{3+} and Ti^{4+} in O_h (Octahedral) Symmetry", deGroot, F. M. F., Fuggle, J. C., Thole, B. T. and Sawatzky, G. A., *Phys. Rev. B*, **41**, 928-937 (1990).
- [37.] "2p X-Ray Absorption of 3d Transition Metal Compounds - An Atomic Multiplet Description Including the Crystal Field", deGroot, F. M. F., Fuggle, J. C., Thole, B. T. and Sawatzky, G. A., *Phys. Rev. B*, **42**, 5459-5468 (1990).
- [38.] "The 2p Absorption Spectra of 3d Transition Metal Compounds in Tetrahedral and Octahedral Symmetry", van der Laan, G. and Kirkman, I. W., *J. Phys. - Condensed Matter*, **4**, 4189-4204 (1992).
- [39.] "Complementary Roles of Co 2p X-Ray Absorption and Photoemission Spectra in CoO", Okada, K. and Kotani, A., *J. Phys. Soc. Jap.*, **61**, 449-453 (1992).
- [40.] "Nickel Hydrogenases - In Search of the Active Site", Albracht, S. P. J., *Biochim. Biophys. Acta*, **1188**, 167-204 (1994).
- [41.] "Crystal Structure of the Nickel-Iron Hydrogenase from *Desulfovibrio gigas*", Volbeda, A., H., C. M., Piras, C., C., H. E. and et al., *Nature*, **373**, 580-587 (1995).
- [42.] "Nickel L-Edge X-ray Absorption Spectroscopy of *Pyrococcus furiosus* Hydrogenase", van Elp, J., Peng, G., Zhou, Z. H., Adams, M. W. W., Baidya, N., Mascharak, P. K. and Cramer, S. P., *Inorg. Chem.*, **34**, 2501-2504 (1995).
- [43.] "The Nickel Site in Active *Desulfovibrio baculatus* [NiFeSe] Hydrogenase is Diamagnetic - Multifield Saturation Magnetization Measurement of the Spin State of Ni(II)", Wang, C. P., Franco, R., Moura, J. J. G., Moura, I. and et al., *J. Biol. Chem.*, **267**, 7378-7380 (1992).
- [44.] Ralston, C. Y. (1997) , Ph. D. Thesis, University of California, Davis.

- [45.] Doyle, S. A. C. (1892) The Silver Blaze.
- [46.] "Electronic Structure of the Oxidized and Reduced Blue Copper Sites - Contributions to the Electron Transfer Pathway, Reduction Potential, and Geometry", Solomon, E. I., Penfield, K. W., Gewirth, A. A., Lowery, M. D., Shadle, S. E., Guckert, J. A. and Lacroix, L. B., *Inorg. Chim. Acta*, **243**, 67-78 (1996).
- [47.] "Structural and Functional Aspects of Metal Sites in Biology", Holm, R. H., Kennepohl, P. and Solomon, E. I., *Chem. Rev.*, **96**, 2239-2314 (1996).
- [48.] "Copper L-Edge Spectral Studies - A Direct Experimental Probe of the Ground-State Covalency in the Blue Copper Site in Plastocyanin", George, S. J., Lowery, M. D., Solomon, E. I. and Cramer, S. P., *J. Am. Chem. Soc.*, **115**, 2968-2969 (1993).
- [49.] Nakajima, R. (1997), Ph. D. Thesis, Stanford University.
- [50.] "X-ray Magnetic Circular Dichroism Spectroscopy of Transition Metal Thin Films", Stöhr, J., *J. Electron Spec. Rel. Phen.*, **75**, 253-272 (1995).
- [51.] "Absorption of Circularly Polarized X Rays in Iron", Schütz, G., Wagner, W., Wilhelm, W., Kienle, P., Zeller, R., Frahm, R. and Materlik, G., *Phys. Rev. Lett.*, **58**, 737 (1987).
- [52.] "Soft X-Ray Magnetic Circular Dichroism of the $L_{2,3}$ Edges of Nickel", Chen, C. T., Sette, F., Ma, Y.-J. and Modesti, S., *Phys. Rev. B*, **42**, 7262-7265 (1990).
- [53.] "Giant X-Ray Absorption Circular Dichroism In Magnetic Ultrathin Films Of Fe/Cu(001)", Tobin, J. G., Waddill, G. D. and Pappas, D. P., *Phys. Rev. Lett.*, **68**, 3642-3645 (1992).
- [54.] "Magnetic X-Ray Dichroism in the Spectroscopy of Ultrathin Magnetic Alloy Films", Tobin, J. G., Goodman, K. W., Mankey, G. J., Willis, R. F. and et al., *J. Vac. Sci. Tech. B*, **14**, 3171-3175 (1996).
- [55.] "Magnetic Moments in a Gadolinium Iron Garnet Studied by Soft-X-Ray Magnetic Circular Dichroism", Rudolf, P., Sette, F., Tjeng, L. H., Meigs, G. and Chen, C. T., *J. Mag. Mag. Mat.*, **109**, 109-112 (1992).
- [56.] "Element-Specific Magnetic Microscopy With Circularly Polarized X-Rays", Stöhr, J., Wu, Y., Hermsmeier, B. D., Samant, M. G., Harp, G. R., Koranda, S., Dunham, D. and Tonner, B. P., *Science*, **259**, 658-661 (1993).
- [57.] Atkins, P. W. (1974) *Quanta - A Handbook of Concepts*, Oxford University Press, Oxford.
- [58.] "Magnetic Dichroism in the X-Ray-Absorption Branching Ratio", van der Laan, G. and Thole, B. T., *Phys. Rev. B*, **42**, 6670-6674 (1990).
- [59.] "Strong Magnetic X-Ray Dichroism in 2p Absorption Spectra of 3d Transition-Metal Ions", van der Laan, G. and Thole, B. T., *Phys. Rev. B*, **43**, 13401-13411 (1991).
- [60.] "Double-Headed Dragon Monochromator for Soft X-Ray Circular Dichroism Studies", Chen, C. T., Sette, F. and Smith, N. V., *Applied Optics*, **29**, 4535-4536 (1990).
- [61.] "Insertion Devices For The New Generation Of Synchrotron Sources - A Review", Elleaume, P., *Rev. Sci. Inst.*, **63**, 321-326 (1992).
- [62.] Cullity, B. D. (1972) *Introduction to Magnetic Materials*, Addison-Wesley, Reading, Mass.
- [63.] "From the third to the fourth generation of synchrotron radiation light sources", Laclare, J. L., *Journal de Physique*, **7**, 39-46 (1997).
- [64.] "Free-Electron Laser Simulation Techniques", Tran, T. M. and Wurtele, J. S., *Phys. Reports*, **195**, 1-21 (1990).

- [65.] "High-resolution Superconducting X-ray Spectrometers with an Active Area of 282 μm x 282 μm ", Mears, C. A., Labov, S. E., Frank, M., Netel, H., Hiller, L. J., Lindeman, M. A., Chow, D. and Barfknecht, A. T., *IEEE Transactions on Applied Superconductivity*, **7**, 3415-3418 (1997).
- [66.] "The Use of X-Ray Capillary Optics for Lithography and Microscopy", Arkadiev, V. A., Gorny, H. E., Gruev, D. I., Karnaukhov, A. A., Kolomiitsev, A. I., Kumakhov, M. A., Langhoff, N., Shandintsev, D. V. and Wedell, R., *Optical and Quantum Electronics*, **28**, 309-314 (1996).
- [67.] "Perfect Crystal and Mosaic Crystal Quarter-Wave Plates for Circular Magnetic X-Ray Dichroism Experiment", Giles, C., Malgrange, C., Goulon, J., Debergevin, F., Vettier, C., Fontaine, A., Dartyge, E., Pizzini, S., Baudelet, F. and Freund, A., *Rev. Sci. Instr.*, **66**, 1549-1553 (1995).
- [68.] "X-ray Raman Spectra from Low-Z Elements", Udagawa, Y., Watanabe, N. and Hayashi, H., *Journal de Physique*, **7**, 347-352 (1997).
- [69.] "High Resolution X-Ray Resonant Raman Scattering", Carra, P., Fabrizio, M. and Thole, B. T., *Phys. Rev. Lett.*, **74**, 3700-3703 (1995).
- [70.] "Dichroism and Spin Information in Soft X-ray Emission", Eisebitt, S., Luning, J., Rubensson, J. E., Schmitz, D., Blugel, S. and Eberhardt, W., *Sol. State Comm.*, **104**, 173-177 (1997).
- [71.] "Theoretical Analysis of the Magnetic Circular Dichroism in the 2p3d and 2p4d x-ray emission of Gd", deGroot, F. M. F., Nakazawa, M., Kotani, A., Krisch, M. H. and Sette, F., *Phys. Rev. B*, **56**, 7285-7292 (1997).
- [72.] "Site-Selective XANES and EXAFS - A Demonstration With Manganese Mixtures and Mixed-Valence Complexes", Grush, M. M., Christou, G., Hamalainen, K. and Cramer, S. P., *J. Am. Chem. Soc.*, **117**, 5895-5896 (1995).

Chapter 9

Electronic Structure Calculations: Density Functional Methods for Spin Polarization, Charge Transfer, and Solvent Effects in Transition Metal Complexes

Jian Li and Louis Noodleman

Department of Molecular Biology, The Scripps Research Institute,
La Jolla, CA 92037

Results of density functional calculations are presented for 16 mononuclear transition metal complexes (high-spin and low-spin systems), and 11 bridged dinuclear complexes. The dinuclear complexes are spin-coupled and the broken symmetry method is quite effective for predicting optimal geometries. The local Vosko-Stoll (VS) exchange-correlation potential predicts both mononuclear and dinuclear geometries well. Redox potentials for the entire first row transition metal ion series $M^{2+,3+}$ in aqueous solution are calculated by metal-hexa-aquo ion calculations with extrapolation from calculations on $Mn^{2+,3+}$ and $Fe^{2+,3+}$. Both experimental trends and energies are well portrayed (largest error about 350 mV out of a 2000 mV range). Overall, the long range environment is more critical for energetics than for geometries where the local coordination environment dominates.

There is great diversity in the electronic structures, geometries, and energetics seen in transition metal complexes [1]. This is true both for inorganic complexes, and for the transition metal active sites in proteins (bioinorganic complexes) [2]. The spin state of a transition metal complex depends on the metal d electron count and on the strength of the surrounding ligand field, with weak field ligands and low coordination numbers favoring high spin ground states [3]. The spin state strongly affects molecular geometry, redox energetics, and the strength of ligand binding. Many biologically relevant ligands including water, thiolates, and carboxylates (constituting the side chains of cysteine, and glutamate or aspartate amino acids) are weak field ligands, while the imidazole side chain of histidine is of moderate field strength [4]. As a consequence, many bioinorganic complexes are high spin (HS) rather than low spin (LS) while others exhibit intermediate spin (IS) ground states or undergo $HS \leftrightarrow IS$, $IS \leftrightarrow LS$ or $HS \leftrightarrow LS$ interconversion. In dinuclear and polynuclear ligand-bridged transition metal complexes, a net low spin ground state often arises from spin coupling between neighboring high spin transition metal sites [5]. Much of the essential electronic structure of each

high spin metal site is carried over into the spin-coupled complex along with additional features characteristic of the spin-coupling [6]. Bioinorganic complexes of this type are also prevalent as seen in dinuclear iron-oxo-carboxylate bridged active sites in enzymes [7], in dinuclear and polynuclear iron-sulfur electron transfer proteins, in other iron-sulfur hydrolytic enzymes [8] and in dinuclear and polynuclear manganese-oxo-carboxylate active site enzymes [9]. For a number of bioinorganic sites in proteins, synthetic analogues have been constructed resembling these in various aspects of coordination geometry. "True" functional analogues of metalloenzymes are much more difficult to construct than structural analogues [10]; the extended protein/solvent environment must often play an important role in functional activity.

In this brief review, we present results of density functional calculations for selected transition metal complexes, illustrating some aspects of spin states, geometries, charge distributions, and the binding energy of the metal ion with the first shell ligands and interaction energy with the extended environment [11, 12]. We focus on open-shell complexes involving first row transition metals, because of their prevalence in bioinorganic systems [5]. The aqueous chemistry of transition metal ions (mainly high-spin for first row metal ions) is also biologically relevant, both because ions are often extracted or sequestered from aqueous solution [13] when these are inserted into metalloproteins, and because a transition metal site in aqueous solution has important features in common with active sites in some metalloproteins [11,12]. Because transition metal active sites in proteins are often charged, the complex with the first ligand-shell also interacts strongly with the extended environment of the protein plus solvent. Such transition metal active sites are part of an extended charged hydrogen-bonding network, as are metal ions in aqueous solution.

High spin transition metal complexes will show a substantial spin-polarization splitting between majority spin and minority spin levels [14-16]. In the context of density functional methods, the self-consistent-field potentials for α (spin-up) and β (spin-down) electrons will differ when there are different numbers of α and β spin electrons (or more generally, different densities of α versus β in particular regions). The filling of the ligand field mainly metal (3d) levels is different in high-spin vs. low spin complexes. Further, the spin- polarization splitting of the majority spin (3d) levels compared to the minority spin levels also changes the relative position of the occupied and empty metal (3d) levels compared to the mainly ligand based high-lying levels [6].

In a compact, partially filled metal (3d) shell (where strong electron-electron repulsion is carefully balanced against strong nuclear-electron attraction), the changes in electron density upon oxidation or reduction always involve both metal and ligand sites. Further, changes in the total electron density are not well-described from changes in the density of the "active orbital" alone (defined as the orbital filled or emptied upon one electron reduction or oxidation, respectively-these orbitals are generally different [6].) The remaining "passive orbitals" will change their net density as well, and collectively this is usually a strong effect, called "electron relaxation" [17]. Both spin-polarization and electron relaxation require a spin-polarized self-consistent-field approach for an appropriate description.

Since metalloenzymes are often redox active, and use catalytic mechanisms involving either one-electron or multi-electron oxidation or reduction, sometimes with coupled proton transfer events as well, the fundamental features of oxidation/reduction energies and associated energies of protonation/deprotonation are highly relevant. Throughout the catalytic cycle, electron transfer, proton transfer, and ligand binding or dissociation lead to changes in active site geometry and electronic structure. The ability of density functional methods to properly depict these geometric changes and the associated energy changes is of considerable interest, particularly because typically only some of the geometries throughout a catalytic cycle are well-characterized.

We will consider examples both of monomeric transition metal complexes and

ligand bridged dinuclear complexes. For some mononuclear complexes ($\text{Fe}^{2+,3+}$, $\text{Mn}^{2+,3+}$ aquo-ions) [11] we will examine interactions with the second ligand shell (considered explicitly in the quantum mechanical description), and interactions with the extended solvent environment represented by a "classical" continuum dielectric representation. For dinuclear complexes, both ligand bridging and spin coupling influence geometries, while the extended environment is also important for redox energetics. Again, the solvent environment can be represented by a continuum dielectric representation [18]. The spin-coupled dimeric complex can be described by the broken symmetry (BS) method, and this gives a good overall view of geometry and energetics of the system. The broken symmetry state contrasts in geometry and energetics with the high spin (HS) state, (obtained with parallel alignment of metal site spin vectors), which is typically higher in energy (since most dimeric complexes are antiferromagnetically coupled). While the combination of the HS and BS energies can be used to construct a complete ladder of pure spin states, we will emphasize here that the BS state has considerable value for energies, geometries, and charge or spin distribution, even prior to consideration of spin coupling parameters and construction of pure spin states $E(S)$ (where S is the total spin quantum number), and their potential energy curves.

Methods

Density Functional Methods Density functional methods are now widely known as a high level technique for quantum chemical calculations, particularly on systems containing transition metal sites. These calculations are difficult to carry out with more conventional *ab initio* methods. The distinctive aspect of density functional theory is that the exchange and correlation energies are approximated using functionals of the electron density alone. For spin polarized systems, there are separate energy terms for the α and β (spin-up and spin-down) electron densities, and correspondingly, separate potentials for these in the one-electron energy equations of the self-consistent-field. Since density functional methods scale as a lower power of basis set size than with conventional Hartree-Fock or more complex *ab initio* methods, it is often feasible to use large basis sets with density functional methods even for fairly large, low symmetry systems, containing 20-70 atoms.

Recent improvements in density functional theory emphasize the introduction of non-local terms which depend on both the α and β densities and on their gradients. These non-local terms allow an improved description of molecular bond energies and vibrational frequencies. Bond energies which are typically too strong using a local Vosko-Wilk-Nusair (VWN, referred to as V below) [19] type potential, are reduced to values much closer to experiment using non-local potentials. The best currently available non-local exchange and correlation potentials are the Becke (B) [20,21] potential for exchange, and the Perdew (P) [22,23] or Lee, Yang, Parr (LYP) [24] potentials for correlation. These are added to the local potential Vosko-Wilk-Nusair potential to give the VBP potential, or the BLYP potential from the B plus LYP combination. One source of the excessive binding energy in the VWN potential is a large term for parallel spin correlation; elimination of this term improves bonding energies, and can be done with a local term, called the Stoll (S) [25,26] term. The resulting VS potential is local, yet more accurate for bonding energies than VWN. Addition of the Becke term to this yields a VSB potential which is close to the quality of VBP. Surprisingly, for molecular geometries, particularly in transition metal complexes, the simpler local VWN potential gives results of similar quality (or better) than the VBP; while VWN usually gives M-L bonds that are too short compared to experiment, VBP usually gives M-L bonds that are too long, which is likely due to the Becke term [27]. This behavior is also noted with BLYP; bond energies are again improved compared to the local VWN

potential, but geometries are not [28]. We have found in recent studies that the local VS potential gives M-L bond lengths between these two limits, and because this potential is local, there is a considerable improvement in computational speed. A number of examples comparing VS with VWN and VBP optimized geometries will be presented below. Examples are drawn from first row transition metal complexes (both high spin and low spin) with net charge.

We should also mention hybrid density functional-Hartree-Fock potentials [29], which combine both HF and DFT energy terms. Different forms of these have been proposed. They are known to give both improved energies and geometries with respect to purely DFT non-local functionals [28]. They are, however, at present, as time consuming as pure Hartree-Fock calculations.

All the calculations from our group employed modified forms of the Amsterdam Density Functional (ADF) code [30, 31] and its predecessor AMOL [32]. Details of published calculations are in the original papers. We will emphasize only a few important points here. The ADF code employs a charge density fitting procedure to fit the density matrix formed from a basis set of Slater type orbitals (and consisting of a linear combination of products of these functions) to a linear combination of different STO's on different centers (a sum of single center functions called the fit density). The Coulomb potential of the fit density can be determined accurately on a three dimensional grid of points along with the exchange and correlation terms at each SCF cycle, and the Hamiltonian matrix elements are constructed by numerical integration of the potentials with the basis functions over a grid of points. The kinetic-energy matrix elements are constructed analytically as usual. The use of the density fitting procedure and the numerical integration over the grid allows for the use of large STO basis sets. Also, when the electrostatic potential due to solvation or other terms from the extended environment are added, these are conveniently constructed over the same grid. While the quality of the result depends on that of the basis set, fit set, and the grid, the numerical grid based methods are well-adapted for parallel computers and scale well with the number of processors.

The bonding energies are calculated with respect to a reference state composed of spin-restricted atoms making up the molecule. In practice, these bonding energies can be calculated with respect to physically realistic spin-polarized atom fragments. Alternately, energy differences between different states or geometries can be evaluated, and the reference state then subtracts out.

Geometry Optimization Geometry optimization of cluster models was done according to the analytic gradient method for local potentials by Versluis et al. [33], and at the non-local level by Fan et al. [34]. The optimization used the Newton-Raphson method, and the second derivative (hessian matrix) was updated with the Broyden-Fletcher-Goldfarb-Shanno strategy [35].

Fitting of Electrostatic Potential Charges (ESP) A modified version of the CHELPG code of Breneman and Wiberg [36]. was used to fit the point charges from the molecular electrostatic potentials (ESP) calculated from the ADF code.

Electrostatics/Solvation Methods-Continuum Dielectric Model for Solvation Once the ESP charges are determined, the reaction field potential ($\phi^*(r)$) can be determined by solving the linearized Poisson-Boltzmann equation [37]. The reaction field potential represents the potential due to polarization of the solvent treated as a continuum dielectric. A similar methodology allows the treatment of extended protein environments as a set of charges embedded in a dielectric medium [38]. With the ESP charges and the reaction field potential, an electrostatic solvation energy can be calculated in a single step process [18]. In a more accurate, but also more computationally intensive process,

the reaction field potential can be incorporated into the self-consistent-field (SCF) of the total system, producing a self-consistent-reaction-field (SCRf) [12,37]. Then, in addition to the solvation energy of interaction with the gas phase quantum cluster, there is an additional energy due to polarization of cluster density to the final solvated value. Further, there is a smaller, but significant energy cost ("electronic strain energy") associated with changing the cluster density.

Broken Symmetry Approach for Dimer States The transition metal dimer systems we will examine are all spin-coupled systems. In density functional theory, we can represent an antiferromagnetic spin-coupled state by a "broken symmetry" state, where the spin densities on the two metal sites are oppositely aligned. The broken symmetry (BS) state is not a pure spin state; rather, it is a specific weighted sum of pure spin states, and lies above the pure spin ground state energy. If we consider that the spin-coupling interactions constitute "spin-bonding" between the alternate metal sites (this being a part of the overall net bridge bonding), then the BS state is net "spin-bonding" and lies fairly close to the spin ground state, while the high spin (HS) state is "spin-antibonding", and considerably higher in energy (assuming that the dominant coupling is antiferromagnetic, and of Heisenberg form $H_{\text{spin}} = J \mathbf{S}_1 \cdot \mathbf{S}_2$). As a simple example, for a dimer with sites of equal valence, the energy difference between the HS and singlet ground state ($S=0$) ($E(\text{HS}) - E(S=0) = J S_{\text{max}}(S_{\text{max}} + 1) / 2$, where S_{max} is the maximum total spin quantum number) while the BS to singlet separation is only $E_{\text{BS}} - E(S=0) = JS_{\text{max}} / 2$.

This is helpful also since the geometry of the system is generally spin-state dependent (a concept called "exchange striction") [39]. A good initial approximation for the ground spin state geometry is then to compute the geometry of E_{BS} . At a higher level of accuracy, separate optimized geometries can be calculated for E_{BS} and $E(\text{HS})$, and a path defined between these geometries, and just beyond them (by Cartesian interpolation and extrapolation). Then $J(\mathbf{x})$ can be evaluated over this path, and the minimum energy and optimized geometry of $E(S=0)$ can be found. A number of examples of optimized geometries will be given in the section on dimers.

For a mixed-valence system, the higher spin states can gain energy from a spin dependent delocalization mechanism (resonance term) with [6, 40] a spin Hamiltonian $H_{\text{spin}} = JS_1 \cdot S_2 \pm B(S + 1/2)$ while for lower spin states (and for the BS state), vibronic coupling or solvent effects quench the resonance term and leave only a Heisenberg spin coupling ($H_{\text{spin}} = JS_1 \cdot S_2$). Since the resonance term favors large spin, and both $J(\mathbf{x})$ and $B(\mathbf{x})$ are geometry dependent, the minima of the $E(\text{HS})$ and E_{BS} states are often closer than in the equal valence case. $-B(\mathbf{x})(S + 1/2)$ is a metal-metal bonding interaction which strengthens and shortens the bond for higher spin states. This effect will be discussed in the context of $[\text{Fe}_2\text{S}_2(\text{SR})_4]^{2-,3-}$ complexes and related systems.

Results and Discussion

Monomer and Dimer Complexes Some of the complexes we will examine are shown in Fig.1. A metal-hexa-aquo complex, representing the first coordination shell of aquated metal ions ($M^{2+,3+}$) is shown in Fig.1a, and this can be compared with the active site of the enzyme manganese-superoxide dismutase (MnSOD) shown in Fig.1d. The five-coordinate active site of MnSOD contains three imidazole side chains from histidines, one carboxylate from aspartate, and one bound water (or hydroxyl). It is expected that the superoxide anion adds to occupy the sixth coordination site during the catalytic cycle. Most first row metal-hexa-aquo complexes are high-spin in both $M^{2+,3+}$ oxidation states, as is MnSOD; these experimental results are also found by

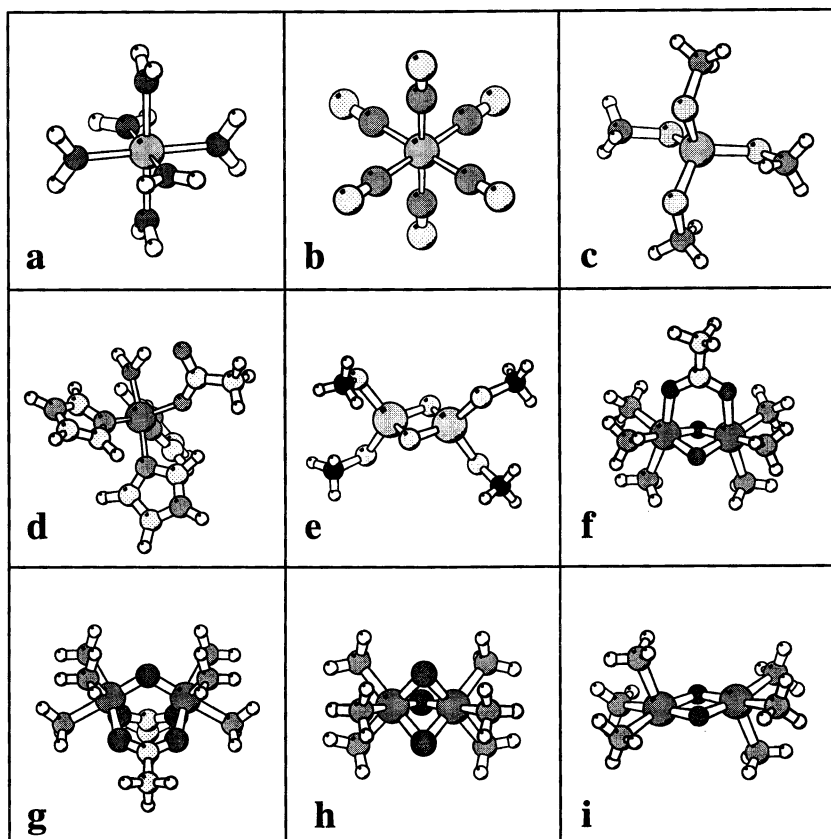


Figure 1. Structures of some monomer and dimer complexes.

density functional calculations. Fig.1b shows structures of low-spin metal-hexacyanide complexes with the low-spin resulting from the strong cyanide ligand field. Fig.1c shows the structure of a monomeric metal-tetrathiolate system. The $\text{Fe}(\text{SR})_4^{1-2-}$ structure is found in the active site of rubredoxin. Fig.1e shows a 2Fe2S center which is typical of 2Fe2S protein active sites, and of a variety of 2Fe2S synthetic analogues. The terminal ligands are organic thiolates in the synthetic systems and cysteine side chains in proteins. Fig.1f,g,h show metal-oxo-dimer complexes similar to those found in synthetic iron-oxo and manganese-oxo dimers. These are largely antiferromagnetically coupled systems with high-spin (or intermediate-spin) metal sites. Structurally and electronically similar sites are found in a variety of metalloproteins. Fig.1i shows a structure of an oxo-bridged copper dimer complex related to some complexes recently synthesized by Tolman and coworkers [41]. Related active site structures are found in the copper dimer proteins hemocyanin (an oxygen carrier), and in tyrosinase [3].

Geometry Optimization of Mononuclear Transition Metal Complexes Most transition metal sites in biological systems are found as metal cations coordinated by nitrogen, sulfur, and oxygen from amino acid side-chains. To evaluate the accuracy of

density functional methods for predicting geometries for such systems, we have optimized the geometries for a series of simple mononuclear complexes including high-spin $M(\text{H}_2\text{O})_6^{n+}$, low-spin $M(\text{CN})_6^{n-}$, and high-spin $M(\text{SCH}_3)_4^{n-}$ where the transition metals are $M = \text{Mn}^{2+,3+}$, $\text{Fe}^{2+,3+}$, $\text{Cu}^{1+,2+}$. These are among the most abundant transition elements in biological complexes. For these complexes (or closely related ones), experimental structural data is available, so that a direct comparison is possible. Figure 2 summarizes calculated versus experimental metal-ligand bond lengths for 16 complexes. The geometry optimizations are done at VWN, VS, and VBP levels.

The calculated metal-ligand bond lengths depicted in Figure 2 are in good agreement overall with experimental values over a wide range of bond lengths from 1.9 Å to 2.5 Å. It should be noted that the experimental bond lengths were measured in crystalline environments while the calculations were done on the isolated complexes in vacuo, without considering the effects of extended environments of either the crystal lattice or solvent/counterions in solution. There appears to be a substantial degree of decoupling between the geometry imposed by the immediate coordination environment and geometric distortions caused by longer range covalent and electrostatic environment even in these charged complexes. As we discuss in the next section the energetic effects of the extended environment are critical for example in redox potential calculations, but geometric effects of the extended environment are much less apparent. Similar observations hold for the dimer complexes examined later. This can be rationalized by thinking

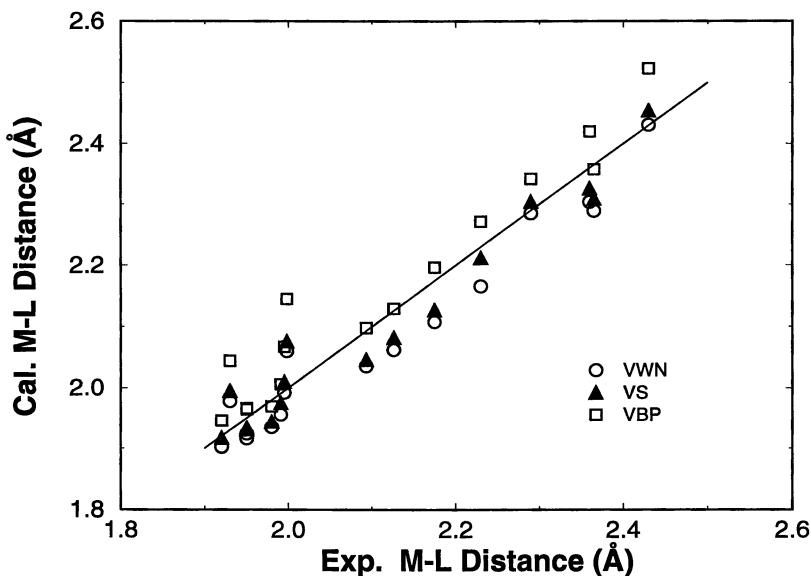


Figure 2. Calculated versus experimental metal-ligand distances in $[\text{M}(\text{H}_2\text{O})_6]^{n+}$ ($M = \text{Fe}^{2+}$, Fe^{3+} , Mn^{2+} , Mn^{3+} , Cu^+ , Cu^{2+} ; $n = 1, 2, 3$), $[\text{M}(\text{CN})_6]^{n-}$ ($M = \text{Fe}^{2+}$, Fe^{3+} , Mn^{2+} , Mn^{3+} ; $n = 3, 4$), $[\text{M}(\text{CN})_4]^{n-}$ ($M = \text{Cu}^+$, Cu^{2+} ; $n = 2, 3$) and $[\text{M}(\text{SCH}_3)_4]^{n-}$ ($M = \text{Fe}^{2+}$, Fe^{3+} , Mn^{2+} , Mn^{3+} ; $n = 1, 2$).

of the second coordination shells and more extended environments as opportunistic, being able to arrange taking advantage of the strong binding in the first shell without significant disruption. This is particularly true when the more distant coordination shells can closely pack around the first shell, and when the metal and first coordination shell are charged, which serves to orient surrounding dipolar and charged ligands. These observations apply both to synthetic systems and to proteins [42].

Comparing the different density functional methods, the VBP results overestimate the metal-ligand bond lengths, while VS and VWN underestimate these. The VS values are in general better than the VBP values, and are also an improvement on the VWN values. This contrasts with the observation for zero-valent, uncharged transition metal organometallic compounds like metal-carbonyls where the VBP metal-carbon distances are consistently superior to VWN results [43].

Deeth et al. [27] applied the same methods to optimize the M-X bond lengths for a variety of $[MX_6]^{2-}$ complexes where M are some first-, second-, and third-row transition metals and X are halogens. They reached the same conclusion that VWN gives better M-X distances than those from VBP. They even built an "in crystal" cluster model $\{K_8[PtCl_6]\}^{6+}$ to simulate the charge effects from the second layer and counterions. It turns out that the M-Cl bond lengths are not sensitive to such environmental effects.

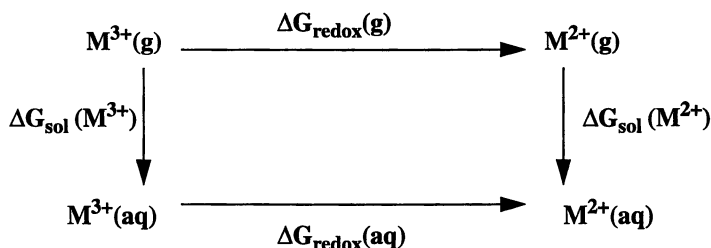
Energetics — Calculated Redox Potentials of M^{3+}/M^{2+} in Aqueous Solution

Redox potentials are key properties of transition metal complexes which function as electron transfer centers in bioinorganic systems. Calculations of redox potentials require not only an accurate evaluation of the energetics for removing or adding electrons to complexes, but also a precise accounting of environment effects like solvation energies and geometric relaxation. We use density functional methods to compute gas phase ionization potentials or electron affinities and a dielectric continuum model to deal with solvent effects. In addition to the electrostatic interaction between the solute and solvent, highly charged transition metal complexes also induce charge transfer between the metal cation center and surrounding environment and affect the hydrogen bond network of the solvent. For this reason, it is important to include some solvent shells beyond the first coordination shell in the quantum cluster model. Our calculation of redox potentials for Mn^{3+}/Mn^{2+} and Fe^{3+}/Fe^{2+} in aqueous solution demonstrates how these effects can be taken into account [11].

We began with a discrete cluster model $[M(H_2O)_6]^{m+}$ which describes the first hydration shell of the metal cations. The structure of this cluster was optimized by density functional methods (VBP). The calculated Mn-OH₂ and Fe-OH₂ bond lengths, as shown in Figure 2, agree fairly well with the data determined by x-ray diffraction for Alum and Tutton salts in crystalline phase and other diffraction methods in solution. To examine the effects of the second hydration shell, twelve water molecules were added to $[M(H_2O)_6]^{m+}$ to construct a larger cluster $[M(H_2O)_{18}]^{m+}$, in which every second shell water molecule forms a hydrogen bond to H atoms in $[M(H_2O)_6]^{m+}$. A high symmetry constraint was applied to the larger cluster and the O(second shell)...H(first shell) distances were optimized using force field methods (Discover module in Insight II, Biosym/MSI). After the outer shell was built, the inner shell was allowed to breathe over a small range and the M-O(first shell) distances were adjusted by a quadratic fitting based on a series of single point density functional calculations. As the result of presence of second hydration shell, the first shell expands slightly. The typical change in first shell M-O bond lengths due to the presence of the second coordination shell of waters is calculated as 0.01 to 0.04 Å (with the larger values for d^4 and d^6 metal ions).

For these metal-aquo ions, the first coordination shell largely controls the metal site geometry [11].

The calculation of redox potentials is based on the following thermodynamic cycle:



and

$$\Delta G_{\text{redox}}(\text{aq}) = \Delta G_{\text{redox}}(\text{g}) - \Delta G_{\text{sol}}(\text{M}^{3+}) + \Delta G_{\text{redox}}(\text{M}^{2+}).$$

By using the calculated gas phase ionization potentials $\text{IP}_{\text{red}}(\text{g})$ and differences in solvation energy $\Delta\Delta E_{\text{sol}} = \Delta G_{\text{sol}}(\text{M}^{2+}) - \Delta G_{\text{sol}}(\text{M}^{3+})$, the redox potential $E_{\text{redox}}^0[\text{M}^{3+}/\text{M}^{2+}]$ can be calculated as:

$$E_{\text{redox}}^0 = \text{IP}_{\text{red}}(\text{g}) - \Delta\Delta E_{\text{sol}} + T\Delta S(\text{aq}) + \Delta\text{SHE} + \Delta E_{\text{corr}}$$

where ΔSHE represents the standard hydrogen electrode potential of -4.43 V. ΔE_{corr} stands for relativistic and geometry relaxation corrections to $\text{IP}_{\text{red}}(\text{g})$. $T\Delta S$ term is the entropy contribution and the experimental value for $\text{Fe}^{3+}(\text{aq}) \rightarrow \text{Fe}^{2+}(\text{aq})$ is 0.55 eV. There is no trivial way to estimate this term theoretically and we used the experimental data for both $\text{Fe}^{3+}/\text{Fe}^{2+}$ and $\text{Mn}^{3+}/\text{Mn}^{2+}$. The calculated and experimental redox potentials for $\text{Fe}^{3+}/\text{Fe}^{2+}$ and $\text{Mn}^{3+}/\text{Mn}^{2+}$ in aqueous solution are listed in Table I and depicted in Figure 3. Figure 3 clearly shows that the calculated $E_{\text{redox}}^0[\text{M}^{3+}/\text{M}^{2+}]$ converge toward the experimental values with increasing size of the cluster model. The inclusion of the second hydration shell in the quantum cluster greatly improves the agreement between calculated and experimental results. Similar convergence has been also observed for calculated absolute pK_a values of hydrated metal cations. These results illustrates that a reasonable discrete supermolecular cluster model is important in order to obtain correct energetics for charged metal systems in condensed environments like aqueous solvent. The water molecules in the first hydration shell form direct

Table I. Calculated and experimental redox potentials ^a.

	IP_{red}	$\Delta\Delta E_{\text{sol}}$	$T\Delta S$	ΔE_{corr}	E_{redox}^0 Calc.	E_{redox}^0 Exp.
$[\text{Mn}(\text{H}_2\text{O})_6]^{3+/2+}$	17.76	10.93	0.55	-0.29	2.66	
$[\text{Mn}(\text{H}_2\text{O})_{18}]^{3+/2+}$	12.27	6.51	0.55	-0.29	1.59	1.56
$[\text{Fe}(\text{H}_2\text{O})_6]^{3+/2+}$	16.78	10.64	0.55	-0.26	2.00	
$[\text{Fe}(\text{H}_2\text{O})_{18}]^{3+/2+}$	11.63	6.43	0.55	-0.26	1.06	0.77

^a. E_{redox}^0 in V and other terms in eV.

polar covalent bonds to the metal center and supply a ligand field to stabilize the cations. The inclusion of the second shell retains the inter-shell strong hydrogen bond network, allows partial electron transfer and offers a better description of the solute-solvent interaction.

A closer look at the data in Table I is very instructive. First, it can be seen that the $\Delta\Delta E_{\text{sol}}$ of $[\text{M}(\text{H}_2\text{O})_{18}]^{\text{m}+}$ is almost constant for Fe and Mn with an average of 6.47 eV. This is understandable since the solvation energy we calculated originates from electrostatic interactions of the cluster polarizing and interacting with the solvent. The charge distribution of $[\text{M}(\text{H}_2\text{O})_{18}]^{\text{m}+}$ clusters are quite similar for either Fe or Mn central atoms. Secondly, the $\text{IP}_{\text{red}}(\text{g})$ difference between $[\text{M}(\text{H}_2\text{O})_{18}]^{2+}$ and $[\text{M}(\text{H}_2\text{O})_6]^{2+}$ clusters, $\Delta\text{IP}_{\text{red}} = \text{IP}_{\text{red}}([\text{M}(\text{H}_2\text{O})_{18}]^{2+}) - \text{IP}_{\text{red}}([\text{M}(\text{H}_2\text{O})_6]^{2+})$, is also nearly constant because this term is governed by the hydrogen bonding strength between the waters in first and second hydration shells. The average of $\Delta\text{IP}_{\text{red}}$ for Fe and Mn clusters is -5.32 eV. From these two parameters, we can go further to estimate approximately the redox potentials $E_{\text{redox}}^0[\text{M}^{3+}/\text{M}^{2+}]$ for the entire first-row transition metal series. We calculated $\text{IP}_{\text{red}}([\text{M}(\text{H}_2\text{O})_6]^{2+})$ for $\text{M} = \text{Sc} - \text{Zn}$, and added $\Delta\text{IP}_{\text{red}}$ to $\text{IP}_{\text{red}}([\text{M}(\text{H}_2\text{O})_6]^{2+})$, giving a good estimate of $\text{IP}_{\text{red}}([\text{M}(\text{H}_2\text{O})_{18}]^{2+})$. We then used the average $\Delta\Delta E_{\text{sol}}$ of $[\text{M}(\text{H}_2\text{O})_{18}]$ (6.47 eV) and the same $\text{T}\Delta\text{S}$ (0.55 eV) and ΔE_{corr} (-0.28 eV) terms to calculate the redox potentials $E_{\text{redox}}^0[\text{M}^{3+}/\text{M}^{2+}]$ for $\text{M} = \text{Sc} - \text{Zn}$. The calculated and experimental $E_{\text{redox}}^0[\text{M}^{3+}/\text{M}^{2+}]$ are shown in Figure 4. For five elements V, Cr, Mn, Fe and Co where experimental data are available, our calculated results compare very well with experimental values with the largest error about 350 mV. This indicates that the cluster models and the theoretical strategies we used in these calculations already include the most important physical contributions and are of good overall accuracy.

A similar methodology has been applied to calculate the redox potential of the active site model of manganese superoxide dismutase [12]. The active site model is shown in Fig 1d. The calculated redox potential for water bound active site model in aqueous solution is 0.17 V, compared to 0.26 and 0.31 V determined for *B. stearothermophilus* and *E. coli* enzymes. However, it should be noticed that the redox process in this enzyme is much more complex because the protonation/deprotonation is likely coupled with the redox electron transfer. Our calculations on this system indicate that the immediate coordination environment of the manganese site in Mn(SOD) depicted in Fig.1d is not sufficient to predict physically reasonable redox potentials when coupled redox and protonation are treated. In our initial calculations, we represented the extended environment by aqueous solution in the dielectric continuum model, but this is clearly insufficient. Rather, it now appears that the extended protein environment needs to be included, and a combined quantum region for the first shell and some second shell ligands plus a much larger electrostatic protein/solvent region are currently being developed, along with geometry optimization of the active site complex in various redox and protonation states.

Electron Density Difference vs. LUMO Orbital Density: The Example of Manganese Superoxide Dismutase Superoxide dismutases are a diverse group of metalloenzymes critical to the existence of aerobic organisms. Manganese superoxide dismutase enzymes are found in prokaryotes and in mammalian mitochondria. Fig.1d shows the Mn(SOD) active site with the central Mn ion, three histidine imidazoles, one aspartate carboxylate (monodentate), and one bound water (alternatively hydroxyl in the oxidized form). The overall catalytic dismutation proceeds via an alternating reduction of

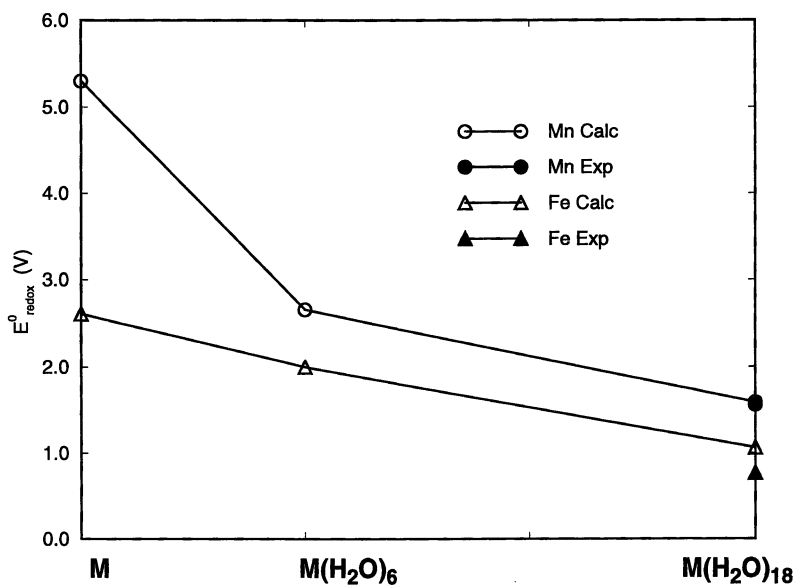


Figure 3. Convergence of calculated one-electron redox potentials $E_{\text{redox}}^{\circ}(\text{M}^{3+}/\text{M}^{2+})$ with increasing size of cluster models $[\text{M}(\text{H}_2\text{O})_n]^{2+/3+}$ ($n=0,6,18$).

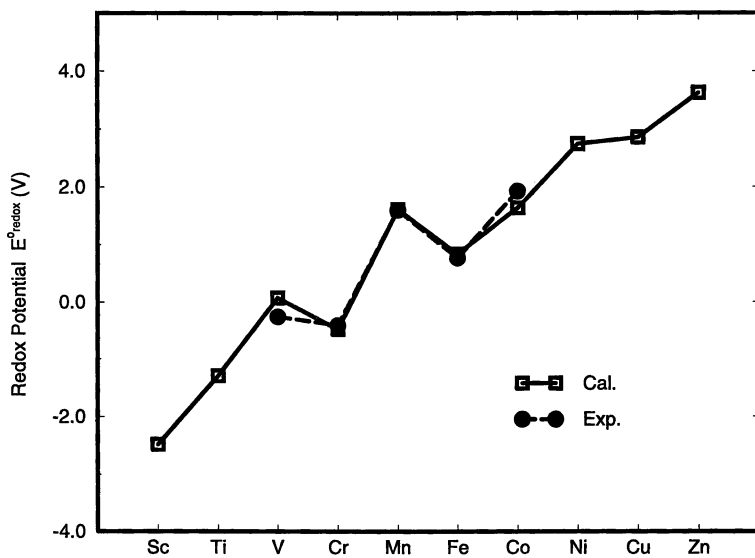
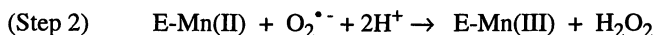
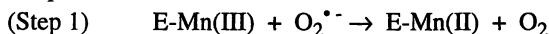


Figure 4. Calculated and experimental one-electron redox potentials $E_{\text{redox}}^{\circ}(\text{M}^{3+}/\text{M}^{2+})$ for first-row transition metals in aqueous solution.

Mn(III) and then oxidation of the Mn(II) enzyme by successive encounters with two different superoxide radical anions:



The full reaction pathway is complicated, and only partially understood. Three features are mechanistically and energetically very significant [12, 44-47]: 1) the electrostatic encounter of separate $\text{O}_2^{\bullet -}$ anions with the positively charged active site in 2 steps (the first and second superoxides encountered); 2) the energetics of the redox transfer to and from the E-Mn(III) and E-Mn(II); 3) the coupling of the redox events with proton transfer to the bound hydroxyl (oxidized form), and then to peroxide after reduction of superoxide in the second step. In feature (1) above, compared with the uncatalyzed dismutation reaction which is inhibited by repulsion of two superoxide anions, the electrostatic encounter of the second $\text{O}_2^{\bullet -}$ (Step 2) with the active site is more favorable when the preceding electron donated is delocalized. Figure 5 (a) shows that the total electron density difference between E-Mn(II) and E-Mn(III) is quite delocalized (calculated with bound H_2O for both states). Further, this density difference is far more delocalized than the density of the E-Mn(III) LUMO alone, due to electron relaxation effects, as shown by comparison with Figure 5 (b). The favorable electrostatic encounter of $\text{O}_2^{\bullet -}$ with E-Mn(II) is further promoted since it is very probable that protonation of hydroxyl precedes the binding of the second superoxide. Then the electrostatic encounter of the second $\text{O}_2^{\bullet -}$ via facilitated diffusion should be fairly comparable with that of the first $\text{O}_2^{\bullet -}$. Relaxation effects of this type are commonly predicted by density functional methods and facilitate metal-ligand covalency (electron delocalization between metal and ligands) in many transition metal complexes [48].

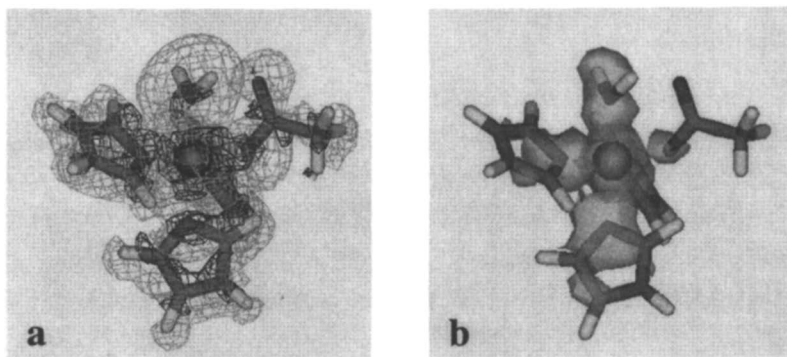


Figure 5. (a) Total density difference and (b) LUMO Charge density (square of the LUMO wave function of the oxidized form) of MnSOD active site model.

Geometries of Dimer Complexes In Table II, we present calculated optimized geometries of 11 ligand bridged transition metal complexes containing manganese-oxo, iron-oxo, copper-oxo (and copper-peroxo) and iron-sulfur centers. (See also Figure 1 for coordination geometries.) The calculated structures for model complexes (with simple amines and methyl-thiolate as terminal ligands) using the broken symmetry method

and VS exchange-correlation potential are compared with those in related synthetic complexes. The calculated geometries are for isolated molecules in vacuo, without accounting for environmental effects on geometries. We have compared geometries in the core region M-X (bridging), M-M distances and M-O-M angle versus metal oxidation state and also protonation state of the μ oxo (or hydroxyl) bridge (complexes 5-7).

Table II. Comparison of optimized and experimental core geometries of ligand bridged transition metal dimer complexes ^a

		M-M	M-X _{μ} ^b	M-X _{μ} -M
[Mn(III) ₂ O(Oac) ₂ (NH ₃) ₆] ²⁺ 1	Calc.	3.104	1.780	121.3
[Mn(III) ₂ O(Oac) ₂ (TACN) ₂](ClO ₄) ₂	Exp.	3.084	1.790	117.9
[Mn(III)Mn(IV)O(Oac) ₂ (NH ₃) ₆] ³⁺ 2	Calc.	3.160	1.795	123.3
[Mn(III)Mn(IV)O(Oac) ₂ (Me ₃ TACN) ₂](ClO ₄) ₃	Exp.	3.230	1.887	125.1
[Mn(III)Mn(IV)O ₂ (Oac)(NH ₃) ₆] ³⁺ 3	Calc.	2.568	1.798	91.0
[Mn(III)Mn(IV)O ₂ (Oac)(TACN) ₂](BPh ₄) ₂	Exp.	2.588	1.81	91.1
[Mn(IV) ₂ (μ -O) ₃ (NH ₃) ₆] ²⁺ 4	Calc.	2.229	1.813	75.7
[Mn(IV) ₂ (μ -O) ₃ (Me ₃ TACN) ₂](PF ₆)	Exp.	2.296	1.82	78
[Fe(III) ₂ O(Oac) ₂ (NH ₃) ₆] ²⁺ 5	Calc.	3.000	1.755	117.4
[Fe(III) ₂ O(Oac) ₂ (TACN) ₂] ₂	Exp.	3.063	1.781	118.7
[Fe(II) ₂ (OH)(Oac) ₂ (NH ₃) ₆] ⁺ 6	Calc.	3.280	2.027	108.0
[Fe(II) ₂ (OH)(Oac) ₂ (Me ₃ TACN) ₂](ClO ₄)	Exp.	3.32	1.99	113.2
[Fe(III) ₂ (OH)(Oac) ₂ (NH ₃) ₆] ³⁺ 7	Calc.	3.400	2.003	116.1
[Fe(III) ₂ (OH)(Oac) ₂ (HBPz ₃) ₂](ClO ₄)	Exp.	3.439	1.960	124
[Cu(III) ₂ (μ -O) ₂ (NH ₃) ₆] ²⁺ 8	Calc.	2.799	1.822	100.3
[L ^{Bn3} Cu(III) ₂ (μ -O) ₂](ClO ₄) ₂	Exp.	2.794	1.805	101.4
[Cu(II) ₂ (O ₂)(NH ₃) ₆] ²⁺ 9	Calc.	3.637	1.951	137.5
[Cu(II)(HB(3,5-R ₂ pz) ₃) ₂] ₂ (O ₂)	Exp.	3.560	1.915	136.7
[Fe(III) ₂ S ₂ (SCH ₃) ₄] ²⁻ 10 (HS)	Calc.	3.072	2.318	83.0
[Fe(III) ₂ S ₂ (SCH ₃) ₄] ²⁻ 10 (BS)	Calc.	2.736	2.226	75.8
[Fe(III) ₂ S ₂ (s-p-MeC ₆ H ₄) ₄] ²⁻	Exp.	2.691	2.201	75.0
[Fe(II)Fe(III)S ₂ (SCH ₃) ₄] ³⁻ 11 (HS)	Calc.	2.792	2.322	73.9
[Fe(II)Fe(III)S ₂ (SCH ₃) ₄] ³⁻ 11 (BS)	Calc.	2.735	2.250 red 2.196 oxd	75.9

^a. Bond lengths in Å and angles in deg.

^b. X=O for **1 - 9**; X=S for **10 - 11**.

Overall, the agreement between calculations and experiment is surprisingly good, particularly considering that these are charged complexes embedded in crystalline environments, and that the ligands are simplified in the calculations. For the Mn complexes, the large variations seen experimentally showing an M-M distance shortening as the number of bridging oxo ligands is increased and the number of bridging carboxylates decreased is reproduced well by the calculations. The M-M distance shows much more variation with these changes in bridging ligand than with changes in Mn oxidation state. This is consistent with the predicted high metal-ligand covalency in the Mn(III)-O and Mn(IV)-O bonds so that calculated Mn ESP charges change only modestly with changes in formal oxidation state. (For a detailed analysis of electronic structures and charge distributions in manganese-oxo-carboxylate-TACN systems, see [49]. It is the ability of the oxo ligands to covalently bond with and to screen the interaction of the Mn cations that accounts for the M-M geometric variations. Similar conclusions can be reached about the iron-oxo and hydroxo complexes (5-7). Protonation of the bridging oxo-ligands produces a much larger change in the Fe-O and Fe-Fe distances comparing the diferric complexes (5) and (7) than does the two electron reduction of complex (7) to the diferrous complex (6). The bonding of the Fe cations to the negatively charged bridge is diminished by protonating the oxo, leading to the greater Fe-O and Fe-Fe separation. In contrast, the strong metal-ligand covalency leads to smaller effects on $\text{Fe(III)}_2 + 2e^- \leftrightarrow \text{Fe(II)}_2$ reduction or oxidation (7) \leftrightarrow (6) of the hydroxyl complexes. Here the greater Fe-Fe separation and larger Fe-O-Fe angle in the diferric hydroxyl complex compared to the diferrous hydroxyl is probably due to the larger Fe(III)_2 than Fe(II)_2 repulsion. We note also that the Fe-O distances for these two hydroxyl complexes are very similar, in contrast to the diferric-oxo complex (5).

For the dicopper complexes (8-9), the large Cu-Cu bond length change for the two isomers, the first formally Cu(III)_2 -di- μ -oxo and the second Cu(II)_2 -di-peroxo is well represented by the calculations.

In Figure 6, calculated energies versus M-M distance are presented for complexes (4) $[\text{Mn(IV)}_2(\mu\text{-O})_3(\text{NH}_3)_6]^{2+}$ and (10) $[\text{Fe(III)}_2\text{S}_2(\text{SCH}_3)_4]^{2-}$ for the BS and HS states (assuming HS is $S=3$ for the Mn(IV)_2 system and $S=5$ for the Fe(III)_2 system). Using the $E(\text{HS}) - E(\text{BS}) = J_{\text{max}}^2 / 2$ energy difference equation, the position of the $E(S=0)$ ground state is determined by interpolation.

The Mn(IV) -tri- μ -oxo shows a much shorter BS minimum than for HS as expected for a strongly antiferromagnetically coupled system. The spin-projected $S=0$ ground state Mn-Mn distance is shorter than the calculated BS state, and both are shorter than found experimentally. The HS state used in the calculation has $S=3$; however, if at short M-M distances, the Mn-Mn σ bond is delocalized, then an $S=2$ state is more appropriate for use as the upper state in the spin-projection equation in the "weak coupling regime" [48]. Further studies of systems of this type are in progress by our group and by Stranger's group in Australia.

For the $[\text{Fe(III)}_2\text{S}_2(\text{SCH}_3)_4]^{2-}$ both high spin states and BS optimized geometries are given in Table 2 (also see Figure 6). For the diferric complex (10), the predicted broken symmetry geometry is close to that in related synthetic complexes. The corresponding "spin antibonding" high-spin state shows a much longer Fe-Fe distance minimum, with a much higher energy. The spin-projected $S=0$ ground state has a shorter Fe-Fe distance, so that $S=0$ and BS bracket the experimental Fe-Fe geometry. The mixed-valence geometries (complex (11)) show a very different pattern. The Fe-Fe distances are similar for the HS and BS optimized geometries, and the BS state is predicted to lie only about 0.3 eV below HS at their respective energy minima. This result, in strong contrast to the diferric complex, is a consequence of the competition between

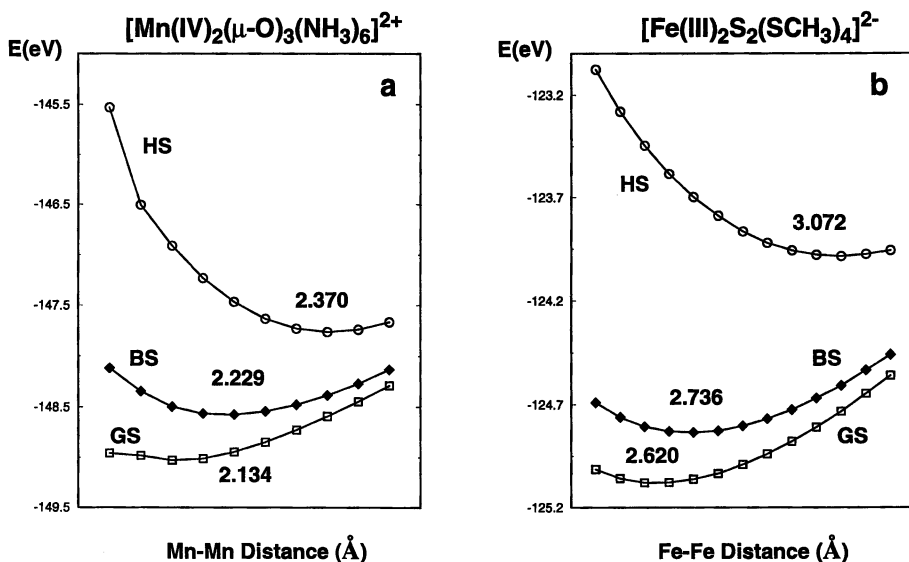


Figure 6. Potential energy curves for high spin (HS) state, broken symmetry (BS) state and ground state (GS). (a) $[\text{Mn(III)}_2(\mu\text{-O})_3(\text{NH}_3)_6]^{2-}$; (b) $[\text{Fe}_2\text{S}_2(\text{SCH}_3)_4]^{2-}$.

Heisenberg exchange (J term) favoring the BS state, and resonance delocalization (double exchange or spin dependent delocalization) favoring the delocalized HS state. While no X-ray structures for reduced synthetic complexes are available for comparison, the predicted Fe-S and Fe-Fe distances of the BS state are close to those expected for the reduced complex (noting also the Fe-S bond length difference between oxidized and reduced sites as expected for a “trapped valence” system with considerable Fe-S covalency). For the HS state, the Fe sites are geometrically equivalent with delocalized valence. Further, these Fe-Fe and Fe-S bond distances are very close to those seen in the valence delocalized high spin dimeric subunits of synthetic $[\text{Fe}_4\text{S}_4(\text{SR})_4]^{2-}$ cubane complexes [18, 48]. The close proximity in both energy and geometry between HS and BS states in the reduced 2Fe2S system provides an initial framework for understanding the coexistence of a trapped valence low spin $S=1/2$ and a delocalized high-spin $S=9/2$ ground state in certain reduced 2Fe ferredoxin mutant species (where one cysteine (SR)⁻ terminal ligand is mutated to serine (OH)⁻) [50-52].

Conclusions

In this review, we have presented results of density functional calculations for geometries of both mononuclear and bridged dinuclear transition metal complexes. These are open shell systems and the dinuclear systems are spin coupled. For the dinuclear systems, the broken symmetry method was shown to be quite effective for predicting optimal geometries. Monomer geometries are fairly well represented either with GGA (VBP) or with simpler (VS) exchange-correlation potential; in fact, the latter has proven more accurate for the systems we have examined with a non-relativistic potential, triple zeta level basis sets and $M(3s,3p)$ frozen core for the first row transition ele-

ments. Effects of smaller metal cores, relativity, and environmental potential still need further study to see whether further improvements are feasible. (2) For dimer complexes, BS state optimized geometries already are fairly good. These are much better than HS state curves for most systems (AF ground state), and from previous work [53], much better than the spin-restricted state geometry and energy (unless the ground state is strongly M-M bonding or closed shell for other reasons- in these cases, the associated BS state goes over directly into the spin-restricted solution). From the potential energy curve for BS and for the HS state, the S=0 and higher spin state potential energy curves can be derived, and spin coupling parameters obtained. The quantitative description of energetics at charged transition metal active sites requires description of the extended environment. Continuum dielectric description of solvation is quite valuable for long range solvent. If there is significant covalent interaction (and/or charge transfer) between the 1st shell ligands and the 2nd shell, then an extended quantum region is indicated, beyond which a continuum dielectric description of solvent, or electrostatic description of protein with a continuum dielectric description of long range solvent can describe the extended environment. The energetics of charged transition metal complexes in proteins and in synthetic inorganic systems are far more sensitive to the extended environment than is the immediate coordination shell geometry. For the latter, geometry optimization of the metal complex with the first coordination shell followed by molecular mechanics for the second shell provides a good initial model for energetic analysis. Of course, there may be more subtle effects of the longer range environment on geometries [53] and reaction pathways. An example of the latter may be the well known carboxylate shift [54].

Acknowledgments

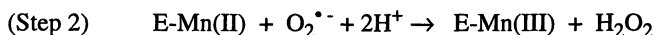
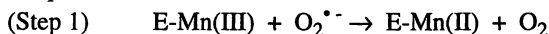
This work was supported by NIH grants GM50154, GM43278 and GM39914. We thank Dave Case, Don Bashford and Cindy Fisher for many helpful discussions.

Literature Cited

1. Shriver, D.F.; Atkins, P.W.; Langford, C.H. *Inorganic Chemistry*; W.H. Freeman: New York, 1990.
2. Frausto da Silva, J.J.R.; Williams, *The Biological Chemistry of the Elements*; Clarendon Press: Oxford, 1991.
3. Holm, R.H.; Kennepohl, P.; Solomon, E.I. *Chem. Rev.* **1996**, *96*, 2239.
4. Lippard, S.J.; Berg, J.M. *Principles of Bioinorganic Chemistry*; University Science Books: Mill Valley, CA., 1994.
5. Ibers, J.A.; Holm, R.H. *Science* **1980**, *209*, 223.
6. Noodleman, L.; Baerends, E.J. *J. Am. Chem. Soc.* **1984**, *106*, 2316.
7. Que Jr., L.; True, A.E. *Prog. Inorg. Chem.* **1990**, *38*, 97.
8. Beinert, H.; Kennedy, M.C.; Stout, C.D. *Chem. Rev.* **1996**, *96*, 2335.
9. Wieghardt, K. *Angew. Chem. Int. Ed. Engl.* **1994**, *33*, 725.
10. Pecoraro, V.L.; Baldwin, M.J.; Gelasco, A. *Chem. Rev.* **1994**, *94*, 807.
11. Li, J.; Fisher, C.L.; Chen, J.L.; Bashford, D.; Noodleman, L. *Inorg. Chem.* **1996**, *35*, 4694.
12. Fisher, C.L.; Chen, J.L.; Li, J.; Bashford, D.; Noodleman, L. *J. Phys. Chem.* **1996**, *100*, 13498.
13. Raymond, K.N. *Top. Curr. Chem.* **1984**, *123*, 49.
14. Norman Jr., J.G.; Jackels, S.C. *J. Am. Chem. Soc.* **1975**, *97*, 3833.
15. Norman Jr., J.G.; Ryan, P.B.; Noodleman, L. *J. Am. Chem. Soc.* **1980**, *102*, 4279.
16. Butcher, K.D.; Didziulis, S.V.; Briat, B.; Solomon, E.I. *J. Am. Chem. Soc.* **1990**, *112*, 2231.

17. Ziegler, T.; Rauk, A.; Baerends, E.J. *Chem. Phys.* **1976**, *16*, 209.
18. Mouesca, J.-M.; Chen, J.L.; Noodleman, L.; Bashford, D.; Case, D.A. *J. Am. Chem. Soc.* **1994**, *116*, 11898.
19. Vosko, S.H.; Wilk, L.; Nusair, M. *Can. J. Phys.* **1980**, *58*, 1200.
20. Becke, A.D. *J. Chem. Phys.* **1986**, *84*, 4524.
21. Becke, A.D. in *The Challenge of d and f Electrons*; Salahub, D.R.; Zerner, M.C. Eds.; American Chemical Society: Washington, D.C. 1989; p 165.
22. Perdew, J.P. *Phys. Rev. B* **1986**, *33*, 8822.
23. Perdew, J.P. *Phys. Rev. B* **1986**, *34*, 7406.
24. Kohn, W.; Becke, A.D.; Parr, R.G. *J. Phys. Chem.* **1996**, *100*, 12974.
25. Stoll, H.; Pavlidou, C.M.E.; Preuss, H. *Theoret. Chim. Acta* **1978**, *49*, 143.
26. Stoll, H.; Golka, E.; Preuss, H. *Theoret. Chim. Acta* **1980**, *55*, 29.
27. Deeth, R.J.; Jenkins, H.J.B. *J. Phys. Chem. A* **1997**, *101*, 4793.
28. Russo, T.V.; Martins, R.L.; Hay, P.J. *J. Chem. Phys.* **1995**, *102*, 8023.
29. Becke, A.D. *J. Chem. Phys.* **1992**, *97*, 9173.
30. te Velde, G.; Baerends, E.J. *J. Comput. Phys.* **1992**, *99*, 84.
31. ADF codes version 2.0.1, Department of Theoretical Chemistry, Vrije Universiteit, Amsterdam (December 1995).
32. AMOL, Department of Theoretical Chemistry, Vrije Universiteit, Amsterdam (August 1992).
33. Versluis, L.; Ziegler, T. *J. Chem. Phys.* **1988**, *88*, 322.
34. Fan, L.; Ziegler, T. *J. Chem. Phys.* **1991**, *94*, 6057.
35. Schlegel, H.B. *Adv. Chem. Phys.* **1987**, *67*, 249.
36. Breneman, C.M.; Wiberg, K.B. *J. Comput. Chem.* **1990**, *11*, 361.
37. Chen, J.L.; Noodleman, L.; Case, D.A.; Bashford, D. *J. Phys. Chem.* **1994**, *98*, 11059.
38. Botuyan, M.V.; Toy-Palmer, A.; Chung, J.; Blake II, R.C.; Beroza, P.; Case, D.A.; Dyson, H.J. *J. Mol. Biol.* **1996**, *263*, 752.
39. Owen, J.; Harris, E.A. in *Electron Paramagnetic Resonance*; Geschwind, S. Ed.; Plenum Press: New York, 1972; p 427.
40. Blondin, G.; Girerd, J.J. *Chem. Rev.* **1990**, *90*, 1359.
41. Tolman, W.B. *Acc. Chem. Res.* **1997**, *30*, 227.
42. Hellinga, H. *Curr. Op. Biotech.* **1996**, *7*, 437.
43. Li, J.; Schreckenbach, G.; Ziegler, T. *J. Am. Chem. Soc.* **1995**, *117*, 486.
44. Ludwig, M.L.; Metzger, A.L.; Patridge, K.A.; Stallings, W.C. *J. Mol. Biol.* **1991**, *219*, 335.
45. Lah, M.S.; Dixon, M.M.; Patridge, K.A.; Stallings, W.C.; Fee, J.A.; Ludwig, M. L. *Biochemistry* **1995**, *34*, 1646.
46. Whittaker, J.W.; Whittaker, M.M. *J. Am. Chem. Soc.* **1991**, *113*, 5528.
47. Borgstahl, G.E.O.; Parge, H.E.; Hickey, M.J.; Breyer Jr., W.F.; Halliwell, R.A.; Tainer, J.A. *Cell* **1992**, *71*, 107.
48. Noodleman, L.; Peng, C.Y.; Case, D.A.; Mouesca, J.-M. *Coord. Chem. Rev.* **1995**, *144*, 199.
49. Zhao, X.G.; Richardson, W.H.; Chen, J.L.; Li, J.; Noodleman, L.; Tsai, H.-L.; Hendrickson, D.N. *Inorg. Chem.* **1997**, *36*, 1198.
50. Crouse, B.R.; Meyer, J.; Johnson, M.K. *J. Am. Chem. Soc.* **1995**, *117*, 9612.
51. Achim, C.; Golinelli, M.-P.; Bominaar, E.L.; Meyer, J.; Munk, E. *J. Am. Chem. Soc.* **1996**, *118*, 8085.
52. Gamelin, D.R.; Bominaar, E.L.; Kirk, M.L.; Wieghardt, K.; Solomon, E.I. *J. Am. Chem. Soc.* **1996**, *118*, 8168.
53. Lovell, T.; McGrady, J.E.; Stranger, R. MacGregor, S.A. *Inorg. Chem.* **1996**, *35*, 3079.
54. Feig, A.L.; Lippard, S.J. *Chem. Rev.* **1994**, *94*, 759.

Mn(III) and then oxidation of the Mn(II) enzyme by successive encounters with two different superoxide radical anions:



The full reaction pathway is complicated, and only partially understood. Three features are mechanistically and energetically very significant [12, 44-47]: 1) the electrostatic encounter of separate $\text{O}_2^{\bullet-}$ anions with the positively charged active site in 2 steps (the first and second superoxides encountered); 2) the energetics of the redox transfer to and from the E-Mn(III) and E-Mn(II); 3) the coupling of the redox events with proton transfer to the bound hydroxyl (oxidized form), and then to peroxide after reduction of superoxide in the second step. In feature (1) above, compared with the uncatalyzed dismutation reaction which is inhibited by repulsion of two superoxide anions, the electrostatic encounter of the second $\text{O}_2^{\bullet-}$ (Step 2) with the active site is more favorable when the preceding electron donated is delocalized. Figure 5 (a) shows that the total electron density difference between E-Mn(II) and E-Mn(III) is quite delocalized (calculated with bound H_2O for both states). Further, this density difference is far more delocalized than the density of the E-Mn(III) LUMO alone, due to electron relaxation effects, as shown by comparison with Figure 5 (b). The favorable electrostatic encounter of $\text{O}_2^{\bullet-}$ with E-Mn(II) is further promoted since it is very probable that protonation of hydroxyl precedes the binding of the second superoxide. Then the electrostatic encounter of the second $\text{O}_2^{\bullet-}$ via facilitated diffusion should be fairly comparable with that of the first $\text{O}_2^{\bullet-}$. Relaxation effects of this type are commonly predicted by density functional methods and facilitate metal-ligand covalency (electron delocalization between metal and ligands) in many transition metal complexes [48].

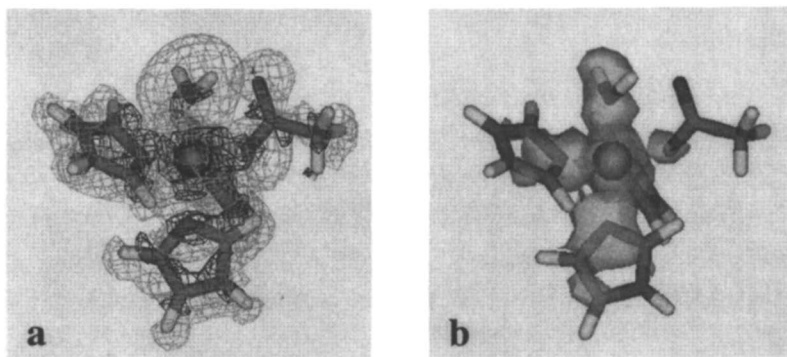


Figure 5. (a) Total density difference and (b) LUMO Charge density (square of the LUMO wave function of the oxidized form) of MnSOD active site model.

Geometries of Dimer Complexes In Table II, we present calculated optimized geometries of 11 ligand bridged transition metal complexes containing manganese-oxo, iron-oxo, copper-oxo (and copper-peroxo) and iron-sulfur centers. (See also Figure 1 for coordination geometries.) The calculated structures for model complexes (with simple amines and methyl-thiolate as terminal ligands) using the broken symmetry method

Chapter 10

Spectroscopic Studies of Ferrocytochrome *c* Folding

Gary A. Mines, Jay R. Winkler, and Harry B. Gray

Beckman Institute 139-74, California Institute of Technology,
Pasadena, CA 91125

Electron-transfer triggering has been employed in a comparison of the folding energetics and kinetics of cytochrome *c* from horse and *Saccharomyces cerevisiae*. These two proteins, with just 60% sequence identity but very similar backbone structures, fold at very different rates at a given denaturant concentration, but at nearly the same rate when their folding free energies are the same. Differences in the amino-acid sequences shift the position of the folding/unfolding equilibrium, but do not appear to alter the location of the transition state along the folding coordinate.

Determining the process by which a polypeptide attains its physiologically relevant conformation is of great current interest. One experimental approach involves measuring the folding kinetics of proteins by stopped-flow mixing: solutions of unfolded protein in high concentrations of a chemical denaturant (typically guanidine hydrochloride (GuHCl) or urea) are rapidly mixed with buffer solutions in order to dilute the denaturant concentration to a level at which the folded form is favored. Although this methodology is very useful, it can only be employed to observe folding processes that occur on timescales greater than ~1 ms, the minimum time required for solutions to mix. Secondary structure fluctuations in small polypeptides can occur on timescales as short as nanoseconds (1,2); these motions may play a role in the early events in folding reactions (3). It also has been suggested that the so-called "burst phase" in folding, referring to the formation of secondary structure and/or a hydrophobic core, can be a submillisecond process (4). Indeed, experimental evidence for a burst phase (≤ 5 ms) has been reported for at least seven proteins or protein fragments: ubiquitin (5), hen lysozyme (6), ferricytochrome *c* (7,8), ribonuclease A (9), *trp* aporepressor (10), barstar (11,12), and the IgG binding domain of protein G (13). If measurements made by time-resolved circular dichroism are included (dead time of about 10-20 ms), several others can be added to the list (14).

Methods have been developed that allow observation of submillisecond events in protein folding: photodissociation of CO from reduced cytochrome *c* has been employed to investigate folding processes occurring in the 10-ns to 1-ms time range (15); conventional temperature-jump methodology has been used to study a 300 μ s folding event in barstar (12); and laser-initiated temperature jump experiments have been employed to probe early events in the folding of apomyoglobin (16). In addition, a continuous-flow mixing apparatus that can achieve time resolution down to 100 μ s has been used to study fast folding events in ferricytochrome *c* (8). These methods are promising, but more techniques are needed to examine the submillisecond kinetics of protein folding.

We have developed an electron-transfer (ET) method of triggering protein folding that can be used to study events in the ns to s time range (17). We have employed this method to investigate the relationship between folding rate and free-energy change in ferrocyclochromes *c* from horse (h-cyt *c*) and yeast (y-cyt *c*). These proteins have similar folds, but distinct stabilities due to differences in amino-acid sequences. We find that the rates of the final folding phase in the two proteins differ significantly at a given denaturant concentration, but are comparable when the free energies of folding are matched.

Materials and Methods

Guanidine hydrochloride (GuHCl, ultrapure grade) was used as received from United States Biochemical. The concentration of GuHCl in all solutions used in equilibrium or kinetics experiments was determined using the empirical relationship between the concentration of GuHCl and the refractive index of GuHCl (18). $K_3[Co(C_2O_4)_3]$ (19) was obtained from T. Pascher. Horse heart cytochrome *c* (Sigma) was used without further purification. The methods used to determine equilibrium unfolding curves and to measure folding kinetics have been described previously (20).

Yeast iso-1-cytochrome *c* (Cys102Ser). The protein was a mutant of *Saccharomyces cerevisiae* iso-1-cytochrome *c* containing serine at position 102 (h-cyt *c* numbering system) in place of cysteine in order to prevent interprotein disulfide formation (21). Protein was isolated from 10-L cultures of a previously prepared GM-3C-2 cell line containing a plasmid with the mutant cyt *c* sequence (22,23); purification followed the procedure of Smith and coworkers (24), with the following modification: after dialysis, the protein was loaded onto a cation exchange column (SP Sepharose, 4 cm \times 2.5 cm i.d.) and eluted with a linear salt gradient (0 to 1 M NaCl, pH 7.0), rather than subjected to a batch adsorption procedure. Final purification was achieved using cation-exchange FPLC (Mono S; salt gradient, 0 to 1 M NaCl, pH 7.0); y-cyt *c* eluted at ~0.30-0.33 M NaCl.

Results and Discussion

Our method is based on the observation that the formal potentials of redox-active metal centers in proteins are "tuned" by the folding of the polypeptide chain around them; that is, metals in the hydrophobic interior of a folded protein often exhibit redox potentials

that are significantly different from those they would possess in an aqueous environment (25). A simple thermodynamic cycle (Figure 1) (26) indicates that such a shift in redox potential ($\Delta E_{F-U} = E_F - E_U$) reflects a difference in conformational stability between the two redox forms of the protein ($-nF\Delta E_{F-U} = \Delta\Delta G_{f,red-ox} = \Delta G_{f,red} - \Delta G_{f,ox}$). If this stability difference is sufficiently large, it should be possible to find conditions at which one redox form of the protein is unfolded and the other form is folded. For example, if the reduced form of the protein (P_{red}) is more stable than the oxidized protein (P_{ox}), it is expected that a higher concentration of a chemical denaturant will be required to unfold the reduced protein compared to the oxidized protein. In solutions with denaturant concentrations above the unfolding transition for the oxidized protein and below that for reduced protein, electron injection into the oxidized protein (unfolded) will lead to the formation of folded reduced protein. If the reduction is rapid enough, the folding of the reduced protein can be observed. Owing to the many well established techniques for reducing or oxidizing proteins on microsecond timescales or shorter (27,28), this method offers promise for studying very early events in protein folding.

Cytochrome *c* is a good candidate for ET-triggered folding studies. First of all, the heme group is linked to the polypeptide through covalent (thioether) bonds to Cys14 and Cys17. This linkage ensures that heme binding is not the rate-limiting step in the folding process. Secondly, it is known that the redox potential of folded cyt *c* (260 mV vs. NHE) (29) is ~ 400 mV higher than the potential for an exposed heme in aqueous solution (*ca.* -150 mV) (30), indicating that the reduced form of the protein is substantially more stable toward unfolding than the oxidized form (26,31). Thus, there should be a wide denaturant-concentration window in which folding can be triggered by rapid reduction of the heme.

Unfolding. The degree of folding of cyt *c* has been determined by monitoring the intensity of fluorescence from tryptophan-59 (32). The fluorescence is nearly completely quenched in the folded state, presumably via energy transfer to the nearby heme group (33). As the protein is unfolded by denaturant, the distance between the two chromophores increases, and the fluorescence signal intensifies dramatically (34).

Unfolding curves generated from fluorescence data for h-cyt *c* and y-cyt *c* in both oxidation states at 22.5 and 40.0 °C are well described as two-state transitions in which the free energy of folding is a linear function of denaturant concentration (slope $\equiv m_D$; Figure 2). It is evident from the unfolding curves (at both temperatures for both species of cyt *c*) that the reduced form is considerably more stable than the oxidized form (as predicted from electrochemical data). Indeed, the extrapolated values of $\Delta\Delta G_{f,red-ox}$ to zero denaturant concentration ($\Delta\Delta G_{f,red-ox}^\circ = -30$ to -35 kJ/mol; Table I) are close to those estimated from the difference in redox potentials ($-\Delta E_{F-U} \sim -400$ mV = -39 kJ/mol). It also is seen that, in both oxidation states at both temperatures, y-cyt *c* is considerably less stable than the corresponding h-cyt *c* protein: the ΔG_f values extrapolated to zero GuHCl concentration (ΔG_f°) are ~ 15 kJ/mol more positive for y-cyt *c* than for h-cyt *c*, and the unfolding midpoints ($[GuHCl]_{1/2}$) occur at GuHCl concentrations ~ 1.5 M lower for y-cyt *c* than for h-cyt *c* (Table I). The observed $[GuHCl]_{1/2}$ and m_D values for h-cyt *c*^{III} and y-cyt *c*^{III} at 22.5 °C are consistent with values reported in prior determinations at similar conditions using identical (or nearly identical) proteins (35-37). The same is true for the values found for y-cyt *c*^{II} at 22.5 °C (37).

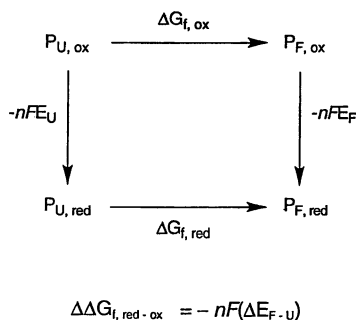


Figure 1. Thermodynamic cycle illustrating the relationship between folding free energies (ΔG_f) and reduction potentials (E) for a redox protein (P). n is the number of electrons transferred and F is the Faraday constant. Subscripts represent the states of the protein: U = unfolded, F = folded; ox = oxidized, red = reduced.

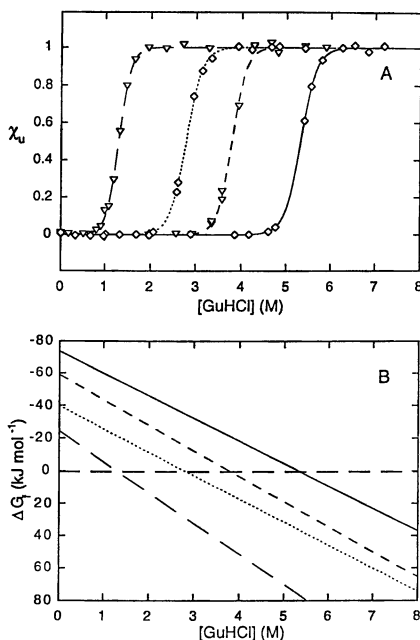


Figure 2. Equilibrium unfolding data for h-cyt c and y-cyt c at 22.5 °C, pH 7. (A) Unfolding curves determined from corrected fluorescence intensity data at 350 nm (y-cyt c , inverted triangles; h-cyt c , diamonds). y-cyt c^{III} (long dashes); y-cyt c^{II} (dashes); h-cyt c^{III} (dotted); h-cyt c^{I} (solid). (B) Plots of calculated ΔG_f vs. [GuHCl] curves based on the data set out in Table I.

Table I. Parameters describing the thermodynamics and kinetics of h-cyt *c* and y-cyt *c* folding and unfolding.

Protein	T (°C)	[GuHCl] _½ (M)	-Δ <i>G</i> _f [°] (kJ mol ⁻¹)	<i>m</i> _D (kJ mol ⁻¹ M ⁻¹)	<i>m</i> _D [‡] (kJ mol ⁻¹ M ⁻¹)	<i>m</i> _D [‡] / <i>m</i> _D
h-cyt <i>c</i> ^{III}	22.5(5)	2.8(1)	40(1)	14.3(4)		
h-cyt <i>c</i> ^{II}	22.5(5)	5.3(1)	74(3)	13.8(4)	5.2(5)	0.38
h-cyt <i>c</i> ^{III}	40.0(5)	2.4(1)	30(1)	12.2(4)		
h-cyt <i>c</i> ^{II}	40.0(5)	4.7(1)	61(10)	13.1(20)	5.5(5)	0.42
y-cyt <i>c</i> ^{III}	22.5(5)	1.3(1)	24(1)	18.9(5)		
y-cyt <i>c</i> ^{II}	22.5(5)	3.8(1)	59(4)	15.7(10)	5.4(5)	0.34
y-cyt <i>c</i> ^{III}	40.0(5)	0.8(1)	15(1)	18.1(8)		
y-cyt <i>c</i> ^{II}	40.0(5)	3.3(1)	45(3)	13.7(8)	5.8(5)	0.42

Error estimates are given in parentheses.

The stability differences between y-cyt *c* and h-cyt *c* must arise from side chain variations. Despite the nearly identical backbone folds of h-cyt *c* and y-cyt *c* (about 80% of the main chain to main chain hydrogen bonds are conserved between h-cyt *c* and y-cyt *c*, and the average deviation between main chain atoms is just 0.45 Å) (38), the two sequences are only 60% identical (39). Examination of the X-ray crystal structures of the two proteins reveals that the majority of the changes occur at surface residues, whereas the most highly conserved side chains are those that form the heme environment or are near the exposed heme edge (38,40,41). This is likely due to the fact that the latter residues play a key role in determining the redox potential of the heme, which allows the protein to carry out its physiological ET function. Six distinct domains can be identified in cytochrome *c*: three α-helical regions (amino terminus, residues 1-13; carboxy terminus, 86-104; 60's helix, 61-69), and three omega loops (residues 20-35, 36-60, and 70-85) (42). Only two of these regions, the 20-35 and 70-85 loops, display a high degree of sequence conservation (>80% identical) between y-cyt *c* and h-cyt *c* (39). The amino- and carboxy-terminal helices exhibit the lowest degree of similarity (58% and 37%, respectively).

We also have measured the absorption spectral changes that accompany unfolding of cyt *c* by GuHCl. The primary change observed for oxidized h-cyt *c* at 22.5 °C and pH 7 is a slight shift of the Soret band to higher energy with an accompanying increase in extinction coefficient (ε). Changes for the reduced protein (22.5 °C, pH 7) include a small shift to lower energy with an increase in ε for the Soret band, and a very slight shift to lower energy with a decrease in ε for the peaks at 520 and 550 nm.

The electronic spectrum of cyt *c* is dominated by the heme group and the observed absorption changes reflect either differences in axial ligation or heme

environment that occur upon unfolding (43). The axial histidine remains bound to the heme upon unfolding of the oxidized protein at pH values above ~ 2.5 (44); the axial methionine, however, is thought to be displaced by non-native histidine residues upon denaturation by GuHCl at pH 7 (8,45). Reduced unfolded cyt *c* is less well characterized but, presumably, the axial histidine remains bound and the methionine is replaced by another ligand at pH 7.

Difference absorption spectra corresponding to formation of unfolded reduced (cyt $c_{\text{U}}^{\text{II}} - \text{cyt } c_{\text{U}}^{\text{III}}$) and folded reduced (cyt $c_{\text{F}}^{\text{II}} - \text{cyt } c_{\text{F}}^{\text{III}}$) proteins exhibit similar overall shapes but differing extinction coefficients at the wavelengths used for most kinetics measurements (400, 420, and 550 nm) (20). Absorption spectral profiles of oxidized y-cyt *c* (in 0.18 M GuHCl) obtained upon thermal unfolding closely resemble those determined by denaturation with GuHCl. The transition is sufficiently steep and occurs at a high enough temperature ($T_{\text{m}} \sim 51$ °C) that the extinction coefficients at 22.5 and 40.0 °C are nearly identical ($\leq 2\%$ difference). These results are consistent with our observation that the shapes of GuHCl-induced unfolding curves at both temperatures are similar; differences are not significant compared to the noise observed in Soret-absorption titrations carried out at 40.0 °C. Thus the same $\Delta\epsilon$ values were used for the two temperatures.

Kinetics. The low reduction potential and kinetic accessibility of the heme group in unfolded cyt *c* place stringent demands on any photochemical ET-triggered folding scheme: a potent reductant must be generated without concomitant generation of oxidants, since reoxidation of the heme removes the driving force for folding. In practice, oxidants can be tolerated as long as the rate of the folding process is competitive with the rate of reoxidation. Microsecond reduction of unfolded cyt *c* by excited ruthenium-polypyridyl complexes has been achieved for both intramolecular (20) and bimolecular reactions (17), but in both cases, reoxidation is observed by photoproducts on a timescale of about 1 ms. Investigations using the bimolecular-reaction approach have indicated that a kinetics phase exhibiting a small heme absorption change may occur early in the folding of reduced cyt *c* at pH 7 (17,46). Here, however, we will restrict our analysis to the events associated with large heme absorption changes that occur on a >1 -ms timescale. For these experiments, a reduction scheme based on the photochemistry of $\text{Co}^{\text{III}}(\text{ox})_3^{3-}$ is used ($\text{ox} = \text{C}_2\text{O}_4^{2-}$) (20). UV-laser excitation of $\text{Co}^{\text{III}}(\text{ox})_3^{3-}$ solutions rapidly generates $\text{Co}_{\text{aq}}^{\text{II}}$ and a strong reductant, probably $\text{CO}_2^{\bullet -}$ ($E^\circ(\text{CO}_2/\text{CO}_2^{\bullet -}) = -2.0$ V) (47-49). This chemistry is thought to arise from the distinctive properties of the ligand-to-metal charge-transfer state that is formed upon excitation, $*[(\text{ox})_2\text{Co}^{\text{II}}(\text{C}_2\text{O}_4^{\bullet -})]$: Co^{II} is quite labile (50), and the oxalate radical anion is unstable with respect to carbon-carbon bond cleavage (51). Importantly, all of the presumed photoproducts in this reaction are either reductants ($\text{CO}_2^{\bullet -}$) or are effectively redox inactive ($\text{Co}_{\text{aq}}^{\text{II}}$, CO_2).

At very low and very high concentrations of denaturant, reduction of oxidized cyt *c* is not expected to lead to folding: at sufficiently low denaturant concentration, oxidized cyt *c* is already folded before the reduction, and at very high GuHCl concentrations, the unfolded reduced cyt *c* that is produced has no thermodynamic driving force to fold (Figure 2). These conditions have been used to characterize the $\text{Co}(\text{ox})_3^{3-}/\text{cyt } c$ photoreduction system. Laser flash photolysis of $\text{Co}(\text{ox})_3^{3-}$ in the

presence of oxidized *folded* y-cyt *c* at pH 7 and 40.0 °C leads to reduced folded y-cyt *c*. The kinetics of reduction are monophasic and, importantly, no secondary changes in absorption are observed out to ~1.0 s, indicating that the final product of reduction, y-cyt $c_{F_2}^{\text{II}}$ undergoes no observable conformational changes or reoxidation under these conditions. When the same experiment is conducted in the presence of 7.6 M GuHCl, significantly different results are obtained: the observed kinetics are biphasic, with the first phase corresponding to an accelerated reduction of the heme ($k_{\text{obs}} \sim 10^4 \text{ s}^{-1}$), and the second corresponding to reoxidation of the heme on a ~100-ms timescale.

Data gathered at a variety of GuHCl concentrations suggest that the accelerated reduction and oxidation seen at high concentrations of GuHCl do not represent an intrinsic dependence of these rates on the concentration of denaturant, but rather reflect differing properties of the folded and unfolded forms of the protein. The faster rate of reduction for the unfolded state is somewhat surprising given that its redox potential is ~0.40 V *lower* than that of the folded conformation. However, analogous behavior has been observed in microperoxidase-8, and has been attributed to increased accessibility of the heme (52). Accelerated reoxidation of unfolded cyt c^{II} is to be expected if oxidants are present, but it was hoped that the lack of oxidized photoproducts would lead to greater longevity of cyt c_{V}^{II} than is observed. Unphotolyzed $\text{Co}(\text{ox})_3^{3-}$ may be acting as the oxidant, although residual traces of oxygen cannot be ruled out as the source of reoxidation. The fact that folded cyt *c* does not reoxidize to any appreciable extent on the timescale of our measurements is a critical observation. Under conditions in which folding experiments are performed, the presence of a signal remaining (a plateau) after ~100 to 500 ms is a clear indication that at least some of the protein has folded to a form that has a near-physiological heme environment (redox potential and degree of solvent accessibility). A rate constant for folding can thus be determined even under conditions in which reoxidation competes with the folding reaction.

Folding. We expect to see protein folding upon rapid reduction of ferricytochrome *c* under conditions in which at least 50% of oxidized cyt *c* is unfolded and 90% of reduced cyt *c* is folded. Inspection of the equilibrium folding data (Figure 2; Table I) yields the following ranges of GuHCl concentration for the designated species and temperature: h-cyt *c* (22.5 °C), 2.8 - 5.0 M; h-cyt *c* (40.0 °C), 2.4 - 4.3 M; y-cyt *c* (22.5 °C), 1.3 - 3.5 M; y-cyt *c* (40.0 °C), 0.8 - 2.9 M. Excitation of $\text{Co}(\text{ox})_3^{3-}$ in the presence of y-cyt *c* at 40.0 °C in 1.0 M GuHCl yields biphasic kinetics (Figure 3). The first phase corresponds to rapid reduction of the heme, as seen above: the traces at 320 and 400 nm exhibit a large rise and bleach, respectively, and the trace at 550 nm shows a more modest signal increase. The second phase corresponds primarily to folding: the traces at 400 and 420 nm tend toward zero, but plateau after about 100 ms. The 550-nm trace does not exhibit a second phase, but simply levels immediately after the reduction phase. This behavior suggests that a fraction of the protein has undergone reoxidation rather than folding since a slight increase is expected at 550 nm for 100% folding, but (partial) reoxidation would contribute a (small) decrease to the signal. These profiles are nearly identical with those observed for h-cyt *c* in 2.7 M GuHCl at 40 °C, conditions at which essentially 100% of the sample folds. In the latter experiment, a full range of wavelengths was monitored, and the full transient spectra, just after reduction (at ~1 ms) and after completion of the folding phase (at ~50 ms), accord closely with the difference spectra of unfolded and folded reduced cyt *c*, respectively (17).

Kinetics of folding of both h-cyt *c* and y-cyt *c* have been measured over a wide range of GuHCl concentrations at both 22.5 and 40.0 °C (pH 7). Kinetics traces cannot always be fit adequately by single-exponential functions, but are well described by biexponential decays or functions describing a distribution of first-order rate constants (20). Many kinetics models can lead to the observation of biexponential behavior; in the case of folding, the most common involves the assumption that the reaction goes through a distinct intermediate, either "on-pathway" or "off-pathway" (53). This could be the case in our system; however, we have no *a priori* reason to suspect that this should be so. The distributed model is appealing because the nonexponential behavior is attributed to heterogeneity in the sample, which is likely to be the case in reactions such as protein folding. As a test of this model, the reoxidation kinetics at very high concentrations of GuHCl were examined. As in the folding reaction, this process involves the unfolded "state" as a reactant, and is therefore expected to exhibit heterogeneous kinetics. Indeed, reoxidation traces cannot be fit adequately using a monoexponential decay function, but are described well by the distributed function with a mean rate constant \bar{k}_{ox} . The kinetics also can be fit to a biexponential function, but assuming just two phases is somewhat arbitrary and chemically unreasonable (one must assume two distinct subpopulations of unfolded molecules with different tendencies for reoxidation). Here we report and discuss reoxidation mean folding rate constants (\bar{k}_f) extracted from fits to the distributed kinetics model. We emphasize, however, that our kinetics data alone provide insufficient evidence to distinguish conclusively between the two models.

For a given protein at 22.5 or 40.0 °C, slower observed rates and smaller final absorption signals are evident as the concentration of GuHCl is increased. Analysis using the distributed model, assuming a competition between folding and reoxidation, yields \bar{k}_f values that decrease as the concentration of GuHCl increases, whereas the reoxidation rate (\bar{k}_{ox}) is roughly constant as a function of GuHCl and (within error) independent of protein and temperature [$\bar{k}_{ox} = 11 \pm 5$ (h-cyt *c*, 40.0 °C); 14 ± 6 (y-cyt *c*, 40.0 °C); 13 ± 6 (h-cyt *c*, 22.5 °C); 7 ± 3 s⁻¹ (y-cyt *c*, 22.5 °C)]. These values for \bar{k}_{ox} are consistent with the observed \bar{k}_{ox} for "pure" reoxidation kinetics of y-cyt_{II} at very high concentrations of GuHCl. The widths of the Gaussian activation-free-energy distributions are similar at all concentrations of GuHCl at a given temperature, but are larger at 40.0 °C than at 22.5 °C. Plots of log \bar{k}_f (and thus ln \bar{k}_f) vs. [GuHCl] are linear for y-cyt *c* and h-cyt *c* at both temperatures (Figure 4). Analysis of the data at 22.5 °C using biexponential fits gives very similar results to those found using distributed fits; values for k_f are typically within 50% of the corresponding \bar{k}_f values.

The \bar{k}_f values in Figure 4 are averages of rates derived from kinetics data at 400, 420, and 550 nm (in cases where 550-nm data are relatively flat as in Figure 3, the mean of the 400 and 420-nm values is given). Close inspection of the data before averaging reveals that although linear behavior is evident, the values extracted from data acquired at different wavelengths often vary substantially. In particular, the values derived from 550-nm data are consistently smaller, often by as much as a factor of 2, than rates derived from 400 and 420-nm data. While this might simply reflect a large intrinsic uncertainty associated with the complexity of the system and the fact that \bar{k}_f is extracted from the observed rate by calculating the yield of folded proteins, it may also be

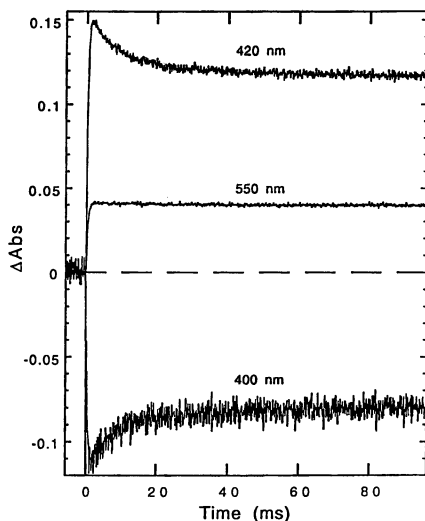


Figure 3. Transient absorption kinetics following excitation of a solution of y-cyt c^{III} ($\sim 15 \mu\text{M}$) and $\text{Co}(\text{ox})_3^{3-}$ ($32 \mu\text{M}$) in 1.0 M GuHCl (pH 7, 40 °C) monitored at 420, 550, and 400 nm.

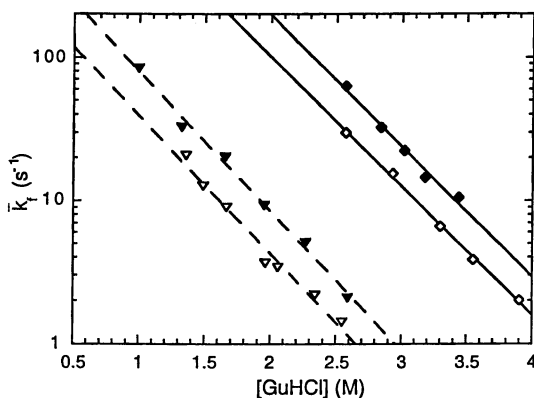


Figure 4. Plot of the folding rates extracted using distributed fits (\bar{k}_f) as a function of GuHCl concentration for y-cyt c (inverted triangles) and h-cyt c (diamonds) at 22.5 °C (open symbols) and 40.0 °C (filled symbols). Note that the y-axis is a log scale; thus linear fits to the data (solid lines, h-cyt c ; dashed, y-cyt c) indicate a linear relationship between ΔG_f^\ddagger and [GuHCl].

indicative of a systematic error in our analysis. One possible explanation is that the protein does not achieve the "final" folded form in the kinetics phase that we observe, but rather a *nearly* native state (in which the polypeptide has collapsed around the heme to afford a near-physiological redox potential) that exhibits a decreased intensity at 550 nm in the absorption spectrum relative to the fully folded form (possibly due to the lack of proper Met80 ligation). This would result in a decreased calculated yield of folding in our analysis of the 550-nm data and could account for the lower \bar{k}_f values that are observed relative to values obtained from 400 and 420-nm traces.

Assuming transition-state theory with a constant pre-exponential factor, a linear relationship between $\ln \bar{k}_f$ and [GuHCl] corresponds to a linear relationship between the activation free energy of folding (ΔG_f^\ddagger) and [GuHCl] (54,55):

$$\Delta G_f^\ddagger = \Delta G_f^{\ddagger 0} + m_D^\ddagger [\text{GuHCl}]$$

where m_D^\ddagger equals the slope of a plot of $RT \ln \bar{k}_f$ vs. [GuHCl]. Recalling that ΔG_f is also linearly related to [GuHCl] with a slope of m_D , ΔG_f^\ddagger (and thus $\ln \bar{k}_f$) must also be a linear function of ΔG_f with a slope equal to m_D^\ddagger/m_D . Plots of $\log \bar{k}_f$ vs. ΔG_f are shown in Figure 5; values of m_D^\ddagger and m_D^\ddagger/m_D obtained from the plots in Figures 4 and 5 are given in Table I.

Examination of the rate behavior exhibited by y-cyt *c* and h-cyt *c* yields a remarkable observation: at a given concentration of GuHCl at either 22.5 or 40.0 °C, the observed or extrapolated mean folding rate constant for h-cyt *c* is over an order of magnitude larger than that for y-cyt *c*; however, at a given folding free energy at either temperature, the rates of folding for the two proteins are comparable (Figures 4, 5). This result strongly suggests that the height of the barrier for this step in cyt *c*^{II} folding depends only on the relative energies of the initial and final states. This finding also provides compelling experimental support for the theoretical notion that the folding free energy is a key factor in determining folding rates (56,57). Furthermore, the fact that the h-cyt *c* and y-cyt *c* values of \bar{k}_f have distinct dependences on the concentration of GuHCl indicates that this denaturant serves to shift the folding/unfolding equilibrium, but does not have a specific effect in determining the folding rate.

The Hammond postulate states that for a chemical reaction with a single transition state, $\partial \ln k / \partial \ln K = \beta$, where β represents the position of the transition state along the reaction coordinate (58). Fersht and coworkers have applied this principle to the study of protein folding, assuming that $\partial \ln k / \partial \ln K = \partial \Delta G_f^\ddagger / \partial \Delta G_f = m_D^\ddagger / m_D$ (55). Although we do not have conclusive evidence that cyt *c*^{II} folding involves an intermediate, neither have we clearly demonstrated that the process is two-state. Nonetheless, recent studies have suggested that cyt *c*^{III} folding can be a two-state process under certain conditions (59), and we will proceed with the analysis noting the assumption made. Values of m_D^\ddagger/m_D for y-cyt *c* and h-cyt *c* at both temperatures studied are all near 0.4 (Table I), suggesting a relatively early transition state along the folding coordinate. The similarity in these values, a reflection of the striking agreement in rate/free energy behavior noted above, suggests that the residues that are not conserved between the two sequences do not significantly affect the location of the transition state, and the two proteins follow similar folding pathways. Interestingly, the m_D^\ddagger/m_D value reported for cyt *c*^{III} also is near 0.4 (0.46) (59), suggesting that the location of the transition state also is fairly insensitive to the oxidation state of the iron atom.

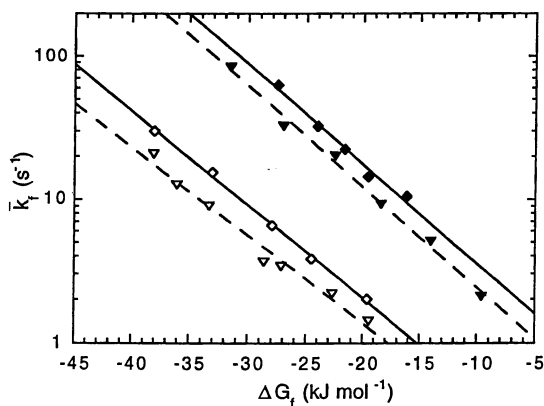


Figure 5. Plot of the folding rates extracted using distributed fits (\bar{k}_f) as a function of folding free energy (ΔG_f) for y-cyt *c* (inverted triangles) and h-cyt *c* (diamonds) at 22.5 °C (open symbols) and 40.0 °C (filled symbols). Note that the y-axis is a log scale; thus linear fits to the data (solid lines, h-cyt *c*; dashed, y-cyt *c*) indicate a linear relationship between ΔG_f^\ddagger and ΔG_f .

Another parameter, Φ_F , has been used to assess the environment of particular residues (mutations) in the transition state of folding (60). Φ_F is defined as $\Delta\Delta G_f^\ddagger/\Delta\Delta G_f$, where $\Delta\Delta G_f^\ddagger$ is the difference in the activation free energy of folding between the mutant and the wild-type, and $\Delta\Delta G_f$ is the difference in folding free energy between the two. Its value represents the extent to which the residue involved in the mutation experiences a native-like environment (often interpreted as "structure") in the transition state; a value of 0 corresponds to an unfolded environment for the residue, whereas a value of 1 implies a completely native-like environment (61). Again, this analysis is only meaningful when applied to a system in which there is only one transition state. With this assumption for cyt *c*^{II}, and viewing y-cyt *c* as a "mutant" of h-cyt *c*, we calculate a Φ_F value of ~0.5 over the concentration range of 1-3 M GuHCl (at 22.5 and 40.0 °C). This value suggests that (on average) the ~40 residues that differ between h-cyt *c* and y-cyt *c* find themselves in a partially folded environment in the transition state. With so many mutations, it is difficult to make a specific interpretation of this result. However, the value of ~0.5 is consistent with results of kinetics studies of h-cyt *c*^{III} that suggest early formation of structure in the N- and C-terminal helices, the two regions with the lowest homology between the yeast and horse proteins.

Summary

We have demonstrated that electron transfer can trigger protein folding. This initiation technique allows direct observation of folding kinetics over a wide range of timescales, including those in the submillisecond regime. Here we have used this method to compare the folding energetics and kinetics of h-cyt *c* and y-cyt *c*. These two proteins, with just 60% sequence identity but very similar backbone structures, fold at very different rates at a given denaturant concentration, but at nearly the same rate when their folding free energies are the same. The differences in the amino-acid sequences shift the position of the folding/unfolding equilibrium, but do not appear to alter the location of the transition state along the folding coordinate.

Acknowledgment

This work was supported by the National Science Foundation (MCB-9630465), the National Institutes of Health, and the Arnold and Mabel Beckman Foundation.

Literature Cited

- (1) Beals, J. M.; Haas, E.; Krausz, S.; Scheraga, H. A. *Biochemistry* **1991**, *30*, 7680-7692.
- (2) Williams, S.; Causgrove, T. P.; Gilmanshin, R.; Fang, K. S.; Callender, R. H.; Woodruff, W. H.; Dyer, R. B. *Biochemistry* **1996**, *35*, 691-697.
- (3) Wright, P. E.; Dyson, H. J.; Lerner, R. A. *Biochemistry* **1988**, *27*, 7167-7175.
- (4) Ptitsyn, O. B. *Prot. Eng.* **1994**, *7*, 593-596.
- (5) Khorasanizadeh, S.; Peters, I. D.; Butt, T. R.; Roder, H. *Biochemistry* **1993**, *32*, 7054-7063.

- (6) Itzhaki, L. S.; Evans, P. A.; Dobson, C. M.; Radford, S. E. *Biochemistry* **1994**, *33*, 5212-5220.
- (7) Elöve, G. A.; Bhuyan, A. K.; Roder, H. *Biochemistry* **1992**, *33*, 6925-6935.
- (8) Takahashi, S.; Yeh, S.-R.; Das, T. K.; Chan, C.-K.; Gottfried, D. S.; Rousseau, D. L. *Nat. Struct. Biol.* **1997**, *4*, 44-50.
- (9) Houry, W. A.; Rothwarf, D. M.; Scheraga, H. A. *Biochemistry* **1996**, *35*, 10125-10133.
- (10) Mann, C. J.; Matthews, C. R. *Biochemistry* **1993**, *32*, 5282-5290.
- (11) Agashe, V. R.; Shastry, M. C. R.; Udgaonkar, J. B. *Nature* **1995**, *377*, 754-757.
- (12) Nölting, B.; Golbik, R.; Fersht, A. R. *Proc. Natl. Acad. Sci. U.S.A.* **1995**, *92*, 10668-10672.
- (13) Kuszewski, J.; Clore, G. M.; Gronenborn, A. M. *Prot. Sci.* **1994**, *3*, 1945-1952.
- (14) Kuwajima, K.; Semisotnov, G. V.; Finkelstein, A. V.; Sugai, S.; Ptitsyn, O. B. *FEBS Lett.* **1993**, *334*, 265-268.
- (15) Jones, C. M.; Henry, E. R.; Hu, Y.; Chan, C.-K.; Luck, S. D.; Bhuyan, A.; Roder, H.; Hofrichter, J.; Eaton, W. A. *Proc. Natl. Acad. Sci. U.S.A.* **1993**, *90*, 11860-11864.
- (16) Ballew, R. M.; Sabelko, J.; Gruebele, M. *Nat. Struct. Biol.* **1996**, *3*, 923-926.
- (17) Pascher, T.; Chesick, J. P.; Winkler, J. R.; Gray, H. B. *Science* **1996**, *271*, 1558-1560.
- (18) Nozaki, Y. In *Methods in Enzymology*; C. H. W. Hirs and S. N. Timasheff, Eds.; Academic Press: New York, 1972; Vol. 26; pp 43-50.
- (19) Booth, H. S. *Inorganic Syntheses*; McGraw-Hill Book Company, Inc.: New York, 1939; Vol. 1.
- (20) Mines, G. A. Ph.D. Thesis, California Institute of Technology, 1997.
- (21) Narita, K.; Titani, K. *J. Biochem. (Tokyo)* **1969**, *65*, 259-267.
- (22) Bowler, B. E.; Meade, T. J.; Mayo, S. L.; Richards, J. H.; Gray, H. B. *J. Am. Chem. Soc.* **1989**, *111*, 8757-8759.
- (23) Mayo, S. L. Ph.D. Thesis, California Institute of Technology, 1988.
- (24) Cutler, R. L.; Pielak, G. J.; Mauk, A. G.; Smith, M. *Prot. Eng.* **1987**, *1*, 95-99.
- (25) Churg, A. K.; Warshel, A. *Biochemistry* **1986**, *25*, 1675-1681.
- (26) Bixler, J.; Bakker, G.; McLendon, G. *J. Am. Chem. Soc.* **1992**, *114*, 6938-6939.
- (27) Wuttke, D. S.; Bjerrum, M. J.; Chang, I.-J.; Winkler, J. R.; Gray, H. B. *Biochim. Biophys. Acta* **1992**, *1101*, 168-170.
- (28) Winkler, J. R.; Malmström, B. G.; Gray, H. B. *Biophys. Chem.* **1995**, *54*, 199-209.
- (29) Taniguchi, V. T.; Sailasuta-Scott, N.; Anson, F. C.; Gray, H. B. *Pure Appl. Chem.* **1980**, *52*, 2275-2281.
- (30) Santucci, R.; Reinhard, H.; Brunori, M. *J. Am. Chem. Soc.* **1988**, *110*, 8536-8537.
- (31) Hilgen-Willis, S.; Bowden, E. F.; Pielak, G. J. *J. Inorg. Biochem.* **1993**, *51*, 649-653.
- (32) Tsong, T. Y. *Biochemistry* **1976**, *15*, 5467-5473.
- (33) Fisher, W.; Taniuchi, H.; Anfinsen, C. B. *J. Biol. Chem.* **1973**, *248*, 3188-3195.
- (34) Tsong, T. Y. *J. Biol. Chem.* **1974**, *249*, 1988-1990.
- (35) Hickey, D. R.; Berghuis, A. M.; Lafond, G.; Jaeger, J. A.; Cardillo, T. S.; McLendon, D.; Das, G.; Sherman, F.; Brayer, G. D.; McLendon, G. *J. Biol. Chem.* **1991**, *266*, 11686-11694.

- (36) McLendon, G.; Smith, M. *J. Biol. Chem.* **1978**, *253*, 4004-4008.
- (37) Doyle, D. F.; Waldner, J. C.; Parikh, S.; Alcazar-Roman, L.; Pielak, G. J. *Biochemistry* **1996**, *35*, 7403-7411.
- (38) Brayer, G. D.; Murphy, M. E. P. In *Cytochrome c: a Multidisciplinary Approach*; R. A. Scott and A. G. Mauk, Eds.; University Science Books: Sausalito, 1996.
- (39) Moore, G. R.; Pettigrew, G. W. *Cytochromes c: Evolutionary, Structural, and Physicochemical Aspects*; Springer-Verlag: New York, 1990.
- (40) Bushnell, G. W.; Louie, G. V.; Brayer, G. D. *J. Mol. Biol.* **1990**, *213*, 585-595.
- (41) Berghuis, A. M.; Brayer, G. D. *J. Mol. Biol.* **1992**, *223*, 959-976.
- (42) Bai, Y.; Sosnick, T. R.; Mayne, L.; Englander, S. W. *Science* **1995**, *269*, 192-197.
- (43) Margoliash, E.; Schejter, A. *Adv. Protein Chem.* **1966**, *21*, 113-286.
- (44) Babul, J.; Stellwagen, E. *Biochemistry* **1972**, *11*, 1195-1200.
- (45) Muthukrishanan, K.; Nall, B. T. *Biochemistry* **1991**, *30*, 4706-4710.
- (46) Tezcan, F. A.; Telford, J. R., unpublished results.
- (47) Breitenkamp, M.; Henglein, A.; Lilie, J. *Ber. Bunsenges. Phys. Chem.* **1976**, *80*, 973.
- (48) Adamson, A. W.; Sporer, A. H. *J. Am. Chem. Soc.* **1958**, *80*, 3865-3870.
- (49) Pina, F.; Mulazzani, Q. G.; Venturi, M.; Ciano, M.; Balzani, V. *Inorg. Chem.* **1985**, *24*, 848-851.
- (50) Shinohara, N.; Lilie, J.; Simic, M. G. *Inorg. Chem.* **1977**, *16*, 2809-2813.
- (51) Chang, M.-M.; Saji, T.; Bard, A. J. *J. Am. Chem. Soc.* **1977**, *99*, 5399-5403.
- (52) McLendon, G.; Smith, M. *Inorg. Chem.* **1982**, *21*, 847-850.
- (53) Baldwin, R. L. *Fold. Des.* **1996**, *1*, R1-R8.
- (54) Chen, B. L.; Baase, W. A.; Nicholson, H.; Schellman, J. A. *Biochemistry* **1992**, *31*, 1464-1476.
- (55) Matouschek, A.; Fersht, A. R. *Proc. Natl. Acad. Sci. U.S.A.* **1993**, *90*, 7814-7818.
- (56) Bryngelson, J. D.; Onuchic, J. N.; Wolynes, P. G. *Proteins: Struct. Func. Gen.* **1995**, *21*, 167-195.
- (57) Onuchic, J. N.; Wolynes, P. G.; Luthey-Schulten, Z.; Socci, N. D. *Proc. Natl. Acad. Sci. U.S.A.* **1995**, *92*, 3626-3630.
- (58) Hammond, G. S. *J. Am. Chem. Soc.* **1955**, *77*, 334-338.
- (59) Sosnick, T. R.; Mayne, L.; Englander, S. W. *Proteins: Struct. Func. Gen.* **1996**, *24*, 413-426.
- (60) Fersht, A. R.; Matouschek, A.; Serrano, L. *J. Mol. Biol.* **1992**, *224*, 771-782.
- (61) Otzen, D. E.; Itzhaki, L. S.; El Masry, N. F.; Jackson, S. E.; Fersht, A. R. *Proc. Natl. Acad. Sci. U.S.A.* **1994**, *91*, 10422-10425.

Photoreduction-Triggered Folding of Cytochrome *c*: UV and Visible Resonance Raman Markers of Structure

T. S. Rush III and T. G. Spiro

Department of Chemistry, Princeton University, Princeton, NJ 08544

Gray and coworkers [1] have shown that early folding events can be monitored for cytochrome *c* by photoreducing the oxidized protein in the presence of 2.3 to 4.6 M guanidine hydrochloride (GuHCl); a range in which Fe[II] cytochrome *c* (cyt *c*^{II}) is folded while Fe[III] cytochrome *c* (cyt *c*^{III}) is not, as judged by tryptophan [Trp] fluorescence. We have monitored the state of the proteins *via* visible and UV resonance Raman [RR] spectroscopy, and find that the folding transitions are heterogeneous. Markers of heme distortion in the visible RR spectra, and also UVRR markers of the Trp H-bond, relax at significantly lower denaturant concentrations than does the Trp fluorescence. Thus there are multiple partially folded states of the protein; these transition off-sets are particularly pronounced for cyt *c*^{II}. At 4.5 M GuHCl, the Trp H-bond is broken in cyt *c*^{II}, while the heme is partially relaxed. Thus the early folding events following cyt *c*^{III} photoreduction at this denaturant concentration, probably lead to some partially folded state instead of to the fully folded native state.

It is possible to use photo-induced electron transfer to investigate early events in protein folding if the protein under study shows a substantial difference in the folding free energies of its oxidized and reduced forms [1,2]. In this case, denaturing conditions may be found in which one form of the protein is unfolded while the other is folded. Rapid photo-reduction or oxidation could therefore promote folding. Photo-triggering of this type was first demonstrated for cyt *c* [1a], which, in the presence of guanidine hydrochloride [GuHCl] at concentrations between 2.3 and 4.6 M, is largely unfolded when oxidized and largely folded when reduced. It was shown that photoreduction of the unfolded oxidized protein, *via* Ru(2,2'-bipyridine)₃²⁺ or Co(C₂O₄)₃³⁻, initiated the folding process. Transient heme absorption identified two folding phases with time constants of approximately 40 μs and 11 ms.

To elucidate the nature of these early folding events, one needs structural information on the folding intermediates. Such information can in principal be provided by vibrational spectroscopy since band positions and intensities are sensitive to molecular structure. Both infrared and Raman spectroscopy can be applied in a time resolved mode, and are adaptable to photo-initiation procedures [3,4]. Raman spectra can be resonance-enhanced, producing high sensitivity and selectivity for vibrational modes that are

sensitive to the heme structure [6]. In regard to protein folding, this type of resonance enhancement has recently been used to monitor heme ligation events occurring after 100 μ s in ultrarapid mixing-triggered folding studies [7]. For cyt *c*, visible enhancement primarily allows for the detection of the pronounced ruffling distortion of the porphyrin ring which is induced by the protein in the native state [8,9], as well as the heme's spin and oxidation state. In addition, ultraviolet excitation can be used to enhance vibrations of the aromatic residues. 230 nm excitation is selective for tryptophan and tyrosine, whose RR bands are sensitive to environmental effects, particularly H-bonding [10].

Preparatory to time-resolved RR studies of cyt *c* folding *via* photo-triggering, we have determined the dependence of the visible and UV RR spectra on GuHCl concentration in both Fe[III] and Fe[II] states. To our surprise, the different monitors of structure reveal distinctly different transition mid-points from those observed *via* Trp fluorescence measurements, establishing the existence of multiple partially folded forms. This heterogeneity in folding events has important implications for the investigation of folding dynamics.

Materials and Methods.

Horse heart cytochrome *c* (type VI) was purchased from Sigma and used without further purification. The chemically oxidized and reduced forms of the protein were obtained by the addition of excess $K_3Fe(CN)_6$ and sodium hydrosulfite, respectively. These oxidizing and reducing agents and their reaction products were dialyzed out overnight. Reduced samples were prepared, and handled thereafter, under high purity N_2 gas. Spectroscopic samples were prepared by adding aliquots of either the reduced or oxidized form of the protein to 100 mM phosphate buffered solutions containing the appropriate guanidine-HCl concentration. All samples were allowed to equilibrate at room temperature for at least 1 hour.

The fluorescence unfolding curve produced by 15 μ M protein solutions was obtained with a Perkin Elmer LS50 luminescence spectrometer. The tryptophan fluorescence was excited with 280 nm light, and detected at 350 nm [11]. Electronic absorption spectra of 0.25 mM protein solutions were recorded on a Hewlett Packard 8451A UV-Visible spectrophotometer. The RR spectra of 0.25 mM protein solutions were recorded on custom spectrometers composed of an appropriate excitation source, monochromator, and detector. The visible RR spectrometer consisted of a Krypton ion laser, a Spex triple-stage monochromator, and a Princeton Instruments diode array detector. The UVRR spectrometer consisted of a frequency doubled Argon ion laser, a Spex single grating monochromator, and a Princeton Instruments diode array detector. In both spectrometers, the samples were contained in spinning quartz NMR tubes, and illuminated in a 135° backscattering geometry. The scattered light was collected, *f*-matched and focused onto the slit of the monochromator. The laser power at the sample was 20 mW for the visible-excited spectra, and 1 mW for the UV-excited spectra. Sample integrity was checked by electronic absorption spectroscopy before and after the experiments.

Results and Discussion.

Cyt *c* denaturation can be monitored via the fluorescence produced by the single tryptophan residue, Trp 59 [11]. In the native state, the indole ring donates a H-bond to a heme propionate sidechain, resulting in fluorescence quenching *via* Förster energy transfer to the heme. Denaturation releases the indole ring, resulting in fluorescence recovery. Our measurements [figure 1] are in agreement with those published previously [1]. The fluorescence reveals cooperative denaturation curves, with transition midpoints at ~ 2.8 M and ~ 5.0 M GuHCl, for oxidized and reduced

cyt *c*. The extra stability of the reduced form means that cyt c^{III} reduction is accompanied by folding in the 2.8 to 5.0 M GuHCl concentration range[1]. However, we note that the cyt c^{III} fluorescence is not constant beyond the folding transition, but increases linearly between 3.4 and 7.0 M GuHCl. This behavior implies that the average indole-heme distance continues to increase after the cooperative unfolding transition, and that the unfolded state is not homogeneous.

Moreover the unfolded state cannot be an ideal random coil polypeptide, because the Fe[III] ion continues to be bound by two protein residues. It has been shown [11b,12] that the native Met 80 ligand is replaced by non-native His sidechains at high GuHCl concentration, while the native His 18 remains intact. Consistent with this finding is the absorption spectrum of cyt c^{III} , whose characteristic 695 nm [Met]S \rightarrow Fe charge transfer transition is found to be lost at \sim 3 M GuHCl [11b], but whose Soret and α/β absorption bands remain characteristic of a low-spin Fe[III] heme. Likewise, the Soret-excited RR spectrum in 3.5 M GuHCl [Figure 2] shows high-frequency porphyrin skeletal modes which are at characteristic positions for low-spin Fe[III] heme[6], although their frequencies are slightly higher than in the native form. These small upshifts can be reproduced by adding imidazole to native cyt c^{III} , resulting in displacement of the Met 80 ligand [7]. Thus the denatured cyt c^{III} RR spectrum is that expected of a bis-histidine heme.

However, the heme structure is partially relaxed upon denaturation, as is indicated by the changes in the low-frequency RR spectrum [figure 2]. These changes include frequency shifts of the porphyrin in-plane skeletal modes [e.g. ν_8 (349 cm^{-1}), ν_7 (702 cm^{-1}) and ν_{10} (1636 cm^{-1})], frequency shifts in the propionate modes [e.g. $\delta(\text{C}_\beta\text{C}_\alpha\text{C}_\alpha)$ (381 cm^{-1})], and most importantly, the loss of intensity of the out-of-plane skeletal modes [e.g. γ_{22} (447 cm^{-1}), γ_{12} (521 cm^{-1}) and γ_{21} (568 cm^{-1})]. The latter out-of-plane modes are activated in the native cyt *c* RR spectrum [9] by the pronounced ruffling distortion imposed on the heme by the protein [8]. The out-of-plane bands are known to only disappear completely upon very harsh acid denaturation of cyt c^{III} , conditions which favor protonation and release of the native His 18, as well as the Met 80 ligand, leaving a bis-aquo heme[13]. In the acid-denatured and molten globule "A state" of cyt c^{III} [prepared by adding salt to acid-denatured cyt c^{III} in order to screen the electrostatic repulsion of the surface charges] the out-of-plane mode intensity is diminished by about one-half [13]. Similar behavior can be seen in neutral 3.5 M GuHCl [Figure 2]; the weak γ_{12} band can no longer be seen, while the strong γ_{21} band has lost about half its intensity. Thus the protein-induced ruffling of the heme is partially, but not completely abolished in the unfolding transition. As in the A state, there is evidence of remnant protein structure around the heme, although the secondary structure of the polypeptide is severely diminished, as judged by CD measurements [14].

Similar relaxation of the heme accompanies cyt c^{II} unfolding [Figure 3]; γ_{22} , γ_{12} and γ_{21} lose intensity, and the propionate bending and in-plane skeletal modes are shifted in frequency. At 5.0 M GuHCl the reduced heme becomes partially oxidized, despite careful exclusion of O_2 with a N_2 purge, as evidenced by the upshift of the ν_4 band [Figure 3], a marker of the oxidation state [6]. This band displays two components, at $1363\text{ [Fe}^{\text{II}}]$ and $1373\text{ [Fe}^{\text{III}}]\text{ cm}^{-1}$; the latter shows up weakly at 4.5 M GuHCl, and strongly at 5.0 M. Unfolding is expected to lower the heme reduction potential appreciably [15], because of the Met/His ligand replacement, and because of exposure of the heme to water. Evidently trace oxidants in the buffer are then able to oxidize the heme.

When the 230 nm-excited UVR spectra are examined [Figures 4 and 5], denaturation is seen to result in striking changes of the Tyr and Trp signals. The band intensities are all diminished, relative to the native protein, reflecting red-shifts in the excitation profiles, as a result of H-bond breaking [10]. [Three of the four Tyr residues are H-bonded in the native structure, as is the one Trp residue.] Moreover,

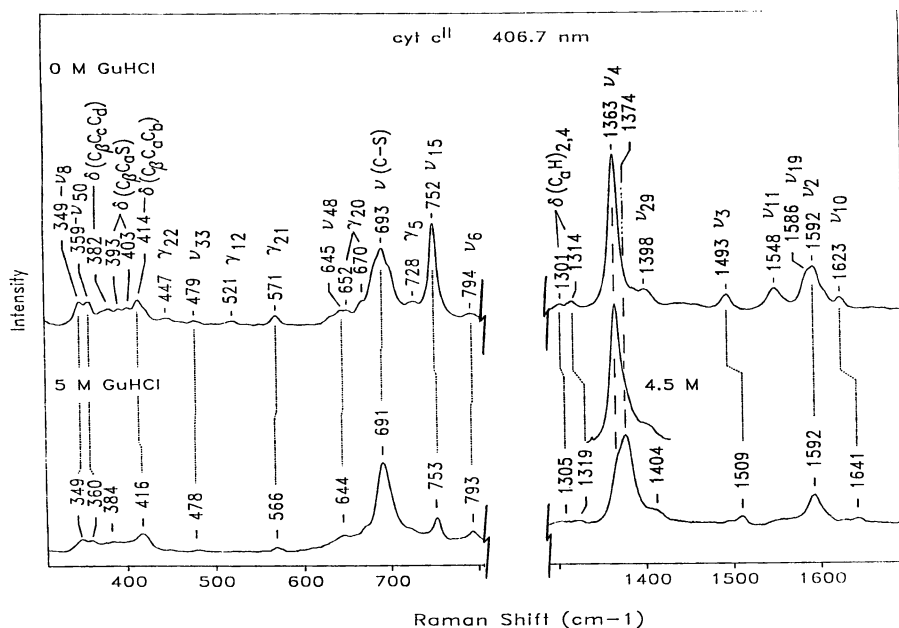


Figure 3. Visible RR spectra of Fe[II] Cytochrome *c* in 0 M (top) and 5 M (bottom) GuHCl.

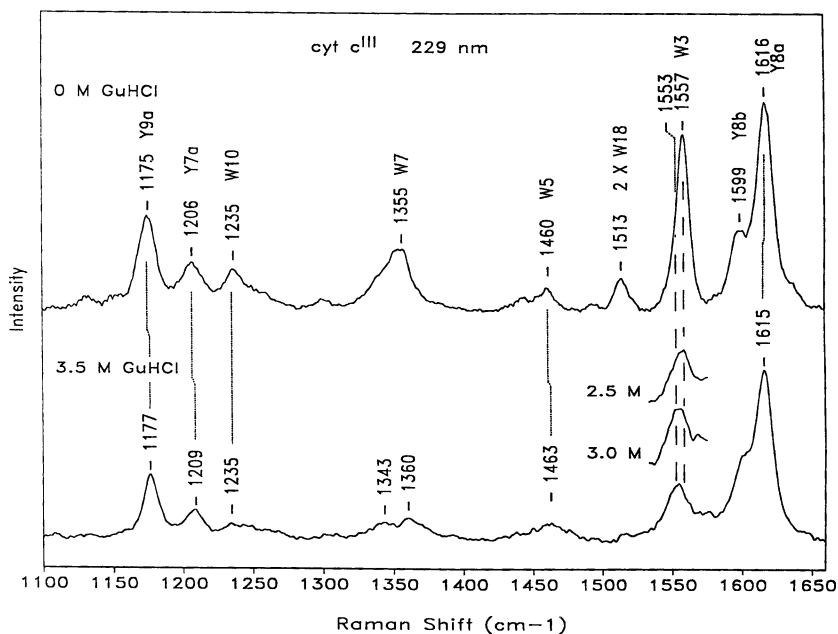


Figure 4. UVRR spectra of Fe[III] Cytochrome *c* in 0 M (top) and 3.5 M (bottom) GuHCl; the inset peaks show the evolving W3 band shape.

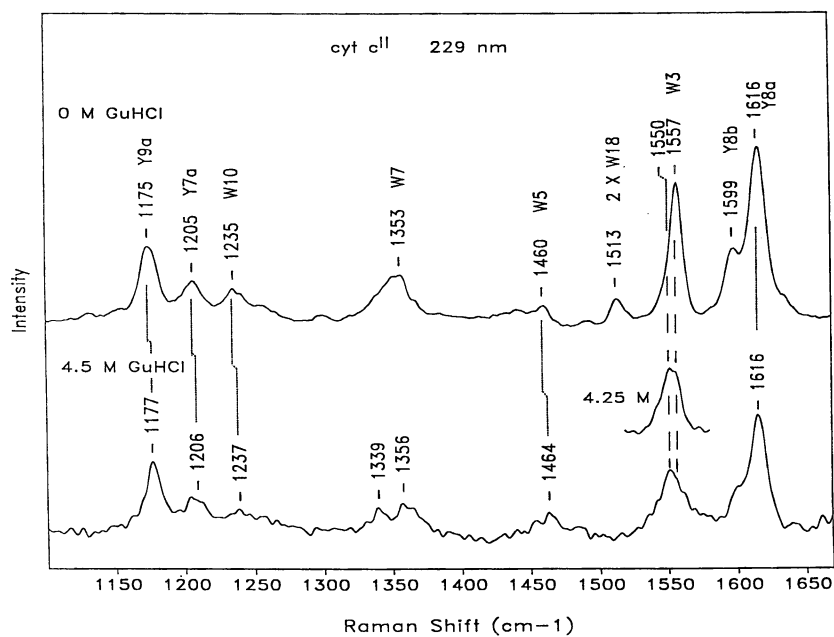


Figure 5. UVRR spectra of Fe[II] Cytochrome *c* in 0 M (top) and 5 M (bottom) GuHCl; the inset peak shows the mid-point transition for W3.

the Trp W3 band is downshifted [1557 - 1550 cm^{-1}] and broadened. The frequency of this ring mode is known to respond to changes in the dihedral angle between the indole ring and the C_β atom [9]. Its shift and broadening upon denaturation reflect the population of multiple side-chain orientations, once the H-bond to the heme propionate is broken [10,16]. Finally the Trp W7 changes from an asymmetric band at 1354 cm^{-1} to a 1360/1343 cm^{-1} doublet, consistent with exposure of the indole sidechain to water [10,17]. These changes are all similar to those seen upon acid unfolding of cyt c^{III} [13].

Importantly, the Raman changes do not track the Trp fluorescence changes as a function of GuHCl concentration [Figure 1]. The Raman transitions precede the fluorescence transitions significantly, showing that denaturation is not a two-state process. The mid-points for the heme out-of-plane RR intensity loss are lower by ~0.5 M in GuHCl concentration, establishing a range of denaturant concentrations over which the heme distortion is relaxed, even while the Trp sidechain remains in the vicinity of the heme.

Even more telling is the behavior of the W3 UVRR band, which shifts and broadens before the Trp fluorescence recovery, implying that the Trp H-bond breaks, allowing multiple sidechain orientations, before the Trp departs the vicinity of the heme. Similar behavior was observed for the cyt c^{III} A state, which has low fluorescence, but a broadened W3 UVRR band [13]. It is plausible that a similar state is produced by GuHCl, prior to complete unfolding. The transition mid-points for fluorescence and for W3 differ only slightly for cyt c^{III} , but greatly for cyt c^{II} [Figure 1]. The W3 midpoint for cyt c^{II} is reached at 4.25 M and the transition is complete by 4.5 M GuHCl [Figure 5], while the fluorescence transition is more gradual, with a 5.2 M mid-point [Figure 1]. Thus cyt c^{II} has a larger stability range for partially unfolded forms than cyt c^{III} .

These findings have important implications for the study of cyt c folding dynamics. The existence of partially unfolded states makes it unlikely that folding can be treated as a homogenous process. Different probes of structure are likely to yield different time constants for early folding events.

Acknowledgments.

This work was supported by NIH grant GM 33576 from the National Institutes of General Medical Sciences. T.S.R. is additionally supported by a NIH postdoctoral fellowship.

References.

1. (a) Pascher, T.; Chesick, J.P.; Winkler, J.R.; Gray, H.B. *Science*, **1996**, *271*, 1558-1560. (b) Mines, G.A.; Pascher, T.; Lee, S.C.; Winkler, J.R.; Gray, H.B. *Chemistry & Biology*, **1996**, *3*, 491-497.
2. Wittung-Stafshede, P.; Gray, H.B.; Winkler, J.R. *J. Am. Chem. Soc.*, in press (1997).
3. (a) Phillips, C.M.; Mizutani, Y.; Hochstrasser, R.M. *Proc. Natl. Acad. Sci. USA*, **1995**, *92*, 7292-7296. (b) Williams, S.; Causgrove, T.P.; Gilmanshin, R.; Fang, K.S.; Callender, R.H.; Woodruff, W.H.; Dyer, R.B. *Biochemistry*, **1996**, *35*, 691-697. (c) Gilmanshin, R.; Williams, S.; Callender, R.H.; Woodruff, W.H.; Dyer, R.B. *Proc. Natl. Acad. Sci. USA*, **1997**, *94*, 3709-3713.
4. (a) Rodgers, K.R.; Su, C.; Subramaniam, S.; Spiro, T.G.; *J. Am. Chem. Soc.*, **1992**, *114*, 3697-3709. (b) Jayaraman, V.; Rodgers, K.R.; Mukerji, I.; Spiro, T.G. *Science*, **1995**, *269*, 1843-1848.
5. For example see: (a) Carey, P. *Biochemical Applications of Raman and Resonance Raman Spectroscopies*; Academic Press: New York, NY, 1992. (b)

- Tu, A. *Raman Spectroscopy in Biology: Principles and Applications*; John Wiley & Sons: New York, NY, 1982.
6. For example see: (a) Spiro, T.G. in *Iron Porphyrins, part II*; Lever, A.B.P. and Gray, H.B. eds.; Addison-Wesley Publishing Co.: Reading, MA, 1983; pp 89-159. (b) Spiro, T.G. *Adv. Protein Chem.*, **1985**, *37*, 111-159. (c) Spiro, T.G.; Li, X.Y. in *Biological Applications of Resonance Raman Spectroscopy*; Spiro, T.G. ed.; John Wiley & Sons: New York, NY, 1988; pp 1-37.
 7. Takahashi, S.; Yeh, S.-R.; Das, T.K.; Chan, C.-K.; Gottfried, D.S.; Rousseau, D.L. *Nature Struct. Biol.*, **1997**, *4*, 44-50.
 8. (a) Louie, G.; Brayer, G.D. *J. Mol. Biol.*, **1990**, *214*, 527-555. (b) Berghuis, A.M.; Brayer, G.D. *J. Mol. Biol.*, **1992**, *223*, 959-976.
 9. Hu, S.; Morris, I.K.; Singh, J.P.; Smith, K.M.; Spiro, T.G. *J. Am. Chem. Soc.*, **1993**, *115*, 12446-12458.
 10. For example see: (a) Harada, I.; Takeuchi, H. in *Spectroscopy of Biological Systems*; Lark, R.J.H and Hester, R.E. eds.; John Wiley & Sons: New York, NY, 1986; pp 113-175. (b) Austin, J.C.; Jordan, T.; Spiro, T.G. in *Advances in Spectroscopy: Biomolecular Spectroscopy*; Hester, R.E. and Clark, R.J.H. eds.; John Wiley & Sons: New York, NY, 1993, Vol. 20A; pp 55-127.
 11. (a) Tsong, T.Y. *Biochemistry*, **1976**, *15*, 5467-5473. (b) Brems, D.N.; Stellwagen, E. *J. Biol. Chem.*, **1983**, *258*, 3655-3660.
 12. (a) Muthukrishnan, K.; Nall, B.T. *Biochemistry*, **1991**, *30*, 4706-4710. (b) Elove, G.A.; Bhuyan, A.; Roder, H. *Biochemistry*, **1994**, *33*, 6925-6935.
 13. Jordan, T.; Eads, J.C.; Spiro, T.G. *Protein Science*, **1995**, *4*, 716-728.
 14. McLendon, G.; Smith, M. *J. Biol. Chem.*, **1978**, *253*, 4004-4008.
 15. Bixler, J.; Bakker, G.; McLendon, G. *J. Am. Chem. Soc.*, **1992**, *114*, 6938-6939.
 16. Miura, T.; Takeuchi, H.; Harada, I. *J. Raman Spectrosc.*, **1989**, *20*, 667-671.
 17. Miura, T.; Takeuchi, H.; Harada, I. *Biochemistry*, **1988**, *27*, 88-94.

Chapter 12

A Probe of Metal–Ligand Interactions in Cupredoxin by Active Site Redesign and Resonance Raman Spectroscopy

R. S. Czernuszewicz¹, B. C. Dave², and J. P. Germanas¹

¹Department of Chemistry, University of Houston, Houston, TX 77204

²Department of Chemistry, Southern Illinois University, Carbondale, IL 62901

High-resolution resonance Raman (RR) spectra are reported for bacterially expressed azurin from *Pseudomonas aeruginosa* (wild type, WT) and its three Cu-site mutants, two with Met121 replaced by Leu (M121L) or Gly (M121G) and one with His46 replaced by Asp (H46D). Each protein shows the characteristic type 1 Cu RR spectrum with four dominant bands near 400 cm⁻¹. The spectral assignments are supported by S and Cu isotope substitutions and the bands showing the highest intensity and largest ^{34/32}S and ^{65/63}Cu shifts, 408 (WT), 405 (M121L), 401 (M121G), and 399 cm⁻¹ (H46D), are identified with the predominantly Cu–S_{Cys} stretching vibration, $\nu(\text{CuS})$. The decreased $\nu(\text{CuS})$ frequency in M121G and H46D implies a weakening of the Cu–S_{Cys} interaction in the mutants. This weakening is ascribed to a displacement of the Cu atom from the trigonal N₂S coordination plane in the direction of the fourth ligand (tetrahedrality of the Cu site), consistent with the appearance of a rhombic EPR spectrum and intensification of an absorption band near 460 nm. Examination of the overtone and combination RR bands suggests pronounced structural distortions along the (Cys)S → Cu(II) charge transfer transition in the mutants. The M121G azurin binds exogenous azide ligand, whereupon the extent of the Cu–S_{Cys} interaction is greatly diminished, generating an extremely tetrahedrally distorted Cu coordination environment.

The mononuclear blue (or type 1) copper proteins (cupredoxins) are ubiquitous metalloproteins found in plants and bacteria that show an intense absorption near 600 nm. The members of this class of relatively small (10–20 kDa) metalloproteins, which act as electron transport agents in nature due to their facile electron transfer dynamics coupled with ready accessibility of Cu(I) and Cu(II) oxidation states (1, 2), have long been a subject of vigorous physicochemical investigation. Besides the characteristic electronic absorption spectra, the cupredoxins also share an unusually rare set of physical and chemical properties (3, 4) which include an axial or rhombic EPR signal in the oxidized form with extremely narrow hyperfine splitting constants (< 60 × 10⁻⁴ cm⁻¹). For an active site comprised of a mononuclear copper center, these proteins display a wide range of relatively high redox potentials varying from 170 to 680 mV as compared to 160 mV for an isolated Cu²⁺/Cu⁺ couple. These unique properties and the highly different reactivities as compared to smaller inorganic analogs are assumed

to be enforced by the protein biopolymer leading to imposition of peculiar geometric and electronic configurations at the active site.

High-resolution X-ray crystal structures are now available for a number of cupredoxins (5, 6), including four plastocyanins from *Populus nigra* (7, 8), *Oleander nerium* (9), *Enteromorpha prolifera* (10), and *Chlamydomonas reinhardtii* (11), two azurins from *Alcaligenes denitrificans* (12) and *Pseudomonas aeruginosa* (13), two pseudoazurins from *Alcaligenes faecalis* (14, 15) and *Methylobacterium extorquens* (16), two amicyanins from *Paracoccus denitrificans* (17) and *Thiobacillus versutus* (18), a stellacyanin from *Cucumis sativus* (19), and the cucumber basic protein (CBP) (20). In spite of their widely disparate sources, a great degree of homology is observed in their structures. The coordinating environment around Cu is comprised of three strongly interacting ligands: one thiolate S atom from cysteine and two imidazole N atoms from histidines forming a distorted trigonal planar geometry with highly covalent copper-ligand bonds (~1.9–2.2 Å). These three residues are found to be conserved in all cupredoxins. The crystal structures also implicate a weakly interacting fourth ligand, usually a thioether S atom from methionine, which is ligated axially to the metal center at a longer distance (~2.6–3.1 Å); sometimes a peptide carbonyl oxygen atom is found on the other side of the trigonal plane, at an even longer distance (~3.1–3.9 Å). Although methionine is a conserved residue in most of the cupredoxins, it is absent in *C. sativus* (19) and *Rhus vernicifera* (21) stellacyanins, zucchini mavycyanin (22, 23), *Arabidopsis thaliana* blue Cu-binding protein (24), horseradish uromyocyanin (25), and *Neurospora crassa* laccase (26). In azurin from *P. aeruginosa*, which is the subject of this research, the strong trigonal coordination to the Cu center is from His46, Cys112, and His117, and the two weak axial interactions are from Met121 and Gly45 (13, 27, 28), as shown schematically in Figure 1.

In order to explain the variable and unusual reactivities for an ostensibly similar type 1 Cu site in cupredoxins, Eyring *et al.* (29, 30) formulated a rack mechanism (31–33) based on the hypothesis that the key functional groups are distorted by the overall protein conformation, thereby leading to altered active site properties. A similar mechanism was put forth by Vallee and Williams, who called the altered state the entatic state (34). As it is not possible for unrestrained ligands to adjust to the entatic state on their own, the conformational effects of polypeptide chains become exceedingly important to manipulate the protein reactivity. A very effective method of changing the ground state energy is to modify the active site by substitution of the coordinating residues with other amino acids by the site-directed mutagenesis.

The *P. aeruginosa* azurin gene has been cloned (35) and expressed in *E. coli* (36). Exchange of the conserved residues by site-directed mutagenesis has opened new avenues to target and study the type 1 Cu site. The mutations of conserved residues lead to large differences in the ground and excited state properties, sometimes leading even to the destruction of the blue Cu center. Recently, by characterizing a series of azurin mutants where the Met121 site was replaced with a variety of amino acids, Karlsson *et al.* showed that the Met residue is not a prerequisite for forming a type 1 Cu center (37). The overall properties of the type 1 Cu center were preserved; however, large differences in the electronic absorption spectra, EPR characteristics and the redox potentials were observed as a result of the mutations. Similarly, Germanas *et al.* have shown that replacement of the His46 residue with Asp preserves the blue Cu active site, but with the EPR signal acquiring an increased rhombic component (38, 39). Apparently, the blue Cu center can retain most of its properties under different coordinating environments with a considerable flexibility in the range of metal-ligand interactions.

The unique structural, electronic and physical properties of the type 1 Cu site are believed to be due mainly to the short Cu–S(Cys) interaction. Normal copper proteins (type 2) (3, 5) with (N/O)₄ coordination spheres have physical properties that resemble small inorganic analog complexes: weak ligand field ($d \rightarrow d$) transitions, characteristic of tetragonal Cu(II), and hyperfine constants in the EPR spectra between 130 and 180 × 10⁻⁴ cm⁻¹. Also, model complexes with long Cu–S interactions (40) fail to reproduce the blue color and the reduced hyperfine coupling constants so

characteristic of the type 1 Cu site. Recently Kitajima *et al.* (41) have succeeded in preparing a series of Cu(II) thiolate complexes with the sterically hindered tris-(pyrazolyl)borate ligand that successfully mimic the short Cu-S(thiolate) bond and display the intense blue color and the small A_{\parallel} values of type 1 Cu sites. However, these complexes have redox potentials that are more negative than those of cupredoxins. On the other hand, a genetically engineered variant of Cu, Zn superoxide dismutase (SOD) with one of its coordinated His residues replaced with Cys was shown recently by Valentine and co-workers (42) to form a cupredoxin-like center. The mutant SOD protein, however, showed a very strong electronic absorption around 450 nm and a relatively weak one at 595 nm along with a very strongly rhombically distorted EPR signal.

Increased optical absorbance near 450 nm and the rhombic EPR signal have been observed to be correlated in cupredoxins. In comparing spectral features of a large number of cupredoxins, Han *et al.* (43) have noticed that the ratio of the molar absorptivities for electronic transitions in the violet and red regions, $R_f = \epsilon(450 \text{ nm})/\epsilon(600 \text{ nm})$, increases as the EPR signal becomes more rhombic. Based on this observation, they proposed that the high absorbance at ~ 450 nm and the rhombic EPR signal are manifestations of a distortion of the Cu active site toward a more tetrahedral geometry via changes in the Cu-ligand bond lengths. As judged by the range of the R_f values and EPR signals associated with different cupredoxins and mutants, it can be safely concluded that, although a short (~ 2.1 Å) Cu-S bond is an absolute necessity for a type 1 Cu active site (39), the choice of other ligands and the local geometry of the Cu coordination sphere is not highly restrictive. In other words, it is a small but finite range of highly covalent interactions between the Cu(II) ion and thiolate S of the Cys side chain that grants a specific cupredoxin with the variable physical properties.

The differences in the Cu-S_{Cys} interactions are clearly evident in the resonance Raman (RR) spectra of cupredoxins, which have long been known to show intense bands in the region between 350 and 450 cm^{-1} associated with vibrations of the Cu(II)-Cys unit (44-46). However, different families of cupredoxins, as well as individual members and site-specific mutants of the same protein, exhibit considerable dissimilarities with respect to the number of RR modes observed, their frequencies, relative intensities, and band widths (44-53). All these point to a "non-conserved" nature of the Cu-S_{Cys} interaction which is presumably controlled and regulated by conformational influence of the polypeptide sub-matrix.

In the present study, the Cu-S_{Cys} interaction in cupredoxins is investigated with a combination of the site-directed mutagenesis, production of isotopically labeled proteins, and cryogenic temperature resonance Raman spectroscopy carried out on azurin from *P. aeruginosa*. We first demonstrate the existence of the (predominantly) Cu-S_{Cys} stretching vibration, $\nu(\text{CuS})$, in the type 1 Cu vibrational spectrum by examining the frozen solution (77K) RR spectra of natural isotope abundance and ^{34}S and $^{63/65}\text{Cu}$ isotope-labeled wild type (WT) azurin and its three Cu site mutants, two with Met121 replaced by Leu (M121L) or Gly (M121G) (37) and one with His46 replaced by Asp (H46D) (38, 39). We then assign and interpret the azurin RR vibrational modes in terms of the type 1 Cu structure and describe the differences in the dominant Cu-S_{Cys} interaction at the metal site due to endogenous protein ligand replacements and binding of exogenous ligands.

Materials and Methods

Sample Preparations. The ^{34}S enriched samples of *P. aeruginosa* azurin and its site-specific mutants were prepared by growing bacterial cultures in minimal medium M9 using 1 g/L of 90% ^{34}S enriched ammonium sulfate (ICON, Summit, NJ). The ^{63}Cu and ^{65}Cu isotopically substituted azurins were prepared from the respective apoproteins by reconstituting with $^{63/65}\text{Cu}$ -labeled nitrate salts (99 % enrichments) which were a generous gift from Dr. J. Sanders-Loehr (Oregon Graduate Institute). All protein isolation and purification was carried out according to established

procedures (37–39). The M121G–azide derivative was prepared by titration with 1M NaN_3 until the ratio of molar absorptivities of the 420 and 615 nm absorption bands equaled 2.5 (54, 55).

Spectroscopy. To improve spectral resolution all the RR spectra were obtained at ~ 77 K by collecting backscattered photons with 2–3 cm^{-1} slit widths at 0.2–0.5 cm^{-1} increments directly off the surface of a frozen protein solution (~ 1 mM in 10 mM pH 8 tris buffer) kept in a liquid- N_2 dewar (56). To ensure accurate isotope shift measurements, two protein samples to be compared were placed side by side on the cold finger so that the RR data could be collected under the same conditions. Excitation provided by a Coherent K-2 Kr^+ ion laser (413.1, 568.2, and 647.1 nm) and conventional scanning Raman instrumentation equipped with a Spex 1403 double monochromator (with 1800 grooves/mm gratings) and a Hamamatsu 928 photomultiplier detection system were used to record the spectra under the control of a Spex DM3000 microcomputer system (57). Typical laser power was 100 to 150 mW, and average of three to four scans at 1 sec/point and 0.2–0.5 $\text{cm}^{-1}/\text{sec}$ increments were taken to improve signal-to-noise ratios. The slit widths and the number of scans were both increased for acquiring the data in the overtone and combination band regions (>600 cm^{-1}), typically by a factor of two. All spectra were calibrated using the known vibrational frequencies of CCl_4 and CH_2Cl_2 . Raman data manipulation was performed using LabCalc software (Galactic Industries Inc.) on a 486-DX 33 MHz PC microcomputer. The quality of the observed Raman signal was very high and no baseline correction or smoothing were applied. UV-visible absorption spectra were obtained at room temperature using an HP-8542 diode array spectrophotometer.

Identification of Cu(II)–S(Cys) Stretching Vibration

Despite the low effective coordination number of the metal site, the RR spectra of cupredoxins (44–53) are unusually complicated and exhibit a complex set of dominant bands (up to 9) of variable frequencies and relative intensities in the 300–450 cm^{-1} region which derive their RR activity from laser excitation into the (Cys)S \rightarrow Cu(II) charge-transfer (CT) transition near 600 nm (3). This multiplicity of vibrational features is generally believed to be due to kinematic coupling of the Cu– S_{Cys} stretch, $\nu(\text{CuS})$, with mainly internal Cys ligand deformation modes (47–53, 58).

Figure 2 displays the low-temperature (77 K) RR spectra for the natural abundance WT and two Cu center mutants, M121G and H46D, of *P. aeruginosa* azurin, and their corresponding ^{34}S -Cys substituted proteins obtained in the 350–450 cm^{-1} region with 647.1 (WT) and 568.2 nm (M121G, H46D) excitation wavelengths (49). Each spectrum shows four strong RR peaks in this region that are characteristic for the type 1 structure of the Cu(II)–Cys chromophores (44–46). The most intense peak in WT azurin occurs at 408 cm^{-1} with a shoulder at 400 cm^{-1} . Both of these peaks shift downward when the protein is enriched in ^{34}S by -3.8 and ~ -1.2 cm^{-1} , respectively. High intensity and relatively large ^{34}S isotope sensitivity unambiguously demonstrate that the Cu– S_{Cys} stretching vibration, $\nu(\text{CuS})$, is a major contributor to these bands (46–53, 58–61). Assuming an isolated two-body oscillator model for the Cu– S_{Cys} stretch, an isotope shift of -7.7 cm^{-1} is calculated for the 408 cm^{-1} frequency (49). Although the $^{34}\text{S}/^{32}\text{S}$ experiment shows a significantly smaller shift than expected by the two-body model, this simple calculation predicts that the strongest RR band of WT azurin arises from the vibrational mode which is at least 45% $\nu(\text{CuS})$ in character. This assignment is also corroborated by the $^{63}/^{65}\text{Cu}$ isotope shifts, shown in Figure 3 and Table I, and by normal mode analysis calculations (61).

The other two dominant peaks are found at 373 and 428 cm^{-1} in WT azurin (Fig. 2) and remain largely unaltered by replacing Met121 with Gly (M121G) or His46 with Asp (H46D); the 373- cm^{-1} peak shifts slightly to lower (371 cm^{-1}) and higher (375 cm^{-1}) frequencies in M121G and H46D mutants, respectively, whereas the 428- cm^{-1} peak loses less than 1 cm^{-1} in M121G and about 2 cm^{-1} in H46D azurins. The

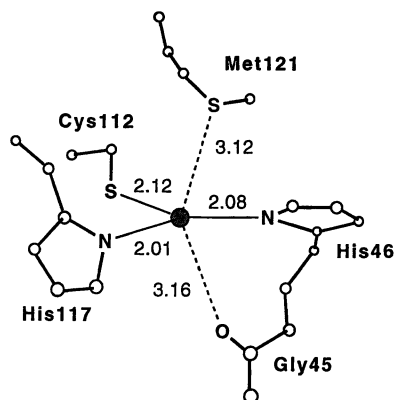


Figure 1. The arrangement of the ligands about Cu(II) ion in *P. aeruginosa* azurin (13). Bond distances (Å) from crystal structure of *A. denitrificans* azurin (12).

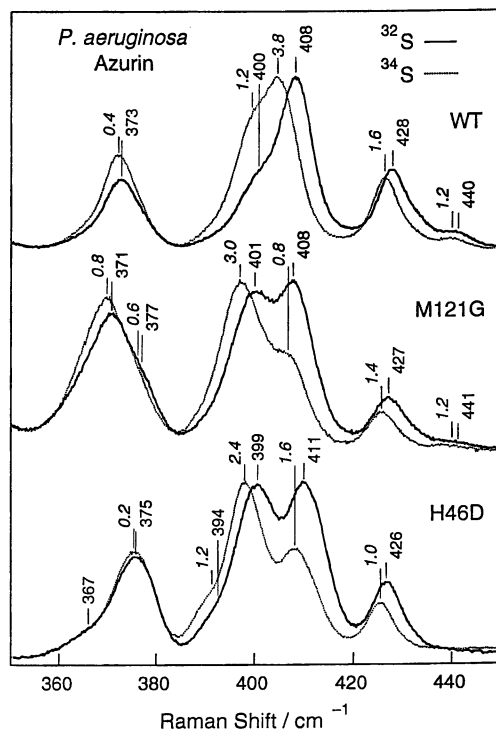


Figure 2. Low-temperature (77 K) RR spectra of *P. aeruginosa* azurins and their ^{34}S -Cys labeled proteins in the region between 360 and 435 cm^{-1} obtained with 647.1 (WT) and 568.2 nm (mutants) excitation wavelengths. Italic numbers show the $\nu(^{32}\text{S})-\nu(^{34}\text{S})$ band shifts.

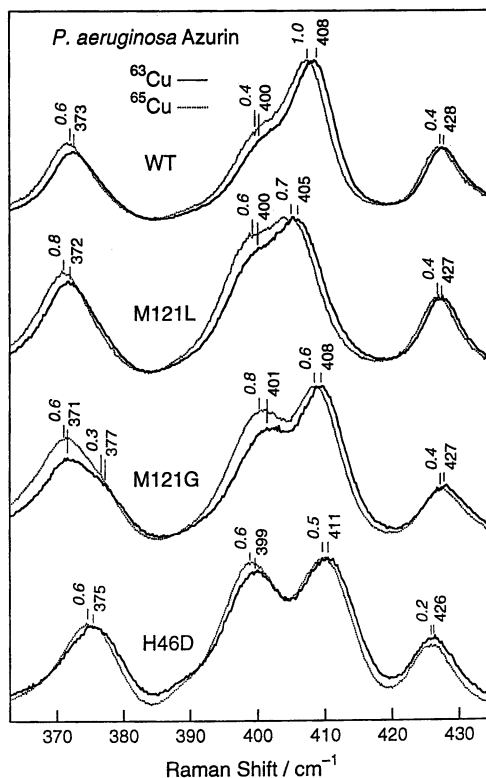


Figure 3. Low-temperature (77 K) RR spectra of *P. aeruginosa* ^{63}Cu -azurins and their ^{65}Cu labeled proteins in the region between 360 and 440 cm^{-1} obtained with 647.1 (WT, M121L) and 568.2 nm (M121G, H46D) excitation wavelengths. Italic numbers show the $\nu(^{63}\text{Cu})-\nu(^{65}\text{Cu})$ band shifts

Table I. Effects of ^{34}S , ^{65}Cu , and D_2O Substitutions on Frequencies of the 370–430- cm^{-1} RR Bands for Type 1 Cu Sites in Azurins

Azurin	RR Frequency and Isotope Shift				Total Shift
Wild-type	373	400	408	428	
$^{32}\text{S} \rightarrow ^{34}\text{S}$	-0.4	-1.2	-3.8	-1.6	-7.0
$^{63}\text{Cu} \rightarrow ^{65}\text{Cu}$	-0.6	-0.4	-1.0	-0.4	-2.4
$\text{H}_2\text{O} \rightarrow \text{D}_2\text{O}$	-0.5	-1.0	-0.5	-1.5	-3.5
M121L ^a	372	400	405	427	
$^{63}\text{Cu} \rightarrow ^{65}\text{Cu}$	-0.8	-0.6	-0.7	-0.4	-2.5
$\text{H}_2\text{O} \rightarrow \text{D}_2\text{O}$	-0.5	-1.0	-0.5	-2.0	-4.0
M121G ^b	371	401	408	427	
$^{32}\text{S} \rightarrow ^{34}\text{S}$	-0.8	-3.0	-0.8	-1.4	-6.4
$^{63}\text{Cu} \rightarrow ^{65}\text{Cu}$	-0.6	-0.8	-0.6	-0.4	-2.4
$\text{H}_2\text{O} \rightarrow \text{D}_2\text{O}$	-2.5	-1.5	-2.0	-2.0	-7.0
H46D ^c	375	399	411	426	
$^{32}\text{S} \rightarrow ^{34}\text{S}$	-0.2	-2.4	-1.6	-1.0	-5.2
$^{63}\text{Cu} \rightarrow ^{65}\text{Cu}$	-0.6	-0.6	-0.5	-0.2	-1.9
$\text{H}_2\text{O} \rightarrow \text{D}_2\text{O}$	-1.5	-3.5	-3.0	-4.5	-12.5

^a ^{34}S data not available for M121L azurin. ^b M121G azurin shows a shoulder at 377 cm^{-1} which shifts ~ -0.6 and ~ -0.3 cm^{-1} on ^{34}S and ^{65}Cu substitutions, respectively. ^c H46D azurin shows a shoulder at 394 cm^{-1} which shifts ~ -1.2 cm^{-1} on ^{34}S substitution.

$\sim 370\text{ cm}^{-1}$ band is virtually insensitive to the ^{34}S substitution in all three proteins. The 428 cm^{-1} band is somewhat sensitive, its ^{34}S isotope shift decreasing from -1.6 cm^{-1} in WT to -1.4 cm^{-1} in M121G to -1.0 cm^{-1} in H46D. This indicates that the 428-cm^{-1} band also arises from the vibrational mode which involves some motion of the cysteinyl sulfur atom; however, sulfur participation in this mode decreases as the protein coordination environment is altered at the Cu site (49).

In contrast, the dominant 408-cm^{-1} RR band of WT azurin and its weak shoulder at 400 cm^{-1} are significantly affected by both mutations at the Cu site, and a splitting into two distinct bands at 399 and 411 cm^{-1} becomes especially apparent when the Cu-bound His46 is replaced with aspartate in H46D. While in the WT protein the higher energy peak at 408 cm^{-1} is predominantly resonance enhanced with either the 647.1 or 568.2 nm (not shown) excitations, the lower energy peak at 399 cm^{-1} becomes as intense as the 411-cm^{-1} line in the H46D mutant when excited at 568.2 nm (Fig. 2) and becomes the strongest feature when excited at 647.1 nm (not shown). Likewise, the 401-cm^{-1} shoulder of M121G mutant intensifies markedly relative to the 408-cm^{-1} peak in the 568.2 nm -excited spectrum and becomes the dominant band in the 647.1 nm -excited spectrum (not shown), implying a redistribution of the Cu-Cys normal coordinates which give rise to these vibrational modes. This redistribution is clearly evidenced by ^{34}S isotope shifts (Table I); the lower frequency components of the M121G and H46D doublet are downshifted much more than the higher frequency ones, -3.0 cm^{-1} versus -0.8 cm^{-1} in M12G and -2.4 cm^{-1} versus -1.6 cm^{-1} in H46D on ^{34}S -Cys substitution. This suggests a maximum contribution of the $\nu(\text{CuS})$ coordinate to the $\sim 400\text{ cm}^{-1}$ rather than $408\text{--}411\text{ cm}^{-1}$ peaks in azurin mutants and, consequently, a decreased Cu-S bond strength as compared to the WT (49, 59).

This apparent weakening of the Cu-S_{Cys} bond is also obvious if one takes into account the changes in the frequency of the β -carbon-sulfur(Cys) stretch, $\nu(\text{CS})$, observed at $\sim 750\text{ cm}^{-1}$ in the WT spectrum. A weaker Cu-S_{Cys} bond is expected to result in increased bonding between the S and C $_{\beta}$ atoms of the Cys unit and the corresponding $\nu(\text{CS})$ frequency should show an opposite trend to the one observed for $\nu(\text{CuS})$. Indeed, we found that the $\nu(\text{CS})$ mode shifts up to $\sim 760\text{ cm}^{-1}$ in the M121G mutant and to a still higher energy, $\sim 770\text{ cm}^{-1}$, in the H46D mutant (see Fig. 8 later in the text).

Previously, Han *et al.* (43) had postulated that increased absorption at $\sim 450\text{ nm}$ and rhombicity of the EPR signal of cupredoxins are related to a more tetrahedral site where the Cu atom has moved away from the plane formed by the three strong ligands. In the case at hand, while the EPR spectrum of the WT protein is axial, the spectra of the M121G (37) and H46D (38, 39) proteins are rhombic. In addition, while the electronic absorption spectrum of the WT displays a weak feature at 473 nm ($\epsilon = 580$), the corresponding absorption in the spectra of M121G (458 nm , $\epsilon = 900$) and H46D (452 nm , $\epsilon = 1200$) azurins is significantly enhanced. Thus the EPR and optical spectra suggest significant separation between the Cu atom and the plane formed by the three strong ligands (N₂S in WT and M121G, NOS in H46D) in the mutant proteins relative to the WT.

In the crystallographically characterized mutant of azurin, M121Q, which displays a rhombic EPR signal and an increased $\sim 450\text{ nm}$ absorption similar to those of the M121G and H46D azurins, the Cu center is significantly out of the N₂S plane (0.3 \AA) (28). Thus, we proposed that the metal center in the M121G and H46D mutants is also displaced from the equatorial plane due to its increased interaction with axial ligands (49), as seen in crystals of M121Q azurin. The possible axial ligands include water and the side chain of Met121. Water coordination is likely for M121G azurin since its spectroscopic properties are nearly identical to the M121(stop codon) mutant that is proposed to have a water molecule as a fourth ligand (62, 63). In the H46D azurin, a weakened coordination of Cu to carboxylate side chain of Asp46 is expected to lead to increased interaction with the side chain of Met121. The RR spectra of the ^{34}S -labeled azurins clearly show a weakened Cu-S interaction in the M121G and H46D mutant proteins relative to the WT. Increases in copper-ligand bond lengths would be expected in the mutant azurins if the Cu atom is moved out of

the trigonal plane relative to the ligand atom positions that are fixed within the protein framework (47, 49).

Effects of Replacement of Conserved Residues on the Ground and Excited States of Blue Cu Active Site in Azurin

Structural information about the nature of extremely subtle and minor variations in metal-ligand interactions effected by the replacement of conserved residues, at present, can not be assessed by X-ray diffraction data due to the sub-resolution level of the changes involved. Additionally, the average nature of the structural information forthcoming from X-ray investigation precludes the determination of dynamical effects causing geometrical perturbations. However, the inherently higher sensitivity and selectivity of the RR scattering can provide a precise and accurate structural information at atomic resolution. Also, the uniqueness of RR spectroscopy to provide information simultaneously about the ground state (frequency changes), and the excited state (intensity redistribution) makes it particularly suitable to assess differential dynamics as a result of active site redesign.

For example, as discussed in the preceding paragraphs, RR studies on the *P. aeruginosa* azurin mutants reveal an envelope of at least four intense bands in the 350–450 cm^{-1} region which show appreciable variations in the frequencies and intensities. An altered active site should result in a redistribution of the copper valence electrons and, hence, lead to differences in bond strengths and corresponding stretching frequencies as compared to the WT active site. These frequency changes in the RR spectral pattern contain information about the geometric changes undergone by the polypeptide sub-matrix to accommodate the redesigned Cu site. Furthermore, the differences in the intensity patterns reflect the electronic distribution of the excited state. This section focuses on structural and electronic information obtainable from the RR spectroscopic data in both the fundamental and overtone band regions. The UV-visible absorption spectra of the WT *P. aeruginosa* azurin and its M121L, M121G, and H46D mutants were also obtained and show systematic changes in band absorbances and λ_{max} positions.

Electronic Absorption Spectra. Figure 4 compares the UV-visible spectra of WT, M121L, M121G, and H46D azurins from *P. aeruginosa* in 10 mM Tris buffer at pH 8. The spectra all show at least one more band of variable intensity and energy in the violet region (450–475 nm) in addition to the intense bands centered near 615 nm. The strong band in the red region was originally assigned to a $(\text{Cys})\text{S}_\sigma \rightarrow \text{Cu}(d_{x^2-y^2})$ CT transition by Ainscough *et al.* (64), but more recent studies by Solomon *et al.* favor the assignment as $(\text{Cys})\text{S}_\pi \rightarrow \text{Cu}(d_{x^2-y^2})$ charge transfer (3, 65). Recent RR studies on cupredoxins by Han *et al.* have shown that both the ~460- and the ~600-nm electronic transitions give rise to the same RR frequencies (43). In addition, the excitation profile measurements between 400 and 700 nm (plots of Raman band intensity versus excitation wavelengths) on the enhanced Raman bands revealed a $(\text{Cys})\text{S} \rightarrow \text{Cu(II)}$ CT character for both transitions. These workers have also developed a correlation between the ratio $R_f(\epsilon_{460}/\epsilon_{600})$ and the EPR characteristics; the more intense the absorption at ~460 nm for a given protein the more rhombic is its EPR signal (43).

Examination of Figure 4 reveals that the λ_{max} and absorbance of the absorption bands near 460 and 615 nm of azurins both depend markedly on the ligating residues to the type I Cu site. Thus, the WT azurin with the coordination sphere involving two His, one Cys, and one Met shows a (very) weak band at 473 nm and an intense band at 627 nm. In the M121L mutant protein the energy of both bands is decreased; $\lambda_{\text{max}} = 475$ and 633 nm. Both proteins show also an axial Cu(II) EPR signal (22–24) consistent with the low energy CT bands for the trigonal bonding arrangement about Cu(II). Evidently, a replacement of the weakly interacting Met residue of azurin with a non-coordinating Leu in M121L mutant results in a loss of electron density on the copper(II) atom, thereby lowering the energy of the $(\text{Cys})\text{S} \rightarrow \text{Cu(II)}$ CT transitions.

However, a similar trend is not observed in the absorption spectra of the M121G and H46D mutants where the Met residue is replaced with non-coordinating Gly residue in M121G and the His46 residue is substituted with negatively charged Asp in H46D. The M121G ($\lambda_{\max} = 458$ and 615 nm) and H46D ($\lambda_{\max} = 452$ and 610 nm) proteins both show bands at much higher energies than those observed in the WT and M121L azurins, which implies a buildup of charge on the Cu atoms. Unlike WT and M121L azurins, these two proteins were found to have rhombic Cu(II) EPR signals (37–39), consistent with tetrahedrally distorted Cu site. As discussed in the previous section, such a distortion of the Cu(II) coordination sphere weakens the Cu–S_{Cys} bond and increases the interaction with an axial ligand, a water molecule in M121G and a S atom of the Met121 residue in H46D. The increased axial interaction in tetrahedral bonding arrangement increases the energy of the half-filled $d_{x^2-y^2}$ orbital, relative to its energy in the trigonal geometry, and in addition orients $d_{x^2-y^2}$ for less optimal overlap with the π orbital of the cysteine S atom. All these factors account for the higher energy CT bands in M12G and H46D relative to the WT and M121L.

Resonance Raman Spectra. In general, the vibrational pattern of resonance-enhanced bands for the wild type and Cu center site-specific mutants of azurin from *P. aeruginosa* studied in this work (M121L, M121G, H46D) are similar, each showing the characteristic type 1 Cu RR spectrum with a group of four dominant bands centered near 400 cm^{-1} , a series of weak to moderate bands below 300 cm^{-1} , and groups of weaker features in the first (~800 cm^{-1}) and second (~1200 cm^{-1}) overtone regions of the ~400 cm^{-1} fundamentals. This is exemplified by Figure 5 which shows the survey spectra of WT protein and H46D mutant obtained with 647.1 and 568.2 nm excitation wavelengths, respectively, in the region between 75 and 1400 cm^{-1} . Expanded views for each spectral region of WT, M121L, M121G, and H46D azurins are shown in Figures 6–8 where appreciable variations in both the frequencies and intensities of the enhanced bands can be easily seen, suggesting significant changes in the ground and excited electronic states among the four blue Cu sites.

Fundamental Vibrations. Figure 6 compares the RR spectra below 500 cm^{-1} for WT azurin and three site-specific mutants, M121L, M121G, and H46D, where most of the copper-ligand vibrations are expected to occur. The energy range of 350–500 cm^{-1} for WT, M121G, and H46D proteins, together with the ^{34}S isotopic shifts, has already been discussed in the previous paragraphs. This region contains the Cu–S_{Cys} stretch, which is the main normal mode coordinate that carries RR intensity in the fundamental region, as expected from excitation within the (Cys)S \rightarrow Cu(II) CT transition. As it was also proven in the previous section via ^{34}S -isotope labeling of the Cys112 ligand, the predominantly $\nu(\text{CuS})$ band downshifts from 408 cm^{-1} in WT to 399 cm^{-1} in the H46D mutant. Since there are still a total of at least four bands observed between 370 and 430 cm^{-1} , this implies an increase in frequency for the shoulder at 400 cm^{-1} observed in WT that now has moved to higher energies in the mutants (408 cm^{-1} in M121G and 411 cm^{-1} in H46D). Such a frequency cross-over is indicative of differences in kinematic coupling between vibrations of the Cu–Cys moiety as a result of ground state perturbations.

In the M121L azurin the strongest peak is observed at 405 cm^{-1} (Fig. 6). This apparent weakening of the Cu–S_{Cys} bond in M121L as compared to WT is rather unexpected, since, based on purely electrostatic arguments, one would expect the opposite to occur. In WT azurin active site copper is bound to four ligands (one Cys, two His and one Met), and a mutation by replacement of the Met residue with Leu should result in one less bonding interaction in M121L azurin as the Leu residue lacks any donor atoms. Even though the Cu–S_{Met} interaction is very weak, its elimination should, if at all, lead to a strengthening of the bonding with the rest of the ligands (1 Cys, 2 His).

This observation of a weaker Cu–S_{Cys} bond in M121L relative to WT indicates influence of the protein sub-matrix in controlling and regulating the ground state potential. Also, as mentioned before, in M121G and H46D azurins the ground state

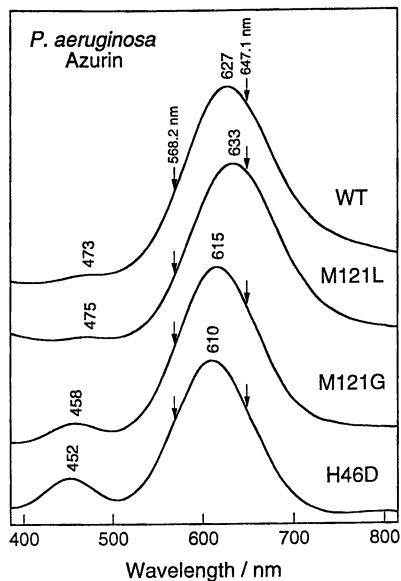


Figure 4. UV-visible absorption spectra of wild type (WT) *P. aeruginosa* azurin and its M121L, M121G, and H46D Cu site-specific mutants in 10 mM Tris buffer (pH 8).

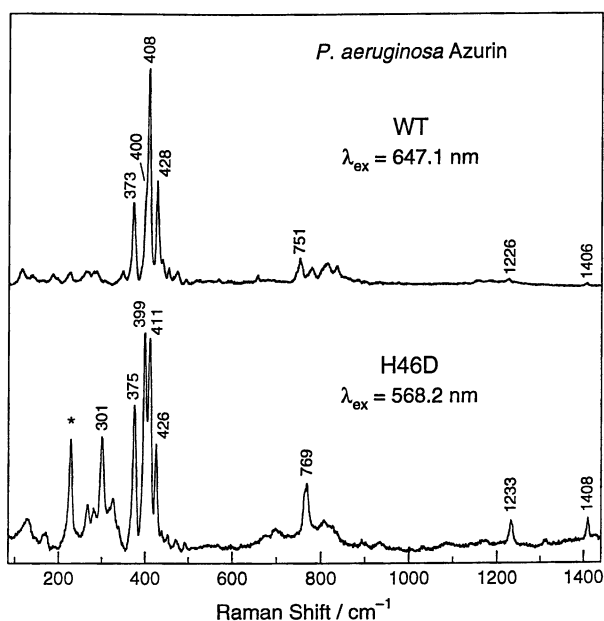


Figure 5. Low-temperature (77 K) survey RR spectra of *P. aeruginosa* azurin and its H46D mutant obtained in the 75–1600 cm^{-1} region with 647.1 and 568.2 nm excitation wavelengths, respectively. (*) denotes ice band.

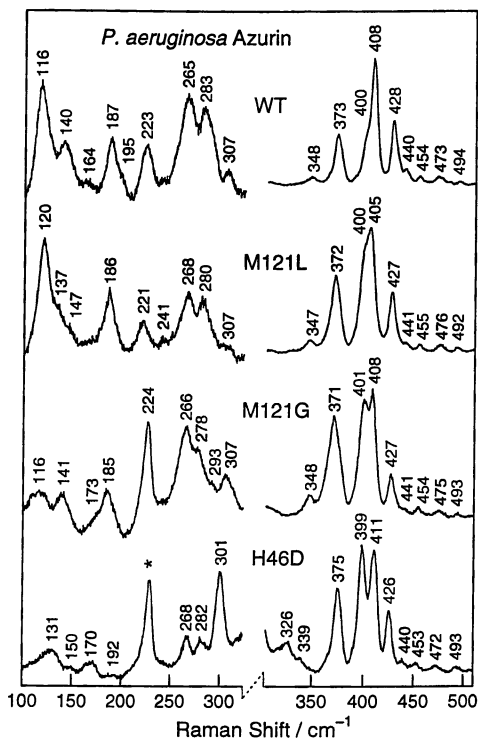


Figure 6. Low-temperature (77 K) RR spectra of *P. aeruginosa* azurin and indicated site-specific mutants in the fundamental region obtained with 647.1 (WT, M121L) and 568.2 nm (M121G, H46D) excitations. (*) denotes ice band.

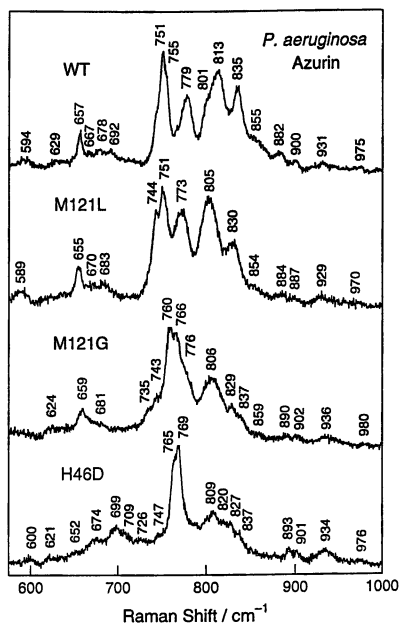


Figure 7. Low-temperature (77 K) RR spectra of *P. aeruginosa* azurin and indicated site-specific mutants in the first overtone region obtained with 647.1 (WT, M121L) and 568.2 nm (M121G, H46D) excitation wavelengths.

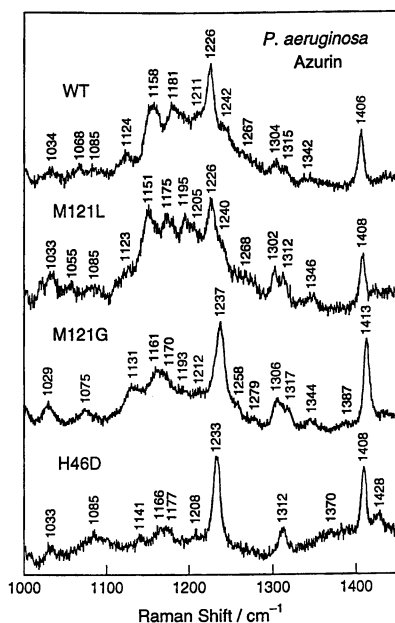


Figure 8. Low-temperature (77 K) RR spectra of *P. aeruginosa* azurin and indicated site-specific mutants in the second overtone region obtained with 647.1 (WT, M121L) and 568.2 nm (M121G, H46D) excitation wavelengths.

resorts to a stronger axial interaction with water and Met121, respectively, resulting in a tetrahedral distortion of the active site. This regulating influence of the polypeptide is particularly apparent in the case of H46D, where the replacement of strongly donating neutral His with charged Asp should, to a first approximation, strengthen the Cu–S_{Cys} bond if active site geometry were to be retained identical to the WT.

In the low-frequency range from 100 to 300 cm⁻¹, the deformation metal-ligand motions are expected to occur, such as $\delta(\text{N}_{\text{His}}\text{CuN}_{\text{His}})$, $\delta(\text{N}_{\text{His}}\text{CuS}_{\text{Cys}})$, $\delta(\text{N}_{\text{His}}\text{CuS}_{\text{Met}})$, and $\delta(\text{S}_{\text{Cys}}\text{CuS}_{\text{Met}})$ angle bendings. Previously, the RR band at 116 cm⁻¹ in WT azurin was attributed to a predominantly $\delta(\text{S}_{\text{Cys}}\text{CuS}_{\text{Met}})$ vibration (66). However, the observation of the same mode at 120 cm⁻¹ in the M121L mutant, which lacks the terminal Met coordination, disproves this assignment. Instead, we assigned this band to a normal mode involving mainly $\delta(\text{S}_{\text{Cys}}\text{CuN}_{\text{His}})$ motion because it downshifts nearly 2 cm⁻¹ upon substitution of ³⁴S for ³²S and ¹⁵N for ¹⁴N in WT of *P. aeruginosa* azurin (61). From the ^{65/63}Cu isotope shift data, the doublet of the modes at 265 and 286 cm⁻¹ was ascribed to stretching motions involving the in- and out-of-phase movements of His nitrogens (58). As can be seen in Figure 6, the center of the doublet is more or less preserved in WT as well as in mutants. Particularly convincing against the origin of these modes being both due to His participation, is the observation of two bands in this region for the H46D mutant that lacks one His residue. Finally, a prominent band is observed at 301 cm⁻¹ in the H46D mutant, which is tentatively assigned to the Cu(II)–O(Asp46) stretching mode, since the other proteins do not show a similarly intense peak and the H46D azurin has a covalent Cu–Asp interaction (38, 39). Detailed assignment of this complex 100–500 cm⁻¹ spectral region must await a complete normal mode analysis calculations.

Nevertheless, the observed differences in the ground state potential, as judged by the differences in frequencies and ³⁴S isotope shifts of bands in the fundamental region, implies a preorganized protein matrix which regulates and, hence, controls the coordination environment of the metal center. A combination of tertiary structure and H-bonding interactions are believed to enforce the coordinating environment around the metal center and thus, fine tune the structural and electronic nuances of the active site (31–33). In order to measure the H-bonding interactions RR spectra of the WT protein and its mutants were obtained in H₂O versus D₂O. As shown in Table I, the strongest peaks in the spectra with the maximum $\nu(\text{CuS})$ contribution are also the ones which are the most affected by replacement of H₂O with D₂O. Thus, while the WT spectrum is not much perturbed in D₂O, the H46D mutant shows the largest ²H isotope shifts. Another observation that can be made is that the isotope shift for the predominantly $\nu(\text{CuS})$ peak increases as its frequency decreases, suggesting an increased H-bonding interaction with Cu–S unit in the mutant azurins as compared to the WT. From these observations, it is apparent that bonding in Cu–Cys chromophore is closely related to the H-bonding interactions.

Overtone and Combination Bands. The region from 550 to 1000 cm⁻¹ (Fig. 7) primarily shows the overtones and combination modes of the ~400 cm⁻¹ fundamental vibrations, as expected for RR scattering. Another prominent feature in this region is the strongly enhanced $\nu(\text{CS})$ vibrational mode of the Cys112 side chain residue, at 751 cm⁻¹ in WT. A similar band is seen for the M121L mutant at an identical frequency, which is consistent with the trigonal Cu site in both azurins. On the other hand, the frequency of $\nu(\text{CS})$ is found to be increased in the mutants that show rhombic EPR signals and enhanced absorbances near 460 nm relative to WT, i.e., the $\nu(\text{CS})$ occurs at ~760 cm⁻¹ in M121G and at ~769 cm⁻¹ in H46D. As was noted previously, a decrease in Cu–S interaction should manifest itself in a concomitant increased S–C interaction. The increased frequency of this vibration provides a semi-definitive proof for reduced Cu–S interaction in the mutant proteins. The Cys112 $\nu(\text{CS})$ stretch of each azurin forms its own series of combination modes with the intense ~400-cm⁻¹ fundamentals, which appear as weak ³⁴S-sensitive bands between 1120 and 1220 cm⁻¹ (Fig. 8). The remaining bands between 720 and 900 cm⁻¹ all fit either overtone or combination frequencies of the four strong fundamentals observed

in the 400 cm^{-1} region, and the most intense bands at ~ 813 (WT) and ~ 805 cm^{-1} (M121L) are assigned to the first overtones of the predominantly $\nu(\text{CuS})$ mode.

Apart from the obvious changes in the frequencies of the vibrational modes associated with overtones and combination modes in this region as a result of ground state modification via active site redesign, spectacular differences in the intensities are observed which reflect excited state modifications. Whereas the fundamental modes derive intensity from the Franck-Condon vibronic pathways via displacement of the excited state nuclear coordinates, the overtones and combinations are enhanced by slightly different mechanisms (67–69). Enhancement of overtones requires that the force constants be changed in the ground and excited state as a result of the CT excitation (67). On the other hand, the enhancement of combinations is by mixing of the ground state normal modes with the excited state, the so-called Duschinsky mixing (68, 69). Intensification of the combinations by Duschinsky mixing requires that the excited state normal modes differ from those of the ground state and therefore suggests a large perturbation of the CT excited state.

The 720–900 cm^{-1} region of the WT azurin spectrum is dominated by overtone bands, whereas the mutant proteins show only broad features that arise from enhancement of all possible permutations of the combination modes; the overtones lose most of their intensity or are not observed. This trend toward "disappearing overtones" (68, 69) while combinations persist is most evident in the H46D mutant as compared to WT azurin (Fig. 7), implying a strong Duschinsky mixing in the excited state of the strongly tetrahedrally distorted H46D azurin. This suggests pronounced structural distortions in the (Cys)S \rightarrow Cu(II) CT transition in the mutant azurins, whereas the WT azurin shows a somewhat constrained active site such that the excited state "Cu(I)" coordination geometry is not grossly different from the ground state.

Effects of Exogenous Ligand Coordination on Blue Cu Active Site

Replacement of the Met121 ligand with a smaller Gly residue creates a spatial aperture, whereby small ligands ought to be able to bind to the active site. Indeed, the anion azide binds to the M121G mutant (54, 55), and the binding can be monitored by optical absorption and RR spectroscopies. Figure 9 shows the effects on the UV-visible spectrum for M121G azurin upon titration with azide. It is seen that, as the amount of added azide increases, a new absorption band develops at 420 nm with a concomitant decrease in intensity of the "blue" 615-nm band. The equilibrium reaction between M121G and azide ion is well-behaved, showing an isosbestic point at 544 nm (54).

The low-temperature (77 K) RR spectra of M121G azurin and its azide adduct are shown in Figure 10, obtained with 568.2 and 413.1 nm excitation wavelengths, respectively. These two excitations are in close resonance with the UV-visible absorption bands at 615 (M121G) and 420 nm (M121G-azide), respectively. The most striking difference between the two spectra is that, while M121G azurin shows the most strongly enhanced vibrational mode at 401 cm^{-1} , assigned to $\nu(\text{CuS})$, the strongest band in the azido adduct occurs at 357 cm^{-1} . Since the new absorption band in the azide adduct at 420 nm occurs in the range where azide-to-metal CT transitions occur, the origin of the strongest peak could be attributed to an enhanced Cu(II)–N_{azide} stretching vibration. However, the 413.1-nm excited RR spectrum of $^{15}\text{N}^{14}\text{N}_2$ adduct (not shown) is identical to that of the natural abundance sample. The non-involvement of azide vibrations also implicates the nature of CT from a moiety other than the exogenous azide. Therefore it seems logical to assume that the origin of the absorption in violet is inherent to the Cu(II)–Cys chromophore, and the new band at 420 nm is due to a structural distortion of the Cu site leading to different energy of (Cys)S \rightarrow Cu(II) charge transfer.

To provide a firmer basis for these electronic and vibrational assignments, we have obtained the 413.1-nm excited RR spectrum on the ^{34}S -labeled M121G azurin mixed with aqueous NaN_3 . As can be seen in Figure 11, the spectrum shows the

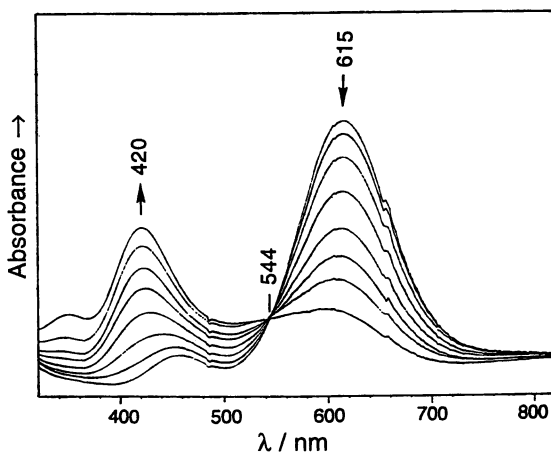


Figure 9. Changes in the UV-visible absorption spectra of *P. aeruginosa* M121G azurin on sequential addition of aqueous NaN_3 .

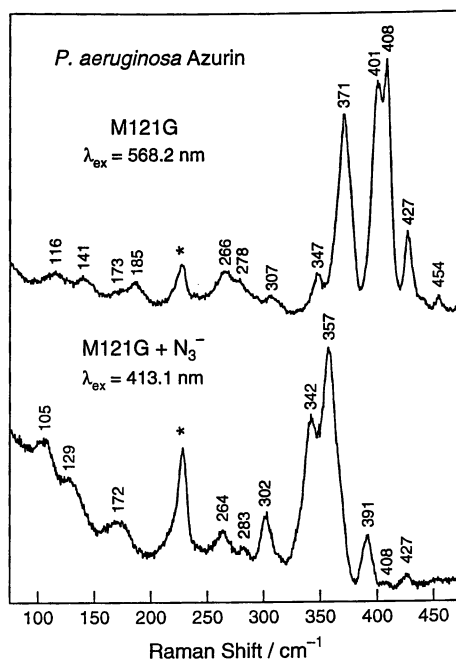


Figure 10. Low-temperature (77 K) RR spectra of *P. aeruginosa* M121G azurin and its azide adduct obtained in the 75–475 cm^{-1} region with 568.2 (M121G) and 413.1 nm (M121G–azide) excitation wavelengths. (*) denotes ice band.

greatest ^{34}S mass effect on the frequency of the most intense peak at 357-cm^{-1} , which shifts 3.0 cm^{-1} to lower frequency. This substantial isotope shift identifies the 357-cm^{-1} mode of M121G-azide as predominantly due to stretching of the Cu–S_{Cys} bond. The decreased energy of the Cu–S oscillator (by $>50\text{ cm}^{-1}$) implies a large elongation of the Cu–S_{Cys} interaction (*vide infra*). This RR experiment also proves the nature of the CT transition as due to (Cys)S → Cu(II) rather than azide → Cu(II).

A Model of Copper-Ligand Interactions in Azurins

The range of Cu–S_{Cys} interactions observed in azurins with corresponding changes in EPR, optical, and resonance Raman characteristics strongly implicates a structure-function correlation that is dependent on the Cu–S_{Cys} interaction coordinate. From the preceding sections, it can be safely concluded that a decrease in $\nu(\text{CuS})$ frequency manifests structurally a tetrahedral distortion of the active site. Such a distortion results in Cu-atom adopting an above the trigonal plane geometry characterized by a weakened Cu–S_{Cys} bond brought with a stronger axial interaction.

The equations used by Woodruff and co-workers (44, 47), originally derived from the familiar empirical Badger's rule of dependence between bond stretching frequencies and their force constants (70), can be adopted to calculate a change in Cu–S distance in the tetrahedrally distorted Cu sites relative to WT azurin for which the Cu–S distance is known to be $\sim 2.1\text{ \AA}$. In this model, $(r_x - r_{\text{ref}}) = 1.96 \log(\nu_{\text{ref}}/\nu_x)$, where r and ν are the Cu–S bond length and $\nu(\text{CuS})$ frequency, respectively, and the subscript "ref" refers to the values of r and ν in WT azurin; $r_{\text{ref}} = 2.1\text{ \AA}$, and $\nu_{\text{ref}} = 408\text{ cm}^{-1}$. Now, assuming that the Cu atom moves out of the N₂S plane along the trigonal axis as shown in Scheme 1, and applying simple trigonometry, the displacement estimate, b , can be derived as $b = (x^2 + 4.2x)^{1/2}$, where $x = 1.96 \log(408/\nu_x)$ and ν_x is the $\nu(\text{CuS})$ frequency in tetrahedrally distorted azurin.

Using these equations, the Cu–S bond lengths and the displacement of the Cu atom along the trigonal plane axis (b) can be calculated. Thus, for the M121G-azide adduct the Cu–S bond length is estimated to be 2.21 \AA from $\nu_x = 357\text{ cm}^{-1}$, an effective expansion of 0.11 \AA relative to WT azurin. The corresponding value of b can then be calculated as 0.65 \AA . Although simple, this model calculation predicts a substantial out-of-plane displacement of central metal and strongly tetrahedrally distorted Cu site consistent with rhombic EPR signal ($A_{\parallel} = 80 \times 10^{-4}\text{ cm}^{-1}$) (54, 55). Strong axial interaction provided by azide is no doubt the major driving force responsible for distortion towards tetrahedral geometry.

An increasingly rhombic nature of the Cu(II) EPR signal due to a splitting of g_{\perp} (i.e. $g_x \neq g_y$) suggests a mixing of d_z^2 into the $d_x^2-y^2$ ground state (42). Electronically this mixing would occur if the axial ligand field strength was increased. The hypsochromic shift of the (Cys)S → Cu(II) CT transitions in M121G and H46D mutants implies an increased ligand field strength around the Cu(II) atom. The mixing of the d_z^2 into the $d_x^2-y^2$ orbitals would be structurally manifested in a tetrahedral distortion of the Cu center, due to a stronger interaction with axial ligand. Lu *et al.* (42) have proposed an orbital model which correlates the R_f ratio and the EPR characteristics of the blue Cu active site. According to this model, an increased mixing of the d_z^2 into the $d_x^2-y^2$ orbital that splits g_{\perp} , results in effective weakening of the overlap between Cu $d_x^2-y^2$ and S π orbitals and thereby reducing the intensity of absorption at 600 nm .

This reduced overlap is also evident in the RR spectra of M121G and H46D mutant proteins which show an overall weaker RR scattering as compared to WT. Taken together, the preceding arguments imply an increasing mixing of the d_z^2 orbital into the $d_x^2-y^2$ orbital as a result of the tetrahedral distortion in the two azurin mutants and the azide adduct as compared to WT. An increased mixing of the d_z^2 orbital, as implied by the rhombic EPR signals of the azurins employed in this study, suggests an increased charge transfer density to d_z^2 orbital of the metal as a result of the (Cys)S π → Cu($d_x^2-y^2$) CT transition. This suggests different excited state dynamics in tetrahedrally distorted azurins.

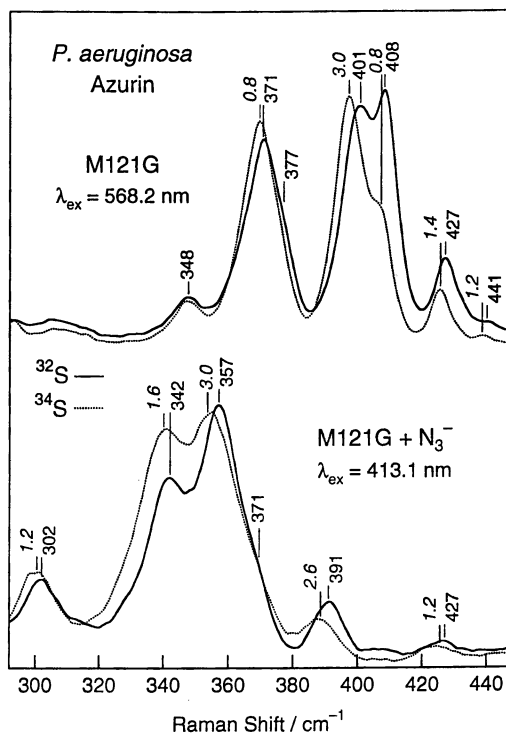
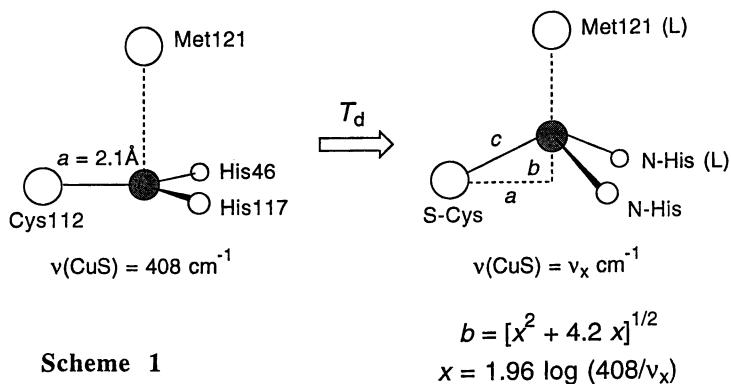


Figure 11. Low-temperature (77 K) RR spectra of *P. aeruginosa* M121G azurin and its azide adduct in the natural abundance and ^{34}S -labeled obtained in the 275–450 cm^{-1} region with 568.2 (M121G) and 413.1 nm (M121G-azide) excitation wavelengths. Italic numbers show the $\nu(^{32}\text{S})$ – $\nu(^{34}\text{S})$ band shifts.



Particularly informative in this regard is the first overtone region of the cupredoxin RR spectra, which indicates substantial variations in the (Cys)S \rightarrow Cu(II) CT excited state geometries. Probing this CT transition by RR spectroscopy, indeed, reveals different enhancement patterns for overtones and combinations as already discussed. The stronger Duschinsky mixing observed for the tetrahedrally distorted azurins is indicative of larger Cu site perturbations. As it can be inferred, the in-plane motions of the Cu atoms are strongly restrained due to strongly interacting equatorial ligands, and the only degrees of freedom available are along the axial direction. The increased extent of charge-transfer to the d_{z^2} orbital in the tetrahedrally distorted azurins should result in an excited state that contains the "Cu(I)" ion showing substantially reduced axial interaction. In other words, as a result of (Cys)S \rightarrow Cu(II) CT the tetrahedrally distorted azurins show an excited state where the effective geometry of "Cu(I)" is more consistent with being trigonal planar.

The most intriguing aspect of the blue single-Cu active sites is their variability of the redox reactivity. The differences in electron transfer rates can be thermodynamic (changes in redox enthalpies) or kinetic (altered potential barriers). Whereas the redox enthalpies are dependent on the ground state geometry, the kinetic effects are governed by the differences in the potentials of the excited states. Due to unavailability of sufficient data, generalizations are difficult to make. Nevertheless, the results of this study show that Cu-S_{Cys} interaction should play an important role in influencing the reactivity and thus the functional properties of the blue Cu active site. While the tetrahedral azurins inhibit large amplitude motions of the copper atom perpendicular to N₂S plane in the ground state, facile dephasing of the modes associated with the in-plane structure in the (Cys)S \rightarrow Cu(II) CT excited state should have profound effects upon the quantum dynamics of electron transfer by providing an efficient superexchange pathway for electron transfer (3).

Summary

1. ³⁴S isotopic substitution and RR spectroscopy provide valuable insight into the strengths of Cu-S_{Cys} interactions in cupredoxins and the geometric features of their metal centers.
2. Positive identification of the predominantly Cu-S_{Cys} stretching vibration with the strongest band in the RR spectrum allows a direct correlation with the EPR signal, the R_f value (43), and the geometry of azurin active site.
3. The comparative RR study of the azurin and its Cu center mutant proteins shows the variations in the ground and excited state Cu active site structure as a result of the active site redesign.
4. The intensity and frequency redistribution in the fundamental region is indicative of altered ground state dynamics resulting in differential kinematic coupling in the mutant proteins relative to WT.
5. The effects of hydrogen bonding interactions could be important in ground state structural dynamics of the azurins as shown by highly disparate D₂O shifts.
6. The overtone and combination region imply a strong Duschinsky mixing in the (Cys)S \rightarrow Cu(II) CT excited state of M121G and H46D mutant azurins, providing a basis for the varied excited state dynamics as a result of perturbation in the ground state.
7. All these results strongly point to a very "constrained" copper active site in WT azurin, whereas the mutant proteins acquire more degrees of freedom.
8. The M121G mutant, due to spatial flexibility allows small exogenous ligands such as water and azide anion to interact with the copper active site. The strong axial interaction with the azide anion leads to an extreme attenuation in the Cu-S_{Cys} interaction as evidenced by the downshift of the predominantly $\nu(\text{CuS})$ stretch from 401 cm⁻¹ in the M121G azurin to 357 cm⁻¹ in the azide adduct.

Acknowledgments. This work was supported by grants from the National Institute of General Medical Sciences (GM48370) and Robert A. Welch Foundation (E-1184).

References

1. Gray, H. B.; Solomon, E. I. In *Copper Proteins*; Spiro, T. G., Ed.; John Wiley: New York, 1981; Vol. 3, pp 1–39.
2. Farver, O., Pecht, I. In *Copper Proteins and Copper Enzymes*; Lontie, R., Ed.; CRC Press: Boca Raton, FL, 1984; Vol.1, pp 183–214.
3. Solomon, E. I.; Baldwin, M. J.; Lowery, M. D. *Chem. Rev.* **1992**, *92*, 521.
4. Adman, E. T. In *Topics in Molecular and Structural Biology: Metalloproteins*; Harrison, P. M., Ed.; Macmillan: New York, 1985; Vol. I, pp 1–42.
5. Adman, E. T. *Adv. Protein Chem.* **1991**, *45*, 145.
6. Sykes, A. G. *Struct. Bonding* **1991**, *75*, 175.
7. Guss, J. M.; Freeman, H. C. *J. Mol. Biol.* **1983**, *169*, 521.
8. Guss, J. M.; Bartunik, H. D.; Freeman, H. C. *Acta Crystallog.* **1992**, *B48*, 790.
9. Tong, H., Ph. D. Dissertation, University of Sydney, Australia.
10. Collyer, C. A.; Guss, J. M.; Sugimura, Y.; Yoshizaki, F.; Freeman, H. C. *J. Mol. Biol.* **1990**, *211*, 617.
11. Redinbo, M. R.; Cascio, D.; Choukair, M. K.; Rice, R.; Merchant, S.; Yeates, T. O. *Biochemistry*, **1993**, *32*, 10560.
12. Baker, E. N. *J. Mol. Biol.* **1988**, *203*, 1071.
13. Nar, H.; Messerschmidt, A.; Huber, R.; van de Kamp, M.; Canters, G. W. *J. Mol. Biol.* **1991**, *218*, 427.
14. Petratos, K.; Dauter, Z.; Wilson, K. S. *Acta Crystallogr.* **1988**, *B44*, 628.
15. Adman, E. T.; Turley, S.; Bramson, R.; Petratos, K.; Banner, D.; Tsernoglou, D.; Beppu, T.; Watanabe, H. *J. Biol. Chem.* **1989**, *264*, 87.
16. Inoue, T.; Kai, Y.; Harada, S.; Kasai, N.; Ohsiro, Y.; Susuki, S.; Kohzuma, T.; Tobari, J. *Acta Crystallogr.* **1994**, *D50*, 317.
17. Durley, R.; Chen, L.; Lim, L. W.; Mathews, F. S.; Davidson, V. L. *Protein Sci.* **1993**, *2*, 739.
18. Romero, A.; Nar, H.; Huber, R.; Messerschmidt, A.; Kalverda, A. P.; Canters, G. W.; Durley, R.; Mathews, F. S. *J. Mol. Biol.* **1994**, *236*, 1196.
19. Hart, P. J.; Nersissian, A. M.; Herrmann, R. G.; Nalbandyan, R. M.; Valentine, J. S.; Eisenberg, D. *Protein Sci.* **1996**, *5*, 2175.
20. Guss, J. M.; Merritt, E. A.; Phizackerley, R. P.; Freeman, H. C. *J. Mol. Biol.* **1996**, *262*, 686.
21. Bergman, C.; Gandvik, E. K.; Nyman, P. O.; Strid, L. *Biochem. Biophys. Res. Commun.* **1977**, *77*, 1052.
22. Shinina, M. E.; Maritano, S.; Barra, D.; Mondovi, B.; Marchesini, A. *Biochem. Biophys. Acta* **1996**, *1297*, 28.
23. Maritano, S.; Marchesini, A.; Susuki, S. *J. Biol. Inorg. Chem.* **1997**, *2*, 177.
24. Van Gysel, A.; Van Montagu, M.; Inze, D. *Gene* **1993**, *136*, 79.
25. Van Driessche, G.; Dennison, C.; Sykes, A. G.; Van Beeumen, J. *Protein Sci.* **1995**, *4*, 209.
26. Germann, U. A.; Muller, G.; Hunziker, P. E.; Lerch, K. *J. Biol. Chem.* **1988**, *263*, 885.
27. Adman, E. T.; Jensen, L. H. *Isr. J. Chem.* **1981**, *21*, 8.
28. Romero, A.; Hoitink, C. W. G.; Nar, H.; Huber, R.; Messerschmidt, A.; Canters, G. W. *J. Mol. Biol.* **1993**, *229*, 1007.
29. Eyring, H.; Lumry, R.; Spikes, J. D. In *The Mechanism of Enzyme Action*; McElroy, W. D.; Glass, B., Eds.; Johns Hopkins Press: Baltimore, 1954; pp 123–136.
30. Lumry, R.; Eyring, H. *J. Phys. Chem.* **1954**, *58*, 110.
31. Malmström, B. G. In *Oxidases and Related Redox Systems*; King, T. E.; Mason, H. S.; Morrison, M., Eds.; Wiley: New York, 1965, Vol. 1, pp 207–216.
32. Gray, H. B.; Malmström, B. G. *Comments Inorg. Chem.* **1983**, *2*, 203.
33. Malmström, B. G. *Eur. J. Biochem.* **1994**, *223*, 711.
34. Vallee, B. L.; Williams, R. J. P. *Proc. Natl. Acad. Sci. USA* **1968**, *59*, 498.

35. Arvidsson, R. H. A.; Nordling, M.; Lundberg, L. G. *Eur. J. Biochem.* **1989**, *179*, 195.
36. Karlsson, B. G.; Pascher, T.; Nordling, M.; Arvidsson, R. H. A.; Lundberg, L. G. *FEBS Lett.* **1989**, *246*, 211.
37. Karlsson, B. G.; Nordling, M.; Pascher, T.; Tsai, L. -C.; Sjölin, L.; Lundberg, L. G. *Protein Eng.* **1991**, *4*, 343.
38. Chang, T. K.; Iverson, S. A.; Rodrigues, C. G.; Kiser, C. N.; Lew, A. Y. C.; Germanas, J. P.; Richards, J. H. *Proc. Natl. Acad. Sci. USA* **1991**, *113*, 5050.
39. Germanas, J. P.; Di Bilio, A. J.; Gray, H. B.; Richards, J. H. *Biochemistry* **1993**, *32*, 7698-7702.
40. Hughey, J. L.; Fawcett, T. G.; Rudich, S. M.; Lalancette, R. A.; Potenza, J. A.; Schugar, H. J. *Am. Chem. Soc.* **1979**, *101*, 2617.
41. Kitajima, N.; Fujisawa, K.; Moro-oka, Y.; *J. Am. Chem. Soc.* **1990**, *112*, 3210.
42. Lu, Y.; LaCroix, L. B.; Lowery, M. D.; Solomon, E. I.; Bender, C. J.; Peisach, J.; Roe, J. A.; Gralla, E. B.; Valentine, J. S. *J. Am. Chem. Soc.* **1993**, *115*, 5907.
43. Han, J.; Loehr, T. M.; Lu, Y.; Valentine, J. S.; Averill, B. A.; Sanders-Loehr, J. J. *Am. Chem. Soc.* **1993**, *115*, 4256.
44. Woodruff, W. H.; Dyer, R. B.; Schoonover, J. R. In *Biological Applications of Raman Spectroscopy*; Spiro, T. G., Ed.; John Wiley: New York, 1988, Vol. 3, pp 413-438.
45. Sanders-Loehr, J. In *Bioinorganic Chemistry of Copper*; Karlin, K. D.; Tyeklar, Z., Eds.; Chapman and Hall: New York, 1993, pp 51-63.
46. Andrew, C. R.; Sanders-Loehr, J. *Acc. Chem. Res.* **1996**, *29*, 365.
47. Blair, D. F.; Campbell, G. W.; Schoonover, J. R.; Chan, S. I.; Gray, H. B.; Malmström, B. G.; Pecht, I.; Swanson, B. I.; Woodruff, W. H.; Cho, W. K.; English, A. M.; Fry, H. A.; Lum, V.; Norton, K. A. *J. Am. Chem. Soc.* **1985**, *107*, 5755.
48. Han, J.; Adman, E. T.; Beppu, T.; Codd, R.; Freeman, H. C.; Huq, L.; Loehr, T. M.; Sanders-Loehr, J. *Biochemistry* **1991**, *30*, 10904.
49. Dave, B. C.; Czernuszewicz, R. S.; Germanas, J. P. *J. Am. Chem. Soc.* **1993**, *115*, 12175.
50. Andrew, C. R.; Yeom, H.; Valentine, J. S.; Karlsson, B. G.; Bonander, N.; van Pouderooyen, G.; Canters, G. W.; Loehr, T. M.; Sanders-Loehr, J. *J. Am. Chem. Soc.* **1994**, *116*, 11489.
51. Qiu, D.; Dong, S.; Ybe, J. A.; Hecht, M. H.; Spiro, T. G. *J. Am. Chem. Soc.* **1995**, *117*, 6443.
52. Nersissian, A. M.; Mehrabian, Z. B.; Nalbandyan, R. M.; Hart, P. J.; Fraczkiewicz, G.; Czernuszewicz, R. S.; Bender, C. J.; Peisach, J.; Herrmann, R. G.; Valentine, J. S. *Protein Sci.* **1996**, *5*, 2184.
53. Andrew, C. R.; Han, J.; den Blaauwen, T.; van Pouderooyen, G.; Vijgenboom, E.; Canters, G. W.; Loehr, T. M.; Sanders-Loehr, J. *J. Biol. Inorg. Chem.* **1997**, *2*, 98.
54. Vidakovic, M.; Germanas, J. P. *Angew. Chem. Int. Ed. Engl.* **1995**, *34*, 1622.
55. Bonander, N.; Karlsson, G. B.; Vänngård, T. *Biochemistry* **1996**, *35*, 2429.
56. Czernuszewicz, R. S.; Johnson, M. K. *Appl. Spectrosc.* **1983**, *37*, 297.
57. Czernuszewicz, R. S. In *Methods in Molecular Biology*; Jones, C.; Mulloy, B.; Thomas, A. H., Eds.; 1993, Humana Press: Totowa, NJ, Vol. 17, pp 345-374.
58. Nestor, L. M.; Larrabee, J. A.; Woolery, G.; Reinhammer, B.; Spiro, T. G. *Biochemistry* **1984**, *23*, 1084.
59. Czernuszewicz, R. S.; Fraczkiewicz, G.; Fraczkiewicz, R.; Dave, B. C.; Germanas, J. P. In *Spectroscopy of Biological Molecules*, Merlin, J. C., Ed.; 1995, Kluwer Acad. Publ.: The Netherlands, pp 273-276.
60. Fraczkiewicz, G.; Fraczkiewicz, R.; Germanas, J. P.; Czernuszewicz, R. S. *Proc. XV-th Int. Conf. Raman Spectrosc.*, Asher, S. A.; Stein, P., Eds.; John Wiley & Sons: New York, 1996, pp 404-405.
61. Fraczkiewicz, R., Ph.D. Dissertation, University of Houston, 1996.

62. Pascher, T.; Karlsson, B. G.; Nordling, M.; Malmström, B. G.; Vänngård, T. *Eur. J. Biochem.* **1993**, *212*, 289.
63. Murphy, L. M.; Strange, R. W.; Karlsson, B. G. *Biochemistry* **1993**, *32*, 1965.
64. Ainscough, E. W.; Bingham, A. G.; Brodie, A. M.; Ellis, W. R.; Gray, H. B.; Loehr, T. M.; Plowman, J. E.; Norris, G. E.; Baker, E. N. *Biochemistry* **1987**, *26*, 71.
65. Solomon, E. I.; Lowery, M. D. *Science* **1993**, *259*, 1575.
66. Thamann, T. J.; Frank, P.; Willis, L. J.; Loehr, T. M. *Proc. Natl. Acad. Sci. USA* **1982**, *79*, 6396.
67. Spiro, T. G.; Stein, P. *Annu. Rev. Phys. Chem.* **1977**, *28*, 501.
68. Heller, E. *Acc. Chem. Res.* **1981**, *14*, 368.
69. Heller, E. J.; Sundberg, R. L.; Tannor, D. *J. Phys. Chem.* **1982**, *86*, 1822.
70. Herschbach, D. R.; Laurie, V. W. *J. Chem. Phys.* **1961**, *35*, 458.
71. Gewirth, A. A.; Cohen, S. L.; Schugar, H. J.; Solomon, E. I. *Inorg. Chem.* **1987**, *26*, 1133.

Chapter 13

XAS Studies on the Cu_A Centers of Heme–Copper Oxidases and Loop-Directed Mutants of Azurin: Implications for Redox Reactivity

N. J. Blackburn¹, M. Ralle¹, D. Sanders², J. A. Fee², S. de Vries³,
R. P. Houser⁴, W. B. Tolman⁴, M. T. Hay⁵, and Y. Lu⁵

¹Department of Biochemistry and Molecular Biology, Oregon Graduate Institute of Science and Technology, P.O. Box 91000, Portland, OR 97291–1000

²Department of Biology, University of California at San Diego, La Jolla, CA 92093

³Department of Microbiology and Enzymology, Technical University of Delft, 2628 BC Delft, Netherlands

⁴Department of Chemistry and Center for Metal in Biocatalysis, University of Minnesota, Minneapolis, MN 55455

⁵Department of Chemistry, University of Illinois at Urbana-Champaign, Urbana, IL 61801

The heme–copper oxidases (historically termed cytochrome oxidases) are ubiquitous in both prokaryotic and eukaryotic aerobic organisms. They function to catalyze the 4-proton, 4-electron reduction of dioxygen to water and transduce the energy made available from O–O bond cleavage to the translocation of an additional 4 protons across the cytoplasmic or mitochondrial membrane. The energy released is stored as an electrochemical gradient and utilized to drive ATP synthesis in the process known as oxidative phosphorylation. For these reasons, heme–copper oxidases are arguably the most important enzymes in mammalian cells, providing the energy for most metabolic processes and consuming 80–90% of the oxygen we breathe.

The catalytic activity of the heme copper oxidases resides in subunit I which is a membrane-spanning polypeptide, containing a dinuclear high-spin heme–Cu_B dioxygen binding site and a low-spin heme center. A second subunit (II) contains the binding site for the electron donor. A number of differing classes of heme–copper oxidases have been characterized depending on the nature of the electron donor and the type of heme centers present in subunit I. Cytochrome *c* is used as the electron donor by the *caa*₃ (cytochrome *c*, low-spin heme *a*, high-spin heme *a*₃–Cu_B) class of enzymes found in mammalian mitochondria, yeasts, and a number of bacterial systems [*Rhodobacter spheroides* (1,2), *Paracoccus denitrificans* (3–5), *Bacillus subtilis* (6)] and by the *cba*₃ oxidase from *Thermus thermophilus* (7). These enzymes all contain an additional redox center, Cu_A, within subunit II. A second major branch of the family, exemplified by the cytochrome *bo*₃ oxidase of

Escherichia coli (8–10) and the *aa*₃-600 oxidase of *Bacillus subtilis* (11,12), use ubiquinol as the reducing substrate, and in these cases the Cu_A-binding site is absent.

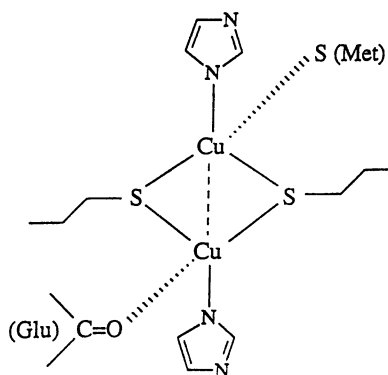
As recently reviewed in detail by Bienert (13), a combination of spectroscopic and molecular biological methodologies had already predicted the coordination chemistry of the metal centers with remarkable accuracy (8) prior to the publication of the X-ray crystal structures of the mitochondrial beef-heart (14) and *Paracoccus denitrificans* enzymes (15). These structures show the coordination chemistry of the metal centers in considerable detail. The site of initial electron entry into the protein is the Cu_A center, an unusual bis-thiolate-bridged mixed-valence dinuclear cluster (16–19) (Fig. 1). An electron entering the cytochrome oxidase molecule via Cu_A is transferred onwards to the 6-coordinate, low-spin heme *a* and thence to the binuclear dioxygen binding center comprised of a 5-coordinate, high-spin heme *a*₃ magnetically coupled to Cu_B. The latter is coordinated to three histidine ligands and carries a water or hydroxide as a fourth ligand in the oxidized form of the enzyme (20).

Although the mechanism of reductive O–O bond cleavage is complex (21), a crucial step is sequential electron transfer from the electron donor to preload the redox centers with electrons prior to reduction of the dioxygen molecule. The Cu_A center exhibits remarkable electron-transfer reactivity. Electron transfer from cytochrome *c* to Cu_A involves rate-limiting binding of cytochrome *c* followed by a very rapid electron transfer to Cu_A (22). Intramolecular electron transfer from Cu_A to Fe_a is also fast, proceeding with a unimolecular rate constant of $\sim 1.8 \times 10^4 \text{ s}^{-1}$ (16). This latter rate is particularly remarkable, as the intersite distance is in excess of 20 Å.

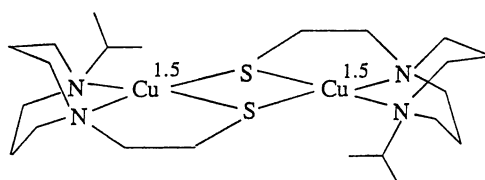
A major question related to the mechanism of the cytochrome oxidase reaction is how the structure of the Cu_A center facilitates this extreme electron-transfer reactivity. X-ray crystallography has revealed a unique structure for the Cu_A center (23). The two copper ions are bridged by the thiolate groups of two cysteine residues, and each has a single histidine ligand as the terminal ligand. A methionine and a main-chain carbonyl oxygen from glutamate provide a second more distant ligand to each copper. The unusual feature of the site is the very short $\sim 2.5\text{-}\text{\AA}$ Cu–Cu separation, which was previously determined from EXAFS spectroscopy (24). This site is the first example of a thiolate-bridged dicopper cluster active in electron transfer; such centers are well characterized in the 2Fe2S clusters of plant ferredoxins and as building blocks of 4Fe4S clusters of bacterial iron–sulfur proteins. However, the Cu_A center is only superficially similar to its 2Fe2S analogue. First, Cu_A is fully electron delocalized, while 2Fe2S clusters are valence-localized systems (25–29). Second, the metal–metal distance in Cu_A is 0.3 Å shorter than that found in FeS clusters. This raises the question of whether the valence delocalization is an essential element of the electron-transfer properties of the Cu_A site and, if so, whether it is mediated via a metal–metal bond as is believed to occur in the class III delocalized $[\text{Fe}_2(\text{OH})_2(\text{tmtacn})_2]^{2+}$ model complex (30).

To provide answers to these questions, we have carried out an X-ray absorption spectroscopic (XAS) study of the Cu_A center. Since crystallographic information is only available on the oxidized (mixed-valence) form of Cu_A, a particular goal of this work was to determine precise metrical information on both

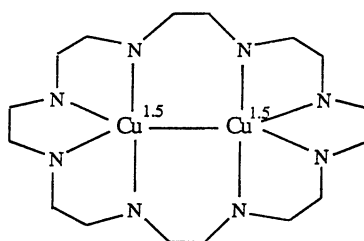
the electron-delocalized mixed-valence and the fully reduced forms of the enzyme to probe the structural changes that accompany the electron-transfer process. As reviewed by Scott (31), XAS featured prominently in the arsenal of techniques applied previously to determine the structure of the metal centers in the heme-copper oxidases. However, these XAS studies were carried out exclusively on mammalian enzymes which contained all three copper ions in their differing environments, and produced an erroneous interpretation of the Cu_A center as a mononuclear CuS_2N_2 site



The Cu_A center



Compound 1



Compound 2

Figure 1. Structures of the Cu_A center and model compounds 1 ($\text{L}^{\text{iPrdacoS}}\text{Cu})_2(\text{O}_3\text{SCF}_3)$ and 2 ($\text{LCu}_2(\text{NO}_3)_3$).

(32), rather than the dinuclear bis-thiolate-bridged center with a short and intense Cu–Cu interaction.

More recently a number of new constructs produced by overexpression of soluble subunit II domains have allowed the Cu_A center to be studied independently. These include reintroduction of a Cu_A site into subunit II of the *E. coli* quinol oxidase by site-directed mutagenesis, forming the so-called *cyoA* construct (33,34), and expression of soluble fragments of subunit II of *P. denitrificans* (3), *B. subtilis* (6), and *T. thermophilus* (35) in *E. coli*. These soluble Cu_A domains have now been studied extensively by spectroscopic techniques, including UV/vis (3,33,34), EPR (6,27,28), resonance Raman (36–39), EXAFS (24,40), MCD (26,41), and NMR (42). Mutagenesis experiments implicated two cysteines, two histidines and a methionine as the only important copper-binding ligands (34), and a number of acidic residues as binding sites for cytochrome *c* (22). Prior to the publication of the crystal structures, EXAFS evidence from our own laboratory for a directly bonded Cu–Cu unit (Cu–Cu = 2.5 Å) (24), and MCD studies on these soluble constructs, led to the conclusion that there were in fact only two viable structural models for Cu_A, viz our directly-bonded Cu–Cu proposal and an alternative involving a bis-thiolate bridge between the two copper atoms (41,43). A crystal structure of the *cyoA* Cu_A construct (23) at close to atomic resolution showed that the thiolate-bridged model was correct, but that the Cu–Cu distance was unusually short as predicted by the EXAFS study.

The study of these soluble subunit II domains by XAS has allowed us to examine the metrical details of a number of isolated Cu_A centers in considerable detail. To calibrate our analysis, we have also studied the EXAFS of two inorganic model complexes whose structures are compared with that of Cu_A in Fig. 1. The first of these is the bis-thiolate-bridged fully electron-delocalized Cu_A model complex, **1**, recently described by the Tolman laboratory (44). The second is the octaazacryptand electron-delocalized complex, **2**, described by Barr and coworkers (45). Complex **1** is the closest available model for Cu_A. The complex accurately mimics the electron-delocalized mixed-valence redox state and provides the bis-thiolate-bridging geometry characteristic of the Cu_A core. However the Cu–Cu distance in the model (2.93 Å) is not as short as in the protein (~2.5 Å), with significantly less acute Cu–S–Cu bridging angles. Complex **2** on the other hand exhibits a very short Cu–Cu interaction (2.41 Å). The lack of any coordinated bridging ligands implicates copper–copper bonding as the origin of the strong Cu–Cu interaction. Both complexes thus model different elements of the Cu_A site.

Calibration of the Cu–Cu Distance

In previous work comparing the Cu_A center of the *B. subtilis* Cu_A center and compound **2**, the Cu–Cu distance was found to be overestimated by ~0.07 Å as a result of inaccuracies in the Cu scatterer phase shift. Therefore, we began our detailed study by carefully calibrating the Cu–Cu distance. Compound **1** was chosen as the most accurate model for the Cu_A center, and the Cu scatterer phase shift was refined, with the Cu–Cu distance set at the crystallographic value of 2.93 Å. Fig. 2 shows the fit obtained using this procedure. Also shown in Fig. 2 is the result of simulating the EXAFS of compound **2** using this refined phase shift. The Cu–Cu

distance obtained for compound **2** was 2.41 Å, in close agreement with the crystallographic value of 2.415 Å, providing confidence in the simulation methodology for the determination of Cu-Cu distances in the proteins.

EXAFS Analysis of Soluble Cu_A Domains

Next we compared the EXAFS of oxidized (mixed-valence) and fully reduced forms of soluble Cu_A domains. The experimental versus simulated data for *T. thermophilus* and *B. subtilis* Cu_A are shown in Figs. 3 and 4, respectively. The metrical parameters derived from these fits are given in Table I. A number of important features can be seen. First, the Cu-Cu distances for both species of bacterial Cu_A are almost identical. The Cu-Cu distance in the mixed-valence form is 2.44 Å, with Cu-S and Cu-N distances of 2.29 and 1.96 Å, respectively. Reduction causes only minor perturbations in the site, with a small increase in the Cu-Cu to 2.51 Å and in the Cu-S to 2.33 Å. Although the crystal structures show a methionine and a main-chain carbonyl group from a glutamic acid residue weakly coordinated to each copper, the EXAFS analysis found no evidence for these ligands.

Core Dimensions of Oxidized and Reduced Cu_A

The metrical parameters determined from EXAFS analysis can be combined to provide a more detailed description of the core geometry than that available from crystallography. Additionally, the new data on the reduced enzyme have allowed us to observe the structural changes that accompany reduction and thus provide insights into the electron-transfer process. Fig. 5 shows a comparison of the core dimensions of the oxidized and reduced forms of *T. thermophilus* Cu_A. (The metrical details of the *B. subtilis* enzyme are essentially identical.) For mixed-valence Cu_A, the Cu₂S₂ diamond has Cu-S and Cu-Cu distances of 2.29 and 2.43 Å, respectively, leading to a Cu-S-Cu angle of 65°. In the reduced form, the diamond core expands slightly, as evidenced by the small increase of Cu-S and Cu-Cu to 2.33 and 2.51 Å, respectively, but the Cu-S-Cu angle remains unchanged at 65°. This suggests that the structure of the Cu₂S₂ core is highly conserved between mixed-valence and fully reduced forms and that structural reorganization accompanying cluster redox involves little more than a vibrational breathing mode of the core.

Confirmation of the strong similarity in structure between oxidized and reduced Cu_A comes from the comparison of the Cu K absorption edges shown in Fig. 6. The edges of the mixed-valence and fully reduced enzymes are essentially identical except for a ~1 eV shift to lower energy in the fully reduced derivative. This shift is less than that usually observed for reduction of Cu(II) to Cu(I) sites in enzymes and models (46) which can be as much as 5 eV for systems involving only N and O ligands, where the charge is localized and the bonding primarily electrostatic. The observed small shift most likely reflects the complete delocalization of electronic charge over the Cu₂S₂ core.

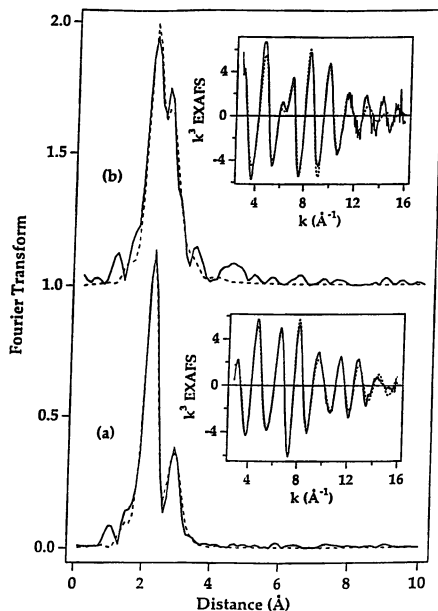


Figure 2. Calibration of Cu-Cu distances via EXAFS simulation of compounds 1 and 2. (a) Simulated versus experimental Fourier transforms and EXAFS (inset) of compound 1. (b) Simulated versus experimental Fourier transforms and EXAFS (inset) of compound 2.

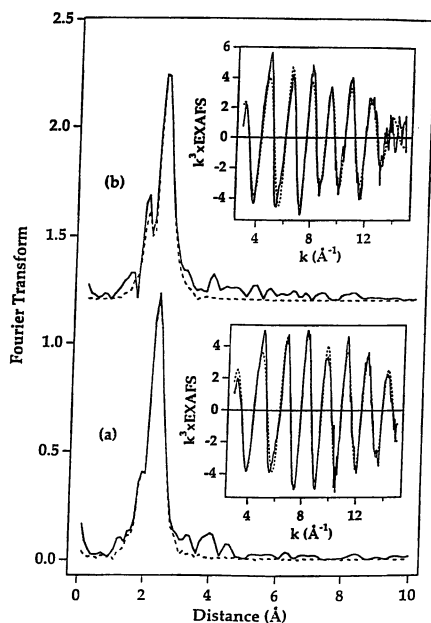


Figure 3. EXAFS of *T. thermophilus* Cu_A. (a) Simulated versus experimental Fourier transforms and EXAFS (inset) of oxidized protein. (b) Simulated versus experimental Fourier transforms and EXAFS (inset) of reduced protein.

Table I. Comparison of EXAFS-Derived Cu-N(His), Cu-S(Cys), and Cu-Cu Distances for Oxidized and Reduced Forms of Different Cu_A Constructs at 10 K

FI	Cu-N(His)		Cu-S(Cys)		Cu-Cu	
	R(Å ⁻¹)	2σ ² (Å ²)	R(Å ⁻¹)	2σ ² (Å ²)	R(Å ⁻¹)	2σ ² (Å ²)
<i>T. thermophilus</i> oxidized	0.84	0.004	2.29	0.011	2.43	0.002
<i>T. thermophilus</i> reduced	1.47	0.001	2.33	0.014	2.51	0.007
<i>B. subtilis</i> oxidized	1.28	0.005	2.30	0.014	2.44	0.005
<i>B. subtilis</i> reduced	0.95	0.011	2.23	0.022	2.52	0.010
Azurin Cu _A oxidized	1.47	0.002	2.28	0.007	2.39	0.003
Azurin Cu _A reduced	0.52	0.010	2.22	0.027	2.51	0.025
Compound 1	0.34	0.011	2.25	0.009	2.93	0.013
Compound 2	1.23	0.011	2.07	0.011	2.41	0.006

The coordination numbers in the protein simulations were fixed at 1.0 N, 2.0 S, and 1.0 Cu scatterers per Cu_A absorber. The metrical parameters used to fit compounds 1 (2.0 N, 2.0 S, 1.0 Cu per Cu absorber) and 2 (4.0 N, 1.0 Cu) are also given for comparison. Distances are accurate to ±0.02 Å.

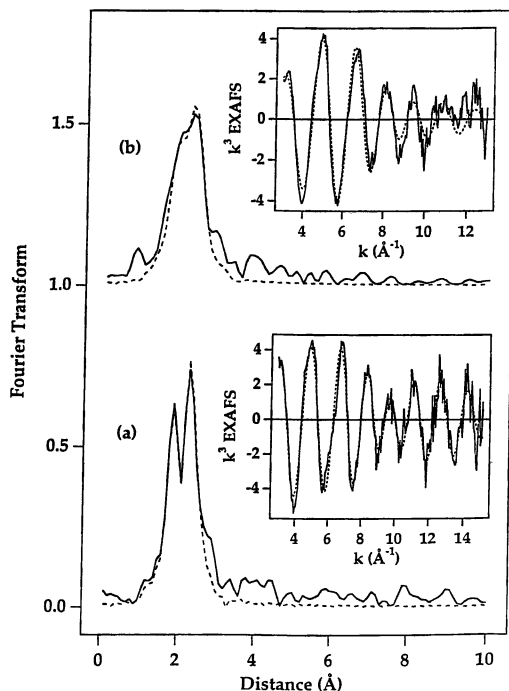


Figure 4. EXAFS of *B. subtilis* Cu_A. (a) Simulated versus experimental Fourier transforms and EXAFS (inset) of oxidized protein. (b) Simulated versus experimental Fourier transforms and EXAFS (inset) of reduced protein.

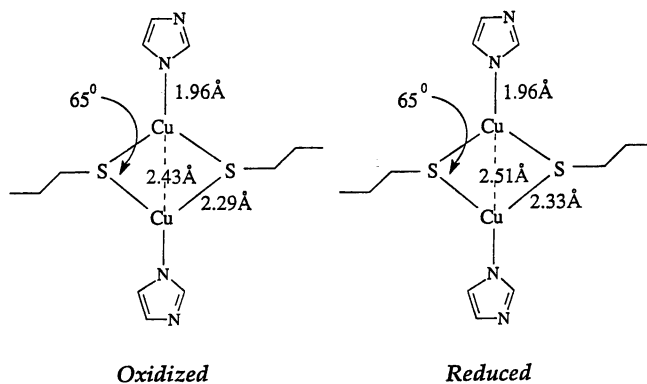


Figure 5. The core dimensions of oxidized and reduced Cu_A.

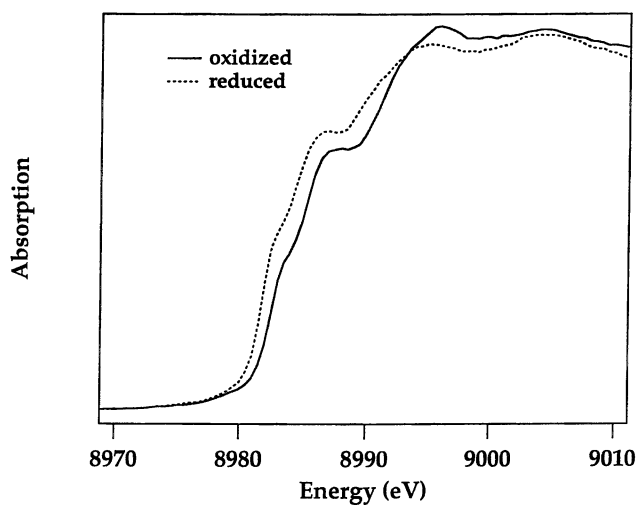


Figure 6. Cu K absorption edges for oxidized and reduced *T. thermophilus* Cu_A.

Implications for Electron Transfer

The similarity between the oxidized and reduced structures is important with respect to the mechanism of electron transfer in cytochrome *c* oxidase. Electron transfer from cytochrome *c* to dioxygen bound at the Fe_{a3}-Cu_B dinuclear center is known to proceed from cytochrome *c* → Cu_A → Fe_a → Fe_{a3}. Thus the Cu_A center is the site of initial electron entry from cytochrome *c*. Studies on the interaction of the *P. denitrificans* soluble subunit II domain with its biological electron-transfer partner cytochrome *c*-550 (22) have determined a second-order rate constant of $1.5 \times 10^6 \text{ M}^{-1} \text{ s}^{-1}$ which is similar to the values previously observed for the reaction of the intact oxidase with its substrate cytochrome *c*. In addition, site-directed mutagenesis has implicated a number of anionic residues in cytochrome *c*-550 binding to the Cu_A domain, which suggest a single cytochrome *c* binding site. These studies confirm that the electron transfer from cytochrome *c* to Cu_A occurs in a monophasic reaction involving rate-limiting binding of substrate at a single site, followed by a very rapid electron transfer (22). A more quantitative treatment of the electron transfer from Cu_A to Fe_a (16) has identified a 16-bond (14 covalent bonds, 2 H bonds) through-bond pathway between Cu_A and heme *a*, initiating on the H224 Cu_A terminal ligand (*P. denitrificans* structure). Using the rate constant of $1.8 \times 10^4 \text{ s}^{-1}$ and reasonable values for covalent and H-bond coupling efficiencies, Ramirez and coworkers calculated an electron-transfer reorganizational energy, λ , between 0.15 and 0.5 eV for the Cu_A center. Typical values for other protein electron-transfer reactions are in the range 0.7–1.3 eV.

These arguments suggest that the very rapid electron-transfer rates for the intermolecular cytochrome *c* to Cu_A and for the intramolecular Cu_A to heme *a* electron-transfer reactions can be traced to an unusually low reorganizational energy, λ , for the Cu_A cluster. The reorganizational energy is made up of contributions from redox-induced structural reorganization of the cluster and from changes in the degree of solvent/polypeptide ordering around the electron-transfer site. The relatively small reaction entropy (–5.4 eu) determined from electrochemical measurements of *T. thermophilus* Cu_A indicates minimal solvent ordering in the vicinity of the Cu_A cluster (47). Our EXAFS data show that structural reorganization of the cluster is small and provide a structural framework to interpret the origin of the low value of λ . The structural interconversion of mixed-valence and fully reduced Cu_A centers requires only a symmetric breathing mode of the diamond core involving small displacements along the Cu–Cu and Cu–S axes, but no change in the Cu–S–Cu angle. These displacements closely parallel the atomic displacements of the lowest energy A_{1g} modes calculated from a normal coordinate analysis of the Cu_A resonance Raman spectrum (38) [observed experimentally at 138 and 339 cm⁻¹ (38,39,48)], and thus rationalize the extremely low reorganizational energy for the site.

Temperature Dependence of the Cu–Cu Debye–Waller Factor and Cu–Cu Bonding

As discussed in the introduction, Cu_A is fully electron delocalized. An intriguing question which then arises is whether the valence delocalization is an essential

element of the electron-transfer properties of the Cu_A site, and if so, whether it is mediated via a metal-metal bond. In a classical sense, it may be argued that electron delocalization provides a superconducting pathway for an electron from the point of entry into the Cu_A site from cytochrome *c* to the point of exit (His 224) for the subsequent electron transfer to heme *a*. It was thus of great interest to determine whether our data could provide any direct evidence for the presence of a metal-metal bond. The temperature dependence of the Debye-Waller terms for the Cu_A center has provided evidence that supports the presence of some degree of Cu-Cu bonding.

Temperature dependences of the Cu-Cu Debye-Waller terms of the Cu_A enzyme sites and of compound 1 are shown in Figs. 7-9. Although the data range is limited for oxidized *T. thermophilus* Cu_A due to photoreduction above 100 K, it is clear that the Cu-Cu Debye-Waller is much smaller, and has a steeper T dependence (Fig. 9) than reduced Cu_A or compound 1. This suggests that the normal mode(s) that give rise to vibrational damping of the EXAFS oscillations induces significant change in Cu-Cu distance, and hence must include a component of Cu-Cu stretching. On the other hand, lack of any strong T dependence of the Cu-S components of the EXAFS of oxidized and reduced Cu_A and compound 1 in this same T range implies little or no change in Cu-S bond length in the normal mode. These considerations suggest that the normal mode that mediates the T dependence is the lowest energy A_g mode identified near 140 cm^{-1} , and assigned by normal coordinate analysis as either predominately Cu-Cu stretching or Cu-S-Cu bending (38,39,48) (Figs. 7 and 8, bottom right). We may also observe that the fully reduced Cu_A has a markedly larger Cu-Cu Debye-Waller at 10 K than mixed-valence, and a flatter T dependence which approximates that of compound 1. The latter clearly has no Cu-Cu bond as the Cu-Cu distance is 2.93 \AA . This suggests that a greater degree of Cu-Cu interaction is present in the oxidized protein than in either the reduced protein or compound 1. Given the near identical Cu_2S_2 core structures of oxidized and reduced Cu_A centers, a component of Cu-Cu bonding involving the unpaired (b_{3u}) d-electron (26,49) in the mixed-valence form seems a more likely explanation than an increase in Cu-S-Cu bending frequency. Thus we conclude that a possible explanation for the very small Debye-Waller term in mixed-valence Cu_A is the presence of a metal-metal bond.

Recent electronic structural calculations on *B. subtilis* Cu_A and compound 1 have reached similar conclusions (29). Assignment of the lowest energy electronic absorption bands as class III mixed-valence transitions has allowed the calculation of the ground-state electronic coupling energy $2H_{AB}$ (responsible for the valence delocalization) as $13,000$ and $4,800\text{ cm}^{-1}$ for Cu_A and compound 1, respectively. Since S K-edge spectroscopy indicated almost identical degrees of S covalency in their respective HOMOs, the additional interaction energy was attributed to direct overlap of Cu 3d orbitals resulting in Cu-Cu $\sigma^b - \sigma^*$ splitting.

Loop-Directed Mutants of Azurin

Blue copper proteins such as azurin and amicyanin have strong sequence homologies to the Cu_A -binding domains of cytochrome *c* oxidases but lack a short 5-residue sequence (XELCG), which contains one extra cysteine residue and a glutamic acid

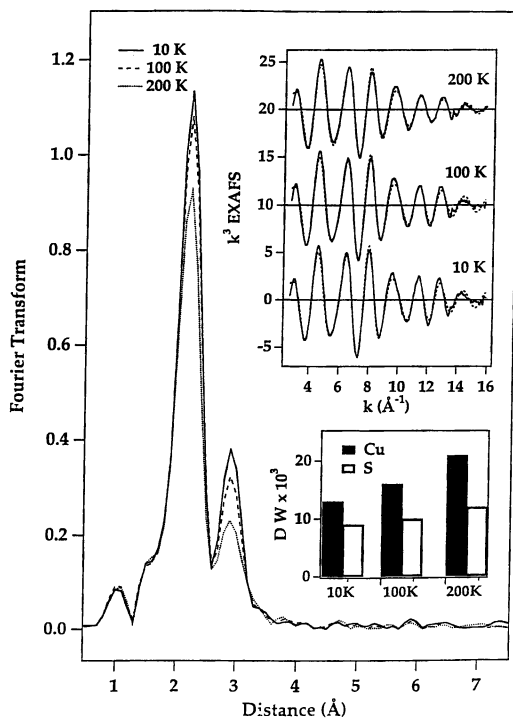


Figure 7. Temperature dependence of the Fourier transforms and EXAFS (inset top) of compound 1. For the Fourier transform data, the solid line represents data taken at 10 K, dashed line 100 K, and dotted line 200 K. For the EXAFS (inset top), solid lines are experimental data, dashed lines are simulated data, in which distances, coordination numbers and E_0 were kept constant while the Debye-Waller terms were floated in the fit. The bottom inset gives a graphical representation of the variation of Cu-Cu (solid bars) and Cu-S (open bars) Debye-Waller terms with temperature.

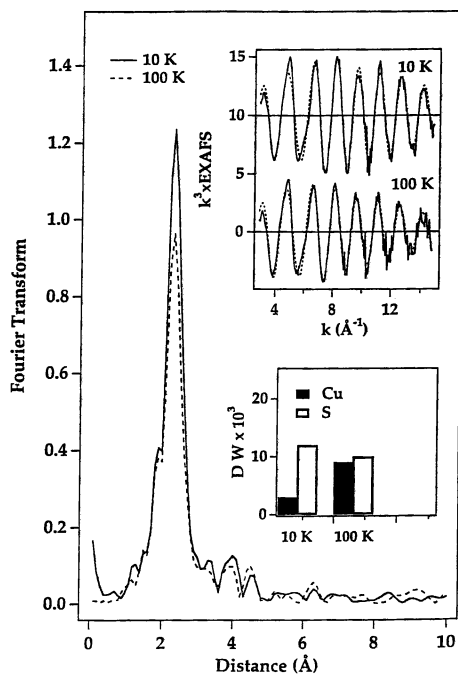


Figure 8. Temperature dependence of the Fourier transforms and EXAFS (inset top) of mixed-valence *T. thermophilus* Cu_A. For the Fourier transform data, the solid line represents data taken at 10 K, dashed line 100 K. For the EXAFS (inset top), solid lines are experimental data, dashed lines are simulated data, in which distances, coordination numbers, and E₀ were kept constant while the Debye-Waller terms were floated in the fit. The bottom inset gives a graphical representation of the variation of Cu-Cu (solid bars) and Cu-S (open bars) Debye-Waller terms with temperature.

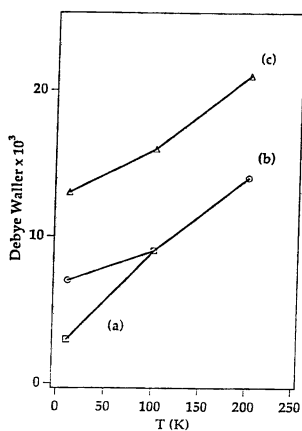


Figure 9. Temperature dependence of the Cu-Cu Debye-Waller terms. (a) Oxidized *T. thermophilus*; (b) reduced *T. thermophilus*; (c) compound 1.

residue. It had been predicted earlier that the subunit II Cu_A domains would share the cupredoxin folding motif common to all blue copper proteins, and the three-dimensional structure of the *cyoA* Cu_A construct shows that this is the case (23). The near-identical protein fold between Cu_A and blue copper proteins has been exploited in independent work from the laboratories of Canters (50) and Lu (51) to construct amicyanin and azurin mutants which contain the binuclear Cu_A center. Whereas the blue copper proteins have two His, one Cys, and one Met as ligands to the mononuclear copper atom, insertion of SELCGIN between C112 and H117 into the azurin sequence converts the blue copper center into a purple Cu_A -like protein, with optical and EPR spectral characteristics resembling those of genuine Cu_A -binding domains. Although no crystal structure is available for either loop-directed mutant, it is likely that the additional Cys and Glu residues complete the required coordination for the dinuclear Cu_A site.

We have carried out XAS studies of the loop-directed mutant of azurin in both the purple oxidized (mixed-valence) and colorless fully reduced forms. Comparison with results on the *T. thermophilus* and *B. subtilis* soluble cytochrome oxidase subunit II domains indicates significant differences between cytochrome oxidase and the mutant cupredoxin Cu_A site. The Fourier transform and EXAFS (top inset) for oxidized (purple) Cu_A azurin are shown in Fig. 10. The FT shows a single peak around $R = 2.4 \text{ \AA}$, similar to that observed for the Cu_A sites of the soluble domain of *T. thermophilus* subunit II, suggesting a similarly short Cu-Cu distance in purple azurin. XAS results presented here, together with other spectroscopic data reported previously (51), provide strong evidence for structural homology between the purple copper azurin and the crystallographically characterized Cu_A centers of beef heart and *P. denitrificans* cytochrome oxidase, and the reengineered *cyoA* construct. Therefore, we used the cytochrome *c* oxidase Cu_A ligand atom donor set as the basis for our EXAFS analysis, but excluded the more distant methionine and main-chain carbonyl ligand atoms, as these did not contribute to the EXAFS of either *T. thermophilus* or *B. subtilis*. For the oxidized azurin mutant, the best fit to the data was obtained with 1 Cu-N(His) at 1.92 \AA , 2 Cu-S(Cys) at 2.28 \AA , and 1 Cu-Cu at 2.39 \AA (Table I). The Cu-S(Cys) distance is comparable to that found in *T. thermophilus*, but the Cu-N(His) and Cu-Cu are 0.04 and 0.05 \AA shorter, respectively. This may reflect a more sterically compressed Cu_A center, perhaps as the result of forcing the normally mononuclear blue copper center in azurin to accept a dinuclear Cu_A center. The Cu-Cu Debye-Waller term for the oxidized purple azurin is also comparable to *T. thermophilus*, suggesting that Cu-Cu bonding also plays a role in eliciting electron-delocalized behavior via an even shorter copper-copper distance.

Analysis of the data for the reduced azurin mutant, however, tells a very different story. Here, the characteristic oscillations due to the short copper-copper distance are severely attenuated (Fig. 10, top inset, top spectrum). In addition to Cu-N(His) and Cu-S(Cys) shells at 2.09 and 2.22 \AA , respectively, a weak Cu-Cu interaction is observed at 2.51 \AA but with a Debye-Waller factor of 0.027 \AA^2 , as compared with 0.007 \AA^2 in reduced *T. thermophilus* (Table I). The electrospray mass spectrum of the reduced azurin sample indicated that one of the two coppers was lost from the majority of the Cu_A sites on reduction, leaving only a small fraction observable as intact reduced Cu_A centers in the EXAFS analysis. The

metrical details of the reduced Cu_A azurin site thus reflect those of a reduced mononuclear type 1 center. Unlike the functional Cu_A sites of the soluble cytochrome oxidase subunit II domains, the loop-directed mutant appears to be unstable with respect to reduction.

Further evidence for a dramatic change in structure accompanying reduction is found in the comparison of the Cu K-absorption edges of oxidized and reduced forms of the azurin mutant shown in Fig. 11. While the absorption edges of oxidized *T. thermophilus* and purple azurin Cu_A mutants are superimposable (indicative of closely related geometric and electronic structure) (Fig. 10, bottom inset), the reduced azurin edge shows little resemblance to its oxidized counterpart and more closely resembles that of the reduced wild-type azurin (data not shown).

Conclusions

We have used XAS to determine the structures of the oxidized and reduced forms of a number of different Cu_A constructs. The main conclusions are as follows.

I. The Cu_2S_2 diamond core is preserved in all the oxidized (mixed-valence) derivatives, with closely similar distances and geometries.

II. Reduction causes a small expansion of the core in the cytochrome oxidase subunit II constructs, but leads to fragmentation of the cluster in the loop-directed azurin mutant.

III. The rapid rate of electron transfer exhibited by the cytochrome oxidase subunit II constructs is due at least in part to minimal structural change in the core cluster geometry accompanying the redox process, resulting in a very small reorganizational energy for electron transfer.

IV. The temperature dependence of the Debye-Waller factors suggest that copper-copper bonding is significant in the oxidized (mixed-valence) forms, but is probably absent in the fully reduced forms. The instability of the loop-directed mutants supports the premise that Cu-Cu bonding is a contributing factor in stabilizing the oxidized form of the azurin mutant.

Acknowledgments. This work was supported by the following grants from the National Institutes of Health: GM52830 to NJB, GM47365 to WBT, and GM35342 to JAF. We gratefully acknowledge the use of facilities at the Stanford Synchrotron Radiation Laboratory, which is supported by the National Institutes of Health Biomedical Research Technology Program, Division of Research Resources, and by the Department of Energy, Office of Health and Environmental Research.

Literature Cited

(1) Shapleigh, J. P.; Hosler, J. P.; Tecklenburg, M. M. J.; Kim, Y.; Babcock, G. T.; Gennis, R. B.; Ferguson, M. S. *Proc. Natl. Acad. Sci. U.S.A.* **1992**, *89*, 4786-4790.

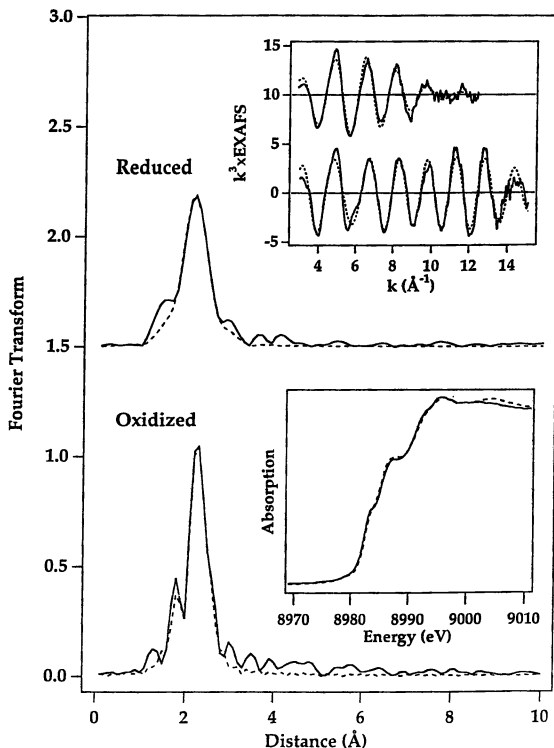


Figure 10. EXAFS analysis of oxidized and reduced azurin Cu_A . The top inset shows experimental (solid) versus simulated (dashed) spectra for oxidized (bottom spectrum) and reduced (top spectrum). The bottom inset shows the superposition of the Cu K absorption edges of oxidized azurin Cu_A (solid) and oxidized *T. thermophilus* (dashed).

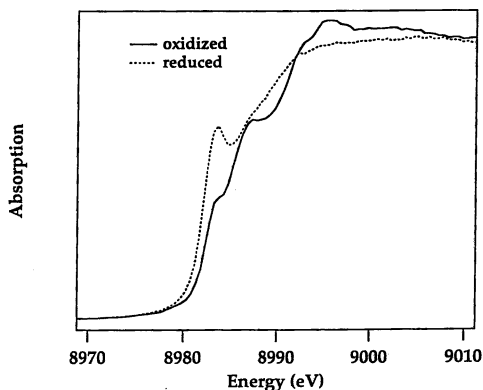


Figure 11. Cu K absorption edges for oxidized (solid) and reduced (dashed) azurin Cu_A .

- (2) Shapleigh, J. P.; Hill, J. J.; Alben, J. O.; Gennis, R. B. *J. Bacteriol.* **1992**, *174*, 2338–2343.
- (3) Lappalainen, P.; Aasa, R.; Malmstrom, B. G.; Saraste, M. *J. Biol. Chem.* **1993**, *268*, 26416–26421.
- (4) Mueller, M.; Schlaepfer, B.; Azzi, A. *Proc. Natl. Acad. Sci. U.S.A.* **1988**, *85*, 6647–6651.
- (5) Steinruecke, P.; Steffens, G. C. M.; Panskus, G.; Buse, G.; Ludwig, B. *Eur. J. Biochem.* **1987**, *167*, 431–439.
- (6) von Wachenfeldt, C.; de Vries, S.; van der Oost, J. *FEBS Lett.* **1994**, *340*, 109–113.
- (7) Fee, J. A.; Yoshida, T.; Surerus, K. K.; Mather, M. W. *J. Bioenerg. Biomembr.* **1993**, *25*, 103–114.
- (8) Hosler, J. P.; Ferguson-Miller, S.; Calhoun, M. W.; Thomas, J. W.; Hill, J.; Lemieux, L.; Ma, J.; Georgiou, C.; Fetter, J.; Shapleigh, J.; Tecklenburg, M. M. J.; Babcock, G. T.; Gennis, R. B. *J. Bioenerg. Biomembr.* **1993**, *25*, 121–136.
- (9) Calhoun, M. W.; Thomas, J. W.; Gennis, R. B. *Trends Biochem. Sci.* **1994**, *19*, 325–330.
- (10) Minghetti, K. C.; Goswitz, V. C.; Gabriel, N. E.; Hill, J. J.; Barassi, C. A.; Georgiou, C. D.; Chan, S. I.; Gennis, R. B. *Biochemistry* **1992**, *31*, 6917–6924.
- (11) Santana, M.; Kunst, F.; Hullo, M. F.; Rappoport, G.; Danchin, A.; Glaser, P. *J. Biol. Chem.* **1992**, *267*, 10225–10231.
- (12) Lauraeus, M.; Haltia, T.; Saraste, M.; Wikstrom, M. *Eur. J. Biochem.* **1991**, *197*, 699–705.
- (13) Beinert, H. *Eur. J. Biochem.* **1997**, *245*, 521–532.
- (14) Tsukihara, T.; Aoyama, H.; Yamashita, E.; Tomizaki, T.; Yamaguchi, H.; Shinzawa-Itoh, K.; Nakashima, R.; Yaono, R.; Yoshikawa, S. *Science* **1995**, *269*, 1069–1074.
- (15) Iwata, S.; Ostermeier, C.; Ludwig, B.; Michel, H. *Nature* **1995**, *376*, 660–669.
- (16) Ramirez, B. E.; Malmstrom, B. G.; Winkler, J. R.; Gray, H. B. *Proc. Natl. Acad. Sci. U.S.A.* **1995**, *92*, 11949–11951.
- (17) Hill, B. C. *J. Biol. Chem.* **1991**, *266*, 2219–2226.
- (18) Hill, B. C. *J. Biol. Chem.* **1994**, *269*, 2419–2425.
- (19) Adelroth, P.; Brezinski, P.; Malmstrom, B. G. *Biochemistry* **1995**, *34*, 2844–2849.
- (20) Fan, Y. C.; Ahmed, I.; Blackburn, N. J.; Boswell, J. S.; Verkhovskaya, M. L.; Hoffman, B. M.; Wikstrom, M. *Biochemistry* **1995**, *34*, 10245–10255.
- (21) Ferguson-Miller, S.; Babcock, G. T. *Chem. Rev.* **1996**, *96*, 2889–2907.
- (22) Lappalainen, P.; Watmough, N. J.; Greenwood, C.; Saraste, M. *Biochemistry* **1995**, *34*, 5824–5830.
- (23) Wilmanns, M.; Lappalainen, P.; Kelly, M.; Sauer-Eriksson, E.; Saraste, M. *Proc. Natl. Acad. Sci. U.S.A.* **1995**, *92*, 11955–11959.
- (24) Blackburn, N. J.; Barr, M. E.; Woodruff, W. H.; van der Oost, J.; de Vries, S. *Biochemistry* **1994**, *33*, 10401–10407.
- (25) Antholine, W. E.; Kastrau, D. H. W.; Steffens, G. C. M.; Buse, G.; Zumft, W. G.; Kroneck, P. M. H. *Eur. J. Biochem.* **1992**, *209*, 875–881.

- (26) Farrar, J. A.; Neese, F.; Lappalainen, P.; Kroneck, P. M. H.; Saraste, M.; Zumft, W. G.; Thompson, A. J. *J. Am. Chem. Soc.* **1996**, *118*, 11501–11514.
- (27) Fee, J. A.; Sanders, D.; Slutter, C. E.; Doan, P. E.; Aasa, R.; Karpefors, M.; Vanngard, T. *Biochem. Biophys. Res. Commun.* **1995**, *212*, 77–83.
- (28) Karpefors, M.; Slutter, C. E.; Fee, J. A.; Aasa, R.; Kallebring, B.; Larsson, S.; Vanngard, T. *Biophys. J.* **1996**, *71*, 2823–2829.
- (29) Williams, K. R.; Gamelin, D. R.; Lacroix, L. B.; Houser, R. P.; Tolman, W. B.; Mulder, M. C.; de Vries, S.; Hedman, B.; Hodgson, K. O.; Solomon, E. I. *J. Am. Chem. Soc.* **1997**, *119*, 613–614.
- (30) Gamelin, D. R.; Bominaar, E. L.; Kirk, M. L.; Weighardt, K.; Solomon, E. I. *J. Am. Chem. Soc.* **1996**, *118*, 8085–8097.
- (31) Scott, R. A. *Annu. Rev. Biophys. Biophys. Chem.* **1989**, *18*, 137–158.
- (32) Li, P. M.; Malmstrom, B. G.; Chan, S. I. *FEBS Lett.* **1989**, *248*, 210–211.
- (33) van der Oost, J.; Lappalainen, P.; Musacchio, A.; Warne, A.; Lemieux, L.; Rumbley, J.; Gennis, R. B.; Aasa, R.; Pascher, T.; Malmstrom, B. G.; Saraste, M. *EMBO J.* **1992**, *11*, 3209–3217.
- (34) Kelly, M.; Lappalainen, P.; Talbo, G.; Haltia, T.; van der Oost, J.; Saraste, M. *J. Biol. Chem.* **1993**, *268*, 16781–16787.
- (35) Slutter, C. E.; Sanders, D.; Wittung, P.; Malmstrom, B. G.; Aasa, R.; Richards, J. H.; Gray, H.; Fee, J. A. *Biochemistry* **1996**, *35*, 3387–3395.
- (36) Andrew, C. R.; Han, J.; de Vries, S.; van der Oost, J.; Averill, B. A.; Loehr, T. M.; Sanders-Loehr, J. *J. Am. Chem. Soc.* **1994**, *116*, 10805–10806.
- (37) Andrew, C. R.; Lappalainen, P.; Saraste, M.; Hay, M. T.; Lu, Y.; Dennison, C.; Canters, G. W.; Fee, J. A.; Slutter, C. E.; Nakamura, N.; Sanders-Loehr, J. *J. Am. Chem. Soc.* **1995**, *117*, 10759–10760.
- (38) Andrew, C. R.; Fraczkiwicz, R.; Czernuszewicz, R. S.; Lappalainen, P.; Saraste, M.; Sanders-Loehr, J. *J. Am. Chem. Soc.* **1996**, *118*, 10436–10445.
- (39) Andrew, C. R.; Sanders-Loehr, J. *Acc. Chem. Res.* **1996**, *29*, 365–372.
- (40) Blackburn, N. J.; de Vries, S.; Barr, M. E.; Houser, R. P.; Tolman, W. B.; Sanders, D.; Fee, J. A. *J. Am. Chem. Soc.* **1997**, *119*, 6135–6143.
- (41) Farrar, J. A.; Lappalainen, P.; Zumft, W. G.; Saraste, M.; Thompson, A. J. *Eur. J. Biochem.* **1995**, *232*, 294–303.
- (42) Bertini, I.; Bren, K. L.; Clemente, A.; Fee, J. A.; Gray, H.; Luchinat, C.; Malmstrom, B. G.; Richards, J. H.; Sanders, D.; Slutter, C. E. *J. Am. Chem. Soc.* **1996**, *118*, 11658–11659.
- (43) Lappalainen, P.; Saraste, M. *Biochim. Biophys. Acta* **1994**, *1187*, 222–225.
- (44) Houser, R. P.; Young, V. G. J.; Tolman, W. B. *J. Am. Chem. Soc.* **1996**, *118*, 2101–2102.
- (45) Barr, M. E.; Smith, P. H.; Antholine, W. E.; Spencer, B. *J. Chem. Soc. Chem. Commun.* **1993**, 1649–1652.
- (46) Boswell, J. S.; Reedy, B. J.; Kulathila, R.; Merkler, D. J.; Blackburn, N. J. *Biochemistry* **1995**, *35*, 12241–12250.
- (47) Immoos, C.; Hill, M. G.; Sanders, D.; Fee, J. A.; Slutter, C. E.; Richards, J. H.; Gray, H. B. *J. Biol. Inorg. Chem.* **1996**, *1*, 529–531.
- (48) Wallace-Williams, S. E.; James, C. A.; de Vries, S.; Saraste, M.; Lappalainen, P.; van der Oost, J.; Fabian, M.; Palmer, G.; Woodruff, W. H. *J. Am. Chem. Soc.* **1996**, *118*, 3986–3987.

- (49) Neese, F.; Zumft, W. G.; Antholine, W. G.; Kroneck, P. M. H. *J. Am. Chem. Soc.* **1996**, *118*, 8692–8699.
- (50) Dennison, C.; Vijgenboom, E.; de Vries, S.; van der Oost, J.; Canters, G. W. *FEBS Lett.* **1995**, *365*, 92–94.
- (51) Hay, M.; Richards, J. H.; Lu, Y. *Proc. Natl. Acad. Sci. U.S.A.* **1996**, *93*, 461–464.

Antiferromagnetic Exchange, Biquadratic Exchange, and Metal–Metal Bond in Metal Clusters: Application to the Multielectron versus Successive Monoelectron Steps Dilemma

J. J. Girerd and E. Anxolabéhère-Mallart

Laboratoire de Chimie Inorganique, URA CNRS 420, Institut de Chimie Moléculaire d'Orsay, Université Paris-Sud, 91405 Orsay, France

It is recalled that the Hubbard model constitutes a simple unified theory of metal-metal interactions in clusters, from weak ones leading to magnetic exchange to strong ones leading to metal-metal bond. This theory is then specifically applied to the study of the electronic factors which govern the difference ΔE^0 in redox potentials for two successive events in a homodinuclear system. It is found that $V < e\Delta E^0 < (U + V) / 2$ in which U and V are respectively the intra and intersite electron-electron repulsion and e is the charge of the electron. For small delocalization energy $|\beta|$ versus $U - V$, i.e. for metal clusters presenting magnetic exchange phenomena, one finds $e\Delta E^0 = V + 2|\beta|$. We propose that in dimanganese di- μ -oxo systems (Mn-Mn distance = 2.7 Å), the origin of the redox gap $\Delta E^0 = E^0(\text{Mn}^{\text{IV}}\text{Mn}^{\text{IV}}/\text{Mn}^{\text{III}}\text{Mn}^{\text{IV}}) - E^0(\text{Mn}^{\text{III}}\text{Mn}^{\text{IV}}/\text{Mn}^{\text{III}}\text{Mn}^{\text{III}})$ (around 1 V) is due to the intersite electron-electron repulsion. In this framework any interaction between the two metal centers increase the redox gap. This effect can be diminished or annihilated by coupling chemical events like protonation. In that case the system can present a multielectron behavior versus successive mono-electronic steps in the former case.

Bioinorganic spectroscopists are discovering more and more examples of metal clusters in proteins. This is a fascinating field since those systems are really original and truly intriguing. In a large number of systems, these clusters are implicated in redox reactions. Relevant examples are the tetranuclear Mn-oxo cluster of the Oxygen Evolving Complex in plants and the FeMo cofactor of nitrogenase. In a first part, we will briefly review the basic features of the electronic structure of metal clusters using Hückel¹ or Hubbard² models. The first one is well known in organic chemistry; it takes into account only the Coulomb integral (α) and the resonance integral (β). The second one is well known in solid state physics and is basically an extension of the Hückel model by taking into account also electron-electron repulsions on-site (U) and intersite (V). The Hubbard model is very convenient for a description of the electronic properties of metal clusters. In particular it allows in a very simple way to illustrate the continuity between exchange interaction and metal-metal bonding. In a second part, we will discuss a simple

application of the Hubbard model to redox properties of metal clusters, specifically to the problem of which electronic factors determine a multielectron behavior versus a sequential one. We will give a simple formula to relate the separation in potential of two successive redox events in a homodinuclear cluster to the parameters of the Hubbard model. These considerations can be applied to metal clusters of bioinorganic interest.

Hückel model: metal clusters as conjugated hydrocarbons.

The first step in such a model theory is to select among all the orbitals of the problem, a subset which are thought to be the most implicated ones for the particular chemical problem under scrutiny. In Hückel theory of conjugated hydrocarbons, the only orbitals taken into account are the p_z orbitals on the carbon atoms. The second step is to choose the integrals which are retained in the calculation. This choice results from a compromise between simplicity desired in calculations and inclusion of all integrals. In Hückel model, the overlap integral between p_z orbitals is neglected (due to its small value) although the resonance integral β between adjacent carbon atoms is retained. The energy of the p_z orbital in the molecule is called Coulomb integral and is noted α . The Hückel model has had a tremendous impact on organic chemistry allowing simple molecular orbital calculations.¹

It is legitimate to extend Hückel theory to metal clusters. Indeed a linear Cu(II) trinuclear cluster has some analogy with an allyl radical. Three orbitals may be selected, a, b, c, one on each Cu(II). We will neglect the overlaps between these orbitals. We will also assume that these orbitals have the same Coulomb integral α and we will designate the resonance integral between two adjacent Cu(II) as β . So one sees that the same type of calculations can be made for metal clusters than for conjugated hydrocarbons. One can even consider clusters of clusters (see for instance dimers of Fe-S cubanes in R. H. Holm's chapter, this volume).

In such a theory a Cu(II) dimer (formally analogous to an ethylene molecule) will give rise to two molecular orbitals

$$\phi_{\pm} = (a \pm b)/\sqrt{2}$$

of energy $\alpha \pm \beta$. By populating these molecular orbitals, the following states will be obtained:

- a singlet $^1\Gamma_g$: energy $E = 2\alpha + 2\beta$, wavefunction $|\phi_+\alpha\phi_+\beta\rangle$
- a triplet $^3\Gamma_u$: energy $E = 2\alpha$, wavefunction $|\phi_+\alpha\phi_-\alpha\rangle$ ($M_S = +1$)
- a singlet $^1\Gamma_u$: energy $E = 2\alpha$, wavefunction $(1/\sqrt{2})(|\phi_+\alpha\phi_-\beta\rangle - |\phi_+\beta\phi_-\alpha\rangle)$
- a singlet $^1\Gamma_g$: energy $E = 2\alpha - 2\beta$, wavefunction $|\phi_-\alpha\phi_-\beta\rangle$

The notation $\phi_+\alpha$ stands for a spinorbital with spin up and $\phi_+\beta$ for a spinorbital with spin down; $|\phi_+\alpha\phi_+\beta\rangle$ stands for the antisymmetric two electrons wavefunction and is equivalent to a Slater determinant. Its sign will change if one permutes the two spinorbitals. The energies of these states are represented in Figure 1. It can be seen that for $|\beta| \neq 0$, the ground state of the Cu(II)₂ pair will be a spin singlet $^1\Gamma_g$ state. This seems fine since it is well known from magnetic susceptibility measurements that the vast majority of Cu(II)₂ dimers have a spin singlet ground state. Nevertheless, the Hückel model predicts for the first excited states one spin singlet degenerate with a spin triplet. This is in contradiction with what is observed in those Cu(II) dimers in which the first excited state is only a spin triplet: an excited spin singlet state close in energy is

not observed. Indeed the very fact that those Cu(II) dimers present a spin singlet ground state and an excited spin triplet state which can be understood as arising from the coupling of the spin doublet ground states of both Cu(II) ions, constitutes the phenomenon of antiferromagnetic coupling.³ This failure of the Hückel model for small $|\beta|$ values is well known. In fact, when $|\beta|$ is small, electron-electron interactions can no longer be neglected. Hubbard model implements Hückel model in taking into account electron-electron interactions in the simplest way.

In order to help the reader who is not familiar with the Hubbard model, we will describe the Hückel model a second time but using now the formalism adapted to the Hubbard model. It will look pedantic but indeed will help to go from one model to the other. Instead of molecular orbitals as above, we will use multielectronic wavefunctions built on the local orbital basis selected, orbitals a and b. For instance, for a Cu(II) dinuclear system one has six possible wavefunctions $|a\alpha b\alpha\rangle$, $|a\beta b\beta\rangle$, $|a\alpha b\beta\rangle$, $|a\beta b\alpha\rangle$ (covalent wavefunctions) and $|a\alpha a\beta\rangle$ and $|b\alpha b\beta\rangle$ (ionic wavefunctions). The Hückel Hamiltonian will be written as

$$H = \sum_i \alpha_i n_i + \sum_{i<j} \beta_{ij} t_{ij}$$

where n_i is the occupation operator for site i and t_{ij} is the transfer operator between sites i and j .⁴ For a symmetric Cu(II) dimer the previous Hamiltonian can be written as

$$H = \alpha (n_a + n_b) + \beta t_{ab} = 2\alpha + \beta t_{ab}$$

since $(n_a + n_b) = 2$. The transfer operator t_{ab} moves the electron, keeping its spin unchanged, and acts as follows:

$$t_{ab} |a\alpha b\beta\rangle = |b\alpha b\beta\rangle + |a\alpha a\beta\rangle$$

Four states are obtained:

- a singlet $^1\Gamma_g$: energy $E = 2\alpha + 2\beta$, wavefunction $(1/2)(|a\alpha b\beta\rangle - |a\beta b\alpha\rangle + |a\alpha a\beta\rangle + |b\alpha b\beta\rangle)$
- a triplet $^3\Gamma_u$: energy $E = 2\alpha$, wavefunction $|a\alpha b\alpha\rangle$ ($M_S = +1$)
- a singlet $^1\Gamma_u$: energy $E = 2\alpha$, wavefunction $(1/\sqrt{2})(|a\alpha a\beta\rangle - |b\alpha b\beta\rangle)$
- a singlet $^1\Gamma_g$: energy $E = 2\alpha - 2\beta$, wavefunction $(1/2)(|a\alpha b\beta\rangle - |a\beta b\alpha\rangle - |a\alpha a\beta\rangle - |b\alpha b\beta\rangle)$

Comparison of the energy values obtained in both ways immediately shows that as expected, the formalism does not change the result. One can check that the wavefunctions are identical too. We will now introduce simply the Hubbard model using this formalism.

Hubbard model: electrons avoid each other.

Hubbard model is well known in solid state physics and is basically an extension of Hückel theory by taking into account also electron-electron repulsions. Originally, Hubbard² proposed to take into account only on-site repulsion U

$$U = \int a(1)a(2)(1/r_{12})a(1)a(2)d\tau_1d\tau_2$$

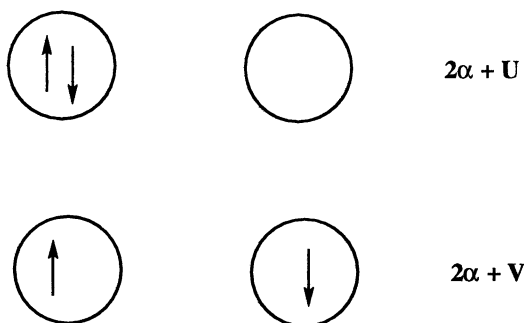
when two electrons occupy the same orbital. A modern presentation of Hubbard model can be found in ref ⁵. Intuitively this on-site repulsion will, for instance in a Cu(II)Cu(II) dimer, make the two unpaired electrons to avoid each other, which

chemically means that a Cu(III)Cu(I) electron repartition will be less sensible. Recently, the Hubbard model has been much applied by solid-state physicists in the context of the study of cuprate superconductors following a suggestion by Anderson in 1987.⁶

Very often the intersite repulsion V

$$V = \int a(1)b(2)(1/r_{12})a(1)b(2)d\tau_1d\tau_2$$

is also taken into account. We will propose below that this term plays an important role in electrochemical properties of metal clusters. The terms U and V are illustrated in the following scheme which gives the energies of two neighboring sites



One sees immediately that taking into account the U and V terms makes these two situations non equivalent: the electrons will no longer be described as moving freely from one center to the other as it is done in Hückel model.

From a formal point of view, Hubbard Hamiltonian is written as

$$H = \sum_i \alpha_i n_i + \sum_{i<j} \beta_{ij} t_{ij} + \sum_i U_i n_{i\alpha} n_{i\beta} + \sum_{i<j} V_{ij} n_i n_j$$

in which $n_{i\alpha(\beta)}$ counts electron on site i with spin up (down). One has $n_i = n_{i\alpha} + n_{i\beta}$.

For a symmetric Cu(II) dimer the previous Hamiltonian can be written as

$$H = 2 \alpha + \beta t_{ab} + U (n_{a\alpha} n_{a\beta} + n_{b\alpha} n_{b\beta}) + V n_a n_b$$

The energy of the triplet ${}^3\Gamma_u$ becomes $E = 2 \alpha + V$ and that of the singlet ${}^1\Gamma_u$, $E = 2 \alpha + U$. The singlets ${}^1\Gamma_g$ are now mixed by the repulsion terms and one gets two states of energy⁷

$$E = 2 \alpha + V + (U - V \pm \sqrt{(U - V)^2 + 16 \beta^2})/2$$

The energies of these states are represented in Figure 2. Hubbard theory correctly predicts a singlet ground state with an excited triplet state.⁸ It is interesting to study those lowest states. In the limit of small $|\beta|$, one can expand the energy difference between the spin triplet and the spin singlet states to find

$$E(\text{triplet}) - E(\text{singlet}) = -(U - V - \sqrt{(U - V)^2 + 16 \beta^2})/2 = 4 \beta^2 / (U - V)$$

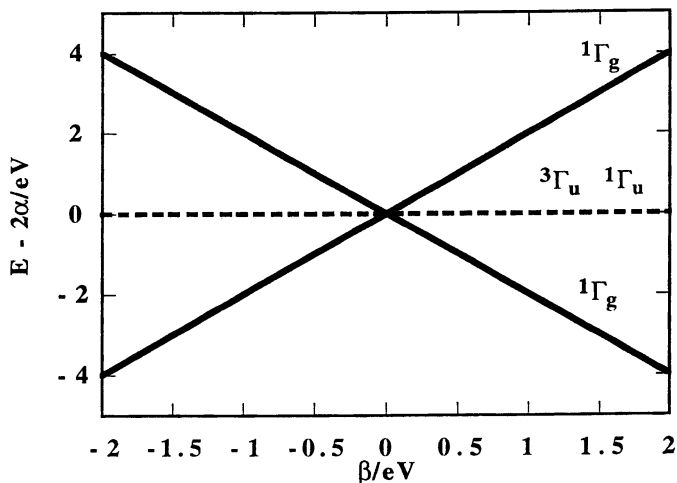


Figure 1. Energy of the states obtained in Hückel theory for a homodinuclear system with two electrons and one orbital per site as a function of the resonance integral β . i) (—) spin singlets ${}^1\Gamma_g$ of energy $E = 2\alpha \pm 2\beta$; ii) (- - -) spin triplet ${}^3\Gamma_u$ of energy $E = 2\alpha$ and spin singlet ${}^1\Gamma_u$ of energy $E = 2\alpha$. The quantity $E - 2\alpha$ is plotted.

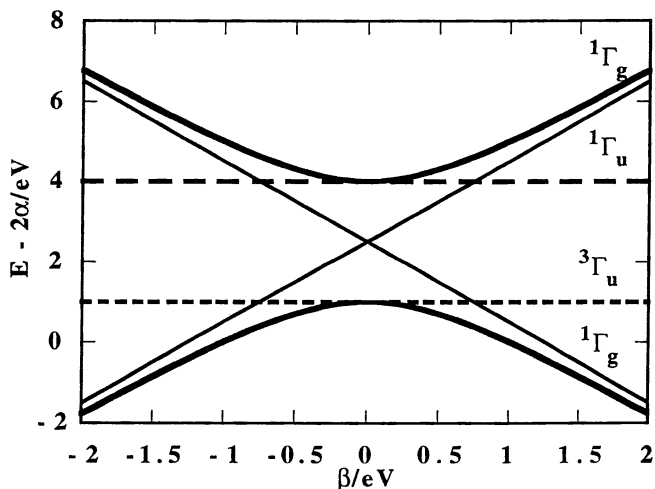


Figure 2. Energy of the states obtained in Hubbard theory for a homodinuclear system with two electrons and one orbital per site as a function of the resonance integral β . i) (—) spin singlets ${}^1\Gamma_g$; ii) (- - -) spin triplet ${}^3\Gamma_u$ of energy $E = 2\alpha + V$; iii) (_ _ _) spin singlet ${}^1\Gamma_u$ of energy $E = 2\alpha + U$. The states corresponding to double occupancy of the MO's (metal-metal single bond) are represented by thin lines. The area around $|\beta| = 0$ corresponds to antiferromagnetic exchange. The quantity $E - 2\alpha$ is plotted. $U = 4\text{ eV}$, $V = 1\text{ eV}$.

assuming $U > V$. This expression relates the antiferromagnetic exchange constant appearing in Heisenberg Hamiltonian $H = -J \mathbf{S}_a \mathbf{S}_b$ to the fundamental integrals of the Hubbard model⁹

$$J = -4 \beta^2 / (U - V)$$

The central part of Figure 2 (corresponding to small $|\beta|$) thus corresponds to magnetic exchange phenomena. The mixing of the $^1\Gamma_g$ spin singlet states leads also to a redefinition of the wavefunctions. In the limit of small $|\beta|$, the lowest singlet wavefunctions becomes $(1/\sqrt{2})(|\alpha\alpha\beta\rangle - |\alpha\beta\alpha\rangle)$, i. e. double occupancy of one site is avoided.

Expanding the energy difference to higher order we obtain

$$E(\text{triplet}) - E(\text{singlet}) = 4 \beta^2 / (U - V) - 16 \beta^4 / (U - V)^3$$

The term in $\beta^4 / (U - V)^3$ corresponds to biquadratic exchange although in the simple case of two Cu(II) ions, biquadratic exchange contributes only to a redefinition of the singlet-triplet gap.¹⁰

In the limit of large $|\beta|$, the energy of the singlet states becomes asymptotically equal to

$$E = 2 \alpha - 2 |\beta| + (U + V) / 2$$

This is precisely the energy of the lowest Hückel state corresponding to the occupation of the lowest MO by the two electrons, the average electron-electron repulsion in that MO being added. This corresponds to the classical description of a metal-metal bond.

Thus Hubbard theory offers an unified theory of metal-metal interaction from antiferromagnetic exchange to metal-metal bond. There is a continuum of situations between these two limits, depending on $|\beta|$, or more precisely on the value of the ratio $|\beta| / (U - V)$.

Application to redox properties of metal clusters: the case of manganese - oxo clusters.

Let us consider the simple case of a symmetrical dinuclear system with one active orbital per site. Hubbard theory allows to compute the energy of the different redox states $A^i B^j$ where i and j refer to the number of electrons. One has

$$E(A^0 B^0) = 0$$

$$E(A^1 B^0) = \alpha - |\beta|$$

$$E(A^1 B^1) = 2 \alpha + V + (U - V - \sqrt{(U - V)^2 + 16 \beta^2})/2$$

This leads to

$$eE^0(A^0 B^0/A^1 B^0) = -(\alpha - |\beta|)$$

$$eE^0(A^1 B^0/A^1 B^1) = -(\alpha + V + (U - V - \sqrt{(U - V)^2 + 16 \beta^2})/2 + |\beta|)$$

where e is the charge of the electron. Clearly these expressions are oversimplified, neglecting solvation energy and entropy effects. We will use only their difference

$$e\Delta E^0 = e\{E^0(A^0B^0/A^1B^0) - E^0(A^1B^0/A^1B^1)\} = V + (U - V - \sqrt{(U - V)^2 + 16\beta^2})/2 + 2|\beta|$$

This is the expression we found for the difference between the potentials of two successive redox events in a dinuclear system. In this difference the effects we have neglected will largely cancel out and we propose that this expression can help in understanding the origin of multielectron behavior versus successive mono-electronic steps. In Figure 3 the expression ΔE^0 is represented as a function of $|\beta|$. Mathematically, one finds that $\min(U, V) < e\Delta E^0 < (U + V) / 2$. Here we assume $U > V$ so that one has $V < e\Delta E^0 < (U + V) / 2$. This means that in a dinuclear system in which the orbital interaction $|\beta|$ is negligible, ΔE^0 mainly reflects the electron - electron repulsion from one site to the other. This will mainly depend of the intercenter distance and if the centers are far apart one will evidently observe the reduction of both centers at the same potential. When the orbital interaction $|\beta|$ will increase but stay smaller than $U - V$ as usual in metal clusters presenting magnetic exchange phenomena, ΔE^0 will increase as $e\Delta E^0 = V + 2|\beta|$: orbital communication will increase the difference between the two redox steps. In this approach a multielectron process will be observed only for non-interacting systems ($V = \beta = 0$). The role of the intersite electron-electron repulsion V in the determination of the value of the redox gap for a dimer has already been proposed through a different road by Sutton et al.¹¹ One notice in Figure 3, that if $U = V$, $e\Delta E^0 = V$, whatever $|\beta|$ is.

The above considerations are summarized in Figure 4. Figure 4a corresponds to $\beta = V = 0$. One has $E(A^0B^0) = 0$, $E(A^1B^0) = \alpha$ and $E(A^1B^1) = 2\alpha$. The states are equidistant and the two redox steps will have the same potential ($\Delta E^0 = 0$). Figure 4b shows the effect of the intersite electron-electron repulsion V . The potentials will become different ($e\Delta E^0 = V$). Figure 4c illustrates the effect of delocalization β . The A^1B^0 state will be more stabilized (stabilization of the order of β) than the A^1B^1 one (stabilization of the order of J). The separation between the potentials will increase ($e\Delta E^0 = V + 2|\beta|$).

The previous very simple theory ignores chemical changes which could accompany redox transformations. One simple example is protonation of an oxo bridge between two metal ions upon reduction of the dinuclear entity.¹² This will stabilize the A^1B^1 state (Figure 4d) and makes the potentials closer. This can lead to multielectron redox behavior.

We would like to briefly illustrates the previous consideration with dinuclear $Mn^{III,IV}$ systems which are currently under study to help to the understanding of the role of manganese in the photosynthetic Oxygen Evolving Complex.¹³

A very common motif is the dimanganese di- μ -oxo entity. In several cases the potentials of the couples $Mn^{IV}Mn^{IV}/Mn^{III}Mn^{IV}$ and $Mn^{III}Mn^{IV}/Mn^{III}Mn^{III}$ are known.¹⁴ Although those potentials differ from one case to the other, a remarkable feature is that the potential separation in acetonitrile is rather constant, of the order of 1 V. From the above calculation, we propose that this separation reflects mainly the electron-electron intersite repulsion in the $Mn^{III}Mn^{III}$ state (Mn-Mn distance = 2.7 Å). In the μ -oxo-di- μ -carboxylato [(TACN') $Mn^{III}O(CH_3CO_2)_2Mn^{III}(TACN')$]²⁺ cation where TACN' stands for N,N',N''-1,4,7-triazacyclononane,¹⁵ the difference $\Delta E^0 =$

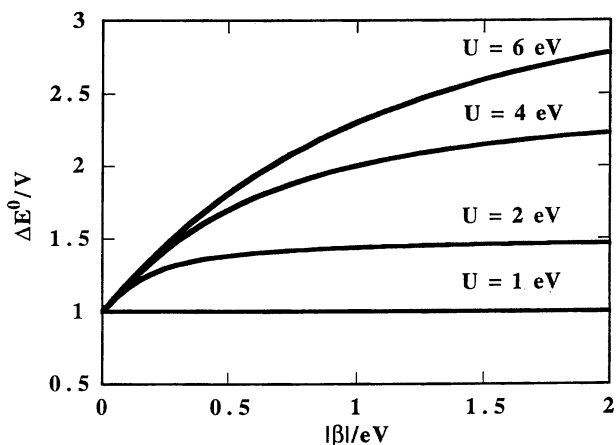


Figure 3. Difference in successive redox potentials $\Delta E^0 = E^0(A^0B^0/A^1B^0) - E^0(A^1B^0/A^1B^1)$ for a dimer AB as a function of absolute value of the resonance integral $|\beta|$. $V = 1$ eV. The value of U is indicated. Notice the linear regime for small $|\beta|$ values corresponding to $e\Delta E^0 = V + 2|\beta|$.

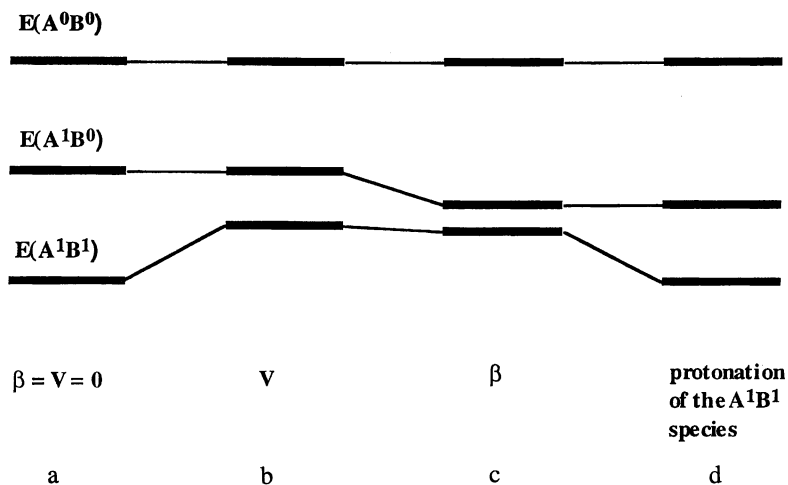


Figure 4. Pictorial representation of the different factors influencing the energy of different redox states of a dimer and henceforth the difference in successive redox potentials. (a) $\beta = V = 0$. One has $E(A^0B^0) = 0$, $E(A^1B^0) = \alpha$ and $E(A^1B^1) = 2\alpha$. The states are equidistant and the two redox steps will have the same potential ($\Delta E^0 = 0$). (b) $V \neq 0$. The potentials will become different ($e\Delta E^0 = V$). (c) $V \neq 0$, $\beta \neq 0$. The A^1B^0 state will be more stabilized (stabilization of the order of β) than the A^1B^1 one (stabilization of the order of J). The separation between the potentials will increase ($e\Delta E^0 = V + 2|\beta|$). (d) A chemical change like a protonation of the oxo bridge of the most reduced species can decrease ΔE^0 .

$E^0(\text{Mn}^{\text{IV}}\text{Mn}^{\text{IV}}/\text{Mn}^{\text{III}}\text{Mn}^{\text{IV}}) - E^0(\text{Mn}^{\text{III}}\text{Mn}^{\text{IV}}/\text{Mn}^{\text{III}}\text{Mn}^{\text{III}}) = 0.66 \text{ V}$, smaller than that of 1 V mentioned above for di- μ -oxo systems. This is expected from the larger Mn-Mn distance = 3.1 Å which leads to a smaller V repulsion energy.

An example from the iron-sulfur field can be taken from the work of the group of Coucouvanis on double cubane systems singly (N_2H_4 or pyrazine) or doubly bridged (N_2H_4 and sulfur).¹⁶ The singly bridged systems are extended and the cubanes ignore each other from a redox point of view. In the doubly bridged systems, in which the cubanes are brought closer to each other, a 230 mV split of the voltammetric waves was observed. This interaction must be due to both the V and β terms. The authors have proposed that delocalization is the principal factor in that case. From our approach, the role of V cannot be ignored either.

Conclusions and perspectives

Application of Hubbard Hamiltonian to metal clusters allows a simple unified treatment of metal-metal interactions from magnetic exchange to metal-metal bond.

Inside that framework we deduced a simplified expression for the redox-potential separation ΔE^0 for an homodinuclear system. We found that for small delocalization energy, $e\Delta E^0 = V + 2|\beta|$ where V is the intersite electron-electron repulsion. The importance of this V term in the determination of the redox gap had already been proposed,¹¹ although through a different approach. Within this framework it is clear that any interaction between the two centers will lead to a redox gap. The only possibility to explain multielectron behavior is the introduction of chemical events, such as protonation of bridging oxygen atoms.

Applying this theory to dimanganese di- μ -oxo units (important for the photosynthetic OEC problem) we found that the separation in potential in this series is mainly due to the V term.

One can envision developments of the application of Hubbard model to higher nuclearity metal clusters with an arbitrary number of electrons, some of these situations leading possibly to an expression for the separation in potential between successive steps different from that proposed here. This problem deserves to be studied both theoretically and experimentally.

Literature Cited

¹ See for instance Salem, L. *The Molecular Orbital Theory of Conjugated Systems*, Benjamin, New York, 1966.

² Hubbard, J. *Proc. Roy. Soc. (London)* **1963**, A276, 238-257.

³ Kahn, O. *Molecular Magnetism*, VCH, Springer-Verlag: New-York, 1986.

⁴ Usually the Hubbard Hamiltonian is presented with second quantization operators. For the reader familiar with second quantization, one has simply $t_{ij} = \sum_{\sigma} (c_{i\sigma}^+ c_{j\sigma} + c_{j\sigma}^+ c_{i\sigma})$ where $i\sigma$ corresponds to the spinorbital on center i with spin σ .

⁵ Schatz, G. C.; Ratner, M. A. *Quantum Mechanics in Chemistry*, Prentice Hall 1993. See also simple introduction in the field of p conjugate systems by Matsen, F. A.; Fox, M. A. *J. Chem. Ed.* **1985**, 62, 367-373.

⁶ Anderson, P. W. *Science* **1987**, 235, 1196-1198.

⁷ Falicov, L. M.; Harris, R. A. *J. Chem. Phys.* **1969**, 51, 3153-3158.

⁸ The Hubbard Hamiltonian as such cannot explain ferromagnetic coupling since positive exchange integrals are not included in the model. It can be done when necessary.

-
- ⁹ Anderson, P. W. in *Magnetism*, G. T. Rado and H. Suhl, vol 1, Academic Press, New York, 1963.
- ¹⁰ For ions with spins $S > 1/2$, biquadratic exchange can lead to qualitative change in the energy spectrum.
- ¹¹ Sutton, J. E.; Sutton, P. M.; Taube, H. *Inorg. Chem.* **1979**, *18*, 1017-1021.
- ¹² Baldwin, M. J.; Pecoraro, V. L. *J. Am. Chem. Soc.* **1996**, *118*, 11325-11326.
- ¹³ Yachandra, V.; Sauer, K.; Klein, M. P. *Chem. Rev.* **1996**, *96*, 2927-2950.
- ¹⁴ Y.-M. Frapart, A. Boussac, R. Albach, E. Anxolebèhère-Mallart, M. Delroisse, J.-B. Verlhac, G. Blondin, J.-J. Girerd, J. Guilhem, M. Césario, A.W. Rutherford, D. Lexa, *J. Am. Chem. Soc.*, 1996, **118**, 2669-2678 and references therein.
- ¹⁵ Wieghardt, K.; Bossek, U.; Nuber, B.; Weiss, J.; Bonvoisin, J.; Corbella, M.; Vitols, S. E.; Girerd, J.-J. *J. Am. Chem. Soc.* **1988**, *110*, 7398-7411.
- ¹⁶ Mosier, P. E.; Kim, C. G.; Coucouvanis, D. *Inorg. Chem.* **1993**, *32*, 2620-2621.

Progress in Characterization of the Photosystem II Oxygen Evolving Complex Using Advanced EPR Methods

R. David Britt¹, Dee Ann Force¹, Kristy A. Campbell¹, David W. Randall¹, Lane M. Gilchrist, Jr.¹, Keri L. Clemens¹, David M. Gingell¹, Jeffrey M. Peloquin¹, Donna P. Pham², and Richard J. Debus²

¹Department of Chemistry, University of California, Davis, CA 95616

²Department of Biochemistry, University of California, Riverside, CA 92521

We have utilized both continuous wave (CW) EPR and pulsed EPR spectroscopies to characterize the structure and function of the oxygen-evolving complex (OEC) of Photosystem II (PSII). Parallel polarization CW EPR spectroscopy of the dark-stable S_1 -state of the OEC in PSII particles isolated from the cyanobacterium *Synechocystis* sp. PCC 6803 reveals a $\Delta M_S = 0$ signal, centered at a g -value of approximately 12, with 18 or more well-resolved ^{55}Mn hyperfine lines. This signal provides direct evidence for the presence of a tri- or tetranuclear coupled Mn cluster in the S_1 -state. Electron spin echo (ESE) envelope modulation (ESEEM) and ESE-ENDOR experiments indicate that substrate water and small alcohol derived ligands are bound to the Mn cluster in the S_2 -state of the cycle. Progress in modeling the magnetic interaction between the photo-oxidized Y_Z^{\bullet} tyrosine and the Mn cluster is described, along with new pulsed EPR evidence supporting recent models that suggest Y_Z^{\bullet} is directly involved in the water oxidation chemistry.

Photosystem II (PSII) oxygen evolution occurs through a cycle of five “ S -state” intermediates, S_0 through S_4 , where the subscript represents the number of oxidizing equivalents abstracted from the PSII *oxygen evolving complex* (OEC) by the photooxidized P680^+ Chl moiety (1). The OEC consists of a tetranuclear Mn cluster, the redox-active tyrosine Y_Z (D1-Tyr161, *Synechocystis* notation), and the essential cofactors Cl^- and Ca^{2+} (2-4). Electron paramagnetic resonance spectroscopy has proven to be a powerful tool in studying the structure and function of the OEC. Extensive CW and pulsed EPR characterization of the odd-electron S_2 state has led to much of our current knowledge of the structure, protein ligation, and substrate and inhibitor binding modes of the Mn cluster (3). Further insights into the workings of the OEC have come from EPR studies of inhibited PSII samples poised in states two equivalents oxidized relative to the dark-stable S_1 state. Such PSII samples exhibit “ S_3 ”-state EPR signals (5) that have been

shown to arise from the oxidized tyrosine Y_Z^{\bullet} radical interacting magnetically with the paramagnetic Mn cluster (6,7). There have also been reports of an integer spin EPR signal from the S_1 -state detected via parallel polarization EPR spectroscopy (8,9). In this chapter we described recent CW and pulsed EPR results that further our knowledge of the magnetic properties of the S_1 -state, the substrate ligation to the Mn cluster in the S_2 -state, and the proximity of Y_Z^{\bullet} to the Mn cluster and its function in proton or H atom abstraction.

The S_1 -State Multiline Signal

For integer spin systems with nonnegligible zero-field splitting interactions, the EPR experiment, performed with the oscillating magnetic field \vec{B}_1 polarized parallel to the static magnetic field \vec{B}_0 , can provide for sensitive detection of " $\Delta M_S = 0$ " electron spin transitions (10,11). Dexheimer and Klein (8) applied such parallel polarization EPR spectroscopy to the study of the OEC in PSII-enriched spinach thylakoid membranes, and reported a broad (600 G peak-to-peak width), featureless EPR signal centered about the $g=4.8$ region of the spectrum, which they assigned to an $S=1$ spin state present in the S_1 -state of the OEC. This signal was recently reproduced by Yamauchi et al. (9). The spectrum bears some similarity to the parallel polarization EPR spectrum reported from a synthetic $2Mn(III)2Mn(IV)$ cluster (11). However no ^{55}Mn hyperfine structure is observed on the S_1 -state EPR signal, despite the resolution of ^{55}Mn hyperfine features in the parallel polarization EPR spectra of some integer spin Mn(III) complexes (12). Thus, although the disappearance of the signal upon illumination is correlated with the appearance of the S_2 -state multiline EPR signal, and the signal is abolished by a hydroxylamine treatment that destroys the manganese cluster, the most direct indication of a manganese origin of the signal, the detection of ^{55}Mn hyperfine features, is absent.

We have recently obtained parallel polarization EPR spectra of PSII particles isolated (13) from the cyanobacterium *Synechocystis* sp. PCC 6803. Figure 1 displays the "dark minus illuminated" parallel polarization EPR difference spectrum that results from subtracting the spectrum obtained after PSII sample illumination (195 K illumination temperature) from the spectrum of the dark-adapted sample taken before the illumination, a process that isolates the spectrum of the dark-stable S_1 -state. The S_1 -state spectrum consists of a well-resolved multiline EPR spectrum, with at least 18 hyperfine lines with an average splitting of 32 G, centered at an effective g -value of approximately 12. In exactly equivalent fashion to the conclusions generated by the observation of such multiline hyperfine structure in the $g=2$ (14) and $g=4.1$ (15) S_2 -state signals, this hyperfine pattern provides unambiguous evidence for the existence of a multinuclear exchange-coupled paramagnetic Mn cluster in the S_1 -state of *Synechocystis* PSII particles.

The contrast between this highly resolved cyanobacterial S_1 -state Mn multiline EPR signal and the broad featureless signal ascribed to the S_1 -state in spinach PSII membranes is quite dramatic. Preliminary simulations indicate that this $g \approx 12$ signal could arise from an $S = 1$ state with a near axial zero-field splitting tensor with a D value of approximately -0.280 cm^{-1} , in contrast to the $D = -0.125 \text{ cm}^{-1}$ and -0.140 cm^{-1} values utilized to simulate the spinach signal (8,9). Dexheimer and Klein (8) and Yamauchi et al. (9) noted that the spectrum assigned to the S_1 -state in spinach

PSII preparations could arise from the first excited state of a dinuclear Mn(III)Mn(III) cluster. However, this would not appear to be a sufficient "minimal unit" to explain the highly-structured EPR signal that we observe in *Synechocystis* PSII particles. The ^{55}Mn hyperfine splitting observed for Mn(III) mononuclear and dinuclear clusters is greater than 50 G (12), appreciably greater than the 32 G splitting observed here. More importantly, the hyperfine interactions for the two Mn ions of either Mn(III)Mn(III) or Mn(IV)Mn(IV) dinuclear clusters would be expected to be approximately equivalent, giving rise to 11-line EPR spectra. (The number of hyperfine lines for a system with k different classes of n_i equivalent spin I_i nuclei is $\prod_{i=1}^k (2n_i I_i + 1)$). In contrast, our S_1 -state signal consists of at least 18 hyperfine lines. The S_1 EPR signal exhibits this same lineshape over a temperature range of 3.6 to 9.0 K, and the signal amplitude closely follows a Curie law $1/T$ dependence, indicating that the signal arises from a single ground or very low-lying integer spin state. We therefore conclude that at least three of the four Mn ions of the OEC must be exchange-coupled in the S_1 -state to give rise to this integer spin EPR signal. Moreover, this highly-structured EPR signal, with at least 18 resolved ^{55}Mn hyperfine lines, will provide a new spectroscopic handle to study the S_1 -state that should prove equivalent to that which has been provided to the study of the S_2 -state by the $g = 2$ multiline signal.

Water Binding at the S_2 -State

The synchronization of the S -State cycle is defined by O_2 release during the $S_4 \rightarrow S_0$ transition. However, it has been more difficult to identify the transitions during which substrate waters bind to the OEC. One limiting view would have two waters binding in Mn ligation sites cleared upon the release of O_2 in the $S_4 \rightarrow S_0$ transition. In this case, the water ligands to Mn would be present in the most reduced state, S_0 . Alternatively, the OEC may exclude water from the catalytic site during early S states to prevent formation of unwanted oxidation byproducts. Thus, the other limiting view would be to have waters bind to Mn only upon the $S_3 \rightarrow S_4$ transition, with an immediate concerted four-electron oxidation to form O_2 . Of course the binding can occur at one or two intermediate S -state transitions as well. If water binds before the $S_3 \rightarrow S_4$ transition, the mechanistic question of whether water oxidation occurs sequentially or concertedly arises.

We are addressing the water binding question with the electron spin echo (ESE) methods of ESE envelope modulation (ESEEM) and ESE-ENDOR (16, 17). The experiments are performed on the S_2 -state multiline signal (14). Previous ENDOR and ESEEM experiments have favored a "dry" substrate environment for the S_2 state (18, 19). However our results provide strong evidence for water or hydroxide ligation to the Mn cluster in the S_2 -state.

Figure 2 displays the 2-pulse time-domain ESEEM of the S_2 -state multiline EPR signal of spinach PSII-membranes incubated in $^2\text{H}_2\text{O}$ -enriched buffer. Specifically, the experimental trace (solid line) is the ($^2\text{H}_2\text{O}/^1\text{H}_2\text{O}$) ratioed spectrum. The ratioing technique nulls modulation contributions from histidine ^{14}N nuclei (20). The Fourier transform of this time-domain spectrum shows a single peak at the 2.1 MHz deuteron Larmor frequency (not shown). The dashed trace is a simulation of the experimental spectrum utilizing several shells of proximal deuterons, including a pair of deuterons with

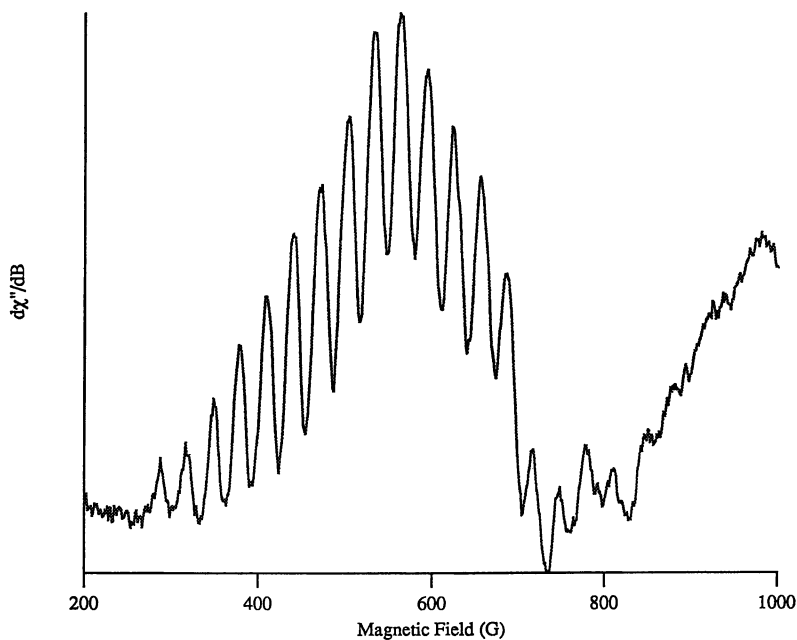


Figure 1. The S_1 -state (dark minus illuminated) parallel polarization EPR difference spectrum of a PSII sample isolated from the cyanobacterium *Synechocystis* 6803.

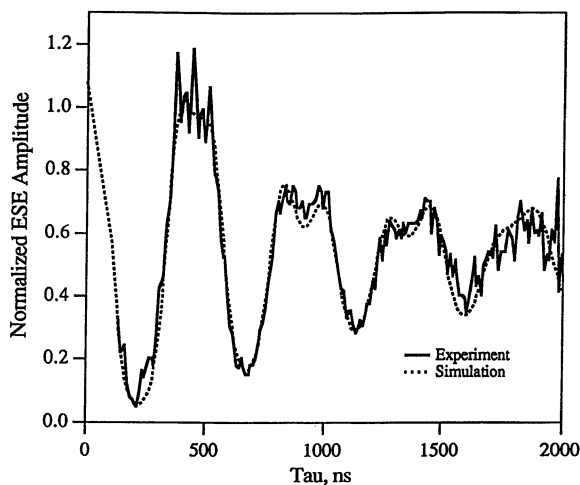


Figure 2. Experimental ($^2\text{H}_2\text{O}/^1\text{H}_2\text{O}$) ratioed 2-pulse time-domain ESEEM for the S_2 -state multiline EPR signal (solid line) and simulation (dashed line).

relatively strong hyperfine couplings to the Mn cluster ($A_{iso}=-0.6$ MHz; $A_{dipolar}=0.75$ MHz; ^2H values). The 0.75 MHz dipolar coupling corresponds to a distance of only 2.5 Å in the point-dipolar coupling approximation.

A disadvantage of the ESEEM method for studying weakly coupled deuterons and protons is that the modulation depth drops to zero at the parallel and perpendicular orientations that provide well-resolved peaks in an ENDOR powder pattern. Thus it is advantageous to also perform ENDOR experiments. Figure 3 shows the proton ESE-ENDOR spectrum for the S_2 -state multiline EPR signal. There are a number of partially-resolved peaks and powder pattern turning points in the spectrum, and those most displaced from the 16 MHz proton Larmor frequency disappear following deuteron exchange (not shown). The simulated proton ENDOR powder pattern in Figure 3 was generated using the ^2H ESEEM-derived parameters scaled up in frequency by the ratio of proton to deuteron magnetic moments ($\times 6.5$; $A_{iso}=-3.9$ MHz; $A_{dipolar}=4.9$ MHz). We observe that the outermost transitions in the proton ENDOR powder pattern match closely what is predicted by the deuteron ESEEM experiment.

However, the 2.5 Å distance that corresponds to the 4.9 MHz proton dipolar coupling is only valid in the limit in which the Mn cluster is represented as a point dipole. We have been working to more properly model the hyperfine interactions with a tetranuclear Mn cluster. For a dinuclear Mn cluster, one can develop analytical expressions for the hyperfine tensor elements as a function of the nuclear coordinates with respect to the two Mn ions (21, 22). Such calculations show that the hyperfine tensor may have rhombic symmetry for finite-size clusters. Figure 4 (23) shows an example of a numerical calculation extension of this method for the tetranuclear cluster geometry proposed by Sauer and Klein and coworkers (24), using the quantum mechanical projection factors that successfully describe the ^{55}Mn hyperfine couplings of the multiline EPR signal as determined by spectral simulation of both the CW EPR signal (25) and the ^{55}Mn ENDOR (26). The bold concentric lines represent constant contours of the through-space hyperfine component that gives rise to the largest peak in the predicted ENDOR powder pattern. The rhombicity of the hyperfine tensor is illustrated with the thin lines. The large majority of the surface of the 4.9 MHz coupling contour is with 2.9 Å of the closest Mn nucleus, i.e. is close enough to be assigned with reasonable certainty to a proton/deuteron of a water or hydroxide ligand to the Mn cluster. The farthest excursion of the 4.9 MHz contour is 3.1 Å. For a more symmetric cubane geometry, a maximum distance of 2.9 Å is calculated. We conclude that the most likely interpretation of the ESEEM and ESE-ENDOR data is that water and/or hydroxide ligands are bound to the Mn cluster in the S_2 -state.

Alcohol Binding at the S_2 -State

A disadvantage of the previously described $^2\text{H}_2\text{O}$ exchange experiments is that the chemical identities of the proximal deuterons/protons are not uniquely determined. Deuterons may populate exchangeable sites near the Mn cluster other than those of bound water or hydroxide. Thus, in these experiments, we cannot absolutely rule out the possibility that we are observing other nearby exchangeable sites with ESEEM and ENDOR. This led us to perform ESEEM experiments with small alcohols labelled with deuterons at the *nonexchangeable* aliphatic positions. Additional motivation is provided by the fact

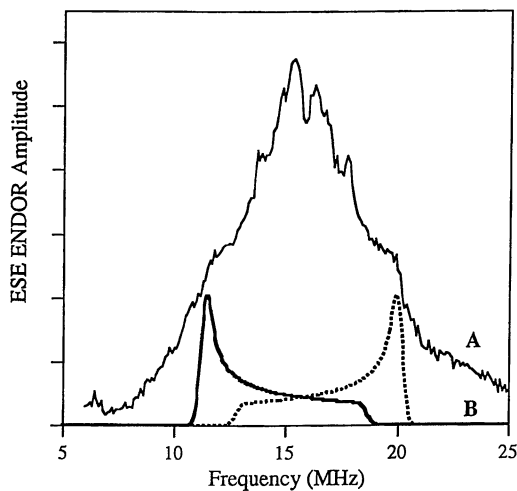


Figure 3. The proton ESE-ENDOR spectrum of the S_2 -state multiline EPR signal, along with a powder pattern simulation utilizing the ESEEM-determined parameters for the most strongly-coupled protons.

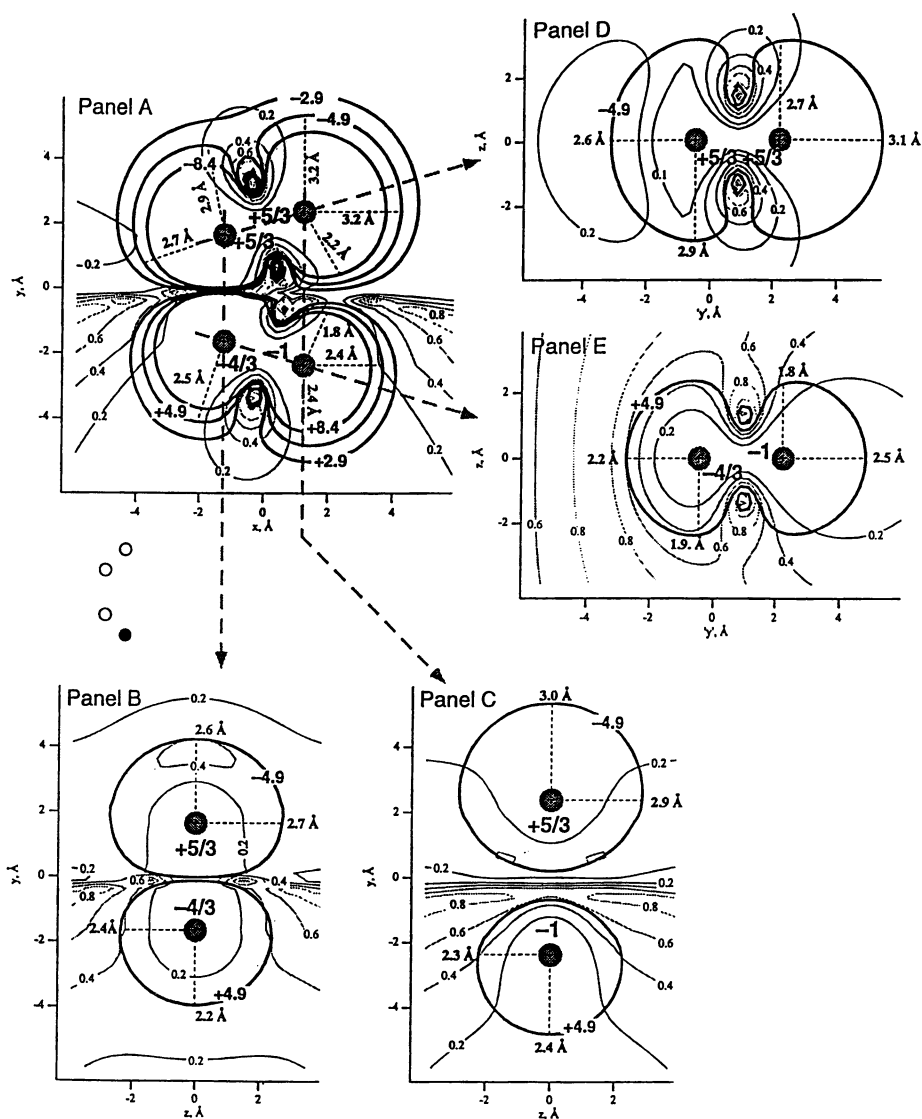


Figure 4. Hyperfine tensor components for a specific tetranuclear Mn cluster geometry (23) proposed to exist in the S_2 -state. The bold concentric lines represent contours of constant through-space coupling strength, and the thin lines represent the rhombicity of the hyperfine interaction.

that small alcohols affect the magnetic properties of the Mn cluster, altering the balance between $g=2$ and $g=4.1$ signals (27).

Figure 5 shows the ratioed (deuterated divided by natural abundance) ESEEM Fourier transforms for deuterated methanol, ethanol, n-propanol, and isopropanol samples prepared at various alcohol concentrations. A 1 M $^2\text{H}_2\text{O}$ pattern is included to show that the strong modulation cannot be accounted for by the minor contribution from the exchangeable alcohol hydrogen, which was initially deuterated in most of these samples. The smaller alcohols, methanol and ethanol, show deep time domain modulation at higher concentration, with significant Fourier transform peaks at the 2.1 MHz deuteron Larmor frequency (Figure 5). The deuteron modulation from these samples can be simulated assuming an 80mM dissociation constant binding site that presents respectively three or two deuterons with ^2H dipolar couplings in the 1.15-2.92 MHz range. In a point dipolar limit, these coupling corresponds to distances between 3.0 to 4.1 Å, which are reasonable distances from Mn to the three methyl hydrogens (methanol case) or two methylene hydrogens (ethanol case) of these alcohols ligated to Mn through via their oxygen groups. The peak height for the n-propanol sample is somewhat diminished, but not negligible at the 1 M concentration, indicating that n-propanol can bind to Mn with somewhat lowered affinity. On the other hand, the 1 M isopropanol sample shows virtually no modulation. We take this as evidence that the binding pocket is too small to accommodate the bulky isopropanol molecule.

Proximity of Y_Z^\bullet to the Mn Cluster

Several treatments allow for the tyrosine radical Y_Z^\bullet to be trapped by illumination and freezing in PSII membranes where the Mn cluster is present, albeit in an inhibited form. In such inhibited systems, the Y_Z^\bullet EPR signal is broadened by magnetic interaction with the Mn cluster, resulting in a characteristic "split-signal" lineshape (5-7). The split-signal has often been referred to as an " S_3 "-state signal because it arises from the electron donor side of PSII trapped in a state three oxidation equivalents removed from S_0 . Recent models have invoked the redox-active tyrosine Y_Z directly in the water-splitting chemistry (6, 28). In these models, the neutral Y_Z^\bullet tyrosine radical, present as an oxidized electron transfer intermediate between P_{680}^+ and the Mn cluster, acts to abstract protons (6) or hydrogen atoms (28) from substrate water molecules bound to the Mn cluster. A requirement for these models to be correct is a close proximity between Y_Z and water ligands to the Mn cluster, and in part these models were inspired by our previous estimation, assuming purely dipolar coupling, of a 4.5 Å distance between the Mn cluster and Y_Z in Ca^{2+} -depleted PSII membranes (6). It is important to further refine our estimate of the distance between Y_Z and the Mn cluster and its substrate water ligands in order to better define possible mechanistic roles for Y_Z in the PSII water-splitting chemistry.

Acetate incubation is one treatment that gives rise to the broadened split-signal version of the Y_Z^\bullet radical EPR signal (29, 30, 7). Figure 6 displays the split-signal obtained under conditions of acetate inhibition, along with an EPR simulation based on an assignment of the major split-signal features to the perpendicular turning points of a Pake powder pattern with exchange and dipolar coupling components. In this assignment, the flanking features correspond to the parallel turning points of the powder pattern. The

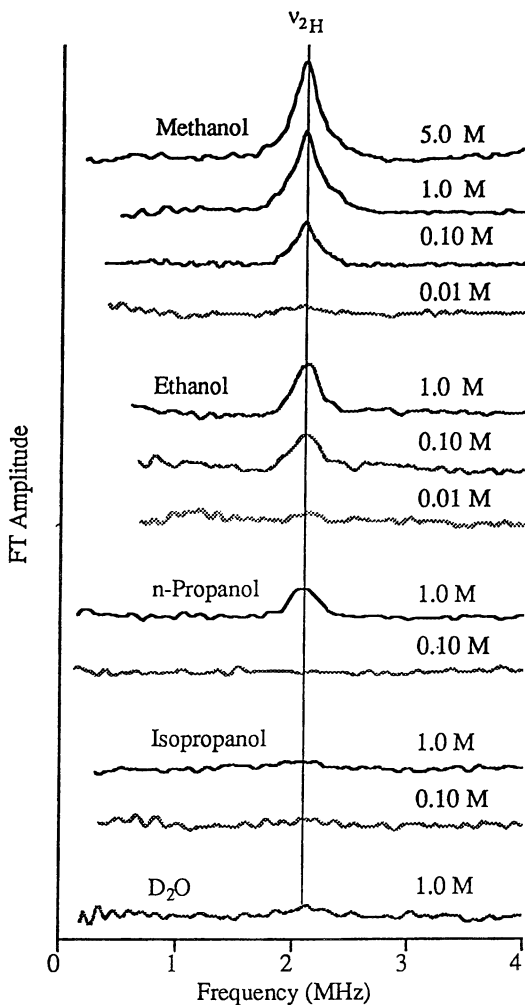


Figure 5. 3-pulse ESEEM Fourier transform traces for deuterated methanol, ethanol, n-propanol, and isopropanol. Each trace is generated as the FFT of the ratioed time-domain data set that results from point-by-point division of the deuterated alcohol data by the natural abundance alcohol data.

simulation, generated with a relatively large dipolar coupling of 1260 MHz and a smaller exchange interaction of -28 MHz, is reasonably good. In the limit of a point dipole approximation, this dipolar coupling corresponds to a Mn–Y_Z[•] distance of only 3.5 Å. However, recent data that we have obtained with acetate-inhibited PSII membranes oriented on plastic sheets (15, 31) indicate that the story is not so simple. Figure 7 displays the “split-signal” lineshape obtained with the membrane normal aligned parallel to the applied magnetic field. For that unique orientation, the membrane internal vector that describes the position of Y_Z[•] relative to the Mn cluster is at a fixed angle θ with respect to the applied magnetic field vector. Because there is no orientation within the plane of the membrane, the ensemble of individual vectors form a cone of half-angle θ whose axis of revolution is aligned along the static field (Figure 7 inset). If the Mn–Y_Z[•] interaction consists of point-dipole and exchange components, this interaction would be of axial symmetry, and for this geometry of constant θ the coupled spectrum would consist of a pair of isotropic derivative-shaped lines. This is not what is observed in Figure 7. Instead the field-modulated EPR spectrum shows a positive-going feature on the low field side, and a negative-going feature on the high field side, indicative of a powder pattern that extends from one side to the other, i.e. a powder pattern of rhombic symmetry. This rhombicity likely originates from the finite size of the Mn cluster and a close proximity to Y_Z[•], providing rhombicity to the interaction tensor exactly along the lines illustrated in Figure 4 for the hyperfine interaction.

Evidence of Y_Z[•] Participation in Proton Transfer

In addition to the essential tyrosine Y_Z, there is a second, symmetry related PSII tyrosine, Y_D (D2-Tyr160, *Synechocystis* notation), that forms a relatively stable neutral radical, Y_D[•]. Y_D is bypassed by the rapid electron transfer involved in oxygen evolution. We have fully characterized the hydrogen bonding interaction of the Y_D[•] tyrosine. The hydrogen bond donor to the neutral Y_D[•] radical is the τ -nitrogen of D2 histidine 189 (32). We have used ²H ESE-ENDOR to characterize the magnetic dipolar ($A_{dip}=570$ kHz) and nuclear quadrupolar ($e^2qQ=200$ kHz) couplings for ²H exchanged into the hydrogen bond (33). From the dipolar coupling and the newly established $\rho(^{17}\text{O})=0.28$ spin density for the Y_D[•] tyrosyl oxygen (34), we obtain an O...H distance of 1.81 Å.

Figure 8 shows the 3-pulse ESEEM for ²H₂O exchanged Y_D[•] (time domain: trace a; frequency domain: trace a'). Using the parameters determined from our ESE-ENDOR data, we can attempt to simulate the time domain ESEEM using one (upper dashed line) or two (lower dashed line) coupled deuterons. We observe a very good match to the experimental data with only one coupled deuteron. This is consistent with the picture, illustrated in Figure 9a, that Y_D participates in a single hydrogen bonding interaction with the adjacent histidine residue, with the proton shifting back and forth between the tyrosine and the histidine depending on the oxidation state of the tyrosine.

We can utilize this spectroscopic information about Y_D[•] as a basis for interpreting similar spectral information obtained for Y_Z[•] trapped in the split signal form. If Y_Z were to serve only as an electron transfer agent, there would be no functional need for more than one hydrogen bonding partner – the proton could shuttle back and forth in the same way as described for the Y_D tyrosine (Figure 9b). On the other hand, if Y_Z[•] were to act to abstract protons or H atoms from substrate water, then there would be two separate

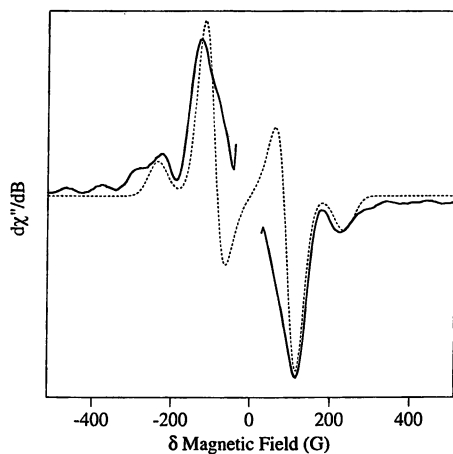


Figure 6. The Y_Z° split-signal generated in acetate-inhibited PSII membranes along with a spectral simulation (dashed line).

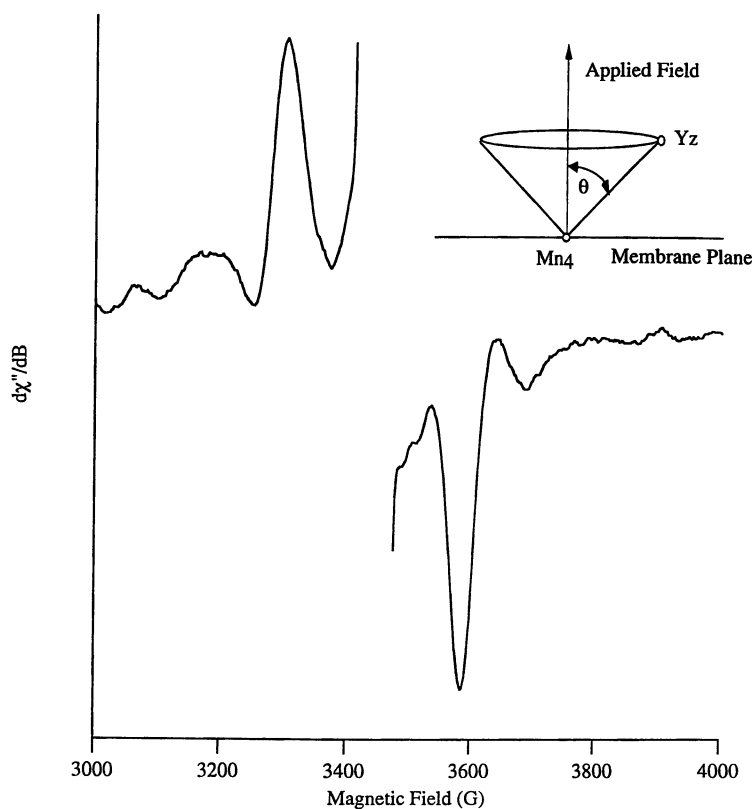


Figure 7. The split-signal observed in acetate-inhibited PSII membranes oriented on plastic sheets with the membrane normal parallel to the applied magnetic field.

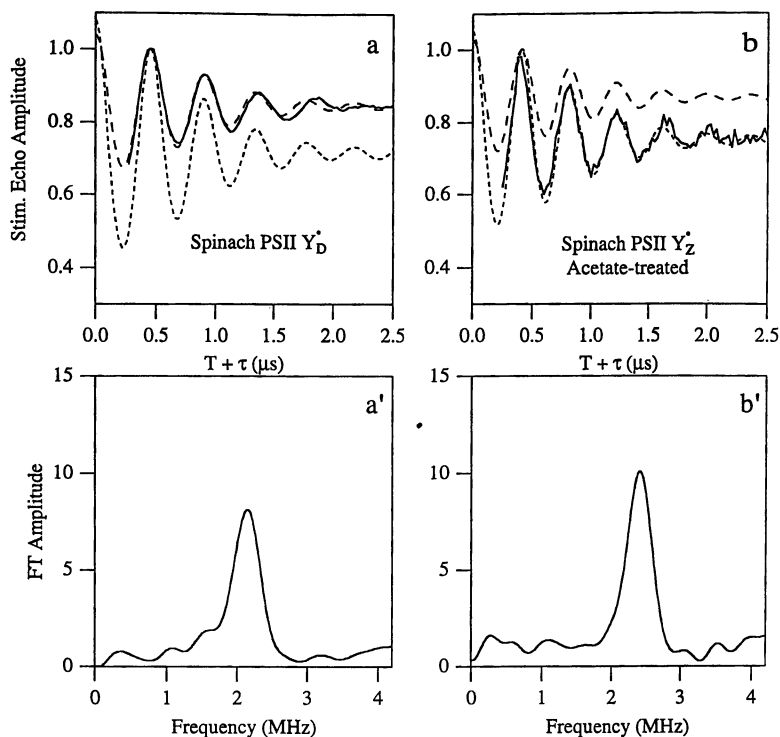


Figure 8. Ratioed $^2\text{H}/^1\text{H}$ ESEEM of $^2\text{H}_2\text{O}$ exchanged PSII membranes. Y_D^* : time domain (a); frequency domain (a'). Y_Z^* , acetate-inhibited split-signal form: time domain (b); frequency domain (b'). ESEEM simulations for one (upper dashed) or two (lower dashed) deuterons are displayed with the experimental time domain traces.

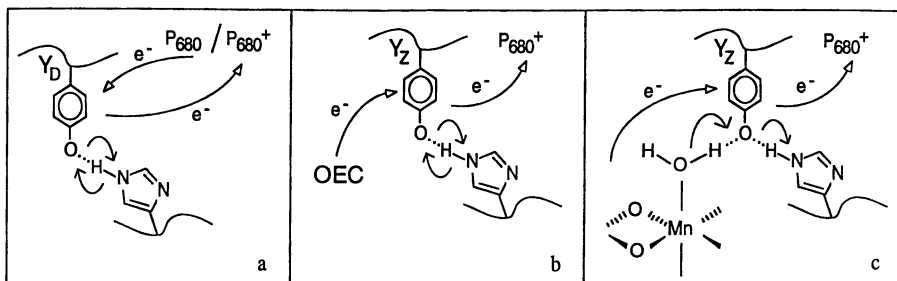


Figure 9. (a) Hydrogen bonding for Y_D^* . (b) Expected hydrogen bonding for Y_Z^* if it were only involved in electron transfer. (c) Expected hydrogen bonding for Y_Z^* if it were involved in electron *and* proton (or H atom) transfer.

hydrogen bonding interaction sites. One site would provide for proton donation to Y_Z upon the $Y_Z^{\bullet} \rightarrow Y_Z$ reduction, either directly from substrate water or through a proton transfer intermediate, while the other site would accept protons from Y_Z during the $Y_Z \rightarrow Y_Z^{\bullet}$ oxidation, as the first step in proton translocation to the luminal phase (Figure 9c). The ^2H ESE ENDOR spectrum of Y_Z^{\bullet} trapped in the split-signal form in acetate-inhibited PSII membranes is similar to that of Y_D^{\bullet} , albeit slightly less resolved (data not shown (35)). We therefore can simulate the ESEEM of Y_Z^{\bullet} (Figure 8b,b') with one or two deuterons, using the same parameters as used for the Y_D^{\bullet} simulations. In this case, we observe a very good match between the experimental data and a simulation using two coupled deuterons, indicating the presence of two hydrogen bonds to the Y_Z^{\bullet} radical. As illustrated in Figure 9 and discussed above, this result provides strong additional support for the proton/H atom transfer models.

Acknowledgments:

We acknowledge the National Science Foundation (MCB 9513648 for RDB) and the National Institutes of Health (GM48242 for RDB and GM43496 for RJD) for support of this research.

Literature Cited

- (1.) Kok, B.; Forbush, B.; McGloin, M. *Photochem. Photobiol.* **1970**, *11*, 457-475.
- (2.) Debus, R. J. *Biochim. Biophys. Acta* **1992**, *1102*, 269-352.
- (3.) Britt, R. D. In *Oxygenic Photosynthesis: The Light Reactions*; Ort, D., Yocum, C. F., Eds.; Kluwer Academic: Dordrecht, The Netherlands, 1996; pp 137-164.
- (4.) Yachandra, V. K.; Sauer, K.; Klein, M. P. *Chem. Rev.* **1996**, *96*, 2927-2950.
- (5.) Boussac, A.; Zimmermann, J.-L.; Rutherford, A. W. *Biochemistry* **1989**, *28*, 8984-8989.
- (6.) Gilchrist, M. L.; Ball, J. A.; Randall, D. W.; Britt, R. D. *Proc. Natl. Acad. Sci. U.S.A.* **1995**, *92*, 9545-9549.
- (7.) Tang, X.-S.; Randall, D. W.; Force, D. A.; Diner, B. A.; Britt, R. D. *J. Am. Chem. Soc.* **1996**, *118*, 7638-7639.
- (8.) Dexheimer, S. L.; Klein, M. P. *J. Am. Chem. Soc.* **1992**, *114*, 2821-2826.
- (9.) Yamauchi, T.; Mino, H.; Matsukawa, R.; Kawamori, A.; Ono, T.-A. *Biochemistry* **1997**, *36*, 7520-7526.
- (10.) Hagen, W. R. *Biochim. Biophys. Acta* **1982**, *708*, 82-98.
- (11.) Hendrich, M. P.; Debrunner, P. G. *Biophys. J.* **1989**, *56*, 489-506.
- (11.) Chan, M. K.; Armstrong, W. H. *J. Am. Chem. Soc.* **1991**, *113*, 5055-5057.
- (12.) Dexheimer, S. L.; Gohdes, J. W.; Chan, M. K.; Hagen, K. S.; Armstrong, M. H.; Klein, M. P. *J. Am. Chem. Soc.* **1989**, *111*, 8923-8925.
- (13.) Tang, X.-S.; Diner, B. A. *Biochemistry* **1994**, *33*, 4594-4603.
- (14.) Dismukes, G. C.; Siderer, Y. *Proc. Natl. Acad. Sci. USA* **1981**, *78*, 274-278.
- (15.) Kim, D. H.; Britt, R. D.; Klein; Sauer, K. *J. Am. Chem. Soc.* **1990**, *112*, 9389-9391.

- (16.) Britt, R. D. In *Biophysical Techniques in Photosynthesis*; Amesz, J., Hoff, A. J., Eds.; Kluwer Academic Publishers: Dordrecht, The Netherlands, 1996; pp 235-253.
- (17.) Hoffman, B. M.; DeRose, V. J.; Doan, P. E.; Gurbiel, R. J.; Houseman, A. L. P.; Telsler, J. In *Biological Magnetic Resonance*; Berliner, L. J., Reuben, J., Eds.; Plenum: New York, 1993; Vol. 13, pp 151-218.
- (18.) Tang, X.-S.; Sivaraja, M.; Dismukes, G. C. *J. Am. Chem. Soc.* **1993**, *115*, 2382-2389.
- (19.) Turconi, S.; MacLachlan, D. J., Bratt, P. J.; Nugent, J. H. A.; Evan, M. C. W. *Biochemistry* **1997**, *36*, 879-885.
- (20.) Tang, X.-S.; Diner, B. A.; Larsen, B. S.; Gilchrist, M. L.; Lorigan, G. A.; Britt, R. D. *Proc. Natl. Acad. Sci. U.S.A.* **1994**, *91*, 704-708.
- (21.) Fiege, R.; Zweggart, W.; Bittl, R.; Adir, N.; Genger, G.; Lubitz, W. *Photosyn. Res.* **1996**, *48*, 227-237.
- (22.) Randall, D. W.; Gelasco, A.; Caudle, M. Y.; Pecoraro, V. L.; Britt, R. D. *J. Am. Chem. Soc.* **1997**, *119*, 4481-4491.
- (23.) Randall, D. W. Ph.D. Dissertation, University of California-Davis, 1997.
- (24.) Yachandra, V.; DeRose, V. J.; Latimer, M. J.; Mukerji, I.; Sauer, K.; Klein, M. P. *Science* **1993**, *260*, 675-679.
- (25.) Zheng, M.; Dismukes, G. C. *Inorg. Chem.* **1996**, *35*, 3307-3319.
- (26.) Randall, D. W.; Sturgeon, B. E.; Ball, J. A.; Lorigan, G. A.; Chan, M. K.; Klein, M. P.; Armstrong, W. H.; Britt, R. D. *J. Am. Chem. Soc.* **1995**, *117*, 11780-11789.
- (27.) Zimmermann, J. L.; Rutherford, A. W. *Biochemistry* **1986**, *25*, 4609-4615.
- (28.) Hoganson, C. W.; Lydakis-Simantiris, N.; Tang, X.-S.; Tommos, C.; Warncke, K.; Babcock, G. T.; Diner, B. A.; McCracken, J.; Styring, S. *Photosynth. Res.* **1995**, *46*, 177-184.
- (29.) MacLachlan, D. J.; Nugent, J. H. A. *Biochemistry* **1993**, *32*, 9772-9780.
- (30.) Szalai, V. A.; Brudvig, G. W. *Biochemistry* **1996**, *35*, 1946-1953.
- (31.) Rutherford, A. W. *Biochim. Biophys. Acta* **1985**, *807*, 189-201.
- (32.) Campbell, K. A.; Peloquin, J. M.; Diner, B. A.; Tang, X.-S.; Chisholm, D. A. Britt, R. D. *J. Am. Chem. Soc.* **1997**, *119*, 4787-4788.
- (33.) Force, D. A.; Randall, D. W.; Britt, R. D.; Tang, X. S.; Diner, B. A. *J. Am. Chem. Soc.* **1995**, *117*, 12643-12644
- (34.) Dole, F.; Diner, B. A.; Hoganson, C. W.; Babcock, G. T.; Britt, R. D. *J. Am. Chem. Soc.*, *in press*.
- (35.) Force, D. A.; Randall, D. W.; Britt, R. D. *Biochemistry* **1997**, *in press*.

Chapter 16

Valence-Delocalized $[\text{Fe}_2\text{S}_2]^+$ Clusters

M. K. Johnson¹, E. C. Duin¹, B. R. Crouse¹, M.-P. Golinelli², and J. Meyer²

¹Department of Chemistry and Center for Metalloenzyme Studies, University of Georgia, Athens, GA 30602

²Département de Biologie Moléculaire et Structurale, CEA-Grenoble, 38054 Grenoble, France

The $[\text{Fe}_2\text{S}_2]^+$ clusters in the C56S and C60S mutated forms of *Clostridium pasteurianum* 2Fe ferredoxin are shown to reversibly interconvert between valence-delocalized $S = 9/2$ and valence-localized $S = 1/2$ forms as a function of pH. This provides a unique opportunity to investigate the ground and excited state electronic properties and the vibrational modes of a valence-delocalized $[\text{Fe}_2\text{S}_2]^+$ cluster using the combination of EPR, variable-temperature magnetic circular dichroism (VTMCD) and resonance Raman spectroscopies. Near-IR electronic transitions arising from Fe–Fe interactions have been identified and assigned by VTMCD and resonance Raman studies. Moreover, the same set of transitions are also observed in the VTMCD spectra of $[\text{Fe}_3\text{S}_4]^0$, $[\text{ZnFe}_3\text{S}_4]^+$ and $[\text{Fe}_4\text{S}_4]^+$ clusters, indicating the presence of valence-delocalized $[\text{Fe}_2\text{S}_2]^+$ fragments in these systems. Assignment of the z-polarized $\sigma \rightarrow \sigma^*$ transition provides the first direct measurement of the magnitude of spin dependent resonance delocalization in Fe–S clusters. The double exchange parameter, B , is shown to be in the range $790\text{--}930\text{ cm}^{-1}$ for valence-delocalized $[\text{Fe}_2\text{S}_2]^+$ units in $[\text{Fe}_2\text{S}_2]^+$, $[\text{Fe}_3\text{S}_4]^0$, $[\text{ZnFe}_3\text{S}_4]^+$ and $[\text{Fe}_4\text{S}_4]^+$ clusters indicating resonance delocalization energies in the range $3950\text{--}4650\text{ cm}^{-1}$.

Detailed understanding of intracuster valence delocalization in Fe–S centers is crucial for understanding ground and excited state properties as a well as rationalizing the thermodynamics and kinetics of intercluster electron transfer. Structural studies have shown that $\text{Fe}_2(\mu_2\text{-S})_2$ units are the building block for more complex clusters and the electronic properties of these units hold the key to understanding electron delocalization in Fe–S clusters. Although synthetic and biological $[\text{Fe}_2\text{S}_2]^+$ clusters are valence localized with $S = 1/2$ ground states (I), Mössbauer and NMR data for higher nuclearity homometallic and heterometallic Fe–S clusters have been interpreted in terms of valence-delocalized $S = 9/2$ $[\text{Fe}_2\text{S}_2]^+$ fragments in at least one oxidation state (2-7). Moreover, theoretical studies have shown that the ground and excited

properties of $[\text{Fe}_2\text{S}_2]^+$ clusters are critically dependent on the interplay of Heisenberg exchange, spin-dependent resonance delocalization (double exchange) and vibronic interactions (8-14). This has led to rationalization of the ground state properties of a range of trinuclear and tetranuclear clusters in terms of antiferromagnetic exchange interactions involving valence-delocalized $S = 9/2$ $[\text{Fe}_2\text{S}_2]^+$ fragments: $[\text{Fe}_3\text{S}_4]^-$ (in $[\text{ZnFe}_3\text{S}_4]^+$) (2); $[\text{Fe}_3\text{S}_4]^0$ (2,12); $[\text{Fe}_4\text{S}_4]^{3+}$ (13); $[\text{Fe}_4\text{S}_4]^{2+}$ (14). However, recent analyses of the hyperfine coupling constants for $[\text{Fe}_4\text{S}_4]^{3+}$ and $[\text{Fe}_4\text{S}_4]^+$ clusters suggest that $S = 7/2$ or intermediate between $S = 7/2$ and $5/2$ are more appropriate formal spin states for the valence-delocalized $[\text{Fe}_2\text{S}_2]^+$ fragments in these cases (15,16).

The dependence of the ground state properties of a $[\text{Fe}_2\text{S}_2]^+$ cluster fragment on the relative magnitude of Heisenberg exchange and spin-dependent resonance delocalization is illustrated in Figure 1. The energy level scheme is based on a Hamiltonian with both Heisenberg (J) and double exchange (B) terms that results in $E = -JS(S + 1) \pm B(S + 1/2)$ (17). This simple model neglects vibronic interactions and assumes that the valence-localized species with the extra electron on Fe_A and Fe_B are isoenergetic. As the extent of resonance delocalization (B/J) increases, the ground state changes from $S = 1/2$ to $9/2$ in integer steps, becoming $S = 9/2$ for $|B/J| > 9$. Inclusion of the factors responsible for valence localization, i.e. vibronic coupling and inequivalence in the energies of the valence trapped species, decreases the B/J range in which the ground state has $3/2 \leq S \leq 7/2$ (18,19). This diminishes the likelihood of observing these intermediate-spin ground states and leads towards a situation in which the ground state changes directly from valence-localized $S = 1/2$ to valence-delocalized $S = 9/2$ with increasing B/J (18,19). Hence the value of B , relative to J and the energetic factors responsible for valence localization, determines both the ground state spin and the extent of valence delocalization. However, there is as yet no reliable experimental estimate of B , and the theoretical estimates span a wide range, $30\text{-}970 \text{ cm}^{-1}$, as gauged by the recent set of *JBIC* commentaries on exchange versus double exchange in polymetallic systems (19-22).

Figure 1 illustrates a potential experimental method for measuring B . For a valence-delocalized $S = 9/2$ $[\text{Fe}_2\text{S}_2]^+$ cluster, the model predicts a spin-allowed, electric-dipole-allowed, z-polarized $\sigma \rightarrow \sigma^*$ transition in the near-IR region at energy $10B (= 2\beta)$, where β is the resonance energy). This type of direct measurement of B requires detailed optical studies of a valence-delocalized $S = 9/2$ $[\text{Fe}_2\text{S}_2]^+$ cluster and the discovery and characterization of such clusters in C56S and C60S mutated forms of *Clostridium pasteurianum* (*Cp*) 2Fe ferredoxin (Fd) are the subject of this chapter.

C56S and C60S Mutated Forms of *Cp* 2Fe Fd

Cp 2Fe Fd is a low molecular weight protein (102 amino acids) containing one $[\text{Fe}_2\text{S}_2]^{2+,+}$ cluster with complete cysteinyl-S ligation. Although structural characterization by x-ray crystallography or NMR is not available, the combination of mutagenesis and spectroscopic studies has revealed a unique arrangement of coordinating cysteine residues (in positions 11, 24, 56 and 60) (23-25) compared to other $[\text{Fe}_2\text{S}_2]$ -containing proteins (26). In the wild-type protein, the $[\text{Fe}_2\text{S}_2]^+$ cluster is valence localized with an $S = 1/2$ ground state and the non-reducible Fe site is coordinated by cysteines 11 and 24 which occur in a flexible loop region (25). The

initial discovery of $S = 9/2$ $[\text{Fe}_2\text{S}_2]^+$ clusters in the C56S and C60S mutated forms came from VTCD and EPR studies (27). Moreover, the close similarity in the near-IR VTCD spectra to those of clusters known to contain valence-delocalized $S = 9/2$ $[\text{Fe}_2\text{S}_2]^+$ clusters lead to the suggestion that these unique ground state properties were the consequence of valence delocalization. This was subsequently confirmed by Mössbauer studies, which provided the definitive proof that these $S = 9/2$ $[\text{Fe}_2\text{S}_2]^+$ clusters were valence delocalized on the time scale of $\sim 10^{-7}$ s (18). However, detailed characterization of the properties of this unique $[\text{Fe}_2\text{S}_2]^+$ cluster were hindered by the observation that the reduced samples were mixtures of valence-localized ($S = 1/2$) and valence-delocalized ($S = 9/2$) species (18,27). The subsequent observation that the C56S and C60S mutated forms, but not the wild-type Fd, had pH dependent midpoint potentials, led to the discovery of reversible interconversion between valence-delocalized $S = 9/2$ and valence-localized $S = 1/2$ forms as a function of pH (28). This has provided a unique opportunity to compare the ground state, excited state and vibrational properties of valence-delocalized $S = 9/2$ $[\text{Fe}_2\text{S}_2]^+$ and valence-localized $S = 1/2$ $[\text{Fe}_2\text{S}_2]^+$ clusters in the same protein (28) and a summary of these recent results is presented below

Redox Properties. At pH 7.0, the C56S and C60S mutations result in a 102-108-mV decrease in midpoint potential compared to wild type ($E_m = -260$ mV vs NHE and independent of pH over the range 5-10). Negative shifts in midpoint potential have previously been reported for $[\text{Fe}_2\text{S}_2]^{2+,+}$ couples on replacing a cysteine ligating the reducible Fe site by a serine: $\Delta E_m = -100$ and -240 mV at pH 7 in *Escherichia coli* fumarate reductase (29) and $\Delta E_m = -18$ mV (pH not specified) in *Anabaena* Fd (30). However, the absolute magnitudes of these serine-induced changes in midpoint potential should not be compared, since the pH dependence was not investigated for *E. coli* fumarate reductase and *Anabaena* Fd. The midpoint potentials of the C56S and C60S mutated forms are both strongly pH dependent; approximately constant at -460 mV above pH 10 and increasing with a slope of ~ 50 mV/pH unit below pH 8. Such behavior is indicative of protonation of the reduced clusters with a $\text{p}K_a \approx 9$, with the serine oxygen as the logical site for protonation. These redox results are, therefore, interpreted in terms of serinate ligation at pH > 10 , with the nature of the fourth ligand at pH < 8 unclear at present, i.e. serine OH, water or some other amino acid side chain. Precedent for serinate ligation of a $[\text{Fe}_2\text{S}_2]$ cluster comes from the crystallographic studies of the C49S mutated form of *Anabaena* Fd (31) and redox-dependent serinate coordination of an Fe-S cluster has recently been observed for the nitrogenase P-clusters (32). As shown below, the pH-induced changes in the nature of the fourth cluster ligand in the C56S and C60S mutated forms have dramatic consequences for the properties of the $[\text{Fe}_2\text{S}_2]^+$ clusters.

Ground State Properties. The ground state properties of $[\text{Fe}_2\text{S}_2]^+$ clusters in the high pH (pH 10-11) and low pH (pH 6-8) forms of the C56S and C60S variants have been investigated by EPR and MCD saturation magnetization studies (28). Both approaches indicate that the low-pH forms are exclusively $S = 1/2$ and that the high-pH forms are predominantly ($> 80\%$) $S = 9/2$. The low pH forms exhibit identical $S = 1/2$ EPR signals ($g = 2.01, 1.92, 1.88$) with increased anisotropy compared to wild-type ($g = 2.00, 1.95, 1.92$), indicative of a change of ligation at the Fe^{2+} site of a localized

valence $[\text{Fe}_2\text{S}_2]^+$ cluster (29,33,34). MCD magnetization data at selected wavelengths are well fit at all temperatures by theoretical data constructed using the EPR-determined g -values, indicating that all transitions originate from the $S = 1/2$ ground state responsible for the EPR signal. Both EPR spin quantitations and the incomplete reversibility of absorption changes following redox cycling show that the reduced cluster is stable at pH 8, but readily degraded at pH 6.

For both the C56S and C60S variants at pH 11, weak $S = 1/2$ resonances were observed, accounting for 0.18 and 0.10 spins/molecule, respectively. The resonances are distinct from those associated with low pH forms in terms of both g -value anisotropy ($g = 2.01, 1.91, 1.87$ for C56S and $g = 2.02, 1.93, 1.86$ for C60S) and substantially increased linewidths. Hence they are interpreted as minor components of localized-valence species with serinate as the fourth cluster ligand (as opposed to protonated serine, water, or some other protein ligand at low pH). However, the majority ($> 80\%$) of the serinate-coordinated clusters in the high pH forms of both variants are present as valence-delocalized $S = 9/2$ $[\text{Fe}_2\text{S}_2]^+$ clusters as evidenced by EPR and MCD studies. Low field resonances that are uniquely indicative of $S = 9/2$ ground states ($E/D = 0.12, D = -2.7 \text{ cm}^{-1}$ for C56S, and $E/D = 0.17, D = -1.4 \text{ cm}^{-1}$ for C60S) were observed at temperatures between 4 and 60 K (28). For the C56S variant, Fig. 2 shows the temperature-dependence of the low-field EPR signals and the analysis in terms of a conventional $S = 9/2$ spin Hamiltonian with $g_0 = 2$:

$$\mathcal{H}_e = g_0\beta\mathbf{H}\cdot\mathbf{S} + D(\mathbf{S}_z^2 - S(S + 1)/3) + E(\mathbf{S}_x^2 - \mathbf{S}_y^2) \quad (1)$$

Observed g -values are given in parenthesis and the low transition probability of the resonances within the two lowest doublets results in the sample being almost devoid of low field resonances below 4.5 K except for the derivative feature centered at $g = 4.3$ from adventitious Fe^{3+} . The value of D was determined by estimating the energy difference between the $M_s = \pm 3/2$ and $\pm 5/2$ doublets from the slope of a plot of the log of the ratio of the intensities at $g = 9.59$ and 8.53 versus $1/T$. MCD magnetization studies for both variants are consistent with the dominant bands being xy -polarized transitions originating from the highly anisotropic $M_s = \pm 9/2$ doublet, $g_{\parallel} \approx 18$ and $g_{\perp} \approx 0$, of an $S = 9/2$ ground state with $D < 0$ (see below).

Excited State Properties. The UV/visible/near-IR absorption spectra of both variants in the oxidized state (23) are independent of pH over the range 6-11. In contrast, the reduced absorption and VTMCD spectra are strongly pH dependent (28) with analogous changes for both variants. This is illustrated by the high and low pH VTMCD spectra for reduced C60S shown in Figure 3. At or below pH 8, both the absorption and VTMCD spectra are characteristic of valence-localized $S = 1/2$ $[\text{Fe}_2\text{S}_2]^+$ clusters (35,36). The variants and wild type all exhibit a pronounced absorption and positive MCD band at $\sim 540 \text{ nm}$ that has been tentatively attributed to the $\text{Fe}^{2+} \rightarrow \text{Fe}^{3+}$ intervalence transition (35,36). We have noted previously that the temperature-dependent MCD intensity of this band argues against this assignment, since it is formally a uniaxial transition and MCD C -terms require two non-zero perpendicular transition dipole moments. It is of course possible that the anomalously high MCD intensity arises from out-of-state spin orbit coupling involving an

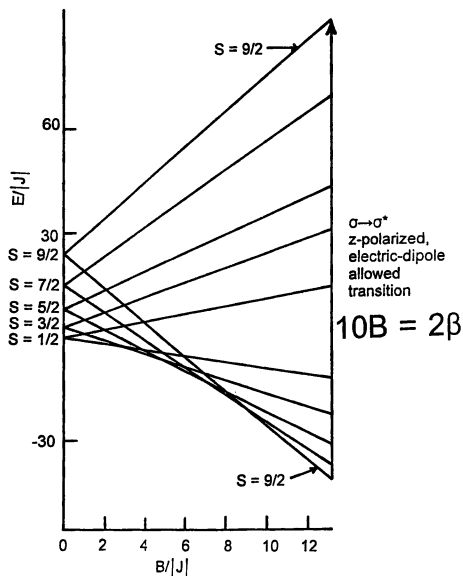
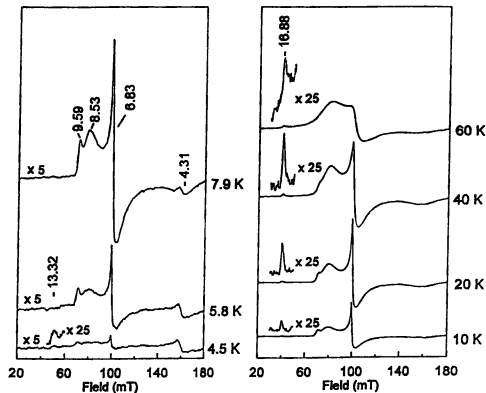


Figure 1. Energy level diagram for an exchange coupled $[\text{Fe}_2\text{S}_2]^+$ cluster as a function of increasing spin dependent resonance delocalization.



$E/D = 0.12, D = -2.7 \text{ cm}^{-1}, g_0 = 2.00$			
$ \pm 1/2\rangle$	0.63	16.86 (16.88)	1.36
$ \pm 3/2\rangle$	4.23 (4.31)	8.51 (8.53)	6.62 (6.83)
$ \pm 5/2\rangle$	9.52 (9.59)	1.72	1.94
$ \pm 7/2\rangle$	13.90 (13.32)	0.07	0.08
$ \pm 9/2\rangle$	17.98	0.000	0.001

Figure 2. Temperature dependence of the low-field EPR spectrum of dithionite-reduced C56S Cp 2Fe Fd at pH 11. The tabulated data is the analysis in terms of a $S = 9/2$ spin Hamiltonian with the g -values in parenthesis corresponding to observed values. Adapted from ref. 28.

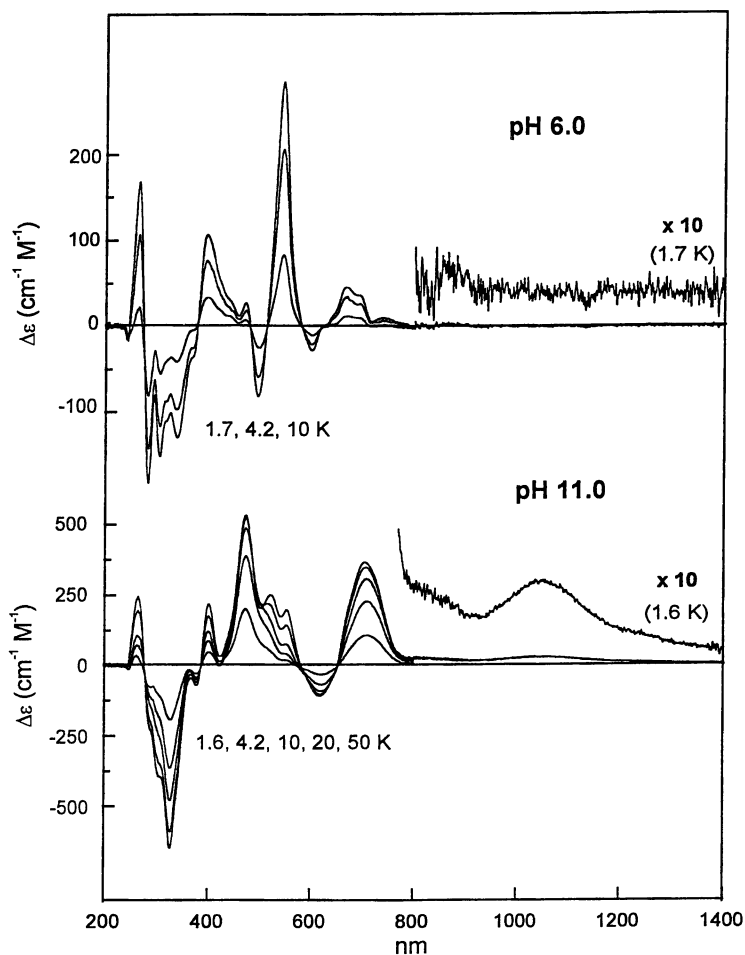


Figure 3. UV/visible/near-IR VTMCD spectra (6.0 T) of the dithionite-reduced C60S mutated form of *Cp 2Fe Fd* at pH 6.0 and 11.0. All transitions increase in intensity with decreasing temperature. Adapted from ref. 28.

energetically similar and orbitally degenerate excited state (37). However, the observation that the energy of this transition is not significantly perturbed by changes in ligation at the Fe^{2+} site (i.e. replacing a cysteinate by an oxygenic ligand as in this work or replacing both cysteinates with histidines in Rieske protein (unpublished MCD results from this laboratory)) is more difficult to reconcile with this assignment. In light of the resonance Raman excitation profiles (35), we therefore currently favor assignment of this band to a $\mu_2\text{-S}^{2-} \rightarrow \text{Fe}^{3+}$ charge transfer transition, with $\text{Cys-S}^- \rightarrow \text{Fe}^{3+}$ charge transfer transitions occurring to higher energies (350-525 nm). The most significant differences in the low-pH VTMC spectra of the variants compared to wild-type, occur in the 250-350 nm region, which is primarily associated with charge transfer transitions involving the Fe^{2+} site (35). Hence, the VTMC data for the variants are also consistent with a change in ligation at the Fe^{2+} site of a valence-localized $[\text{Fe}_2\text{S}_2]^+$ cluster.

The absorption and VTMC spectra of both variants at pH 11 are unique compared to any known type of $[\text{Fe}_2\text{S}_2]^+$ cluster. In the visible region, the absorption spectrum comprises a broad shoulder with inflections at 420 and 470 nm and weaker lower energy band centered at 670 nm (28). These features correlate with intense positive MCD bands at 420 and 480 nm and a derivative-shaped feature centered at 660 nm (positive and negative components at 705 and 610 nm, respectively), see Figure 3. MCD magnetization studies for the positive bands centered near 480 nm and 705 nm indicate that both arise almost exclusively from xy -polarized transitions from an $S = 9/2$ ground state with $D < 0$. For example, the lowest temperature data for the C60S variant collected at 705 nm (Figure 4) are well fit by theoretical data (computed according to the equations in ref. 38 and indicated by the solid line) corresponding to 93% of the MCD intensity at this wavelength arising from an $S = 9/2$ ground state (transition originating from the lowest doublet with $g_{\parallel} = 18$ and $g_{\perp} = 0$) and 7% from an $S = 1/2$ ground state ($g = 2.02, 1.93, 1.86$). The minor components of serinate-ligated localized-valence $S = 1/2$ $[\text{Fe}_2\text{S}_2]^+$ clusters that were apparent in the EPR studies of both variants at pH 11, are also evident in the VTMC spectra by the presence of bands with $S = 1/2$ temperature dependence in the 500-580 nm region (Figure 3).

The 480-nm MCD band of valence-delocalized $S = 9/2$ $[\text{Fe}_2\text{S}_2]^+$ clusters is the logical counterpart of the 540-nm band of the valence-localized $S = 1/2$ $[\text{Fe}_2\text{S}_2]^+$ clusters, and is, therefore, assigned to a $\mu_2\text{-S}^{2-} \rightarrow \text{Fe}^{2.5+}$ charge transfer transition. Likewise, the higher energy bands of the $S = 9/2$ clusters are assigned to $\text{Cys-S}^- \rightarrow \text{Fe}^{2.5+}$ charge transfer transitions with each shifted to higher energy relative to the $\text{Cys-S}^- \rightarrow \text{Fe}^{3+}$ counterparts in $S = 1/2$ clusters. However, the near-IR MCD bands, i.e. intense positive bands at 710 nm and weaker positive bands at ~ 850 nm (shoulder in C60S) and 1070 nm (Figure 3), are unique to the $S = 9/2$ species and hence appear to be a direct consequence of the Fe-Fe interactions that lead to the spin dependent valence delocalization (37). Since MCD magnetization studies indicate that the 710 nm is xy -polarized, it is not a candidate for the z -polarized $\sigma \rightarrow \sigma^*$ transition that would result from direct σ overlap of the Fe d_{z^2} orbitals. Rather this transition is assigned to the weak MCD band at 1070-nm which is shown to be predominantly z -polarized by MCD magnetization studies (Figure 4). The anomalous magnetization behavior at this wavelength, i.e. increasing to a maximum and then decreasing as a function of $\beta B/2kT$, is predicted for predominantly z -polarized C -terms arising from

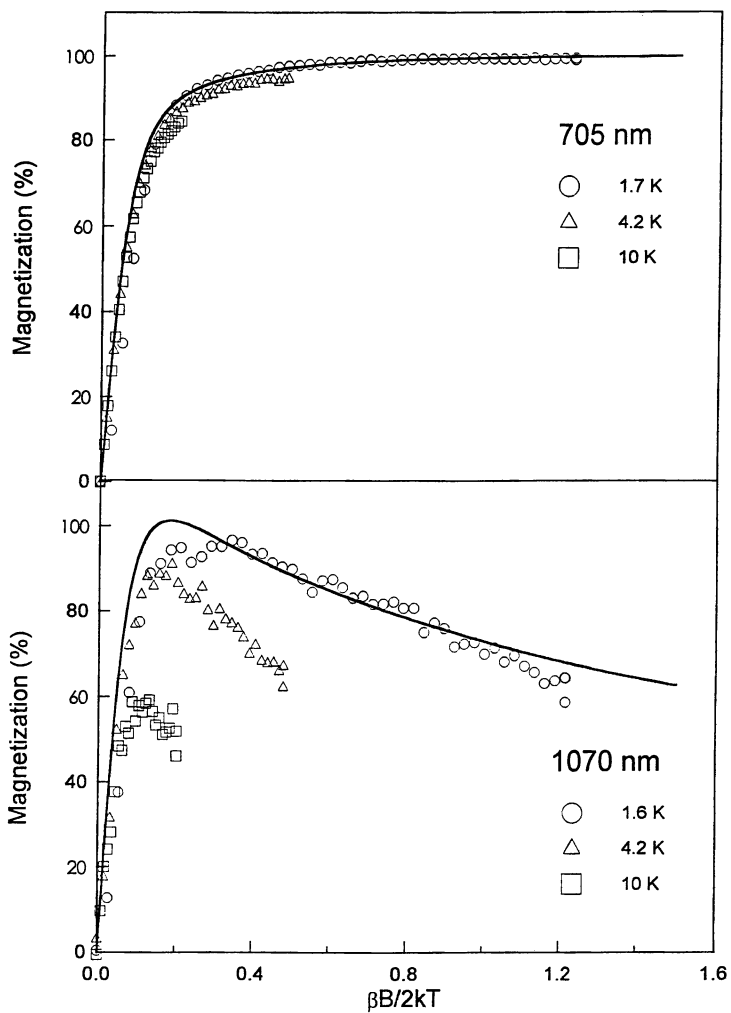


Figure 4. MCD magnetization data collected at 705 and 1070 nm for the dithionite-reduced C60S mutated form of *Cp 2Fe Fd* at pH 11.0. Adapted from ref. 28.

highly anisotropic doublet ground states, when both the z -polarized and xy -polarized transition dipole moments (m_z and m_{xy} , respectively) have the same sign (38). The theoretical data shown by the solid line in Figure 4 was computed using the effective g -values for the $M_s = \pm 9/2$ doublet of the C60S variant derived from the spin Hamiltonian analysis of the EPR resonances ($g_{\parallel} = 17.96$ and $g_{\perp} = 0.003$) and $m_z/m_{xy} = 300$.

These polarization assignments facilitate rationalization of the near-IR MCD bands in terms of a schematic molecular orbital diagram for the Fe–Fe interactions in the valence-delocalized $S = 9/2$ $[\text{Fe}_2\text{S}_2]^+$ cluster (Figure 5). The estimate of the tetrahedral crystal field splitting at each $\text{Fe}^{2.5+}$ site ($10Dq_t \sim 5000 \text{ cm}^{-1}$) is based on the detailed electronic studies of tetrahedral Fe^{2+} and Fe^{3+} complexes with thiolate ligands (39,40). The dominant interaction (responsible for the $S = 9/2$ ground state) is the σ overlap between the pair of d_{z^2} orbitals, with progressively smaller π interactions, between pairs of d_{xz} and d_{yz} orbitals, and δ interactions, between pairs of d_{xy} and $d_{x^2-y^2}$ orbitals. The $\sigma \rightarrow \sigma^*$ transition (1070 nm, 9300 cm^{-1}) is electric dipole allowed, but z -polarized resulting in weak VT-MCD intensity. The $\sigma \rightarrow \pi$ and $\sigma \rightarrow \pi^*$ transitions will be effectively xy -polarized if the d_{xz} and d_{yz} orbitals are close in energy and both should therefore exhibit broad derivative shaped temperature-dependent MCD bands (pseudo A -terms). The former is electric-dipole forbidden and hence weak in the MCD. Only the positive feature is observed as a shoulder at ~ 850 nm in C60S (it is more clearly observed in the C56S variant (28)) with the negative component buried under the intense band 710 nm. The latter is electric-dipole allowed and xy -polarized and hence gives rise to the intense pseudo A -term centered at 660 nm (15000 cm^{-1}).

The energy of the $\sigma \rightarrow \sigma^*$ transition corresponds to $10B$ (2β) and hence provides the first direct measurement of the double exchange parameter and resonance energy for a valence-delocalized $[\text{Fe}_2\text{S}_2]^+$ cluster; $B = 930 \text{ cm}^{-1}$ and $\beta = 4650 \text{ cm}^{-1}$. These values are in good agreement with those estimated for a $[\text{Fe}_2\text{S}_2]^+$ cluster ($B = 965 \text{ cm}^{-1}$ and $\beta = 4825 \text{ cm}^{-1}$) based on extrapolation from the Fe–Fe electronic coupling observed in $[\text{Fe}_2(\text{OH})_3(\text{tmtacn})_2]^{2+}$ (37). This synthetic complex is by far the best characterized valence-delocalized $S = 9/2$ diiron system investigated thus far (37,41).

Vibrational Properties. The high pH forms of dithionite-reduced C56S and C60S C_p 2Fe Fd offer the first opportunity to investigate the vibrational consequences of valence delocalization in a $[\text{Fe}_2\text{S}_2]^+$ unit. Moreover, since vibrations involving displacement along the Fe–Fe coordinate should be enhanced in the Raman spectrum by excitation into the low energy $\sigma \rightarrow \sigma^*$ and $\sigma \rightarrow \pi^*$ transitions, resonance Raman spectroscopy provides a method for testing the above assignments. Thus far resonance Raman studies have been confined to the C56S variant using excitation wavelengths in the range 406–676 nm, and a detailed discussion of spectra and the rationale for the preliminary assignments presented in Table I can be found in ref. 28. As indicated by the frequencies listed in Table I, the valence-delocalized and valence-localized $[\text{Fe}_2\text{S}_2]^+$ clusters in the C56S variant have remarkably different resonance Raman spectra, showing that the former is valence delocalized on the vibrational time scale (10^{-12} – 10^{-13} s)

⁵⁴Fe- and ³⁴S-isotope shifts are not yet available for C_p 2Fe Fd, since cluster

reconstitution by the standard protocols produces a protein different from wild-type (42). Nevertheless, Fe–S stretching modes have been assigned for both the $[\text{Fe}_2\text{S}_2]^{2+}$ and valence-localized $[\text{Fe}_2\text{S}_2]^+$ clusters in wild type *Cp* 2Fe Fd (35,43,44), under effective D_{2h} and C_{2v} symmetry, respectively, by analogy to other Fds and model complexes (35,43–45), see Table I. The resonance Raman spectrum of the oxidized C56S variant is very similar to that of the wild-type except for significant upshifts (7–9 cm^{-1}) in the predominantly terminal A_g^t and B_{3u}^t Fe–S stretching modes. This is attributed to the mass effect resulting from replacement of a coordinating S by O (24). The same general trend is observed in comparing the frequencies of the valence-localized reduced cluster in the low pH C56S variant and wild-type, i.e. upshifts of 0–14 cm^{-1} . However, the significant upshifts that are observed for the B_2 mode, which is almost exclusively Fe–S^t stretching at the Fe^{3+} site, and for the modes at 370 and 390 cm^{-1} in the wild-type, which primarily involve Fe–S^b stretching, are unexpected and probably reflect a change in the overall cluster environment resulting from replacing the serinate ligand with water or another protein ligand in the C56S variant at low pH. The resonance Raman spectra of the valence-delocalized cluster in the reduced C56S variant at pH 11 are assigned under D_{2h} symmetry by analogy to the oxidized C56S sample. Each band is shifted down in frequency by 12–35 cm^{-1} , which is consistent with weakening of the Fe–S bonds on going from Fe^{3+} to $\text{Fe}^{2.5+}$.

Table I. Fe–S stretching frequencies (cm^{-1}) for wild-type and C56S *Cp* 2Fe Fd^a

Mode ^a (D_{2h})	WT (ox)	C56S (ox)	C56S (red, VD)	Mode (C_{2v})	C56S (red, VL)	WT (red)
B_{2u}^b	404	406	385	B_1	404	390
A_g^b	387	387	368	A_1	375	370
B_{3u}^b	366	366	341	A_1	320	310
B_{1u}^t, B_{2g}^t	353	353	341	B_2	341	328
A_g^t	335	344	317	A_1	320	310
B_{1g}^b	313	314	299	B_1	280	280
B_{3u}^t	290	297	268	A_1	280	267
$A_g(\text{Fe–Fe})$	208	211	176			

^aThe t and b superscripts refer to Fe–S stretching modes that predominantly involve terminal (cysteiny) and bridging (inorganic) S, respectively. VD, valence delocalized; VL, valence localized. Adapted from ref. 28

A particularly striking difference between the resonance Raman spectra of the valence-localized and valence-delocalized $[\text{Fe}_2\text{S}_2]^+$ clusters in the C56S is seen with 676-nm excitation (Figure 6). In accord with the assignment of the absorption and MCD bands near 670 nm to the Fe–Fe $\sigma \rightarrow \pi^*$ transition in the high-pH form of C56S, excitation at this wavelength results in enhancement of the totally symmetric Fe–Fe stretching mode at 176 cm^{-1} and the totally symmetric breathing mode of the Fe_2S_2 core at 368 cm^{-1} . Both modes involve displacement along the Fe–Fe coordinate. Hence their enhancement with near-IR excitation provides strong evidence that the near-IR electronic transitions of the valence delocalized cluster arise from Fe–Fe interactions. Confirmation of these assignments via ⁵⁴Fe-isotope shifts and attempts to use excitation into the $\sigma \rightarrow \sigma^*$ transition at 1050 nm are in progress.

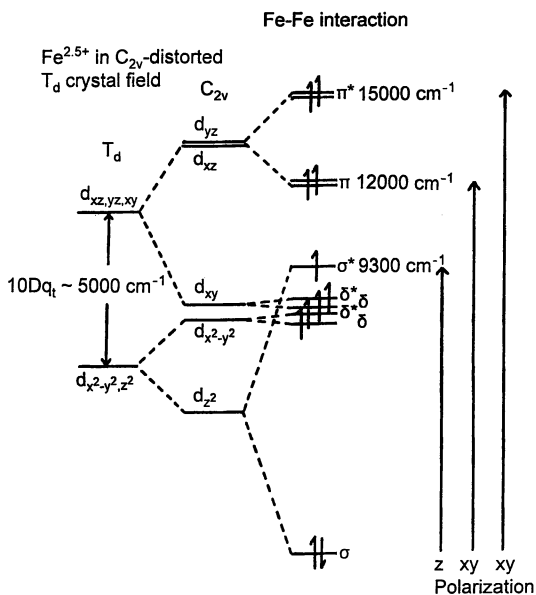


Figure 5. Schematic MO diagram for the Fe–Fe interactions in the valence-delocalized $S = 9/2$ $[\text{Fe}_2\text{S}_2]^+$ cluster based on the observed electronic transitions. The z -axis is along the Fe–Fe coordinate. Adapted from ref. 28.

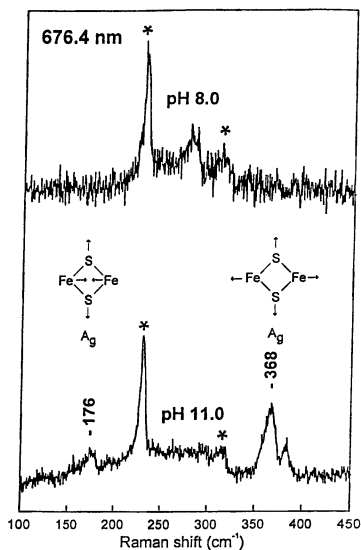


Figure 6. Comparison of the resonance Raman spectra (676-nm excitation) of dithionite-reduced C56S Cp 2Fe Fd at pH 8 and 11. The asterisks indicate lattice modes of ice.

Origin of Valence Delocalization. The discovery of valence-delocalized $S = 9/2$ $[\text{Fe}_2\text{S}_2]^+$ clusters in the C56S and C60S mutated forms of *Cp* 2Fe Fd begs for the question of why such clusters are observed in this case, whereas all other biological and synthetic $[\text{Fe}_2\text{S}_2]^+$ clusters investigated thus far are valence localized with $S = 1/2$ ground states. A detailed discussion of the extensive literature on "static" and "vibronic" mechanisms for electron trapping in exchange-coupled systems is beyond the scope of this chapter. The interested reader is referred to reviews by Blondin and Girerd (9) and the recent *JBIC* commentary articles (19-22). However, we have tried below to summarize our initial thoughts on this interesting question.

Valence delocalization resulting in an $S = 9/2$ ground state requires $|B/J| > 9$ in an idealized system in which the two valence-localized configurations have the same energy (Figure 1). This can be accomplished by increasing B , decreasing J , or a combination of both. Asymmetric Fe coordination as a result of serinate coordination might be expected to decrease J (46), and this is probably an important contributing factor to the observed valence delocalization. Whether or not B increases in the serinate-coordinated valence-delocalized forms remains to be determined. Since B is expected to correlate with the Fe-Fe distance (37), this question can be directly addressed by EXAFS studies of low-pH (valence-localized) and high-pH (valence-delocalized) forms of these two variants and such studies are in progress.

The degree of valence delocalization for a given spin state is determined by the ratio of B to the localization energy, ΔE , which contains the energetic terms reflecting both the vibronic and static preference for valence localization. On the basis of the simple resonance Hamiltonian model, valence trapping will generally occur unless $2|B(S + 1/2)| > \Delta E$. Although it is difficult to separate the vibronic and static contributions to ΔE , the static component, which corresponds to the energy difference when the extra electron is on Fe_A or Fe_B , is likely to be minimized in the C56S and C60S variants. By decreasing the potential at the "reducible" Fe site by approximately 200 mV, we hypothesize that serinate coordination accidentally makes the two Fe sites equipotential and that this is a major determinant for valence delocalization in the C56S and C60S variants.

On the basis of this discussion, it seems probable that further examples of valence delocalized $S = 9/2$ $[\text{Fe}_2\text{S}_2]^+$ clusters will come through mutagenesis studies of proteins rather than from chemical synthesis. In order to decrease the Heisenberg exchange coupling, asymmetric Fe coordination is probably required, but it is difficult to see how this can be accomplished in a synthetic cluster while maintaining isopotential Fe sites. In contrast, the nature of the Fe ligands in a protein-bound cluster is only one of the factors that determines the redox potentials at the Fe sites, making it possible to obtain isopotential Fe sites with asymmetric Fe coordination via site-directed mutagenesis.

Implications for Higher Nuclearity Fe-S Clusters

Now that the unique electronic and vibrational properties of a valence delocalized $[\text{Fe}_2\text{S}_2]^+$ clusters have been established, can this information be used to identify and characterize similar units in higher nuclearity clusters? At least in the case of VT-MCD spectroscopy, the answer appears to be a resounding yes.

Figure 7 shows a comparison of the low temperature MCD spectra of

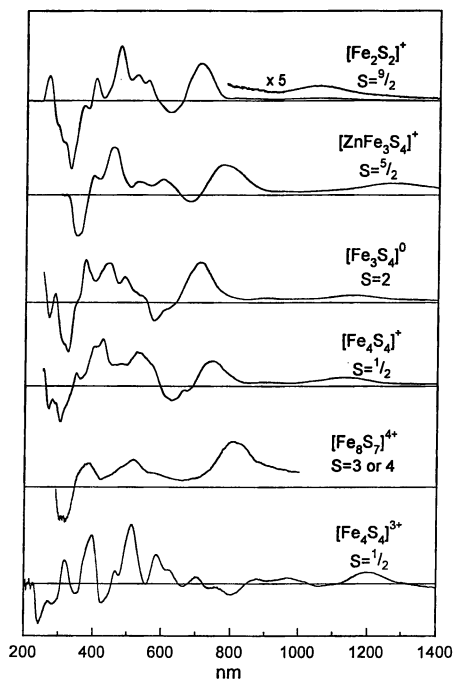


Figure 7. Comparison of the low temperature MCD spectra of different types of paramagnetic Fe-S clusters. Adapted from ref. 28.

representative examples of each type of paramagnetic Fe-S cluster that has been proposed to contain a valence delocalized $[\text{Fe}_2\text{S}_2]^+$ fragment, i.e. $S = 5/2$ $[\text{Fe}_3\text{S}_4]^-$ fragment in $[\text{ZnFe}_3\text{S}_4]^+$ Fd (2), $S = 2$ $[\text{Fe}_3\text{S}_4]^0$ Fd, $S = 1/2$ $[\text{Fe}_4\text{S}_4]^+$ Fd, $S = 3$ or 4 $[\text{Fe}_8\text{S}_7]^{4+}$ nitrogenase P-cluster, and $S = 1/2$ $[\text{Fe}_4\text{S}_4]^{3+}$ HiPIP. The origin of the intense positive band between 700-800 nm that dominates the near-IR MCD of many paramagnetic Fe-S has long been a puzzling feature of the spectra of Fe-S proteins (47). It is now evident that this is the hallmark of a valence delocalized $[\text{Fe}_2\text{S}_2]^+$ fragment. Indeed inspection of Figure 7, suggests that the electronic transitions from this fragment dominate the UV/visible/near-IR MCD spectra of $[\text{ZnFe}_3\text{S}_4]^+$, $[\text{Fe}_3\text{S}_4]^0$, $[\text{Fe}_4\text{S}_4]^+$ and $[\text{Fe}_8\text{S}_7]^{4+}$ clusters. This is not surprising since, with the exception of $[\text{Fe}_3\text{S}_4]^0$ cluster, the remaining Fe is all Fe^{2+} which is expected to contribute charge transfer bands only below 400 nm. What is particularly striking is that $[\text{ZnFe}_3\text{S}_4]^+$, $[\text{Fe}_3\text{S}_4]^0$, $[\text{Fe}_4\text{S}_4]^+$ clusters all exhibit the same pattern of near-IR MCD bands that were assigned to Fe-Fe $\sigma \rightarrow \sigma^*$, $\sigma \rightarrow \pi$ and $\sigma \rightarrow \pi^*$ transitions for the valence-delocalized $[\text{Fe}_2\text{S}_2]^+$ clusters. Hence we conclude that all three clusters contain a valence-delocalized $[\text{Fe}_2\text{S}_2]^+$ cluster fragment and the energy of the $\sigma \rightarrow \sigma^*$ transition provides a direct measure of the double exchange parameter, $B = 790 \text{ cm}^{-1}$ in $[\text{ZnFe}_3\text{S}_4]^+$, 870 cm^{-1} in $[\text{Fe}_3\text{S}_4]^0$, and 890 cm^{-1} in $[\text{Fe}_4\text{S}_4]^+$.

In the case of the $[\text{ZnFe}_3\text{S}_4]^+$ and $[\text{Fe}_3\text{S}_4]^0$ clusters, the Mössbauer data leave little doubt that the valence-delocalized $[\text{Fe}_2\text{S}_2]^+$ fragment is $S = 9/2$ (2,12). Based on the similarity in the VT-MCD data, it is tempting to draw the same conclusion for the spin state of this fragment in $[\text{Fe}_4\text{S}_4]^+$ clusters. However, a similar set of MCD bands might also be expected for valence-delocalized $[\text{Fe}_2\text{S}_2]^+$ clusters with $S = 7/2$ or $5/2$ ground states, based on the schematic energy level scheme shown in Figure 5. It may prove possible to discriminate between these alternatives by obtaining MCD data to lower energies, since only the lower spin states would be expected to have observable transitions at wavelengths $> 1400 \text{ nm}$. Such measurements are in progress for a wide range of Fe-S clusters. At this stage, it remains to be determined if near-IR VT-MCD can provide a means of assessing the spin state of the valence-delocalized $[\text{Fe}_2\text{S}_2]^+$ fragments in higher nuclearity clusters.

The presence of an intense MCD band at 800 nm in oxidized P-clusters clearly suggests the presence of valence-delocalized $[\text{Fe}_2\text{S}_2]^+$ fragments. Although near-IR VT-MCD data clearly needs to be extended to lower energy in this case, analysis will be more difficult, since there are likely to be two different valence delocalized $[\text{Fe}_2\text{S}_2]^+$ fragments in the oxidized form of this double cubane cluster (32). A surprising aspect of the MCD data shown in Figure 7, is that the VT-MCD spectrum of the $[\text{Fe}_4\text{S}_4]^{3+}$ cluster in oxidized HiPIPs does not conform to the pattern expected for cluster containing a valence delocalized $[\text{Fe}_2\text{S}_2]^+$ fragment. Whether this is a consequence of overlapping electronic transitions from the Fe^{3+} pair and/or a spin state $< 9/2$ for the valence-delocalized $[\text{Fe}_2\text{S}_2]^+$ fragment is unclear at present.

This brief discussion demonstrates that the discovery and characterization of $S = 9/2$ valence-delocalized $[\text{Fe}_2\text{S}_2]^+$ clusters in mutated forms of *Cp* 2Fe Fd represents a major step forward in understanding the electronic structure of Fe-S clusters. Moreover, the ability of VT-MCD spectroscopy to identify and determine the resonance energy of these fragments in higher nuclearity clusters indicates that this technique is destined to play an increasingly important role in investigations of valence delocalization in Fe-S clusters.

Acknowledgments

This work was supported by a grant from the National Institutes of Health (GM51962 to M.K.J.)

Literature Cited

1. Münck, E.; Kent, T. A. *Hyperfine Interact.* **1986**, *27*, 161-172.
2. Münck, E.; Papaefthymiou, V.; Surerus, K. K.; Girerd, J.-J. In *Metal Clusters in Proteins*; Que, L., Jr. Ed.; ACS Symposium Series; American Chemical Society: Washington, D. C. 1988; pp 302-325.
3. Papaefthymiou, V.; Millar, M. M.; Münck, E. *Inorg. Chem.* **1986**, *25*, 3010-3014.
4. Banci, L.; Bertini, I.; Ciurli, S.; Ferretti, C.; Luchinat, C.; Piccioli, M. *Biochemistry* **1993**, *32*, 9387-9397.
5. Middleton, P.; Dickson, D. P. E.; Johnson, C. E.; Rush, J. D. *Eur. J. Biochem.* **1978**, *88*, 135-141.
6. Bertini, I.; Briganti, F.; Luchinat, C.; Scozzafava, A.; Sola, M. *J. Am. Chem. Soc.* **1991**, *113*, 1237-1245.
7. Christner, J. A.; Janick, P. A.; Siegel, L. M.; Münck, E. *J. Biol. Chem.* **1983**, *258*, 11157-11164.
8. Girerd, J.-J. *J. Chem. Phys.* **1983**, *79*, 1766-1775.
9. Blondin, G.; Girerd, J.-J. *Chem. Rev.* **1990**, *90*, 1359-1376.
10. Noodleman, L.; Baerends, E. J. *J. Am. Chem. Soc.* **1984**, *106*, 2316-2327.
11. Noodleman, L.; Case, D. A. *Adv. Inorg. Chem.* **1992**, *38*, 423-470.
12. Borshch, S. A.; Bominaar, E. L.; Blondin, G.; Girerd, J.-J. *J. Am. Chem. Soc.* **1993**, *115*, 5155-5168.
13. Bominaar, E. L.; Borshch, S. A.; Girerd, J.-J. *J. Am. Chem. Soc.* **1994**, *116*, 5362-5372.
14. Bominaar, E. L.; Hu, Z.; Münck, E.; Girerd, J.-J.; Borshch, S. A. *J. Am. Chem. Soc.* **1995**, *117*, 6976-6989.
15. Mouesca, J.-M.; Rius, G.; Lamotte, B. *J. Am. Chem. Soc.* **1993**, *115*, 4714-4731.
16. Mouesca, J.-M.; Noodleman, L.; Case, D. A.; Lamotte, B. *Inorg. Chem.* **1995**, *34*, 4347-4359.
17. Anderson, P. W.; Hasegawa, H. *Phys. Rev.* **1955**, *100*, 675-681.
18. Achim, C.; Golinelli, M.-P.; Bominaar, E. L.; Meyer, J.; Münck, E. *J. Am. Chem. Soc.* **1996**, *118*, 8168-8169.
19. Kröckel, M.; Grodzicki, M.; Papaefthymiou, V.; Trautwein, A. X.; Kostikas, A. *JBIC* **1996**, *1*, 173-176.
20. Blondin, G.; Girerd, J.-J. *JBIC* **1996**, *1*, 170-172.
21. Noodleman, L.; Case, D. A.; Mouesca, J.-M. *JBIC* **1996**, *1*, 177-182.
22. Bertini, I.; Luchinat, C. *JBIC* **1996**, *1*, 183-185.
23. Fujinaga, J.; Gaillard, J.; Meyer, J. *Biochem. Biophys. Res. Commun.* **1993**, *194*, 104-111.

24. Meyer, J.; Fujinaga, J.; Gaillard, J.; Lutz, M. *Biochemistry* **1994**, *33*, 13642-13650.
25. Golinelli, M.-P.; Akin, L. A.; Crouse, B. R.; Johnson, M. K.; Meyer, J. *Biochemistry* **1996**, *35*, 8995-9002.
26. Johnson, M.K. In *Encyclopedia of Inorganic Chemistry*; King, R.B., Ed.; John Wiley & Sons: Chichester, 1994; pp 1896-1915.
27. Crouse, B. R.; Meyer, J.; Johnson, M. K. *J. Am. Chem. Soc.* **1995**, *117*, 9612-9613.
28. Duin, E. C.; Crouse, B. R.; Golinelli, M.-P.; Meyer, J.; Fawcett, S.; Armstrong, F. A.; Johnson, M. K. *J. Am. Chem. Soc.*, submitted.
29. Werth, M. T.; Cecchini, G.; Manodori, A.; Ackrell, B. A. C.; Schroder, I.; Gunsalus, R. P.; Johnson, M. K. *Proc. Natl. Acad. Sci. U.S.A.* **1990**, *87*, 8965-8969.
30. Cheng, H.; Xia, B.; Reed, G. H.; Markley, J. L. *Biochemistry* **1994**, *33*, 3155-3164.
31. Holden, H. M.; Jacobson, B. L.; Hurley, J. K.; Tollin, G.; Oh, B.-H.; Skjeldal, L.; Chae, Y. K.; Xia, B.; Markley, J. L. *J. Bioenerg. Biomembr.* **1994**, *26*, 67-88.
32. Peters, J. W.; Stowell, M. H. B.; Soltis, S. M.; Finnegan, M. G.; Johnson, M. K.; Rees, D. C. *Biochemistry* **1997**, *36*, 1181-1187.
33. Bertrand, P.; Gayda, J.-P. *Biochim. Biophys. Acta* **1979**, *579*, 107-121.
34. Bertrand, P.; Guigliarelli, B.; Gayda, J.-P.; Beardwood, P.; Gibson, J. F. *Biochim. Biophys. Acta* **1985**, *831*, 261-266.
35. Fu, W.; Drozdowski, P. M.; Davies, M. D.; Sligar, S. G.; Johnson, M. K. *J. Biol. Chem.* **1992**, *267*, 15502-15510.
36. Thomson, A. J.; Cammack, R.; Hall, D. O.; Rao, K. K.; Briat, B.; Rivoal, J.; Badoz, J. *Biochim. Biophys. Acta* **1977**, *493*, 132-141.
37. Gamelin, D. R.; Bominaar, E. L.; Kirk, M. L.; Wieghardt, K.; Solomon, E. I. *J. Am. Chem. Soc.* **1996**, *118*, 8085-8097.
38. Bennett, D. E.; Johnson, M. K. *Biochim. Biophys. Acta* **1987**, *911*, 71-80.
39. Gebhard, M. S.; Deaton, J. C.; Koch, S. A.; Millar, M.; Solomon, E. I. *J. Am. Chem. Soc.* **1990**, *112*, 2217-2231.
40. Gebhard, M. S.; Koch, S. A.; Millar, M.; Devlin, F. J.; Stephens, P. J.; Solomon, E. I. *J. Am. Chem. Soc.* **1991**, *113*, 1640-1649.
41. Gamelin, D. R.; Bominaar, E. L.; Mathonière, C.; Kirk, M. L.; Wieghardt, K.; Girerd, J.-J.; Solomon, E. I. *Inorg. Chem.* **1996**, *35*, 4323-4335.
42. Meyer, J.; Moulis, J.-M.; Gaillard, J.; Lutz, M. *Adv. Inorg. Chem.* **1992**, *38*, 73-115.
43. Meyer, J.; Moulis, J.-M.; Lutz, M. *Biochim. Biophys. Acta* **1986**, *873*, 108-118.
44. Han, S.; Czernuszewicz, R. S.; Kimura, T.; Adams, M. W. W.; Spiro, T. G. *J. Am. Chem. Soc.* **1989**, *111*, 3505-3511.
45. Han, S.; Czernuszewicz, R. S.; Spiro, T. G. *J. Am. Chem. Soc.* **1989**, *111*, 3496-3504.
46. Kahn, O. In *Molecular Magnetism*; VCH Publishers: New York, 1993; pp 103-134.
47. Johnson, M. K.; Robinson, A. E.; Thomson, A. J. In *Iron-sulfur Proteins*; Spiro, T.G. Ed.; Metals in Biology; Wiley: New York, 1982, Vol. 4; pp 367-406.

Chapter 17

NMR of FeS Proteins

Ivano Bertini¹, Claudio Luchinat², and Aileen Soriano¹

¹Department of Chemistry, University of Florence, via Gino Capponi 7, 50121 Florence, Italy

²Department of Soil Science and Plant Nutrition, University of Florence, P.le delle Cascine 28, 50144 Florence, Italy

The NMR linewidths of FeS polymetallic centers are discussed herein in terms of electronic relaxation rates and of the possibility of performing high resolution NMR spectroscopy on these systems. The linewidths depend on a single effective electron relaxation time, equal to or smaller than 5×10^{-11} s, which is our estimate from the iron-containing reduced rubredoxin. A summary of what is learned from NMR studies on the three polymetallic centers $[\text{Fe}_2\text{S}_2]^+$, $[\text{Fe}_4\text{S}_4]^{3+}$ and $[\text{Fe}_3\text{S}_4]^+$, all having $S=1/2$ ground state, is presented.

The NMR of FeS proteins is largely the NMR of systems containing iron ions that are magnetically coupled in any of the naturally occurring polymetallic centers (Figure 1) (1,2). The synthetic models have permitted an enormous progress to be made in the understanding of these polymetallic centers (3,4). However, the effect of magnetic coupling on the electronic relaxation times and on the electronic structures of the synthetic systems has not been pursued as deeply as has been done on the corresponding proteins, one of the many reasons being the averaged symmetry of the synthetic models on the NMR time scale, at least at room temperature. The lack of any symmetry, the rigid frame provided by the polypeptide chain, and the slow tumbling times resulted in great advantages for the direct investigation of iron-sulfur centers in the proteins themselves.

The observability of the NMR lines in paramagnetic proteins depends on electron relaxation: the faster the electron relaxation, the sharper the NMR lines. In turn, electronic relaxation is efficient when there are excited electronic states close in energy. The ground state in tetrahedral Fe^{3+} is ${}^6\text{A}_1\text{g}$ with $S = 5/2$. Therefore, there are no low-lying excited states. Estimates of zero field splitting (ZFS) of the $S = 5/2$ multiplet in oxidized rubredoxin indicate that it is too small ($1\text{--}2 \text{ cm}^{-1}$) (5,6) to make effective Raman type (7) or Orbach type (8) electron relaxation. From the linewidths of ${}^1\text{H}$ and ${}^2\text{H}$ NMR signals we can estimate an effective electronic relaxation time at room temperature to be of the order of 10^{-9} - 5×10^{-10} s. This makes ${}^1\text{H}$ NMR lines, for example of $\beta\text{-CH}_2$ protons of the coordinated cysteines, broad beyond detection.

Indeed, the β -CH₂ protons of the coordinated cysteines in oxidized rubredoxin have not been observed. The corresponding ²H signals, which should be a factor of 42 narrower, have been located at 800-1000 ppm downfield (9).

The situation of Fe²⁺ is somewhat better: $S = 2$ makes the linewidths 2/3 those of $S = 5/2$. Furthermore, the ground state is ⁵E which is further split by low symmetry. Estimates of such splitting range between 600 and 1400 cm⁻¹ (10-12) which should provide relatively fast electron relaxation. Indeed, ¹H NMR signals from the β -CH₂ protons of the coordinated cysteines in reduced rubredoxin have been observed (9), but they are still very broad (in the 10 kHz range), and we can estimate an effective electronic relaxation time for Fe²⁺ to be around 5×10^{-11} s.

The effect of magnetic coupling on electronic relaxation times is very complex and only partly understood. In every polynuclear system with a magnetic coupling constant J larger than a few wavenumbers, we can probably define a single effective electronic relaxation time at each temperature (13). This should be equal to or smaller than that of the fastest relaxing ion by itself, in this case Fe²⁺ (Bertini, I.; Galas, O.; Luchinat, C.; Parigi, G.; Spina, G.; manuscript submitted, 1997). In the absence of new electronic relaxation mechanisms, only the mechanisms of the fastest relaxing metal ion should be effective for all metal ions due to magnetic exchange coupling. However, the new energy levels arising from magnetic coupling may experience new and efficient relaxation pathways and thus decrease the overall electronic relaxation time. Therefore, whenever there is a Fe²⁺ ion, the effective electronic relaxation time can be set to be less than 5×10^{-11} s. Thus, ¹H NMR can be attempted for any FeS system except [Fe₂S₂]²⁺, which contains only Fe³⁺, and [Fe₃S₄]⁰, possibly because of the presence of chemical equilibria (Bertini, I.; Luchinat, C.; Mincione, G.; Soriano, A.; manuscript submitted, 1997). Here we discuss three cases with resulting spin $S' = 1/2$: [Fe₂S₂]⁺, [Fe₄S₄]³⁺, and [Fe₃S₄]⁺. The latter contains three Fe³⁺ ions.

The [Fe₂S₂]⁺ case

A great advantage of ¹H NMR spectroscopy is that we can follow the magnetic exchange coupling at room temperature whenever the ground state has total spin larger than zero. The Fe-S-Fe superexchange mechanism provides antiferromagnetic coupling (1). Thus, a system constituted by $S_1 = 5/2$ (Fe³⁺) and $S_2 = 2$ (Fe²⁺) will provide a ground state with $S' = 1/2$ (the prime refers to spin states resulting from magnetic coupling). The larger spin, $S_1 = 5/2$, will orient along the applied external magnetic field. The smaller spin $S_2 = 2$ will, on the contrary, orient against the external magnetic field if $J \geq kT$ because in the ground state the antiferromagnetic coupling prevails (Figure 2) (14,15). We recall the definition of $\langle S_{1z} \rangle$ and $\langle S_{2z} \rangle$ as the expectation values of S_{1z} and S_{2z} operators on the S_1 and S_2 spin wavefunctions, respectively. In the isolated systems, these expectation values are negative. In the coupled systems, S_{1z} and S_{2z} operate on the spin coupled wavefunction S' . As a result of magnetic coupling, $\langle S_{1z} \rangle$ will be negative as for any isolated system and $\langle S_{2z} \rangle$ will be positive. Since the contact shift is proportional to $-\langle S_{iz} \rangle$ (through the positive proportionality constant which is the hyperfine coupling constant) (16), the contact shifts will be positive (downfield) for nuclei sensing $S_1 = 5/2$ (Fe³⁺) and negative (upfield) for nuclei interacting with $S_2 = 2$ (Fe²⁺). Also, if the antiferromagnetic coupling constant J is much smaller than kT , all the S' levels are equally populated and there is no effect from magnetic coupling (13). When $J = kT$, intermediate cases are

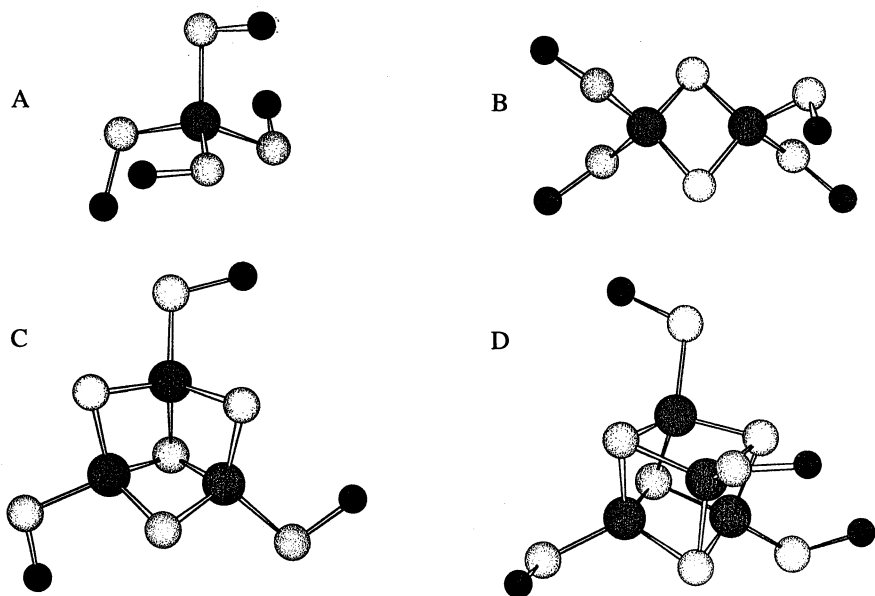


Figure 1. Cysteinate ligands coordinating $\text{Fe}^{2+/3+}$ in rubredoxins (A); $[\text{Fe}_2\text{S}_2]^{1+/2+}$ (B) and $[\text{Fe}_3\text{S}_4]^{0/1+}$ (C) in ferredoxins; and $[\text{Fe}_4\text{S}_4]^{1+/2+/3+}$ (D) in ferredoxins (1+/2+) or HiPIPs (2+/3+), respectively.

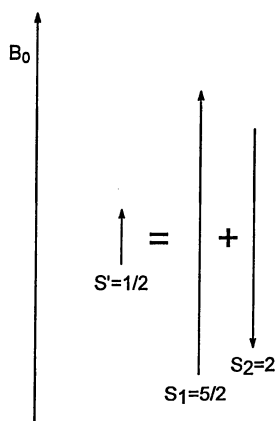


Figure 2. The $S' = 1/2$ spin resulting from antiferromagnetic coupling between $S_1 = 5/2$ and $S_2 = 2$ spins orients along an external magnetic field B_0 . As a result, the $S_2 = 2$ spin is oriented against the field, and its hyperfine interaction with nuclei changes sign.

observed. This is the case for $[\text{Fe}_2\text{S}_2]^+$ clusters in ferredoxins ($J \cong 200 \text{ cm}^{-1}$). A representative NMR spectrum is shown in Figure 3. The less shifted cys $\beta\text{-CH}_2$ signals ($f - i$) arise from the iron(II) site and their low temperature limiting shift is upfield, as expected from the magnetic coupling scheme discussed above. The different linewidths between the iron(III) and the iron(II) sites are explained in terms of the different $\langle S_{1z} \rangle$ and $\langle S_{2z} \rangle$ values in the coupled system (15). The values are consistent with a single electron relaxation time for the pair, as expected. Our estimate, however, is about $2 \times 10^{-12} \text{ s}$ which is shorter than that of iron(II) in rubredoxin. Apparently, there are additional relaxation mechanisms made available by the exchange coupling. Note that if electron delocalization occurred, all signals would experience the same average $\langle S_z \rangle$ value and all NMR signals would be downfield.

In short, ^1H NMR provides a tool (*i*) for knowing whether or not there is a localized valence system with Fe^{3+} and Fe^{2+} and if so, as is the case for $[\text{Fe}_2\text{S}_2]^+$ systems, (*ii*) for recognizing the protons of each domain (17). Then, through the techniques of NMR of paramagnetic molecules we can (*i*) perform the sequence specific assignment of the signals of each domain and then (*ii*) recognize which is the reducible iron (17). The reducible iron is that close to the surface of the protein on account of the large dielectric constant experienced by the region occupied by the solvent (18). In principle, it is possible to solve the whole structure in solution (19) as has been done for other Fe-S proteins (20-22).

The $[\text{Fe}_4\text{S}_4]^{3+}$ case (oxidized HiPIP)

The ^1H NMR spectrum of oxidized HiPIP II from *E. halophila* shows four signals downfield and four upfield (Figure 4) (23). This has been reconciled with the idea of having $S_{12} = 9/2$ antiferromagnetically coupled with $S_{34} = 4$ where 1, 2, 3 and 4 denote each individual iron ion (24). The $S_{12} = 9/2$ occurs everytime there is a mixed valence (non localized) iron(II)-iron(III) pair (25). The $S_{34} = 4$ is due to the ferric pair. The values 9/2 and 4 for the S_{12} and S_{34} spin pairs are the result of applying the Heisenberg Hamiltonian, $\mathcal{H} = JS_i \cdot S_j$, to each pair of *i* and *j* metal ions. Under antiferromagnetic coupling ($J > 0$), if J_{12} is the smallest, S_1 and S_2 are forced to be ferromagnetically coupled with $S_{12} = 9/2$. This is because not all spins can be antiferromagnetically coupled one to the other in a close circular arrangement. Therefore, the pair experiencing the smallest antiferromagnetic coupling indeed acquires a ground state typical of ferromagnetic systems. S_{34} has a value smaller than 5, and indeed is 4, for a very large range of *J* values. Actually, to explain the low temperature hyperfine values with ^{57}Fe and the EPR data, it has been proposed that the ground state is the following linear combination of $|9/2, 4\rangle$ and $|7/2, 4\rangle$ wavefunctions (26,27):

$$\Psi = 0.95|9/2, 4\rangle + 0.31|4, 7/2\rangle \quad (1)$$

This ground state is obtained with a *J* coupling scheme with C_s symmetry.

Thus, the two cysteines bound to the mixed valence pair will experience downfield shift and the two cysteines bound to the ferric pair will experience upfield shift. The sequence specific assignment of the cysteines recently became available (23) and shortly after, the solution structures of this type of proteins were solved (20-22) (Figure 5).

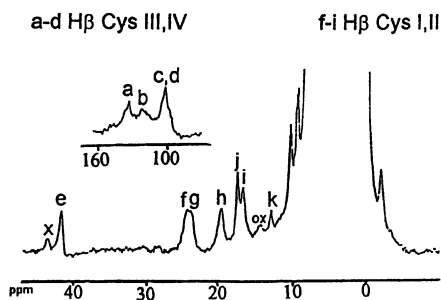


Figure 3. ^1H NMR spectrum of the $[\text{Fe}_2\text{S}_2]^+$ -containing reduced ferredoxin from spinach (43). The eight signals (*a-d, f-i*) arise from the β - CH_2 protons of the four cluster-coordinated cysteines. The four far downfield signals (*a-d*) originate from the ferric site whose $S = 5/2$ spin is oriented along the magnetic field; the less shifted signals (*f-i*) originate from the ferrous site whose ground $S = 2$ spin is oriented against the field in the ground state (see Figure 2). The low temperature limiting shift value of the latter signals is in fact upfield. The sequential assignment of the signals to the cluster-bound cysteines is also shown.

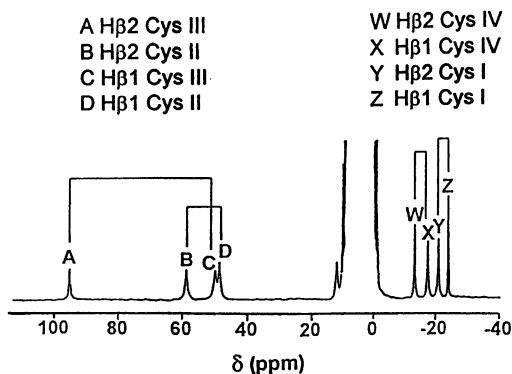


Figure 4. ^1H NMR spectrum of the $[\text{Fe}_4\text{S}_4]^{3+}$ -containing oxidized HiPIP II from *E. halophila* (23). The eight signals arise from the β - CH_2 protons of the four cluster-coordinated cysteines. The four downfield signals (*a-d*) originate from the mixed-valence $\text{Fe}^{2.5+}\text{-Fe}^{2.5+}$ pair whose ground state $S_{12} = 9/2$ spin is oriented along the magnetic field; the four upfield signals (*w-z*) originate from the ferric $\text{Fe}^{3+}\text{-Fe}^{3+}$ pair whose ground state $S_{34} = 4$ spin is oriented against the field. The sequential assignment of the signals to the cluster-bound cysteines is also shown.

Some oxidized HiPIPs may have a more complicated behavior owing to the possibility that electron delocalization occurs in more than one pair of iron ions. This has been reviewed in a previous ACS series book (28).

The ^1H NMR lines in $[\text{Fe}_4\text{S}_4]^{3+}$ systems are very sharp, and particularly much sharper than in $[\text{Fe}_2\text{S}_2]^{2+}$ systems. Again, the data are consistent with a single τ_s value, much shorter than that of iron(II) in rubredoxin.

The $[\text{Fe}_3\text{S}_4]^+$ case

This case is interesting because the cluster contains only iron(III) ions, as in the oxidized $[\text{Fe}_2\text{S}_2]^{2+}$ ferredoxins, the latter giving very broad NMR lines. The ground state of the $[\text{Fe}_3\text{S}_4]^+$ cluster has $S'=1/2$ with g values around 2.02, 2.00 and 1.97 (1,29). Its ^1H NMR lines are almost as sharp as in $[\text{Fe}_4\text{S}_4]^{3+}$ systems (compare Figures 4 and 6). Apparently, a dramatic shortening of the overall τ_s with respect to the isolated Fe^{3+} ion by exchange coupling has occurred and the shortening is sizable also with respect to the $[\text{Fe}_2\text{S}_2]^{2+}$ case. This may be a general phenomenon due to the existence of excited states with the same spin as the ground state in trinuclear (and higher nuclearity) clusters. It is possible that the sharpening of the NMR signals increase with the nuclearity of the cluster. The NMR investigation of $[\text{Fe}_3\text{S}_4]^+$ systems has been recently extended to a number of proteins, and the ambiguities in the assignment resolved (30-36). It appears that the $[\text{Fe}_3\text{S}_4]^+$ environment in 3Fe4S proteins is slightly different from that of $[\text{Fe}_3\text{S}_4]^+$ in 7Fe8S proteins (Figure 6 A and B, respectively). This has been related (36) to the difference in primary sequences (Figure 7) (37). The 3Fe4S proteins look more symmetric, as the protons of one cysteine are far downfield shifted and those of the other two cysteines are less shifted (Figure 6A). In the $[\text{Fe}_3\text{S}_4]^+$ cluster of 7Fe8S proteins there is also one far shifted cysteine $\beta\text{-CH}_2$ pair, but the other two $\beta\text{-CH}_2$ pairs are more inequivalent as one proton of a pair is slightly upfield (Figure 6B). We have proposed (36) that, with one possible exception (31), Cys IV in the primary sequence is the one far shifted downfield and Cys I is shifted around zero or upfield (Table I). We have also drawn energy diagrams for the two cases (Figure 8) (36) depending on the J values in the following Hamiltonian:

$$\mathcal{H} = J_{12}S_1S_2 + J_{13}S_1S_3 + J_{23}S_2S_3 \quad (2)$$

The experimental temperature dependence is also consistent with the theoretical expectations from the proposed electronic structure, both for the more symmetric (32,33) as well as for the less symmetric clusters (35,36). In Figure 9, the experimental and calculated values for the less symmetric cases are reported. In the more symmetric cases, the shifts for the B , I' , I , W tend to be similar to their average value.

Concluding remarks

^1H NMR spectroscopy is a powerful tool for monitoring the contribution of each metal ion to each spin level in a magnetic coupled system. This permits the investigation of the valence distribution in Fe_nS_m polymetallic centers, where average oxidation states of 2+, 2.5+ and 3+ have been found. If the sequence specific assignment of the protein is available, this then frames the valence distribution inside the protein structure. At this point, on one side we can proceed to obtain the solution structure of the protein,



Figure 5. Schematic representation of the solution structure of the $[\text{Fe}_4\text{S}_4]^{5+}$ -containing oxidized HiPIP I from *E. halophila* (21). The thickness of the tube is proportional to the backbone RMSD. Note the high resolution even in the proximity of the paramagnetic center.

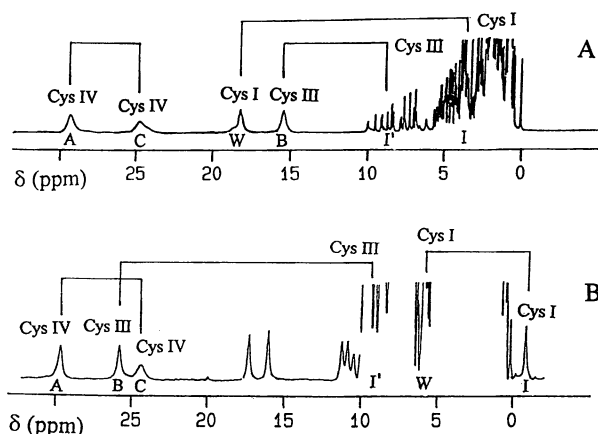


Figure 6. ^1H NMR spectra of the $[\text{Fe}_3\text{S}_4]^+$ -containing oxidized ferredoxins from *D. gigas* (3Fe4S ferredoxin) (A) (33) and *R. palustris* (7Fe8S ferredoxin) (B) (36). Signals in A and B are labelled according to the sequence-specific assignment in B. The sequential numbering of the corresponding cysteines is also shown. The sequential numbering of the $[\text{Fe}_4\text{S}_4]^{2+}$ cluster in B is omitted for clarity. Cys IV β - CH_2 protons are most downfield and show a Curie-type temperature dependence in both cases. Cys I and III β - CH_2 protons are almost equivalent and all antiCurie in A, whereas they are strongly inequivalent in B, with signal I being upfield with a pseudoCurie behavior (see also Figure 8).

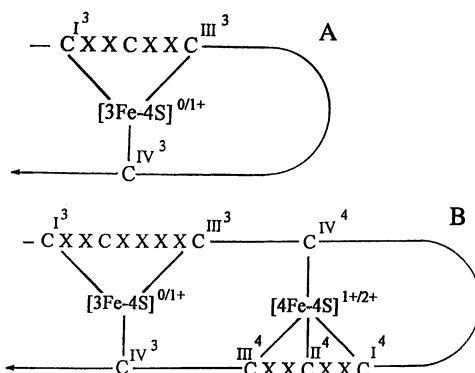


Figure 7. Different primary sequences characterizing most 3Fe4S (A) and 7Fe8S (B) ferredoxins (36,37). Arabic numerals refer to the type of cluster, and roman numerals refer to the sequential cysteine ordering in the cluster.

Table I. Summary of the available NMR data on 3Fe4S and 7Fe8S ferredoxins. ^a

	Cys-I ³ antiCurie	Cys-III ³ antiCurie	Cys-IV ³ Curie	Cys-IV ⁴ antiCurie	Cys-I ⁴ antiCurie	Cys-II ⁴ antiCurie	Cys-III ⁴ antiCurie
<i>D. gigas</i> ^b (33)	~ 18, ~3.5	~ 15.2, ~ 8.5	29.2, 24.5				
<i>T. litoralis</i> ^b (32,39)	17.4, 4.9	16.6, 8.1	29.2, 24.0				
<i>P. furiosus</i> ^b (31,32)	19.7, 17.1 Curie	14.3, 5.2	23.6, 11.8 antiCurie				
<i>P. putida</i> ^c (30,40)	(0-10), (0-10)	21.8, (0-10)	31.8, 26.3 ^d	9.8, 9.3 ^{d, e}	9.8, 9.3 ^{d, e}	17.3, (0-10) ^d	15.3, (0-10)
<i>A. vinelandii</i> ^f (30)	(0-10), (0-10)	21.1, 8.6	32.2, 26.1 ^d	(0-10), (0-10)	(0-10), (0-10)	16.9, 9.1 ^d	15.2, 5.6
<i>B. schlegelii</i> ^g (35)	(0-9), (0-9)	18.3, 6.6	32.2, 23.4	10.35, ~ 9	11.1, 9.0	15.8, 9.7	15.9, 5.2
<i>R. palustris</i> ^{d, g} (36)	-0.8 ^h , 5.8	25.8, 9.5	29.6, 24.4	10.2, 9.6	10.6, 9.7	17.15, 9.3	15.9, 6.0
<i>D. ambivalens</i> ^b (41)	20.0, 9.2	17.1, 7.5	21.7, 18.9	14.2, 7.9	10.9, 9.3	17.9, 9.2	14.0, 6.3
<i>P. ovalis</i> ^{d, i} (42)	(0-10), (0-10)	22.3, (0-10)	30.9, 25.7	10.5 ^e , (0-10)	10.5 ^e , (0-10)	17.7, (0-10) ^j	15.7, (0-10) ^j
<i>M. smegmatis</i> ^{d, i} (42)	(0-10), (0-10)	22.9, (0-10)	29.8, 21.5	11.0 ^e , (0-10)	11.0 ^e , (0-10)	17.1, (0-10) ^j	16.2, (0-10) ^j
<i>T. thermophilus</i> ^{d, i} (42)	(0-10), (0-10)	21.8, (0-10)	29.0, 21.1	11.1 ^e , (0-10)	11.1 ^e , (0-10)	17.4, (0-10) ^j	17.0, (0-10) ^j

^a Chemical shifts in ppm and their temperature dependence; ^b 303 K; ^c 281 K; ^d sequence specific assignment proposed in (36); ^e only one signal or one pair is observed. It is impossible to discriminate between Cys-IV⁴ and Cys-I⁴; ^f 280 K; ^g 298 K; ^h pseudoCurie; ⁱ 300 K; ^j the assignment to Cys-II⁴ or Cys-III⁴ could be reversed.

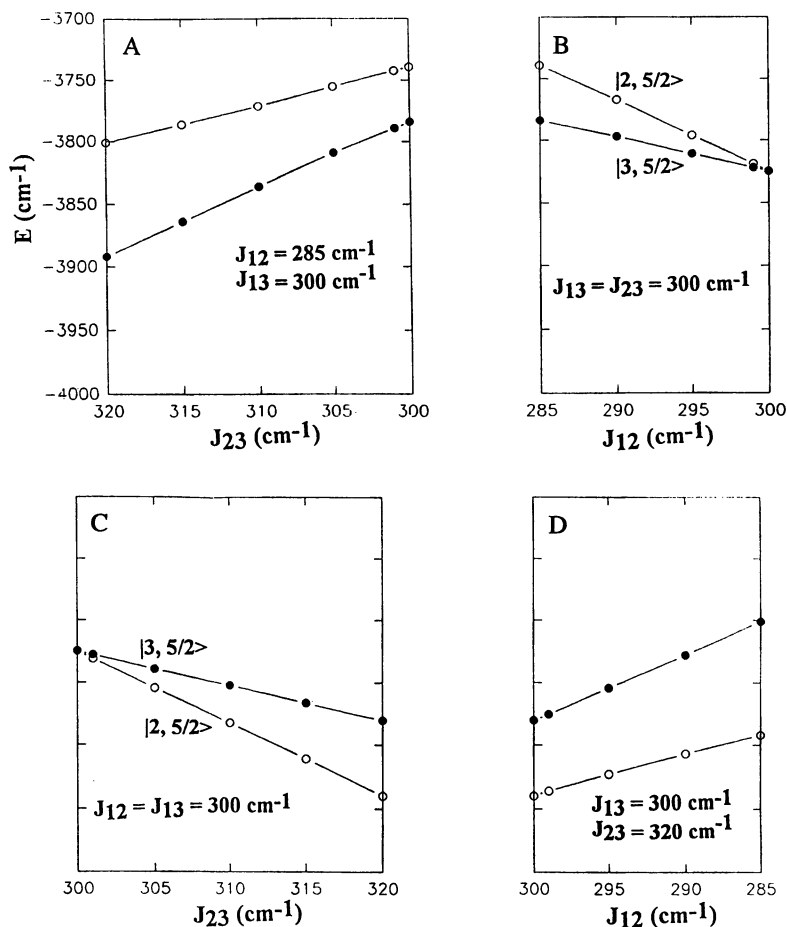


Figure 8. Calculated eigenvalues for the two lowest lying energy states of the Hamiltonian (equation 2) in $[\text{Fe}_3\text{S}_4]^+$ clusters for different J values. B and C refer to the more symmetric case encountered in 3Fe4S ferredoxins (two equal J values), while A and D refer to the more asymmetric case encountered in the $[\text{Fe}_3\text{S}_4]^+$ cluster of 7Fe8S ferredoxins (three different J values). Cases A and B can be described by S_{12} (or S_{23}) = 3 (or 2) and S_3 (or S_J) = 5/2, respectively, while in the asymmetric C and D cases these are no longer good quantum numbers. The set of J values that qualitatively reproduces the experimental temperature dependence for the asymmetric cases (see Figure 9) is shown both at the extreme left of A and at the extreme right of D, which are in fact coincident.

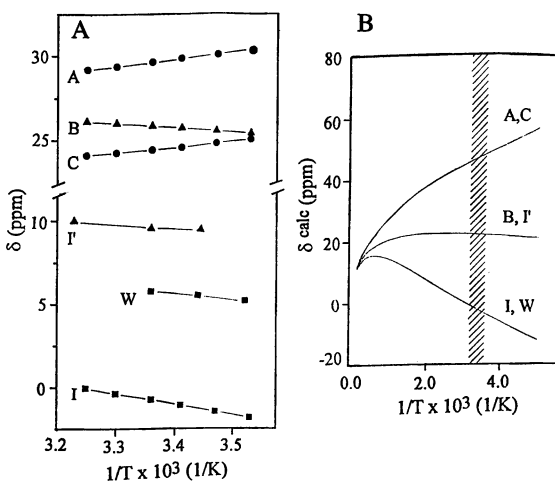


Figure 9. Experimental (A) and calculated (B) temperature dependences for the hyperfine shifts of the cysteine β -CH₂ protons in asymmetric $[\text{Fe}_3\text{S}_4]^+$ clusters (35, 36). The curves in B are calculated using $J_{I2} = 285 \text{ cm}^{-1}$, $J_{I3} = 300 \text{ cm}^{-1}$ and $J_{23} = 320 \text{ cm}^{-1}$ in the Hamiltonian (equation 2). The signal labelling refers to Figure 6B.

and on the other, the factors determining a given valence distribution and overall reduction potential can be investigated (38).

Literature Cited

1. Bertini, I.; Ciurli, S.; Luchinat, C. In *Structure and Bonding*; Springer-Verlag: Berlin Heidelberg, 1995; Vol. 83, pp. 1-54.
2. Bertini, I.; Luchinat, C. *NMR of paramagnetic substances*; Coord.Chem.Rev.150, Elsevier: Amsterdam, 1996; pp. 1-300.
3. Holm, R. H.; Kennepohl, P.; Solomon, E. I. *Chem. Rev.* **1996**, *96*, 2239-2314.
4. Holm, R.H.; Ciurli, S.; Weigel, J.A. In *Progress in Inorganic Chemistry: Bioinorganic Chemistry, Vol. 38*; Lippard, S.J. Ed.; John Wiley & Sons, Inc. New York, 1990; pp. 1-74.
5. Moura, I.; Huynh, B. H.; Hausinger, R. P.; LeGall, J.; Xavier, A. V.; Münck, E. *J. Biol. Chem.* **1980**, *255*, 2493-2498.
6. Bennett, D. E.; Johnson, M. K. *Biochim. Biophys. Acta* **1987**, *911*, 71-80.
7. Van Vleck, J. H. *Phys. Rev.* **1940**, *57*, 426
8. Orbach, R. *Proc. R. Soc. London, Ser.* **1961**, *A264*, 458
9. Xia, B.; Westler, W. M.; Cheng, H.; Meyer, J.; Moulis, J.-M.; Markley, J. L. *J. Am. Chem. Soc.* **1995**, *117*, 5347-5350.
10. Rao, K. K.; Evans, M. C. W.; Cammack, R.; Hall, D. O.; Thompson, C. L.; Jackson, P. J.; Johnson, C. E. *Biochem. J.* **1972**, *129*, 1063-1070.
11. Eaton, N.A.; Lovenberg, W. In *Iron-Sulfur Proteins*; Lovenberg, W. Ed.; Academic Press: New York, 1973, *Vol. 2*; pp. 131-162.
12. Gebhard, M. S.; Koch, S. A.; Millar, M.; Devlin, F. J.; Stephens, P. J.; Solomon, E. I. *J. Am. Chem. Soc.* **1991**, *113*, 1640-1649.
13. Banci, L.; Bertini, I.; Luchinat, C. *Nuclear and electron relaxation. The magnetic nucleus-unpaired electron coupling in solution*; VCH: Weinheim, 1991.
14. Dunham, W. R.; Palmer, G.; Sands, R. H.; Bearden, A. J. *Biochim. Biophys. Acta* **1971**, *253*, 373-384.
15. Banci, L.; Bertini, I.; Luchinat, C. *Struct. Bonding* **1990**, *72*, 113-135.
16. McConnell, H. M.; Chestnut, D. B. *J. Chem. Phys.* **1958**, *28*, 107-117.
17. Dugad, L. B.; La Mar, G. N.; Banci, L.; Bertini, I. *Biochemistry* **1990**, *29*, 2263-2271.
18. Banci, L.; Bertini, I.; Gori Savellini, G.; Luchinat, C. *Inorg. Chem.* **1996**, *35*, 4248-4253.
19. Pochapsky, T. C.; Mei Ye, X.; Ratnaswamy, G.; Lyons, T. A. *Biochemistry* **1994**, *33*, 6424-6432.
20. Banci, L.; Bertini, I.; Eltis, L. D.; Felli, I. C.; Kastrau, D. H. W.; Luchinat, C.; Piccioli, M.; Pierattelli, R.; Smith, M. *Eur. J. Biochem.* **1994**, *225*, 715-725.
21. Bertini, I.; Eltis, L. D.; Felli, I. C.; Kastrau, D. H. W.; Luchinat, C.; Piccioli, M. *Chemistry - A European Journal* **1995**, *1*, 598-607.
22. Bertini, I.; Luchinat, C.; Rosato, A. *Prog. Biophys. Mol. Biol.* **1996**, *66*, 43-80.
23. Banci, L.; Bertini, I.; Capozzi, F.; Carloni, P.; Ciurli, S.; Luchinat, C.; Piccioli, M. *J. Am. Chem. Soc.* **1993**, *115*, 3431-3440.
24. Noodleman, L. *Inorg. Chem.* **1988**, *27*, 3677-3679.
25. Papaefthymiou, V.; Girerd, J.-J.; Moura, I.; Moura, J. J. G.; Münck, E. *J. Am. Chem. Soc.* **1987**, *109*, 4703-4710.

26. Belinskii, M. I.; Bertini, I.; Galas, O.; Luchinat, C. *Z. Naturforsch.* **1995**, *50a*, 75-80.
27. Belinskii, M. I.; Bertini, I.; Galas, O.; Luchinat, C. *Inorg. Chim. Acta* **1996**, *243*, 91-99.
28. Bertini, I.; Luchinat, C. In *Transition metal sulfur chemistry: biological and industrial significance*; Stiefel, E.I., Matsumoto, K. Eds.; ACS Symposium Series N. 653: Washington DC, 1996; pp. 57-73.
29. Huynh, B. H.; Moura, J. J. G.; Moura, I.; Kent, T. A.; LeGall, J.; Xavier, A. V.; Münck, E. *J. Biol. Chem.* **1980**, *255*, 3242-3244.
30. Cheng, H.; Grohmann, K.; Sweeney, W. V. *J. Biol. Chem.* **1992**, *267*, 8073-8080.
31. Gorst, C. M.; Yeh, Y.-H.; Teng, Q.; Calzolari, L.; Zhou, Z.-H.; Adams, M. W. W.; La Mar, G. N. *Biochemistry* **1995**, *34*, 600-610.
32. Busse, S. C.; La Mar, G. N.; Yu, L. P.; Howard, J. B.; Smith, E. T.; Zhou, Z. H.; Adams, M. W. W. *Biochemistry* **1992**, *31*, 11952-11962.
33. Macedo, A. L.; Moura, I.; Moura, J. J. G.; LeGall, J.; Huynh, B. H. *Inorg. Chem.* **1993**, *32*, 1101-1105.
34. Macedo, A. L.; Palma, P. N.; Moura, I.; LeGall, J.; Wray, V.; Moura, J. J. G. *Magn. Reson. Chem.* **1993**, *31*, S59-S67.
35. Aono, S.; Bertini, I.; Cowan, J. A.; Luchinat, C.; Rosato, A.; Viezzoli, M. S. *JBIC* **1996**, *1*, 523-528.
36. Bertini, I.; Dikiy, A.; Luchinat, C.; Macinai, R.; Viezzoli, M. S.; Vincenzini, M. *Biochemistry* **1997**, *36*, 3570-3579.
37. Cammack, R. *Adv. Inorg. Chem.* **1992**, *38*, 281-322.
38. Bertini, I.; Capozzi, F.; Eltis, L. D.; Felli, I. C.; Luchinat, C.; Piccioli, M. *Inorg. Chem.* **1995**, *34*, 2516-2523.
39. Donaire, A.; Gorst, C. M.; Zhou, Z. H.; Adams, M. W. W.; La Mar, G. N. *J. Am. Chem. Soc.* **1994**, *116*, 6841-6849.
40. Cheng, H.; Grohmann, K.; Sweeney, W. V. *J. Biol. Chem.* **1990**, *265*, 12388-12392.
41. Bentrop, D.; Bertini, I.; Luchinat, C.; Mendes, J.; Piccioli, M.; Teixeira, M. *Eur. J. Biochem.* **1996**, *236*, 92-99.
42. Nagayama, K.; Ohmori, D.; Imai, Y.; Oshima, T. *FEBS Lett.* **1983**, *158*, 208-212.
43. Bertini, I.; Lanini, G.; Luchinat, C. *Inorg. Chem.* **1984**, *23*, 2729-2730.

Chapter 18

The Electronic Structure of Linear Thiophenolate-Bridged Heterotrinnuclear Complexes: Localized versus Delocalized Models

Thorsten Glaser and Karl Wieghardt

Max-Planck-Institut für Strahlenchemie, Stiftstrasse 34-36, D-45470 Mülheim an der Ruhr, Germany

The electronic structure of a series of linear heterotrinnuclear complexes containing six thiophenolato bridges has been established by magnetochemical methods and complementary spectroscopies (electron paramagnetic resonance (EPR), X-ray absorption spectroscopy (XAS), ^{57}Fe Mössbauer). The complexes $[\text{LFeCrFeL}]^{1+/2+/3+}$, $[\text{LFeCoFeL}]^{2+/3+}$, and $[\text{LFeFeFeL}]^{2+/3+}$ contain the same ligand matrix comprising two 1,4,7-tris(4-*tert*-butyl-2-mercaptobenzyl)-1,4,7-triazacyclononane (L^{3-}) ligands. Their electronic structures are discussed in terms of superexchange mechanisms for localized oxidation states and by double exchange for delocalized systems. The isoelectronic systems (low spin d^5 d^6 d^5) $[\text{LFeCoFeL}]^{3+}$ and $[\text{LFeFeFeL}]^{2+}$ are shown to have different electronic structures despite a common $S_{\text{T}}=1$ ground state. A consistent qualitative model is discussed.

Iron-sulfur metalloproteins are probably the structurally and spectroscopically most intensively studied metalloproteins (1). These proteins contain active sites comprised of tetrahedrally coordinated Fe^{II} and/or Fe^{III} ions, sulfido and S-bound cysteinato ligands. Mono-, di-, tri- and tetranuclear core structures have been identified (Figure 1) which exist in a variety of oxidation levels. The magnetic properties of these iron-sulfur clusters are well established (2). High spin d^6 and d^5 electronic configurations prevail in the Fe^{II} and Fe^{III} ions which lead to antiferromagnetic exchange coupling in the dinuclear $[\text{2Fe-2S}]^{2+,1+}$ cores either between two Fe^{III} ions as in $[\text{2Fe-2S}]^{2+}$ yielding an $S=0$ ground state or one Fe^{II} and one Fe^{III} ion in the mixed valent form $[\text{2Fe-2S}]^{1+}$ in which both oxidation states are localized (class I or II) and an $S=1/2$ ground state is obtained. For the latter an $S=9/2$ ground state (ferromagnetic coupling) has recently been shown to exist in a mutant of *Clostridium pasteurianum* 2Fe

ferredoxin (3). Intramolecular antiferromagnetic coupling between three Fe^{III} ions in the oxidized form [3Fe-4S]¹⁺ yields an S=1/2 ground state.

In the mixed valent [3Fe-4S]⁰ form of ferredoxin II of *Desulfovibrio gigas* comprising formally two Fe^{III} and one Fe^{II} the valencies are delocalized. A Fe^{2.5}₂ pair with an S=9/2 ground state is antiferromagnetically coupled to one Fe^{III} (S=5/2) generating the observed S_T=2 ground state of the trinuclear cluster (4). The double exchange mechanism originally introduced by Zener, Anderson, and Hasegawa (5) has been invoked to explain the spin alignment in the Fe^{2.5}₂ pair. In the cubane-type core structures [4Fe-4S]^{3+,2+,1+} such a mixed valent Fe^{2.5}₂ pair with S=9/2 ground state and delocalized excess electron occurs in all three oxidation levels. For example the S_T=0 ground state results from an antiferromagnetic coupling of two such pairs in the [4Fe-4S]²⁺ cluster.

Remarkably, neither in these trinuclear nor in the tetranuclear clusters has delocalization of the excess electron been experimentally observed over all three or four iron ions. This observation has recently been rationalized by Girerd et al (6) by taking into account vibronic coupling in the double exchange Hamiltonian which considers impeded electron transfer between tetrahedral high spin Fe^{II} and high spin Fe^{III} due to differing Fe-S bond lengths (large Frank-Condon barrier).

Accordingly, systems with smaller bond length differences between their oxidized and reduced forms should facilitate electron transfer and, consequently, electron delocalization. We have been inspired by the fact that the ionic radius of tetrahedrally coordinated Fe^{III} increases upon reduction to Fe^{II} by 22% which, in contrast, is only 9% for octahedrally coordinated low spin Fe^{III} and Fe^{II} and have investigated the electronic structure of sulfur bridged, trinuclear complexes containing two terminal, octahedral Fe^{III}/Fe^{II} ions and a di- or trivalent central heterometal ion.

We describe here a series of such linear, thiophenolato bridged trinuclear species with the trianionic ligand 1,4,7-tris(4-*tert*-butyl-2-mercaptobenzyl)-1,4,7-triazacyclononane (L³⁻) which with Fe^{III} forms an extremely stable mononuclear complex [LFe^{III}] with a facial N₃S₃ donor set (Figure 2) (7). Two mononuclear units can then bind via the facial S₃ donors in an octahedral fashion to a central metal ion Mⁿ⁺ yielding the corresponding trinuclear complex (8). The central metal ion possesses an octahedral MS₆ core structure (M = Cr, Co, Fe). Figure 3 shows a schematic representation of the resulting linear heterotrinuclear species and gives a compilation of the complexes synthesized and their labels.

From detailed electrochemical investigations of the three series, where the terminal ions are always Fe ions and the central metal ion is either Cr, Co, or Fe, one or two reversible one electron-transfer processes at well separated redox potentials have been identified, respectively. By choosing the appropriate one-electron oxidant such as ferrocenium hexafluorophosphate or, alternatively, a one-electron reductant such as L'M(CO)₃ where L' represents 1,4,7-trimethyl-1,4,7-triazacyclononane and M⁰ = Cr, Mo, W (9) we have been able to chemically generate and isolate as pure crystalline materials the corresponding one-electron oxidized or reduced trinuclear tri- or monocation.

The structures of complexes 3, 5, 6, and 7 have been determined by X-ray crystallography. Figure 4 gives a perspective view of one representative example of

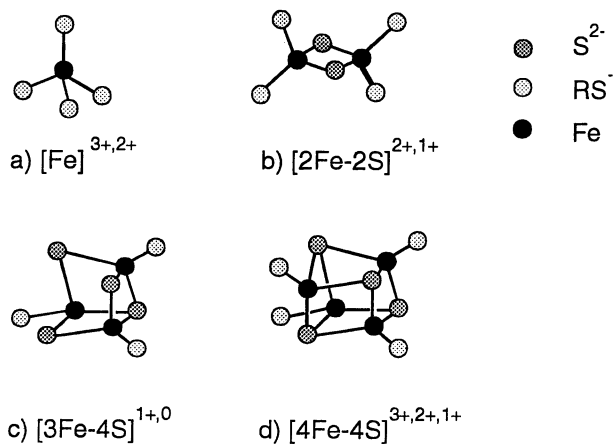


Figure 1. Schematic representation of the structures of the active sites of known iron-sulfur metalloproteins.

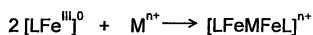
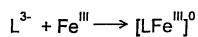
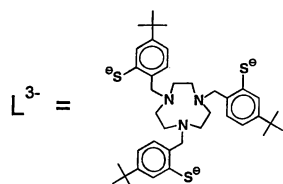
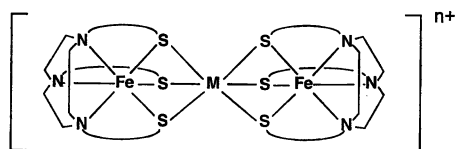


Figure 2. The ligand L^{3-} and synthesis of complexes.



	S_i
1 [LFeCrFeL](PF ₆)	3/2
2 [LFeCrFeL](PF ₆) ₂	2
3 [LFeCrFeL](PF ₆) ₃	1/2
4 [LFeCoFeL][BPh ₄] ₂	1/2
5 [LFeCoFeL](PF ₆) ₃	1
6 [LFeFeFeL][BPh ₄] ₂	1
7 [LFeFeFeL][BPh ₄] ₃	1/2

Figure 3. Complexes synthesized and labeling scheme.

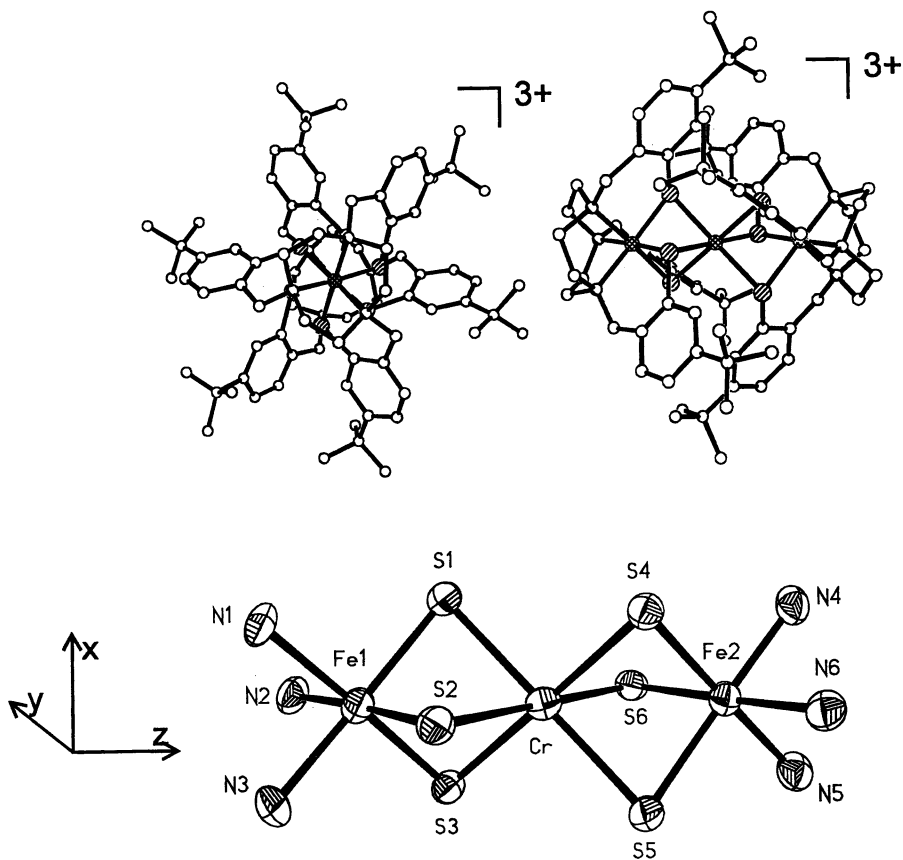


Figure 4. Perspective views of [LFeCrFeL]³⁺ in crystals of 3.

[LFeCrFeL](PF₆)₂(ClO₄) and Table I lists some pertinent bond distances and angles of the respective N₃FeS₃MS₃FeN₃ core.

Table I. Selected Average Bond-Distances (Å) and Angles (deg) in [LFeMFeL]ⁿ⁺

		Fe - M _c	Fe - N	Fe - S	M - S	Fe - S - M
[LFeCrFeL] ³⁺	3	2.95	2.06	2.26	2.40	78.3
[LFeCoFeL] ³⁺	5	2.87	2.04	2.23	2.29	78.8
[LFeFeFeL] ²⁺	6	2.84	2.05	2.30	2.24	77.7
[LFeFeFeL] ³⁺	7	2.79	2.06	2.24	2.30	75.9

Since complexes 1-7 are available as pure crystalline solids it appeared to be appealing to characterize their electronic structure in considerable detail by using magnetochemical methods and spectroscopies such as electron paramagnetic resonance (EPR) and ⁵⁷Fe Mössbauer. *It is thus possible to study the effect of a variable valence electron configuration of seven molecules having essentially the same ligand matrix.* We will attempt to rationalize the electronic ground states in a qualitative but consistent picture by using the established rules of superexchange mechanisms for localized and spin-dependent delocalization models for delocalized systems.

The Series [LFeCrFeL]ⁿ⁺ (1-3)

The X-band EPR spectrum of **1** in a frozen acetonitrile solution at 4.2 K displays an axial signal at $g_{\perp}=3.94$ and $g_{\parallel}=1.99$ which is typical for an S=3/2 ground state. This is in excellent agreement with variable-temperature magnetic susceptibility measurements of powdered **1** which exhibit a temperature-independent magnetic moment of 3.81 μ_B in the temperature range from 4-300 K. Thus the S=3/2 ground state is the only populated state up to 300 K. The Mössbauer spectrum of **1** displays *one* weakly quadrupole split doublet (Table II) in the same temperature range. Thus both iron ions in **1** are equivalent. Formulation of **1** as a species with two low spin Fe^{II} ions (S=0) and a Cr^{III} (S=3/2) with localized oxidation states is in perfect accordance with the above spectroscopic data: [LFe^{II}Cr^{III}Fe^{II}L]¹⁺.

The two-electron oxidized form of monocationic **1** yields the trication **3** which exhibits at 4.2 K an S_t=1/2 ground state (EPR). Again the Mössbauer spectrum displays a single quadrupole doublet albeit with a *decreased* isomer shift, δ , and an enormously *increased* quadrupole splitting, ΔE_Q , as compared to the values reported for **1** (see Table II). The temperature-dependence of the magnetic moment of **3** (4.2-300 K) confirms the S=1/2 ground state (1.70 μ_B 4-80 K). Above 80 K μ_{eff} increases to 2.62 μ_B at 300 K. This temperature-dependence was satisfactorily modeled by using the Hamiltonian given in equation 1 with S₁=S₃=1/2 (low spin Fe^{III}), S₂=3/2

Table II. Isomer shift (δ), quadrupole splitting (ΔE_Q) parameters, and relative peak areas of the Mössbauer spectra of $[\text{LFeMFeL}]^{n+}$ at 4.2 K

		donor set	$\delta / \text{mm s}^{-1}$	$\Delta E_Q / \text{mm s}^{-1}$	area / %
$[\text{LFeCrFeL}]^{1+}$	1	N_3S_3	0.54	+0.14	100
$[\text{LFeCrFeL}]^{2+}$	2	N_3S_3	0.42	+1.08	100
$[\text{LFeCrFeL}]^{3+}$	3	N_3S_3	0.34	+2.00	100
$[\text{LFeCoFeL}]^{2+}$	4	N_3S_3	0.34	+1.70	50
		S_6	0.45	+0.23	50
$[\text{LFeCoFeL}]^{3+}$	5	N_3S_3	0.30	+1.94	100
$[\text{LFeFeFeL}]^{2+}$	6	N_3S_3	0.39	+1.36	66
		S_6	0.53	+0.87	34
$[\text{LFeFeFeL}]^{3+}$	7	N_3S_3	0.33	+1.85	71
		S_6	0.47	+1.76	29

(Cr^{III}) where J_a represents the exchange coupling constant of two adjacent metal ions ($\text{Fe}^{\text{III}} \text{Cr}^{\text{III}}$) and J_t is the corresponding coupling constant for the two terminal Fe^{III} ions.

$$\hat{H} = -2J_a(S_1S_2 + S_2S_3) - 2J_tS_1S_3 \quad (1)$$

Numerical values of $J_a = -128(2) \text{ cm}^{-1}$ and $J_t = -41(5) \text{ cm}^{-1}$ indicate a strong intramolecular antiferromagnetic exchange coupling yielding the observed $S_t = 1/2$ ground state. Thus **3** can be described as an $[\text{LFe}^{\text{III}}\text{Cr}^{\text{III}}\text{Fe}^{\text{III}}\text{L}]^{3+}$ ion with localized oxidation states. The analysis of the Mössbauer spectra of **3** in an applied external magnetic field clearly shows that the unpaired electron of the low spin Fe^{III} ions is in a d_{z^2} metal orbital where the z-axis coincides with the $\text{Fe}\cdots\text{Cr}\cdots\text{Fe}$ C_3 axis. Thus antiferromagnetic coupling between the metal ions results from interaction of three half-filled d_{z^2} orbitals (a_1 in D_{3d} symmetry). This is depicted in Figure 5. Note that this classical superexchange mechanism leading to antiferromagnetic coupling has been identified in a vast number of face-sharing bioctahedral complexes containing two paramagnetic metal ions (e.g. V^{II} , Cr^{III} , Mn^{IV}) with a_1 magnetic orbitals (10).

It is now an interesting problem to investigate the electronic structure of the mixed valence dication in **2** since localized and delocalized models lead to differing ground states. Temperature-dependent zero-field Mössbauer spectra of **2** immediately reveal that the two iron ions in **2** are equivalent on the time scale of this spectroscopic method ($\sim 10^{-7}$ s). Thus only a single quadrupole doublet is observed over the temperature range 2-300 K where both the isomer shift and the quadrupole splitting

parameters of **2** represent the exact average of those values reported above for **1** and **3**. Again, on the time scale of a Mössbauer experiment **2** is a fully delocalized, mixed valent species of class III which then can be described as a $[\text{LFe}^{2.5}\text{Cr}^{\text{III}}\text{Fe}^{2.5}\text{L}]^{2+}$ species. Interestingly, **2** displays a temperature-dependent intervalence band in the infrared region at 3125 nm (3200 cm^{-1}) which is shown in Figure 6 (bottom).

With the experimental data obtained so far for **1-3** in mind we briefly analyze the possibilities for the electronic ground state of **2**. If the valencies were localized (which they are not) one would predict an antiferromagnetic coupling between a low spin Fe^{III} ($S=1/2$) and an adjacent Cr^{III} ($S=3/2$) yielding an $S_{\text{T}}=1$ ground state (note that the low spin Fe^{II} ion would be diamagnetic; Figure 7). If, on the other hand, the excess electron in **2** is fully delocalized, a double exchange mechanism must be taken into account and an $S_{\text{T}}=2$ ground state results.

As we have shown previously (10), one can construct simple resonance structures for such trinuclear complexes following two simple rules:

- a) These resonance structures are interrelated by simple one-electron transfer steps between adjacent and terminal a_1 orbitals of the metal ions.
- b) Resonance structures requiring the moving electron to undergo a spin flip (which otherwise would lead to a Pauli-forbidden state) are not considered (constructed).

Figure 8 shows this schematically for **2**. The quintet state is stabilized by allowed one-electron transfer steps over all three metal ions (including the central Cr^{III} ion) whereas the corresponding triplet is less effectively stabilized because only two resonance structures interrelated by one-electron transfer steps over two metal sites (the Fe^{III} and Cr^{III}) are constructable.

Gratifyingly, variable-temperature magnetic susceptibility measurements of **2** confirm the $S_{\text{T}}=2$ ground state with an excited $S_{\text{T}}=1$ state ($\Delta E=40\text{ cm}^{-1}$). The energy difference between these two states is significantly smaller than in other known $\text{Fe}^{2.5}_2$ pairs with $S_{\text{T}}=9/2$ ground state (11). There the first excited $S_{\text{T}}=7/2$ state is at least 700 cm^{-1} above the ground state of $S_{\text{T}}=9/2$. This is in good agreement with the fact that in **2** the two iron centers are $\sim 6\text{ \AA}$ apart (in the other $\text{Fe}^{2.5}_2$ pairs this difference is $< 3.0\text{ \AA}$ (11)) and, most importantly, the resonance structure involving $\text{Cr}(\text{II})$ contributes very little.

The above model for localized **1** and **3** and delocalized **2** implies that the spin density variation in going from **1** to **3** is prevalent at the iron sites (and, probably, the sulfur bridges) whereas the central Cr^{III} ion is not significantly involved. This has been experimentally verified by measuring the Fe and Cr K-edge energies of **1**, **2**, and **3** by XAS spectroscopy. Thus the Cr K-edge energy is invariant in complexes **1-3** whereas the Fe K-edge energy increases by 0.6 eV per oxidation step on going from **1** to **3**. Furthermore, a detailed analysis of the Debye-Waller factors shows that the two iron ions in **2** are equivalent (i.e. not a mixture of localized Fe^{II} and Fe^{III}). The time scale of an XAS experiment is $\sim 10^{-15}\text{ s}$.

The Series $[\text{LFeCoFeL}]^{2+/3+}$ (**4**, **5**)

If the above analysis of the electronic structures of **1 - 3** is essentially correct, we anticipate dramatic differences in the degree of electronic delocalization in a $[\text{Fe}^{2.5}\text{M}$

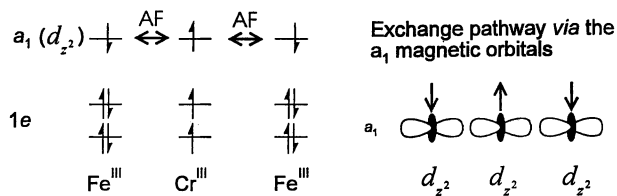


Figure 5. Orbital interaction scheme for $[\text{LFeCrFeL}]^{3+}$.

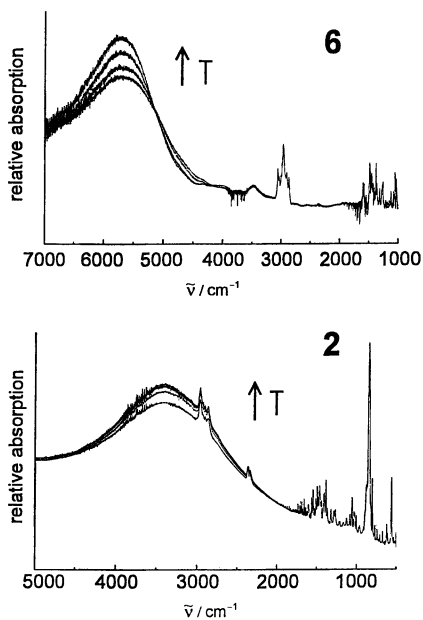


Figure 6. Intervallence band of **6** (top) and **2** (bottom) at 12, 100, 200, and 294 K.

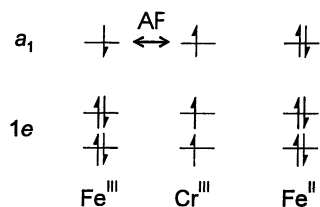


Figure 7. Orbital interaction scheme for **2** assuming localized oxidation states $\text{Fe}^{\text{III}} \text{Cr}^{\text{III}} \text{Fe}^{\text{II}}$.

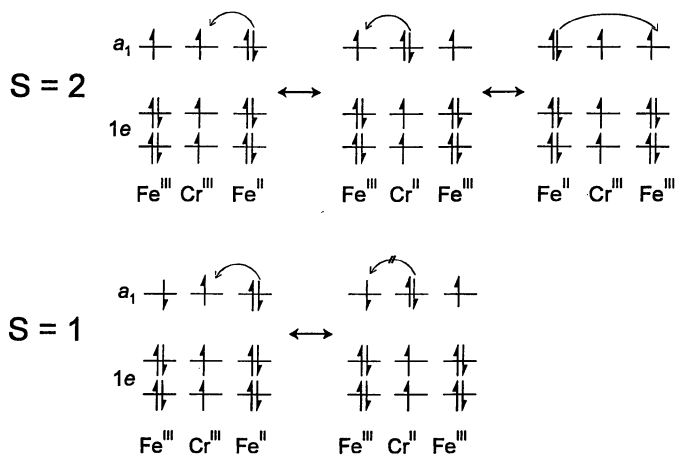


Figure 8. Orbital interaction schemes for **2** yielding an $S_t=2$ or an $S_t=1$ ground state.

Fe^{2.5}] species if the central metal M possesses a filled t_{2g} subshell. The question we ask is: does a low spin cobalt(III) ion (t_{2g}^6) block the electron transfer (or delocalization) between a formally Fe^{II} (low spin) and an Fe^{III} (low spin) in the species [LFeCo^{III}FeL]²⁺ (**4**)?

Before dealing with this case we present the clear-cut case of **5** which formally contains an Fe^{III}Co^{III}Fe^{III} oxidation state distribution. As in **3**, both iron ions in **5** are low spin Fe^{III} which display very similar Mössbauer parameters in both complexes (Table II). Thus complex **5** contains two low spin Fe^{III} ions in terminal positions and a central diamagnetic low spin cobalt(III) (d^6) ion. It appears natural to assume localized oxidation states. The ground state of **5** can either be $S_t=0$ assuming antiferromagnetic exchange coupling or $S_t=1$ with a ferromagnetic interaction between the terminal Fe^{III} ions separated by 6 Å. EPR spectra and susceptibility measurements prove that the triplet state is the ground state with the singlet excited state at $\Delta E \sim 80 \text{ cm}^{-1}$. Thus a *ferromagnetic* coupling prevails. Details of the superexchange mechanism leading to an $S_t=1$ ground state will be discussed below.

One-electron reduction of **5** yields the mixed valent species **4** as is clearly seen from its Mössbauer spectra which conclusively rule out the alternative formulation of **4** as [Fe^{III}Co^{II}Fe^{III}]²⁺ species. In zero-field at 5 K *two* doublets (ratio 1:1) are detected. Their respective isomer shift and quadrupole splitting parameters are typical for one low spin Fe^{II} and one low spin Fe^{III} ion (Table II). Therefore, **4** must be described as mixed valent [LFe^{III}Co^{III}Fe^{II}]²⁺ species with trapped (localized) valencies at 5 K. EPR and magnetic susceptibility measurements prove the $S_t=1/2$ ground state of **4** over the temperature range 4–300 K.

Figure 9 shows variable-temperature, zero-field Mössbauer spectra of **4** in the range 5–353 K. Interestingly, with increasing temperature a third doublet with intermediate isomer shift and quadrupole splitting parameters grows in at the expense of the former two doublets. At temperatures >100 °C only this third doublet is observed. Cooling of the sample reverses the effect. *Complex 4 is a mixed valent species of class II.* At very low temperatures localized valencies are observed within the time window of a Mössbauer experiment whereas at higher temperatures thermally activated electron hopping is fast on this time scale. Thus, we observe the dynamic process of electron hopping (hopping) between the two iron centers. Nota bene: we do not observe line-broadening at elevated temperatures. Instead, a new doublet appears. This phenomenon of lacking coalescence and line-broadening for a dynamic process has been described previously by Gütlich and coworkers (12).

Up to this point we have described two trinuclear mixed valent complexes containing an Fe^{II} and an Fe^{III} ion in the terminal positions, namely **2** and **4**. Complex **2** has a central Cr^{III} with a half-filled t_{2g} subshell which allows complete electron delocalization of the excess electron (class III). Substitution of the Cr^{III} by a low spin Co^{III} (t_{2g}^6) leads to a situation where this delocalization is effectively blocked and thermally activated electron transfer with an, in principle, measurable intramolecular electron transfer rate ($k_{et} \sim 10^7 \text{ s}^{-1}$) is observed (class II). In other words, the potential energy curve of the ground state of **2** has a single minimum whereas that of **4** has a double minimum.

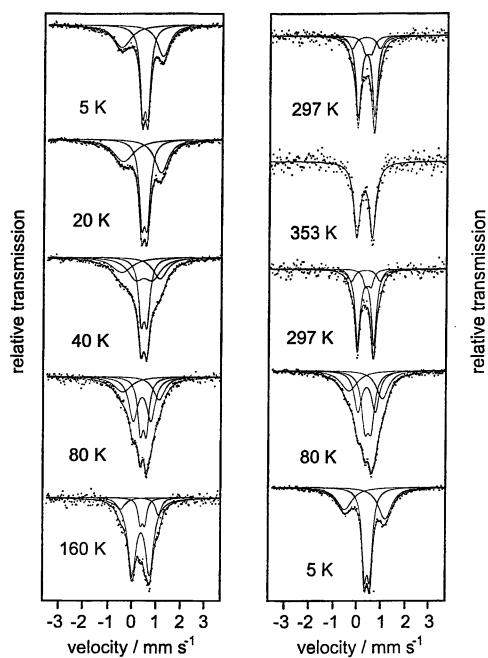


Figure 9. Temperature-dependence of the zero-field Mössbauer spectra of **4** (warming up and cooling down).

The Series [LFeFeFeL]^{2+/3+} (6, 7)

For the sake of simplicity we first present the case of the trication [LFeFeFeL]³⁺ (7) containing three low spin Fe^{III} ions. The Mössbauer spectrum of 7 displays two doublets (ratio 2:1) (see Table II). The more intense doublet is assigned to the two terminal Fe^{III} ions with an N₃S₃ donor set whereas the less intense doublet corresponds to the central Fe^{III}S₆ unit which has a slightly larger isomer shift as compared to all other complexes with N₃Fe^{III}S₃ units. This effect is due to a comparatively increased electron density at the central Fe^{III} ion brought about by six (*vs* three) π -donating thiophenolato ligands. Complex 7 contains, therefore, three Fe^{III} low spin ions with localized valencies, [LFe^{III}Fe^{III}Fe^{III}L]³⁺. From Mössbauer spectra measured in a strong external magnetic field it is readily deduced that the magnetic orbital is the d_{z^2} , respectively (see Figure 5). Intramolecular antiferromagnetic exchange coupling as described for 3 should therefore yield an S_T=1/2 ground state for 7. Indeed, the EPR spectrum and variable-temperature magnetic susceptibility measurements of 7 prove the S_T=1/2 ground state. Interestingly, up to 300 K only the S_T=1/2 state is populated which implies that the exchange coupling is very strong ($J_a < -350$ cm⁻¹). Thus, 7 represents a case where we move away from the weak interaction regime (exchange coupling) toward the strong interaction regime or direct metal-metal bonding. Note that the Fe...Fe distance in 7 is only 2.79 Å.

We now take a close look at the one-electron reduced form of 7, namely the mixed valent species 6. The question as to whether the excess electron is localized (e.g. Fe^{III} Fe^{II} Fe^{III}) or delocalized is by no means a trivial one.

If one considers the dication in 6 as consisting of two "electron poor" N₃FeS₃ units and a central "electron rich" FeS₆ moiety, simple electrostatic considerations would imply a preferential occupation of the excess electron at the two terminal sites. Since these are identical, a truly mixed valent species (as opposed to a distribution Fe^{III} Fe^{II} Fe^{III}) is generated containing a central low spin Fe^{III}S₆ unit with a hole in the t_{2g} subshell. This would allow delocalization over all three sites as in 2. Note that in 6 the resonance structure with the excess electron at the central iron ion possesses a larger weight as compared to 2 because the orbital energy in a Fe^{II}S₆ moiety is close to that of the N₃Fe^{II}S₃ units, closer than in the corresponding resonance structure for 2 containing an energetically unfavourable Cr^{II}S₆. Along these arguments, we would then expect that the excess electron in 6 is delocalized over the three iron sites with a small preference for the terminal sites.

This is experimentally nicely verifiable by Mössbauer spectroscopy (Table II). The zero-field spectra are temperature-independent in the range 2-300 K; two doublets at (ratio 2:1) are clearly observed. From their observed isomer shifts and quadrupole splitting parameters it is concluded that both types of iron possess some Fe^{II} character. A detailed analysis also allows the conclusion that the terminal sites are slightly more affected than the central one. An oxidation state distribution of roughly [L Fe^{2.63} Fe^{2.74} Fe^{2.63} L]²⁺ describes the situation quite accurately. Note that 6 displays a

temperature-dependent intervalence band at 1820 nm (5500 cm^{-1}) as is shown in Figure 6 (top).

Variable-temperature magnetic susceptibility measurements on **6** (4-300 K) show a temperature-independent magnetic moment of $2.89\ \mu_B$. Thus, **6** possesses an $S_T=1$ ground state and the excited state ($S_T=0$) is not populated up to 300 K.

Since complexes **5** and **6** are isoelectronic (formally low spin $d^5\ d^6\ d^5$) it is now an interesting problem to investigate why the superexchange mechanism proposed for **5** (localized valencies) and the double exchange mechanism operative in **6** (delocalized valencies) afford the same $S_T=1$ ground state.

Discussion of the low spin $d^5\ d^6\ d^5$ Case

As stated above, the dication $[\text{LFeFeFeL}]^{2+}$ (**6**) and the trication $[\text{LFeCoFeL}]^{3+}$ (**5**) are isoelectronic and may be formally represented as a low spin $d^5\ d^6\ d^5$ system. The electronic differences between the two cations have been experimentally clearly demonstrated: **5** is best described as $[\text{Fe}^{\text{III}}\ \text{Co}^{\text{III}}\ \text{Fe}^{\text{III}}]^{3+}$ with localized oxidation states whereas for **6** a delocalized model must apply (class III).

In both cases the magnetic orbital at each metal site is the a_1 orbital (in D_{3d} symmetry; or d_{z^2} type metal orbital). In the following we denote the terminal sites as a, c, and the central site is b. The two magnetic orbitals at the terminal sites have the same energy, $+\Delta/2$, and the energy of the central site has an energy $-\Delta/2$ (Figure 10 top). The parameter Δ accounts for the fact that the central metal ions (Co in **5** and Fe in **6**) have a different first coordination sphere and consequently different energies than the terminal ones. For **5** this parameter Δ is significantly larger than for **6** because a CoS_6 in **5** is formally replaced by an FeS_6 moiety in **6**. Therefore, one has to assume that in **5** $\Delta \gg 0$ and in **6** $\Delta \leq 0$ is valid, respectively.

Distribution of 4 electrons over the three a_1 orbitals yields three triplet and three singlet states:

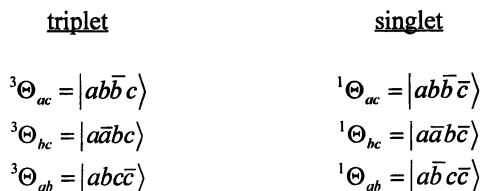


Figure 10 (bottom) depicts these states in a - for chemists more readily understood - pictorial fashion. We can then derive the following matrix neglecting at this point all interactions between the sites ($\beta=\beta'=0$; zeroth order).

$$\begin{array}{c|ccc}
 & |^3\Theta_{ac}^u\rangle & |^3\Theta_{bc}\rangle & |^3\Theta_{ab}\rangle \\
 \hline
 \langle^3\Theta_{ac}^u| & 0 & & \\
 \langle^3\Theta_{bc}| & & \Delta & \\
 \langle^3\Theta_{ab}| & & & \Delta
 \end{array}$$

This is a mathematical description for the chemists view of **5** with fully localized valencies ($\Delta \gg 0$). The ground state electron distribution is low spin $d^5 d^6 d^5$ with a central Co^{III} . There are two excited metal-to-metal one-electron charge-transfer states at an energy Δ . At this level the origin of the ferromagnetism of **5** is not yet clear. In both excited states the orbital symmetry is cancelled (the inversion center at the central site b is lost) and both represent mixed valent $\text{Fe}^{\text{II}} \text{Fe}^{\text{III}}$ pairs.

Taking now into account the resonance integral β' (electron transfer between the terminal sites a and c) the two excited states will mix. We can construct the symmetry adapted wavefunctions as

$$\begin{aligned}
 |^3\Theta_+^u\rangle &= \frac{1}{\sqrt{2}} [|^3\Theta_{ab}\rangle + |^3\Theta_{bc}\rangle] \\
 |^3\Theta_-^g\rangle &= \frac{1}{\sqrt{2}} [|^3\Theta_{ab}\rangle - |^3\Theta_{bc}\rangle]
 \end{aligned}$$

and the matrix as

$$\begin{array}{c|ccc}
 & |^3\Theta_{ac}^u\rangle & |^3\Theta_+^u\rangle & |^3\Theta_-^g\rangle \\
 \hline
 \langle^3\Theta_{ac}^u| & 0 & & \\
 \langle^3\Theta_+^u| & & \Delta + \beta' & \\
 \langle^3\Theta_-^g| & & & \Delta - \beta'
 \end{array}$$

This is a resonance phenomenon (first order perturbation, no off diagonal matrix elements) for which the term 'intramolecular electron transfer in the excited state' may be used. The same procedure must now be performed for the singlet states (not shown explicitly).

From Extended-Hückel calculations we know that the sign of β' is negative. One can then construct a qualitative energy level diagram as shown in Figure 11. For both the triplet and singlet states there are two states of the same symmetry (**u** in the triplet; **g** in the singlet) which now mix by virtue of the resonance integral β (interaction between the central site b and one terminal site a or c):

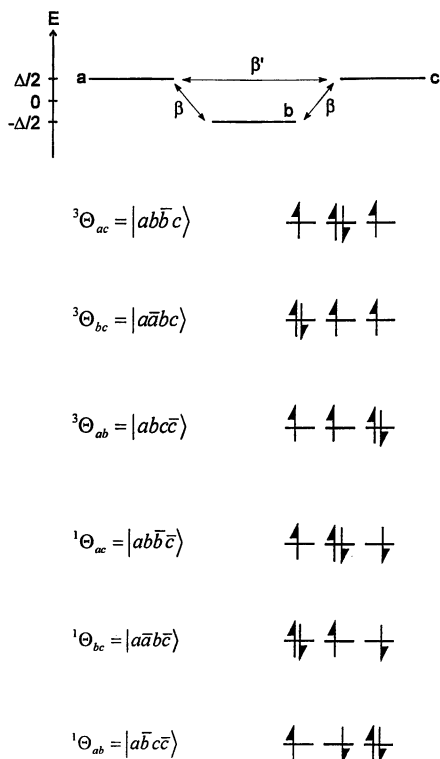


Figure 10. Schematic representation of the relative energies of the a_1 orbitals (terminal sites a , c and central site b) in the linear heterotrinnuclear complexes (top). Simplified representation of the triplet and singlet states for low spin $d^5 d^6 d^5$ (bottom). *Note:* For the pictorial description of states we have shown one part of the antisymmetrized wavefunction only (also in Figure 13).

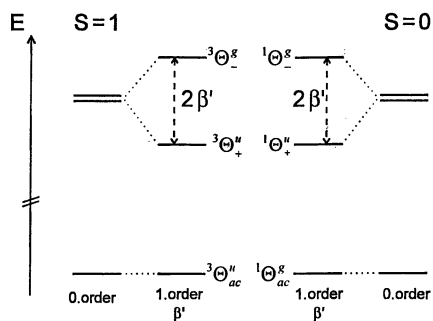


Figure 11. Relative energy levels of the ground and excited states with and without taking into account the resonance integral β' (0^{th} and 1^{st} order perturbation).

$$\begin{array}{c|ccc}
 & |^3\Theta_{ac}^u\rangle & |^3\Theta_+^u\rangle & |^3\Theta_-^g\rangle \\
 \langle^3\Theta_{ac}^u| & 0 & -\sqrt{2}\beta & \\
 \langle^3\Theta_+^u| & -\sqrt{2}\beta & \Delta + \beta' & \\
 \langle^3\Theta_-^g| & & & \Delta - \beta'
 \end{array}$$

For complex **5** the energy Δ is much larger than β ($\Delta \gg \beta > \beta'$) and, therefore, this mixing can be achieved by a second-order perturbation. Qualitatively, this mixing is more efficient for states lying energetically closer together. Therefore, the $S_t=1$ state is the ground state in **5** (Figure 12).

For the delocalized complex **6** the above treatment is not correct because here the energies β , β' , and Δ are of the same order of magnitude. Upon diagonalization of the above matrix we arrive at the following energies for the triplet and singlet states:

triplet	singlet
$E_{\pm} = \frac{1}{2} \left[\Delta + \beta' \pm \sqrt{(\Delta + \beta')^2 + 8\beta^2} \right]$ $E = \Delta - \beta'$	$E_{\pm} = \frac{1}{2} \left[\Delta - \beta' \pm \sqrt{(\Delta - \beta')^2 + 8\beta^2} \right]$ $E = \Delta + \beta'$

Again, the triplet state is stabilized if β' is negative but the triplet-singlet gap is significantly larger for **5** because here we have mixed the metal-to-metal charge-transfer states as a perturbation into the ground state only. In **6** we have an approximately equal mixing of all three states and, consequently, the stabilization of the $S_t=1$ ground state is much more effective.

In the following we attempt to translate the above quantum mechanical treatment into a more readily comprehensible - and for chemists adaptable - pictorial representation. To this end, we have a look at the configurational mixing with β and β' not in the wavefunction formalism given above but use pictorial orbital and spin representations of these wavefunctions as shown in Figure 13 (top), instead.

From this picture it immediately follows that moving one electron over all three sites requires a spin-flip in the singlet case whereas it does not in the triplet case.

An even simpler case may be envisaged in an equilateral triangle of two Fe^{III} and one Fe^{II} where the three magnetic orbitals are at the same energy as are the three β . In this case a negative β stabilizes the triplet ground state (*13*) because for neighboring centers the net orbital overlap integral is positive yielding a single molecular orbital (metal-metal bonding). The excess electron in this delocalized orbital has an antiparallel spin as compared to those in three 'localized' MO's (Figure 13 bottom). In essence, this is the MO description of the double exchange mechanism. If, on the other hand, β is positive, the overlap-integral will be negative and there will be no delocalized MO and the singlet becomes the ground state via a superexchange mechanism.

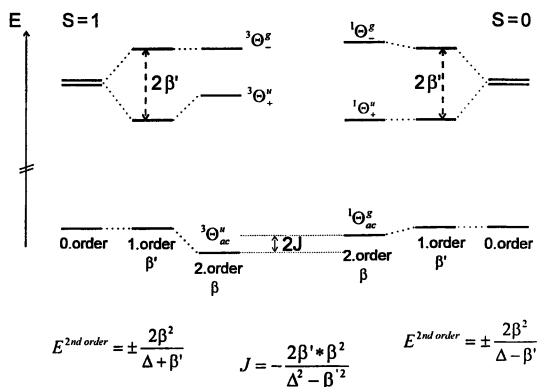


Figure 12. Relative energy levels of the ground and excited states with and without taking into account the resonance integral β' and β with $\Delta \gg \beta > \beta'$ (2nd order perturbation).

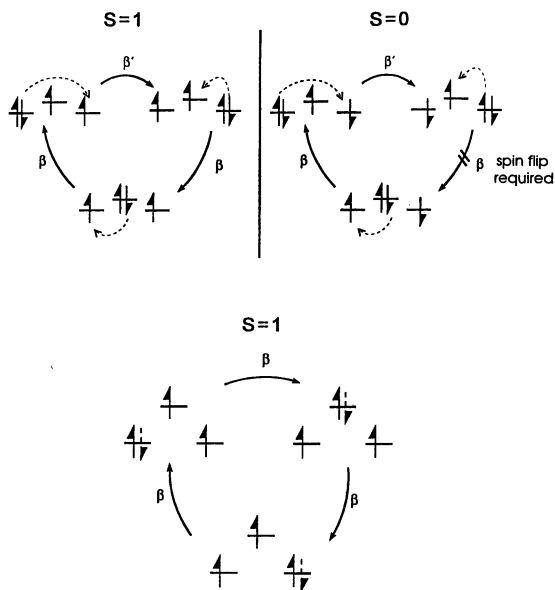


Figure 13. Schematic, simplified representation of the three a_1 magnetic orbitals occupied by 4 electrons for a linear (top) and an equilateral triangular (bottom) trinuclear complex. The arrows indicate allowed one-electron transfer steps without requiring a spin-flip.

Acknowledgement. We are grateful to Dr. J.-J. Girerd (Orsay, Paris-Sud) for his never diminishing interest and help. We thank Dr. E. Bill and his coworkers for many hours of Mössbauer, EPR, and SQUID measurements and discussions. Dr. T. Weyhermüller is thanked for the X-ray structure determinations.

Literature Cited.

- (1) *Iron-sulfur Proteins*; Lovenberg, W, Ed.; Academic Press: New York, 1973-1977; Vols. I-III; b) *Iron-sulfur Proteins*; Spiro, T. G., Ed.; John Wiley & Sons: New York, 1982; Vol. IV; c) *Iron-sulfur Proteins*; Cammack, R., (Ed.); *Advances in Inorganic Chemistry*; Academic Press: San Diego, 1992; Vol 38; d) Beinert, H. *FASEB J.* **1990**, *4*, 2483.
- (2) Trautwein, A. X.; Bill, E.; Bominaar, E. L.; Winkler, H. *Structure and Bonding*; Springer: Berlin, Heidelberg, 1991; Vol. 78, 1-95.
- (3) Crouse, B. R.; Meyer, J.; Johnson, M. K. *J. Am. Chem. Soc.* **1995**, *117*, 9613; b) Achim, C.; Golinelli, M.-P.; Bominaar, E. L.; Meyer, J.; Münck, E. *J. Am. Chem. Soc.* **1996**, *118*, 8168.
- (4) Münck, E.; Kent, T. A. *Hyperfine Interactions* **1986**, *27*, 161; b) Papaefthymiou, V.; Girerd, J.-J.; Moura, I.; Moura, J. J. G.; Münck, E. *J. Am. Chem. Soc.* **1987**, *109*, 4703 b) Münck, E.; Papaefthymiou, V.; Surerus, K. K.; Girerd, J.-J. In *Metal Clusters in Proteins*; Que, Jr., L., Ed.; ACS Symposium Series No. 372; American Chemical Society, Washington, D. C., 1988.
- (5) Zener, C. *Phys. Rev.* **1951**, *82*, 403; Anderson, P. W.; Hasegawa, H. *Phys. Rev.* **1955**, *100*, 675.
- (6) Borshch, S. A.; Bominaar, E. L.; Girerd, J.-J. *New. J. Chem.* **1993**, *17*, 39; b) Borshch, S. A.; Bominaar, E. L.; Blondin, G.; Girerd, J.-J. *J. Am. Chem. Soc.* **1993**, *115*, 5155; c) Bominaar, E. L.; Borshch, S. A.; Girerd, J.-J. *J. Am. Chem. Soc.* **1994**, *116*, 5362; d) Bominaar, E. L.; Hu, Z.; Münck, E.; Girerd, J.-J.; Borshch, S. A. *J. Am. Chem. Soc.* **1993**, *115*, 5155.
- (7) Beissel, T.; Bürger, K.-S.; Voigt, G.; Wieghardt, K. *Inorg. Chem.* **1993**, *32*, 124 b) Beissel, T.; Glaser, T.; Kesting, F.; Wieghardt, K.; Nuber, B. *Inorg. Chem.* **1996**, 3936.
- (8) Beissel, T.; Birkelbach, F.; Bill, E.; Glaser, T.; Kesting, F.; Krebs, C.; Weyhermüller, T.; Wieghardt, K.; Butzlaff, C.; Trautwein, A. X. *J. Am. Chem. Soc.* **1996**, *118*, 12376.
- (9) Backes-Dahmann, G.; Herrmann, W.; Wieghardt, K.; Weiss, J. *Inorg. Chem.* **1985**, *24*, 485; b) Beissel, T.; Della Vedova, B. S. P. C.; Wieghardt, K.; Boese, R. *Inorg. Chem.* **1990**, *29*, 1736.
- (10) Leuenberger, B.; Güdel, H. U. *Inorg. Chem.* **1986**, *25*, 181; b) Niemann, A.; Bossek, U.; Wieghardt, K.; Butzlaff, C.; Trautwein, A. X.; Nuber, B. *Angew. Chem. Int. Ed. Engl.* **1992**, *31*, 311 and literature cited therein.
- (11) Ding, X.-Q.; Bominaar, E.L.; Bill, E.; Winkler, H.; Trautwein, A. X.; Drüke, S.; Chaudhuri, P.; Wieghardt, K. *J. Chem. Phys.* **1990**, *92*, 178; b) Gamelin, D. R.; Bominaar, E. L.; Kirk, M. L.; Wieghardt, K.; Solomon, E. I. *J. Am. Chem. Soc.* **1996**, *118*, 8085.
- (12) Wu, C.-C.; Jang, H. G.; Rheingold, A. L.; Gütllich, P.; Hendrickson, D. N. *Inorg. Chem.* **1996**, *35*, 4137.
- (13) Nagaoka, Y. *Phys. Rev.* **1966**, *147*, 392.

Chapter 19

Amino Acid Side Chain Movements in the Active Site of the Hydroxylase Enzyme from Soluble Methane Monooxygenase

Douglas A. Whittington and Stephen J. Lippard

Department of Chemistry, Massachusetts Institute of Technology,
Cambridge, MA 02139

Examination of crystal structures of the hydroxylase enzyme (MMOH) from *Methylococcus capsulatus* (Bath) reveals alternate conformations for amino acid side chains Leu110, Asn214, and Glu243. These alternate side chain orientations may regulate access of substrates to the active site via cavities in the enzyme or make available coordination sites on the iron atoms required for activation of dioxygen. X-ray crystal structures of MMOH containing bound xenon demonstrate the accessibility of cavities in the enzyme to gaseous substrates. MMOH is spectroscopically well characterized, and evidence for changes in its structure upon binding of protein B and the reductase is summarized.

Obligate methanotrophic bacteria have evolved a metabolism which derives energy to support life processes and carbon for cellular growth from the oxidation of CH₄ to CO₂. The production of methanol from methane is the first step in this process. One member of this class of bacteria is the organism *Methylococcus capsulatus* (Bath), originally isolated from a thermal spa in Bath, England (1). Metalloenzymes enable these bacteria to consume methane as indicated in equation 1, the mechanism of which



is of considerable interest. Understanding the biological process would greatly facilitate attempts to duplicate such oxidation chemistry with small inorganic compounds.

M. capsulatus (Bath) can express either a particulate, membrane-bound methane monooxygenase containing copper or a soluble form containing iron (2). The soluble methane monooxygenase (sMMO), produced when there is a deficiency of copper in the environment, has been the subject of extensive research (3,4). Three proteins are used by the sMMO system to oxidize methane to methanol. The largest

protein is a 251 kDa hydroxylase (MMOH), which contains dinuclear iron centers at the active sites in the α subunits of an $(\alpha\beta\gamma)_2$ dimer. A second protein (MMOB) plays a regulatory role during catalysis, as first suggested in (5), while electron transfer to the diiron centers of MMOH is mediated by the reductase protein (MMOR). The latter receives its electrons from nicotinamide adenine dinucleotide (NADH). These electrons pass sequentially through a flavin adenine dinucleotide (FAD) cofactor, an Fe_2S_2 center, and ultimately to the hydroxylase (6). Turnover linked to NADH consumption requires all three components (7). Oxidation in the analogous system from *M. trichosporium* OB3b apparently can proceed with only the hydroxylase and reductase, but is greatly stimulated in the presence of protein B (8). Similar requirements for substrate oxidation by enzymes requiring three or more protein components have also been observed in toluene monooxygenase (9,10), alkene monooxygenase (11,12), and phenol hydroxylase (13) systems.

Methane monooxygenase is one of a family of proteins that contain carboxylate-bridged, dinuclear iron centers, including hemerythrin, purple acid phosphatase, toluene monooxygenase, stearyl-ACP $\Delta 9$ desaturase, ribonucleotide reductase R2 protein, and rubrerythrin (14). In the last four proteins and sMMO, the two iron atoms at the active site are anchored within a four-helix bundle by glutamate and histidine residues comprising Glu-X-X-His motifs (14). The iron atoms are bridged by either oxo-, hydroxo-, or aqua ligands and the remaining coordination sites are filled by glutamate, aspartate, or water-derived groups. Despite similarities in active site architecture, each of these proteins performs a unique function. Only methane monooxygenase can achieve the difficult, selective oxidation of methane to methanol. The varying functions indicate that important differences must occur in the protein structure surrounding the transition metal active site centers to tune their reactivity (15).

The geometry of the sMMO hydroxylase is well established from X-ray structure determinations on two crystal forms each from both *M. capsulatus* (Bath) (16,17) and *M. trichosporium* OB3b (18). The hydroxylase proteins from these two organisms display essentially identical folds, which is not unexpected given their 89% sequence similarity (19). The structure of the hydroxylase from *M. capsulatus* (Bath) has been solved in the oxidized, diiron(III), and reduced, diiron(II), states (20), as well as in crystals bathed in dimethyl sulfoxide (DMSO) (21). These multiple determinations have demonstrated a flexibility manifest by alternate conformations of side chains at the active site (20,21). Such side chain movements, when considered in the present context, suggest a possible regulatory role involving amino acids located in the vicinity of the active site ligands. The manner by which this regulatory control might be manifest for the methane monooxygenase hydroxylase is the subject of this chapter. Two of the more intriguing questions regarding the mechanism of sMMO are: How does the enzyme control substrate access to and product egress from the active site? And, by what mechanism are dioxygen and the C—H bond of methane activated to perform the chemical oxidation?

Cavity Structure of the α Subunit in sMMOH

The hydroxylase protein contains a large amount of open interior space. Five hydrophobic cavities have been identified within each α subunit, as illustrated in Figure 1. These cavities are postulated to serve as components of a channel by which

substrates or products could traverse the protein exterior and the active site, which is buried in the interior of the protein (16). Such large amounts of open space are not unique to the sMMO hydroxylase, for many large globular proteins contain cavities of some sort (22). Interior pockets exist for many reasons, the simplest of which derives from natural defects which occur when folding a hydrophobic polypeptide chain (23). The presence of cavities, especially in large proteins, has also been proposed to allow for hinge motions between different domains (24). In many cases, cavities are postulated also to play a role in providing substrate access to an active site, examples being myoglobin (25), cytochrome P450 (26), and a Ni-Fe hydrogenase (27). Molecular dynamics simulations with myoglobin and the Ni-Fe hydrogenase, which also contain buried active sites and several internal cavities, suggest that small diatomic molecules traverse much of the space provided by cavities until they escape the interior through natural "checkpoints" in the protein structure (25,27).

In the hydroxylase protein of methane monooxygenase, the five cavities of the α subunit are separated from one another by amino acid side chains. In order to pass freely through these openings, even small molecules such as dioxygen and methane would require movement of the residues from their crystallographically identified orientations. This series of cavities does not trace the shortest path to the active site from the surface of the protein, which instead passes directly between two of the four helices that provide ligands to coordinate the iron atoms and into cavity 1. Although the distance along this route is only about 12 Å, the pathway is blocked by multiple amino acid side chains.

A docking study performed by using the coordinates of the oxidized structure of the *M. capsulatus* (Bath) hydroxylase identified three primary substrate binding sites in the active site region (28). The major binding site for small molecules such as methane or propylene was assigned in the active site cavity approximately 3 Å from each iron atom and corresponds to cavity 1 in Figure 1. The remaining two sites accommodated larger substrates and were located approximately 14 Å from the iron atoms. In order for these sites to be competent during catalysis, one must invoke substantial motions of the protein to allow access to the interior. There is experimental evidence that a wide range of substrates can be oxidized by sMMO (29-31). Such broad substrate specificity is reminiscent of cytochromes P450 (32) and is one of the more remarkable aspects of the enzyme. In addition to methane, molecules such as propylene, nitrobenzene, adamantane, and methylphenylcyclopropane can all be oxidized (29-31). Such a broad range of size in acceptable substrates indicates that changes from the crystallographically determined structure must occur during catalysis, perhaps induced by the formation of a complex with protein B.

There is direct experimental evidence that small gaseous molecules bind in at least one of the series of hydrophobic cavities located within the α subunit. X-ray structural studies on hydroxylase crystals which had been pressurized with Xe gas revealed a xenon atom bound in the hydrophobic cavity adjacent to the active site cavity (33), as illustrated in Figure 2 (34). Since xenon has a van der Waals radius similar to that of methane, but many more electrons, it serves as a good crystallographic probe for methane binding. The finding of Xe in cavity 2 indicates that there are mechanisms for accessing hydrophobic interior cavities, but the question remains as to whether the protein actually uses this depot as part of a longer pathway to the surface. Xenon binding has also been explored as a probe in myoglobin (35,36) and a Ni-Fe hydrogenase (27) in order to identify putative gas-binding sites within the

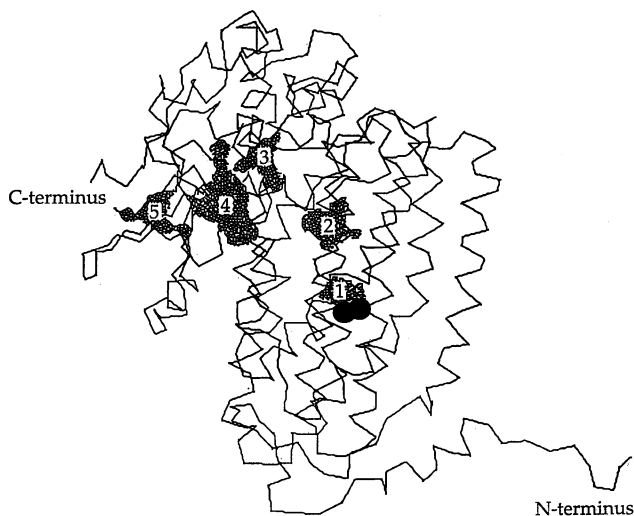


Figure 1. The α subunit of the hydroxylase displaying the five hydrophobic cavities identified within the subunit structure. The two iron atoms are represented by two black spheres.

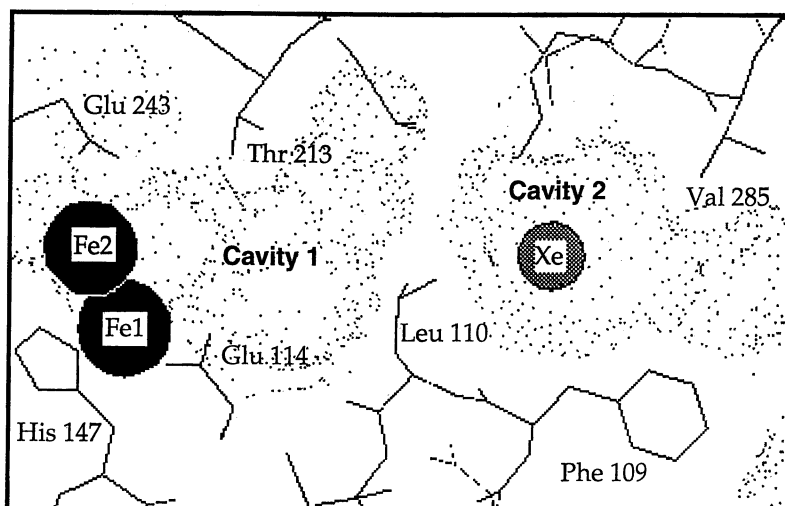


Figure 2. Location of the bound xenon atom in cavity 2 within the α subunit of the hydroxylase structure. The dot surfaces represent Connolly surfaces calculated by using the program MAIN (34) with a 1.2 Å probe. The two iron atoms and several representative amino acid side chains are labeled.

protein matrix. Despite the discovery of an ordered Xe atom in the crystal structure, kinetic measurements in solution indicate that the reaction of methane with the oxidizing intermediate Q is second order (37), implying diffusion of methane molecules within the protein on the time scale of the hydroxylation step ($t_{1/2}$ 4.0 sec).

Flexibility of Side Chains

One feature shared by several members of the family of carboxylate-bridged dinuclear iron proteins is the large number of coordinated glutamate and aspartate residues. From studies of polymanganese and polyiron carboxylate complexes, the existence of numerous modes of carboxylate binding to polymetallic centers was discerned, and it was proposed that shifts in the carboxylate binding mode might be of functional significance in metalloenzyme mechanisms (38). Crystal structure analyses of MMOH from *M. capsulatus* (Bath) in the diiron(II) oxidation state and following treatment with DMSO revealed significant carboxylate shifting of Glu243, and, to a lesser extent, Glu144, as illustrated in Figure 3 (20,21). Glu243 can adopt a monodentate binding mode as found in the resting state, a bidentate chelating mode, as in the DMSO-treated crystals, or a mixed mode involving monodentate bridging between two iron atoms and bidentate chelation to Fe²⁺ in the reduced state. In the reduced diiron(II) state, the bridging hydroxide ligands are no longer present. Since the reduced state is reactive toward dioxygen, it would appear that the resulting rearrangement of the active site ligands prepares the diiron center for this chemistry by opening sites for oxygen atom binding to the metal atoms.

In addition to Glu243, the side chain of Asn214 adopts one of two different conformations in the various structures, as illustrated in Figure 4 (Whittington, D.A.; Lippard, S.J., unpublished observation, 1997). This finding is interesting since Asn214 lies along the shortest distance from the iron atoms to the exterior of the protein passing between helices E and F in the α subunit of the hydroxylase. The conformation found in the reduced structure and in one protomer of the DMSO-soaked crystal serves to open a deeper crevice extending from the exterior of the protein towards the active site. The accessibility and flexibility of this residue suggest that it may function to shuttle electrons or protons to the active site. Both Asn214 and the adjacent Thr213, one of two hydrophilic residues situated in the active site pocket and implicated in proton shuttling, are conserved in the *M. capsulatus* (Bath) and *M. trichosporium* OB3b hydroxylases, toluene-4-monooxygenase from *Pseudomonas mendocina*, and phenol hydroxylase from *Pseudomonas sporium* CF600 (39).

Analysis of electron density differences between the two crystal forms of the *M. capsulatus* (Bath) MMOH also revealed two different orientations of the Leu110 side chain, one of several hydrophobic residues lining the active site cavity (17). Rotation of the isopropyl group of Leu110 around C β partially opens a connection between cavities 1 and 2. Such movement suggests a possible role for Leu110 to serve as a gate, controlling access between the two pockets, and supports the hypothesis that the protein may use the series of hydrophobic cavities to shuttle substrates and/or products. Recent work has revealed that leucine residues near iron-containing active sites may serve regulatory roles in other proteins as well. Site-directed mutagenesis of Leu98 to Ala in hemerythrin (Hr) increased the autoxidation rates of the protein, whereas the rates decreased significantly in the L98Y mutants (Farmer,

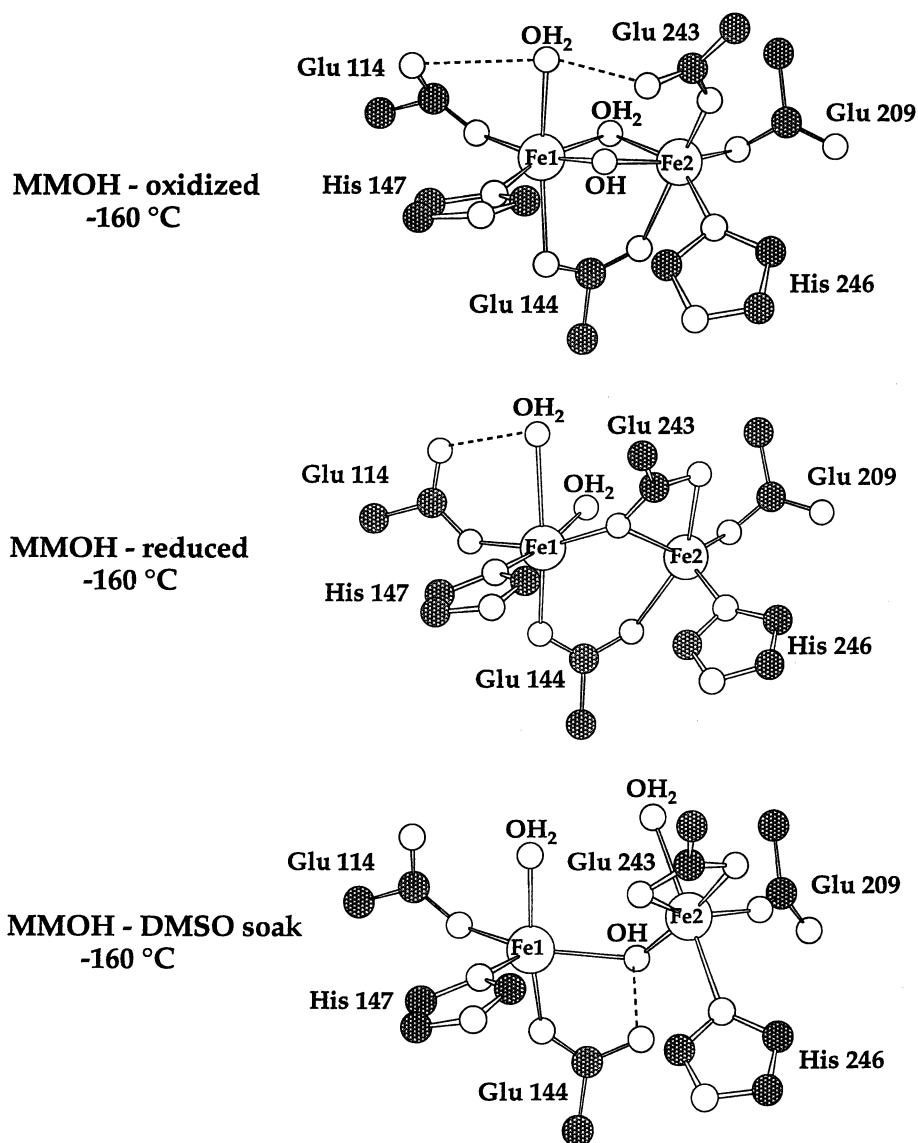


Figure 3. Three different views of the hydroxylase active site as determined by X-ray crystallography showing three different coordinating modes of Glu243 (16,20,21).

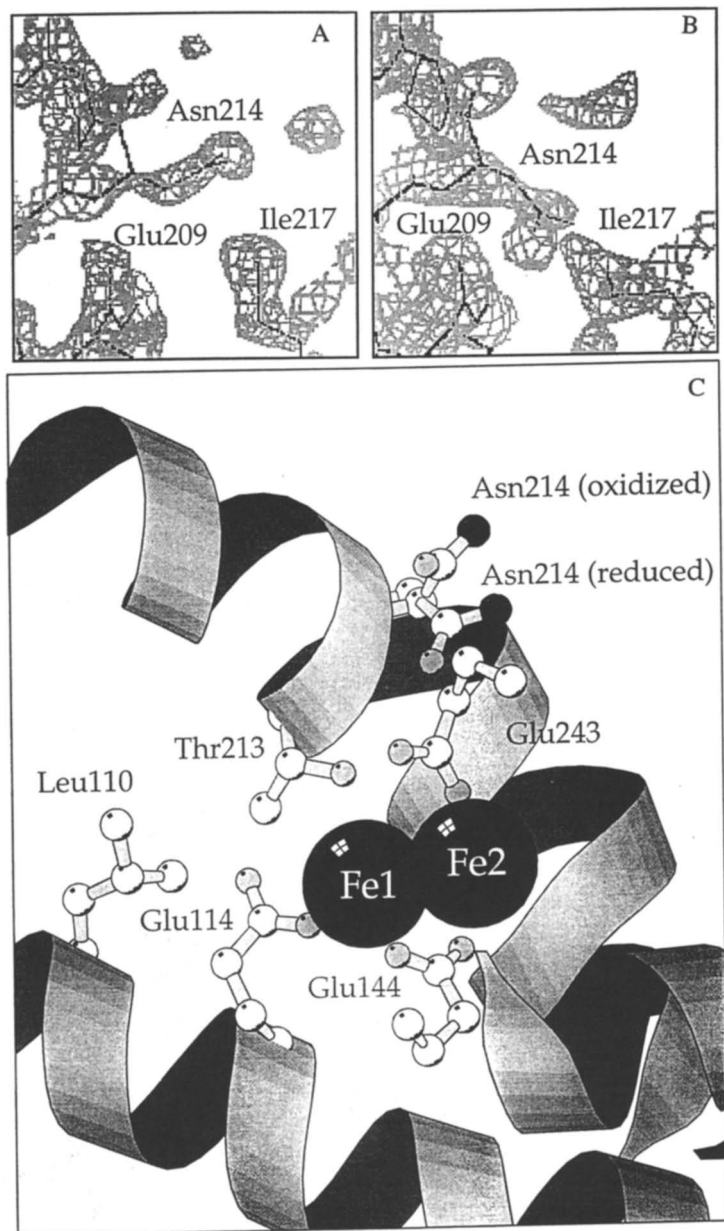


Figure 4. Overlaid oxidized and reduced MMOH structures showing (A) the electron density for residue Asn214 in the 1.7 Å oxidized structure and (B) electron density for residue Asn214 in the 1.7 Å reduced structure. (C) Location of the altered Asn214 residue in relation to the diiron active site in MMOH. The two iron atoms and important amino acids are labeled. Additional ligands to the iron atoms and two of the four helices in the four helix bundle have been removed for clarity.

C.S.; Xiong, J.; Arastu, S.; Kurtz, Jr., D.M., personal communication, 1997). The active site cavity and an adjacent cavity in Hr are separated by Leu98 in a manner similar to the separation of cavities 1 and 2 by Leu110 in MMOH (17). Mutants for Leu103 in myohemerythrin, L103V and L103N, have also been constructed and neither formed a stable dioxygen adduct (40,41). The side chain terminus of this residue comes into van der Waals contact with the bound dioxygen molecule in oxyhemerythrin. Finally, molecular dynamics calculations of the reduced and oxidized structures of cytochrome c have demonstrated a functional role for Leu68 in gating access of water to the active site (42).

The propensity for movement of an amino acid side chain or its ability to adopt multiple conformations can sometimes be quantitated by analysis of its Debye-Waller factors derived from the refinement of a protein X-ray crystal structure. It has already been noted that several different crystal structures of MMOH from *M. capsulatus* (Bath) have been solved. By taking an average value for the atoms in each amino acid residue directly coordinated to an iron atom or lining the active site pocket, it is possible to estimate those residues which are prone to movement. Figure 5 shows the isotropic temperature factors (B) for many such atoms in the MMOH active site. From these values, we suggest that Asn214, Thr213, Glu243, Glu209, and Leu110 are the most prone to move during catalysis.

Role of Protein B and the Reductase

In addition to the hydroxylase, the oxidation of methane to methanol by sMMO in the *M. capsulatus* (Bath) system requires the presence of both protein B and the reductase. The presence of one FAD and one Fe₂S₂ center in the reductase provided early evidence for its role as an electron transfer protein (7,43). Subsequent stopped-flow experiments involving the hydroxylase, the reductase and NADH substantiated this claim (6). Initial analysis of protein B showed that it contained no metals or other cofactors but its importance as a coupling protein, linking the consumption of NADH with oxidation of substrate, soon became evident (5). When protein B was added to solutions containing hydroxylase and reductase in the absence of substrate, NADH consumption was greatly reduced. Addition of substrate resulted in productive turnover. For sMMO from both *M. capsulatus* (Bath) and *M. trichosporium* OB3b, electron paramagnetic resonance (EPR) experiments of the hydroxylase in the presence and absence of the other two protein components revealed that both B and R could shift the reduction potentials of the diiron center (44-46). Whereas it is more difficult to add the second than the first electron to the diiron(III) form of the hydroxylase, in the presence of MMOR the potentials are such that it is easier to add the second electron, thereby minimizing formation of the catalytically inactive mixed valent, Fe(II)Fe(III), species. Subsequent work has revealed an even more complex role for these two protein components.

The presence of a carboxylate-bridged diiron center within each α subunit of MMOH allows for numerous spectroscopic methods to be applied to the sMMO system, and the interactions of protein B and the reductase have been investigated by using several of these techniques. The presence of protein B results in significant changes in the EPR spectra of the mixed-valent and reduced hydroxylase from both organisms [(47-49) and Liu, K.E.; Lippard, S.J., unpublished observations, 1994]. Since EPR spectroscopy is very sensitive to magnetic coupling between the iron

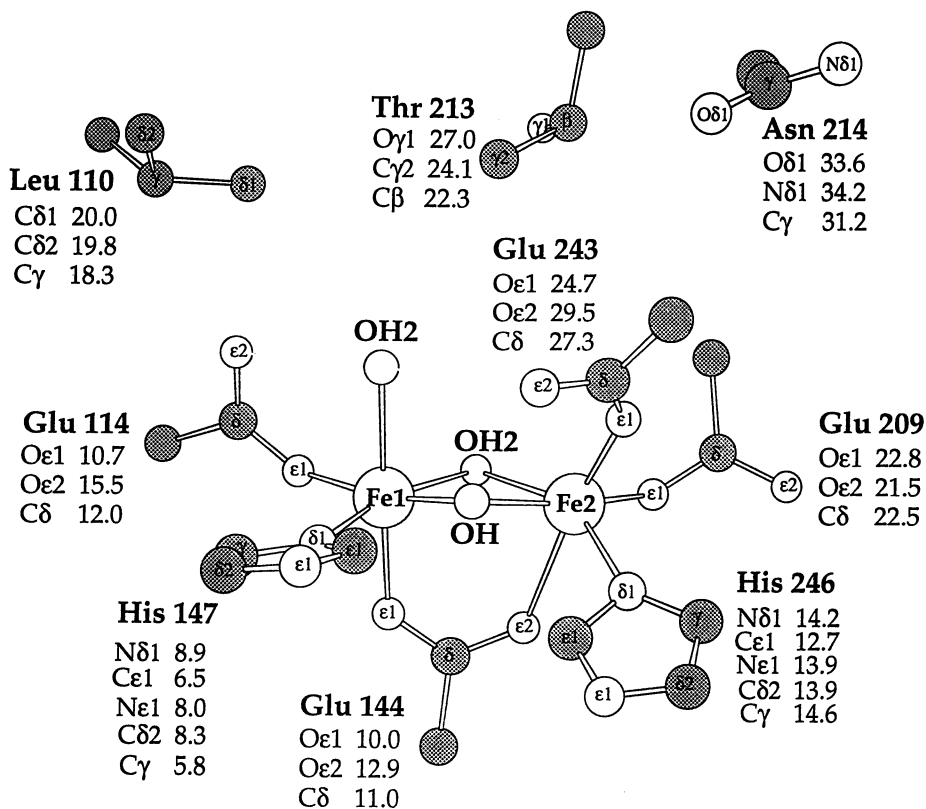


Figure 5. The active site of the hydroxylase showing important amino acid side chains along with the average temperature factors as determined by averaging the B values from all published structures of the *M. capsulatus* (Bath) hydroxylase.

atoms and the symmetry of their coordination environments, it is likely that the binding of protein B perturbs these features. One limitation to the use of EPR spectroscopy, however, is its inability to probe the effects of protein B binding to the diferric MMOH, which is EPR silent at 4.2 K owing to antiferromagnetic coupling between the two iron atoms (50). By radiolytic reduction of the diferric centers in frozen solutions of MMOH, an EPR signal can be generated (51,52). Irradiation with γ -rays of a frozen solution of oxidized diiron(III) MMOH at 77 K yields the EPR-active Fe(II)Fe(III) state, the features of which reflect the geometry of the diferric state. Experiments of this type demonstrate that protein B interacts with the oxidized hydroxylase in such a manner as to alter the EPR signature of the cryogenically photo-reduced active site (51).

X-ray absorption spectroscopy (XAS) of metalloenzymes allows one to probe both the oxidation state and coordination environment of the metal centers. Experiments with the sMMO hydroxylase from both organisms in the presence and absence of protein B revealed no substantial differences (53,54). Since XAS spectra are sensitive to changes in oxidation state, coordination number and types of ligand donor atoms, protein B binding to the hydroxylase must not affect these parameters. Mössbauer spectroscopy can also probe the oxidation state, spin state and the local symmetry at iron centers. Protein B binding does not significantly affect the Mössbauer spectrum of the hydroxylase enzyme (49). Differences were observed in circular dichroism (CD) experiments of the *M. trichosporium* OB3b hydroxylase with and without protein B, however (55). Addition of MMOB to reduced MMOH perturbed the spectrum, and the substrate *trans*-1,2-dichloroethylene or inhibitor tetrachloro-ethylene altered the spectral signature only when protein B was present. A full analysis of these CD data indicated that protein B binding itself changes the ligand field environment of one iron atom in the active site, whereas substrate or inhibitor binding perturbed that at the other iron atom (55). Complementary magnetic circular dichroism data showed no change upon protein B binding to the hydroxylase. Taken together, these results indicate that MMOB binding alters the active site cavity in MMOH without changing the ligands bound to iron.

Analysis of product distributions during catalytic turnover and of reaction rates during catalytic and single turnover experiments revealed further effects of protein B on sMMO behavior. When isopentane was oxidized by MMOH in the presence and absence of protein B in the *M. trichosporium* OB3b system, significant shifts in the ratios of secondary and tertiary alcohol to primary alcohol were observed (48). Altered product distributions were also seen during the oxidation of nitrobenzene by MMOH, depending upon the presence of protein B (48). Moreover, protein B increased the rates of reaction in both hydroxylase enzymes under steady-state conditions and during single turnover reactions, which reached a maximum at a 2:1 MMOB:MMOH ratio, although a 0.1:1.0 MMOB:MMOH ratio was enough to effect the change in product distributions with isopentane (48,56). It has therefore been proposed that protein B not only causes conformational changes near the active site, in accord with much of the spectroscopic evidence, but that it results in a type of hysteresis such that the conformational changes remain after dissociation of protein B from the hydroxylase (45,48). Finally, work with both systems has shown that the presence of protein B increases the rate of formation of intermediates in the reaction cycle (56,57).

The role of the reductase has been less thoroughly investigated than that of protein B. The most important function of the reductase is to shuttle electrons from NADH to the diiron sites of the hydroxylase. The reductase also alters product distributions during the oxidation of isopentane (48) and nitrobenzene (56), however. In addition, MMOR shifts the reduction potentials of the diiron center, as monitored by EPR spectroscopy (46), although only one-tenth the concentration of MMOR relative to MMOH active sites is required to effect fully the shifts. Furthermore, steady-state experiments with *M. capsulatus* (Bath) have demonstrated that a substoichiometric ratio of 1.0:0.1 MMOH:MMOR can sustain catalytic oxidation of propylene (58). This observation is significant because it may indicate a hysteretic effect for the reductase as well, or at the very least rapid on and off rates in conjunction with very quick electron transfer events such that a small population of the reductase can reduce a large population of the hydroxylase. Although the evidence is much less dramatic in the case of the reductase, it too may cause conformational changes in the hydroxylase upon binding, thereby altering the orientation of residues near the active site and facilitating the transfer of electrons.

Concluding Remarks

Many metalloenzymes are grouped into families based upon related active site structures. Despite similar architectures, the functions carried out by such enzymes are diverse. The family of structurally related, carboxylate-bridged dinuclear iron proteins is an excellent example of such disparity of function. Tailoring of specific functions to the individual enzymes is performed by the choice and orientation of amino acid side chains as ligands to the metal and as components of the active site pocket, which can greatly affect the behavior of the transition metal core. In a recent example, site directed mutagenesis studies on the diiron-containing toluene 4-monooxygenase demonstrated that the mutants Q141C and F205I, involving simple hydrophobic residues postulated to line the hydrophobic active site cavity, shifted the regioselectivity of aromatic hydroxylation (59).

A combination of X-ray diffraction and solution spectroscopic methods has revealed several protein side chain movements which are likely to be critical features of the mechanism by which sMMO oxidizes methane to methanol. X-ray structural studies identified residues near the active site which exist in multiple conformations, including Glu243, Leu110, and Asn214. The alternate Leu110 conformations may be part of a gate connecting the active site cavity to cavity 2 in a series of hydrophobic pockets proposed to play a role in substrate access to the active site (17). Similar gating roles for leucine have been observed in hemerythrin and cytochrome c [(40,42) and Farmer, C.S.; Xiong, J.; Arastu, S.; Kurtz, Jr., D.M., personal communication, 1997]. Cavity 2 binds a xenon atom, a result which may indicate its functional relevance. Spectroscopic work suggests that protein B and the reductase cause changes in the active site, but not by altering ligands coordinated to the iron atoms. No significant difference is observed in XAS or Mössbauer spectra of MMOH:MMOB mixtures when compared with MMOH solutions alone, although circular dichroism and EPR spectra reveal different features upon MMOB binding to the hydroxylase. Since these latter techniques monitor the environment around the iron atoms, changes must be occurring in the active site pocket, perhaps through altered hydrogen bonding interactions. Direct structural evidence for amino acid side

chain movements upon protein-protein binding is not yet available, but one or more of the residues identified as being important by the crystallographic studies are likely involved. Further X-ray structural work with protein complexes or experiments with site-directed mutants are required to address this issue.

Acknowledgments. This work was supported by grants GM32134 and GM48388 from the National Institute of General Medical Sciences. DAW is an NIH Biotechnology Predoctoral Trainee.

Literature Cited

- (1) Whittenbury, R.; Phillips, K. C.; Wilkinson, J. F. *J. Gen. Microbiol.* **1970**, *61*, 205-218.
- (2) Nielsen, A. K.; Gerdes, K.; Degn, H.; Murrell, J. C. *Microbiol.* **1996**, *142*, 1289-1296.
- (3) Liu, K. E.; Lippard, S. J. *Adv. Inorg. Chem.* **1995**, *42*, 263-289.
- (4) Wallar, B. J.; Lipscomb, J. D. *Chem. Rev.* **1996**, *96*, 2625-2657.
- (5) Green, J.; Dalton, H. *J. Biol. Chem.* **1985**, *260*, 15795-15801.
- (6) Lund, J.; Dalton, H. *Eur. J. Biochem.* **1985**, *147*, 291-296.
- (7) Colby, J.; Dalton, H. *Biochem. J.* **1978**, *171*, 461-468.
- (8) Fox, B. G.; Froland, W. A.; Dege, J. E.; Lipscomb, J. D. *J. Biol. Chem.* **1989**, *264*, 10023-10033.
- (9) Newman, L. M.; Wackett, L. P. *Biochemistry* **1995**, *34*, 14066-14076.
- (10) Pikus, J. D.; Studts, J. M.; Achim, C.; Kauffmann, K. E.; Münck, E.; Steffan, R. J.; McClay, K.; Fox, B. G. *Biochemistry* **1996**, *35*, 9106-9119.
- (11) Small, F. J.; Ensign, S. A. *J. Biol. Chem.* **1997**, *272*, 24913-24920.
- (12) Muira, A.; Dalton, H. *Biosci. Biotechnol. Biochem.* **1995**, *59*, 853-859.
- (13) Powlowski, J.; Shingler, V. *Biodegradation* **1994**, *5*, 219-236.
- (14) Nordlund, P.; Eklund, H. *Curr. Opin. Struct. Biol.* **1995**, *5*, 758-766.
- (15) Lippard, S. J.; Berg, J. M. *Principles of Bioinorganic Chemistry*; University Science Books: Mill Valley, CA, 1994.
- (16) Rosenzweig, A. C.; Frederick, C. A.; Lippard, S. J.; Nordlund, P. *Nature* **1993**, *366*, 537-543.
- (17) Rosenzweig, A. C.; Brandstetter, H.; Whittington, D. A.; Nordlund, P.; Lippard, S. J.; Frederick, C. A. *Proteins: Struct. Funct. Genet.* **1997**, *29*, 141-152.
- (18) Elango, N.; Radhakrishnan, R.; Froland, W. A.; Wallar, B. J.; Earhart, C. A.; Lipscomb, J. D.; Ohlendorf, D. H. *Protein Sci.* **1997**, *6*, 556-568.
- (19) Cardy, D. L. N.; Laidler, V.; Salmond, G. P. C.; Murrell, J. C. *Molec. Microbiol.* **1991**, *5*, 335-342.
- (20) Rosenzweig, A. C.; Nordlund, P.; Takahara, P. M.; Frederick, C. A.; Lippard, S. J. *Chem. & Biol.* **1995**, *2*, 409-418.
- (21) Rosenzweig, A. C.; Frederick, C. A.; Lippard, S. J. In *Microbial Growth on Cl Compounds*; Lidstrom, M. E. and Tabita, F. R., Eds.; Kluwer Academic Publishers: 1996; pp 141-149.
- (22) Hubbard, S. J.; Gross, K.-H.; Argos, P. *Protein Eng.* **1994**, *7*, 613-626.
- (23) Hubbard, S. J.; Argos, P. *Protein Eng.* **1995**, *8*, 1011-1015.

- (24) Hubbard, S. J.; Argos, P. *J. Mol. Biol.* **1996**, *261*, 289-300.
- (25) Elber, R.; Karplus, M. *J. Am. Chem. Soc.* **1990**, *112*, 9161-9175.
- (26) Deprez, E.; Gerber, N. C.; Di Primo, C.; Douzou, P.; Sligar, S. G.; Hoa, G. H. B. *Biochemistry* **1994**, *33*, 14464-14468.
- (27) Montet, Y.; Amara, P.; Volbeda, A.; Vernede, X.; Hatchikian, E. C.; Field, M. J.; Frey, M.; Fontecilla-Camps, J. C. *Nature Struct. Biol.* **1997**, *4*, 523-526.
- (28) George, A. R.; Wilkins, P. C.; Dalton, H. *J. Molec. Cat. B* **1996**, *2*, 103-113.
- (29) Colby, J.; Stirling, D. I.; Dalton, H. *Biochem. J.* **1977**, *165*, 395-402.
- (30) Green, J.; Dalton, H. *J. Biol. Chem.* **1989**, *264*, 17698-17703.
- (31) Liu, K. E.; Johnson, C. C.; Newcomb, M.; Lippard, S. J. *J. Amer. Chem. Soc.* **1993**, *115*, 939-947.
- (32) Dawson, J. H.; Sono, M. *Chem. Rev.* **1987**, *87*, 1255-1276.
- (33) Rosenzweig, A. C.; Whittington, D. A.; Frederick, C. A.; Lippard, S. J. **1997**, manuscript in preparation.
- (34) Turk, D. **1992**, Ph.D. Thesis, Technische Universität München.
- (35) Schoenborn, B. P.; Watson, H. C.; Kendrew, J. C. *Nature* **1965**, *207*, 28-30.
- (36) Tilton, Jr., R. F.; Kuntz Jr., I. D.; Petsko, G. A. *Biochemistry* **1984**, *23*, 2849-2857.
- (37) Lee, S.-K.; Nesheim, J. C.; Lipscomb, J. D. *J. Biol. Chem.* **1993**, *268*, 21569-21577.
- (38) Rardin, R. L.; Tolman, W. B.; Lippard, S. J. *New. J. Chem.* **1991**, *15*, 417-430.
- (39) Fox, B. G.; Shanklin, J.; Ai, J.; Loehr, T. M.; Sanders-Loehr, J. *Biochemistry* **1994**, *33*, 12776-12786.
- (40) Raner, G. M.; Martins, L. J.; Ellis, Jr., W. R. *Biochemistry* **1997**, *36*, 7037-7043.
- (41) Martins, L. J.; Hill, C. P.; Ellis, Jr., W. R. *Biochemistry* **1997**, *36*, 7044-7049.
- (42) Banci, L.; Gori-Savellini, G.; Turano, P. *Eur. J. Biochem.* **1997**, In press.
- (43) Colby, J.; Dalton, H. *Biochem. J.* **1979**, *177*, 903-908.
- (44) Liu, K. E.; Lippard, S. J. *J. Biol. Chem.* **1991**, *266*, 12836-12839.
- (45) Paulsen, K. E.; Liu, Y.; Fox, B. G.; Lipscomb, J. D.; Münck, E.; Stankovich, M. T. *Biochemistry* **1994**, *33*, 713-722.
- (46) Liu, Y.; Nesheim, J. C.; Paulsen, K. E.; Stankovich, M. T.; Lipscomb, J. D. *Biochemistry* **1997**, *36*, 5223-5233.
- (47) Fox, B. G.; Liu, Y.; Dege, J. E.; Lipscomb, J. D. *J. Biol. Chem.* **1991**, *266*, 540-550.
- (48) Froland, W. A.; Andersson, K. K.; Lee, S.-K.; Liu, Y.; Lipscomb, J. D. *J. Biol. Chem.* **1992**, *267*, 17588-17597.
- (49) Fox, B. G.; Hendrich, M. P.; Surerus, K. K.; Andersson, K. K.; Froland, W. A.; Lipscomb, J. D.; Münck, E. *J. Am. Chem. Soc.* **1993**, *115*, 3688-3701.
- (50) Woodland, M. P.; Patil, D. S.; Cammack, R.; Dalton, H. *Biochim. Biophys. Acta* **1986**, *873*, 237-242.
- (51) Davydov, A.; Davydov, R.; Gräslund, A.; Lipscomb, J. D.; Andersson, K. K. *J. Biol. Chem.* **1997**, *272*, 7022-7026.
- (52) Davydov, R.; Komar-Panicucci, S.; Valentine, A. M.; Hoffman, B.; Lippard, S. J. **1997**, manuscript in preparation.
- (53) Shu, L.; Liu, Y.; Lipscomb, J. D.; Que, Jr., L. *J. Bioinorg. Chem.* **1996**, *1*, 297-304.

- (54) DeWitt, J. G.; Rosenzweig, A. C.; Salifoglou, A.; Hedman, B.; Lippard, S. J.; Hodgson, K. O. *Inorg. Chem.* **1995**, *34*, 2505-2515.
- (55) Pulver, S. C.; Froland, W. A.; Lipscomb, J. D.; Solomon, E. I. *J. Am. Chem. Soc.* **1997**, *119*, 387-395.
- (56) Liu, K. E.; Valentine, A. M.; Wang, D.; Huynh, B. H.; Edmondson, D. E.; Salifoglou, A.; Lippard, S. J. *J. Am. Chem. Soc.* **1995**, *117*, 10174-10185.
- (57) Liu, Y.; Nesheim, J. C.; Lee, S.-K.; Lipscomb, J. D. *J. Biol. Chem.* **1995**, *270*, 24662-24665.
- (58) Gassner, G. T.; Lippard, S. J. **1997**, manuscript in preparation.
- (59) Pikus, J. D.; Studts, J. M.; McClay, K.; Steffan, R. J.; Fox, B. G. *Biochemistry* **1997**, *36*, 9283-9289.

Chapter 20

Applications of X-ray Absorption Spectroscopy to Characterization of the Mn Cluster in the Photosynthetic Oxygen Evolving Complex

Pamel DeMarois¹, Pamela J. Riggs-Gelasco^{2,4}, Charles F. Yocum^{2,3},
and James E. Penner-Hahn²

¹Biophysics Research Division and ²Department of Chemistry, The University
of Michigan, Ann Arbor, MI 48109-1055

³Department of Biology, The University of Michigan, Ann Arbor, MI 48109-1048

The active site structure and the redox reactivity of the tetranuclear manganese cluster in the photosynthetic oxygen evolving complex of photosystem II have been probed using x-ray absorption spectroscopy. Extended x-ray absorption fine structure analysis has provided information about the manganese-nearest neighbor (ligand) interactions and, to a lesser extent, about the longer distance Mn-metal interactions. On the basis of cation substitution experiments, the outer (~3.3 Å) Mn-metal interactions appear to be dominated by Mn-Mn scattering. X-ray absorption near edge spectroscopy has been used to address mechanistic questions by characterizing the effects of chemical reductants on the edge energy and by comparing these with the effects of photooxidation. The combined data support a model in which two different Mn sites, which may or may not be spatially distinct, undergo differential reactivity.

Most of the chemical energy used in life is derived from solar energy, which is captured and converted to a chemically useful form by photosynthetic organisms. Reduced hydrocarbons are produced from CO₂, using electrons that are ultimately derived from the oxidation of H₂O to O₂ (equation 1).



The reaction in equation 1 takes place at a tetranuclear Mn cluster known as the oxygen evolving complex (OEC) found in Photosystem II (see for example, 1,2-4).

Insight into the molecular mechanism of water oxidation came with the demonstration (5) that photosynthetic membranes which are illuminated with short (ca. 5 μsec) but saturating flashes of light evolve oxygen maximally every fourth flash starting with the third flash. This demonstrated that each reaction center acts independently to acquire four oxidizing equivalents in a sequential manner and led to the kinetic model shown in Figure 1(6). This model is based on four kinetically

⁴Current address: Department of Chemistry, Massachusetts Institute of Technology, Cambridge, MA 02139

resolvable intermediates known as S_n states, where the subscript refers to the number of stored oxidizing equivalents. The dark stable state of the OEC is the S_1 state. Three flashes oxidize this to the transient S_4 state, which evolves O_2 , regenerating S_0 and beginning a new period-four oscillation.

It is generally accepted that the OEC contains four Mn ions, together with at least one Ca^{2+} and one Cl^- per reaction center (2). Most of the spectroscopic studies of the OEC have been done on the so-called BBY (7) preparations. These contain: the D1 and D2 peptides, which bind the principal redox co-factors; the light-harvesting antennae proteins CP43 and CP47; peptides α and β which bind cytochrome b_{559} ; and a 28 kDa peptide that plays a role in quinone binding (2). In addition to these intrinsic transmembrane polypeptides, there are three extrinsic polypeptides, with molecular masses of approximately 17, 24, and 33 kDa. The 33 kDa polypeptide helps to stabilize the Mn, while the two smaller extrinsic polypeptides enhance the retention of Ca^{2+} and Cl^- by the OEC.

A more highly purified preparation of the OEC known as the reaction center complex (RCC) (8) lacks the 17 and 24 kDa extrinsic polypeptides and most of the light harvesting complex (LHCII). This preparation requires added Ca^{2+} and Cl^- for activity, but appears spectroscopically to be similar or identical to BBY preparations. An important advantage of RCC preparations is that they have an approximately 3-fold higher Mn concentration on a chlorophyll basis than BBY preparations, and consequently give spectra having a better signal/noise ratio.

Spectroscopic characterization of the OEC is difficult since the portions of greatest interest (Mn, Cl, Ca) are elements that are generally hard to study. Optical methods (UV-visible, MCD, fluorescence, resonance Raman, etc.) are particularly difficult due to the interference from chlorophyll. Although most of the relevant spectroscopic techniques have been applied to the OEC, the most useful information has come from studies that employ magnetic resonance and x-ray absorption spectroscopies.

X-ray absorption spectroscopy

X-ray absorption spectroscopy (XAS) refers to the structured absorption on the high energy side of an x-ray absorption "edge" (the abrupt increase in absorption resulting from excitation of a core electron) (9-11). For Mn, the "K" (1s initial state) edge occurs at ca. 6500 eV \approx 2 Å. X-ray absorption spectra are frequently divided into the x-ray absorption near edge structure (XANES) region, for structure within ca. 50 eV of the edge, and the extended x-ray absorption fine structure (EXAFS) region, for structure from \sim 50 eV to \sim 1000 eV above the edge. The structure in x-ray absorption spectra is due to the modulation of x-ray photoabsorption cross-section that occurs as a consequence of interference between the x-ray excited and the back-scattered photoelectron waves.

Information content of XANES. The energy of an x-ray absorption edge is correlated with the oxidation state of the absorbing atom, with higher oxidation states giving higher energy edge thresholds (12). The physical basis of this effect probably involves both electrostatic effects (edge energy increases with increasing nuclear charge as it becomes more difficult to ionize the core electron) and continuum resonance effects (edge energy $\propto 1/R^2$ where R =absorber-scatterer distance) (13,14). Since higher oxidation state complexes typically have shorter bond lengths, both effects are likely to contribute to the oxidation-state dependent changes that are seen in XANES. In addition to changes in *energy*, there are also changes in the *shape* of XANES spectra as the molecular structure of the absorber changes. These are generally understood to arise from multiple-scattering of the photoelectron by the

surrounding atoms, and thus to contain information about geometry. However, quantitative interpretation of XANES is not generally possible.

Information content of EXAFS. EXAFS spectra contain oscillations from all of the neighbors around the absorbing atom, with each neighbor contributing oscillations of a characteristic frequency $2R$ when spectra are plotted in k space, where k (equation 2) is the photoelectron wave vector and E_0 is the threshold energy for photoelectron excitation. The fractional modulation in x-ray absorption cross-section, $\chi(k)$, is given by equation 3, where N_s is the number of scattering atoms at distance R_{as} from the absorbing atom, σ_{as}^2 is the rms deviation in R_{as} , and A_s and ϕ_{as} , the amplitude and phase of the scattering, respectively. The sum in equation 3 is taken over each "shell" of scatterers, where "shell" refers to a group of atoms of similar atomic type (e.g. N or O) at the same distance from the absorbing atom.

$$k = \sqrt{2m_e(E - E_0) / \hbar^2} \quad (2)$$

$$\chi(k) = \sum_s \frac{N_s A_s(k)}{k R_{as}^2} \exp(-2k^2 \sigma_{as}^2) \cdot \sin(2k R_{as} + \phi_{as}(k)) \quad (3)$$

EXAFS bond lengths, which depend on frequency, are generally well defined. In contrast, the coordination number and Debye-Waller factor (σ_{as}^2), which depend on amplitude, are less well defined. It is generally accepted that EXAFS can be used to determine $R_{as} \pm 0.02 \text{ \AA}$, and N_s to ± 1 (10,11), at least for analyses of first-coordination shells. Somewhat lower accuracy is generally obtained for more distant atoms. The values of A_s and ϕ_{as} depend on the chemical identity of the scatterer, thus it is also possible to identify the scatterer, typically to within one row of the periodic table (e.g., N and Cl are distinguishable but N and O are not). Data analysis typically involves using equation 3 together with A_s and ϕ_{as} , often calculated theoretically (15,16), to fit the data, refining R , N , and σ^2 .

The Fourier transform of equation 3 is a pseudo radial distribution function, with each shell of scatterers giving rise to a peak at $R + \alpha$ ($\alpha \approx -0.4 \text{ \AA}$ is a consequence of ϕ_{as} in equation 3). For perfect data, over an unlimited k range, each shell of scatterers in equation 3 would give a separate peak in the Fourier transform. In reality, the EXAFS amplitudes are damped due to both the A_s/k and the $\exp(-2k^2\sigma^2)$ terms in equation 3, and thus data can be measured only over a finite k range. For biological Mn EXAFS, the available k range is usually further limited by the Fe K absorption edge at 7100 eV (i.e., $k_{\max} \approx 11.9 \text{ \AA}^{-1}$). The limited k range means that, under the best conditions, the closest shells that can be resolved are separated by $\Delta R \geq \pi/2\Delta k \approx 0.14 \text{ \AA}$. In practice, the true resolution limit is generally somewhat worse than this (17). This decreased resolution means that the peaks in the Fourier transform are not well resolved, and consequently that the presence of different scatterers (e.g., different ligand atoms) can be difficult to establish (17).

Because EXAFS spectra are band-limited (i.e., only a limited band of frequencies contribute to the observed EXAFS), the amount of information contained in a spectrum is determined by the range of the spectrum (Δk) and by the range of distances that contribute to the spectrum (ΔR) (18). The number of independent data points, $N_{\text{idp}} = 2 \Delta k \Delta R / \pi$, is typically ≤ 15 and this number can drop dramatically for fits to Fourier "filtered" data, where a back Fourier transform is used to isolate a single peak from the overall radial distribution (17).

Applications of XAS to proteins. The principal attraction of XAS, particularly in the context of the OEC, is that it is able to provide element specific structural

information about non-crystalline systems. Unlike magnetic resonance, XAS spectra are always detectable, regardless of the spin-state of the sample. This is, however, also a potential weakness. *All* of the metal in a sample (e.g. all of the Mn in the OEC) contributes to the observed XAS spectrum. This makes it difficult, if not impossible, to determine the structure of each of the metal sites in a protein. Instead, only the average structure can be determined. The present chapter illustrates how chemical perturbations can be used to minimize the difficulties associated with the low information content of XAS.

Structural Characterization of the OEC

Magnetic properties. A key breakthrough in understanding the OEC was the discovery that the S_2 state is EPR active (19). Illumination at 200 K, which limits the OEC to a single S-state advance, gives a multiline EPR signal centered at $g \approx 2$ with 18-20 resolved lines spread over ca. 1900 G (for reviews, see 20,21). This S_2 multiline EPR signal, which arises from an $S=1/2$ ground state, is generally similar to those seen for mixed valence Mn dimers, although the signal for the OEC is considerably broader. Different conditions (e.g. low temperature illumination or the presence of inhibitors such as fluoride or ammonia) give instead a broad EPR signal at $g \approx 4.1$ for S_2 (22,23). Attempts to simulate the S_2 multiline signal have shown that at least two, and possibly all four, Mn ions are magnetically coupled to the paramagnetic center that accounts for this signal. Although extremely useful in helping to define the structural possibilities for the OEC (see e.g. 2), magnetic resonance measurements have previously been limited to the S_2 state as the only known EPR active species of the OEC. Very recently a Mn multiline EPR signal, similar to the S_2 multiline signal, has been reported for the S_0 state in the presence of methanol (24). This discovery may provide structural information on the OEC in the future, but currently is not well characterized.

Chloride is presumed to have some influence on the Mn site, as Cl^- is required for low temperature formation of the characteristic multiline EPR signal of the S_2 state. Cl^- has been suggested as a Mn ligand (25,26), possibly serving as a redox regulator of the Mn complex. The Ca^{2+} site also influences the formation of the S_2 multiline EPR signal; samples depleted of Ca^{2+} by addition of chelators form a modified multiline signal with narrower lines, and samples substituted with Sr^{2+} in the Ca^{2+} site form a $g \approx 4.1$ signal instead of the $g \approx 2$ multiline signal. This suggests that the Ca^{2+} site is also located near the Mn cluster.

Oxidation state assignments. It is only possible to have an $S=1/2$ EPR signal for S_2 if the cluster that gives rise to this signal contains an odd number of half-integer spin ions. For Mn, the only commonly available oxidation states with an odd number of electrons are Mn(II) and Mn(IV). EXAFS data (see below) suggest that the OEC contains $\text{Mn}(\mu\text{-O})_2\text{Mn}$ units characteristic of Mn(III) and Mn(IV) oxidation states. Together, these observations suggest that S_2 is either $\text{Mn(III)}_3\text{Mn(IV)}$ or Mn(III)Mn(IV)_3 and thus that S_1 is either Mn(III)_4 or $\text{Mn(III)}_2\text{Mn(IV)}_2$. The XANES data for S_1 are most consistent with the latter oxidation state assignment (4,27-29). In contrast, EPR interpretations have favored a Mn(III)_4 assignment for S_1 (30).

Preparation of reduced derivatives. The OEC shows a two flash delay in production of oxygen after treatment with reductants such as NH_2OH or N_2H_4 (31,32). The delay is consistent either with a two-electron reduction of the Mn cluster to form an " S_{-1} " state (33) or with formation of a state such as $S_1 \cdot \text{NH}_2\text{OH}$ where the bound NH_2OH serves to reduce a higher S state (e.g., S_2) following photooxidation (34). Initial XANES measurements suggested that NH_2OH treated samples were not reduced in the dark (35). More recently, we have reported XANES data consistent

with reduction of the Mn in the dark, and re-oxidation to S_1 on exposure to light (29,36). The data in the two reports are very similar; the different conclusions depend on whether the observed edge shifts are attributed to reduction of Mn to S_{-1} or to production of inactive Mn(II). In the more recent work, the NH_2OH effect has been shown to be photoreversible, demonstrating that there is no significant sample decomposition, and thus that the observed edge shift represents reduction of Mn by NH_2OH in the dark. The edge energy for S_{-1} is most consistent with an average oxidation state of Mn(III) (29), which is reasonable if S_1 has an average oxidation state of 3.5 (see above).

Structure of reduced species. Perhaps the most striking feature of S_{-1} is the near identity of its EXAFS spectrum to that seen for S_1 (37). Both spectra (see Figure 2, bottom) are dominated by three resolvable shells, attributable to Mn-(O/N) nearest neighbors ($R+\alpha \approx 1.6 \text{ \AA}$), Mn \cdots Mn interactions at ca. 2.7 \AA ($R+\alpha \approx 2.3 \text{ \AA}$), and a weaker outer shell peak ($R+\alpha \approx 3 \text{ \AA}$) attributable to Mn \cdots M interactions, where M is one (or more) metal at ca. 3.3 \AA from Mn (see below). The 2.7 \AA Mn \cdots Mn interaction is characteristic of di- μ -oxo bridged Mn(III) and Mn(IV) dimers, suggesting that this unit is a basic building block of the OEC Mn cluster. The retention of the 2.7 \AA Mn-Mn feature in S_{-1} adds strong support to the XANES finding (29) that this S_{-1} state does not contain Mn(II). Reduction to Mn(II) would have been expected to result in loss of one (or more) of the 2.7 \AA Mn-Mn interactions, and thus to a decrease in this feature in the Fourier transform. A Mn(III)₄ oxidation state for S_{-1} implies that S_0 and S_1 have oxidation states Mn(III)₃Mn(IV) and Mn(III)₂Mn(IV)₂, respectively.

In addition to NH_2OH , larger reductants, such as hydroquinone (H_2Q), can also reduce the OEC. The latter gives a form of the OEC that contains ca. 50% Mn(II), as judged by a six-line EPR signal, but that is nevertheless completely photoreversible, thus demonstrating that no Mn has been lost (38). The Mn(II) appears to be tightly sequestered near its active site. Hydroquinone reduction gives a significant decrease in XANES edge energy that is best modeled (36) by a 50:50 mixture of Mn(II):Mn(IV), and, as expected, results in major structural changes (see Figure 2, top), consistent with loss of a 2.7 \AA Mn-Mn interaction. This probably reflects reduction of one Mn(μ -O)₂Mn unit.

The NH_2OH and H_2Q treatments show strong synergism in their ability to attack the OEC (38). This, together with the EXAFS results, suggested (36) a two-site model in which large reductants (e.g. H_2Q) are only able to attack at one site (A) while small water soluble reductants (e.g. NH_2OH) preferentially attack at a different site (B) but can also slowly attack at A. When both A and B are reduced, the OEC is unstable and loses Mn to solution. In this model, the structural change that accompanies H_2Q reduction of A blocks internal electron transfer that would normally produce similar products when different reducing agents are used (36). The significance of the two site reduction model is that it suggests that the OEC Mn may be organized into two functionally distinct units. This in turn raises the possibility of a two step mechanism for water oxidation. It is important to note, however, that the observation of two functional dimers does not necessarily reflect the presence of two uncoupled dimers, especially in the case of S_2 where EPR data point to the presence of a magnetic tetranuclear arrangement.

Photooxidation of the OEC. It has been known for some time(39,40) that low temperature illumination of S_1 results in a shift of the XANES features to higher energy, consistent with oxidation of Mn. Although the $S_1 \rightarrow S_2$ transition is generally considered to represent a one electron oxidation of the Mn cluster, the edge shift has been reported to be as small as 0.6 eV (41) and as large as 1.8 eV (28). As shown in Figure 3, a similar shift is also seen following low temperature illumination of S_{-1} . Isostructural mononuclear model compounds show that the edge shift expected for a

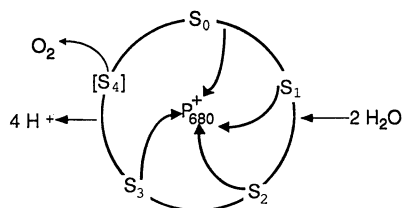


Figure 1. Kok scheme for photooxidation.

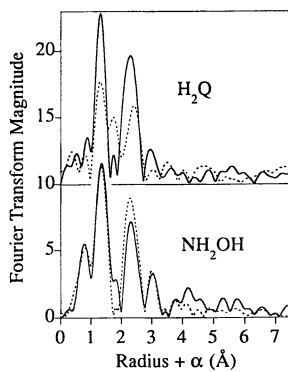


Figure 2. Fourier transforms of EXAFS spectra for control S_1 (solid lines) and for samples reduced with NH_2OH (bottom) or H_2Q (top).

Mn(III) to Mn(IV) oxidation is on the order of 2 eV. It is reasonable to expect the OEC to show an edge shift about one fourth as large (i.e., ca. 0.5 eV) when one of the four Mn ions is oxidized. All of the edge shifts in Figure 3 are consistent with this expectation. The uniform shape and features of these edges support the assignment of a Mn(III)→Mn(IV) oxidation on each transition.

Although the edge shifts due to NH_2OH and H_2Q are both fully reversible when the reduced samples are illuminated continuously at 4° C (29), only the NH_2OH reduced species can be photooxidized at 200 K (data not shown). This is consistent with the model (above) in which different reductants attack different Mn sites. The site that is reduced to Mn(II) by H_2Q is evidently not photooxidizable at low temperature, either because of the structural changes that are required for a Mn(II)→Mn(III) oxidation are blocked at 200 K or because the site that is reduced by H_2Q is too far from the redox active tyrosine Y_Z to permit low temperature photooxidation.

The Role of Ca^{2+} . The outer shell peak in Figure 2 ($R+\alpha \approx 3 \text{ \AA}$) reflects the long range structure in the OEC cluster. The relatively large intensity of the third shell peak, together with the absence of a significant number of histidine ligands (which give outer shell peaks) suggests that the third shell peak in the OEC is due to a Mn-metal interaction. The likely candidates for the metal are Mn and Ca. Although it has been reported that Mn-Ca interactions give better fits to this peak than do Mn-Mn interactions (42), it is now generally agreed that it is probably not possible distinguish Mn-Mn from Mn-Ca scattering, at least not in these samples (43,44). Although the peak can be fit with two shells (e.g. Mn-Mn+Mn-Ca), these fits were difficult to justify compared to single shell fits (44,45). This does not, of course, exclude the possibility that Mn, Ca (and potentially C) all contribute to the third shell (46,47).

In an effort to determine unambiguously whether Ca scattering contributes to the 3.3 Å feature, several groups have removed the Ca^{2+} or replaced the Ca^{2+} with other metals and determined the effect of these perturbations on the EXAFS. One such study (48), found that replacement of Ca^{2+} by Sr^{2+} gave an increase in the amplitude of the 3.3 Å interaction and that fits to the substituted data were slightly better with Sr+Mn scattering than with Ca+Mn scattering, suggesting that at least some of the outer shell scattering is due to a Mn-Ca interaction. In contrast, we found no change in the third shell peak when Ca^{2+} was replaced by Sr^{2+} , La^{3+} , or Dy^{3+} (37), as shown in Figure 4. In some cases, the fits were slightly better using Sr rather than Ca as the scatterer. However, this was true both for control samples that had never been exposed to Sr and for Sr-substituted samples, thus illustrating the difficulty in using fit quality to distinguish between fits for outer shell scattering (17). Our experiments were done in the absence of the 17 and 24 kDa extrinsic polypeptides, while these peptides were present in the other studies. If one or both peptides contributes ligands that bridge the Mn-Ca interaction, the interaction would be expected to be stronger (and thus more readily detectable) in the presence of the extrinsic polypeptides. However, this explanation is difficult to reconcile with the observation that three biochemically distinct, Ca^{2+} sufficient preparations (thylakoids, intact BBY preparations and reaction centers reconstituted with Ca^{2+}) give essentially identical EXAFS results.

Although we did not find any changes in the 3.3 Å feature, we did observe small, but reproducible, changes in the 2.7 Å peak when Ca was replaced (37). The average Mn-Mn distance decreased 0.013±0.004 Å when Ca was replaced with Sr and increased 0.015±0.004 Å when Ca was replaced with a lanthanide. This is direct evidence of a role for Ca in controlling the Mn core structure. The average Mn-Mn distance appears to increase with increasing Lewis acidity of the cation that is bound in the Ca site. The changes in $R_{\text{Mn-Mn}}$ are too small to be due to protonation (49,50) but could arise if the Mn-Mn distance is affected by hydrogen bonding, with the Ca

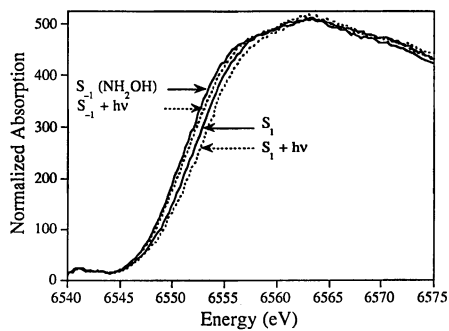


Figure 3. XANES spectra for S_{-1} , S_0 , S_1 , and S_2 .

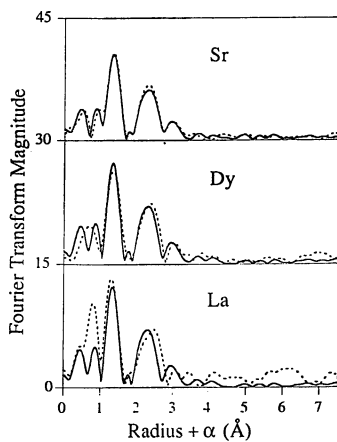


Figure 4. Fourier transforms of EXAFS data for native (solid lines) vs. Sr, Dy, and La substituted OEC.

site modulating the acidity of a proton bound near an oxo bridge of one of the di- μ -oxo bridged dimers. A Ca-(H₂O)-Mn₂O₂ hydrogen bond would explain the observation that Ca²⁺ is bound most tightly in S₁ (3), since the basicity of the oxo-bridge decreases when the Mn is oxidized (50). The change in the multiline EPR spectrum following Sr substitution would be consistent with the fact that protonation alters intradimer exchange couplings and the inability to form S₂ when lanthanides are bound at the Ca site and the stability of S₂ when Ca is depleted might be related, at least in part, to alterations in the redox potential of the Mn(μ -O)₂Mn dimers as a function variations in hydrogen bonding.

Mechanistic Possibilities

A variety of mechanisms have been suggested for water oxidation (see 4,26,51,52) but little definitive information is available. It is generally agreed that water oxidation cannot proceed in one electron steps, since these would produce high energy intermediates. If Mn is oxidized on each S-state transition, then the mechanism of water oxidation can rely on conventional Mn redox chemistry with, for example, each of the four Mn accepting one electron. If a non-manganese radical is produced in a higher S-states, e.g. S₄, fewer (perhaps only two) Mn need to be redox active. If only a single Mn dimer is redox active (4) then it most likely transfers all four electrons simultaneously. However, if all four Mn are redox active, then they can potentially be arranged to carry out either a single four-electron oxidation or two two-electron oxidations. In addition to electrons, it is also necessary to transfer four protons. Proton and electron transfer can be either sequential or concurrent, the latter representing hydrogen atom transfer. If indeed H-atom transfer is important, it is likely that this takes place at YZ (26,53). Using the finding (above) that the Mn appear to be organized into functional (if not necessarily structural) dimers, a possible scheme for water oxidation can be constructed, using standard oxidation states for Mn in all S states, with the possible exception of the transient S₄. One such scheme is shown in Figure 5.

Conclusions and Future Directions

X-ray absorption spectroscopy has made important contributions to understanding the structure and mechanism of the OEC. The ability to obtain direct structural information from a variety of different states of the OEC has been crucial for defining the Mn cluster structure. Although oxidation states are not as well defined by XANES as is molecular structure by EXAFS, the oxidation state information provided for the OEC has been crucial in defining the limits to useful structural models. As with all spectroscopies, the data from XAS are most useful when combined with data from other techniques. In particular, the availability of chemically perturbed OEC samples has been essential for interpretation of XAS results and has, to some extent, been able to overcome the inherent limitations of poor site selectivity (and consequent loss of information) in EXAFS. The future prospects for even more detailed characterization of the OEC seem bright. The expectation of better signal/noise ratio data from third generation synchrotron sources, the use of other absorption edges to improve the specificity of XAS structures (54), and the development of high-resolution x-ray spectroscopies that have the potential to give site-specific structural information (55,56) should all improve our ability to characterize the Mn site.

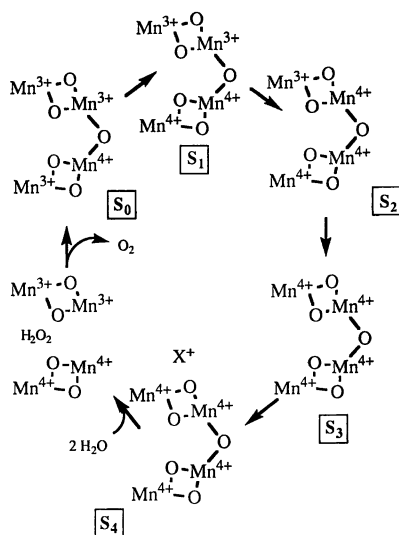


Figure 5. Possible scheme for water oxidation by the OEC based on conventional Mn oxidation states and two-electron dimer-like reactivity. The transient oxidant in S₄ is shown as X⁺; this may be as a tyrosine radical based on evidence (46,47) suggesting that H-atom transfer is important. Other states (e.g., Mn(V) could also be drawn for S₄. The water molecules that are oxidized by S₄ are shown as free in solution since XAS does not provide any direct information on their location. These are likely to be coordinated to Mn and/or Ca.

Acknowledgments

Supported in part by the NIH (GM-45205 to JPH) and the USDA Photosynthesis Program of the Competitive Research Grants Office, USDA (G-96-35306-3399 to C.F.Y.). We thank Prof. V. Pecoraro for helpful discussions. XAS data were measured at SSRL, which is supported by the US DOE, Office of Basic Energy Sciences, with additional support from the DOE Office of Health and Environmental Research and the NIH Research Resource program.

Literature Cited

- Ghanotakis, D. F.; Yocum, C. F. *Annu. Rev. Plant Physiol. Plant Mol. Biol* **1990**,
- Debus, R. J. *Biochim. Biophys. Acta* **1992**, *1102*, 269-352.
- Yocum, C. F. In *Manganese Redox Enzymes*; V. L. Pecoraro, Ed.; VCH Publishers: New York, 1992.
- Yachandra, V. K.; Sauer, K.; Klein, M. P. *Chem. Rev.* **1996**, *96*, 2927-2950.
- Joliot, P.; Barbieri, G.; Chabaud, R. *Photochem. Photobiol.* **1969**, *10*, 309-29.
- Kok, B.; Forbush, B.; McGloin, M. *Photochem. Photobiol.* **1970**, *11*, 457-75.
- Berthold, D. A.; Babcock, G. T.; Yocum, C. F. *FEBS Letters* **1981**, *134*, 231-234.
- Ghanotakis, D. F.; Demetriou, D. M.; Yocum, C. F. *Biochimica et Biophysica Acta* **1987**, *891*, 15-21.
- Lee, P. A.; Citrin, P. H.; Eisenberger, P.; Kincaid, B. M. *Rev. Mod. Phys.* **1981**, *53*, 769-806.

10. Scott, R. A. *Methods Enzymol* **1985**, *117*, 414-59.
11. Teo, B. K. *EXAFS: Basic Principles and Data Analysis*; Springer-Verlag: New York, 1986; Vol. 9.
12. Kirby, J. A.; Goodin, J. A.; Wydrynski, T.; Robertson, A. S.; Klein, M. P. *J. Am. Chem. Soc.* **1981**, *103*, 5537-5542.
13. Wong, J.; Lytle, F. W.; Messmer, R. P.; Maylotte, D. H. *Phys. Rev.* **1984**, *B30*, 5596-5610.
14. Natoli, C. R. In *Springer Series in Chemical Physics*; A. Bianconi; L. Incoccia and S. Stipcich, Ed.; Springer-Verlag: Berlin, 1983; Vol. 27; pp 43-56.
15. Rehr, J. J.; Mustre, d. L. J.; Zabinsky, S. I.; Albers, R. C. *J. Am. Chem. Soc.* **1991**, *113*, 5135-40.
16. Binsted, N.; Hasnain, S. S. *J. Synchr. Rad.* **1996**, *3*, 185-196.
17. Riggs-Gelasco, P. J.; Stemmler, T. L.; Penner-Hahn, J. E. *Coord. Chem. Rev.* **1995**, *144*, 245-286.
18. Bunker, G.; Hasnain, S.; Sayers, D. In *X-ray Absorption Fine Structure*; S. S. Hasnain, Ed.; Ellis Horwood: New York, 1991; pp 751-770.
19. Dismukes, G. C.; Siderer, Y. *FEBS Lett* **1980**, *121*, 78-80.
20. Rutherford, A. W.; Boussac, A.; Zimmermann, J. L. *New J. Chem* **1991**, *15*, 491-500.
21. Miller, A.-F.; Brudvig, G. W. *Biochim. Biophys. Acta* **1991**, *1056*, 1-18.
22. Zimmermann, J. L.; Rutherford, A. W. *Biochim. Biophys. Acta* **1984**, *767*, 160-7.
23. Casey, J. L.; Sauer, K. *Biochim. Biophys. Acta* **1984**, *767*, 21-8.
24. Messinger, J. N., J. H. A.; Evans, M. C. W. *Biochemistry* **1997**, *36*, 11055-11060.
25. Sandusky, P. O.; Yocum, C. F. *Biochim. Biophys. Acta.* **1986**, *849*, 85-93.
26. Hoganson, C. W.; Lydakakis, S. N.; Tang, X. S.; Tommos, C.; Warncke, K.; Babcock, G. T.; Diner, B. A.; McCracken, J.; Styring, S. *Photosynth. Res* **1995**, *46*, 177-84.
27. Ono, T.-a.; Noguchi, T.; Inoue, Y.; Kusunoki, M.; Matsushita, T.; Oyanagi, H. *Science* **1992**, *258*, 1335-1337.
28. Roelofs, T. A.; Liang, W.; Latimer, M. J.; Cinco, R. M.; Rompel, A.; Andrews, J. C.; Sauer, K.; Yachandra, V. K.; Klein, M. *Proc. Natl. Acad. Sci. U. S. A* **1996**, *93*, 3335-40.
29. Riggs, P., J.; Yocum, C. F.; Penner-Hahn, J. E.; Mei, R. *J. Am. Chem. Soc* **1992**, *114*, 10650-1.
30. Zheng, M. D., G. C. *Inorg. Chem.* **1996**, *35*, 3307-3319.
31. Bouges, B. *Biochim. Biophys. Acta* **1971**, *234*, 103-112.
32. Renger, G.; Bader, K. P.; Schmid, G. H. *Biochimica et Biophysica Acta* **1990**, *1015*, 288-294.
33. Messinger, J., Renger, G. *Biochemistry* **1993**, *32*, 9379-9386.
34. Radmer, R. *Biochimica et Biophysica Acta* **1981**, *637*, 80-87.
35. Guiles, R. D.; Yachandra, V. K.; McDermott, A. E.; Cole, J. L.; Dexheimer, S. L.; Britt, R. D.; Sauer, K.; Klein, M. P. *Biochemistry* **1990**, *29*, 486-96.
36. Riggs-Gelasco, P. J.; Mei, R.; Yocum, C. F.; Penner-Hahn, J. E. *J. Am. Chem. Soc* **1996**, *118*, 2387-99.
37. Riggs-Gelasco, P.; Mei, R.; Ghanotakis, D.; Yocum, C. F.; Penner-Hahn, J. E. *J. Am. Chem. Soc.* **1996**, *118*, 2400-2410.
38. Mei, R.; Yocum, C. F. *Biochemistry* **1992**, *31*, 8449-8454.
39. Yachandra, V. K.; Guiles, R. D.; McDermott, A. E.; Cole, J. L.; Britt, R. D.; Dexheimer, S. L.; Sauer, K.; Klein, M. P. *Biochemistry* **1987**, *26*, 5974-81.
40. Goodin, D. B.; Yachandra, V. K.; Britt, R. D.; Sauer, K.; Klein, M. *Biochimica Biophysica Acta* **1984**, *767*, 209-216.
41. MacLachlan, D. J.; Nugent, J. H. A.; Evans, M. C. W. *Biochim. Biophys. Acta* **1994**, *1185*, 103-11.
42. MacLachlan, D. J.; Hallahan, B. J.; Ruffle, S. V.; Nugent, J. H. A.; Evans, M. C. W.; Strange, R. W.; Hasnain, S. S. *Biochem. J* **1992**, *285*, 569-76.

43. MacLachlan, D. J.; Nugent, J. H. A.; Bratt, P. J.; Evans, M. C. W. *Biochim. Biophys. Acta* **1994**, *1186*, 186-200.
44. DeRose, V. J.; Mukerji, I.; Latimer, M. J.; Yachandra, V. K.; Sauer, K.; Klein, M. P. *J. Am. Chem. Soc.* **1994**, *116*, 5239-49.
45. Dau, H.; Andrews, J. C.; Roelofs, T. A.; Latimer, M. J.; Liang, W.; Yachandra, V. K.; Sauer, K.; Klein, M. P. *Biochemistry* **1995**, *34*, 5274-87.
46. Liang, W.; Latimer, M. J.; Dau, H.; Roelofs, T. A.; Yachandra, V. K.; Sauer, K.; Klein, M. P. *Biochemistry* **1994**, *33*, 4923-32.
47. Mukerji, I.; Andrews, J. C.; DeRose, V. J.; Latimer, M. J.; Yachandra, V. K.; Sauer, K.; Klein, M. P. *Biochemistry* **1994**, *33*, 9712-21.
48. Latimer, M. J.; DeRose, V. J.; Mukerji, I.; Yachandra, V. K.; Sauer, K.; Klein, M. P. *Biochemistry* **1995**, *34*, 10898-909.
49. Larson, E. J.; Pecoraro, V. L. In *Manganese Redox Enzymes*; V. L. Pecoraro, Ed.; VCH Publishers: New York, 1992.
50. Baldwin, M. J.; Stemmler, T. L.; Riggs, G. P. J.; Kirk, M. L.; Penner-Hahn, J. E.; Pecoraro, V. L. *J. Am. Chem. Soc.* **1994**, *116*, 11349-56.
51. Wydrzynski, T.; Hillier, W.; Messinger, J. *Physiol. Plant* **1996**, *96*, 342-350.
52. Pecoraro, V. L.; Gelasco, A.; Baldwin, M. J. *Adv. Chem. Ser.* **1995**, *246*, 265-301.
53. Gilchrist, M. L.; Ball, J. A.; Randall, D. W.; Britt, R. D. *Proc. Natl. Acad. Sci., USA* **1995**, *92*, 9545-9549.
54. Rompel, A.; Andrews, J. C.; Cinco, R. M.; Wemple, M. W.; Christou, G.; Law, N. A.; Pecoraro, V. L.; Sauer, K.; Yachandra, V. K.; Klein, M. P. *J. Am. Chem. Soc.* **1997**, *119*, 4465-4470.
55. Grush, M. M.; Chen, J.; Stemmler, T. L.; George, S. J.; C. Ralston; Stibrany, R. T.; Gelasco, A.; Christou, G.; Gorun, S. M.; Penner-Hahn, J. E.; Cramer, S. P. *J. Am. Chem. Soc.* **1996**, *118*, 65-69.
56. Grush, M. M.; Christou, G.; Haemaelainen, K.; Cramer, S. P. *J. Am. Chem. Soc.* **1995**, *117*, 5895-6.

Chapter 21

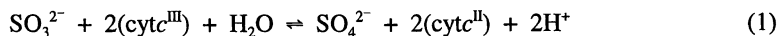
EPR and MCD Studies of Oxomolybdenum Centers in Sulfite Oxidase and Related Model Compounds

John H. Enemark

Department of Chemistry, University of Arizona, Tucson, AZ 85721

The minimal dithiolene coordination of the molybdenum center in sulfite oxidase (SO) has been modeled by $\text{LMoO}(\text{tdt})$, where L is hydrotris(3,5-dimethyl-1-pyrazolyl)borate and tdt is toluene dithiolate. The MCD spectrum shows a low-energy ($\sim 9,000 \text{ cm}^{-1}$) band that is assigned to a $S\pi\text{-Mo } 4d$ charge transfer transition, and which is consistent with the occurrence of g_{\parallel} values > 2 in the EPR spectrum. Electron spin echo envelope modulation (ESEEM) spectroscopy on the low pH and phosphate forms of SO unambiguously demonstrates that they contain Mo-OH and Mo-OPO₃ units, respectively. The crystal structure of chicken liver SO shows five-coordinate square-pyramidal geometry about the Mo atom with an axial oxo ligand; the equatorial donors are two S atoms from the dithiolene fragment of molybdopterin, a S atom from a cysteinyl residue, and an OH (or H₂O) ligand.

Sulfite oxidase (SO), an essential enzyme for sulfur metabolism in animals (1), is a member of a diverse group of enzymes that contain a mononuclear Mo center and which catalyze two-electron oxidation or reduction reactions by what is formally an oxygen atom transfer reaction (2-6). Specifically, SO catalyzes the oxidation of sulfite to sulfate with the concomitant reduction of two equivalents of ferricytochrome *c* (equation 1):



Hille (6) has subdivided this group of molybdoenzymes into three families based upon their reactivity and spectroscopic characteristics. Crystal structures are now available for at least one member of each family: aldehyde oxidoreductase (AOR) from the xanthine oxidase family (7); DMSO reductase (8-11) and formate dehydrogenase (12) from the DMSO reductase family; chicken liver sulfite oxidase (*vide infra*, 13,14) from the sulfite oxidase family. A key structural feature of each family is the coordination of the Mo atom

by the dithiolene fragment of a novel pyranopterin ligand (structure **1**). In some bacterial enzymes the phosphate group is replaced by a dinucleotide, and for enzymes in the DMSO reductase family there are two pterins per Mo atom. Dithiolene coordination of the Mo atom by a substituted pterin was originally proposed by Johnson and Rajagopalan (15). The structure of the novel pyranopterin ligand of **1** was first determined in the tungsten-containing AOR from the hyperthermophilic bacterium *Pyrococcus furiosus*, which contains two pyranopterin per tungsten atom (16).

Sulfite oxidase was first isolated, purified and shown to contain molybdenum in 1971 (17), but its X-ray structure has only recently been determined (13,14). The electronic spectrum of the enzyme is dominated by the absorptions of the *b*-type heme domain of the protein, but the Mo center has been probed directly by EXAFS at the Mo K-edge (18-20) and by EPR spectroscopy (21-25). These spectroscopic investigations of the Mo center of SO as well as recent studies of mutants of the enzyme (26) led to a proposed structure for the oxidized resting enzyme in which a dioxo-Mo(VI) center is coordinated by the dithiolene group of the novel pyranopterin (**1**) as well as a sulfur atom from a cysteinyl residue that is invariant in all SO enzymes (6,20). During turnover, SO cycles among the Mo(IV,V,VI) oxidation states; reoxidation of the enzyme by the physiological oxidant cytochrome *c* is coupled to intramolecular electron transfer from the Mo center to the *b*-type heme of SO. The paramagnetic Mo(V) state has been extensively studied by CW-EPR, and three spectroscopically distinct forms of SO have been identified: one form is obtained at high pH (9-9.5) in low concentrations of chloride or phosphate; the other two forms are observed at low pH (6.5-7) (21-24). The particular low pH form which is observed depends upon whether phosphate is present in the buffer (22). In the absence of phosphate the CW-EPR spectrum of SO gives the so-called "low pH signal" which is characterized by a hyperfine interaction with a strongly coupled exchangeable proton (assigned to a Mo-OH group) and $g_i > 2$ (22,25). For Mo(V), simple ligand field theory predicts that all $g_i < 2$ (27); the large g -value for SO and other molybdoenzymes is characteristic of sulfur coordination to Mo(V), as occurs in structure **1** (28).

Model Oxo-Mo(V) Compounds

In order to investigate the effect of a single coordinated dithiolene on the EPR parameters of an oxo-Mo(V) center, compound **2** (Figure 1) was prepared as a *minimum structural model* for **1** and the Mo center of SO (25). Comparison of the EPR parameters of **2** and of the different forms of SO (Table I) shows that this simple model closely mimics g_1 and g_2 observed for SO at low pH in the absence of phosphate, but that g_3 for the enzyme is larger than for **2**. These EPR data suggest that SO has at least three sulfur atoms coordinated to the Mo atom, as has been proposed from EXAFS (18-20) and mutation studies (26). Single crystal EPR spectra of **2** diluted in a diamagnetic host lattice of LMo(NO)(bdt) are most consistent with the orientation of the g -tensor shown in Figure 2 (29,30). Compound **2** has approximate C_s symmetry; the largest g component lies in the MoS₂ plane approximately perpendicular to the mirror plane, and the second largest component is approximately parallel to the Mo=O bond. These EPR studies of **2** confirm what has long been known; sulfur ligation of oxo-Mo(V) centers increases the g -values

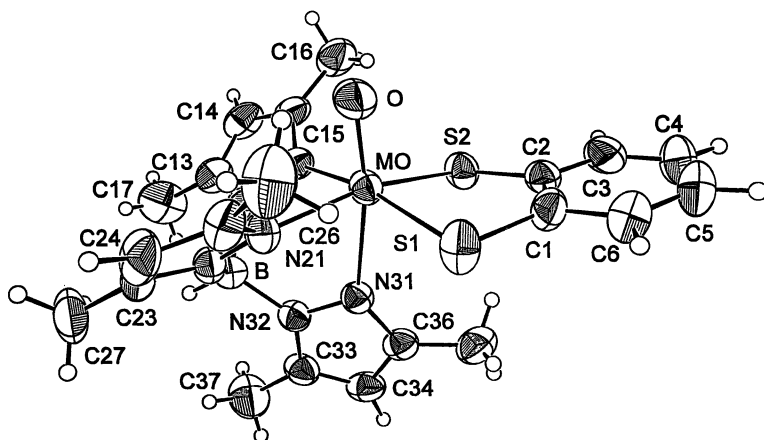
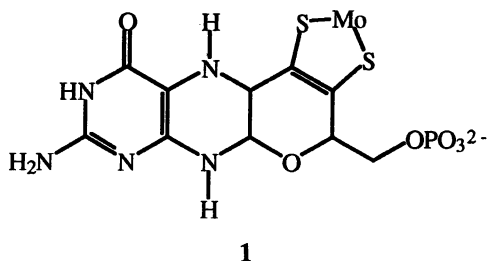


Figure 1. Perspective view of the structure of **2**; Mo-S1 = 2.368(2), Mo-S2 = 2.379(2); Mo-O = 1.678(4) Å (reproduced with permission from ref. 33. Copyright 1996 American Chemical Society).

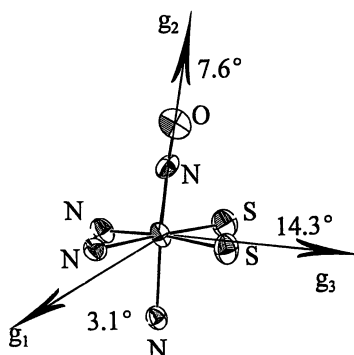


Figure 2. Orientation of the g -tensor of **2** relative to the molecular frame of LMo(NO)(tdt), the diamagnetic host for **2**. The largest component (g_1) lies approximately in the MoS₂ plane and is perpendicular to the mirror plane of the molecule; g_2 is nearly parallel to the Mo=O bond (reproduced with permission from ref. 29).

Table I EPR Data for Sulfite Oxidase and Selected Mo(V) Compounds

<i>Species</i>	g_1	g_2	g_3	$\langle g \rangle$	<i>Reference</i>
sulfite oxidase (low pH, no phosphate)	2.007	1.974	1.968	1.983	34
sulfite oxidase (low pH, phosphate)	1.962	1.970	1.993	1.975	31
sulfite oxidase (high pH, no phosphate)	1.990	1.966	1.954	1.970	34
LMO(bdt) 2	2.004	1.972	1.934	1.971	34
LMO(cat)	1.969	1.969	1.919	1.952	38

(and decreases the $A(^{95,97}\text{Mo})$ hyperfine parameters) (28). However, the EPR results alone do not provide insight concerning the features of the electronic structure of **2** that lead to large g -values.

Magnetic circular dichroism (MCD) spectroscopy is an extremely powerful technique for investigating the electronic structures of metal centers (32). Figure 3 shows the electronic absorption spectra for two isostructural oxo-Mo(V) complexes that differ in the number of sulfur atoms coordinated to the Mo atom; LMO(cat) has only oxygen and nitrogen donor atoms, whereas LMO(tdt) possesses a dithiolene ligand as in **2**. Even cursory inspection of Figure 3 shows that the coordination of a dithiolene ligand leads to a low energy absorption band (ca. 9,000 cm^{-1}) that is absent in the analogous catecholate complex. In addition, LMO(tdt) exhibits a much richer MCD spectrum than LMO(cat). These spectral differences have been rationalized by the molecular orbital energy level diagram derived from Fenske-Hall calculations (Figure 4) (33,34). These calculations indicate that the low energy band at ca. 9,000 cm^{-1} in LMO(tdt) arises from charge transfer transitions from filled sulfur $p\pi$ orbitals to the half-filled Mo 4d orbital that lies in between the ligands in the xy plane. This charge transfer band is relatively weak ($\epsilon \approx 1000 \text{ M}^{-1}\text{cm}^{-1}$) because the orbitals involved in the transition are nearly orthogonal to one another. However, these low-lying charge transfer states and spin-orbit coupling of the sulfur atoms (ca. 370 cm^{-1}) can account for one of the g_i values being greater than the free electron value ($g_e = 2.0023$) according to equation 2 (34-37). Each summation in equation 2 is over all appropriate excited states; ζ_{Mo} is the single-electron spin-orbit coupling constant for an electron in a metal d orbital; F and G are terms that depend upon the composition of the molecular orbitals in the ground and excited states and ligand spin-orbit coupling contributions; ΔE_{d-d} is the d-d transition energy and ΔE_{CT} is the energy associated with a single-electron excitation from a filled molecular orbital of mainly ligand character to the half-filled metal d orbital of the ground state. Comparable contributions from the two terms of opposite sign in equation 2 could result in $g_i > 2$ (Table I). For LMO(cat) all $g_i < 2$ because the second term in equation 2 is negligible due to the large value of ΔE_{CT} and the small spin-orbit coupling constant for oxygen (38).

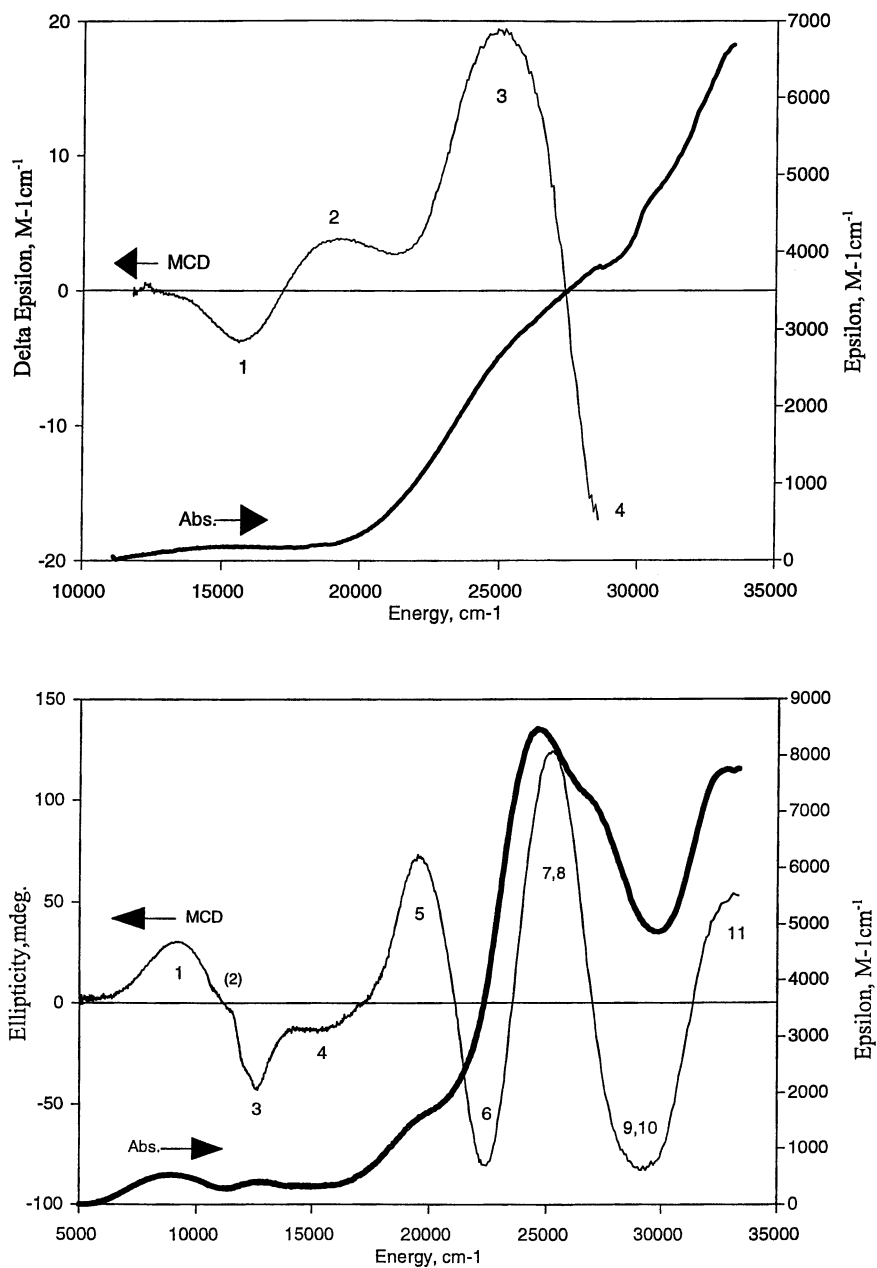


Figure 3. Electronic absorption (dark line) and MCD (light line) spectra for a) LMoO(cat) and b) LMoO(tdt) (reproduced with permission from ref. 32. Copyright 1994 American Chemical Society).

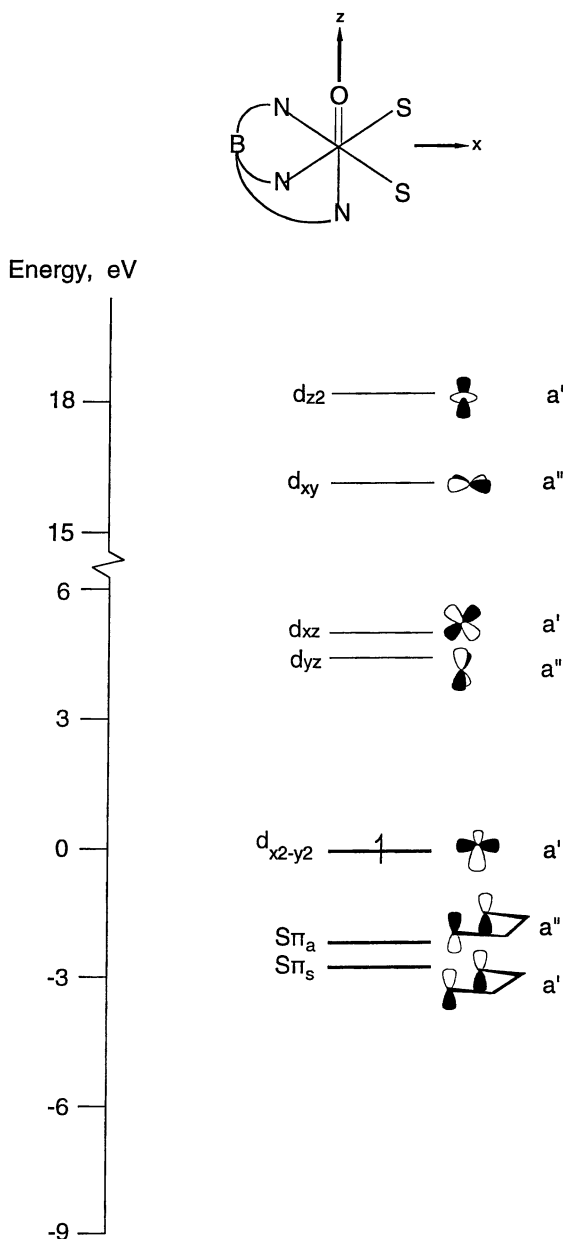


Figure 4. Partial molecular orbital energy level diagram for $\text{LMoO}(\text{tdt})$ and related compounds showing the filled sulfur $p\pi$ orbitals that can be involved in low energy charge transfer bands to the half-filled Mo 4d orbital in structures such as **2** (adapted from ref. 32 and reproduced with permission from ref. 33. Copyright 1996 American Chemical Society).

$$g_i = 2.0023 - \sum \left(\frac{\zeta_{MoF}}{\Delta E_{d-d}} \right) + \sum \left(\frac{\zeta_{MoG}}{\Delta E_{CT}} \right) \quad (2)$$

ESEEM Studies of Sulfite Oxidase

The well-known proton hyperfine splitting observed for SO at low pH in the absence of phosphate has been assigned to an Mo-OH group (22). This proton hyperfine splitting is not observed in phosphate buffer (22), and Bray and coworkers obtained evidence for coordinated phosphate from careful difference CW-EPR measurements between ^{17}O -labelled phosphate and ordinary phosphate (23). Electron spin echo envelope modulation (ESEEM) is a powerful technique for detecting and quantitating weak hyperfine and quadrupole interactions (39,40). This technique has been used here to probe in detail the Mo(V) center of SO at low pH in the presence and absence of phosphate. The ESEEM spectra of SO in D_2O at low pH are shown in Figure 5. In the absence of phosphate (top trace) several deuteron frequencies are observed, including a strong peak near 8 MHz assigned to $2\nu_D$. A detailed analysis of this $2\nu_D$ peak as a function of field using four-pulse ESEEM methods shows a deuterium quadrupole splitting of 0.28-0.30 MHz, which clearly indicates the presence of an Mo-OD group and not an Mo-OD₂ group (Raitsimring, A; Enemark, J. H.; Pacheco, A. to be published). In phosphate buffer (bottom trace) the strong peak near 8 MHz disappears and a new peak appears near 20 MHz due to $2\nu_P$, thereby providing unambiguous direct evidence for coordinated phosphate under these conditions. Multifrequency ESEEM investigations of the Mo(V) center of SO in phosphate buffer suggest that the coordinated phosphate group is monodentate and that it adopts a distribution of orientations (structure 3) (41).

Combining the ESEEM results on SO in phosphate buffer with other spectroscopic, chemical, and mutation (26) data for the enzyme lead to the structural proposal for catalysis and inhibition by phosphate shown in Scheme 1. Initially the reduced form of SO is generated by direct oxygen atom transfer to sulfite, as proposed by Brody and Hille (42). Displacement of the product, sulfate, by water is a necessary step in the regeneration of the starting Mo(VI) species. High phosphate concentrations lead to the formation of the phosphate-inhibited form of the enzyme either by direct displacement of sulfate or by funneling off the hydroxo species (41).

Structure of Sulfite Oxidase

SO is an α_2 dimer with a total mass of about 110 kDa, and each subunit contains a *b*-type heme domain and one molybdenum center (17). Preparation of diffraction quality crystals has proved to be frustratingly difficult over the years because the protein tends to form very thin plates. The preparation of ultra pure enzyme in our laboratory has finally led to crystals that diffract to 1.9 Å with the use of synchrotron radiation and has enabled the structure of chicken liver SO to be determined very recently (13,14). The approximately square pyramidal coordination geometry about the molybdenum atom is shown in Figure 6.

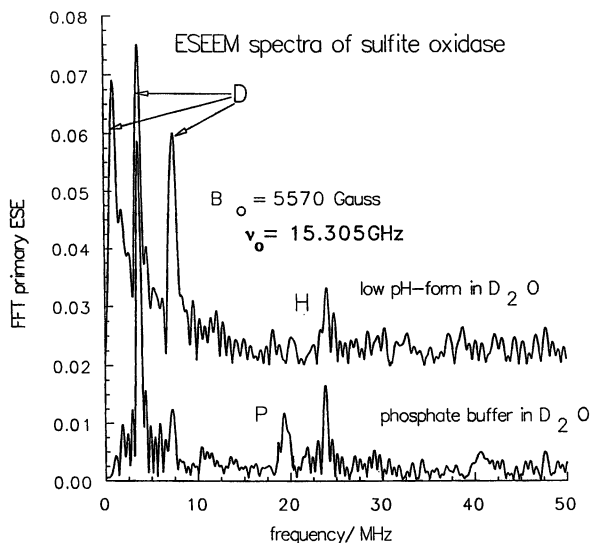
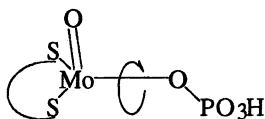
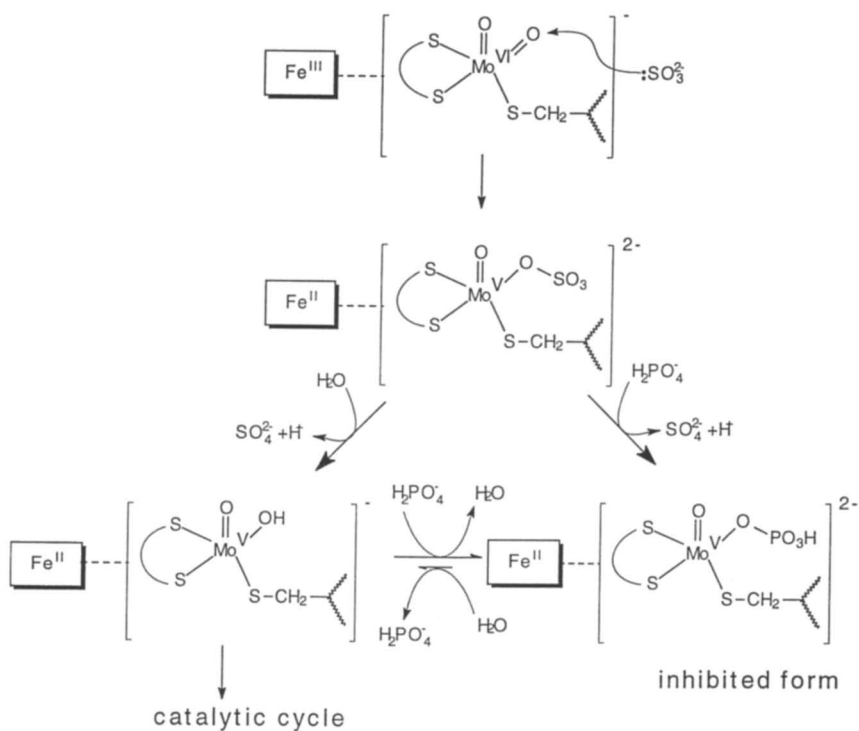


Figure 5. Two pulse ESEEM spectra of sulfite oxidase in D_2O at $pH^* = 6.5$. The top trace shows the spectrum in the absence of phosphate; the strong peak near 8 MHz is due to $2\nu_D$ of the Mo-OD group. The bottom trace shows the spectrum in phosphate buffer; the Mo-OD peak is absent and a new peak appears near 20 MHz due to $2\nu_p$ from the coordinated phosphate group.





Scheme 1.

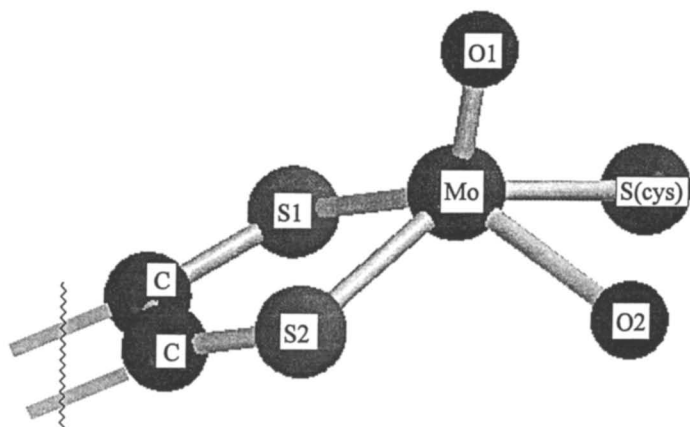


Figure 6. Coordination environment about the Mo atom in chicken liver SO; Mo-O(1) = 1.7, Mo-O(2) = 2.3, Mo-Scys = 2.5, Mo-S1 = 2.3, Mo-S2 = 2.4 Å.

A terminal oxo group (Mo=O, 1.7Å) occupies the axial position, and the equatorial positions are occupied by sulfur atoms from the dithiolene unit of the pyranopterin (1) and from a coordinated cysteinyl residue that is invariant among all sulfite oxidases and nitrate reductases (6). The remaining equatorial position is occupied by an oxygen atom (Mo-O, 2.3 Å) that is most reasonably described as a coordinated water or hydroxide. The position trans to the Mo=O group is blocked by protein residues and not accessible to solvent or anions.

The observation of two very different Mo-O distances is surprising because EXAFS studies of the oxidized resting form of the enzyme have indicated a dioxo-Mo(VI) core with an Mo=O distance of 1.71 Å (18-20). The strikingly inequivalent distances observed in the crystal structure are suggestive of a monooxo-Mo(IV) center. However, the actual oxidation state of the Mo atom in the crystals is unknown at this point, and there is no direct evidence for the active oxidized enzyme becoming reduced either during crystallization or data collection.

The proposed chemical mechanisms of SO (43), including that shown in Scheme 1, involve intramolecular electron transfer from the Mo center to the *b*-type heme center during turnover. The Mo···Fe distance in SO (32 Å) is surprisingly long considering the rates observed for turnover and intramolecular electron transfer. Moreover, the pterin ring, which has been invoked as part of the electron transfer pathway in other molybdenum-containing enzymes (7-12) is not even oriented in the direction of the *b*-type heme in SO (13,14).

Summary

Spectroscopic studies of molybdenum-containing enzymes and molybdenum model compounds have been an active area of research since the first observation of a molybdenum EPR signal from xanthine oxidase in 1959 (44). However, only in the past two years have crystal structures of these enzymes begun to become available (7-14). The very recent determination of the structure of chicken liver SO (13,14) raises questions about the actual oxidation state of the Mo atom in the crystal, the mechanism of sulfite oxidation, and the pathway for intramolecular electron transfer over the 32 Å distance between the Mo and Fe centers. As is often the case, the solution of the crystal structure of SO has raised many new questions about the structure and function of its metal centers. It has been said that bioinorganic chemistry begins when the structure of the protein is known (Solomon, E. I. private communication). Following this dictum, 1997 marks the beginning of the bioinorganic chemistry of SO.

Ligand Abbreviations

Ligand abbreviations: bdt = 1,2-benzenedithiolate; cat = catecholate; L = hydrotris(3,5-dimethyl-1-pyrazolyl)borate; tdt = toluenedithiolate.

Acknowledgments

The contributions of coworkers P. Basu, M.D. Carducci, I.K. Dhawan, A. Pacheco, E. P. Sullivan, Jr., W.A. Wehbi and B. L. Westcott to this research are deeply appreciated. I am indebted to C. Kisker, A. Raitsimring, D. C. Rees, H. Schindelin and E. I. Solomon for fruitful collaborations. Financial support from the National Institutes of Health (grant GM-37773) and the Materials Characterization Program of the University of Arizona is gratefully acknowledged.

References

1. Rajagopalan, K. V. *Nutr. Rev.* **1987**, *45*, 321-328.
2. *Molybdenum Enzymes*; Spiro, T. G., Ed.; John Wiley and Sons: N.Y., 1985.
3. *Molybdenum and Molybdenum-Containing Enzymes*; Coughlan, M.P., Ed.; Pergamon Press: Oxford, U.K., 1980.
4. Enemark, J. H.; Young, C. G.; *Adv. Inorg. Chem.* **1993**, *40*, 1.
5. Pilato, R. S.; Stiefel, E. I. In *Inorganic Catalysis*; Reedijk, J., Ed.; Marcel Dekker, Inc.: New York, 1993; p 131.
6. Hille, R. *Chem. Rev.*, **1966**, *96*, 2757-2816.
7. Romão, M. J.; Archer, M.; Moura, I.; Moura, J. J. G.; LeGall, J.; Engh, R.; Schneider, M.; Hof, P.; Huber, R. *Science* **1995**, *270*, 1170-1176.
8. Schindelin, H.; Kisker, C.; Hilton, J.; Rajagopalan, K. V.; Rees, D. C. *Science*, **1996**, *272*, 1615-1621.
9. Schneider, F.; Löwe, J.; Huber, R.; Schindelin, H.; Kisker, C.; Knäblein, J. J. *Mol. Biol.* **1996**, *263*, 53-59.
10. Bailey, S.; McAlpine, A. S.; Duke, E. M. H.; Benson, N.; McEwan, A. G. *Acta Cryst.* **1996**, *52D*, 194-196.
11. Bailey, S.; McAlpine, A. S.; McEwan, A. G.; Shaw, A. L. *J. Biol. Inorg. Chem.* **1997**, in press.
12. Boyington, J. C.; Gladyshev, V. N.; Khangulov, S. V.; Stadtman, T. C.; Sun, P. D. *Science* **1997**, *275*, 1305-1308.
13. Kisker, C.; Schindelin, H.; Rees, D. C.; Pacheco, A.; Enemark, J. H. *Abstracts, Molybdenum Enzymes Meeting*, University of Sussex, UK, April 12-15, 1997, P28.
14. Kisker, C.; Schindelin, H.; Pacheco, A.; Wehbi, W. A.; Garrett, R. M.; Rajagopalan, K. V.; Enemark, J. H.; Rees, D. C., submitted for publication.
15. Johnson, J. L.; Rajagopalan, K. V. *Proc. Natl. Acad. Sci. USA* **1982**, *79*, 6856-6860.
16. Chan, M. K.; Mukund, S.; Kletzin, A.; Adams, M. W. W.; Rees, D. C. *Science* **1995**, *267*, 1463-1465.
17. Cohen, H. J.; Fridovich, I.; Rajagopalan, K. V. *J. Biol. Chem.* **1971**, *246*, 374-382.
18. Cramer, S.P., Wahl, R., Rajagopalan, K.J. *J. Am. Chem. Soc.* **1981**, *103*, 7721.
19. George, G.N.; Kipke, C.A.; Prince, R.C.; Sunde, R.A.; Enemark, J.H.; Cramer, S.P. *Biochemistry* **1989**, *28*, 5075.

20. George, G. N.; Garrett, R. M.; Prince, R. C.; Rajagopalan, K. V. *J. Am. Chem. Soc.* **1996**, *118*, 8588-8592.
21. Bray, R. C. *Polyhedron* **1986**, *5*, 591-595.
22. Lamy, M. T.; Gutteridge, S.; Bray, R. C. *Biochem. J.* **1980**, *185*, 397-403.
23. Gutteridge, S.; Lamy, M. T.; Bray, R. C. *Biochem. J.* **1980**, *191*, 285-288.
24. Bray, R. C.; Gutteridge, S.; Lamy, M. T.; Wilkinson, T. *Biochem. J.* **1983**, *211*, 227-236.
25. Dhawan, I.K.; Pacheco A.; Enemark, J.H. *J. Am. Chem. Soc.* **1994**, *116*, 7911-7912.
26. Garrett, R. M.; Rajagopalan, K. V. *J. Biol. Chem.* **1996**, *271*, 7387-7391.
27. Mabbs, F. E.; Collison, D. *Electron Paramagnetic Resonance of d Transition Metal Compounds*; Elsevier Science Publishers B. V.: Amsterdam, 1992.
28. W.E. Cleland, Jr., K.M. Barnhart, K. Yamanouchi, D. Collison, F.E. Mabbs, R.B. Ortega, and J.H. Enemark, *Inorg. Chem.* **1987**, *26*, 1017, and references therein.
29. Westcott, B. L.; Dhawan, I.; Raitsimring, A.; Enemark, J. H. *Abstracts, 213th ACS National Meeting*, San Francisco, CA, April 13-17, 1997, poster INOR504.
30. Westcott, B. L., Jr. Ph.D. dissertation, University of Arizona, 1997.
31. George, G.N.; Prince, R.C.; Kipke, C.A.; Sunde, R.A.; Enemark, J.H. *Biochem. J.* **1988**, *256*, 307.
32. Pavel, E. G.; Solomon, E. I., this volume, and references therein.
33. Carducci, M.D.; Brown, C.; Solomon, E.I.; Enemark, J.H. *J. Am. Chem. Soc.* **1994**, *116*, 11856-11868.
34. Dhawan, I.K.; Enemark, J.H. *Inorg. Chem.* **1996**, *35*, 4873-4882.
35. Glarum, S. H.; *J. Chem. Phys.* **1966**, *41*, 1125.
36. Garner, C. D.; Hillier, I. H.; Mabbs, F. E.; Taylor, C; Guest, M. F.; *J. Chem. Soc., Dalton Trans.* **1976**, 2258.
37. Garner, C. D.; Mabbs, F. E. *J. Inorg. Nucl. Chem.* **1979**, *41*, 1125.
38. Basu, P.; Bruck, M.A.; Li, Z.; Dhawan I.K.; Enemark, J.H. *Inorg. Chem.* **1995**, *34*, 405-407.
39. Dikanov, S. A.; Tsvetkov, Yu. D. *Electron Spin Echo Envelope Modulation (ESEEM) Spectroscopy*; CRC Press: Boca Raton, 1992; chapter 1.
40. Willems, J-P.; Lee, H-I.; Burdi, D.; Doan, P.; Stubbee, J.; Hoffman, B. M., this volume, and references therein.
41. Pacheco, A.; Basu, P., Borbat, P., Raitsimring, A.M.; Enemark, J.H. *Inorg. Chem.* **1996**, *35*, 7001-7008.
42. Brody, M. S.; Hille, R. *Biochim. Biophys. Acta*, **1995**, *1253*, 133-135.
43. Sullivan, E.P., Jr.; Hazzard, J.T.; Tollin G.; Enemark, J.H. *Biochemistry* **1993**, *32*, 12465-12470, and references therein.
44. Bray, R. C.; Malmström, B. G.; Vänngård, T. *Biochem. J.* **1966**, *73*, 193.

Spectroscopic Signatures of the Fe₂O₂ Diamond Core

Lawrence Que, Jr., Yanhong Dong, Lijin Shu, and Elizabeth C. Wilkinson

Department of Chemistry and Center for Metals in Biocatalysis, University of Minnesota, Minneapolis, MN 55455

Due to the availability of synthetic precedents, the Fe₂(μ-O)₂ diamond core has emerged as an attractive candidate for the core structures of the high-valent intermediates of nonheme diiron enzymes such as methane monooxygenase and ribonucleotide reductase. Such cores have spectroscopic signatures that distinguish them from other proposed structures, particularly the Fe=O moiety associated with high-valent states of heme enzymes. The Mössbauer, Raman, and EXAFS features of the Fe₂(μ-O)₂ diamond core can be used to ascertain whether the high-valent intermediates of methane monooxygenase and ribonucleotide reductase utilize such structures to access the iron(IV) oxidation state.

Like the heme cofactor, a carboxylate-bridged nonheme diiron unit has emerged as a new common structural motif for the metal sites of a number of metalloproteins (1-4) (Figure 1). Among this class are proteins that reversibly bind dioxygen, hemerythrin and myohemerythrin (5), and enzymes that activate dioxygen such as the hydroxylase component of methane monooxygenase (MMOH) (6-8), the R2 protein of ribonucleotide reductase (RNR R2) (9,10), and stearyl-acyl carrier protein Δ⁹-desaturase (Δ⁹D) (11). Such units are also found in the metal sites of the purple acid phosphatases (12), rubrerythrin (13), and the ferroxidase component of bacterioferritin (14). Given the range of reactivities represented by these proteins, it is clear that the carboxylate-bridged diiron unit, like the heme cofactor and the iron-sulfur cluster, represents another "bioinorganic chip" (15), which Nature can employ to carry out her various functions.

Both heme and nonheme iron enzymes are involved in oxygen activation (16). It is generally accepted that heme enzymes such as cytochrome P450 and peroxidases access a formally Fe^V=O species in their catalytic cycles to effect oxidations of

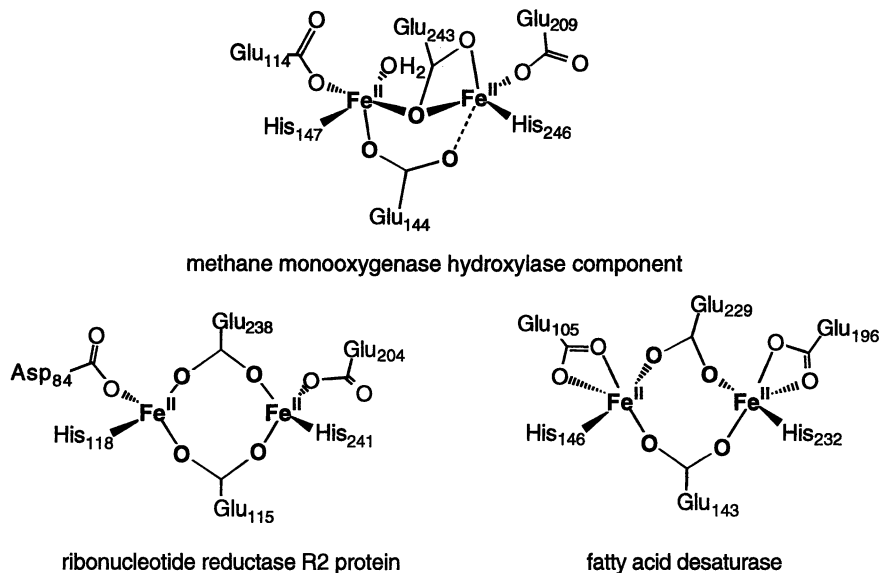


Figure 1. Nonheme diiron(II) active sites of MMOH, RNR R2, and $\Delta 9D$ as determined by x-ray crystallography (from refs 7, 10, and 11).

organic substrates (17). Direct evidence for such an intermediate has been obtained in the catalytic cycles of the heme peroxidases. For these enzymes, the high-valent intermediate is called Compound I and is better described as an oxoiron(IV) complex with a one-electron oxidized porphyrin ligand. Thus the two oxidizing equivalents implied by the Fe^V formalism are actually localized on the metal center and the porphyrin. This intermediate can carry out one- or two-electron oxidations. For cytochrome P450, this intermediate is proposed to effect the two-electron oxidation of alkanes or alkenes to alcohols or epoxides, respectively. For the peroxidases, this intermediate carries out a one-electron oxidation of substrate and is reduced to another intermediate called Compound II, which is an oxoiron(IV) porphyrin complex; Compound II in turn can effect a one-electron oxidation of another molecule of substrate.

High-valent intermediates have also been observed for the nonheme diiron enzymes. For MMOH, an intermediate called **Q**, which is kinetically competent to hydroxylate methane, is characterized as a diiron(IV) species (18-21). For RNR R2, an intermediate called **X**, which is responsible for the oxidation of Tyr122 to its catalytically essential radical form, is described as an iron(III)iron(IV) species (22-24). Thus MMOH-**Q** and RNR-R2-**X** respectively possess two and one oxidizing equivalents relative to the as isolated diiron(III) state and are analogous to Compounds I and II of the heme peroxidase cycle (17). This analogy is illustrated in the mechanistic scheme in Figure 2. In this scheme, the second iron in the nonheme diiron active site replaces the porphyrin as the repository of the second oxidizing equivalent (25).

The structures for the high-valent intermediates in the mechanisms of nonheme diiron enzymes are not yet well characterized. Early proposals for the oxygen activation mechanism invoked intermediates having a high valent iron center with a terminal oxo ligand analogous to the heme mechanism (26-28); subsequently these ideas evolved to include the $\text{Fe}_2(\mu\text{-O})_2$ diamond core structure (1-3, 25, 29) proposed in Figure 2. This notion is attractive for a number of reasons. Firstly, oxo groups are commonly used to stabilize high oxidation states. Secondly, the Fe_2O_2 unit can be construed as arising from the head-to-tail dimerization of two $\text{Fe}=\text{O}$ units, thus relating the proposed mechanistic schemes for heme and nonheme enzymes. Most importantly, complexes with $\text{Fe}_2(\mu\text{-O})_2$ cores have been synthesized by a

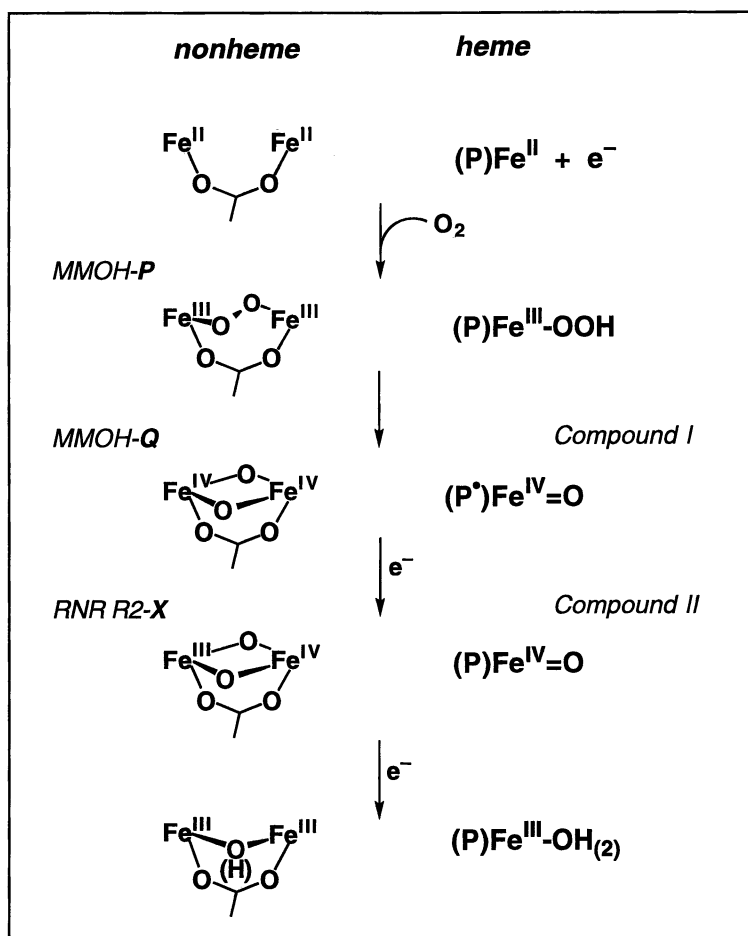


Figure 2. Comparison of mechanisms for oxygen activation by iron centers in heme and nonheme diiron enzymes.

route directly relevant to the chemistry of nonheme diiron enzymes. These complexes result from the reaction of a (μ -oxo)diiron(III) precursor with H_2O_2 , which is electronically equivalent to the reaction of a diiron(II) complex with O_2 . Three such complexes with the formula $[\text{Fe}_2\text{O}_2\text{L}_2]^{3+}$ (**1**, L = TPA; **2**, L = 5-Me₃-TPA; **3**, L = 6-Me-TPA) have been characterized (Figure 3) (30,31). The diiron centers of **1** and **2** are best described as having valence delocalized, low-spin Fe^{III} ($S_1 = 1/2$)-low-spin Fe^{IV} ($S_2 = 1$) pairs that are coupled by double exchange, affording complexes with an $S = 3/2$ ground state. On the other hand, the diiron center of **3** is an antiferromagnetically coupled high-spin Fe^{III} ($S = 5/2$)-high-spin Fe^{IV} ($S = 2$) pair, affording an $S = 1/2$ complex. The availability of these synthetic complexes allows us to determine what spectroscopic properties may uniquely characterize the $\text{Fe}_2(\mu\text{-O})_2$ diamond core.

The Fe_2O_2 core has geometric features that distinguish it from the more familiar carboxylate-bridged (μ -oxo)diiron core found in the diiron(III) forms of hemerythrin, RNR R2, and $\Delta 9\text{D}$ (1,2,4,5,9). The presence of the two oxo bridges constrains the two iron atoms to a distance of 3 Å or less, and the Fe-O-Fe angle approaches 90°. These features are illustrated by $[\text{Fe}^{\text{III}}_2(\mu\text{-O})_2(6\text{-Me}_3\text{-TPA})_2]^{2+}$ (**4**), the only crystallographically characterized example of an iron complex with an $\text{Fe}_2(\mu\text{-O})_2$ core (32). For **4**, the Fe-Fe distance is 2.71 Å, and the Fe-O-Fe angle is 92°, dimensions comparable to those observed in the crystal structures of $\text{Cu}_2(\mu\text{-O})_2$ (33) and $\text{Mn}_2(\mu\text{-O})_2$ complexes (34). However **4** differs from these latter complexes in having a rather asymmetric M-O-M unit; the Fe- μ -O bond trans to the more weakly bonded amine nitrogen is 0.08 Å shorter than the other. Furthermore its Fe- μ -O bond lengths (1.84 and 1.92 Å) are significantly longer than the mean value (1.78-1.80 Å) observed for (μ -oxo)diiron(III) complexes (35).

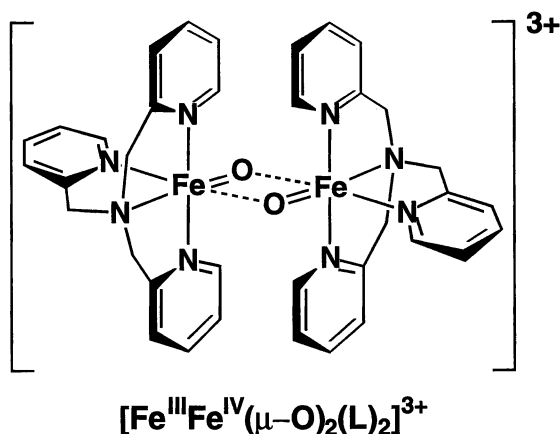


Figure 3. Proposed structure for $[\text{Fe}_2(\mu\text{-O})_2\text{L}_2]^{3+}$ complexes

Studies of **1 - 3** indicate that these complexes can be distinguished from other iron complexes with oxo ligands by their Mössbauer, Raman, and EXAFS properties. Table I compares the Mössbauer isomer shifts (δ) and quadrupole splittings (ΔE_Q) for a number of synthetic Fe^{IV} complexes with O/N ligands. There are a number of iron(IV) complexes with $S = 1$ ground states, but only three with $S = 2$ ground states. The isomer shifts span a range from -0.1 to 0.2 mm/s. The values estimated for the low-spin iron(IV) centers of **1** and **2** and observed for the high-spin iron(IV) center of **3** are in the middle of this range. Unfortunately, the limited number of iron(IV) compounds currently available makes it difficult to interpret the isomer shift values observed. What is more striking perhaps is the fact that **1 - 3** have the smallest quadrupole splittings. The magnitude of ΔE_Q reflects the asymmetry of the electronic environment around the iron center (36). With its d⁴ configuration, an iron(IV) center may be expected to have a large ΔE_Q value, by analogy to a high-spin iron(II) center. But, for reasons not evident at present, the Fe₂(μ -O)₂ cores of **1 - 3** exhibit much less anisotropy, and this feature distinguishes them from the other

Table I. Mössbauer properties of Fe^{IV} centers in proteins and model compounds

Complex	S(Fe ^{IV})	δ (mm/s)	ΔE_Q (mm/s)	ref
[Fe ^{III} Fe ^{IV} (μ -O) ₂ (TPA) ₂] ³⁺ (1)	1	~0 (0.14) ^a	0.53	30
[Fe ^{III} Fe ^{IV} (μ -O) ₂ (5-Me ₃ -TPA) ₂] ³⁺ (2)	1	~0 (0.12) ^a	0.49	30
[Fe ^{III} Fe ^{IV} (μ -O) ₂ (6-Me-TPA) ₂] ³⁺ (3)	2	0.08	0.5	31
[Fe ₂ (μ -N)(Me ₃ TACN) ₂ (Cl ₄ cat) ₂]	1	0.09	0.81	37
[Fe ₂ (μ -N)(Me ₃ TACN) ₂ (Cl ₄ cat) ₂] ⁺	1	0.04	1.55	37
[Fe ₂ (μ -O)(OEC) ₂]	1	0.02	2.35	38
[Fe(OEC)Cl]	1	0.19	2.99	38
[FeCl(η^4 -MAC*)] ⁻	2	-0.02	0.89	39
Fe ^{IV} in perovskites (O ₆)	2	-0.06 – -0.13	0.80 – 1.34	40
[Fe(O)(TMP)] ⁺	1	0.08	1.62	41
[Fe(O)(Cl ₈ TPP)] ⁺	1	0.06	1.48	41
[Fe(O)(TPP)(pyr)]	1	0.10	1.56	42
[Fe(O)(TPP)(1-MeIm)]	1	0.11	1.26	42
HRP Compound I	1	0.08	1.25	42
HRP Compound II	1	0.03	1.61	42
CCP Compound ES	1	0.05	1.55	42
MMOH-Q (<i>M. trichosporium</i>)	2	0.17	0.53	19
MMOH-Q (<i>M. capsulatus</i>)	2	0.14	0.55	21
		0.21	0.68	
RNR-R2-X (<i>E. coli</i>)	2	0.26	0.6	24

^a Estimated isomer shift for the low-spin Fe^{IV} site of the valence-delocalized Fe^{III}Fe^{IV} center based on the observed isomer shift (in parentheses) and an assumed low-spin Fe^{III} isomer shift of 0.2-0.3 mm/s

complexes in Table I. (As will be discussed later, the iron(IV) centers in the high-valent intermediates of MMOH and RNR R2 also have small ΔE_Q values.)

The $\text{Fe}_2(\mu\text{-O})_2$ core may also be expected to exhibit a characteristic core vibration. Figure 4 shows the Raman spectra of **1** and **2** upon laser excitation into the intervalence band at 616 nm. There is a prominent vibration in **1** at 666 cm^{-1} , which appears as a Fermi doublet centered at 667 cm^{-1} in **2** (**30**). This vibration is both iron- and oxygen-isotope sensitive ($\Delta^{54}\text{Fe}^{57}\text{Fe} = -3.7\text{ cm}^{-1}$; $\Delta^{16}\text{O}^{18}\text{O} = 28\text{ cm}^{-1}$) (**43**). These isotope shifts are as expected for an Fe-O harmonic oscillator model (4.0 and 29 cm^{-1} , respectively). However the energy of this vibration is too low for an Fe=O bond (ca. 800 cm^{-1} , Table II) and too high for an Fe-O bond ($450\text{-}550\text{ cm}^{-1}$). This vibration may also derive from the triatomic Fe-O-Fe unit, for which extensive studies have been conducted. Such a core typically exhibits a symmetric Fe-O-Fe stretch at $400\text{-}550\text{ cm}^{-1}$ and an asymmetric mode at $750\text{-}900\text{ cm}^{-1}$ (**44**). The energies of both modes are sensitive to the Fe-O-Fe angle and in fact extrapolate to ca. 650 cm^{-1} as the Fe-O-Fe angle approaches 90° . Since the $\text{Fe}_2(\mu\text{-O})_2$ core would have such a small Fe-O-Fe angle, the values observed for **1** and **2** fit an assignment to a triatomic vibration well. However further isotope studies demonstrate that the 666 cm^{-1} feature is a tetraatomic vibration. When ^{18}O is incorporated into only one oxygen atom of the $\text{Fe}_2(\mu\text{-O})_2$ core in **1**, an isotope shift of 22 cm^{-1} is observed.

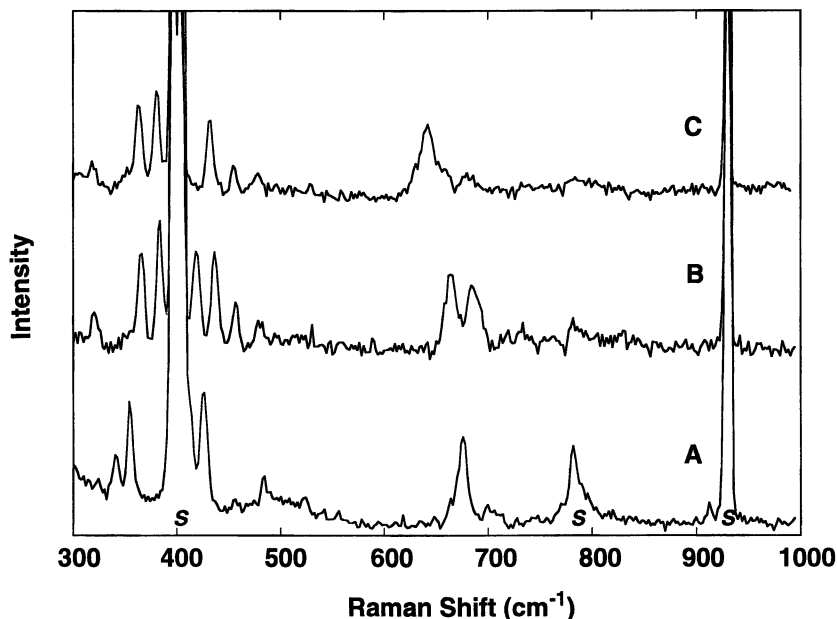


Figure 4. Raman spectra for A) **1**, B) **2**, and C) **2** + H_2^{18}O in CH_3CN . Peaks marked with "s" arise from solvent vibrations. Reprinted from reference **30**

Only for an $\text{Fe}_2(\mu\text{-O})_2$ core vibration would an intermediate isotope shift be observed. Vibrations at similar energies are found for other complexes with $\text{M}_2(\mu\text{-O})_2$ cores (Table II), supporting the notion that an oxygen-isotope sensitive vibration at this energy is a signature of the $\text{Fe}_2(\mu\text{-O})_2$ diamond core.

EXAFS spectra of complexes with the $\text{Fe}_2(\mu\text{-O})_2$ diamond core show two prominent features, one corresponding to the first coordination sphere and the other associated with an Fe scatterer (Figure 5, Table II). The intensity of the latter feature derives from the limited vibrational disorder enforced by the two oxo bridges. Similarly intense features have been found in the spectra of other complexes with $\text{M}_2(\mu\text{-O})_2$ cores (45, 46). The EXAFS analysis of **2** suggests that it has a core core structure comparable to that found crystallographically for **4**. The data can be

Table II. Raman and Structural Data for Metal-Oxo Complexes

Complex	$\nu_{\text{M-O}}$ ($\Delta^{18}\text{O}$), cm^{-1}	$r(\text{M-O})$, \AA	$d(\text{M-M})$, \AA	refs
$[\text{Fe}^{\text{III}}\text{Fe}^{\text{IV}}(\mu\text{-O})_2(\text{TPA})_2]^{3+}$ (1)	666 (-28)	n.a. ^a	n.a.	30
$[\text{Fe}^{\text{III}}\text{Fe}^{\text{IV}}(\mu\text{-O})_2(5\text{-Me}_3\text{-TPA})_2]^{3+}$ (2)	667 (-31)	1.77, (1.94) ^b	2.89	30
$[\text{Fe}^{\text{III}}\text{Fe}^{\text{IV}}(\mu\text{-O})_2(6\text{-Me-TPA})_2]^{3+}$ (3)	n.a. ^a	1.82	3.03	c
$[\text{Fe}^{\text{III}}_2(\mu\text{-O})_2(6\text{-Me}_3\text{-TPA})_2]^{2+}$ (4)	692 (-32)	1.84, 1.92	2.71	32,43
$[\text{Cu}^{\text{II}}_2(\mu\text{-O})_2(\text{Bn}_3\text{TACN})_2]^{2+}$	602, 612 (-24)	1.80, 1.81	2.79	46
$[\text{Cu}^{\text{III}}_2(\mu\text{-O})_2(\text{iPr}_4\text{DTNE})]^{2+}$	600 (-22)	1.82, 1.83	2.78	47
$[\text{Mn}^{\text{III}}\text{Mn}^{\text{IV}}(\mu\text{-O})_2(\text{bpy})_4]^{3+}$	690	1.81	2.72	48,49
$[\text{Mn}^{\text{III}}\text{Mn}^{\text{IV}}(\mu\text{-O})_2(\text{OAc})(\text{TACN})_2]^{2+}$	668, 687	1.81, 1.82	2.59	49,50
$[\text{Fe}^{\text{IV}}_2\text{O}(\text{OEC})_2]$	n.a. ^a	1.71	3.40	38
$[\text{Fe}^{\text{IV}}(\text{O})(\text{salen})]$	851 (-35)	n.a. ^a	—	51
$[\text{Fe}^{\text{IV}}(\text{O})\text{TTP}]$	852 (-34)	n.a. ^a	—	51
$[\text{Fe}^{\text{IV}}(\text{O})(\text{TMP}^*)(\text{CH}_3\text{OH})]^+$	831	1.64	—	52,53
$[\text{Fe}^{\text{IV}}(\text{O})\text{TTP}(1\text{-MeIm})]$		1.64	—	53
HRP Compound I	790 (-35)	1.64	—	53-55
HRP Compound II	788 (-31)	1.64	—	55
MMOH-Q	n.a. ^a	1.77, (2.04) ^b	2.46	56
RNR R2-X	n.a. ^a	1.77, (2.04) ^b	2.47	57

^an.a. = data not available. ^bLonger Fe- μ -O bond incorporated into the major sub-shell of the first sphere. ^cFrom an analysis of a 1:1 mixture of **3** and its (μ -oxo)diiron(III) precursor (Shu, L., unpublished results)

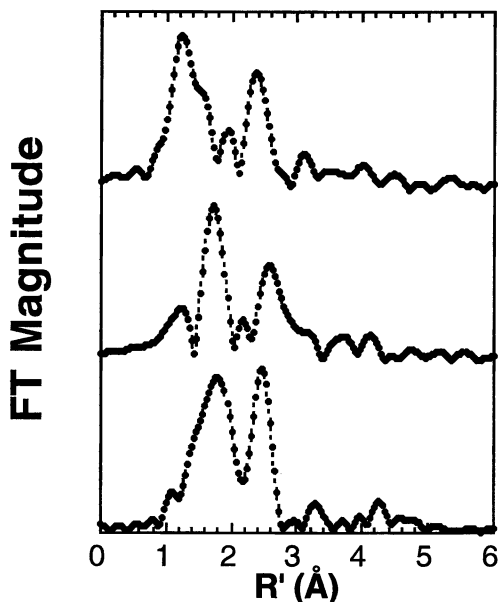


Figure 5. EXAFS spectra of **2** (top), **3** (middle), and **4** (bottom).

fit with only one short Fe-O bond per iron at 1.77 Å, with the other longer Fe- μ -O bond being included in the 1.94 Å sub-shell of the first coordination sphere. The EXAFS analysis of **3** also shows a short (1.82 Å) Fe-O bond, but the quality of the data does not allow us to establish the extent of core asymmetry at present. Interestingly, the Fe-Fe distances found for the higher-valent complexes (2.89 and 3.03 Å, respectively) are somewhat longer than that for **4** (2.71 Å), a difference that cannot yet be explained.

Because of their importance in the oxygen activation mechanisms of MMOH and RNR R2, the high-valent intermediates MMOH-Q and RNR R2-X have been investigated by a number of spectroscopic techniques, including Mössbauer and EXAFS. Resonance Raman data is not yet available for these species. A perusal of the Mössbauer data in Table I shows that the Fe^{IV} sites of MMOH-Q and RNR R2-X have unexpectedly small quadrupole splittings similar to those observed for **1** - **3**. This is in contrast to the large quadrupole splittings (> 1 mm/s) observed for the iron(IV) complexes with only one oxo ligand, be it terminal or bridging. However the Fe^{IV} isomer shifts of the enzyme intermediates are higher than those of the synthetic complexes. This may reflect differences in spin state, ligand environment, and bond covalency, as the ligand environments of **1** - **3** are nitrogen-rich, while those of RNR R2-X and MMOH-Q are oxygen-rich. Clearly, more high-spin Fe^{IV} complexes need

to be synthesized to augment the Mössbauer data base. Nevertheless the similarly small ΔE_Q values of the enzyme intermediates and the high-valent Fe_2O_2 complexes serve as the first hint that RNR R2-X and MMOH-Q may have core structures related to those of 1 - 3.

EXAFS can determine whether an Fe_2O_2 -like core is present in the enzyme intermediates. Because the intermediates cannot be generated in quantitative yield and because EXAFS analysis provides an average of all the metal environments present in the sample, it was necessary to use Mössbauer spectroscopy to determine the relative populations of the various iron species present in the samples. If an Fe_2O_2 core were present, the Fe scatterer would appear as an intense feature at a distance shorter than those associated with the other components likely to be present in the samples, i. e. the diiron(II) and diiron(III) forms of the enzymes, thus mitigating the potential uncertainty associated with analyzing a mixture.

Tandem rapid-freeze-quench Mössbauer/EXAFS experiments have been carried out on MMOH-Q (56) and RNR R2-X (57). The EXAFS spectra of the two intermediates are remarkably similar and show two prominent features. Both intermediates have one short Fe-O bond per iron at 1.77 Å. As can be seen from Table II, this bond is significantly longer than that associated with the terminal oxo ligand in high-valent oxoiron porphyrin complexes (1.64 Å) and that found for the oxo bridge in the only known (μ -oxo)diiron(IV) complex (1.71 Å). It is however comparable to those observed for the synthetic Fe_2O_2 complexes. More importantly, there is an intense feature in the second coordination sphere that is best fit with an Fe scatterer at ca. 2.5 Å. The intensity of this feature indicates a diiron unit that has at least two single atom bridges. To date the only precedent in iron chemistry for a 2.5 Å Fe-Fe distance is the mixed valence diiron(II,III) complex $[\text{Fe}_2(\mu\text{-OH})_3(\text{Me}_3\text{TACN})_2]^{2+}$ which has three hydroxo bridges (58). The high valent nature of the intermediates and the presence of a 1.77-Å Fe-O bond suggest that one or two oxo bridges are likely to be present. Figure 6 shows two structures that may be consistent with the EXAFS analyses. Structure A represents a diiron core with three single-atom bridges, with at least one being an oxo bridge. Structure B represents an $\text{Fe}_2(\mu\text{-O})_2$ core with an additional carboxylate bridge to contract the Fe-Fe distance to the appropriate value. In support of this proposed structure, the

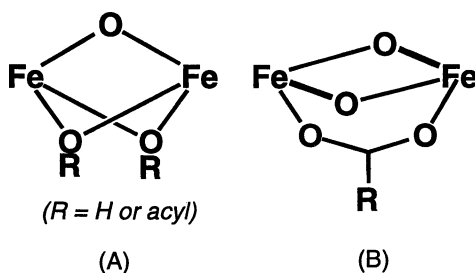


Fig. 6. Possible core structures consistent with the EXAFS analysis for MMOH-Q and RNR R2-X.

typical Mn-Mn distance of 2.7 Å in complexes with bis(μ -oxo) cores is shortened to approximately 2.6 Å upon addition of a bidentate carboxylate bridge (45,59,60). While diiron core structures with one oxo bridge and other single atom bridges such as a hydroxide and/or a monodentate carboxylate (Fig. 6A) cannot be excluded by the EXAFS data, we favor an $\text{Fe}_2(\mu\text{-O})_2$ core structure (Fig. 6B) because this is the only core thus far shown to stabilize the Fe^{IV} oxidation state in a nonheme ligand environment. Siegbahn and Crabtree also favor an $\text{Fe}_2(\mu\text{-O})_2$ core on the basis of density functional theory calculations and correctly predicted the dimensions of the diiron core in MMOH-Q (61).

In conclusion, the synthetic complexes 1 - 3 with high-valent $\text{Fe}_2(\mu\text{-O})_2$ diamond cores exhibit spectroscopic properties that distinguish them from related high-valent complexes with either a terminal oxo ligand or a single oxo bridge. These spectroscopic signatures can be used to ascertain whether such cores may participate in the high-valent chemistry of the nonheme diiron enzymes. Indeed the Mössbauer and EXAFS properties of MMOH-Q and RNR R2-X resemble those of 1 - 3. These observations, coupled with the similar EPR properties of RNR R2-X and 3 (24,31), make the $\text{Fe}_2(\mu\text{-O})_2$ core an attractive motif with which to access the iron(IV) oxidation state in these enzymes. This hypothesis needs to be tested by the synthesis and characterization of more model complexes and further spectroscopic studies on the enzyme intermediates.

Abbreviations used.

Bn_3TACN , 1,4,7-tribenzyl-1,4,7-triazacyclononane; bpy, 2,2'-bipyridine; CCP, cytochrome c peroxidase; Cl_4cat , tetrachlorocatecholate dianion; Cl_8TPP , *meso*-tetrakis(2,6-dichlorophenyl)porphinate dianion; HRP, horseradish peroxidase; iPr_4DTNE , 1,2-bis(4,7-diisopropyl-1,4,7-triaza-1-cyclononyl)ethane; MAC^* , 1,4,8,11-tetraaza-13,13-diethyl-2,2,5,5,7,7,10,10-octamethyl-3,6,9,12,14-pentaoxocyclotetradecane tetraanion; 1-Melm, 1-methylimidazole; Me_3TACN , 1,4,7-trimethyl-1,4,7-triazacyclononane; 5- $\text{Me}_3\text{-TPA}$ tris(5-methyl-2-pyridylmethyl)amine; 6-Me-TPA, (6-methyl-2-pyridylmethyl)bis(2-pyridylmethyl)amine; 6- $\text{Me}_3\text{-TPA}$ tris(6-methyl-2-pyridylmethyl)amine; OEC, octaethylcorrole trianion; pyr, pyridine; salen, 1,2-ethano-bis(salicylideneamine) dianion; TMP, *meso*-tetramesitylporphinate dianion; TPA, (tris(2-pyridylmethyl)amine); TPP, *meso*-tetraphenylporphinate dianion; TTP, *meso*-tetra-*p*-tolylporphinate dianion.

Acknowledgments.

This work was supported by the National Institutes of Health (GM-38767) and the National Science Foundation (MCB-9405723).

Literature Cited

1. Wallar, B. J.; Lipscomb, J. D. *Chem. Rev.* **1996**, *96*, 2625-2657.
2. Feig, A. L.; Lippard, S. J. *Chem. Rev.* **1994**, *94*, 759-805.
3. Que, L., Jr. In *Active Oxygen in Biochemistry*; J. S. Valentine, C. S. Foote, A. Greenberg and J. F. Liebman, Eds.; Chapman and Hall: London, UK, 1995; Vol. 3, pp 232-275.
4. Kurtz, D. M., Jr. *J. Biol. Inorg. Chem.* **1997**, *2*, 159-167.
5. Stenkamp, R. E. *Chem. Rev.* **1994**, *94*, 715-726.
6. Rosenzweig, A. C.; Frederick, C. A.; Lippard, S. J.; Nordlund, P. *Nature* **1993**, *366*, 537-543.
7. Rosenzweig, A. C.; Nordlund, P.; Takahara, P. M.; Frederick, C. A.; Lippard, S. J. *Chem. Biol.* **1995**, *2*, 409-418.
8. Elango, N.; Radhakrishnan, R.; Froland, W. A.; Wallar, B. J.; Earhart, C. A.; Lipscomb, J. D.; Ohlendorf, D. H. *Protein Sci.* **1997**, *6*, 556-568.
9. Nordlund, P.; Eklund, H. *J. Mol. Biol.* **1993**, *232*, 123-164.
10. Logan, D. T.; Su, X.-D.; Åberg, A.; Regnström, K.; Hajdu, J.; Eklund, H.; Nordlund, P. *Structure* **1996**, *4*, 1053-1064.
11. Lindqvist, Y.; Huang, W.; Schneider, G.; Shanklin, J. *EMBO J.* **1996**, *15*, 4081-4092.
12. Sträter, N.; Klabunde, T.; Tucker, P.; Witzel, H.; Krebs, B. *Science* **1995**, *268*, 1489-1492.
13. deMaré, F.; Kurtz, D. M., Jr.; Nordlund, P. *Nature Struct. Biol.* **1996**, *3*, 539-546.
14. Frolow, F.; Kalb (Gilboa), J.; Yariv, J. *Nature Struct. Biol.* **1994**, *1*, 453-460.
15. Lippard, S. J.; Berg, J. M. *Principles of Bioinorganic Chemistry*; University Science Books: Mill Valley, CA, 1994.
16. Valentine, J. S.; Foote, C. S.; Greenberg, A.; Liebman, J. F., Eds. *Active Oxygen in Biochemistry*; Chapman and Hall: London, UK, 1995.
17. Dawson, J. H. *Science* **1988**, *240*, 433-439.
18. Lee, S.-K.; Nesheim, J. C.; Lipscomb, J. D. *J. Biol. Chem.* **1993**, *268*, 21569-21577.
19. Lee, S.-K.; Fox, B. G.; Froland, W. A.; Lipscomb, J. D.; Münck, E. *J. Am. Chem. Soc.* **1993**, *115*, 6450-6451.
20. Liu, K. E.; Wang, D.; Huynh, B. H.; Edmondson, D. E.; Salifoglou, A.; Lippard, S. J. *J. Am. Chem. Soc.* **1994**, *116*, 7465-7466.
21. Liu, K. E.; Valentine, A. M.; Wang, D.; Huynh, B. H.; Edmondson, D. E.; Salifoglou, A.; Lippard, S. J. *J. Am. Chem. Soc.* **1995**, *117*, 10174-10185.
22. Bollinger, J. M., Jr.; Edmondson, D. E.; Huynh, B. H.; Filley, J.; Norton, J.; Stubbe, J. *Science* **1991**, *253*, 292-298.
23. Ravi, N.; Bollinger, J. M., Jr.; Huynh, B. H.; Edmondson, D. E.; Stubbe, J. *J. Am. Chem. Soc.* **1994**, *116*, 8007-8014.
24. Sturgeon, B. E.; Burdi, D.; Chen, S.; Huynh, B. H.; Edmondson, D. E.; Stubbe, J.; Hoffman, B. M. *J. Am. Chem. Soc.* **1996**, *118*, 7551-7557.
25. Que, L., Jr.; Dong, Y. *Acc. Chem. Res.* **1996**, *29*, 190-196.
26. Green, J.; Dalton, H. *J. Biol. Chem.* **1989**, *264*, 17698-17703.

27. Fox, B. G.; Borneman, J. G.; Wackett, L. P.; Lipscomb, J. D. *Biochemistry* **1990**, *29*, 6419-6427.
28. Que, L., Jr. *Science* **1991**, *253*, 273-274.
29. Shteinman, A. A. *FEBS Lett.* **1995**, *362*, 5-9.
30. Dong, Y.; Fujii, H.; Hendrich, M. P.; Leising, R. A.; Pan, G.; Randall, C. R.; Wilkinson, E. C.; Zang, Y.; Que, L., Jr.; Fox, B. G.; Kauffmann, K.; Münck, E. *J. Am. Chem. Soc.* **1995**, *117*, 2778-2792.
31. Dong, Y.; Que, L., Jr.; Kauffmann, K.; Münck, E. *J. Am. Chem. Soc.* **1995**, *117*, 11377-11378.
32. Zang, Y.; Dong, Y.; Que, L., Jr.; Kauffmann, K.; Münck, E. *J. Am. Chem. Soc.* **1995**, *117*, 1169-1170.
33. Tolman, W. B. *Acc. Chem. Res.* **1997**, *30*, 227-237.
34. Manchanda, R.; Brudvig, G. W.; Crabtree, R. H. *Coord. Chem. Rev.* **1995**, *144*, 1-38.
35. Kurtz, D. M., Jr. *Chem. Rev.* **1990**, *90*, 585-606.
36. Drago, R. S. *Physical Methods for Chemists, 2nd Edition*; Saunders:Fort Worth, TX, 1992; Chapter 15.
37. Jüstel, T.; Weyhermüller, T.; Wieghardt, K.; Bill, E.; Lengen, M.; Trautwein, A. X.; Hildebrandt, P. *Angew. Chem. Int. Ed. Engl.* **1995**, *34*, 669-672.
38. Vogel, E.; Will, S.; Tilling, A. S.; Neumann, L.; Lex, J.; Bill, E.; Trautwein, A. X.; Wieghardt, K. *Angew. Chem. Int. Ed. Engl.* **1994**, *33*, 731-734.
39. Kostka, K. L.; Fox, B. G.; Hendrich, M. P.; Collins, T. J.; Richard, C. E. F.; Wright, L. J.; Münck, E. *J. Am. Chem. Soc.* **1993**, *115*, 6746-6757.
40. Demazeau, G.; Chevreau, N.; Fournes, L.; Soubeyroux, J.-L.; Takeda, Y.; Thomas, M.; Pouchard, M. *Rev. Chim. Minerale* **1983**, *20*, 155-172.
41. Mandon, D.; Weiss, R.; Jayaraj, K.; Gold, A.; Ternier, J.; Bill, E.; Trautwein, A. X. *Inorg. Chem.* **1992**, *31*, 4404-4409.
42. Schulz, C. E.; Rutter, R.; Sage, J. T.; Debrunner, P. G.; Hager, L. P. *Biochemistry* **1984**, *23*, 4743-4754.
43. Wilkinson, E. C.; Dong, Y.; Zang, Y.; Fujii, H.; Fraczkiewicz, R.; Fraczkiewicz, G.; Czernuszewicz, R. S.; Que, L., Jr., submitted for publication.
44. Sanders-Loehr, J.; Wheeler, W. D.; Shiemke, A. K.; Averill, B. A.; Loehr, T. M. *J. Am. Chem. Soc.* **1989**, *111*, 8084-8093.
45. Yachandra, V. K.; Sauer, K.; Klein, M. P. *Chem. Rev.* **1996**, *96*, 2927-2950.
46. Mahapatra, S.; Halfen, J. A.; Wilkinson, E. C.; Pan, G.; Wang, X.; Young, V. G., Jr.; Cramer, C. J.; Que, L., Jr.; Tolman, W. B. *J. Am. Chem. Soc.* **1996**, *118*, 11555-11574.
47. Mahapatra, S.; Young, V. G., Jr.; Kaderli, S.; Zuberbühler, A. D.; Tolman, W. B. *Angew. Chem. Int. Ed. Engl.* **1997**, *36*, 130-133.
48. Plaskin, P. M.; Stoufer, R. C.; Mathews, M.; Palenik, G. J. *J. Am. Chem. Soc.* **1972**, *94*, 2121-2122.
49. Czernuszewicz, R. S.; Dave, B.; Rankin, J. G. In *Spectroscopy of Biological Molecules*; Hester, R. E., Girling, B., Eds.; Royal Society of Chemistry: Cambridge, UK, 1991; pp 285-288.
50. Wieghardt, K.; Bossek, U.; Zsolnai, L.; Huttner, G.; Blondin, G.; Girerd, J.-J.; Babonneau, F. *J. Chem. Soc., Chem. Commun.* **1987**, 651-653.

51. Proniewicz, L. M.; Bajdor, K.; Nakamoto, K. *J. Phys. Chem.* **1986**, *90*, 1760-1766.
52. Czarnecki, K.; Nimri, S.; Gross, Z.; Proniewicz, L. M.; Kincaid, J. R. *J. Am. Chem. Soc.* **1996**, *118*, 2929-2935.
53. Penner-Hahn, J. E.; Eble, K. S.; McMurry, T. J.; Renner, M.; Balch, A. L.; Groves, J. T.; Dawson, J. H.; Hodgson, K. O. *J. Am. Chem. Soc.* **1986**, *108*, 7819-7825.
54. Palaniappan, V.; Terner, J. *J. Biol. Chem.* **1989**, *264*, 16046-16053.
55. Kincaid, J. R.; Zheng, Y.; Al-Mustafa, J.; Czarnecki, K. *J. Biol. Chem.* **1996**, *271*, 28805-28811.
56. Shu, L.; Nesheim, J. C.; Kauffmann, K.; Münck, E.; Lipscomb, J. D.; Que, L., Jr. *Science* **1997**, *275*, 515-518.
57. Riggs-Gelasco, P. J.; Shu, L.; Chen, S.; Burdi, D.; Huynh, B. H.; Que, L., Jr.; Stubbe, J., submitted for publication.
58. Gamelin, D. R.; Bominaar, E.; Kirk, M. L.; Wieghardt, K.; Solomon, E. I. *J. Am. Chem. Soc.* **1996**, *118*, 8085-8097.
59. Pal, S.; Gohdes, J. W.; Wilisch, W. C. A.; Armstrong, W. H. *Inorg. Chem.* **1992**, *31*, 713-716.
60. Pal, S.; Olmstead, M. M.; Armstrong, W. H. *Inorg. Chem.* **1995**, *34*, 4708-4715.
61. Siegbahn, P. E. M.; Crabtree, R. H. *J. Am. Chem. Soc.* **1997**, *119*, 3103-3113.

Chapter 23

Intermediates in Non-Heme Iron Intradiol Dioxygenase Catalysis

John D. Lipscomb, Allen M. Orville¹, Richard W. Frazee², Kevin B. Dolbeare, Natesan Elango, and Douglas H. Ohlendorf

Department of Biochemistry, Medical School, and the Center for Metals in Biocatalysis, University of Minnesota, Minneapolis, MN 55455

Protocatechuate 3,4-dioxygenase (3,4-PCD) sequentially binds 3,4-(OH)₂-benzoate (PCA) and O₂ before catalyzing ring fission. Structural and spectroscopic studies show that the 3,4-PCD active site Fe³⁺ has a trigonal bipyramidal ligand coordination with axial Tyr and His and equatorial His, Tyr, and OH ligands. It is proposed from structural and kinetic data that PCA binds progressively: *i*) to the Fe³⁺ via the C4-O⁻ displacing the OH⁻, and *ii*) deeper in the site, yielding octahedral coordination geometry. Subsequently, PCA rotates so that: *i*) the C3-O⁻ becomes an equatorial ligand, *ii*) the C4-O⁻ displaces the axial Tyr to form an Fe³⁺-PCA chelate, and *iii*) rotation of the displaced Tyr opens an O₂ binding site next to PCA from which electrophilic attack on the dianionic PCA can occur. The importance of the axial Tyr ligand to catalysis is indicated by the fact that the turnover number of the Y447H mutant of 3,4-PCD is 600-fold lower than wild type. In accord with the proposed mechanism, kinetic measurements of reaction cycle intermediates showed that the decreased rate is due to slow substrate binding.

Aromatic ring-cleaving dioxygenase enzymes catalyze the key reaction in the biodegradation of aromatic compounds in which the aromatic ring itself is opened (1). Broadly, these ubiquitous enzymes fall into two structural and mechanistic categories based on the redox state of the essential active site mononuclear iron atom found in each type (2). In nearly every case, the aromatic substrates for each dioxygenase type have two OH functions in either *ortho* or *para* orientation. As illustrated in Figure 1, dioxygenases that bind Fe²⁺ catalyze ring cleavage outside of the vicinal OH groups in the catecholic substrates (extradiol cleavage) or between one OH group and another type of substituent in the gentisate-like substrates. Those that bind Fe³⁺ cleave between the

¹Current address: Institute of Molecular Biology, University of Oregon, Eugene, OR 97403.

²Current address: Department of Chemistry, The University of Michigan, Flint, MI 48502.

OH groups (intradiol cleavage) of catecholic substrates and do not metabolize gentisate-like substrates.

Unlike most other oxygenase enzymes, the redox state of the iron in ring cleaving dioxygenases is not observed to change during catalysis for either dioxygenase type. Nevertheless, these remarkable enzymes cleave the O-O bond of O₂ and insert both atoms into the substrate with ~100% efficiency. The mechanism by which this occurs in each dioxygenase type has been extensively studied (2-3). They appear to differ primarily in the strategy used to facilitate the initial interaction of the aromatic substrate and O₂. It is hypothesized that O₂ is activated for nucleophilic attack on the aromatic substrate by binding initially to the Fe²⁺ of extradiol dioxygenases (4-5), while in the intradiol dioxygenases, substrate is activated for electrophilic attack by O₂ by binding to the Fe³⁺ (6-7). The structural basis for these mechanistic hypotheses have derived largely from spectroscopic studies. However, crystal structures of representatives of both types of dioxygenase have recently appeared (8-12). Moreover, we have recently completed an X-ray crystallographic study of the structures of a range of substrate, inhibitor, and small molecule complexes of a well studied intradiol dioxygenase, protocatechuate 3,4-dioxygenase (3,4-PCD) (13-16). In this chapter, these crystallographic studies will be correlated with the spectroscopic data to build a structural model for the substrate binding and catalytic reactions of 3,4-PCD.

A Mechanism for Intradiol Cleavage Based on Kinetic and Spectroscopic Studies

Extensive optical, EPR, Mössbauer, and resonance Raman studies of 3,4-PCD have shown that the active site iron is ferric and is liganded by at least two charge donating tyrosinate ligands (2-3,17). The ligand-to-metal charge transfer (LMCT) transitions from this ligation give the enzyme a burgundy color which provides a probe both for exogenous ligand binding and for the transient formation of intermediates in the catalytic cycle. Under anaerobic conditions, 3,4-PCD was observed to bind substrate to give a new ferric species (ES) in which one or both of the OH groups bind directly to the iron. This interaction was directly detected by the occurrence of characteristic new bands in the resonance Raman spectrum occurring near 1250 cm⁻¹ (17). EPR spectra of the ES complex using substrate analogs labeled specifically in either of the two OH functions with ¹⁷O exhibited hyperfine broadening suggesting that the substrate binds to the iron through both OH functions to form a chelate complex (18). Introduction of O₂ in transient kinetic experiments revealed the occurrence of two additional reaction cycle intermediates. One intermediate, termed ESO₂, forms and decays within milliseconds after O₂ addition and exhibits a bleached optical spectrum (19). The purple second intermediate (ESO₂*) forms at the same rate as the decay of ESO₂, and then decays itself much more slowly at the turnover rate of the enzyme (19-20). Chemical quench experiments were consistent with assignment of ESO₂* as the enzyme-product complex indicating that product release is the rate limiting step overall (21).

Based on these and related observations, we proposed a mechanism for 3,4-PCD initiated by substrate activation rather than the O₂ activation typical of most oxygenase reactions (see Figure 2) (2,6-7). This was required because the Fe³⁺ would not be expected to bind O₂ directly. It was proposed that an initial substrate-Fe³⁺ chelate complex forms in which both OH functions of the catecholic substrate would be

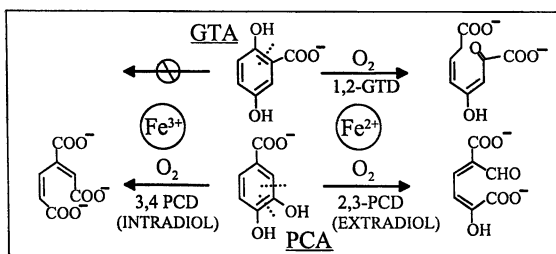


Figure 1. Aromatic ring cleavage reactions catalyzed by typical Fe^{3+} and Fe^{2+} containing dioxygenases. GTA = Gentisic Acid; PCA = Protocatechuic Acid

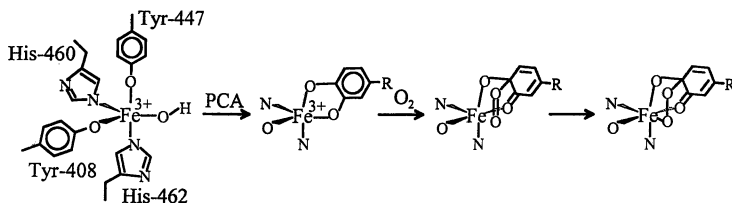


Figure 2. General proposal for the substrate activation of Fe^{3+} dioxygenases.

deprotonated (22). This would provide an anionic substrate that might serve as a site for electrophilic attack by O_2 .

The electrophilic attack would be further facilitated if the substrate were to ketonize either before attack to yield a carbanion at a specific ring carbon or after the attack to stabilize a peroxy intermediate. Ketonization would, in turn, be facilitated if the substrate were to bind asymmetrically to the iron, thus selectively weakening one Fe-O bond. The importance of ketonization was tested by synthesizing N-oxide analogs of the protocatechuate (PCA), such as 2-OH-isonicotinic acid N-oxide (INO), which ketonize spontaneously in solution (23). These analogs were not turned over, but they bound essentially irreversibly to give a final species with spectroscopic properties much like those of the bleached intermediate ESO_2 . Interestingly, the binding process was slow so that at least three intermediates could be detected. One of these spectroscopically resembled the ES complex, suggesting that the usual dianionic chelate complex forms first, followed by a complex of the ketonized adduct. This was the first indication that the substrate binding process occurs in several steps which is one of the major conclusions of the crystallographic study described below. The proposed mechanism provides an intriguing answer to how biology can activate O_2 without a reduced metal, but it also opened new questions: 1) How does the enzyme enforce a specific reaction sequence? 2) How is the putative substrate chelate made asymmetric? and 3) How does the enzyme retain the second O atom from O_2 for incorporation as required by the reaction stoichiometry? Answers to these questions are emerging from the structural and kinetic studies which reveal a fascinating story of the manner in which dynamic changes metal in ligation can be used to determine the course of enzyme reaction chemistry.

Structures of 3,4-PCD and Ligand Complexes

The x-ray crystal structure of 3,4-PCD isolated from *Pseudomonas putida* has been solved to a resolution of 2.1 Å (8-9). The holoenzyme consists of 12 protomers, each with an ($\alpha\beta Fe^{3+}$) structure. Although the active site is formed at the subunit interface, the endogenous active site Fe^{3+} ligands all derive from the β -subunit. The coordination geometry of the iron is trigonal bipyramidal with Tyr447^{On} and His462^{Ne2} as the axial ligands and Tyr408^{On}, His460^{Ne2}, and solvent Wat827 (OH⁻) completing the ligation in the equatorial plane (see Figure 3a). This ligand set results in a neutral iron center, which we believe has significance for the function of the enzymes as explained below. The OH⁻ points into a narrow cavity that extends from the iron to the surface which has the size and shape of PCA. Moreover, the residues that line the cavity complement the structure of PCA, and 5 crystallographically defined solvents in the cavity form a "ghost" of PCA in its absence (8,13). Using computational methods, the structure of PCA was "docked" in the 3,4-PCD structure so as to minimize van der Waals overlaps. This hypothetical ES complex structure predicts that PCA will bind so that the plane of its aromatic ring is aligned approximately along the axial direction of the Fe^{3+} coordination and the PCA^{4O-} group will bind to the iron in place of the solvent. The PCA^{3OH} group is predicted to bind out of bonding distance in a small H-bonding pocket below the iron. This prediction contradicts the spectroscopic studies that predict a PCA- Fe^{3+} chelate, thus a structural change upon substrate binding seemed likely.

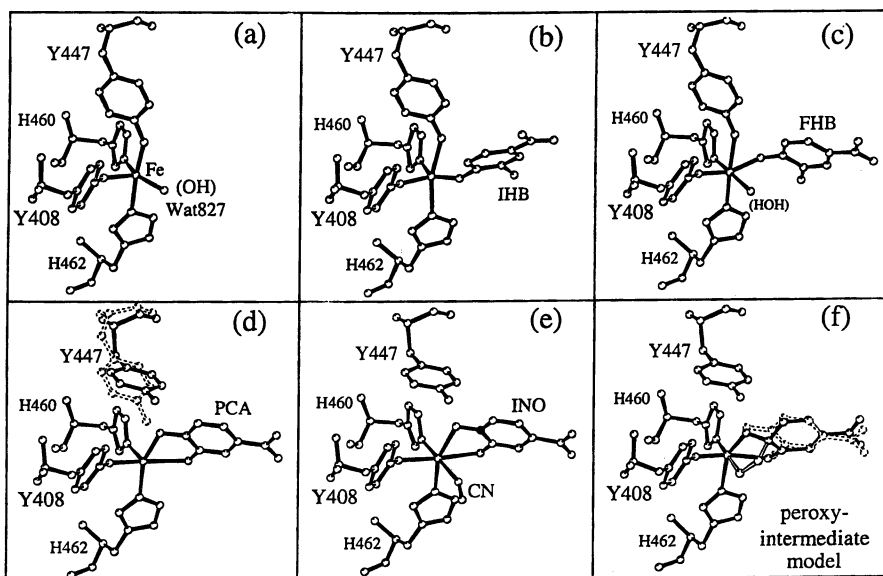


Figure 3. X-ray crystal structures of the active site region of (a) *P. putida* 3,4-PCD and 3,4-PCD complexed with inhibitors: (b) 3-I,4-OH benzoate, (c) 3F,4-OH benzoate. Also shown are: (d) anaerobic 3,4-PCD-PCA complex (original position of Tyr447 is shown in dashed lines) and (e) 3,4-PCD complex with INO (added first) and CN⁻. Panel (f) shows an energy minimized hypothetical model for the peroxy intermediate (PCA is superimposed in dashed lines). Adapted from reference (14).

Structures of 3,4-PCD-Inhibitor Complexes. A large number of PCA analogs bind in the active site but are not turned over. The structures of seven of these inhibitor complexes were recently determined at 2.0–2.2 Å resolution to investigate the substrate binding process (13). Depending upon the substituents present on the aromatic ring, several possible binding orientations were observed. For example, as shown in Figure 3b, 3-I,4-OH-benzoate (IHB) binds in a position similar to that predicted by the PCA docking calculation described above. The IHB^{4O-} group binds to the iron in place of solvent while the IHB¹ binds in the hydrogen binding pocket below the iron. In contrast, 3-F,4-OH-benzoate (FHB) (Figure 3c) binds significantly deeper in the active site pocket, presumably due to less steric interference from the smaller halide substituent. The halide still binds in the hydrogen bonding pocket, but it is positioned to form stronger hydrogen bonds with Arg457 and Gln477. The FHB^{4O-} binds to the iron as in the IHB complex, but instead of displacing the solvent, the iron coordination is converted to 6-coordinate octahedral and the solvent is not displaced. This is readily rationalized by the fact that the trigonal bipyramidal iron coordination of the resting enzyme has a relatively open iron coordination face due to the 140° His460^{Ne2-}–Fe³⁺–Wat827^{OH} bonding angle in the equatorial plane. When the inhibitor can penetrate the active site sufficiently, the 4-OH group can insert into this open face to yield octahedral symmetry. Inhibitors that bind in this way have very little solvent exposed surface area, consistent with their very high affinities.

Structures of 3,4-PCD-Substrate and Transition-State Analog Complexes. A different type of change in the iron coordination is caused by the binding of substrates (such as PCA or homoprotocatechuate (HPCA)) and transition state analogs (such as INO). The structures of 6 of these complexes were determined at 2.1–2.2 Å resolution (14). Relative to the binding orientation of FHB, molecules like PCA appear to rotate about 18° around the C1 carbon to bring the C3–O⁻ group into the equatorial plane of the iron coordination and the C4–O⁻ into the axial position (Figure 3d). This, in turn, forces the displacement of Tyr447 which rotates ~90° and hydrogen bonds to both Tyr16 and Asp413. Although there are a few other cases where the loss of an endogenous iron ligand in a nonheme system is suspected, this is now the best characterized example. The binding process yields PCA chelated to the iron as a dianion in accord with the spectroscopic studies. Analogous dramatic changes in the iron coordination are caused by HPCA (15) or INO (14) binding.

As the Tyr447 rotates away from the iron, space is created around the usual equatorial site of solvent binding. Nevertheless, solvent is not present in this site in the PCA and HPCA complexes. In contrast, it is present in the INO complex as indicated by the spectroscopic studies using ¹⁷O-enriched solvent (7) and the crystal structure. This is apparently not a steric effect because the INO and PCA binding orientations are essentially indistinguishable (14). It seems likely that a tendency to maintain the same neutral charge as found in the resting enzyme is the cause of the difference in the iron ligation. Substrate binding as a dianion, in combination with anionic Tyr408, gives the Fe³⁺ a neutral overall charge, while INO binding as the ketonized tautomer does not. Presumably solvent binds as OH⁻ in the INO complex to reestablish a neutral center.

Structure of 3,4-PCD-INO-CN Complexes. The creation of an empty site adjacent to the iron and the substrate in the protein leads readily to the hypothesis that this site is used to bind O₂ during the catalytic cycle. This would place the O₂ immediately over the bond into which it will insert during the reaction and immediately next to an open iron coordination site that could be used to bind the terminal oxygen of the putative peroxy-intermediate so that dioxygenase stoichiometry could be enforced. Moreover, the creation of this site as a result of substrate binding would provide a structural basis for the observed ordered reaction mechanism in which the substrate binding must precede O₂ binding to the enzyme.

Although the oxygen complex itself is not sufficiently stable for structural studies, the possibility that the new cavity is used to bind small molecules can be tested by determining the structure of the 3,4-PCD-INO-CN⁻ complex (Figure 3e). The analogous 3,4-PCD-PCA-CN⁻ complex has been well characterized kinetically and spectroscopically (7,18) but is also not sufficiently stable for crystallographic study. In this case, CN⁻ binds in two kinetically well resolved steps resulting ultimately in an S=1/2 complex in which CN⁻ occupies multiple ligand sites and displaces PCA. In the high spin S = 5/2 intermediate complex, however, PCA remains bound and only a single CN⁻ associates. The same kinetic phases are observed when INO is used in place of PCA. The 2.1 Å crystal structure of the 3,4-PCD-INO-CN⁻ complex shows that the CN⁻ does bind in the new cavity, but it is coordinated to the iron as expected due to the affinity of CN⁻ for Fe³⁺ (14). It is interesting to note that the Fe-C≡N bonds are not linear in this complex due to constraints within the cavity. This weakens the Fe-CN bond, accounting for the lack of hyperfine coupling from ¹³CN in the complex in spectroscopic studies (Orville, A. M.; Lipscomb, J. D., unpublished data). However, it supports the hypothesis illustrated in Figure 3f that the cavity is designed to stabilize an intermediate Fe-O-O-PCA complex which would preferentially adopt a bent Fe-O-O bond.

Asymmetry in the Binding of Substrates. One intriguing and mechanistically relevant aspect of the 3,4-PCD-substrate complex is the observation that the Fe³⁺-PCA^{3O-} bond is longer (2.41 Å) than the Fe³⁺-PCA^{4O-} bond (2.16 Å) (14). This asymmetry might derive, in part, from the fact that one ligand is axial and the other equatorial in an octahedral ligation, however, the difference in bond length seems too large for this to be the primary explanation. It is more likely that the asymmetry derives primarily from *trans* influences of the endogenous iron ligands. The negative Tyr408^{On} opposite the PCA^{3O-} would tend to lengthen the PCA-Fe bond more than would the neutral His^{Ne2} bond opposite PCA^{4O-}. There are no appropriate model complexes to test the *trans* influence of tyrosinate, however, Fe³⁺ chelate complexes with tertiary amine and carboxylate ligands *trans* to 3,5-di-*tert*-butyl catechol exhibit marked asymmetry in the iron-catechol bond lengths that has been attributed to the *trans* influence (24). The mechanistic consequence of this asymmetry would be that the PCA^{3O-} would have a greater tendency to ketonize, and therefore initial electrophilic attack by O₂ would be directed to the PCA^{C4} where negative charge would develop. An important confirmation of this observation is found in the 3,4-PCD-HPCA structure which is similarly asymmetric (15). However, in this case, it proved impossible to crystallographically distinguish between two HPCA orientations related by an ~180° flip of the aromatic ring. Thus, it was unclear whether the short Fe-HPCA bond was formed with the 3- or

the 4-O⁻. As shown in Figure 4, this was resolved using resonance Raman spectroscopic data from the *Brevibacterium fuscum* 3,4-PCD-HPCA complex. This showed low frequency vibrational bands between 500 and 650 cm⁻¹ as well as a band at ~1320 cm⁻¹ that arise from Fe-HPCA⁰ vibrational modes and a catechol ring mode, respectively. These bands are diagnostic of a HPCA•Fe³⁺ chelate complex (15). ¹⁸O-Labeling of HPCA at either the C-4 or C-3 OH group unambiguously established which band in the 500-640 cm⁻¹ region was associated with each Fe-HPCA⁰ ligand. This showed that the Fe³⁺-HPCA⁴⁰⁻ bond is stronger and therefore shorter than the Fe³⁺-HPCA³⁰⁻ bond indicating that HPCA binds in the same orientation as PCA in the active site. It also demonstrates that the chelate structure and asymmetric binding of substrates pertain to the enzyme in solution as well as in the crystalline state.

A Modified Mechanism Based on the Structural and Spectroscopic Data

The simple mechanism described above can be expanded to encompass the new structural and spectroscopic data as shown in Figure 5. Based on a comparison of the hypothetical "docked" substrate complex and the actual structures of many inhibitor and substrate complexes, it is proposed that the substrate binds in at least three sequential steps which can be described as: *i*) initial weak association with protein in the active site, perhaps involving a bond to the iron through the PCA⁴⁰⁻ with release of the OH⁻ ligand, *ii*) a shift to a position deeper in the active site where strong association with the Fe³⁺ is possible, resulting in conversion of the Fe³⁺ coordination to octahedral and perhaps the return of solvent as neutral H₂O in the new sixth coordination site, and finally, *iii*) rotation into a chelate structure with displacement of the axial Tyr447 and solvent resulting in the creation of a pocket for O₂ binding. Because the ring opening reactions of the dioxygenases are highly specific, it is likely that electrophilic attack of O₂ is directed toward a specific ring carbon of the substrate. The structural models indicate that this specificity derives, at least in part, by the positioning of the putative O₂ binding pocket over the site of ring cleavage between C3 and C4 of the substrate. The asymmetry in the chelate structure apparently caused by the nature of the ligands *trans* to the substrate phenolates favors attack at the C4 position. This mechanism does not require that the iron be reduced. However, the spin forbidden nature of the direct attack of triplet O₂ on the singlet organic substrate would be relieved if some electron density were transferred to the iron, giving the aromatic ring radical character (3). The alternative mechanism in which the radical character of the substrate is developed by a two step reaction in which superoxide is generated in the first step is illustrated in Figure 5.

A Test of the Mechanism Based on CN⁻ and NO Binding to Reduced 3,4-PCD

Although 3,4-PCD is active in the Fe³⁺ (S = 5/2) state, the active site iron can be chemically reduced to the Fe²⁺ (S = 2) state (3,4-PCD¹). This state is readily reoxidized by O₂, but it can also bind NO to give an S = 3/2 species with a characteristic EPR spectrum (25). If the substrate complex with 3,4-PCD¹ is formed before addition of NO, then a markedly different S=3/2 species is formed with much larger rhombicity evident in the EPR spectrum suggesting that the nitrosyl complex is significantly altered when substrate is also bound to the iron. Remarkably, if NO is added first, then the

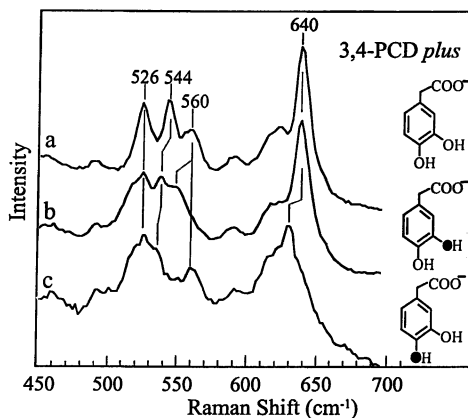


Figure 4. Shown are the low energy resonance Raman features arising from metal-ligand vibrational modes. Shifts engendered by labeling with ^{18}O (filled letters) identify the modes associated with the HPCA^{3-} (560 cm^{-1}) and the HPCA^{4-} (640 cm^{-1}) substituents. The bands at 526 cm^{-1} and 544 derived from the uncomplexed enzyme and a combination mode of the chelated catecholate- Fe^{3+} , respectively. Adapted from reference (15).

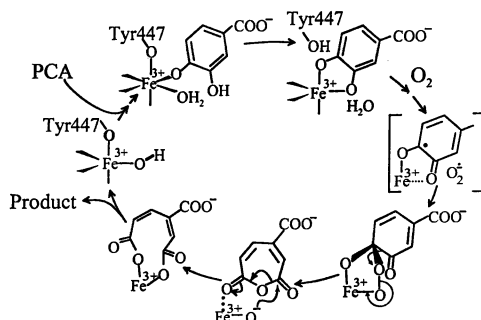


Figure 5. Proposed mechanism for 3,4-PCD and intradiol dioxygenases.

addition of substrate has no effect on the EPR spectrum. Similar order dependence is observed for the binding of CN^- and NO to 3,4-PCD' (16). Initial binding of NO leads to the usual $S = 3/2$ complex independent of the presence or absence of CN^- , but initial binding of CN^- yields a unique $S = 1/2$ species after NO is bound. Once this complex is formed, addition of substrate analogs such as INO give $S = 3/2$ type spectra characteristic of the complex formed in the absence of CN^- when the substrate-like molecule adds before NO . Thus, it appears that CN^- can be displaced by the substrate-like molecule without displacing NO because NO rebinding from solution would presumably exclude all other molecules from the iron. The $S = 1/2$ species gives 3 EPR resonances near $g = 2$ similar to those observed for the NO complex of many heme proteins. As shown in Figure 6, highly resolved hyperfine splitting is observed in each resonance for $^{14/15}\text{NO}$, ^{14}N -His (from the histidine ligands), ^{57}Fe , and ^{13}CN demonstrating that each of these is directly associated with the electronic spin. Interestingly, the EPR spectrum for the complex formed with $^{13}\text{CN}^-$ cannot be simulated by assuming a single binding site for CN^- . As illustrated in Figure 6, two scenarios give good simulations: *i*) CN^- may bind with approximately equal affinity in either of two ligand positions, only one of which exhibits hyperfine coupling to the electronic spin, or *ii*) CN^- may bind simultaneously in two positions that have almost equal hyperfine coupling values. This problem was addressed by forming the complex with a 1:1 mixture of $^{12}\text{CN}^-$ and $^{13}\text{CN}^-$. Simulations indicated that the two possibilities would give quite different EPR spectra under these conditions and the results showed that the second scenario described the predominant form of the complex (compare Figure 6C and D). This shows that three sites in the Fe^{2+} coordination can be occupied simultaneously by exogenous ligands when only a single site seems to be available from the structural studies, suggesting that a conformational change similar to that observed in response to substrate binding to the Fe^{3+} enzyme has occurred to expose these sites in 3,4-PCD'.

In the context of the mechanistic model presented in Figure 5, the observed binding behavior of CN^- and NO can be rationalized under the assumption that the neutral charge of the 3,4-PCD metal center in the resting Fe^{3+} enzyme will tend to be maintained following ligand exchange (Figure 7). In the case of the 3,4-PCD', the metal has one less positive charge, and thus, should preferentially bind one less negatively charged ligand to maintain neutrality. This would most reasonably be effected by binding water rather than OH^- in the solvent site. The subsequent binding of CN^- in this equatorial site opposite Tyr408 would create a -1 charged center which could be returned to neutrality by dissociation of Tyr447 as occurs in the Fe^{3+} form of the enzyme when substrate binds as a dianion. In the Fe^{3+} enzyme, this conformational change also shifts the iron coordination to octahedral and creates two more coordination sites, one *trans* to each of the His ligands. Binding of NO in the putative O_2 binding site opposite His460 would account for the strongly coupled $I = 1$ ligand revealed by the superhyperfine splitting of the $S = 1/2$ EPR spectrum. Once bound in this protected site, the NO apparently does not dissociate. In contrast, the CN^- is bound in the main solvent accessible substrate binding channel where it could readily dissociate. Moreover, the second site that is proposed to be opened as a result of CN^- binding is normally occupied by an anion (either tyrosinate or catecholate), and thus it may bind the second CN^- revealed by the spectroscopic data. The subsequent binding of INO would be expected to displace both of the CN^- molecules because these are in the sites that INO occupies

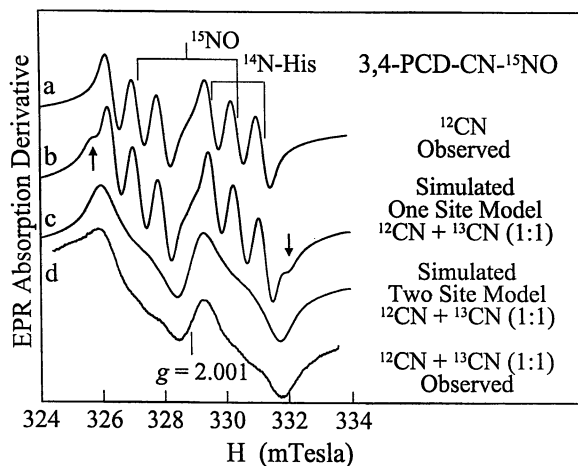


Figure 6. EPR spectra of 3,4-PCD-CN-NO complexes. Only the central resonance is shown. The carbon isotopes of CN⁻ present and their relative abundance are shown on the figure. Spectra (b) and (c) are simulations of two models for CN⁻ binding described in the text. Adapted from reference (16).

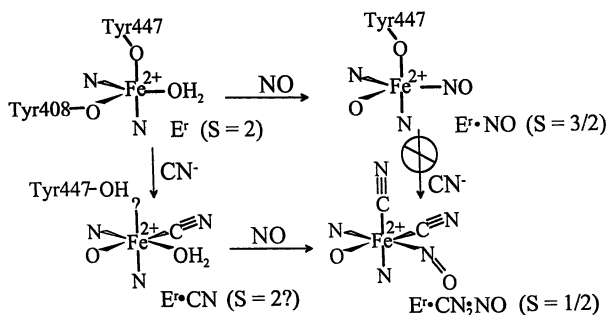


Figure 7. Model for the binding of CN⁻ and NO to reduced 3,4-PCD (E). Adapted from reference (16).

in the ferric enzyme complex (14). The resulting complex would simply be the 3,4-PCD⁻-INO-NO complex as indicated by the $S = 3/2$ EPR spectrum. Since INO is known to bind in the ketonized configuration to 3,4-PCD (23), it would provide only one anionic ligand for the iron as required to maintain charge neutrality. This complex would presumably be more stable than the 3,4-PCD-(CN)₂-NO complex which would have a -1 charge unless one of the cyanides or the NO is protonated.

The binding of NO before CN⁻ would presumably occur in the equatorial plane in the site proposed above for initial cyanide binding because it is the only site available prior to the conformational change. This would result in the displacement of the neutral solvent by another neutral ligand (NO[•]). In addition, the transfer of electron density to the NO molecule from the iron which produces the observed $S = 3/2$ species would not favor the release of the axial Tyr447. Thus, neither of the potential two new sites in the iron coordination would be created. If this iron-NO bond is very stable, its formation would exclude all other ligands in accord with our observations.

A Test of the Mechanism Based Site Directed Mutagenesis of 3,4-PCD

Both the crystallographic and spectroscopic data suggest that Tyr447 undergoes a major reorientation as substrate binds. We hypothesize that this plays a role in both substrate deprotonation and creation of a specific O₂ binding site. If this is correct, then change of this residue should affect catalysis. The two genes for 3,4-PCD from *P. putida* were recently cloned and overexpressed making mutagenesis possible (26). Several mutations were made in the Tyr447 position, but the change to histidine (Y447H) gave a stable protein that could be studied in detail (Frazee, R. F.; Orville, A. M.; Dolbeare, K. D.; Yu, H.; Ohlendorf, D. H.; Lipscomb, J. D., submitted for publication). The mutated enzyme was found to bind Fe³⁺ in more of the available protomers (~10 of 12) than is typically observed for wild type enzyme (~6 of 12), and the K_M values for PCA and O₂ were lower than those observed for wild type. However, the turnover number was decreased by ~600 fold showing that some aspect(s) of the reaction was dramatically altered. The optical spectrum showed a decrease in absorbance in the 450 nm region consistent with the loss of one of the Tyr-to-Fe³⁺ LMCT bands. When the anaerobic complex with PCA was formed, however, the optical spectrum was found to be nearly indistinguishable from that of the wild type ES complex. This is consistent with the conclusion that Tyr447 is displaced in this complex, and thus the wild type and Y447H enzyme complexes should have the same iron ligands.

The step or steps that are slowed down in the reaction cycle of the mutated enzyme were determined using stopped flow transient kinetic techniques. As shown in Figure 8, anaerobic mixing of Y447H with substrate revealed at least two intermediates that occur before the formation of the final stable substrate complex. Moreover, the rate of each of the observed kinetic phases was independent of PCA concentration, suggesting that a third intermediate species is formed essentially irreversibly at short times. It is possible that these intermediates also occur in the wild type enzyme, but they decay too rapidly to be observed. As described above, we proposed from structural studies that substrate binding occurs in several steps (14). One important reason for these steps is to progressively deprotonate PCA so that it can undergo electrophilic attack by O₂. It is possible that in the mutated enzyme, the absence of Tyr447 to act as

a good base to assist in this deprotonation of substrate decreases the rate of substrate binding sufficiently that the intermediates can be directly observed.

The rate of the final step leading to the stable Y447H-PCA complex is approximately equal to the turnover number for catalysis. Thus, the rate limiting step of is shifted in Y447H turnover from product release to substrate binding. Most importantly, mixing of O_2 with the preformed Y447H-PCA complex rapidly gives a species with an optical spectrum that is essentially identical to that of the ESO_2^* complex of the wild type enzyme reaction cycle (19-20) thought to be the product complex. Thus, the chemical steps after substrate binding and before product release remain fast. Since Tyr447 is proposed to be released from the iron during these steps, it is reasonable that the wild type and mutated enzymes should behave similarly.

The decay of the Y447H ESO_2^* complex also occurs in at least two phases, in contrast to the decay of the wild type intermediate which occurs in only one observed phase. This indicates that a new intermediate is also stabilized in the product dissociation phase of the cycle. Like substrate binding, product release is much slower in Y447H than in the wild type enzyme, but it is not slowed as much as the PCA binding steps, accounting for the shift in the rate limiting step. This suggests that Tyr447 also plays some role in product dissociation. It is reasonable that the two new carboxylate groups of the product may remain bound to the Fe^{3+} after ring cleavage to maintain charge neutrality. Product displacement may be facilitated by return of the Tyr447 to the iron resulting in protonation of one of the carboxylates. The intermediates and rate of conversion for Y447H are compared with those of wild type in Figure 9.

Charge Neutrality in the Y447H Mutated Enzyme

The crystal structure of Y447H was determined at a resolution of 2.1 Å and the active site region is shown in Figure 10. The overall structure of the mutated enzyme is not distinguishable from that of the wild type enzyme and all the changes are localized in the active site. The new His in position 447 is not bound to the iron and is stabilized about halfway between the liganding position and the alternate binding position of Tyr447. After refinement, some unassigned electron density near the iron is apparent in the $|F|_o - |F|_c$ maps that could not be assigned to solvent. Trial fitting of the density with several possible molecules showed that it was fit best by $(H)CO_3^-$. If this molecule is actually carbonate, then the mutated enzyme has restored both the 5-coordinate iron site and the charge neutrality of the wild type enzyme by binding a single ligand.

Conclusion

Examination of the spectroscopy, structure, and structural changes that pertain to 3,4-PCD reveals an excellent example of the way in which an enzyme can control the reactivity of a metal through static and dynamic control of its ligation. The ligation of 3,4-PCD Fe^{3+} not only stabilizes the metal binding but also facilitates the activation of substrate. It provides both bases required to deprotonate the substrate thereby promoting reaction with O_2 . Additionally, by controlling the nature of the *trans* ligands, the position of O_2 attack is selected. The protein structure beyond the Fe^{3+} ligation also plays important roles such as the alignment of the aromatic ring so that PCA is forced

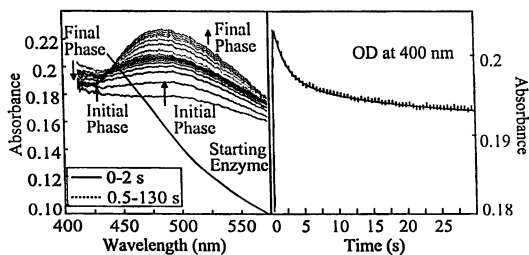


Figure 8. Left: Rapid scan stopped flow spectra recorded during the binding of PCA to Y447H under anaerobic conditions at 25 °C. Spectra were recorded at 20 ms and 500 ms in the early and late parts of the reaction, respectively. Every tenth spectrum in presented in each phase for clarity. Right: Time course of the same reaction recorded at 400 nm. The data (|) was fit by nonlinear regression techniques to three exponential phases (solid line).

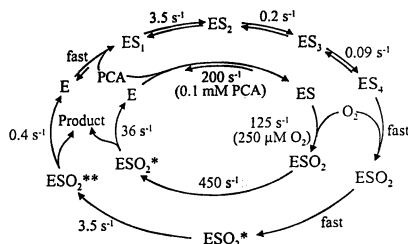


Figure 9. Comparison of the rates of interconversion of intermediates in the catalytic cycles of wild type 3,4-PCD at 4 °C (inner oval) (19-20) and Y447H at 25 °C (outer oval).

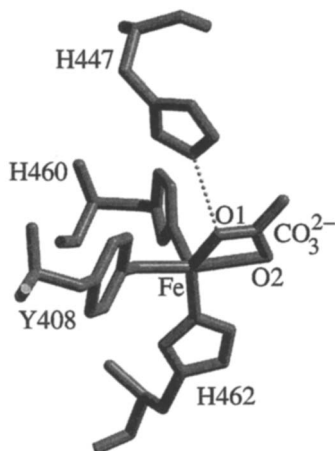


Figure 10. Environment of the iron in the active site of Y447H based on the 2.1 Å crystal structure. The presence of CO_3^{2-} is based on fitting of unassigned density and the maintenance of charge neutrality at the iron center.

to chelate in a manner that would not occur in solution, but which leads to Tyr447 dissociation and hence the generation of one of the *in situ* bases. Finally, the protein apparently provides a method to couple deprotonation of the substrate with O₂ binding through the creation of an O₂ binding pocket in response to Tyr447 release. It seems likely that many metalloenzymes may use similar mechanistic strategies.

Acknowledgment

We thank Profs. Lawrence Que, Jr. and Eckard Münck for collaboration in many aspects of this research. The work was funded by National Institutes of Health Grants GM24689 (JDL) and GM46436 (DHO).

Literature Cited

- (1) Dagley, S. In *The Bacteria*; Sokatch, J. R. and Ornston, L. N., Eds.; Academic Press, Inc.: Orlando, FL, 1986; Vol. 10, pp 527-555.
- (2) Lipscomb, J. D.; Orville, A. M. In *Metal Ions in Biological Systems*; Sigel, H. and Sigel, A., Eds.; Marcel Dekker, Inc.: New York, NY, 1992; Vol. 28.
- (3) Que, L., Jr.; Ho, R. Y. N. *Chem. Rev.* **1996**, *96*, 2607-2624.
- (4) Arciero, D. M.; Lipscomb, J. D. *J. Biol. Chem.* **1986**, *261*, 2170-2178.
- (5) Shu, L. J.; Chiou, Y. M.; Orville, A. M.; Miller, M. A.; Lipscomb, J. D.; Que, L. *Biochemistry* **1995**, *34*, 6649-6659.
- (6) Que, L., Jr.; Lipscomb, J. D.; Münck, E.; Wood, J. M. *Biochim Biophys Acta* **1977**, *485*, 60-74.
- (7) Whittaker, J. W.; Lipscomb, J. D. *J. Biol. Chem.* **1984**, *259*, 4487-4495.
- (8) Ohlendorf, D. H.; Lipscomb, J. D.; Weber, P. C. *Nature* **1988**, *336*, 403-405.
- (9) Ohlendorf, D. H.; Orville, A. M.; Lipscomb, J. D. *J. Mol. Biol.* **1994**, *244*, 586-608.
- (10) Sugiyama, K.; Senda, T.; Narita, H.; Yamamoto, T.; Kimbara, K.; Fukuda, M.; Yano, K.; Mitsui, Y. *Proc. Jpn. Acad.* **1995**, *71B*, 32-35.
- (11) Han, S.; Eltis, L. D.; Timmis, K. N.; Muchmore, S. W.; Bolin, J. *Science* **1995**, *270*, 976-980.
- (12) Senda, T.; Sugiyama, K.; Narita, H.; Yamamoto, T.; Kimbara, K.; Fukuda, M.; Sato, M.; Yano, K.; Mitsui, Y. *J. Mol. Biol.* **1996**, *735*-752.
- (13) Orville, A. M.; Elango, N.; Lipscomb, J. D.; Ohlendorf, D. H. *Biochemistry* **1997**, *36*, 10039-10051.
- (14) Orville, A. M.; Lipscomb, J.D. ; Ohlendorf, D. H. *Biochemistry* **1997**, *36*, 10052-10066.
- (15) Elgren, T. E.; Orville, A. M.; Kelley, K. A.; Lipscomb, J. D.; Ohlendorf, D. H.; Que, L., Jr. *Biochemistry* **1997**, *36*, 11504-11513.
- (16) Orville, A. M.; Lipscomb, J. D. *Biochemistry* **1997**, *36*, *in press*.
- (17) Que, L. In *Iron Carriers and Iron Proteins*; Loehr, T. M., Ed.; VCH, New York, NY, 1989, pp 467-524.
- (18) Orville, A. M.; Lipscomb, J. D. *J. Biol. Chem.* **1989**, *264*, 8791-8801.
- (19) Bull, C.; Ballou, D. P.; Otsuka, S. *J. Biol. Chem.* **1981**, *256*, 12681-12686.

- (20) Fujisawa, H.; Hiromi, K.; Uyeda, M.; Okuno, S.; Nozaki, M. *J. Biol. Chem.* **1972**, *247*, 4422-4428.
- (21) Nakata, H.; Yamauchi, T.; Fujisawa, H. *Biochim. Biophys. Acta* **1978**, *527*, 171-81.
- (22) True, A. E.; Orville, A. M.; Pearce, L. L.; Lipscomb, J. D.; Que, L., Jr. *Biochemistry* **1990**, *29*, 10847-10854.
- (23) Whittaker, J. W.; Lipscomb, J. D. *J. Biol. Chem.* **1984**, *259*, 4476-86.
- (24) Que, L. Jr.; Kolanczyk, R. C.; White, L. S. *J. Am. Chem. Soc.* **1987**, *109*, 5373-5380.
- (25) Orville, A. M.; Lipscomb, J. D. *J. Biol. Chem* **1993**, *268*, 8596-8607.
- (26) Frazee, R. W.; Livingston, D. M.; LaPorte, D. C.; Lipscomb, J. D. *J. Bacteriol.* **1993**, *175*, 6194-202.

Chapter 24

Reaction Intermediates in Oxygen Activation Reactions by Enzymes Containing Carboxylate-Bridged Binuclear Iron Clusters

Boi Hanh Huynh¹, J. Martin Bollinger, Jr.², and Dale E. Edmondson³

¹Department of Physics and ³Departments of Biochemistry and Chemistry, Emory University, Atlanta, GA 30322

²Department of Biochemistry and Molecular Biology, The Pennsylvania State University, University Park, PA 16802

The rapid freeze-quench method was used to trap intermediates in the reaction of O₂ with the dinuclear iron(II) clusters in the soluble methane monooxygenase from *Methylococcus capsulatus* (Bath) and in the R2 subunit of the ribonucleotide reductase from *Escherichia coli*. Mössbauer and EPR spectroscopies were used to characterize the trapped intermediates. For methane monooxygenase, the initial intermediate formed is a peroxodiiron(III) complex which undergoes further structural and electron reorganization to form a high-valent, formally diiron(IV), complex termed *Q*. In the case of R2, reaction of O₂ with the diiron(II) center in the presence of reducing agents generates a mixed valent, formally Fe(III), Fe(IV), complex termed *X*, which is capable of oxidizing the proximal Y122 to its radical form with formation of the resting diiron(III) cluster. In this chapter, spectroscopic characteristics of these intermediates are presented. Structural and mechanistic implications are also discussed.

In the last decade, it has been recognized that a group of proteins containing carboxylate-bridged binuclear iron clusters form a class of enzymes which activate molecular oxygen for diverse biological functions. These include the hydroxylase component of the soluble methane monooxygenase (MMOH) (1, 2), R2 subunit of the Fe-containing ribonucleotide reductase (3-5), stearoyl-acyl carrier protein Δ^9 desaturase (6), toluene monooxygenases (7, 8), xylene monooxygenase (9), phenol hydroxylase and alkane hydroxylase (10). This realization has stimulated increased interest in the study of the structures and oxygen reactivities of these diiron-containing enzymes. Particularly, extensive spectroscopic and kinetic investigations have been performed on the soluble MMO enzyme system and on the R2 subunit of *E. coli* ribonucleotide reductase (1, 2, 11, 12). Applying rapid kinetic techniques, such as stopped-flow and rapid freeze-rapid quench methods, several key

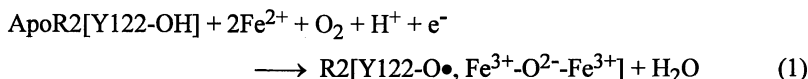
intermediates formed during the oxygen activation reactions by MMOH and R2 were identified and spectroscopically characterized (13-26). In this Chapter, we present the kinetics and spectroscopic properties of these reaction intermediates, point out their physical characteristics and discuss the structural and mechanistic implications. Emphasis is given on the similarities as well as the differences between these two proteins in their active site structures and oxygen activation mechanisms. Our goal is to identify the factors that control their mechanisms and specificities.

The Enzyme Systems and Kinetics of Their Reaction with Oxygen

Ribonucleotide Reductase. Ribonucleotide reductase (RNR) is a group of enzymes that catalyze the reduction of ribonucleotides to deoxyribonucleotides, the first committed and rate limiting step in the biosynthesis of DNA. Three classes of RNR have been characterized: the iron-tyrosyl radical containing RNR (class I), the adenosyl cobalamin-dependent RNR (class II) and the anaerobic RNR (class III) (27, 28). The *E. coli* RNR belongs to the class I enzymes and is composed of two homodimeric subunits, R1 and R2. The larger subunit R1, composed of two 85.7 kDa polypeptides, contains the binding sites for substrate and allosteric effectors, and the redox active cysteine residues involved in ribose reduction. The smaller subunit, R2, composed of two 43.4 kDa polypeptides, contains the catalytically essential tyrosyl radical (Y122•) and the binuclear iron cluster. Crystallographic studies (29) of met R2 (with the Y122 radical reduced) reveal that the two Fe atoms of the diferric center are each six-coordinate. They are bridged by an oxo and a carboxylate group (E115). In addition, each Fe is ligated by one nitrogen atom from a histidine residue, a water molecule and two oxygen atoms from protein carboxylate groups (Figure 1A). This binuclear center is buried within a four helix bundle and is 10 Å from the nearest protein surface. The EXXH amino acid sequence is repeated in the diiron binding site and this repeat of EXXH sequence is now recognized as the binuclear cofactor binding motif for this class of oxygen-activating enzymes (30). The residue Y122 is located approximately 5.3 Å from the nearest Fe site (Fe_A) and the Fe-Fe distance is 3.3 Å. The two ferric ions in R2 are antiferromagnetically coupled to form a diamagnetic ground state (31). They are spectroscopically distinguishable and exhibit two well resolved Mössbauer quadrupole doublets ($\Delta E_Q = 2.41$ mm/s and $\delta = 0.45$ mm/s for doublet 1 and $\Delta E_Q = 1.62$ mm/s and $\delta = 0.55$ mm/s for doublet 2) (23, 31). The unusually large ΔE_Q of 2.41 mm/s observed for one of the ferric site may reflect an asymmetric ligand environment caused by the bidentate binding of D84. More recently, the x-ray crystallographic structure of the reduced R2 has been solved at 1.7-Å resolution (32). Although the same two histidine and four carboxylate residues remain as ligands to the reduced binuclear cluster, substantial ligand rearrangement occurs in comparison to the diferric form; residue E238 undergoes a "carboxylate shift (33)" shifting from a terminal ligand of Fe_B to a bridging ligand between the two ferrous ions and the coordination mode of D84 changes from bidentate to monodentate (See Figure 1B). Most interestingly, both ferrous ions are four-coordinate, resulting from the loss of the μ -oxo group and

a water molecule for each Fe, and the Fe-Fe distance increases to 3.9 Å. These structural alterations upon reduction of the binuclear iron center should facilitate the binding of O₂. A MCD study of the reduced R2 has suggested that one of the Fe is five-coordinate (34). Currently, this discrepancy between the two methods is not yet understood.

It has been known for more than two decades that this complex cofactor of R2 can be reconstituted spontaneously *in vitro* by addition of ferrous ions to apo R2 in the presence of molecular oxygen (35). The reaction can be described by equation 1.



An "exogenous" reducing equivalent is required for this reaction since the reduction of O₂ to water requires four electrons and there are only three available electrons from the diferrous cluster and Y122. The physiological source of the fourth electron has not yet been identified. *In vitro*, however, the fourth reducing equivalent can be provided by chemical reductants, such as ascorbate or excess ferrous ions.

By using the methods of stopped-flow absorption spectroscopy, rapid freeze-quench EPR and Mössbauer spectroscopies, the R2 reconstitution reaction (at 5 °C) has been investigated in detail (22-26). Kinetic data from the three methods indicate that the R2 cofactor assembly proceeds according to Scheme 1, when the reaction is carried out with excess Fe²⁺ or in the presence of ascorbate. A single reaction intermediate, called *X*, forms with a rate constant of ~8 s⁻¹ and decays with a rate constant of ~1 s⁻¹ (23). The decay of *X* is concomitant with the formation of Y122• as well as the production of diiron(III) cluster. In the presence of excess Fe²⁺, the observed first order rate constant for formation of *X* is independent of the concentration of Apo R2, Fe²⁺ and O₂. This observation lead to the suggestion that conformational changes of R2 are required prior to its reaction with O₂ to form *X* (23). In order to examine the validity of such a suggestion and also to investigate the reaction mechanism of reduced R2 with O₂, similar experiments were carried out with Apo R2 preincubated with Fe²⁺ (precomplexed Fe²⁺-R2) before the introduction of O₂ (20). With precomplexed Fe²⁺-R2, the same reaction intermediate *X* forms and decays with concomitant formation of Y122•, demonstrating that the cofactor assembly proceeds by a mechanism similar to that in apo R2. The formation rate of *X*, however, was found to increase by approximately 10 fold (60-80 s⁻¹) while the decay rate of *X* remains similar, supporting the suggestion of conformational changes prior to oxygen reaction (Scheme 1).

Methane Monooxygenase. Methane monooxygenase (MMO) catalyzes the conversion of methane to methanol (equation 2), the first step in carbon assimilation by the methanotrophic bacteria (36).

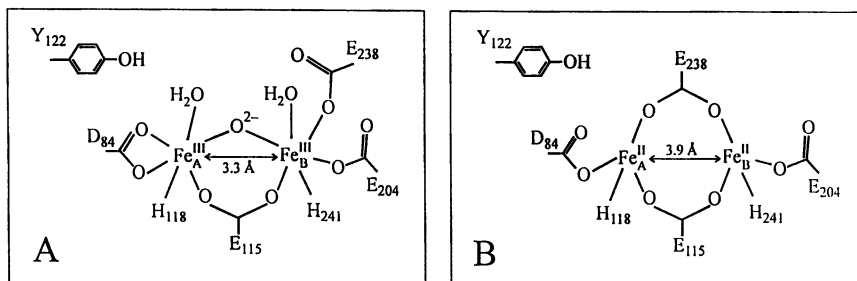
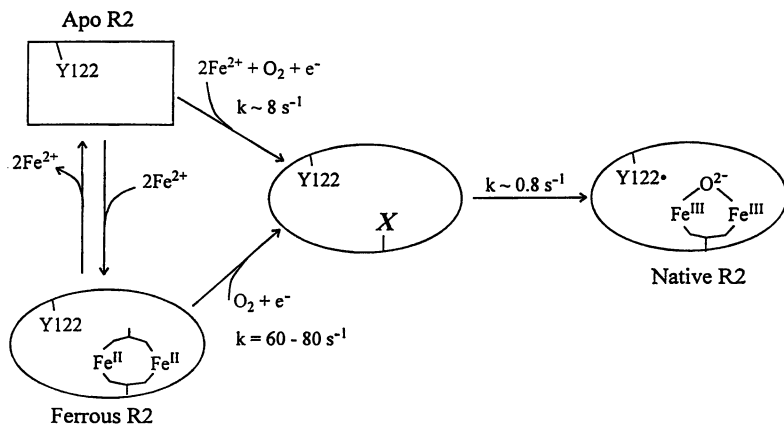


Figure 1. Schematic representation of the oxidized (A) and reduced (B) binuclear iron center of *E. coli* ribonucleotide reductase (adapted from ref. 30 and 33).



Scheme 1.



Two classes of MMO have been identified, a membrane-bound Cu-containing enzyme and a soluble Fe-containing protein complex (37). The soluble protein complexes isolated from *Methylococcus capsulatus* (Bath) and *Methylosinus trichosporium* OB3b are the two most extensively studied MMO systems. They are composed of three protein components, a binuclear Fe cluster-containing hydroxylase (MMOH), an Fe₂S₂- and flavin-containing reductase (MMOR) and a small (16 kDa) metal free protein (MMOB). MMOH binds the substrate, and its binuclear Fe center is the site for hydroxylation. Kinetic investigations (14, 38-41) indicate that the reactivity of MMOH is regulated by both components MMOR and MMOB, most probably through complexation of the protein components involved (38). In particular, MMOB has been shown to have a significant effect on the O₂ reactivity of reduced MMOH (40) as well as on catalysis by MMO (38, 41). Spectroscopic evidence further suggests that interaction of MMOB with MMOH affects the environment of the binuclear Fe center (38, 41-45). For a detailed account on the component interactions, the reader is referred to a recent review on this subject (1). The focus of this chapter is the transient intermediates formed during single turnover reactions of MMOH with O₂ in the absence of substrate. The kinetics described below were results obtained from experiments performed with stoichiometric MMOB per binuclear site, an amount that has been shown to maximize the reactivity of MMOH with O₂.

MMOH is a large molecule of approximately 250 kDa comprised of three polypeptide chains organized in a (αβγ)₂ configuration. The binuclear Fe cluster resides in the α subunit. As purified, MMOH is in the oxidized diferric form (H_{ox}). X-ray crystallographic measurements (46-48) show a similar structures for this center in *M. capsulatus* H_{ox} flash frozen at -160 °C (46) and in *M. trichosporium* H_{ox} determined at 18 °C (48). Similar to the binuclear center of R2, the ferric ions are six-coordinate (Figure 2A), situated at the center of a four helix bundle and coordinated by two EXXH segments. Each Fe ion is ligated by a histidine residue. One of the Fe has two terminal monodentate glutamate ligands. The other Fe has one terminal glutamate and a water ligand. Unlike that of R2, in addition to a bridging carboxylate, the two ferric ions are bridged by two oxygen ligands forming a so called "diamond core" structure (13). In *M. trichosporium* H_{ox}, the two oxygen atoms are from two hydroxo groups and in *M. capsulatus* H_{ox}, one oxygen is from a hydroxide and the other from a water molecule. The Fe-Fe distance is short (~3.0 Å), which appears to be a characteristic for the diamond core structure (49, 50). X-ray crystallographic studies (46, 47) further reveal that the binuclear center in *M. capsulatus* H_{ox} can exist in two structures depending on the conditions used in the X-ray study. At 4 °C, the bridging water molecule is replaced by an exogenous acetate ligand (47), most probably derived from the solvent. The Fe-Fe distance expands to 3.4 Å, a result probably reflecting the loss of the bridging water molecule. Recently, in an EXAFS investigation (51), two populations of molecules with different Fe-Fe distances were also found in a *M. trichosporium* H_{ox} sample. The majority (~60 %)

of the sample exhibits a short Fe-Fe distance of 3.0 Å while the remainder shows a longer Fe-Fe distance of 3.4 Å.

The presence of two structures for the binuclear ferric cluster has also been detected by Mössbauer spectroscopy in a single turnover *M. capsulatus* H_{ox} sample (14). Two oxidized species, termed H_{ox}(1) and H_{ox}(2), are observed. H_{ox}(1) is characterized by two equal intensity quadrupole doublets with $\Delta E_Q = 1.12$ mm/s and 0.79 mm/s and $\delta = 0.51$ mm/s and 0.50 mm/s, respectively, and H_{ox}(2) exhibits two doublets with $\Delta E_Q = 1.46$ mm/s and 1.33 mm/s and $\delta = 0.72$ mm/s and 0.47 mm/s, respectively. Kinetic Mössbauer data (14) indicate that these two oxidized species result from two populations of reduced MMOH, termed H_{red}(1) and H_{red}(2), that react differently with oxygen; H_{ox}(1) arises following a fast reaction of H_{red}(1) with oxygen while H_{ox}(2) results from a much slower reaction of H_{red}(2) with oxygen. For the "as-purified" MMOH from both *M. trichosporium* and *M. capsulatus*, however, H_{ox}(1) is the predominant species (45, 52). Currently, it is not clear whether the heterogeneity observed in the single turnover Mössbauer measurements can be correlated with that detected in the X-ray crystallographic and EXAFS studies.

Upon reduction, the binuclear center of MMOH undergoes a substantial ligand rearrangement without changing the protein ligands (Figure 2) as found to be the case with R2. The terminal monodentate E243 in H_{ox} (equivalent to E238 in R2) becomes a bridging ligand in H_{red}. Both exogenous bridging ligands are lost and the Fe atoms are five-coordinate. However, the bridging mode of E243 in H_{red} is distinct from that of E238 in reduced R2. Only one oxygen of the carboxylate of E243 is bridged between the two reduced Fe atoms. The other oxygen is still ligated to Fe_B (Figure 2). The Fe-Fe distance is 3.4 Å, which is significantly shorter than the 3.9 Å determined for reduced R2. This difference in the Fe-Fe distance could be partly due to the different bridging modes of E243 in H_{red} and E238 in reduced R2 and may be a factor that could influence the oxygen reactivities of the two enzymes. Another major structural difference revealed by X-ray crystallography that may be significant in substrate reactivity is the presence of a hydrophobic cavity adjoining the binuclear center in MMOH, which is not present in R2. Finally the carboxylate ligand E114 in MMOH differs from D84 in R2 by one carbon bond and may provide a better flexibility for the binding of Fe_A.

The reaction of reduced *M. capsulatus* MMOH with O₂ in the presence of 2 equivalents of MMOB and absence of substrate has been examined recently by a method combining rapid freeze quench technique and Mössbauer spectroscopy (14, 15). As mentioned above, two populations of H_{red} were found that react with O₂ at different rates. H_{red}(1) (30-40 % of the total population) reacts with O₂ at a rate (24-28 s⁻¹ at 4 °C) that is about 100-fold faster than that of the enzyme catalytic turnover while H_{red}(2) reacts at a much slower rate (0.01 s⁻¹) that is catalytically insignificant, suggesting that H_{red}(2) may represent non-functional enzyme. The

ratio of these two populations was found to be preparation dependent. The origin for this heterogeneity is currently unknown. The kinetic Mössbauer and stopped-flow absorption data further establish that the reaction of $H_{\text{red}}(1)$ with oxygen proceeds according to scheme 2. Two reaction intermediates, H_{peroxo} and compound Q , were found to accumulate at sufficient concentrations for spectroscopic characterization. Their spectroscopic properties will be described in the following sections. The first intermediate, H_{peroxo} , accumulates at a rate (28 s^{-1}) that is consistent with the rate of disappearance (24 s^{-1}) of $H_{\text{red}}(1)$ and decays with the concomitant formation of compound Q at a rate of $0.4\text{--}0.5 \text{ s}^{-1}$. In the absence of substrate, compound Q decays with a rate of $0.03\text{--}0.07 \text{ s}^{-1}$. The formation and decay rates of Q , monitored by stopped-flow spectroscopy, were found to be independent of oxygen concentration (14) suggesting the irreversible formation of a precursor in the reaction of $H_{\text{red}}(1)$ with O_2 .

The oxygen reactivity of reduced MMOH from *M. trichosporium* has also been investigated extensively by stopped-flow absorption and rapid freeze-quench EPR and Mössbauer spectroscopies (16, 17, 40). The results are consistent with those reported for $H_{\text{red}}(1)$ of the *M. capsulatus* enzyme. The spectroscopic properties, the formation and decay rates of the various spectroscopically detectable species are strikingly similar for these two enzymes. However, it is not clear whether the *M. trichosporium* MMOH also contains two populations of molecules that react differently with oxygen. In the studies of the *M. trichosporium* enzyme, the decay of the reduced MMOH in its reaction with oxygen was monitored by the disappearance of the $g = 16$ EPR signal, which is characteristic of the diferrous cluster in reduced MMOH (53). Based on the observation that the rate of disappearance of the $g = 16$ signal is independent of oxygen concentration, it was proposed that an oxygen intermediate, called compound O , forms irreversibly prior to the formation of H_{peroxo} (40). Since the formation of O does not alter the $g = 16$ signal of the diferrous cluster, compound O was suggested to represent an oxygen adduct of MMOH where the oxygen molecule is not yet associated with the reduced binuclear cluster.

The Spectroscopic Detectable Transient Intermediates

H_{peroxo} of MMOH. The presence of an EPR silent, initial reaction intermediate in the reaction of MMOH with oxygen was first proposed for the *M. trichosporium* enzyme based on the kinetic data obtained from stopped-flow optical and rapid freeze-quench EPR measurements (17). This transient intermediate, H_{peroxo} , however was first spectroscopically characterized in the single turnover reaction of *M. capsulatus* MMOH with oxygen by Mössbauer spectroscopy (14, 15). It exhibits a sharp and symmetric quadrupole doublet with parameters $\Delta E_Q = 1.51 \text{ mm/s}$, $\delta = 0.66 \text{ mm/s}$ and a full-width at half maximum of 0.27 mm/s (Figure 3A). This same intermediate with identical Mössbauer characteristics has now also been identified in the *M. trichosporium* MMOH (13). At the time of its discovery, the observed

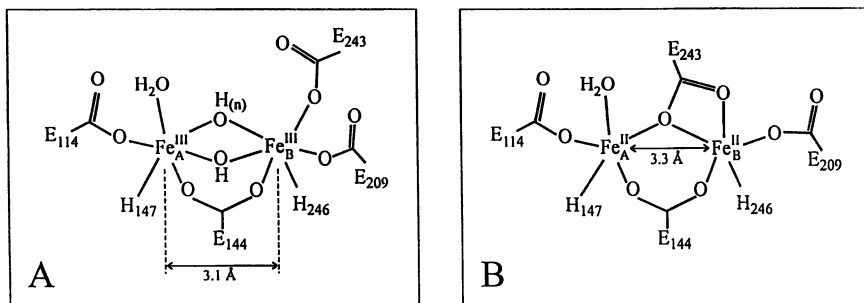
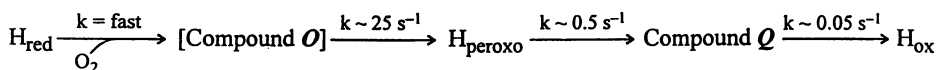


Figure 2. Schematic representation of the oxidized (A) and reduced (B) binuclear iron center of the hydroxylase component of soluble methane monooxygenase (adapted from ref. 47-49).



Scheme 2.

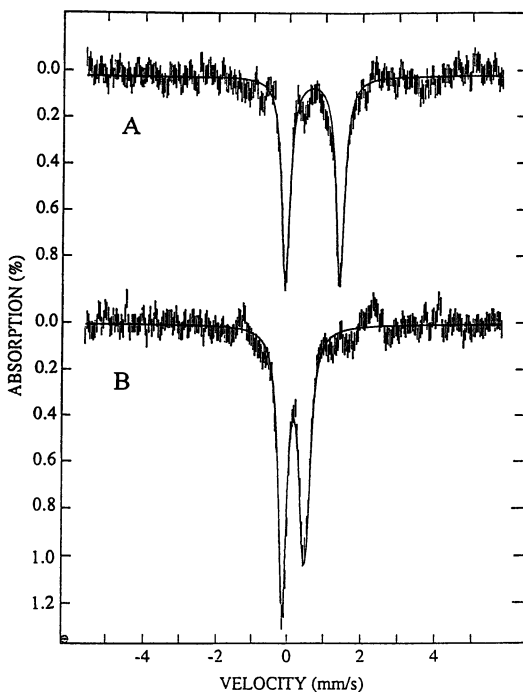


Figure 3. Mössbauer spectra at 4.2 K of intermediates H_{peroxo} (A) and compound \mathcal{Q} (B) formed during the reaction of oxygen with reduced MMOH from *M. capsulatus*. The reaction was freeze-quenched at 155 ms (A) or at 8 s (B). These spectra were prepared from the corresponding raw data by removing contributions of other iron species present in the samples from the total iron absorption (adapted from ref. 16).

Mössbauer parameters were considered to be unique for carboxylate-bridged dinuclear Fe clusters. Based on the kinetic data and chemical considerations this intermediate was proposed to be a peroxodiferric complex even though the isomer shift of 0.66 mm/s was significantly larger than the 0.52-0.54 mm/s observed for the few peroxodiferric model complexes known at the time (54-56). The larger isomer shift of H_{peroxo} can be explained as an indication of considerable electronic charge transfer from the peroxide to the Fe atoms. The fact that only one sharp and symmetric doublet was observed for H_{peroxo} strongly suggested a symmetric binding mode for the peroxide. Mössbauer spectra of H_{peroxo} recorded at strong applied fields (4 - 8 T) further demonstrated that the two ferric ions are antiferromagnetically coupled to form a diamagnetic ground state. A detailed stopped-flow optical absorption study of the reaction of *M. trichosporium* MMOH with oxygen has also shown that H_{peroxo} exhibits a broad optical absorption band with $\lambda_{\text{max}} \approx 725$ nm (see the Chapter by S. J. Lippard in this book).

Table I. Spectroscopic Properties of H_{peroxo} in *M. capsulatus* MMOH and the Peroxodiferric Model Complex $[\text{Fe}_2(\mu\text{-O}_2)(\mu\text{-O}_2\text{CCH}_2\text{Ph})_2\{\text{HB}(\text{pz}')_3\}_2]$

	H_{peroxo} ^a	Diferricperoxo Complex ^b
λ_{max} (nm)	725	694
ϵ (cm ⁻¹ M ⁻¹)		2650
ΔE_Q (mm/s)	1.51	1.40
δ (mm/s)	0.66	0.66
ν (O-O) (cm ⁻¹)		888
$\Delta\nu$ (¹⁶ O ₂ - ¹⁸ O ₂) (cm ⁻¹)		46

^aData taken from references 14. Also, see the chapter by S. J. Lippard in this book.

^bData taken from reference 57. $\text{pz}' = 3,5\text{-bis(isopropyl)-pyrazolyl}$.

Recently, a (μ -peroxo)bis(μ -carboxylato)diferric model complex (57) with a *trans* $\mu\text{-}\eta^1\text{:}\eta^1$ bridging peroxo structure has been reported to exhibit spectroscopic properties resembling those of H_{peroxo} (Table I). In particular, the Mössbauer parameters of the model complex and H_{peroxo} are strikingly similar, indicating that the complex is a potential structural model for the binuclear center in H_{peroxo} .

Compound Q. The transient intermediate, compound **Q**, was first discovered in the reaction of *M. trichosporium* MMOH with O₂ (17). It is EPR silent and exhibits an optical spectrum with λ_{max} at 330 and 430 nm. The same intermediate with similar optical properties was also found later in the *M. capsulatus* enzyme (14) and was demonstrated to be the intermediate formed immediately after the decay of H_{peroxo} . The 4.2-K zero-field Mössbauer spectra of compounds **Q** formed in *M. capsulatus*

MMOH and *M. trichosporium* MMOH are very similar and show a quadrupole doublet with unusual parameters. However, for the *M. trichosporium* compound **Q**, the doublet is symmetric (16) and can be fitted with one set of parameters ($\Delta E_Q = 0.53$ mm/s and $\delta = 0.17$ mm/s) while the *M. capsulatus* compound **Q** exhibits a slightly asymmetric doublet (Figure 3B) that is best fitted with two unresolved doublets ($\Delta E_Q = 0.68$ and 0.55 mm/s and $\delta = 0.21$ and 0.14 mm/s, respectively) (15). For a series of structurally related Fe compounds, the parameter, isomer shift, is a very good measure of the Fe oxidation state, with smaller isomer shift corresponding to higher oxidation state ($\delta_{\text{Fe(IV)}} < \delta_{\text{Fe(III)}} < \delta_{\text{Fe(II)}}$). In general, the isomer shift reduces by 0.4-0.5 mm/s for each unit increase in oxidation state. The observed reduction of δ from 0.66 mm/s in H_{peroxo} to 0.17 mm/s in **Q** is consistent with changing of the diferric state in H_{peroxo} to the formal diferryl state in **Q**. Strong-field Mössbauer spectra indicate that compound **Q** is diamagnetic (15, 16), which is also consistent with the formal diferryl assignment for **Q** with the two Fe(IV) ions antiferromagnetically coupled. However, as mentioned above, the δ value 0.66 mm/s of H_{peroxo} is at the high end of the range for ferric compounds and may represent significant electron charge delocalization from the ligand(s) to the iron ions. A similar argument can be made for compound **Q**, as the value 0.17 mm/s is considerably greater than those reported for Fe(IV) complexes (59-61). If we assume that the iron oxidation state in **Q** is between 3+ and 4+ as suggested by the isomer shift, it may be possible that in the conversion of H_{peroxo} to **Q** one electron is removed from the Fe ions and the other is from a ligand (or ligands). In this respect, it is interesting to note that a recent theoretical investigation on the reaction of MMOH with O_2 has suggested a mixed-valent Fe(III, IV)-ligand radical state as a stable electronic state for the formally Fe(IV, IV) **Q** (61). Also, density functional calculations of Fe-oxo (62) and Mn-oxo(63) dimer complexes suggest strong ligand to metal charge transfer, particularly, from μ -oxo or μ -peroxo ligands.

Very recently, an EXAFS study (13) has provided further insight into the structure of **Q**. The rapid freeze quench technique was used to trap compound **Q** formed during the reaction of reduced *M. trichosporium* MMOH with O_2 . Two samples with significant concentrations of **Q** (40 and 60 % of total Fe content) were examined by Fe EXAFS. Both samples showed a short Fe-Fe interaction of 2.46 Å. This short Fe-Fe distance was not observed in either the reduced or oxidized MMOH and was therefore attributed to compound **Q**. In addition, the data suggested the presence of a short Fe-O interaction at 1.77 Å. Based on these observations and on comparing the results with those of bis(μ -oxo)diiron model complexes (49, 64, 65), it was concluded that compound **Q** contains a bis(μ -oxo) diiron core structure, the so called diamond core structure. For more details in the EXAFS investigation of **Q**, the readers are referred to the Chapter by L. Que, Jr. in this book.

Intermediate X of R2. Optical, EPR and Mössbauer kinetic data established that **X** is the reaction intermediate in R2 that oxidizes Y122 to form the catalytically important tyrosyl radical and the product diferric cluster. The oxidation state of **X**

must therefore be one oxidizing equivalent more than that of the product differic cluster (*i. e.*, formally Fe(III, IV)). The electronic properties of *X* are rather unique and are characterized by a nearly isotropic EPR signal at $g = 2.0$ (Figure 4) measured at X-band frequency, indicating an $S = 1/2$ ground electronic state. Among all known Fe-containing cofactors in proteins, there is only one other that exhibits an isotropic EPR signal around $g = 2.0$, namely, the $[3\text{Fe-4S}]^{1+}$ cluster in iron-sulfur proteins (66). The EPR spectrum of *X* measured at Q band frequency, however, shows resolved signals at $g = 2.007$, 1.999 and 1.994 (21). At 4.2 K, intermediate *X* exhibits a paramagnetic Mössbauer spectrum composed of two spectral components corresponding to the two Fe sites (Figure 5). Mössbauer spectra recorded at various applied fields (1 - 8 T) revealed that the two Fe ions are antiferromagnetically coupled. An ENDOR investigation (21) also showed two Fe sites associated with *X*. One iron site was shown to have a nearly isotropic magnetic hyperfine coupling constant, A , while the other iron site was found to have an anisotropic A . Analysis of the Mössbauer and ENDOR data yielded the characteristic fine and hyperfine parameters for *X* listed in table 2. The ΔE_Q , δ and the isotropic A found for Fe site 1 are consistent with the site being a high-spin $S = 5/2$ ferric ion. The magnitude and sign of A for site 1 is in conformity with it being antiferromagnetically coupled to a $S = 2$ Fe ion (21).

The parameters determined for Fe site 2 are rather unusual and provide interesting information concerning the electronic state of that Fe site. The δ value, 0.26 mm/s, of Fe site 2 in *X* is smaller than those generally observed for high-spin ferric ions with octahedral oxygenous/nitrogenous ligands suggesting an oxidation state higher than Fe(III). On the other hand, the value is considerably greater than those observed for Fe(IV) model complexes (58-60). This situation is rather similar to that of the formally Fe(IV) ions in compound *Q* of MMOH described above. In other words, the Fe site 2 in *X* may also be described as a formally Fe(IV) ion with substantial charge delocalization from the ligands to the metal ion. The magnetic hyperfine tensor **A** of Fe site 2 was determined by ENDOR spectroscopy (21) to be anisotropic, which is expected for an $S = 2$ Fe(IV) ion (21). If we assume that Fe site 2 is indeed an $S = 2$ Fe(IV) ion that is spin-coupled to a $S = 5/2$ Fe(III) ion to form the $S = 1/2$ ground state of *X*, the intrinsic A values for Fe site 2 can be calculated by multiplying the observed A values with the spin coupling factor $-3/4$. The intrinsic anisotropy of **A**, Δa , can then be estimated and is found to be ~ 7.4 MHz which is significantly smaller than the theoretical value, 18 MHz, predicted for a single 3d electron (or hole) in a $S = 2$ Fe ion (21). This observation supports the view that there is substantial charge delocalization between Fe site 2 and its ligands. Among the known binuclear mixed-valent Fe(III, IV) complexes, the $[\text{Fe}_2(\mu\text{-O})_2(6\text{MeTPA})_2]^{3+}$ complex (67) exhibits spectroscopic properties similar to those of *X* and provides a good model for gaining insight on the structure and electronic properties of *X*. The model complex also shows an isotropic EPR signal at $g = 2.0$ region and exhibits Mössbauer spectra composed of two components representing two valence localized and antiferromagnetically coupled Fe(III) and Fe(IV) ions (67). The observed hyperfine parameters are list in Table II for comparison with

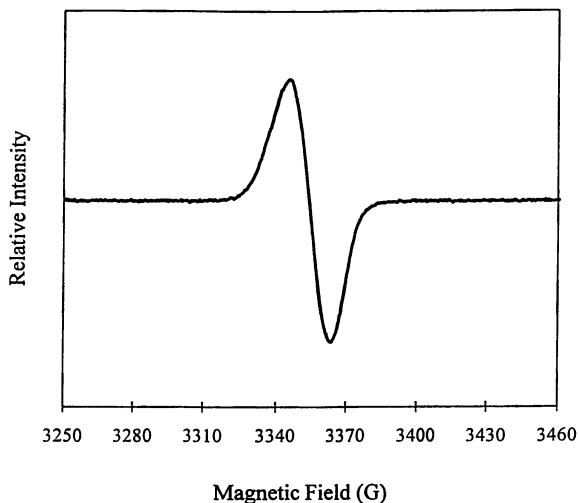


Figure 4. EPR spectrum at 40 K of intermediate *X* formed during the reconstitution of apo Y122F mutant of R2 (adapted from reference 27). The reaction was quenched at 310 ms.

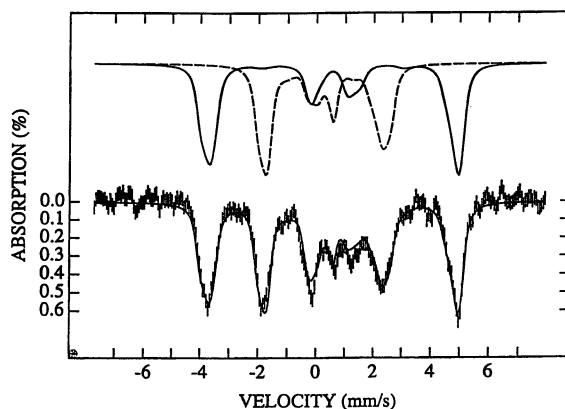


Figure 5. Mössbauer spectrum at 4.2 K of intermediate *X* formed during the reaction of oxygen with precomplexed Fe^{2+} -R2. The reaction was freeze-quenched at 160 ms. This spectrum was prepared from the corresponding raw data by removing contributions of other iron species present in the sample from the total iron absorption. The raw data were recorded with a field of 50 mT applied parallel to the γ -beam. The *solid line* plotted on the experimental data is a simulation using the parameters listed in Table II. Simulations for the two iron sites are also shown on top of the Figure: *solid line*, Fe_A ; *dashed line*, Fe_B .

those of *X*. For the Fe(IV) site of the complex, the isomer shift (0.08 mm/s) is smaller and the intrinsic anisotropy in *A* ($\Delta a = 12.4$ MHz) is considerably greater, respectively, than those for Fe site 2 of *X*, supporting the assignment of an oxidation state intermediate between 3+ and 4+ for the Fe site 2 of *X*.

Table II. ^{57}Fe Hyperfine Parameters for the Diiron Sites of *X* and the Diiron Complex $[\text{Fe}_2(\mu\text{-O})_2(6\text{MeTPA})_2]^{3+}$.

	<i>X</i> ^a		Diiron Complex ^b	
	Fe _A	Fe _B	Fe _A	Fe _B
ΔE_Q (mm/s)	-0.9	-0.6	1.6	0.5
δ (mm/s)	0.56	0.26	0.48	0.08
η (mm/s)	0.5	2.7	1.0	1.0
A_{xx} (MHz)	-74.2	27.5	-64.5	20.0
A_{yy} (MHz)	-72.2	36.8	-64.5	36.5
A_{zz} (MHz)	-73.2	36.8	-64.5	36.5
Δa (MHz)		7.4		12.4

^aData taken from references 21 and 24.

^bData taken from reference 67. TPA = tris(2-pyridylmethyl)amine.

In addition to probing the magnetic hyperfine interaction of *X*, the ENDOR spectroscopy has also been useful in providing information concerning the ligand environment. 2-D proton ENDOR spectra recorded at Q-band revealed the presence of two proton resonances attributable to two protons of a water molecule or a proton of a hydroxide group with two orientations as terminal ligand to the ferric ion in *X* (Burdì, D. et al., unpublished results; also see the Chapter by B. M. Hoffman in this book for details). When $^{17}\text{O}_2$ was used in the generation of *X* in a Y122F mutant of R2, ENDOR spectroscopy further revealed the presence of a single μ -oxo bridge in *X* derived from oxygen gas (19). This observation is consistent with a much earlier Raman study of oxidized Y122F-R2 (68), which suggested that the μ -oxo group of the diferric center originates from molecular oxygen. ENDOR data demonstrated that in *X*, the O-O bond was broken and that the oxo bridge found in the product diferric cluster is already present. The presence of an oxo bridge in *X* is also supported by a recent EXAFS investigation of *X* (Riggs-Gelasco, P. J. et al., unpublished results; also see the Chapter by L. Que, Jr. in this book). More interestingly, the EXAFS data show a short Fe-Fe interaction at 2.5 Å, suggesting a tribridge structure with at least two single-oxygen bridges for *X*.

In an effort to gain more information on the cofactor assembly reaction of R2, we have applied Mössbauer spectroscopy to probe the Fe binding properties of R2. Using two iron isotopes, ^{56}Fe and ^{57}Fe , and the fact that Mössbauer spectroscopy can only detect ^{57}Fe , we showed that the two iron sites in R2 can be selectively enriched with ^{57}Fe depending on the sequence of additions of the two iron isotopes

(69). This experiment demonstrated that the two iron sites have significant different affinities for Fe^{2+} . Exploiting this differential Fe^{2+} binding affinity and the different Mössbauer spectral properties associated with the two Fe sites in *X*, we were able to establish that Fe site 2 is the higher affinity site. Correlating this information with the results of a recent x-ray crystallographic study of R2 from mouse at pH 4.7 (70), which shows Fe occupancy only at the site of Fe_B , we assigned Fe site 2 defined by Mössbauer spectroscopy to Fe_B . In other words, the site with partial Fe(IV) character in *X* is farther away from Y122 than the Fe(III) site. When all of the available spectroscopic data of *X* described above are taken together with the X-ray crystallographic structures of reduced R2 and met R2, a structure of *X* may be proposed and is shown in Figure 6. It should be noted, however, that the proposed single-oxygen bridging mode for E238 is only one of the many possible tribridge configurations that are consistent with the short Fe-Fe distance observed in EXAFS and that the reason for proposing a terminal hydroxide to Fe_A rather than a water ligand is to retain the neutrality of the binuclear center as observed in its reduced and oxidized states.

Mechanistic Implications

As described above, applications of rapid kinetic techniques together with spectroscopic investigations have provided much detailed information about the kinetics and physical properties of the reaction intermediates in the oxygen activation reactions by the soluble MMOH and the R2 subunit of *E. coli* RNR. Although both enzymes contain a similar carboxylate-bridged binuclear Fe cluster as the oxygen activation site, their oxygen reactivities are very different. Figure 7 summarizes the structural and mechanistic information obtained so far for these two enzymes and contrasts the differences in their reactions with oxygen. Such a comparison may also be useful for identifying possible factors controlling the different oxygen reactivities of these two enzymes and for designing experiments to test these possibilities.

In this hypothetical scheme (Figure 7), a common peroxo intermediate for both MMOH and R2 is proposed to be the initial reaction intermediate. In the case of MMOH, the presence of a peroxo intermediate and its kinetic competence have been firmly established. Spectroscopic evidence also suggests a *trans* $\mu\text{-}\eta^1\text{:}\eta^1$ symmetric binding mode for the peroxo molecule. To accommodate the bridging peroxo molecule the monodentate bridging mode of E243 in H_{red} is proposed to shift to a bidentate bridging mode in H_{peroxo} . In the case of R2, the presence of a kinetically competent peroxo intermediate has not yet been established. However, when R2 precomplexed with Fe^{2+} was used in the O_2 reaction, preliminary analysis of the Mössbauer data detected a transient quadrupole doublet with spectral properties characteristics of H_{peroxo} (20). This doublet forms at a very early stage of the reaction (< 25 ms) and is undetectable after 100 ms reaction time. Unfortunately, it accumulated only as a minor species ($< 10\%$ of total Fe absorption) making a definitive characterization difficult. Currently, we are exploring various

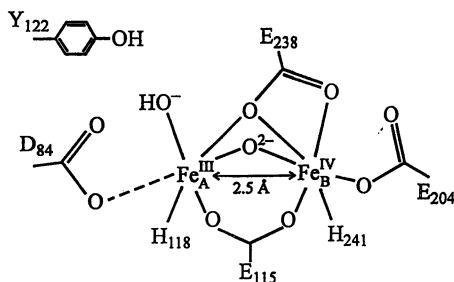


Figure 6. Proposed structure for intermediate X.

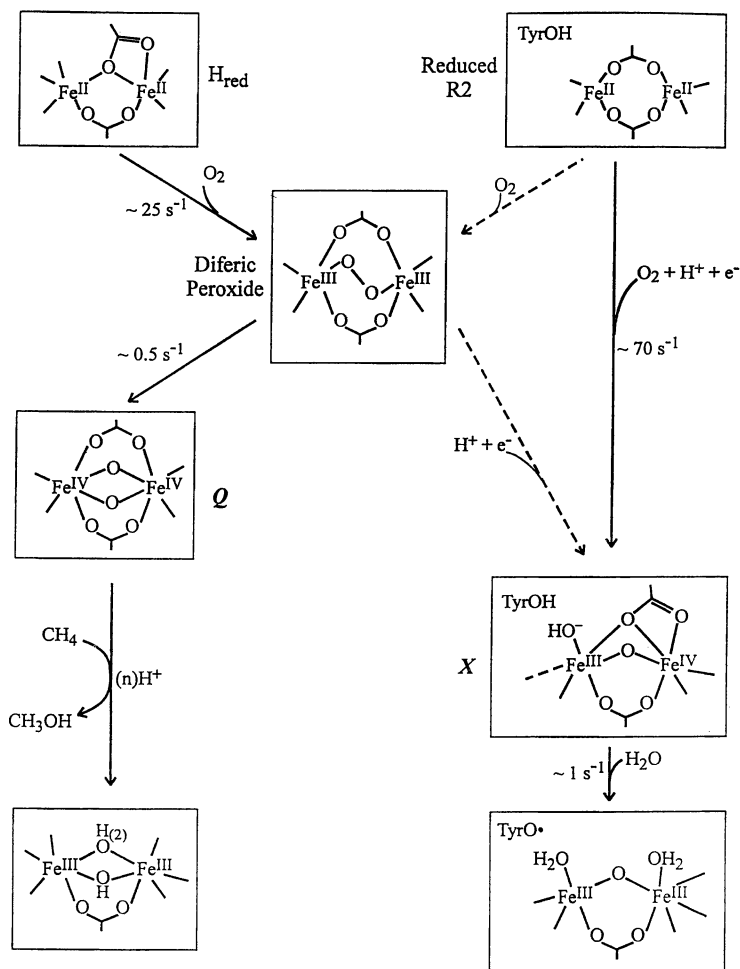


Figure 7. Proposed scheme for the O_2 activation by binuclear iron centers in MMOH and R2.

experimental conditions, such as lowering the reaction temperature or freeze-quenching the reaction at times shorter than 25 ms, in an effort to accumulate more of this elusive species.

The conversion of H_{peroxo} to compound **Q** requires an electronic and ligand rearrangement. The dioxygen bond is proposed to be broken in **Q** and the Fe-Fe distance is shortened to 2.46 Å, forming a $\text{Fe}_2(\mu\text{-oxo})_2$ core structure as suggested by the EXAFS data (13). It is not clear whether the bridging carboxylate group E243 would have already shifted to the terminal binding mode as observed for H_{ox} . Retaining its bridging mode, however, would be consistent with the symmetric spectroscopic properties observed for the two Fe atoms in **Q**. Kinetic data indicate compound **Q** as the key oxidizing species in substrate hydroxylation by MMO (1). This indication is in agreement with the formal Fe(IV, IV) assignment for **Q** since hydroxylation is a two-electron oxidation reaction and diiron(IV) state is two equivalents more oxidizing than the final product, the diferric H_{ox} . A detailed and thorough discussion on the mechanism of and intermediates involved in substrate hydroxylation by MMO has been presented recently in a review article by Wallar and Lipscomb (1).

In the case of R2, compound **Q** is not detected. Instead, intermediate **X** with a formal oxidation state of Fe(III, IV) is observed. This observation is not surprising since the oxygen activation in R2 is for the generation of the tyrosyl radical Y122•, which is a one-electron oxidation reaction, and the observed formal oxidation state, Fe(III, IV), of the key intermediate **X** in R2 is one oxidizing equivalent more than the product diferric cluster. In fact, the formation of a potent two-electron oxidizing species, such as **Q**, is functionally unfavorable for R2. In the proposed scheme, a differentiation in the O_2 activation mechanism for R2 and MMOH is suggested to occur after the formation of the peroxo species. Instead of a rearrangement of the electronic distribution, the dioxygen bond in R2 is proposed to be reductively cleaved by the injection of an exogenous electron, resulting in the formation of the intermediate **X**. One of the oxygen atoms forms the bridging oxo group while the other is proposed to become a terminal ligand to the Fe(III) site as suggested by the ENDOR data. To accommodate the EXAFS data of a short Fe-Fe interaction at 2.5 Å (Riggs-Gelasco, P. J. et al., unpublished data) which suggests the presence of at least two single-oxygen bridges, the bridging E238 is proposed to undergo a carboxylate shift from a bidentate bridging mode to a monodentate bridging mode and a bidentate ligand to Fe_B (Figures 6 and 7). Since the binuclear center is buried in the protein, an electron-transfer pathway must exist for the exogenous electron. Consequently, a possible protein regulation for controlling the reactivities of binuclear iron center in these two proteins may lie in the fundamental question of how proteins control electron transfer.

From the X-ray crystallographic structure of R2, it has been noted that a hydrogen bonding network connects the binuclear center to a near-surface residue W48 and may be a possible electron-transfer pathway (23, 29). To test this hypothesis, a site-specific mutant R2-W48F was engineered and overexpressed in *E. coli*. The apo R2-W48F was found to bind Fe^{2+} (approximately 3Fe/R2) and react

with O_2 . The reconstitution of the mutant R2-W48F was examined by stopped-flow spectrophotometry and rapid freeze-quench EPR and Mössbauer spectroscopy. Preliminary analysis of the data (Bollinger, J. M., Jr. *et al.*, unpublished data) suggests that the *fast* injection of the exogenous electron is disrupted in the mutant protein, that Y122• forms concomitantly with X, and that these two nearby $S = 1/2$ species, Y122• and X, are spin-coupled to form a $S = 1$ EPR active entity, termed X'. The Y122• of X' is found to be unstable and probably decays through either a radical recombination or an oxidation by the remaining oxidizing equivalent of the nearby X. These observations are very intriguing and provide further insight into protein regulation of binuclear center reactivities with O_2 . The results not only demonstrate the essential role played by W48 in the transfer of electrons to generate X in the wild type R2, the fact that X' (which is also two equivalents more oxidized than the diferric state) instead of a Q-like species is observed in the mutant R2 also suggests that there are other important factors controlling the functionality of the binuclear center in R2. At least two possible factors may be identified. First, there is the presence of the nearby oxidizable Y122. Any possible precursor of X with a diiron(IV) oxidation state is capable of oxidizing Y122 and is therefore unstable. Second, with the D84 ligand in R2 being one carbon bond shorter than that of E114 in MMOH, the binuclear site in R2 may not have the required flexibility to accommodate a Q-like intermediate, since the Fe-Fe distance in Q is about 1.4 Å shorter than that of the reduced R2. To stabilize a Q-like species in R2 may therefore require three mutations at W48, Y122 and D84. Currently, experiments are designed to test the above speculations.

Acknowledgments

The authors acknowledge the collaboration with the research groups of Drs. Steve J. Lippard and JoAnne Stubbe which made this work possible. In particular, the authors would like to thank the following research associates in these and in our laboratories for their indispensable contributions: Brenda A. Ley in Bollinger's lab, Shuxian Chen and Natarajan Ravi in Huynh's lab, Katherine E. Liu and Ann M. Valentine in Lippard's lab and Doug Burdi, Pamela J. Riggs-Gelasco and Wing H. Tong in Stubbe's lab. The work described here was partially supported by grants from the National Institutes of Health GM 47295 to B. H. H., GM 29433 to D. E. E. and GM 55365 to J. M. B.

Literature Cited

1. Wallar, B. J.; Lipscomb, J. D. *Chem. Rev.* **1996**, *96*, 2625-2657.
2. Feig, A. L.; Lippard, S. J. *Chem. Rev.* **1994**, *94*, 759-805.
3. Sjöberg, B. M. *Structure* **1994**, *2*, 793-796.
4. Fontecave, M.; Nordlund, P.; Eklund, H.; Reichard, P. *Adv. Enzymol.* **1992**, *59*, 147-183.
5. Stubbe, J. *Adv. Enzymol.* **1990**, *63*, 349-419.

6. Fox, B. G.; Shanklin, J.; Somerville, C.; Münck, E. *Proc. Natl. Acad. Sci., USA* **1993**, *90*, 2486-2490.
7. Newman, L. M.; Wackett, L. P. *Biochemistry* **1995**, *34*, 14066-14076.
8. Pikus, J. D.; Studts, J. M.; Achim, C.; Kauffmann, K. E.; Münck, E.; Steffan, R. J.; McClay, K.; Fox, B. G. *Biochemistry* **1996**, *35*, 9106-9119.
9. Shanklin, J.; Whittle, E.; Fox, B. G. *Biochemistry* **1994**, *33*, 12787-12794.
10. Shanklin, J.; Achim, C.; Schmidt, H.; Fox, B. G.; Münck, E. *Proc. Natl. Acad. Sci. USA* **1997**, *94*, 2981-2986.
11. Kurtz, D. M., Jr. *JBIC* **1997**, *2*, 159-167.
12. Edmondson, D. E.; Huynh, B. H. *Inorg. Chim. Acta* **1996**, *252*, 399-404.
13. Shu, L.; Nesheim, J. C.; Kauffmann, K.; Münck, E.; Lipscomb, J. D.; Que, L., Jr. *Science*, **1997**, *275*, 515-518.
14. Liu, K. E.; Valentine, A. M.; Wang, D.; Huynh, B. H.; Edmondson, D. E.; Salioglou, A.; Lippard, S. J. *J. Am. Chem. Soc.* **1995**, *117*, 10174-10185.
15. Liu, K. E.; Wang, D.; Huynh, B. H.; Edmondson, D. E.; Salifoglou, A.; Lippard, S. J. *J. Am. Chem. Soc.* **1994**, *116*, 7465-7466.
16. Lee, S.-K.; Fox, B. G.; Froland, W.; Lipscomb, J. D.; Münck, E. *J. Am. Chem. Soc.* **1993**, *115*, 6450-6451.
17. Lee, S.-K.; Nesheim, J. C.; Lipscomb, J. D. *J. Biol. Chem.* **1993**, *268*, 21569-21577.
18. Froland, W. A.; Andersson, K. K.; Lee, S. K.; Liu, Y.; Lipscomb, J. D. *J. Biol. Chem.* **1992**, *267*, 17588-17597.
19. Burdi, D.; Sturgeon, B. E.; Tong, W. H.; Stubbe, J.; Hoffman, B. M. *J. Am. Chem. Soc.* **1996**, *118*, 281-282.
20. Tong, W. H.; Chen, S.; Lloyd, S. G.; Edmondson, D. E.; Huynh, B. H.; Stubbe, J. *J. Am. Chem. Soc.* **1996**, *118*, 2107-2108.
21. Sturgeon, B. E.; Burdi, D.; Chen, S.; Huynh, B. H.; Edmondson, D. E.; Stubbe, J.; Hoffman, B. M. *J. Am. Chem. Soc.* **1996**, *118*, 7551-7557.
22. Ravi, N.; Bollinger, J. M., Jr.; Huynh, B. H.; Edmondson, D. E.; Stubbe, J. *J. Am. Chem. Soc.* **1994**, *116*, 8007-8014.
23. Bollinger, J. M., Jr.; Tong, W. H.; Ravi, N.; Huynh, B. H.; Edmondson, D. E.; Stubbe, J. *J. Am. Chem. Soc.* **1994**, *116*, 8015-8023.
24. Bollinger, J. M., Jr.; Tong, W. H.; Ravi, N.; Huynh, B. H.; Edmondson, D. E.; Stubbe, J. *J. Am. Chem. Soc.* **1994**, *116*, 8024-8032.
25. Bollinger, J. M., Jr.; Edmondson, D. E.; Huynh, B. H.; Filley, J.; Norton, J. R.; Stubbe, J. *Science* **1991**, *253*, 292-298.
26. Bollinger, J. M., Jr.; Stubbe, J.; Huynh, B. H.; Edmondson, D. E. *J. Am. Chem. Soc.* **1991**, *113*, 6289-6291.
27. Reichard, P. *Science* **1993**, *260*, 1773-1777.
28. Atkinson, J. K.; Ingold, K. U. *Biochemistry* **1993**, *32*, 9209-9214.
29. Norlund, P.; Sjöberg, B.-M.; Eklund, H. *Nature* **1990**, *345*, 593-598.
30. Fox, B. G.; Shanklin, J.; Ai, J.; Loehr, T. M.; Sanders-Loehr, J. *Biochemistry* **1994**, *33*, 12776-12786.
31. Lynch, J. B.; Juarez-Garcia, C.; Münck, E.; Que, L., Jr. *J. Biol. Chem.* **1989**, *264*, 8091-8096.

32. Logan, D. T.; Su, X.-D.; Åberg, A.; Regnstrom, K.; Hajdu, J.; Eklund, H.; Nordlund, P. *Structure* **1996**, *4*, 1053-1064.
33. Tolman, W. B.; Liu, S.; Bentsen, J. G.; Lippard, S. J. *J. Am. Chem. Soc.* **1991**, *113*, 152-164.
34. Pulver, S. C.; Tong, W. H.; Bollinger, J. M., Jr.; Stubbe, J. and Solomon, E. I. *J. Am. Chem. Soc.* **1995**, *117*, 12664-12678.
35. Atkin, C. L.; Thelander, L.; Reichard, P.; Lang, G. *J. Biol. Chem.* **1973**, *248*, 7464-7472.
36. Anthony, C. *The Biochemistry of Methylotrophs*; Academic Press: New York, NY, 1982; pp 296-379.
37. Prior, S. D.; Dalton, H. *J. Gen. Microbiol.* **1985**, *131*, 155-163
38. Fox, B. G.; Liu, Y.; Dege, J. E.; Lipscomb, J. D. *J. Biol. Chem.* **1991**, *266*, 540-550.
39. Liu, K. E.; Lippard, S. J. *J. Biol. Chem.* **1991**, *266*, 12836-12839.
40. Liu, Y.; Nesheim, J. C.; Lee, S. K.; Lipscomb, J. D. *J. Biol. Chem.* **1995**, *270*, 24662-24665.
41. Froland, W. A.; Anderson, K. K.; Lee, S.-K.; Liu, Y.; Lipscomb, J. D. *J. Biol. Chem.* **1992**, *267*, 17588-17597.
42. Davydov, A.; Davydov, R.; Gräslund, A.; Lipscomb, J. D.; Andersson, K. K. *J. Biol. Chem.* **1997**, *272*, 7022-7026.
43. Paulsen, K. E.; Liu, Y.; Fox, B. G.; Lipscomb, J. D.; Münck, E.; Stankovich, M. T. *Biochemistry* **1994**, *33*, 713-722.
44. Pulver, S.; Froland, W. A.; Fox, B. G.; Lipscomb, J. D.; Solomon, E. I. *J. Am. Chem. Soc.* **1993**, *115*, 12409-12422.
45. Fox, B. G.; Hendrich, M. P.; Surerus, K. K.; Andersson, K. K.; Froland, W. A.; Lipscomb, J. D.; Münck, E. *J. Am. Chem. Soc.* **1993**, *115*, 3688-3701.
46. Rosenzweig, A. C.; Nordlund, P.; Takahara, P. M.; Frederick, C. A.; Lippard, S. *J. Chem. Biol.* **1995**, *2*, 409-418.
47. Rosenzweig, A. C.; Frederick, C. A.; Lippard, S. J.; Nordlund, P. *Nature* **1993**, *366*, 537-543.
48. Elango, N.; Radhakrishnan, R.; Froland, W. A.; Wallar, B. J.; Earhart, C. A.; Lipscomb, J. D.; Ohlendorf, D. H. *Protein Science* **1997**, *6*, 556-568.
49. Dong, Y.; Fujii, H.; Hendrich, M. P.; Leising, R. A.; Pan, G.; Randall, C. R.; Wilkinson, E. C.; Zang, Y. Que, L. Jr.; Fox, B. G.; Kauffmann, K.; Münck, E. *J. Am. Chem. Soc.* **1995**, *117*, 2778-2792.
50. Zang, Y.; Pan, G.; Fox, B. G.; Münck, E.; Que, L., Jr. *J. Am. Chem. Soc.* **1994**, *116*, 3653-3654.
51. Shu, L.; Liu, Y.; Lipscomb, J. D.; Que, L., Jr. *J. Biol. Chem.* **1996**, *1*, 297-304.
52. DeWitt, J. G.; Bentsen, J. G.; Rosenzweig, A. C.; Hedman, B.; Green, J.; Pilkington, S.; Papaefthymiou, G. C.; Dalton, H.; Hodgson, K. O.; Lippard, S. J. *J. Am. Chem. Soc.* **1991**, *113*, 9219-9235.
53. Hendrich, M. P.; Münck, E.; Fox, B. G.; Lipscomb, J. D. *J. Am. Chem. Soc.* **1990**, *112*, 5861-5865.
54. Brennan, B. A.; Chen, Q.; Juarez-Garcia, C.; True, A. E.; O'Connor, C. J.; Que, L. Jr. *Inorg. Chem.* **1991**, *30*, 1937-1943.

55. Menage, S.; Brennan, B. A.; Juarez-Garcia, C.; Münck, E.; Que, L., Jr. *J. Am. Chem. Soc.* **1990**, *112*, 6423-6425.
56. Micklitz, W.; Bott, S. G.; Bentsen, J. G.; Lippard, S. L. *J. Am. Chem. Soc.* **1989**, *111*, 372-374.
57. Kim, K.; Lippard, S. J. *J. Am. Chem. Soc.* **1996**, *118*, 4914-4915.
58. Vogel, E.; Will, S.; Tilling, A. S.; Neuman, L.; Lex, J. Bill, E.; Trautwein, A. X.; Wieghardt, K. *Angew. Chem. Int. Ed. Engl.* **1994**, *33*, 731-735.
59. Kostka, K. L.; Fox, B. G.; Hendrich, M. P.; Collins, T. J.; Rickard, C. E. F.; Wright, L. J.; Münck, E. *J. Am. Chem. Soc.* **1993**, *115*, 6746-6757.
60. Debrunner, P. G. in *Iron Porphyrins, Part 3*; Lever, A. B. P., Gray, H. B., Eds.; VCH: New York, 1990, pp139-234.
61. Siegbahn, P. E. M.; Crabtree, R. H. *J. Am. Chem. Soc.* **1997**, *119*, 3103-3113.
62. Ghosh, A.; Almlöf, J.; Que, L., Jr. *Angew. Chem., Int. Ed. Engl.* **1996**, *35*, 770-772.
63. Zhao, X. G.; Richardson, W. H.; Chen, J.-L.; Noodleman, L.; Tsai, H.-L.; Hendrickson, D. N. *J. Am. Chem. Soc.* **1997**, in press.
64. Zang, Y.; Dong, L.; Que, L., Jr.; Kauffmann, K.; Münck, E. *J. Am. Chem. Soc.* **1995**, *117*, 1169-1170.
65. Percoraro, V. L.; Baldwin, M. J.; Gelasco, A. *Chem. Rev.* **1994**, *94*, 807-826.
66. Beinert, H.; Kennedy, M. C.; Stout, C. D. *Chem. Rev.* **1996**, *96*, 2335-2373.
67. Dong, Y.; Que, L., Jr.; Kauffmann, K.; Münck, E. *J. Am. Chem. Soc.* **1995**, *117*, 11377-11378.
68. Lind, J.; Sahlin, M.; Sjöberg, B.-M.; Loehr, T. M.; Sanders-Loehr, J. *J. Biol. Chem.* **1994**, *269*, 5595-5601.
69. Bollinger, J. M., Jr.; Chen, S.; Parkin, S. E.; Mangravite, L. M.; Ley, B.; Edmondson, D. E.; Huynh, B. H. *J. Am. Chem. Soc.* **1997**, *119*, 5976-5977.
70. Kauppi, B.; Nielsen, B. B.; Ramaswamy, S.; Larsen, I. K.; Thelander, M.; Thelander, L.; Eklund, H. *J. Mol. Biol.* **1996**, *262*, 706-720.

Chapter 25

Spectroscopic Studies of O₂ Intermediates in Copper Proteins: Electronic Structure Contributions to Function in Bioinorganic Chemistry

Edward I. Solomon, Amy E. Palmer, Uma M. Sundaram,
and Timothy E. Machonkin

Department of Chemistry, Stanford University, Stanford, CA 94305-5080

Spectroscopic studies of oxygen intermediates in copper proteins have provided a great deal of insight into the molecular mechanism of these proteins and in doing so have increased our understanding of how electronic and geometric structure correlate with biological function. The electronic structure of oxyhemocyanin is presented and compared to that of oxytyrosinase and the difference in reactivity is correlated with substrate accessibility to the copper site. Implications of the unique electronic structure of this site for both reversible O₂ binding and substrate hydroxylation are discussed. Studies on the oxygen intermediate and peroxide adduct of T1Hg laccase and the oxygen intermediate of native laccase have led to a mechanism for O₂ reduction to H₂O in which the Frank Condon barrier associated with O-O bond cleavage is overcome by the large driving force associated with two 2 electron steps. Finally, the above studies are complemented by studies on Cu-O model complexes in which systematic trends in the peroxide-Cu(II) bond are developed and related to reactivity.

Table I lists the known and proposed copper sites involved in dioxygen binding, activation and multi-electron reduction. The mononuclear copper enzymes (amine oxidase and galactose oxidase) have a Cu(II) center along with a covalently bound organic cofactor (generated by the copper center in a post-translational modification of a nearby tyrosine residue) which couple the oxidation of substrate to the two-electron reduction of O₂ to peroxide. The uncoupled binuclear copper enzymes (dopamine β monooxygenase and peptidylglycine α hydroxylating monooxygenase) have two metal ions at $> 6\text{\AA}$ distance with no bridging ligation. The "uncoupled" indicates that the active site spectral features are those of isolated Cu(II) ions with no antiferromagnetic coupling between the coppers. One copper is considered to be the site of substrate and small molecule activation and the second provides the additional electron for the reaction. The coupled binuclear copper enzymes include hemocyanin and tyrosinase. These have active sites with two Cu(II)s bridged by an exogenous

Table I: Copper Proteins Involved in Oxygen Binding and Activation

Protein	Catalytic Reaction	Protein	Catalytic Reaction
mononuclear copper		trinuclear copper clusters	
amine oxidase (AmO)		laccase (Lc)	
galactose oxidase (GO)		ascorbate oxidase (AO)	
uncoupled binuclear copper		ceruloplasmin (Cp)	
dopamine β-hydroxylase (DBH)		phenoxazinone synthase (PHS)	
peptidylglycine α-hydroxylating monooxygenase (PHM)		bilirubin oxidase (BO)	
coupled binuclear copper		dihydrogocidin/sulochrin oxidase (DHGO/SO)	
hemocyanin (Hc)	$\text{deoxyHc} [\text{Cu}^{\text{II}}\text{Cu}^{\text{I}}] + \text{O}_2 \rightleftharpoons \text{oxyHc} [\text{Cu}^{\text{II}}\text{O}_2\text{-Cu}^{\text{II}}]$	particulate methane monooxygenase (pMMO)	
tyrosinase (Tyr)			

ligand (vide infra). The bridge provides a covalent superexchange pathway for strong antiferromagnetic coupling with an $S_{\text{total}} = 0$ ground state. Hemocyanin is involved in the reversible binding of dioxygen while tyrosinase activates O_2 for hydroxylation of monophenol substrate to catechol which is further oxidized to the *o*-quinone (i.e. an internal monooxygenase). The trinuclear copper cluster containing enzymes are a rapidly expanding class with a wide variety of functions. The most well characterized are laccase, ascorbate oxidase and ceruloplasmin which couple four one electron oxidations of substrate to the four electron reduction of dioxygen to water.

Oxygen intermediates have now been stabilized for the hemocyanins and tyrosinases (oxyhemocyanin and oxytyrosinase) and for the multi-copper oxidase, laccase (the intermediates of the type 1 mercury derivative and of the native enzyme). These exhibit unique spectral features which differ among intermediates. These spectral features reflect new geometric and electronic structures involved in dioxygen binding, activation and multielectron reduction, and further define differences in active site geometric and electronic structure which relate to the differences in biological function.

Hemocyanin: electronic structure contributions to reversible O_2 binding

From Table I, the active site of deoxy hemocyanin contains two Cu(I), which react with dioxygen to form the oxyhemocyanin site with peroxide bound to two Cu(II). This site exhibits unique spectral features compared to those of a model complex with peroxide end-on bound to a single Cu(II). Figure 1A shows the energy level diagram appropriate for a mononuclear peroxide - Cu(II) complex. The valence level on the Cu(II) is the half occupied $d_{x^2-y^2}$ orbital while for peroxide the HOMO is the π^* doubly degenerate set. This splits in energy upon end-on binding to the copper with the π^*_σ orbital (σ bonding to the Cu(II)) stabilized to deeper binding energy which reciprocally destabilizes the $d_{x^2-y^2}$ orbital on the copper. This is characteristic of a σ -donor ligand interaction and should result in a $O_2^{2-} \pi^*_\sigma \rightarrow Cu(II) d_{x^2-y^2}$ charge transfer transition with moderate intensity in the visible spectral region. In the absorption spectrum in Figure 1B, the dotted line is that of the peroxide-Cu(II) monomer model complex which exhibits an $O_2^{2-} \pi^*_\sigma$ to Cu(II) charge transfer transition at ~ 500 nm with an ϵ of $\sim 6000 M^{-1} cm^{-1}$. Also included in Figure 1B, in the solid line is the absorption spectrum of oxyhemocyanin which shows that the $\pi^*_\sigma \rightarrow Cu(II) d_{x^2-y^2}$ charge transfer transition has gone up in energy to 350 nm and its intensity has increased by a factor of ~ 4 (1). Resonance Raman spectra taken upon excitation into these charge transfer transitions also exhibit striking differences (Figure 1C). Peroxide end-on bound to a single Cu(II) exhibits a fairly normal O-O stretching frequency of $803 cm^{-1}$ (2) while for oxyhemocyanin ν_{O-O} has been greatly reduced to $\sim 750 cm^{-1}$ (3). Finally, monomer Cu(II) complexes exhibit a normal $S = 1/2$ EPR spectrum as illustrated by the broken line in Figure 1D, while oxyhemocyanin exhibits no EPR signal (4). The latter has been shown by SQUID magnetic susceptibility studies to result from antiferromagnetic coupling between the two Cu(II)s due to a strong covalent bridging ligand which produces an $S_{\text{total}} = 0$ ground state (5)(6).

The crystal structure of oxyhemocyanin by Magnus *et al* (7)(Figure 2A) shows that an unusual geometric structure, a side-on bridging or $\mu-\eta^2:\eta^2$ peroxide is associated with these unique spectral features. This unusual structure was, in fact, anticipated from the spectral features of the first $\mu-\eta^2:\eta^2$ peroxy binuclear Cu(II) model complex prepared by Kitajima *et al.* (8).

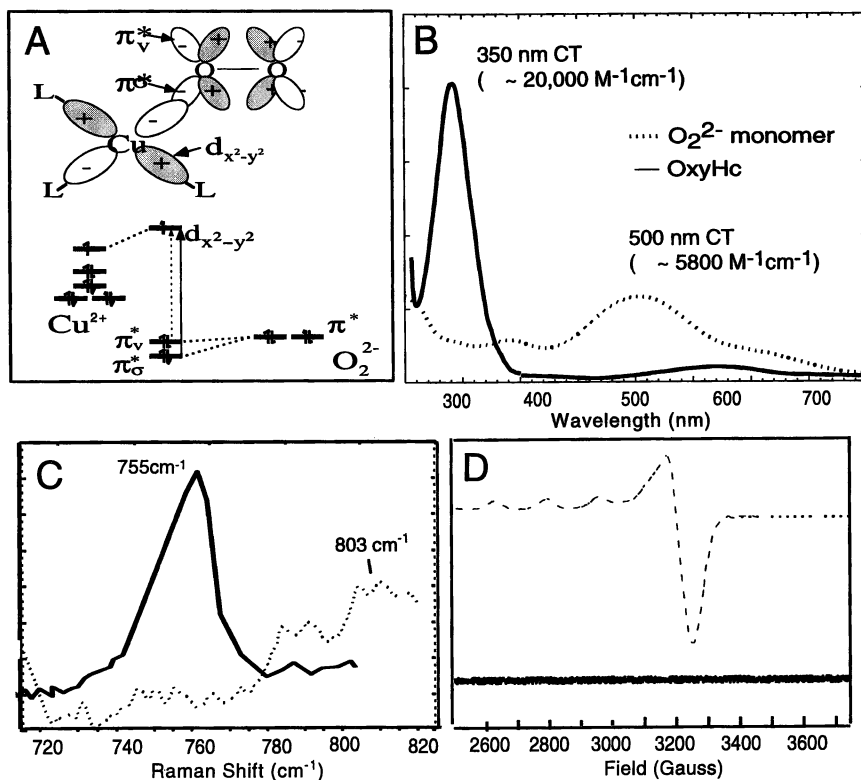


Figure 1: (A) Energy level diagram of a mononuclear peroxide-Cu(II) complex. Spectroscopy of oxyhemocyanin (solid) and a peroxide monomer (dotted) (B) Room temperature absorption (C) resonance Raman (D) EPR.

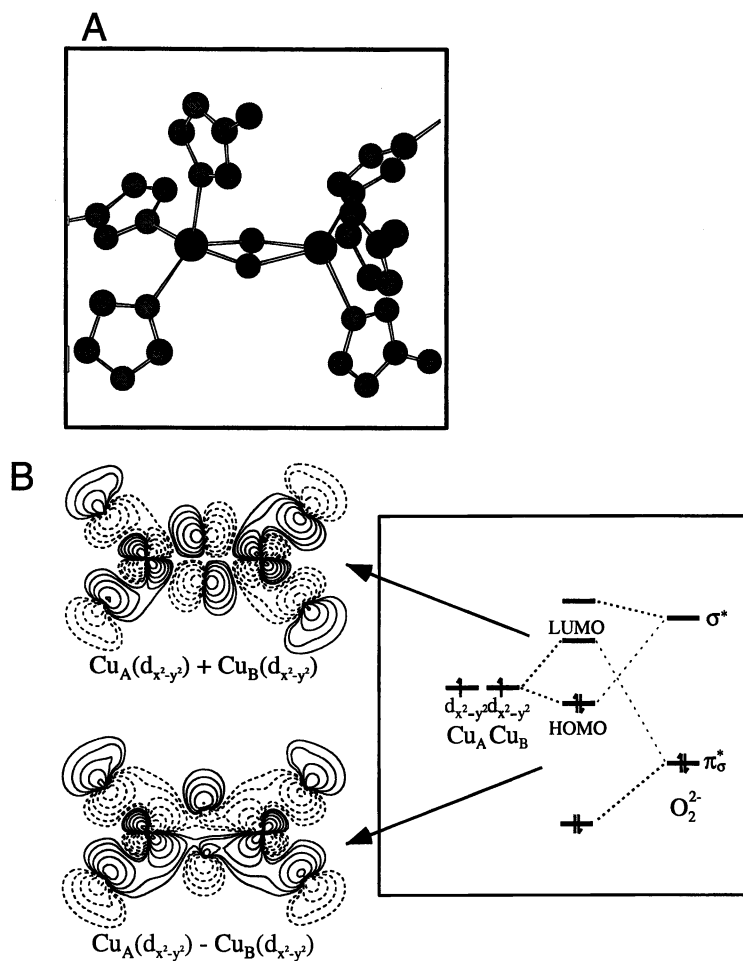


Figure 2: (A) Crystal structure of the oxyhemocyanin active site (Magnus et al) exhibiting a side-on bridged, $\mu\text{-}\eta^2\text{:}\eta^2$ geometry. (B) Energy level diagram and HOMO and LUMO orbital contours from SCF-X α -SW calculations.

We have developed the electronic structure description of this side-on bridging peroxide and have shown that it accounts for the unique spectral features in Figure 1 and provides insight into the reversible O₂ binding by this active site (9). In a binuclear copper system, the valence orbitals are the symmetric and anti-symmetric combinations of the $d_{x^2-y^2}$ orbitals on each copper which form the LUMO and HOMO, respectively. These are then split in energy by bonding interactions with the valence orbitals on the side-on bridging peroxide. There are two remarkable features of the electronic structure in Figure 2B. First, the O₂²⁻π*σ orbital is greatly stabilized which strongly destabilizes the LUMO. This indicates that the peroxide has a very strong σ-donor interaction with the Cu(II)s. The origin of this is clear from the contour of the LUMO in Figure 2B top, left which shows that the peroxide has two donor interactions with each of the two Cu(II)s in the side-on bridging geometry. This strong O₂²⁻σ-donor interaction in the side-on bridging structure accounts for the high energy and intensity of the peroxide π*σ→Cu(II) charge transfer transition in oxyhemocyanin in Figure 1B. Second, in the oxyhemocyanin structure the HOMO is stabilized in energy due to a bonding interaction with the high energy unoccupied σ* orbital on the peroxide. As shown in the HOMO contour in Figure 2B bottom, left this shifts electron density from the copper into the σ* orbital on the peroxide; thus the peroxide also acts as a π-acceptor ligand. The σ* orbital is highly antibonding with respect to O-O bond and the increased electron density in this orbital greatly weakens the bond. This is the origin of the low O-O stretching frequency of oxyhemocyanin in Figure 1C. The combination of strong σ-donor and π-acceptor leads to a large HOMO/LUMO splitting which gives rise to the antiferromagnetic coupling in the oxyhemocyanin active site (Figure 1D). This also leads to a strong peroxide-binuclear cupric bond which is important in the function of oxyhemocyanin. This stabilizes the oxyhemocyanin site from loss of peroxide which would produce a binuclear cupric (*i.e.* oxidized or met site) which would be inactive at further dioxygen binding.

Tyrosinase: comparison to hemocyanin and the molecular mechanism of hydroxylation

The absorption (10) and resonance Raman (11)(3) spectral features of the oxygen intermediate of tyrosinase (oxytyrosinase) are compared to those of oxyhemocyanin in Figures 3A and B respectively. From Figure 3 it is observed that oxytyrosinase exhibits the same unique spectral features: the high energy, intense O₂²⁻π*σ→Cu(II) a_{1g} charge transfer transition ($\lambda \sim 350$ nm, $\epsilon \sim 20,000$ M⁻¹cm⁻¹), and the low ν_{O-O} (~ 750 cm⁻¹). This indicates that the active site of oxytyrosinase has a very similar geometric and electronic structure to that of oxyhemocyanin in Figure 2A. It is important to recognize that the unique electronic structure of the side-on bridging peroxide in Figure 2B contributes greatly to the activation of dioxygen by the oxy site. The strong σ donation involving the O₂²⁻π*σ orbital shifts electron density to the copper and activates this ligand for electrophilic attack on the substrate. Further, the π-acceptor interaction with the O₂²⁻σ* orbital shifts a limited amount of electron density into this orbital which is strongly antibonding with respect to the O-O bond activating it for cleavage. (To our knowledge, this is the weakest known O-O bond with $k_{O-O} = 3.4$ mdyne/Å).

Thus the geometric and electronic structure of the oxytyrosinase and oxyhemocyanin active sites are very similar yet only oxytyrosinase catalyzes the oxygenation of substrate. This difference reflects the fact that tyrosinase has an

active site which is accessible for substrate coordination directly to the copper ion (12) (in contrast to, for example p 450, the heme monooxygenase which has substrate binding in the active site pocket in the vicinity of the heme-oxygen intermediate). Figure 4 shows that the addition of exogenous ligands such as azide to oxyhemocyanin and oxytyrosinase leads to loss of the $O_2^2-\pi\sigma^*\rightarrow Cu(II)$ charge transfer transition at 350 nm indicating displacement of the peroxide. The rates of this associative displacement reaction are included in the insert which show that these vary over four orders of magnitude with tyrosinase having the highest rate indicating that its active site is most accessible (10)(13)(14). This accessibility extends to substrate analogs/competitive inhibitors where only in the case of tyrosinase do these displace the peroxide from the copper site. The spectral features of the mimosine adduct (see Figure 5A for structure) of two derivatives of the tyrosinase site are particularly revealing. The met derivative has two Cu(II)s antiferromagnetically coupled through a bridging OH- which has replaced the $\mu-O_2^2-$ in oxytyrosinase. Addition of mimosine leads to a new absorption band at 400 nm (Figure 5A) which is a mimosine $\rightarrow Cu(II)$ charge transfer transition (10). Since charge transfer intensity requires orbital overlap, this spectrum requires that the mimosine bind directly to the coppers (12). The half-met derivative has a [Cu(II) Cu(I)] site which has an $S = 1/2$ ground state and is EPR detectable. The EPR spectrum at the top of Figure 5B is that of half-met tyrosinase. The addition of mimosine leads to a large change in the spectrum associated with substrate analog binding to the copper. The spectrum at the bottom of Figure 5B is unusual in that it has a large rhombic splitting of g_x and g_y , and a large hyperfine coupling in the $g_{||}$ region. These spectral changes indicate that there is some d_{z^2} mixing into the $d_{x^2-y^2}$ half-occupied orbital ground state. From ligand field theory this mixing requires a trigonal bipyramidal distortion of the copper site in the substrate analog bound form.

The above studies have led to the molecular mechanism for tyrosinase given in Figure 6A (note that axial ligands are not included for clarity). For tyrosinase, the side-on bridging peroxide - binuclear cupric active site is accessible to direct coordination of substrate. This undergoes a trigonal bipyramidal rearrangement at the copper leading to ortho-hydroxylation. Oxidation of the resultant coordinated catecholase by two electrons leads to loss of *o*-quinone and a reduced or deoxy tyrosinase site which is active in further dioxygen binding and reaction. As indicated in Figure 6B a significant point that still needs to be elaborated in this reaction is when the O-O bond cleaves. It is clearly present in oxytyrosinase (the $\nu_{O-O} = 750\text{ cm}^{-1}$ species in Figure 3B). However, the phenolate substrate is a strong donor ligand and coordination could shift enough electron density into the LUMO of the site to break the O-O bond prior to attack on the substrate. Alternatively, O-O bond cleavage could be concerted with electrophilic attack on the ring. Spectral studies of oxygen intermediates in copper model systems capable of hydroxylation are presently underway to obtain insight into this component of the reaction coordinate.

Multicopper oxidases

The Trinuclear Copper Cluster Site. The multicopper oxidases contain three types of sites which together catalyze the four electron reduction of O_2 to H_2O . The type 3 site has some parallels to hemocyanin and tyrosinase in that it is a hydroxide bridged, antiferromagnetically coupled binuclear copper(II) center, while the type 2 site has spectral features which are normal for mononuclear Cu(II) complexes. The type 1 site is a blue copper center (having intense characteristic spectral features, see

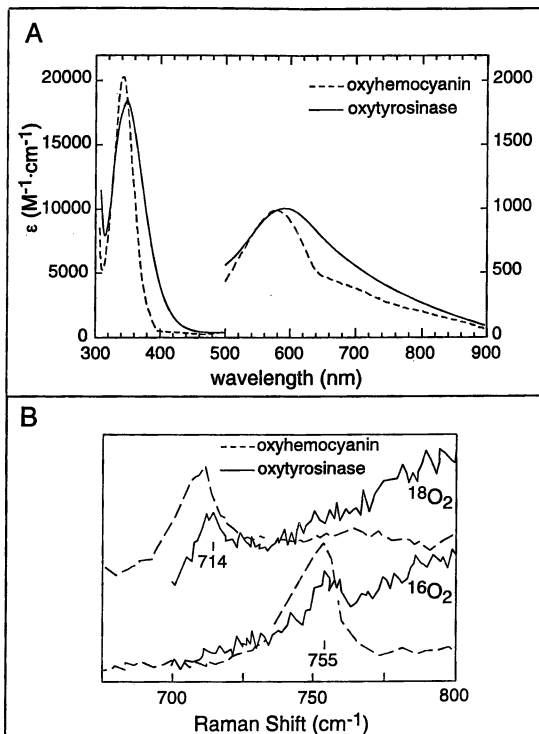


Figure 3: Comparison of the spectral features of oxytyrosinase (solid line) and oxyhemocyanin (dotted line). (A) Absorption (B) Resonance Raman spectra of the O-O peroxide stretch indicating the Raman shift with isotopic substitution

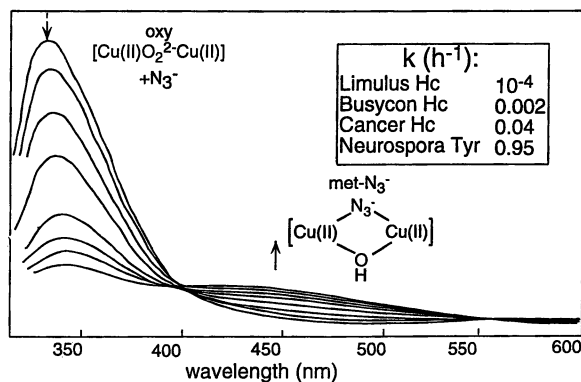


Figure 4: Kinetics of associative peroxide displacement upon addition of N_3^- .

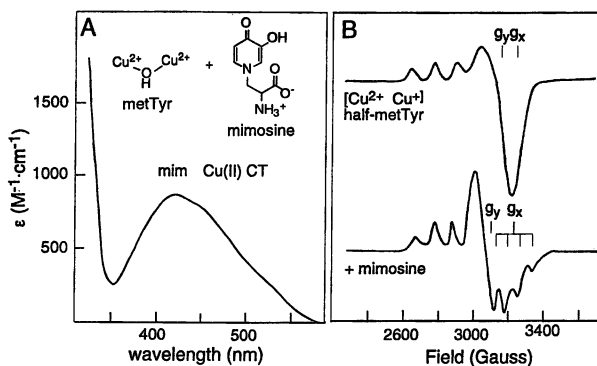


Figure 5: Spectroscopy of the inhibitor mimosine bound derivatives of tyrosinase. (A) Absorption spectrum of met-mimosine tyrosinase (B) EPR spectrum of half met tyrosinase (top) and 1/2 met-tyrosinase + mimosine (bottom).

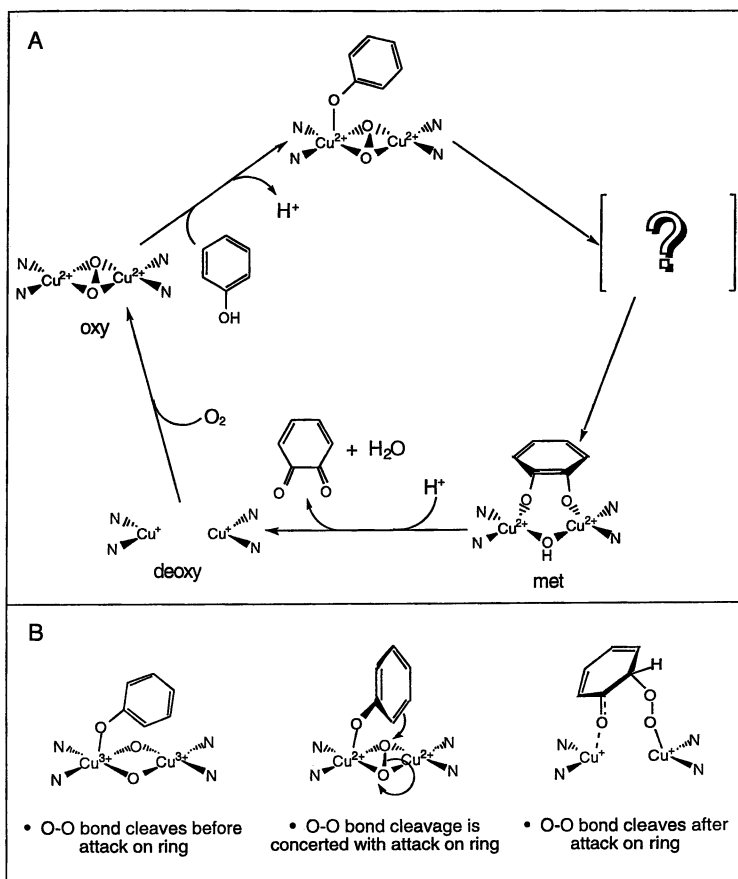


Figure 6: (A) Proposed molecular mechanism of tyrosinase and (B) schematics of three possibilities for O-O bond breakage.

reference (15)) which is $>13\text{\AA}$ from the type 2 and type 3 sites and is capable of rapid electron transfer over this distance. From Table II, laccase has the least complex stoichiometry of the multicopper enzymes with one of each type of site for a total of four copper ions. Ascorbate oxidase can be considered a dimer of laccase molecules while ceruloplasmin has two additional type 1 centers for a total of six copper ions. The role of these additional type 1 coppers is now under investigation.

Due to its simplicity, our spectral studies have focused on laccase and on two of its derivatives. The type 2 depleted derivative (T2D) has a type 2 center reversibly removed (16), while the type 1 mercury substituted derivative (T1Hg) has its blue copper site substituted with a redox inactive and spectroscopically innocent mercuric ion (17)(18)(19). A variety of spectroscopic studies on these derivatives have demonstrated that the type 3 center is fundamentally different from the coupled binuclear copper site in hemocyanin and tyrosinase and have defined the copper centers required for dioxygen reduction by the multicopper oxidases.

These results are nicely represented by X-ray absorption spectral (XAS) studies on the laccase derivatives relative to hemocyanin (20). The copper K-edge exhibits a feature at 8984 eV characteristic of reduced copper with the edge shape indicating the coordination environment of the metal ion. Oxidized copper exhibits no significant edge feature below 8986 eV. (Note that Cu(II) has an 8979 eV $1s \rightarrow 3d$ pre-edge feature which is very weak.) This qualitative difference is illustrated for hemocyanin in Figure 7A where the X-ray absorption spectrum for deoxy hemocyanin (solid line) shows an intense 8984 eV feature which is eliminated upon dioxygen binding (dotted line) to generate the binuclear cupric oxyhemocyanin active site. The extension of these results to the T2D derivative (T1(ox) T3(red)) is given in Figure 7B, which shows that, in striking contrast to hemocyanin, the reduced type 3 center in the multicopper oxidase does not react with dioxygen (20)(21). These studies were then pursued on the fully reduced T2D derivative (T1(red) T3(red)) to determine if three electrons from these two sites could be simultaneously transferred to O_2 in the catalytic mechanism (*vide infra*). As shown in Figure 7C the reduced T2D derivative also does not react with dioxygen. We finally turned to the fully reduced T1Hg substituted laccase derivative (T2(red) T3(red)). As shown in Figure 7C this reduced derivative rapidly reacts with dioxygen generating the oxygen intermediate of T1Hg laccase which will be presented in the next section. These studies clearly demonstrate that the type 2 and type 3 centers together are the minimum structural unit required for O_2 reduction. XAS studies combined with extensive MCD studies (22) first demonstrated the presence of a trinuclear copper cluster site in biology.

The trinuclear copper cluster site has now been supported by the X-ray crystallographic studies of Messerschmidt and Huber on ascorbate oxidase (23)(24). As shown in Figure 8 the site is very much as determined by spectroscopy. The type 3 coppers are antiferromagnetically coupled through a hydroxide bridge. The type 2 center is within 4\AA of the two type 3 coppers but has no bridging interactions. The one structural feature not anticipated by spectroscopy and unprecedented in Cu(II) coordination chemistry is that the oxidized type 2 center is three coordinate. Having specific geometric coordinates and a T2/T3 trinuclear copper cluster in the T1Hg derivative which is not obscured by the usually dominant spectral features of the type 1 center, one could pursue spectral studies in the ligand field region to obtain an initial description of the electronic structure of the trinuclear copper cluster site (25). Low temperature MCD spectroscopy is a powerful probe of paramagnetic metal ions and since the type 3 site is antiferromagnetic coupled, only the type 2 center contributes to the LT MCD spectrum in the ligand field region. This is given in

Table II: Multicopper Oxidases			
Enzyme	Type 1 Blue	# of Centers	
		Type 2 Normal	Type 3 Coupled Binuclear
Laccase	1	1	1
Ascorbate Oxidase	2	2	2
Ceruloplasmin	3	1	1
<u>Laccase Derivatives</u>			
Type 2 Depleted (T2D)	1	---	1
T1 Hg Subst. (T1Hg)	Hg ²⁺	1	1

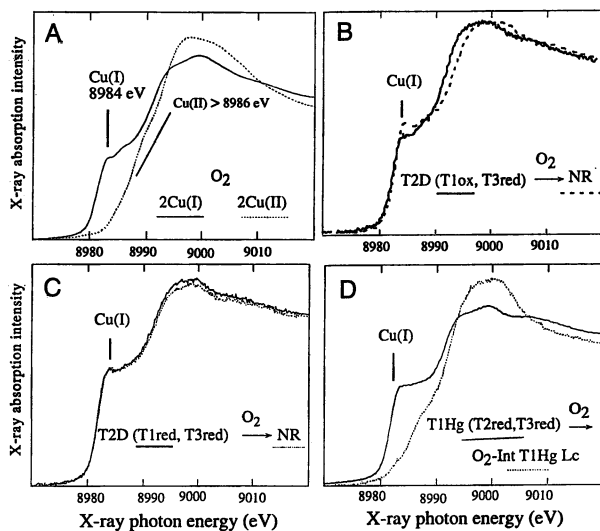


Figure 7: Comparison of X-ray absorption Cu K edges. (A) Reaction of hemocyanin with O_2 . (B) Reaction of T2D laccase ($T1_{ox}$, $T3_{red}$) with O_2 . (C) Reaction of reduced T2D ($T1_{red}$, $T3_{red}$) laccase with O_2 . (D) Reaction of reduced T1Hg laccase ($T2_{red}$, $T3_{red}$) with O_2 .

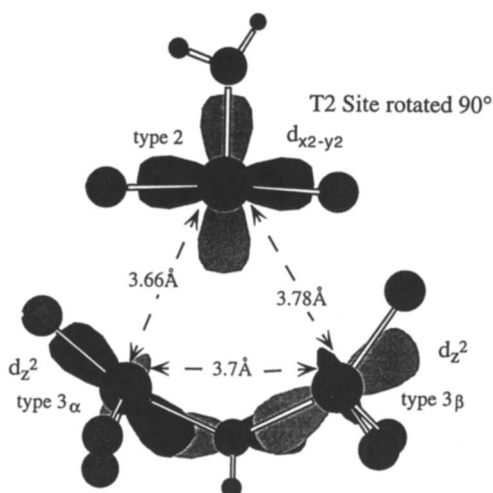


Figure 8: Electronic structure of the trinuclear copper cluster superimposed on the geometric structure as determined by crystallography. The electronic structure was obtained by ligand field calculations and the geometry is based on crystallographic coordinates of AO (see reference 24).

Figure 9A. Figure 9B shows the CD spectrum of the trinuclear copper cluster. Selective reduction of the type 2 center does not change this spectrum indicating that the CD spectrum is dominated by the ligand field transitions of the two type 3 coppers (26)(27). Since there are more than four $d \rightarrow d$ transitions in Figure 9B the two type 3 coppers must be inequivalent, and through ligand binding perturbations a set of $d \rightarrow d$ transitions can be correlated with each of the type 3 coppers (25). These ligand field transition energies combined with the crystal structure allow a ligand field calculation of each of the copper sites in the cluster (28).

From Figure 8, the type 2 center has a half occupied $d_{x^2-y^2}$ ground state. It has a square planar structure with an open coordination position in the equatorial plane oriented toward the two type 3 centers. The two type 3 coppers are best described as having trigonal bipyramidal geometries with open coordination positions in their equatorial planes oriented toward the type 2 center. This ligand field produces a d_{z^2} half occupied ground state which is well oriented for good overlap with the bridging hydroxide ligand leading to an efficient superexchange pathway and strong antiferromagnetic exchange coupling. It should be noted that one of the type 3 coppers has one of its histidine ligands bound in a δ rather than the prevalent ϵ mode (24). This has a shorter ligand-copper bond length and this short bond appears to make a major contribution to the inequivalence between the two type 3 coppers. This trinuclear copper cluster has open coordination positions on all three metal ions organized such that bridging interactions of oxygen intermediates are possible between the type 3 and type 2 centers. This will be considered in the next section.

Oxygen intermediates and the molecular mechanism of the four electron reduction of O_2 to H_2O . This section considers two oxygen intermediates of laccase, a related protein derivative and a series of model complexes. These are summarized in Table III. Reaction of fully reduced native laccase generates an oxygen intermediate (29) (the native intermediate) which has been studied since the mid 1970s. Reaction of the fully reduced T1Hg derivative produces a new oxygen intermediate (25) which can be at least one electron less reduced than the native intermediate since the type 1 copper is substituted with a redox inactive mercuric ion. In the next section, the T1Hg oxygen intermediate is shown to be at the peroxide level. Thus it has also been important to study the T1Hg-peroxide adduct (28) where peroxide is bound to a fully oxidized trinuclear copper cluster site. Finally, these studies on oxy-forms of laccase and our research on oxyhemocyanin and oxytyrosinase have lead to parallel studies on a series of peroxide Cu(II) model complexes (8)(30)(31)(32) to define electronic structure differences associated with the different geometric structures of peroxide binding: terminal, end-on bridged, side-on bridged and the effects of protonation.

Figure 10A presents kinetic data on the formation of both intermediates. Reaction of the fully reduced T1Hg laccase with O_2 generates an oxygen intermediate with an absorption band at 340 nm (Figure 10B). Its rate of formation is linear in O_2 concentration and the plot in Figure 10A gives a second order rate constant for the formation of the T1Hg Lc intermediate of $2.2 \times 10^6 \text{ M}^{-1}\text{s}^{-1}$ (33). Fully reduced native laccase reacts with O_2 to produce a different intermediate with an absorption band at 360 nm (29). Formation of this intermediate also produces an intense absorption band at 614 nm associated with oxidation of the type 1 copper which is present in the native enzyme (but not in the T1Hg Lc derivative). Thus, as anticipated above, the native intermediate is at least one electron further reduced relative to the T1Hg Lc intermediate. From Figure 10A its rate of formation is, within error, the same as that

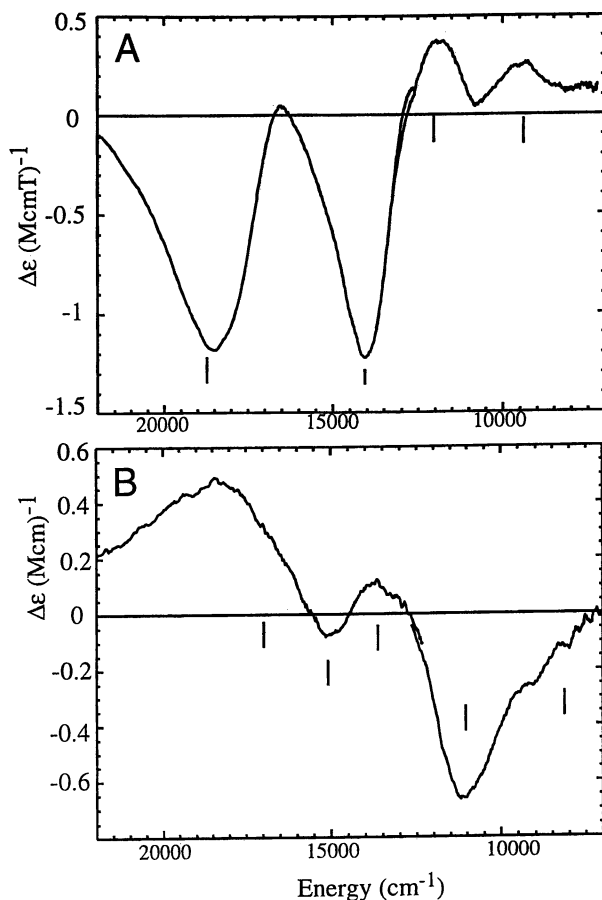
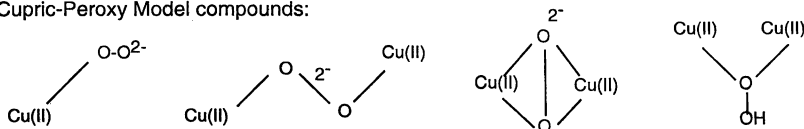
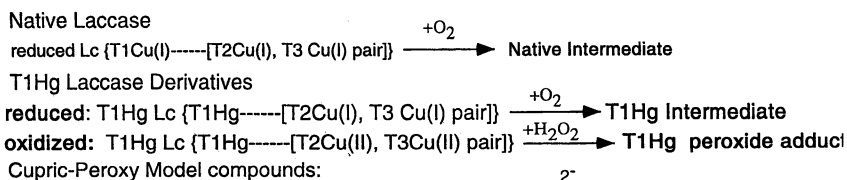


Figure 9: Ligand field spectroscopic features of T1Hg laccase. (A) Low temperature MCD of T1Hg laccase. Because the two T3 Cu's are antiferromagnetically coupled, only the paramagnetic T2 Cu contributes to the MCD spectrum. (B) CD spectrum of T1Hg laccase. The T2 Cu does not contribute to the CD and therefore the transitions observed are only those involving the two T3 Cus.

Table III: Intermediates in the reduction of O_2 to H_2O by the Multicopper Oxidases



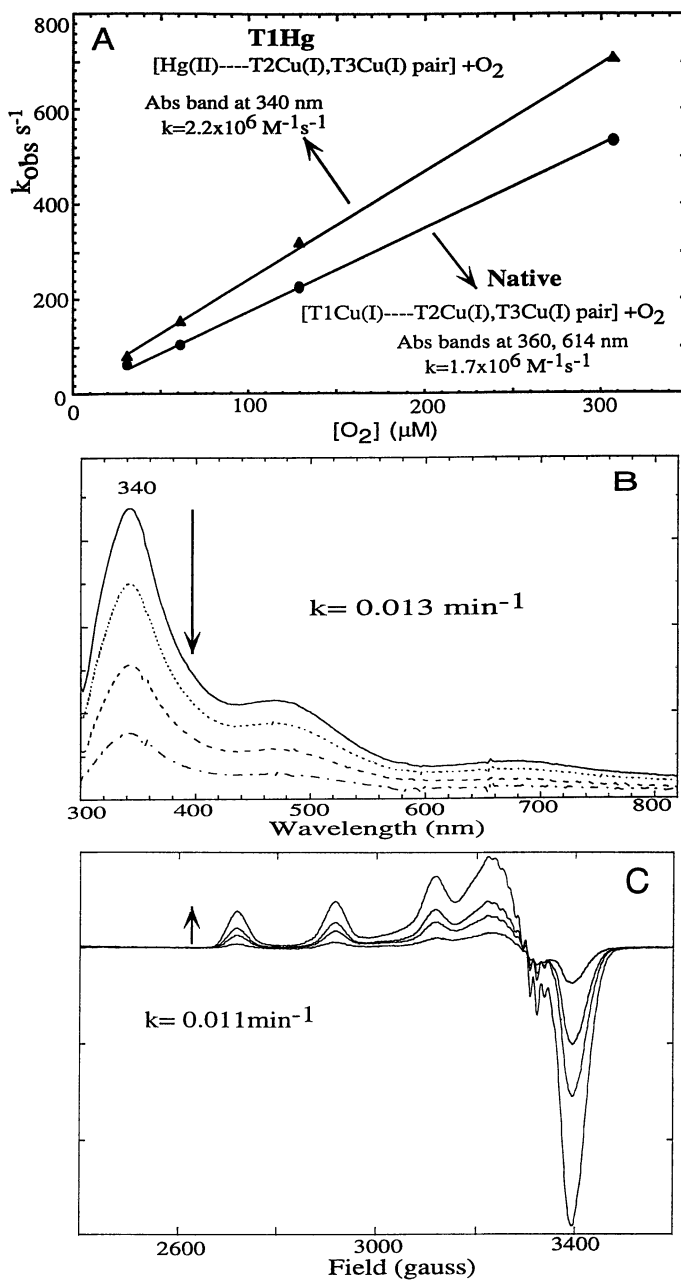


Figure 10: Kinetic data on the T1Hg intermediate (A) Comparison of the kinetics of formation of the T1Hg intermediate and the native intermediate. (B) Kinetics of decay of the T1Hg intermediate, monitored by absorption spectroscopy. (C) Kinetics of decay of the T1Hg intermediate, monitored by EPR spectroscopy.

of the T1Hg Lc intermediate. Thus formation of the T1Hg Lc intermediate can be the rate limiting step in the formation of the native intermediate, and the rate of type 1 to trinuclear copper cluster electron transfer is very fast ($> 10^3 \text{ s}^{-1}$). Figure 10C shows that the T1Hg Lc intermediate exhibits no EPR signal. However, as it decays (indicated by arrows in Figure 10B and C) a normal type 2 copper EPR signal appears. The rate of decay of the T1Hg intermediate is extremely slow and is further reduced at low temperature and high pH. This has allowed a detailed spectroscopic study of this intermediate (34).

The peroxide level intermediate of type 1 mercury laccase: comparison to oxyhemocyanin and oxytyrosinase. Isotope ratio mass spectrometry (IRMS) has been used to define the number of oxygen atoms contained in the T1Hg Lc intermediate. The reduced trinuclear copper cluster site was reacted with $^{18}\text{O}_2$ and the appearance of the ^{18}O label in the H_2O solvent was monitored by IRMS. As shown in Figure 11, the ^{18}O label appears as the T1Hg intermediate decays. From a quantitative analysis of the IRMS data, no oxygen is released into the solvent on formation of the intermediate but both oxygen appear up on its decay. Thus both oxygen atoms are bound in the T1Hg laccase intermediate and it is at the superoxide or peroxide level. We could distinguish between these possibilities by monitoring the oxidation of the coppers in the ligand field spectral region.

As described earlier, the CD spectrum in the ligand field region probes the two type 3 copper centers. From Figure 12A the T1Hg Lc intermediate (solid line) shows all the same ligand field transitions as present in the resting enzyme (dotted line) indicating that both type 3 coppers are oxidized. The limited spectral perturbations are associated with the interaction of the oxygen intermediate with the type 3 center. The low temperature MCD spectrum selectively probes the paramagnetic type 2 site in the resting enzyme, *vide supra* (Figure 12B, dotted line). The T1Hg intermediate shows no low temperature MCD signal in the ligand field region (Figure 12B solid line). This is consistent with the lack of a type 2 Cu EPR signal in the T1Hg intermediate in Figure 10C and indicates that this center is reduced. Thus the reduced trinuclear copper cluster transfers two electrons from the type 3 site to dioxygen and this is a peroxide level intermediate.

It is important to determine the magnetic properties associated with the oxidized type 3 coppers. This was pursued through SQUID magnetic susceptibility studies on the T1Hg laccase intermediate. Figure 13 A and B give the low temperature, increasing magnetic field saturation data, and a Curie plot of the temperature dependence of the susceptibility for a fixed magnetic field, respectively. It is important to note that these figures plot the magnetization of the oxidized trinuclear copper cluster minus the intermediate to correct for protein solution diamagnetism and dissolved dioxygen paramagnetism. The magnetization is positive indicating that the oxidized trinuclear copper cluster is more paramagnetic than the intermediate and quantitates to one more paramagnetic Cu(II). Since the oxidized trinuclear copper cluster has one paramagnetic center (the type 2 Cu(II)) this indicates that the intermediate is diamagnetic and thus the two type 3 Cu(II)s are antiferromagnetically coupled. The error bars in the data allow a lower limit estimate of this coupling as $-2J > 200 \text{ cm}^{-1}$. This antiferromagnetic coupling requires bridging ligation and this possibility was examined through XAS spectral studies.

Figure 14 gives the Fourier transform of the EXAFS spectrum of the T1Hg intermediate (solid line) along with those of the oxidized (broken line) and reduced (dotted line) trinuclear copper cluster sites. It is clear that the intermediate shows a

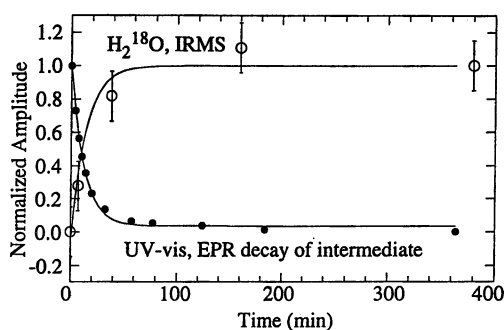


Figure 11: Isotope ratio mass spectrometry of the decay of the T1Hg intermediate compared to the decay as monitored by absorption and EPR.

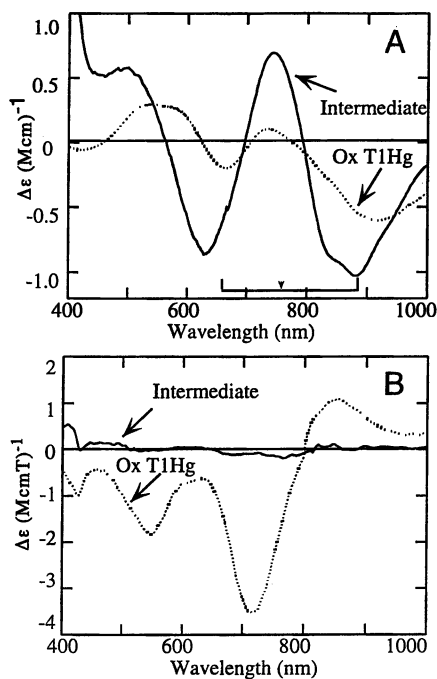


Figure 12: Comparison of (A) CD and (B) LT MCD of oxidized T1Hg Lc (dotted line) and the T1Hg intermediate (solid line).

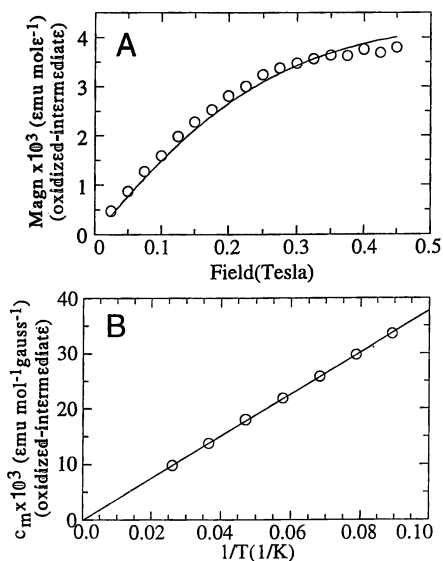


Figure 13: SQUID magnetic susceptibility studies on the T1Hg intermediate. (A) Saturation data at low temperature and increasing magnetic field. (B) Curie plot of the temperature dependence of susceptibility for a fixed magnetic field. The data are referenced to the fully oxidized trinuclear Cu cluster in the T1Hg derivative.

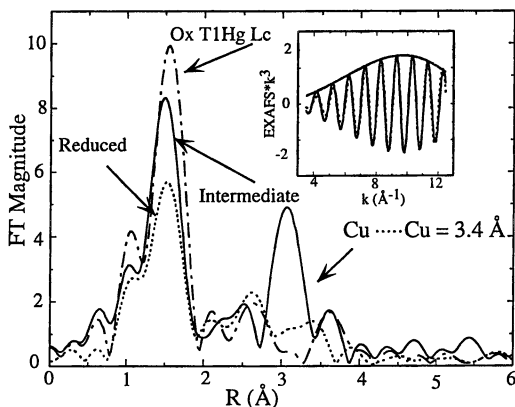


Figure 14: Fourier transforms of the EXAFS spectra of the T1Hg intermediate (solid), oxidized T1Hg Lc (dashed), and reduced T1Hg Lc (dotted). Inset giving back transform of the 3.0 \AA peak with the k dependence of amplitude indicating that it is consistent with a Cu-Cu interaction.

dominant outer shell peak not present in either the oxidized or reduced clusters indicating that two coppers in the intermediate are tightly bridged together at a distance of 3.4 Å. This bridge should be the peroxide species as the hydroxide bridge at the type 3 center in the resting trinuclear cluster does not lead to a significant outer shell Cu-Cu peak. It should also be noted that the EXAFS data rule out the presence of a short, < 1.9 Å, Cu-oxo bond.

The final spectral feature of the T1Hg Lc oxygen intermediate to be discussed here is its charge transfer spectrum. This is shown in Figure 15 (solid line) and compared to the charge transfer spectrum of oxyhemocyanin (dotted line) (*I*) which is very similar to that of oxytyrosinase, the oxyhemocyanin spectrum having been scaled down by a factor of 5. These dramatically different charge transfer spectra demonstrate that there is a fundamentally different geometric and electronic structure associated with dioxygen binding and activation by hemocyanin and tyrosinase (the side-on bridged structure in Figure 16A) relative to the peroxide intermediate in the multicopper oxidases which promotes its further reduction to water. The two key charge transfer features of the intermediate are that the transition has low intensity indicating a limited peroxide donor interaction with Cu(II), while it is at high energy requiring an additional strong bonding interaction with the peroxide. This leads to the proposal that peroxide is protonated and binds as hydroperoxide bridging between the oxidized type 3 and reduced type 2 copper centers (Figure 16B). This bridging peroxide structure is important in understanding the reaction mechanism and has been addressed through spectral studies on the peroxide adduct.

Titration of the oxidized trinuclear copper cluster in the T1Hg derivative of laccase with hydrogen peroxide results in the appearance of O₂²⁻ to Cu(II) charge transfer transitions, one at 335 nm similar to that of the T1Hg intermediate and a second transition at 400 nm (Figure 17A) (28). These indicate that peroxide binds (with a low binding constant, $k_B = 15 \text{ M}^{-1}$) to the oxidized trinuclear copper site. EXAFS data on this peroxide adduct presented in Figure 17B (solid line) exhibit the same outer shell 3.4 Å Cu-Cu peak in the Fourier transform as is present in the T1Hg Lc intermediate (dotted line). Thus peroxide binds in the adduct with a similar geometric and electronic structure as in the T1Hg Lc intermediate. This is important in that the type 2 center in the adduct is a cupric ion with an $S = 1/2$ ground state which is accessible through paramagnetic spectroscopic methods. Figure 18A gives the EPR signal of the type 2 site which is greatly perturbed upon peroxide binding. The signal goes from rhombic to axial indicating that the site has become four coordinate in the adduct. Also the ligand field transitions in the low temperature MCD spectrum (Figure 18B) of the oxidized trinuclear copper cluster show a large shift to higher energy upon peroxide binding. These spectral changes suggest that peroxide binds directly to the type 2 Cu(II) center. This is confirmed by low temperature MCD data on the 400 nm transition in Figure 17A which show that this is a peroxide to paramagnetic type 2 Cu(II) charge transfer transition. Peroxide coordination to the type 3 center is supported by shifts in the type 3 ligand field transitions in the CD spectrum (Figure 18C) and by the presence of a charge transfer band in the CD spectrum at 338 nm which has no corresponding low temperature MCD signal.

The above spectral results indicate that peroxide binds to the oxidized trinuclear copper cluster in a bridging mode between the type 2 and type 3 centers. This can involve a μ -1,1 hydroperoxide structure as in Figure 19A or an all internally bridged $\mu_3(\eta^1)_3$ type structure. Importantly, the structure of both the peroxide intermediate and adduct of laccase in solution are different from that observed in the crystal

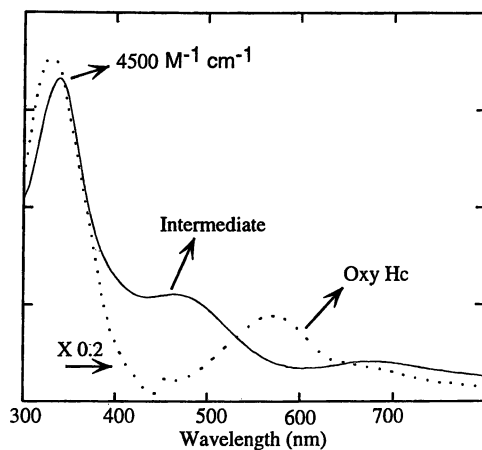


Figure 15: Comparison of the charge transfer absorption spectrum of the T1Hg intermediate (solid) with oxyhemocyanin (dotted). The oxyhemocyanin spectrum has been scaled down by a factor of 5.

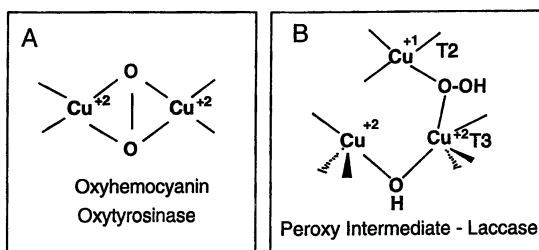


Figure 16: Spectroscopically effective geometric structure of the peroxide level intermediate in (A) oxyhemocyanin and oxytyrosinase and (B) T1Hg Lc.

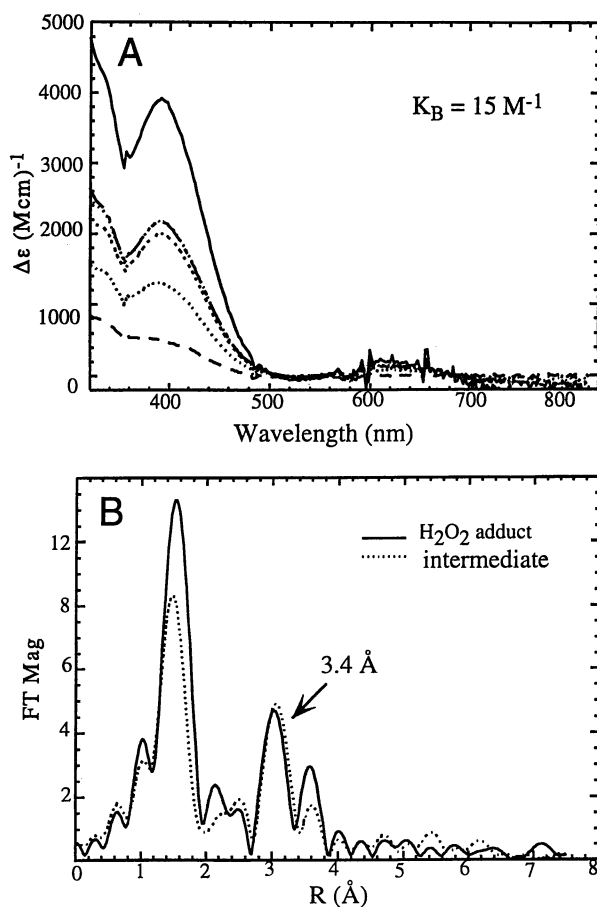


Figure 17: Spectroscopic changes upon titration of oxidized T1Hg Lc with H₂O₂. (A) Absorption spectrum (B) EXAFS.

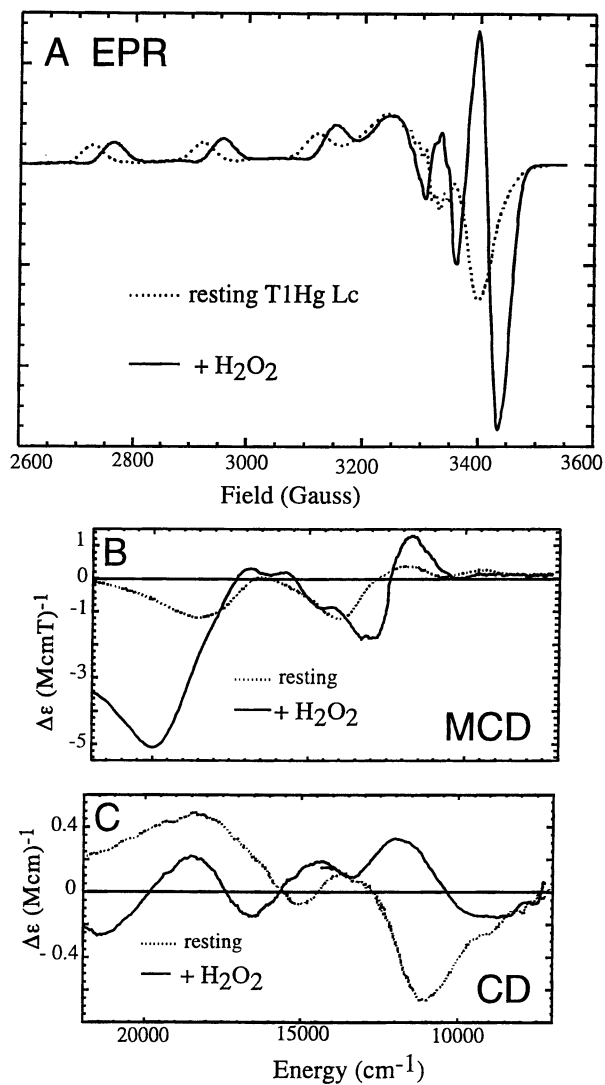


Figure 18: Comparison of the (A) EPR, (B) LT MCD, and (C) CD spectra of resting T1Hg Lc (dotted) and its peroxide adduct (solid)

structure of ascorbate oxidase where peroxide binds to only one copper and all coppers of the trinuclear cluster become uncoupled with Cu-Cu distances of $> \sim 3.7 \text{ \AA}$ with no bridging ligation (35). This is not consistent with the diamagnetism of the T1Hg Lc intermediate, the EPR and MCD spectra of the adduct or with the EXAFS data on both forms.

We finally turned to model studies on a μ -1,1 hydroperoxide bridged binuclear cupric complex (32) to evaluate the electronic structural features associated with protonation that could promote further reduction. The absorption and resonance Raman data on this model complex are given in Figure 20 (36). The resonance Raman spectrum shows an extremely high O-O stretching frequency of 892 cm^{-1} while the excitation profile of the intensity of this feature shows one hydroperoxide to Cu(II) charge transfer transition of moderate intensity ($\epsilon \sim 6000 \text{ M}^{-1}\text{cm}^{-1}$) at $\sim 25000 \text{ cm}^{-1}$. We have studied the series of known peroxide- Cu(II) model complexes listed at the top of Table 4 (36) and have shown that the $\text{O}_2^{2-} \rightarrow \text{Cu(II)}$ charge transfer intensity can be used to quantitate the σ -donor interaction of the peroxide (α_2) with the Cu(II), while the $\nu_{\text{O-O}}$ through a normal coordinate analysis to get the associated force constant $k_{\text{O-O}}$, quantitates the strength of the O-O bond. From Table IV, with the σ -donor strength normalized to that of the complex with peroxide end-on bound to a single Cu(II), it is observed that the μ -1, 1 hydroperoxide has a similar donor strength to this monomer (consistent with its low absorption intensity) even though the peroxide bridges two Cu(II)s. Thus hydroperoxide is a weak σ -donor ligand. Also, Table IV shows that the high value of $\nu_{\text{O-O}}$ corresponds to an extremely strong O-O bond.

This experimental description of the hydroperoxide- Cu(II) bond is supported by density functional theory calculations (Figure 21) (36). These calculations show that protonation increases the electron affinity of the peroxide, shifts its valence orbitals to deeper binding energy and reduces its donor interaction with the copper. For comparison to Figure 21A, the HOMO of the end-on bound peroxide (*i.e.* no protonation) contains 17% peroxide character. Further, from Figure 21B protonation polarizes the $\text{O}_2^{2-} \pi^*$ orbitals which reduces there lone pair - lone pair repulsion and this leads to the increased strength of the O-O bond.

The change in peroxide bonding with protonation has significant implications with respect to the reactivity of the hydroperoxide intermediate in laccase. First, the reduced σ donor interaction with Cu(II) stabilizes the intermediate from reversible O_2 binding. Also the hydroperoxide is not particularly activated for monooxygenase reactivity in that it does not have the extremely weak O-O bond of the side-on peroxide bridging structure of oxytyrosinase. The increased electron affinity does, however, activate the hydroperoxide for further reduction. Finally, the strong O-O bond supports the two electron vs one electron reduction of the peroxide intermediate to form the native intermediate as described in the next section.

The native “intermediate”: molecular mechanism of the four electron reduction of O_2 . As described above, native laccase contains a redox active type 1 copper which is oxidized upon forming the native intermediate (Figure 10A; the native intermediate exhibits an absorption band at 360 nm and the oxidized type 1 Cu(II) center produces the absorption band at 614 nm). Thus this intermediate is at least one electron further reduced than the T1Hg-peroxide intermediate. Consistent with this, a broad EPR signal is observed at low temperature centered at a low *g* value of 1.94 (Figure 22A) (37). The signal broadens further when generated with $^{17}\text{O}_2$ leading researchers to assign it as an oxygen based radical (38) (oxyl or hydroxyl as

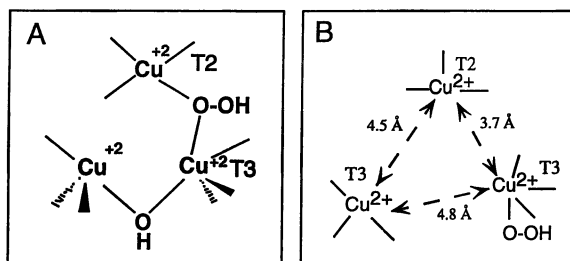


Figure 19: (A) Spectroscopically effective structure of the peroxide adduct of T1Hg laccase compared to (B) the crystallographically determined structure of peroxide bound to AO.

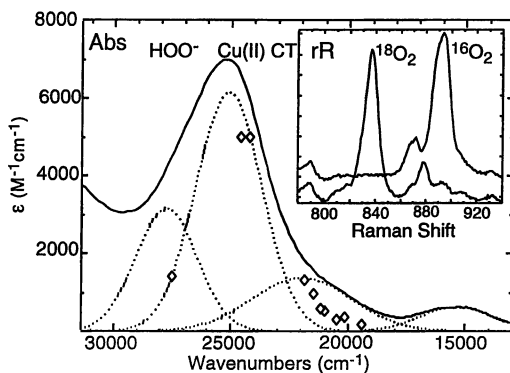
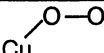
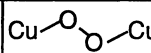
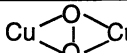
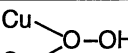


Figure 20: Absorption and resonance Raman excitation profile on a μ -1,1 hydroperoxide bridged binuclear model complex. Inset shows Raman shift upon isotopic substitution.

Table IV: Copper Model Complexes				
				
	K. Karlin	K. Karlin	N. Kitajima	K. Karlin
relative α^2 (osc. str.)	1 (0.105)	1.9 (0.25)	3.7 (0.48)	1.2 (0.23)
O-O str k/mdyne/Å (ν/cm^{-1})	2.9 (803)	3.1 (832)	2.4 (763)	3.4 (892)

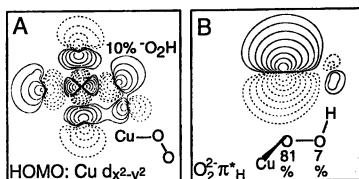


Figure 21: Electronic structure description of the hydroperoxide-Cu(II) bond determined by density functional calculations. (A) $d_{x^2-y^2}$ HOMO contour indicating hydroperoxide σ donor strength as quantitated by % peroxide character. (B) Hydroperoxide π^* orbital coupled in bonding interaction with proton. Large polarization is indicated by differences in O 2p contributions to the contour.

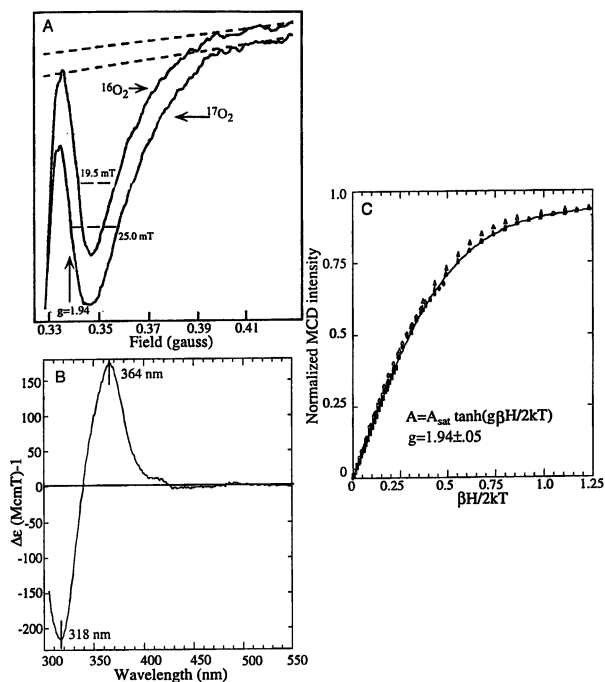


Figure 22: Spectroscopic features of the oxygen intermediate of native laccase. (A) LT EPR exhibiting line broadening upon $^{17}O_2$ substitution (reproduced with permission from ref 38). (B) LT MCD. (C) Saturation magnetization curves for the 318 and 364 nm MCD bands.

in Figure 23A left). We have been able to trap this intermediate in a form suitable for variable-temperature, variable-field MCD (VTVH MCD) spectroscopy (39). The low temperature MCD spectrum is shown in Figure 22B where the positive feature at 364 nm corresponds to the 360 nm absorption band of the native intermediate. VTVH MCD studies on this band produce the saturation magnetization curves in Figure 22C. These demonstrate that the optical intermediate has a $S = 1/2$ ground state with a g value of 1.94, thereby correlating the optical features with the same species observed by EPR in Figure 22A. The important point here is that the low temperature MCD intensity in Figure 22B is very high. This C-term intensity requires a large spin-orbit coupling between excited states which is accessible with a copper but not with an oxygen based radical ($\zeta(\text{Cu(II)}) = 830 \text{ cm}^{-1}$; $\zeta (\sim 70 \text{ cm}^{-1})$). Thus the native intermediate is best described by the resonance structure shown to the right in Figure 23A where the electron is transferred from the type 2 copper to the oxygen and thus this form is, in fact, a hydroxide product bound to a fully oxidized trinuclear cluster site. As summarized in Figure 23B three Cu(II)s bridged by two hydroxides would produce an $S_{\text{total}} = 1/2$ ground state distributed over the three copper centers, which can exhibit the unusual EPR spectrum given in Figure 22A (15).

These studies lead to the mechanism for the four electron reduction of dioxygen to water shown in Figure 24. The reduced multicopper oxidase active site reacts with O_2 to form the peroxide - level intermediate with the two type 3 coppers oxidized and the peroxide bridging between the type 2 and type 3 centers. This is further reduced by two electrons from the type 1 and type 2 centers to generate the native "intermediate" which is best described as a hydroxide product bridged between the type 2 and type 3 centers. Thus the reduction of O_2 to H_2O occurs in two, 2-electron steps. From the kinetics in Figure 10A, the first is rate determining and the second is fast. It is important to recognize that there will be a large Franck Condon barrier associated with the redox cleavage of the O-O bond in the peroxide (Figure 25). Thus a large thermodynamic driving force is required for the rapid reaction in the second step which is available with the two electron but not the one electron reduction of peroxide. Finally, it should be noted that the T2/T3 bridged hydroxide product can relax to produce a hydroxide bound to the type 2 Cu(II) which is observed from $^{17}\text{O}_2$ labeling studies in EPR (40).

Summary

The first point to emphasize here is that the unique spectral features which are often observed in Bioinorganic Chemistry reflect unusual active electronic as well as geometric structures which can make a major contribution to reactivity. For the coupled binuclear copper proteins we find the unique spectral features in Figure 1 and 3 reflect very strong σ -donation combined with π -backbonding for the side-on bridged peroxide. This produces an electrophilic activation mechanism and generates an extremely weak O-O bond which is activated for cleavage. Further, spectral features indicate that tyrosinase has a very similar active site to hemocyanin with the additional feature of substrate coordination directly to the copper center. This leads to the molecular mechanism for hydroxylation given in Figure 6A. For the multicopper oxidases, spectral features demonstrate that the type 3 center is fundamentally different from the coupled binuclear copper site in hemocyanin and tyrosinase. It is part of a type 2/type 3 trinuclear cluster which is required for O_2 reduction. This cluster generates a different peroxide-level intermediate relative to oxyhemocyanin and oxytyrosinase therefore defining geometric and electronic

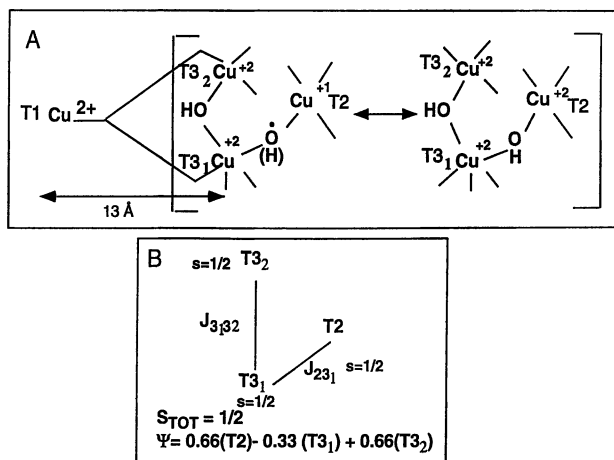


Figure 23: (A) Possible electronic structure descriptions of the oxygen intermediate of native Lc (see text) and (B) exchange coupling model for the trinuclear cluster in (A), right.

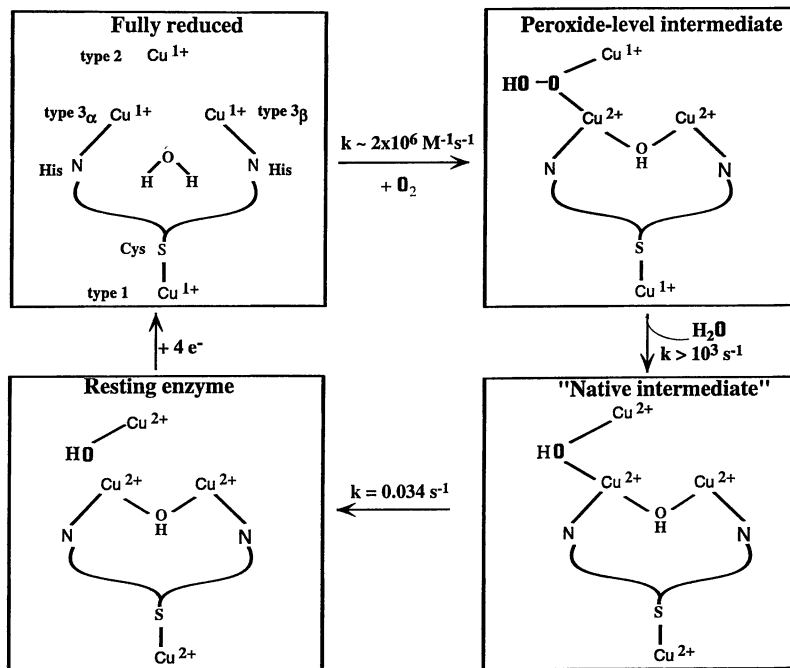


Figure 24: Proposed mechanism for the 4 electron reduction of O₂ to H₂O by the multicopper oxidases.

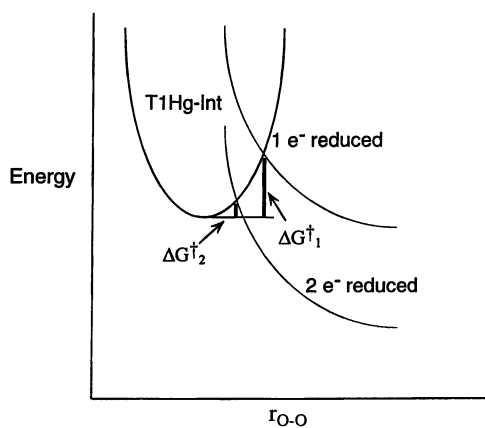


Figure 25: Potential energy diagram for reduction of peroxide by one or two electrons.

structure differences which correlate with differences in function (Figures 15 and 16). Finally, these studies have generated a molecular mechanism for the four electron reduction of O₂ to H₂O (Figure 24). This involves two, 2-electrons steps, the first is rate limiting and the second is fast due to the large driving force associated with the 2-electron reduction which is required to overcome the large Franck Condon barrier associated with reductive cleavage of the O-O bond.

Acknowledgments. E. I. S. would like to thank his past students and collaborators as indicated in the references cited for their contributions to this field. This research is funded by NIH Grant DK31450. T. E. M. acknowledges the NSF for a predoctoral fellowship.

Literature Cited.

1. Eickman, N. C.; Himmelwright, R. S.; Solomon, E. I. *Proc. Nat. Acad. Sci. USA* **1979**, *76*, 2094.
2. Pate, J. E.; Cruse, R. W.; Karlin, K. D.; Solomon, E. I. *J. Am. Chem. Soc.* **1987**, *109*.
3. Freedman, T. B.; Loehr, J. S.; Loehr, T. M. *J. Am. Chem. Soc.* **1976**, *98*, 2809.
4. Himmelwright, R. S.; Eickman, N. C.; Solomon, E. I. *Biochem. Biophys. Res. Comm.* **1979**, *86*, 628.
5. Solomon, E. I.; Dooley, D. M.; Wang, R.-H.; Gray, H. B.; Cerdonio, M.; Mogno, F.; Romani, G. L. *J. Am. Chem. Soc.* **1976**, *98*, 1029.
6. Dooley, D. M.; Scott, R. A.; Ellinghaus, J.; Solomon, E. I.; Gray, H. B. *Proc. Nat. Acad. Sci. USA* **1978**, *75*, 3019.
7. Magnus, K. A.; Hazes, B.; Ton-That, H.; Bonaventura, C.; Bonaventura, J.; Hol, W. G. J. *Proteins* **1994**, *19*, 302.
8. Kitajima, N.; Fujisawa, K.; Moro-oka, Y.; Toriumi, K. *J. Am. Chem. Soc.* **1989**, *111*, 8975.
9. Ross, P. K.; Solomon, E. I. *J. Am. Chem. Soc.* **1991**, *113*, 3246.
10. Himmelwright, R. S.; Eickman, N. C.; Lubein, C. D.; Lerch, K.; Solomon, E. I. *J. Am. Chem. Soc.* **1980**, *102*, 7339.
11. Eickman, N. C.; Solomon, E. I.; Larrabee, J. A.; Spiro, T. G.; Lerch, K. *J. Am. Chem. Soc.* **1978**, *100*, 6529.
12. Winkler, M. E.; Lerch, K.; Solomon, E. I. *J. Am. Chem. Soc.* **1981**, *103*, 7001.
13. Himmelwright, R. S.; Eickman, N. C.; Lubein, C. D.; Solomon, E. I. *J. Am. Chem. Soc.* **1980**, *102*, 5378.
14. Hepp, A. F.; Himmelwright, R. S.; Eickman, N. C.; Solomon, E. I. *Biochem. Biophys. Res. Comm.* **1979**, *89*, 1050.
15. Solomon, E. I.; Baldwin, M. J.; Lowery, M. D. *Chem. Rev.* **1992**, *92*, 521.
16. Graziani, M. T.; Morpurgo, L.; Rotilio, G.; Mondoví, B. *FEBS Letters* **1976**, *70*, 87.
17. Morie-Bebel, M. M.; Morris, M. C.; Menzie, J. L.; McMillin, D. R. *J. Am. Chem. Soc.* **1984**, *106*, 3677.
18. Morie-Bebel, M. M.; Menzie, J. L.; McMillin, D. R. *The preparation and characterization of a mixed metal derivative of laccase*; Morie-Bebel, M. M.; Menzie, J. L.; McMillin, D. R., Ed.; Adenine Press: Guilderland, NY, 1986; Vol. 1, pp 89.

19. Severns, J. C.; McMillin, D. R. *Biochem.* **1990**, *29*, 8592.
20. Kau, L.-S.; Spira-Solomon, D. J.; Penner-Hahn, J. E.; Hodgson, K. O.; Solomon, E. I. *J. Am. Chem. Soc.* **1987**, *109*, 6433.
21. LuBein, C. D.; Winkler, M. E.; Thamann, T. J.; Scott, R. A.; Co, M. S.; Hodgson, K. O.; Solomon, E. I. *J. Am. Chem. Soc.* **1981**, *103*, 7014.
22. Allendorf, M. D.; Spira, D. J.; Solomon, E. I. *Proc. Nat. Acad. Sci. USA* **1985**, *82*, 3063.
23. Messerschmidt, A.; Rossi, A.; Ladenstein, R.; Huber, R.; Bolognesi, M.; Guiseppina, G.; Marchesini, A.; Petruzzelli, R.; Finazzi-Agro, A. *J. Mol. Bio.* **1989**, *206*, 513.
24. Messerschmidt, A.; Ladenstein, R.; Huber, R.; Bolognesi, M.; Avigliano, L.; Petruzzelli, R.; Rossi, A.; Finazzi-Agro, A. *J. Mol. Bio.* **1992**, *224*, 179.
25. Cole, J. L.; Clark, P. A.; Solomon, E. I. *J. Am. Chem. Soc.* **1990**, *112*, 9534.
26. Spira-Solomon, D. J.; Solomon, E. I. *J. Am. Chem. Soc.* **1987**, *109*, 6421.
27. Tamilarasan, R.; McMillin, D. R. *Biochem. J.* **1989**, *263*, 425.
28. Sundaram, U. M.; Zhang, H. H.; Hedman, B.; Hodgson, K.; Solomon, E. I. *Submitted for publication* **1997**.
29. Andréasson, L.-E.; Brändén, R.; Malmström, B. G.; Vänngård, T. *FEBS Letters* **1973**, *32*, 187.
30. Karlin, K. D.; Cruse, R. W.; Gultneh, Y.; Farooq, A.; Hayes, J.; Zubieta, J. *J. Am. Chem. Soc.* **1987**, *109*, 2668.
31. Karlin, K. D.; Ghosh, P.; Cruse, R. W.; Farooq, A.; Gultneh, Y.; Jacobson, R. R.; Blackburn, N. J.; Strange, R. W.; Zubieta, J. *J. Am. Chem. Soc.* **1988**, *110*, 6769.
32. Ghosh, P.; Tyeklar, Z.; Karlin, K. D.; Jacobson, R. R.; Zubieta, J. *J. Am. Chem. Soc.* **1987**, *109*, 6889.
33. Cole, J. L.; Ballou, D. P.; Solomon, E. I. *J. Am. Chem. Soc.* **1991**, *113*, 8544.
34. Shin, W.; Sundaram, U. M.; Cole, J. L.; Zhang, H. H.; Hedman, B.; Hodgson, K.; Solomon, E. I. *J. Am. Chem. Soc.* **1996**, *118*, 3202.
35. Messerschmidt, A.; Luecke, H.; Huber, R. *J. Mol. Bio.* **1993**, 997.
36. Root, D.; Karlin, K.; Solomon, E. I. *Submitted for publication* **1997**.
37. Aasa, R.; Brändén, R.; Deinum, J.; Malmström, B. G.; Reinhammar, B.; Vänngård, T. *FEBS Lett.* **1976**, *61*, 115.
38. Aasa, R.; Brändén, R.; Deinum, J.; Malmström, B. G.; Reinhammar, B.; Vänngård, T. *Biochem. Biophys. Res. Comm.* **1976**, *70*, 1204.
39. Clark, P. A.; Solomon, E. I. *J. Am. Chem. Soc.* **1992**, *114*, 1108.
40. Brändén, R.; Deinum, J. *FEBS Lett.* **1977**, *73*, 144.

Author Index

- Anxolabéhère-Mallart, E., 262
Bertini, Ivano, 302
Blackburn, N. J., 241
Bollinger, J. Martin, Jr., 403
Britt, R. David, 272
Bryant, Craig, 154
Burdi, Doug, 2
Campbell, Kristy A., 272
Clemens, Keri L., 272
Cramer, Stephen P., 154
Crouse, B. R., 286
Czernuszewicz, R. S., 220
Dave, B. C., 220
de Vries, S., 241
Debus, Richard J., 272
DeMarois, Pamel, 348
Doan, Peter E., 2
Dolbeare, Kevin B., 387
Dong, Yanhong, 374
Duin, E. C., 286
Edmondson, Dale E., 403
Elango, Natesan, 387
Enemark, John H., 360
Fee, J. A., 241
Force, Dee Ann, 272
Frazee, Richard W., 387
Freeman, H. C., 62
Germanas, J. P., 220
Gilchrist, Lane M., Jr., 272
Gingell, David M., 272
Girerd, J. J., 262
Glaser, Thornsten, 314
Golinelli, M.-P., 286
Gray, Harry B., 198
Hay, M. T., 241
Hoffman, Brian M., 2
Horne, Craig, 154
Houser, R. P., 241
Huynh, Boi Hanh, 403
Johnson, M. K., 286
Kauffmann, K. E., 16
Lee, Hong-In, 2
Legros, Mark, 154
Li, Jian, 179
Lippard, Stephen J., 334
Lipscomb, John D., 387
Loehr, Thomas M., 136
Lu, Y., 241
Luchinat, Claudio, 302
Machonkin, Timothy E., 423
Meyer, J., 286
Mines, Gary A., 198
Münck, E., 16
Noodleman, Louis, 179
Ohlendorf, Douglas H., 387
Orville, Allen M., 387
Palmer, Amy E., 423
Patel, Daulat, 154
Pavel, Elizabeth G., 119
Peloquin, Jeffrey M., 272
Penner-Hahn, James E., 348
Pham, Donna P., 272
Que, Lawrence, Jr., 374
Ralle, M., 241
Ralston, Corie, 154
Randall, David W., 272
Riggs-Gelasco, Pamela J., 348
Rush, T. S., III, 212
Sanders, D., 241
Shu, Lijin, 374
Solomon, Edward I., 119
Solomon, Edward I., 423
Soriano, Aileen, 302
Spiro, T. G., 212
Stubbe, JoAnne, 2
Sundaram, Uma M., 423
Tolman, W. B., 241
Tuczek, Felix, 98
Walker, F. Ann, 30
Wang, Hongxin, 154
Wang, Xin, 154
Whittington, Douglas A., 334
Wieghardt, Karl, 314
Wilkinson, Elizabeth C., 374
Willems, Jean-Paul, 2
Winkler, Jay R., 198
Yocum, Charles F., 348

Subject Index

A

Ab initio method

Monoraphidium braunii cytochrome c_c
evaluation, 80–81

phase evaluation in crystallography, 79*t*

recent progress, 80–81

shake-and-bake method, 80

superposition of super-sharpened Patterson
functions, 80

Amino acid side chain movement. *See* Methane
monooxygenase hydroxylase (MMOH)

Amsterdam Density Functional (ADF) code, 182

Antiferromagnetic exchange coupling

iron–sulfur by NMR $[\text{Fe}_2\text{S}_2]^+$ case, 303, 304*f*

iron–sulfur metalloproteins, 314–315

See also Metal clusters; Valence-delocalized
 $[\text{Fe}_2\text{S}_2]^+$ clusters

Arthrobacter globiformis amine oxidase

diffraction precision indicator, 92*t*

polymorphism in metalloprotein crystallography
67, 69*t*

two forms of amine oxidase, 71, 72*f*

Atomic resolution, diffraction pattern of protein
structures, 76–77

B

Bacillus subtilis

comparison with loop-directed mutant of azurin,
254

EXAFS analysis of soluble Cu_A domains, 245,
248*f*

Becke potential, density functional method, 181–
182

Biquadratic exchange. *See* Metal clusters

Broken symmetry approach

electronic structure calculations for dimer states,
183

geometries of dimer transition metal complexes,
190–193

Broyden–Fletcher–Goldfarb–Shanno strategy for
geometry optimization, 182

Burst phase in protein folding, 198–199

C

CAMELSPIN experiment. *See* Nuclear magnetic
resonance (NMR) spectroscopy

Carboxylate-bridged binuclear iron clusters

electronic properties of intermediate X of R2 by

EPR and Mössbauer, 412–413, 414*f*

enzyme systems and reaction with oxygen, 404–
409

H_{peroxo} intermediate of MMOH, 409, 410*f*, 411

hyperfine parameters for diiron (^{57}Fe) sites of X
by Mössbauer and ENDOR, 415*t*

intermediate Q of methane monooxygenase

hydroxylase (MMOH), 411–412

intermediate X of R2 subunit of ribonucleotide

reductase (RNR), 412–416

intermediate X possible structure, 417*f*

ligand rearrangement upon reduction of MMOH,
408, 410*f*

mechanistic implications, 416–419

methane monooxygenase and kinetics with
oxygen, 405, 407–409

methane monooxygenase hydroxylase (MMOH),
403–404

Mössbauer parameters of H_{peroxo} intermediate
and potential structural model, 411*t*

ribonucleotide reductase (RNR) and kinetics

with oxygen, 404–405

RNR subunit R2, 403–404

schematic of oxidized and reduced binuclear iron
center of *E. coli* RNR, 406*f*

schematic of oxidized and reduced binuclear iron
center of MMOH, 407, 410*f*

schematic proposed for oxygen activation by

binuclear iron centers in MMOH and R2, 417*f*

spectroscopic detectable transient intermediates,
409, 410*f*, 411–416

tyrosyl radical generation by R2, 412–413, 418–
419

Carr–Purcell–Meiboom–Gill (CPMG) spin-echo
experiment, spin-spin relaxation, 38

Charge-coupled detector devices

resonance Raman spectroscopy, 138, 139*f*

X-ray diffraction detectors, 73

Charge-transfer spectrum, covalency information
of ligands and metal site, 98–99

Charge-transfer transitions. *See* Copper(II) azide
systems; Electronic absorption spectroscopy

CHELPG code, fitting electrostatic potential
charges, 182

Chemically induced dynamic nuclear polarization
(CIDNP), NMR experimental technique, 56

Chemical shifts of paramagnetic complexes by
NMR, 33–36

CIDNP. *See* Chemically induced dynamic nuclear

- polarization (CIDNP)
- Circular dichroism (CD) spectroscopy
metalloenzyme analysis, 343
See also Magnetic circular dichroism (MCD) spectroscopy
- Clostridium pasteurianum* (Cp) 2Fe ferredoxin (Fd). *See* Valence-delocalized $[\text{Fe}_2\text{S}_2]^+$ clusters
- Contact shift, NMR spectroscopy, 33–34
- Copper(II) azide systems
azide analogue for peroxide, 98–99
charge transfer (CT) transitions in mononuclear complexes, 99–102
cis μ -1,3 bridging azide with strong antiferromagnetic coupling, 106, 107f, 108
considerations of CT transitions in binuclear bridged complexes, 102, 104–106
covalency parameter, 100
ferromagnetically coupled dimer with one azido and one OH group, 108–112
ferromagnetically coupled dimer with two bridging azido groups, 112–115
ground and excited state wavefunctions, 101–102
- Heitler–London (HL) or valence-bond (VB) ground state description, 100
- ionic and charge-transfer configuration terms, 100
- molecular orbital (MO) ground state Slater determinant, 99–100
- optical absorption spectrum of monomeric Cu(II) azide complex, 103f
- overlap integral, 99
- valence-bond configuration interaction (VBCI) of mono- and binuclear Cu(II) azide complexes, 103t
See also Electronic absorption spectroscopy
- Copper–heme oxidases. *See* Heme–copper oxidases
- Copper plastocyanin
soft X-ray absorption spectroscopy, 167–168
X-ray magnetic circular dichroism, 173
- Copper proteins
arrangement of ligands about Cu(II) in *P. aeruginosa* azurin, 221, 224f
electron transfer agents in nature, 220–221
high-resolution X-ray crystal structures, 221
rack mechanism, 221
See also Loop-directed mutants of azurin;
Metal–ligand interactions in cupredoxin;
Oxygen intermediates in copper proteins
- Correlated spectroscopy (COSY). *See* Nuclear magnetic resonance (NMR) spectroscopy
- Coulomb integral, Hückel model, 263–264
- Counters, X-ray diffraction detectors, 73
- Covalency, charge-transfer spectrum of metal–substrate complex, 98
- Cruickshank's diffraction precision indicator, metalloprotein crystallography, 91–93
- Cryocrystallography, X-ray at low temperatures, 74–76
- Crystallography. *See* Metalloprotein crystallography
- Cucumber basic protein and stellacyanin, phase evaluation by crystallography, 81
- Cupredoxin. *See* Metal–ligand interactions in cupredoxin
- Curie law, paramagnetic shifts of nuclei, 40–42
- Cyanobacterium *Synechocystis* sp. PCC 6803 photosystem II isolation and EPR spectra, 273, 275f
See also Photosystem II oxygen evolving complex (OEC)
- Cytochrome *c*. *See* Electron-transfer triggering method for protein folding; Photoreduction-triggered folding of cytochrome *c*
- ## D
- Davies pulsed protocol in electron-nuclear double resonance spectroscopy (ENDOR), 3, 5–6
- Deadtime, ENDOR, 5
- Debye–Waller factors
amino acid side chain movement quantification, 341
equivalent iron ions in $[\text{LFeCrFeL}]^{3+}$ complexes, 320
mutants of azurin, 254–255
temperature dependence of Cu–Cu terms of Cu_A enzyme sites, 250–251, 252f, 253f
- Density functional theory calculations
experimental description of hydroperoxide–Cu(II) bond, 445, 447f
recent improvements, 181–182
See also Electronic structure calculations
- Difference absorption spectroscopy of unfolded and folded reduced proteins, 203
- Difference Raman spectroscopy for lactate dehydrogenase and coenzyme NADH, 142, 143f
- Diffraction pattern, resolution quality, 76
- Diffraction precision indicator, crystallography, 91–93
- Dioxygenase catalysis. *See* Protocatechuate 3,4-dioxygenase (3,4-PCD)
- Dipolar or pseudocontact shift of NMR spectroscopy, 34–36
- Double exchange versus super-exchange

- mechanism in heterotrinnuclear complexes, 326–330
- E**
- Electron-nuclear double resonance (ENDOR) spectroscopy
 analysis of intermediate Q of methane monooxygenase hydroxylase (MMOH), 413, 415*t*
 continuous wave ENDOR and analysis methods, 3, 5–6
 Davies pulsed ENDOR protocol, 3, 5–6
 deadline, 5
 Mims and Refocused Mims (ReMims)
 stimulated-echo ENDOR pulse sequence, 5–6
 pulsed ENDOR technique, 5–6
 Electron paramagnetic resonance (EPR) spectroscopy
 correlations with Mössbauer spectroscopy, 16–17
 model compounds of oxomolybdenum centers in sulfite oxidase, 361–366
 reduction potentials of diiron center in MMOH, 341, 343–344
 structure and function analysis of oxygen evolving complex, 272–273
See also Linear thiophenolate-bridged heterotrinnuclear complexes; Photosystem II oxygen evolving complex (OEC)
- Electron relaxation, electronic structure calculations, 180
- Electron spin echo electron-nuclear double resonance (ESE-ENDOR), experiments in photosystem II oxygen evolving complex, 274, 276, 277*f*, 281
- Electron spin echo envelope modulation (ESEEM) photosystem II oxygen evolving complex, 274–276, 281, 283*f*
 sulfite oxidase studies, 366, 367*f*
- Electron spin relaxation time, NMR spectroscopy, 36, 37*t*
- Electron-transfer triggering method for protein folding
 absorption spectral changes accompanying unfolding, 202–203
 biphasic kinetics for excitation of $\text{Co}(\text{ox})_3^{3-}$ in *y*-cyt *c* presence, 204, 206*f*
 competition between folding and reoxidation, 205
 difference absorption spectra of unfolded and folded reduced proteins, 203
 distributed kinetics model, 205
 ferrocyclochromes *c* from horse (*h*-cyt *c*) and yeast (*y*-cyt *c*), 199
 folding kinetics, 204–209
 folding rates from kinetics data, 205, 206*f*, 207
- guanidine hydrochloride (GuHCl) concentrations, 203–204
- Hammond postulate application to protein folding, 207
- horse heart cytochrome *c*, 199
 kinetics of folding process, 203–204
 materials and method, 199
 parameter to assess environment of particular residues in folding transition state, 209
 rate behavior comparison between *y*-cyt *c* and *h*-cyt *c*, 207, 208*f*
 redox-active metal center "tuned" by polypeptide chain folding, 199–200
 redox potential in thermodynamic cycle relation to conformational stability, 200, 201*f*
 reoxidation of heme group competitive with folding rate, 203–204
 stability differences between *y*-cyt *c* and *h*-cyt *c*, 202
 thermodynamics and kinetics of *h*-cyt *c* and *y*-cyt *c* folding and unfolding, 202*t*
 unfolding curves from fluorescence data, 200–203
 very low and very high denaturant concentrations, 203–204
 yeast iso-1-cytochrome *c* (*y*-cyt *c*), 199
- Electronic absorption spectroscopy
 admixed ground state singlet and triplet wavefunctions, 115–117
 electronic-structural information defining reactivity of active site, 98–99
 Heitler–London (HL) or valence-bond (VB) ground state description, 100
 ligand-field transitions, 98
 model in terms of valence-bond configuration interaction (VB CI) formalism, 98–99
 overlap integrals, 99
 super-exchange pathway monitoring, 117
 total covalency, 116–117
See also Copper(II) azide systems
- Electronic structure calculations
 broken symmetry method for dimer states, 183
 calculated and experimental one-electron redox potential for first row transition metals in aqueous solution, 188, 189*f*
 calculated and experimental redox potentials, 187*t*
 calculated energies versus metal–metal distance for dimer complexes, 192–193
 calculated versus experimental metal–ligand bond lengths, 185
 calculating redox potentials of $\text{M}^{3+}/\text{M}^{2+}$ in aqueous solution, 186–188
 comparison of density functional methods for mononuclear transition metal complexes, 186
 continuum dielectric model for solvation, 182–183

density functional methods, 181–182
 electron density difference versus LUMO orbital density, 188, 190
 electrostatics/solvation methods, 182–183
 energetics cluster model, 186–188
 first and second hydration shells, 186–188
 fitting electrostatic potential charges, 182
 geometry optimization for dimer transition metal complexes, 190–193
 geometry optimization for mononuclear transition metal complexes, 184–186
 geometry optimization methods, 182
 manganese superoxide dismutase example, 188, 190
 optimized and experimental core geometries comparison of ligand bridged transition metal dimer complexes, 191t
 structures of monomer and dimer complexes, 183–184
 thermodynamic cycle basis for redox potential calculations, 187
 ENDOR spectroscopy. *See* Electron-nuclear double resonance (ENDOR) spectroscopy
 Energy levels and transitions, NMR spectroscopy, 31–33
 Enterobacter coli amine oxidases
 active site dependent on crystallization conditions, 71, 72f
 EPR. *See* Electron paramagnetic resonance (EPR) spectroscopy
 Escherichia coli, ribonucleotide reductase, 404–405
 ESEEM. *See* Electron spin echo (ESE) envelope modulation (ESEEM)
 ESE-ENDOR (electron spin echo electron-nuclear double resonance), photosystem II oxygen evolving system, 274, 276, 277f, 281
 EXAFS. *See* Extended X-ray absorption fine structure (EXAFS)
 Extended-Hückel calculations, double exchange versus super-exchange mechanism, 327–330
 Extended X-ray absorption fine structure (EXAFS)
 analysis of soluble Cu_A domains in heme-copper oxidases, 245
 oscillations from absorbing neighbor atoms, 350
 rapid-freeze-quench technique for compound Q intermediate of MMOH, 412
See also Heme-copper oxidases

F
 Fe₂O₂ diamond core structure candidate
 characteristic core vibration in Raman spectra, 379–380
 distinguishing geometric features, 377–380

features prominent in EXAFS spectra, 380–381
 high-valent intermediates of methane monooxygenase hydroxylase (MMOH) and ribonucleotide reductase (RNR) subunit R2, 374, 381–383
 mechanism comparison for oxygen activation by iron centers in heme and nonheme diiron enzymes, 375, 376f
 Mössbauer properties distinctive, 378–379
 nonheme diiron enzymes, 374–375
 nonheme diiron(II) active site of MMOH, 374, 375f
 tandem rapid-freeze-quench Mössbauer /EXAFS experiments, 382–383
 Fenske–Hall calculations, spectral differences rationalized by molecular orbital energy level diagram, 363, 365f
 Ferredoxins. *See* Iron-sulfur (FeS) proteins by NMR
 Ferrocytochrome *c* folding. *See* Electron-transfer triggering method for protein folding; Photoreduction-triggered folding of cytochrome *c*
 Ferryl compounds, high-valent metal-oxo complexes by Raman spectroscopy, 147, 149
 Franck Condon barrier, potential energy diagram for peroxide reduction, 448, 450f

G

Guanidine hydrochloride (GuHCl). *See* Electron-transfer triggering method for protein folding; Photoreduction-triggered folding of cytochrome *c*

H

Hamiltonian
 energy diagrams for the case of [Fe₃S₄]⁺-containing ferredoxin, 307, 310f
 energy level scheme based on Heisenberg (J) and double exchange (B) terms, 287, 290f
 Heisenberg of Hubbard model, 267
 Heisenberg for [Fe₄S₄]³⁺ case, 305
 Hubbard model, 265
 Hückel model, 264
 soft X-ray absorption spectroscopy, 161–165
 temperature-dependence of [LFeCrFeL]^{III} series of linear thiophenolate-bridged complexes, 318–320
 theoretical aspects of Mössbauer spectroscopy, 17–19
 Hammond postulate, protein folding study, 207, 209

- Heme-copper oxidases
 calibration of the Cu-Cu distance, 244-245, 246f
 catalytic activity, 241
 core dimensions of oxidized and reduced Cu_A, 245, 248f, 249f
 cytochrome *bo3* oxidase, 241
 cytochrome *c*, 241
 EXAFS analysis of soluble Cu_A domains, 245, 246f, 247i, 248f
 implications for electron transfer, 250
 mechanism of cytochrome oxidase and electron transfer reactivity, 242
 spectroscopic techniques of past study, 244
 structure of Cu_A center and model compounds for study, 241-242, 243f
 structural similarity of reduced and oxidized forms, 245, 249f
 temperature dependence of Cu-Cu Debye-Waller factor and Cu-Cu bonding, 250-251, 252f, 253f
 X-ray absorption spectroscopy (XAS) for metal center structure determination, 242, 244
- Heme-free enzymes. *See* Nonheme iron intradiol dioxygenase intermediates
- Hemocyanin. *See* Oxygen intermediates in copper proteins
- HETCOR (¹³C-detected) and HMQC (¹H-detected) NMR correlation spectra, 53-54
- Homonuclear Hartmann-Hahn (HOHAHA) experiment
 COSY and TOCSY NMR experiments, 51
 NOESY and ROESY experimental methods, 47-48
- Horse heart cytochrome *c*. *See* Electron-transfer triggering method for protein folding
- Hubbard model. *See* Hamiltonian
- Hückel model. *See* Hamiltonian
- Hybrid density functional Hartree-Fock potential, density functional method, 182
- Hydroxylase enzyme of soluble methane monoxygenase. *See* Methane monoxygenase hydroxylase (MMOH)
- Hyperfine selectivity, electron-nuclear double resonance spectroscopy (ENDOR), 5
- I**
- Image plates, two-dimensional X-ray diffraction detectors, 73
- In-house X-ray generators, diffraction sources, 7
- Iron clusters. *See* Carboxylate-bridged binuclear iron clusters
- Iron(II) bleomycin, 2D NMR experiments, 55, 5
- Iron nonheme enzyme intermediate. *See* Nonheme iron intradiol dioxygenase intermediates
- Iron-porphyrin ferryl species, resonance Raman spectroscopy, 149, 150f
- Iron-sulfur (FeS) proteins by NMR
 antiferromagnetic coupling by super-exchange mechanism for [Fe₂S₂]⁺ case, 303, 304f
 case of [Fe₂S₂]⁺ by ¹H NMR, 303, 305
 case of [Fe₃S₄]⁺, 307
 case of [Fe₄S₄]³⁺, 305, 307
 eigenvalues calculated for two lowest energy states of Hamiltonian in [Fe₃S₄]⁺ clusters, 307, 310f, 311f
 electron relaxation rate dependence for NMR line observability, 302-303
 Heisenberg Hamiltonian for [Fe₄S₄]³⁺ case, 305
 NMR data for available ferredoxins, 309t
 primary sequences characterizing ferredoxins, 307, 309f
 solution structure of [Fe₄S₄]³⁺-type protein, 305, 308f
 spectrum of [Fe₂S₂]⁺-containing reduced ferredoxin from spinach, 306f
 spectrum of [Fe₃S₄]⁺-containing oxidized ferredoxins, 308f
 spectrum of [Fe₄S₄]³⁺-containing oxidized HiPIP II from *E. halophila*, 306f
 systems with iron ions magnetically coupled in polymetallic centers, 302, 304f
See also Valence-delocalized [Fe₂S₂]⁺ clusters
- Iron-sulfur metalloproteins
 antiferromagnetic exchange coupling in dinuclear cores, 314-315
 structures of active sites of known FeS metalloproteins, 314, 316f
See also Iron-sulfur (Fe-S) proteins by NMR; Linear thiophenolate-bridged heterotrinnuclear complexes; Valence-delocalized [Fe₂S₂]⁺ clusters
- Isotope ratio mass spectrometry (IRMS), decay of type 1 mercury laccase intermediate, 438, 439f
- K**
- Kramers systems, magnetic circular dichroism for half-integer spin ground states, 124-125, 126f
- L**
- Lanthanide ions bound by porphyrins, NMR experiments, 54
- Lee, Yang, Parr (LYP) potentials, density functional method, 181-182
- Ligand-field transitions, electronic absorption spectroscopy, 98

- Linear thiophenolate-bridged heterotrinnuclear complexes
 average bond distances and angles of selected [LFeMFeL]^{nt} complexes, 318t
 complexes synthesized and labeling scheme, 315, 317f
 delocalization effectively blocked for Co(III) substitution for Cr(III), 323
 discussion of low spin d⁵d⁶d⁵ case, 326–330
 double exchange versus super-exchange mechanism, 326–330
 extended-Hückel calculations, 327–329
 isomer shift, quadrupole splitting parameters, and relative peak areas of [LFeMFeL]^{nt} Mössbauer spectra, 319t
 ligand 1,4,7-tris(4-*tert*-butyl-2-mercaptobenzyl)-1,4,7-triazacyclononane (L³), 315, 316f
 orbital interaction scheme for [LFeCrFeL]³⁺, 319–320, 321f, 322f
 perspective views of representative complex, 315, 317f, 318
 series of [LFeCoFeL]^{nt} complexes, 320, 323–324
 series of [LFeCrFeL]^{2+/3+} complexes, 318–320
 series of [LFeFeFeL]^{2+/3+} complexes, 325–326
- Loop-directed mutants of azurin
 DeBye–Waller term for purple oxidized azurin comparable to *T. thermophilus*, 254
 reduced azurin mutant differences, 254–255
 XAS studies of purple oxidized and colorless reduced forms, 251, 254–255, 256f
- Luzzati plots, precision in metalloprotein crystallography, 90–91
- ## M
- Macromolecular crystallography. *See* Metalloprotein crystallography
- Magnetic circular dichroism (MCD) spectroscopy
 application to lipoygenases, 129, 131–133
 electronic structure of metal centers in oxo–Mo(V) complexes, 363, 364f
 excited state information, 121–124
 ground state information, 124–129
 Kramers systems with half-integer spin doublet ground state, 124–125, 126f
 low-temperature MCD sensitive for paramagnetic center investigations, 134
 mammalian lipoygenases and comparison to soybean lipoygenase-1, 131, 132f, 133
 mechanistic implications of lipoygenase study, 133
 metalloenzyme analysis, 343
 metal site geometry from energies and splittings of d→d bands with low temperature MCD, 122–124
 non-Kramers integer spin systems, 125, 126f, 127–128
 oxygen intermediate of native laccase, 445, 447f, 448
 recent advances related to ground state information, 124
 relation of ground state and ligand field parameters, 128–129
 soybean lipoygenase-1 example, 129, 131, 132f
 theory, 119–121
 variable-temperature variable-field (VTVH) MCD data for ground-state electronic structure information, 124–129
 Zeeman splittings for ground and excited states, 119–121
See also X-ray magnetic circular dichroism (XMCD) spectroscopy
- Magnetometry
 magnetic susceptibility theory, 17–19
See also Mössbauer spectroscopy and magnetometry
- Manganese superoxide dismutase (MnSOD), electronic structure calculations, 183–184
- Manganese tetranuclear cluster. *See* Photosystem II oxygen evolving complex (OEC)
- Mass spectrometry. *See* Isotope ratio mass spectrometry (IRMS)
- MCD. *See* Magnetic circular dichroism (MCD) spectroscopy
- Metal clusters
 application to redox properties of manganese-oxo clusters, 267–270
 clusters as conjugated hydrocarbons in Hückel model, 263–264
 difference in successive redox potentials for dimer, 268, 269f
 electron-electron intersite repulsion separation, 268, 270
 energy of states in Hubbard theory, 266f
 energy of states in Hückel theory, 266f
 Heisenberg Hamiltonian, 267
 Hubbard Hamiltonian, 265
 Hubbard models as electrons avoiding each other, 264–267
 Hückel Hamiltonian, 264
 Hückel model description in Hubbard model formalism, 264
 intersite repulsion, 265
 pictorial representation of factors influencing energy of dimer redox states, 269f
 redox reactions in proteins, 262–263
See also Carboxylate-bridged binuclear iron clusters; Photosystem II oxygen evolving complex (OEC)

- Metal–ligand interactions in cupredoxin
 copper–S bond lengths and Cu atom displacement calculations, 235
 effects of exogenous ligand coordination on blue Cu active site, 233–235, 236f
 effects of residue replacement on ground and excited states of blue Cu active site in azurin, 227–233
 electronic absorption spectra of wild type *P. aeruginosa* azurin and mutants, 227–228, 229f
 fundamental vibrations of RR spectra, 228, 232
 identification of Cu(II)–S(Cys) stretching vibration, 223, 224f, 225–227
 isotopic ^{34}S substitution and RR spectroscopy summary, 237
 low temperature RR spectra of azurin and azide adduct, 233, 234f
 low temperature RR spectra of *P. aeruginosa* azurin and ^{34}S -Cys labeled proteins, 223, 224f
 low temperature RR spectra of *P. aeruginosa* azurin and ^{65}Cu labeled proteins, 223, 225f
 mass effect of ^{34}S labeled *P. aeruginosa* azurin and azide adduct, 233, 235, 236f
 model of copper–ligand interactions in azurins, 235–237
 overtone and combination bands of RR spectra, 232–233
 redox reactivity variability of single Cu active sites, 237
 RR spectra of wild type *P. aeruginosa* azurin and mutants, 228–233
 sample preparations, 222–223
 schematic of Cu atom movement along trigonal axis, 235, 236
 spectroscopic methods, 223
 UV–visible absorption spectra of *P. aeruginosa* azurin, 233, 234f
- Metalloprotein crystallography
 accuracy assessment of metalloprotein structure, 87–88, 89f
 active site in amine oxidases dependence on crystallization conditions, 71, 72f
 avoiding errors in connectivity and protein conformation, 83
 computer methods for model building, 83
 copper metalloprotein examples, 62–63, 65f
 Cruickshank's diffraction precision indicator, 91–93
 cryocrystallography, 74–76
 crystallization conditions, 63
 crystallization experiments, 63, 67
 deviations from ideal dimensions, 88
 diffraction pattern resolution, 76
 diffraction precision indicator, 91–93
 dimensional dependence of Cu(I) site in reduced plastocyanin on crystallization medium pH, 69–71
 error alerts, 88, 89f
 factors affecting metal-site geometry, 90
 free residual and residual as accuracy indicator, 87
 least-squares model refinement, 84
 Luzzati plots for precision, 90–91
 maximum likelihood refinement method, 85, 87
 model building and electron-density map interpretation, 82–83
 model refinement, 83–87
 phase evaluation, 77–82
 plastocyanin Cu–ligand bond lengths, 80, 90, 91f
 precision assessment of metalloprotein structure, 88–93
 precision of metal-site geometries, 88, 90–91
 protein structures at atomic resolution, 76–77
 purity pre-condition, 63
 quality of diffraction pattern, 76
 restrained least-squares model refinement, 84–85
 ribbon diagrams by computer graphics, 63, 64f
 screening variables and procedures, 67
 simulated annealing to escape false energy minimum, 85, 86f
 steps to metalloprotein knowledge, 63, 66f
 structural dependence on crystallization conditions, 67, 69–71, 72f
 suitability of crystals for X-ray measurements, 67, 68f
 X-ray detectors, 71, 73
 X-ray diffraction measurements, 71, 73–76
 X-ray measurement at low temperature, 74–76
 X-ray sources, 74
 See also Phase evaluation in crystallography
- Metalloproteins
 heme enzymes cytochrome P450 and peroxidases, 374–375
 nonheme diiron unit, 374–375
 See also Fe_2O_2 diamond core structure candidate; Iron–sulfur (FeS) proteins by NMR
- Methane monooxygenase hydroxylase (MMOH)
 active site showing important amino acid side chains, 342f
 altered product distributions for isopentane oxidation, 343
 amino acid side chains and conformations, 338–341
 cavity structure of the α subunit in soluble MMOH, 335–338
 circular dichroism experiments, 343
 diamond core structure of hydroxylase (MMOH), 407
 Fe_2O_2 diamond core structure candidate, 374, 381–383

- flexibility of side chains, 338–341, 342*f*
 hydrophobic cavities illustration, 337*f*
 intermediate H_{peroxo} of MMOH, 409, 410*f*, 411
 intermediate Q following H_{peroxo} decay, 411–412
 magnetic circular dichroism complementary data, 343
 methanol production from methane, 334–335
 Mössbauer spectroscopy for oxidation state, spin state, and local symmetry at iron center, 343
 nonheme diiron(II) active site, 375*f*
 overlaid oxidized and reduced MMOH structures, 340*f*
 protein family with carboxylate-bridged dinuclear iron centers, 335
 reductase shuttling electrons to diiron sites, 344
 role of protein B and reductase, 341, 343–344
 schematic of oxidized and reduced binuclear iron center of MMOH, 410*f*
 spectroscopic methods for mechanistic studies, 344–345
 three views of hydroxylase active site as determined by X-ray crystallography, 339*f*
 xenon as crystallographic probe for methane binding, 336, 337*f*
 X-ray absorption spectroscopy, 343
See also Carboxylate-bridged binuclear iron clusters; Fe_2O_2 diamond core structure candidate
- Methane monooxygenase (MMO)
 enzyme system and kinetics with oxygen, 405, 407–409
Methylococcus capsulatus (Bath), 403, 407
Methylosinus trichosporium OB3b, 407
 rapid-freeze-quench technique and Mössbauer spectroscopy, 408–409
See also Carboxylate-bridged binuclear iron clusters; Methane monooxygenase hydroxylase (MMOH)
- Methanol production. *See* Methane monooxygenase hydroxylase (MMOH)
- Methylococcus capsulatus* (Bath)
 methane monooxygenase and kinetics with oxygen, 405, 407–409
See also Carboxylate-bridged binuclear iron clusters; Methane monooxygenase hydroxylase (MMOH)
- Mims stimulated-echo ENDOR pulse sequence, 5–6
- Molecular replacement method
 comparison with other methods, 81–82
 effective for cucumber stellacyanin example, 8
 failure in cucumber basic protein example, 81
 pea seedling amine oxidase example, 81–82, 81
 phase evaluation in crystallography, 79*t*
- Molybdenum-containing enzymes. *See* Oxomolybdenum centers in sulfite oxidase
- Monoraphidium braunii* cytochrome c_6 , first unknown protein solved by *ab initio* phase evaluation method, 80–81
- Mössbauer spectroscopy
 freeze-quenched methods for transient intermediate detection in oxygen activation reactions, 409–416
 oxidation state, spin state, and local symmetry of iron centers in metalloenzymes, 343
See also Carboxylate-bridged binuclear iron clusters; Linear thiophenolate-bridged heterotrimeric complexes
- Mössbauer spectroscopy and magnetometry exchange coupled Cu(II)–Fe(III) heme model complexes, 27, 29
 exchange coupled diiron(III) dimer, 24, 26*f*, 27, 28*f*
 experimental considerations, 20, 23–24, 25*f*
 paramagnetic or magnetically ordered impurities, 20, 23
 sample alignment by magnetic field, 23–24, 25*f*
 sample texture complications, 23–24, 25*f*
 simple example of high-spin ferric porphyrin system, 19–20, 21*f*, 22*f*
 theoretical basis of connections, 17–19
- Multicopper oxidases. *See* Copper proteins; Heme-copper oxidases; Oxygen intermediates in copper proteins
- Multiple isomorphous replacement method, phase evaluation in crystallography, 79*t*
- Multiple wavelength anomalous dispersion method, phase evaluation in crystallography, 79*t*
- Myoglobin
 cavities role in allowing access to enzyme active site, 336
 xenon binding as crystallographic probe, 336–338
- N
- Newton–Raphson method, geometry optimization, 182
- Ni–Fe hydrogenase
 application of soft X-ray absorption spectroscopy, 165–166, 167*f*
 cavities role in allowing access to enzyme active site, 336
 xenon binding as crystallographic probe, 336–338
- NMR. *See* Nuclear magnetic resonance (NMR) spectroscopy
- NOE. *See* Nuclear Overhauser Effect (NOE) spectroscopy
- Nonheme diiron enzymes. *See* Fe_2O_2 diamond

- core structure candidate; Nonheme iron intradiol dioxygenase intermediates
- Nonheme iron intradiol dioxygenase intermediates
- asymmetry in binding of substrates, 393–394
- intradiol cleavage mechanism based on kinetic and spectroscopic studies, 388–390
- mechanism modified based on structural and spectroscopic data, 394, 395*f*
- mechanism test based on CN⁻ and NO binding to reduced 3,4-PCD, 394, 396–398
- mechanism test based on site-directed mutagenesis of 3,4-PCD, 398–399, 400*f*
- protocatechuate 3,4-dioxygenase (3,4-PCD), 387–388
- See also* Protocatechuate 3,4-dioxygenase (3,4-PCD)
- Non-Kramers integer spin systems
- distinguishing sign of the zero-field splitting (ZFS), 128
- magnetic circular dichroism ground state, 125, 126*f*, 127–128
- Nuclear magnetic resonance (NMR) spectroscopy
- ¹³C–¹H correlation spectra, 53–54, 55*f*
- CAMELSPIN experiment, 47–48
- chemically-induced dynamic nuclear polarization (CIDNP), 56
- contact shift, δ_{con} , 33–34
- COSY and TOCSY experiments, 51–53
- definition of chemical shifts, 33
- dipolar or pseudocontact shift, δ_{dip} , 34–36
- electron spin relaxation time, 36, 37*t*
- electronic relaxation times of various metal ions, 37*t*
- energy levels and NMR transitions, 31–33
- experiments for paramagnetic metal complexes, 30–31
- Fe(II) bleomycin by 2D NMR experiments, 55, 56*f*
- lanthanide ions bound by porphyrins, 54
- MCOSY magnitude experiment for low-spin iron chlorins, 51–53
- multi-experiment approaches to structure determination and complex dynamics, 54–56
- NOE (1D) difference spectroscopy, 43–46
- NOESY and ROESY NMR experiments
- experimental methods, 47–51
- FELIX software, 47–48
- Homonuclear Hartmann–Hahn experiment, 47–48
- nuclear line broadening due to dipolar relaxation, 37*t*
- nuclear spin-lattice relaxation time, 36–38
- nuclear spin-spin relaxation time, 38–40
- relaxation times, 36–40
- simple 1D method for paramagnetic complexes, 42–43
- temperature dependence of paramagnetic shifts, 40–42
- See also* Iron–sulfur (FeS) proteins by NMR
- Nuclear Overhauser effect (NOE), 1D difference NMR spectroscopic method, 43–46
- Nuclear Overhauser enhancement and exchange spectroscopy (NOESY). *See* Nuclear magnetic resonance (NMR) spectroscopy
- Nuclear spin-lattice relaxation time in NMR spectroscopy, 36–38
- Nuclear spin-spin relaxation time in NMR spectroscopy, 38–40
- O**
- Orbital degeneracy, magnetic circular dichroism (MCD) requirements, 120–121
- Oxomolybdenum centers in sulfite oxidase
- chemical mechanisms proposed for sulfite oxidase, 369
- coordination environment of Mo atom in chicken liver sulfite oxidase, 368*f*
- EPR data for sulfite oxidase and selected Mo(V) compounds, 363*t*
- ESEEM studies of sulfite oxidase, 366, 367*f*
- model oxo–Mo(V) compounds, 361–366
- structural proposal for catalysis and inhibition by phosphate, 366, 368
- structure of sulfite oxidase, 366, 369
- Oxygen activation reactions. *See* Carboxylate-bridged binuclear iron clusters
- Oxygen activation reactions by enzymes. *See* Carboxylate-bridged binuclear iron clusters
- Oxygen evolving complex (OEC). *See* Photosystem II oxygen evolving complex (OEC)
- Oxygen intermediates in copper proteins
- absorption and resonance Raman of hydroperoxide-bridged binuclear model complex, 445, 446*f*
- azide ligand addition and associative displacement reaction of oxyhemocyanin and oxytyrosinase, 429, 430*f*
- charge transfer absorption spectrum of type 1 mercury (T1Hg) intermediate comparison with oxyhemocyanin, 441, 442*f*
- circular dichroism spectrum of oxidized T1Hg laccase and intermediate, 438, 439*f*
- copper proteins involved in oxygen binding and activation, 424*t*

- crystal structure of oxyhemocyanin active site, 427f
- description of multicopper oxidases, 433t
- electronic structure of trinuclear copper cluster supported by X-ray crystallography, 432, 434f, 435
- energy level diagram of mononuclear peroxide–Cu(II) complex, 426f
- experimental description of hydroperoxide–Cu(II) bond by density functional theory calculations, 445, 447f
- Fourier transforms of EXAFS spectra of T1Hg intermediate reduced and oxidized, 438, 440f, 441
- hemocyanin electronic structure contributions to reversible oxygen binding, 425–428
- isotope ratio mass spectrometry (IRMS) of T1Hg laccase intermediate decay, 438, 439f
- kinetic data for two oxygen intermediates of laccase, 437f
- magnetic susceptibility studies of T1Hg intermediate, 438, 440f
- metal centers of copper enzymes, 423, 425
- native intermediate in molecular mechanism of four electron reduction of oxygen, 445, 447f, 448–450
- oxygen intermediates and molecular mechanism of four electron reduction of oxygen to water, 435, 436t, 437–438
- peroxide–Cu(II) model complexes, 446t
- peroxide level intermediate of T1Hg laccase and comparison to oxyhemocyanin and oxytyrosinase, 438–445
- possible electronic structure descriptions of oxygen intermediate of native laccase, 445, 448, 449f
- potential energy diagram for peroxide reduction, 448, 450f
- proposed mechanism for four electron reduction of oxygen to water by multicopper oxidases, 448, 449f
- proposed mechanism of tyrosinase and three possible O–O bond breakage schemes, 431f
- resonance Raman of hemocyanin reaction with oxygen, 426f
- spectral feature comparison of oxytyrosinase and oxyhemocyanin, 428–429, 430f
- spectroscopy of inhibitor mimosine bound derivatives of tyrosinase, 429, 431f
- titration of oxidized T1Hg derivative of laccase with hydrogen peroxide, 441, 443f, 444f, 446f
- trinuclear copper cluster site, 429, 432–435
- tyrosinase comparison to hemocyanin and molecular mechanism of hydroxylation, 428–429, 430f, 431f
- X-ray absorption spectra comparison of laccase and hemocyanin, 432, 434f
- Oxyhemerythrin, resonance Raman spectroscopy, 145, 146f
- Oxyhemocyanin. *See* Oxygen intermediates in copper proteins
- Oxytyrosinase. *See* Oxygen intermediates in copper proteins
- ## P
- Paramagnetic metal complex
- low-temperature magnetic circular dichroism (MCD) spectroscopy, 119, 124, 134
- structure determination by ENDOR spectroscopy, 2–3
- See also* Electron–nuclear double resonance (ENDOR) spectroscopy
- Paramagnetic metal complex structure determination
- agreement between 2D set optimized Q-band ENDOR spectra and simulations, 11, 13f
- alternate models for protonated oxygenic species of intermediate X, 6–10
- optimized 2D ENDOR spectra for model with bridging hydroxyl, 6, 7f, 8
- optimized ENDOR spectra for model with two inequivalent protons of water terminally bound to iron(III), 7f, 8
- precise metrical parameters and hyperfine tensor components for models, 8, 9t
- proton/deuteron ENDOR of intermediate X, 10–11, 12f
- two models for paramagnetic diiron intermediate of S₂-state ribonucleotide reductase (RNR), 3, 4f
- Pea seedling amine oxidase
- diffraction precision indicators, 92t
- phase evaluation in metalloprotein crystallography, 81–82, 86f
- Perdew potential, density functional method, 181–182
- Phase evaluation in crystallography
- ab initio* method, 79t
- calculated structural factors for molecular model, 78
- cucumber basic protein and stellacyanin examples, 81
- intensity and phase of X-ray reflection, 77
- methods for evaluating phases, 78–80
- molecular replacement method, 79t
- molecular replacement versus other methods, 81–82
- multiple isomorphous replacement method, 79t

- multiple wavelength anomalous dispersion method, 79t
- pea seedling amine oxidase example, 81–82, 86f
- phase information for electron density map calculation, 77–78
- recent progress in *ab initio* method, 80–81
- single isomorphouse replacement with anomalous scattering method, 79t
- solving the structure, 80
- Phosphotungstate ion, $\text{PW}_{12}\text{O}_{40}^{-5}$, combined phase evaluation methods in pea seedling amine oxidase example, 81–82, 86f
- Photographic films, X-ray diffraction detectors, 71, 73
- Photo-induced electron transfer. *See* Photoreduction-triggered folding of cytochrome *c*
- Photoreduction-triggered folding of cytochrome *c* denaturation by Raman transitions, 218
- fluorescence monitoring denaturation of cyt *c*, 213–214, 215f
- horse heart cytochrome *c*, 213
- materials and methods, 213
- resonance Raman (RR) spectroscopy, 213
- UV RR spectra of Fe(II) and Fe(III) cyt *c*, 214, 216f, 217f
- visible RR spectra of Fe(II) cyt *c*, 214, 216f
- visible RR spectra of Fe(III) cyt *c*, 214, 215f
- Photosystem II oxygen evolving complex (OEC) acetate incubation for broadened split-signal version of tyrosine radical EPR signal, 279, 281, 282f
- alcohol binding at the S_2 -state, 276, 279
- applications of XAS to proteins, 350–351
- cycle of five "S-state" intermediates, 272
- ESEEM (3-pulse) Fourier transform traces for deuterated alcohols, 279, 280f
- evidence of tyrosine radical participation in proton transfer, 281, 283f, 284
- experimental ratioed 2-pulse time-domain ESEEM for S_2 -state multiline EPR signal and simulation, 275f
- future directions, 356
- hyperfine tensor components for tetranuclear Mn cluster geometry proposed in S_2 -state, 276, 278f
- information content of EXAFS (extended X-ray absorption fine structure), 350
- information content of XANES (X-ray absorption near edge structure), 349–350
- kinetic model based on four kinetically resolvable intermediates (S_n), 348–349, 353f
- magnetic properties, 351
- mechanistic possibilities, 356
- oxidation state assignments, 351–354
- parallel polarization EPR difference spectrum of PSII isolated from cyanobacterium *Synechocystis* 6803, 275f
- photooxidation of the OEC, 352, 354, 355f
- possible water oxidation scheme, 356, 357f
- preparation of reduced derivatives, 351–352
- proton ESE–ENDOR spectrum for S_2 -state multiline EPR signal, 277f
- proximity of tyrosine radical to Mn cluster, 279, 281, 282f
- role of Ca^{2+} in OEC cluster, 354, 355f, 356
- S_1 -state multiline EPR signal, 273–274, 275f
- similarity to synthetic $2\text{Mn(III)}2\text{Mn(IV)}$ cluster parallel polarization EPR spectrum, 273
- structural characterization of OEC, 351–356
- structure of reduced species, 352, 353f
- tetranuclear Mn cluster, tyrosine radical, and cofactors, 272–273
- tetranuclear Mn cluster for oxidation of water to oxygen, 348–349
- understanding role of manganese, 268, 270
- water binding at the S_2 -state, 274, 275f, 276
- X-ray absorption spectroscopy, 349–351
- Plastocyanin Cu(I) and Cu(II) sites diffraction precision indicator, 92t
- dimensional dependence on crystallization medium pH, 69–71
- precision of metal-site geometry, 88, 90, 91t
- Polymorphism metalloprotein structural dependence on crystallization conditions, 67, 69–71, 72f
- See also* Metalloprotein crystallography
- Protein folding. *See* Electron-transfer triggering method for protein folding; Photoreduction-triggered folding of cytochrome *c*
- Protocatechuate 3,4-dioxygenase (3,4-PCD) aromatic ring cleavage catalyzed by Fe^{3+} and Fe^{2+} containing dioxygenases, 387–388, 389f
- asymmetry in binding of substrates, 393–394
- charge neutrality in Y447H mutated enzyme, 399
- comparison of interconversion rates of intermediates in catalytic cycles of wild type 3,4-PCD and Y447H mutated enzyme, 399, 400f
- crystal structure of Y447H mutated enzyme, 400f
- EPR spectra of 3,4-PCD-CN-NO complexes, 394, 396, 397f
- intradiol cleavage mechanism based on kinetic and spectroscopic studies, 388–390
- low energy resonance Raman features from metal–ligand vibrational modes, 395f
- mechanism test based on CN^- and NO binding to reduced 3,4-PCD, 394, 396–398
- mechanism test based on site-directed mutagenesis of 3,4-PCD, 398–399, 400f

model for binding CN^- and NO to reduced 3,4-PCD, 397f

modified mechanism based on structural and spectroscopic data, 394, 395f

N-oxide analogs of protocatechuate 2-OH-isonicotinic acid N-oxide (INO), 390

structures of 3,4-PCD and ligand complexes, 390–394

structures of 3,4-PCD-inhibitor complexes, 392

structures of 3,4-PCD-INO-CN complexes, 393

structures of 3,4-PCD-substrate and transition-state analog complexes, 392

See also Nonheme iron intradiol dioxygenase intermediates

Pseudocontact or dipolar shift, NMR spectroscopy, 34–36

Pseudomonas aeruginosa azurin

arrangement of ligands about Cu(II) ion, 221, 224f

See also Metal–ligand interactions in cupredoxin

Pseudomonas putida. *See* Protocatechuate 3,4-dioxygenase (3,4-PCD)

Q

Quality of diffraction pattern, resolution, 76

R

Raleigh scattering, most probable contribution to resonance Raman spectroscopy, 137

Raman scattering, 137

Raman shifts, discovery of Stokes and anti-Stokes shifts, 136

Reaction intermediates in oxygen activation reactions. *See* Carboxylate-bridged binuclear iron clusters

Redox potentials calculations, $\text{M}^{3+}/\text{M}^{2+}$ in aqueous solution, 186–188

Refocused–Mims (ReMims) pulse sequence, electron-nuclear double resonance spectroscopy (ENDOR), 5–6

Relaxation times, NMR spectroscopy, 36–40

Resonance Raman (RR) spectroscopy

binding mode of peroxo adducts, 147, 148f

calibration of the CCD detector, 140, 141f

charge-coupled device (CCD) detector, 138, 139f

collection of photomultiplier tubes in CCD, 138

cryogenic temperature RR for cupredoxins, 222–223

description, 137, 139f

difference spectroscopy of lactate hydrogenase and coenzyme NADH, 142, 143f

energy level diagram showing electronic and vibrational processes, 139f

freeze-trapped intermediates and cryosolvent complications, 147

high-valent metal-oxo complexes, 147, 149

holographic notch filter to reduce stray and Rayleigh scattering, 138, 140

identification of specific oxo intermediates, 145, 146f

iron–porphyrin ferryl species, 149, 150f

isotope dependence of non-heme ferryl species, 149, 150f

modern instrumentation, 138, 139f

oxyhemerythrin vibrations through isotope exchange, 145, 146f

Raleigh scattering, 137

resonance Raman effect, 137–138

sample integrity improvements, 140, 142, 143f

time-resolved spectroscopy of cytochrome *bo* oxidase, 142, 144f, 145

vibrational properties of valence-delocalized $[\text{Fe}_2\text{S}_2]^+$ clusters, 294–295, 296f

See also Metal–ligand interactions in cupredoxin; Photoreduction-triggered folding of cytochrome *c*

Ribonucleotide reductase (RNR)

enzyme system and reaction with oxygen, 404–405

Escherichia coli, 2–3, 403–404

Fe_2O_2 diamond core structure candidate for subunit R2, 374, 381–383

intermediate X of R2 subunit, 3, 4f, 412–416

nonheme diiron(II) active site structure, 375f

schematic of oxidized and reduced binuclear iron center, 406

See also Carboxylate-bridged binuclear iron clusters; Paramagnetic metal complex structure determination

Rotating frame nuclear Overhauser effect

spectroscopy (ROESY). *See* Nuclear magnetic resonance (NMR) spectroscopy

S

Saccharomyces cerevisiae iso-1-cytochrome *c*, protein folding studies, 199

Single isomorphous replacement with anomalous scattering method, phase evaluation in crystallography, 79f

Slater-type orbitals, density functional method, 182

Soft X-ray absorption spectroscopy absorption lengths, 157

- advantages for bioinorganic compounds, 160–161
- application to copper proteins, 167–168
- application to nickel proteins, 165–166, 167f
- chemical shifts, 162
- contributions to Hamiltonian, 161–165
- core hole spin-orbit splitting, 162
- coulomb and exchange interactions, 163–164
- covalency effects, 164–165
- detection methods, 157–159
- experimental considerations, 157–159
- integrated cross section sum rule, 167, 168f
- ligand-field splittings, 163, 164f
- pitfalls of fluorescence detection, 158–159
- radiation damage, 160
- schematic of different detection methods, 158f
- Structure determination. *See* Copper(II) azide systems; Electronic absorption spectroscopy
- Sulfite oxidase
- catalysis of sulfite to sulfate, 360–361
- enzyme for sulfur metabolism in animals, 360
- See also* Oxomolybdenum centers in sulfite oxidase
- Super-exchange mechanism
- antiferromagnetic coupling, 108
- case of $[\text{Fe}_2\text{S}_2]^+$ by ^1H NMR, 303, 305
- discussion versus double exchange mechanism in heterotrinuclear complexes, 326–330
- Superoxide dismutases (SOD)
- electron density versus LUMO (lowest unoccupied molecular orbital) orbital density, 188, 190
- LUMO charge density of MnSOD active site model, 190f
- manganese superoxide dismutase (MnSOD), 188, 190
- structure of MnSOD active site, 183, 184f
- total density difference of MnSOD active site model, 190f
- ZnSOD genetically altered variant of copper, 221–222
- Synchrotron radiation sources
- X-ray absorption spectroscopy, 156
- X-ray sources for diffraction, 74
- T**
- Thermus thermophilus*
- comparison with loop-directed mutant of azurir 254, 256f
- core dimensions of oxidized and reduced Cu_A forms, 245, 248f
- EXAFS analysis of soluble Cu_A domains, 245, 246f
- temperature dependence of Cu–Cu Debye–Waller terms, 251, 253f
- Time-resolved spectroscopy, flow-flash experiment for resonance Raman spectroscopic data, 142, 144f, 145
- Total correlation spectroscopy (TOCSY). *See* Nuclear magnetic resonance (NMR) spectroscopy
- Transition metal complexes
- application areas for density functional calculations, 180
- diversity in electronic structures, geometries, and energetics, 179–180
- geometric changes in metalloenzyme active sites, 180
- geometry optimization of dimer complexes, 190–193
- geometry optimization of mononuclear complex, 184–186
- weak field ligands, 179–180
- See also* Electronic structure calculations
- Tyrosinase. *See* Oxygen intermediates in copper proteins
- U**
- UV resonance Raman spectroscopy. *See* Photoreduction-triggered folding of cytochrome *c*
- V**
- Valence-bond configuration interaction (VBCI) model analyzing chain transfer spectral features of monomers and analogous bridged dimers, 98–99, 115–117
- parameters of mono- and binuclear Cu(II) azide complexes, 103f
- See also* Copper(II) azide systems
- Valence-delocalized $[\text{Fe}_2\text{S}_2]^+$ clusters
- building blocks of complex clusters, 286–287
- C56S and C60S mutated forms of *Clostridium pasteurianum* (Cp) 2Fe ferredoxin (Fd), 287–288
- comparison of low temperature MCD spectra of different paramagnetic Fe–S cluster types, 298f
- energy level diagram for exchange-coupled $[\text{Fe}_2\text{S}_2]^+$ cluster as function of spin dependent resonance delocalization, 287, 290f
- energy level scheme based on Hamiltonian with both Heisenberg (J) and double exchange (B) terms, 287, 290f

excited state properties of mutants in oxidized and reduced state, 289, 291–294

Fe–S stretching frequencies for wild type and C56S mutant, 295*t*

first direct measurement of double exchange parameter (B) and resonance energy, 294

ground state properties of C56S and C60S, 288–289

implications for higher nuclearity Fe–S clusters, 297–299

MCD magnetization data for dithionite-reduced C60S mutant, 292, 293*f*, 294

origin of valence delocalization, 297

redox properties of C56S and C60S mutations, 288

schematic molecular orbital diagram for Fe–Fe interaction, 294, 296*f*

temperature dependence of low-field EPR spectrum of dithionite-reduced C56S, 289, 290*f*

UV/visible/near-IR variable temperature MCD spectra of dithionite-reduced C60S mutant, 289, 291*f*, 292

vibrational properties of C56S and C60S mutants, 294–296

See also Carboxylate-bridged binuclear iron clusters; Iron-sulfur (FeS) proteins by NMR; Iron-sulfur metalloproteins

Variable-temperature magnetic circular dichroism (VTMCD) spectroscopy

characterization of high nuclearity Fe–S clusters, 297–299

excited state properties of valence-delocalized $[\text{Fe}_2\text{S}_2]^+$ clusters, 289, 291–294

Variable-temperature variable-field (VTVH) magnetic circular dichroism (MCD) spectroscopy, obtaining ground-state information for paramagnetic species, 124–129

VBCI. *See* Valence-bond configuration interaction (VBCI)

Vosko–Wilk–Nusair (VWN or V) type potential, density functional method, 181–182

VS (Vosko–Wilk–Nusair and Stoll combination) potential

density functional method, 181

geometries of dimer transition metal complexes, 190–191

VTMCD. *See* Variable-temperature magnetic circular dichroism (VTMCD) spectroscopy

W

Water-suppressed equilibrium Fourier transform (WEFT) sequences, NMR experiments, 48–49

Wavefunctions

Hückel model, 263–264

redefinition in Hubbard model, 267

X

X-ray absorption near edge structure (XANES) region, energy and molecular shape changes in photosystem II oxygen evolving complex, 349–350

X-ray absorption spectroscopy (XAS)

extended X-ray absorption fine structure (EXAFS), 154–155

oxidation state and coordination of metal center in metalloenzymes, 343

structural determinations of oxidized and reduced Cu_A constructs, 255

synchrotron radiation, 156

X-ray multiplets, 155

X-ray transitions, 154

See also Heme-copper oxidases; Loop-directed mutants of azurin; Photosystem II oxygen evolving complex (OEC); Soft X-ray absorption spectroscopy

X-ray diffraction measurements

charge-coupled detector devices, 73

cryocrystallography, 74–76

image plates, 73

in-house X-ray generators, 74

synchrotron radiation sources, 74

two-dimensional detectors, 73

X-ray counter detectors, 73

X-ray detectors reading films, 71, 73

X-ray measurement at low temperatures, 74–76

X-ray magnetic circular dichroism (XMCD)

applications, 168–169

application to copper plastocyanin, 173

circular polarization sources, 170–171

effect at 3d transition metal $L_{2,3}$ edges, 169–170

experimental considerations for soft X-ray MCD, 170–171, 172*f*

field and temperature dependence, 171, 172*f*

future prospects, 173–174

information and strengths for bioinorganic compounds, 171–172

orbital (L) and spin (S) angular momentum sum rules, 172, 173*f*

schematic illustration of XMCD for atomic Cu^{+2} , 170*f*

See also Magnetic circular dichroism (MCD) spectroscopy

Y

Yeast iso-1-cytochrome *c* (*y*-cyt *c*). *See* Electron-transfer triggering method for protein folding

Z

Zeeman splitting, magnetic circular dichroism (MCD) spectroscopy, 119–121

Zero-field splitting (ZFS)

distinguishing ZFS sign, 128

non-Kramers integer spin systems, 125, 126*f*, 127–128

orientation averaged MCD intensity, 127